# Fractal Analysis

Edited by: Olga Moreira

ARCLER PRESS

# Fractal Analysis

# Fractal Analysis

*Edited by:*

**Olga Moreira**

ARCLER PRESS

www.arclerpress.com

**Fractal Analysis**

*Olga Moreira*

**Arcler Press**
224 Shoreacres Road
Burlington, ON L7L 2H2
Canada
www.arclerpress.com
Email: orders@arclereducation.com

**e-book Edition 2021**

ISBN: 978-1-77407-900-3 (e-book)



ISBN: 978-1-77407-699-6 (Hardcover)

Arcler Press publishes wide variety of books and eBooks. For more information about Arcler Press and its products, visit our website at www.arclerpress.com

# DECLARATION

# ABOUT THE EDITOR

**Olga Moreira** obtained her Ph.D. in Astrophysics from the University of Liege (Belgium) in 2010, her BSc. in Physics and Applied Mathematics from the University of Porto (Portugal). Her post-graduate travels and international collaborations with the European Space Agency (ESA) and European Southern Observatory (ESO) led to great personal and professional growth as a scientist. Currently, she is working as an independent researcher, technical writer, and editor in the fields of Mathematics, Physics, Astronomy and Astrophysics.

# TABLE OF CONTENTS

# LIST OF CONTRIBUTORS

**Olga Moreira**

**Yi Jin**
School of Resources and Environment, Henan Polytechnic University, Jiaozuo, 454003, China
Collaborative Innovation Center of Coalbed Methane and Shale Gas for Central Plains Economic Region, Henan Province, Jiaozuo, 454003, China

**YingWu**
School of Resources and Environment, Henan Polytechnic University, Jiaozuo, 454003, China

**Hui Li**
School of Resources and Environment, Henan Polytechnic University, Jiaozuo, 454003, China

**Mengyu Zhao**
School of Resources and Environment, Henan Polytechnic University, Jiaozuo, 454003, China

**Jienan Pan**
School of Resources and Environment, Henan Polytechnic University, Jiaozuo, 454003, China
Collaborative Innovation Center of Coalbed Methane and Shale Gas for Central Plains Economic Region, Henan Province, Jiaozuo, 454003, China

**Emanuel Guariglia**
Department of Physics "E. R. Caianiello", University of Salerno, Via Giovanni Paolo II, 84084 Fisciano, Italy
Division of Applied Mathematics, Mälardalen University, 721 23 Västerås, Sweden

**Jun Li**
Division of Engineering and Applied Science, California Institute of Technology, 91125 Pasadena, CA, USA

**Martin Ostoja-Starzewski**
Department of Mechanical Science & Engineering, Institute for Condensed Matter

Theory and Beckman Institute, University of Illinois at Urbana-Champaign, 61801 Urbana, IL, USA

**ElhamNajafi**
Department of Physics, University of Zanjan, Zanjan, Iran

**Amir H. Darooneh**
Department of Physics, University of Zanjan, Zanjan, Iran

**Helmut Ahammer**
Institute of Biophysics, Centre of Physiological Medicine, Medical University of Graz, Graz, Austria

**Mihai Ivanovici**
MIV Imaging Venture Laboratory, Department of Electronics and Computers, Faculty of Electrical Engineering and Computer Science, "Transilvania" University, Str. Politehnicii nr. 1, 500019 Bras¸ov, Romania

**Noel Richard, ¨**
XLIM-SIC UMR CNRS 6172, Signals, Images and Communications Laboratory, University of Poitiers, Poitiers, Bat. SP2MI, ˆ T´el´eport 2, Bvd. Marie et Pierre Currie, BP 30179, 86962 FuturoscopeChasseneuilCedex, France

**Christine Fernandez-Maloigne**
XLIM-SIC UMR CNRS 6172, Signals, Images and Communications Laboratory, University of Poitiers, Poitiers, Bat. SP2MI, ˆ T´el´eport 2, Bvd. Marie et Pierre Currie, BP 30179, 86962 FuturoscopeChasseneuilCedex, France

**Ian Pilgrim**
University of Oregon, Eugene, Oregon, USA

**Richard P. Taylor**
University of Oregon, Eugene, Oregon, USA

**Michael A. Riley**
Department of Psychology, Center for Cognition, Action, and Perception, University of Cincinnati, Cincinnati, OH, USA

**Scott Bonnette**
Department of Psychology, Center for Cognition, Action, and Perception, University of Cincinnati, Cincinnati, OH, USA

**Nikita Kuznetsov**
Department of Psychology, Center for Cognition, Action, and Perception, University of Cincinnati, Cincinnati, OH, USA

**Sebastian Wallot**
MINDLab, Aarhus University, Aarhus, Denmark

**Jianbo Gao**
PMB Intelligence, LLC, West Lafayette, IN, USA
BME, School of Life Sciences and Technology, Xi An Jiao Tong University, Xian, PR China

**Andras Eke**
Institute of Human Physiology and Clinical Experimental Research, Semmelweis University, Budapest, Hungary
Diagnostic Radiology, Yale University, New Haven, CT, USA

**Peter Herman**
Diagnostic Radiology, Yale University, New Haven, CT, USA

**Basavaraju G. Sanganahalli**
Diagnostic Radiology, Yale University, New Haven, CT, USA

**Fahmeed Hyder**
Diagnostic Radiology, Yale University, New Haven, CT, USA
Biomedical Engineering, Yale University, New Haven, CT, USA

**Peter Mukli**
Institute of Human Physiology and Clinical Experimental Research, Semmelweis University, Budapest, Hungary

**Zoltan Nagy**
Institute of Human Physiology and Clinical Experimental Research, Semmelweis University, Budapest, Hungary

**Mohammad Z. Al-Hamdan**
Universities Space Research Association at NASA Marshall Space Flight Center, National Space Science and Technology Center, NASA Global Hydrology and Climate Center, Huntsville, AL 35805, USA

**James F. Cruise**
Civil and Environmental Engineering Department, University of Alabama in Huntsville, Huntsville, AL 35899, USA

**Douglas L. Rickman**
Earth Science Office at NASA Marshall Space Flight Center, National Space Science and Technology Center, NASA Global Hydrology and Climate Center, Huntsville, AL 35805, USA

**Dale A. Quattrochi**
Earth Science Office at NASA Marshall Space Flight Center, National Space Science and Technology Center, NASA Global Hydrology and Climate Center, Huntsville, AL 35805, USA

**Shuguang Ji**
University of Tennessee, 37996 Knoxville TN, USA

**Zhang Zhang**
Tangshan Maritime Safety Administration of People's Republic of China, 100736 Tangshan, China

**Hongbiao Yang**
University of Tennessee, 37996 Knoxville TN, USA

**Dan Liu**
Department of Audio, Visual and Image Technology, National Police University of China, 100038 Shenyang, China

**Rapinder Sawhney**
University of Tennessee, 37996 Knoxville TN, USA

**Xu Shanhua**
School of Civil Engineering, Xi'an University of Architecture and Technology, Xi'an, Shannxi, People's Republic of China

**Ren Songbo**
School of Civil Engineering, Xi'an University of Architecture and Technology, Xi'an, Shannxi, People's Republic of China

**Wang Youde**
School of Civil Engineering, Xi'an University of Architecture and Technology, Xi'an, Shannxi, People's Republic of China

**Zhiwei Zhou**
China University of Petroleum(East), No. 66, Changjiang West Road, Huangdao District, Qingdao 266580, China

**Yuliang Su**
China University of Petroleum(East), No. 66, Changjiang West Road, Huangdao District, Qingdao 266580, China

**Wendong Wang**
China University of Petroleum(East), No. 66, Changjiang West Road, Huangdao District, Qingdao 266580, China

**Yi Yan**
China University of Petroleum(East), No. 66, Changjiang West Road, Huangdao District, Qingdao 266580, China

**KiranNandlal**
Harold Vance Department of Petroleum Engineering, Texas A&M University, 3116 TAMU, College Station, TX 77843-3116, USA

**Ruud Weijermars**
Harold Vance Department of Petroleum Engineering, Texas A&M University, 3116 TAMU, College Station, TX 77843-3116, USA

**Yu-Qin Song**
Hunan Key Laboratory for Computation and Simulation in Science and Engineering and Key Laboratory of Intelligent Computing and Information Processing of Ministry of Education, Xiangtan University, Xiangtan, Hunan 411105, China
College of Science, Hunan University of technology, Zhuzhou, Hunan 412007, China

**Jin-Long Liu**
Hunan Key Laboratory for Computation and Simulation in Science and Engineering and Key Laboratory of Intelligent Computing and Information Processing of Ministry of Education, Xiangtan University, Xiangtan, Hunan 411105, China

**Zu-GuoYu**
Hunan Key Laboratory for Computation and Simulation in Science and Engineering and Key Laboratory of Intelligent Computing and Information Processing of Ministry of Education, Xiangtan University, Xiangtan, Hunan 411105, China
School of Mathematical Sciences, Queensland University of Technology, Brisbane, Q4001, Australia

**Bao-Gen Li**
Hunan Key Laboratory for Computation and Simulation in Science and Engineering and Key Laboratory of Intelligent Computing and Information Processing of Ministry of Education, Xiangtan University, Xiangtan, Hunan 411105, China

**YuankunXue**
Ming Hsieh Department of Electrical Engineering, University of Southern California, 90007, CA, USA

**Paul Bogdan**
Ming Hsieh Department of Electrical Engineering, University of Southern California, 90007, CA, USA

# LIST OF ABBREVIATIONS

| | |
|---|---|
| AVHRR | Advanced Very High-Resolution Radiometer |
| ARMA | American Rock Mechanics Association |
| AWC | Averaged wavelet coefficient |
| BCANw | Box-covering algorithm for weighted networks |
| CBB | Compact-box-burning |
| DBH | Diameter at Breast Height |
| DFN | Discrete fracture network |
| DRV | Drained rock volume |
| ESRI | Environmental Systems Research Institute |
| FFT | Fast Fourier transform |
| fBm | Fractional Brownian motion |
| fGn | Fractional Gaussian noise |
| ICAMS | Image Characterization and Modeling System |
| IMO | International Maritime Organization |
| IFS | Iterated Function Systems |
| LAI | Leaf Area Index |
| LSE | Least square error |
| MSE | Mean-squared error |
| MSE | Microseismic events |
| MODIS | Moderate-Resolution Imaging Spectroradiometer |
| NM | Nautical miles |
| NDVI | Normalized Difference Vegetation Index |
| PEQV | Perceptual Evaluation of Video Quality |
| PSD | Power spectral density |
| ROI | Region of interest |
| SWV | Scaled windowed variance |
| SSC | Signal summation conversion |
| SNR | Signal-to-noise ratio |

| | |
|---|---|
| TM | Thematic Mapper |
| TIGER | Topologically Integrated Geographic Encoding and Referencing System |
| UFM | Unconventional fracture model |
| USGS | United States Geological Survey |
| VQEG | Video Quality Experts Group |
| VSNR | Visual signal-to-noise ratio |
| WTMM | Wavelet Transform Modulus Maxima |
| WMF | Weierstrass-Mandelbrot function |
| WFNs | Weighted fractal networks |

# PREFACE

Fractals are self-similar, self-repeating and scale-invariant structures which were first introduced by Mandelbrot to model the "roughness" in patterns observed in nature, a roughness that could not be described in terms of over-idealized Euclidean geometry. Fractals are not only used to model complex spatial shapes but also time patterns. This book is composed by an introductory chapter and 16 open-access articles describing various aspects of fractal analysis. It overviews concepts such as fractal dimension, fractal time series, symmetrical and asymmetrical bifurcating fractal networks. The book is divided into the following topics:

- Fractal dimension, self-similarity and self-affinity: The first chapter aims to introduce the reader to fundamental concepts in fractal analysis such as self-similarity, self-affinity, Hausdorff dimension and Hurst exponent. The second chapter introduces a unified definition of fractal dimension for self-similar and self-affine fractals.
- Fractal Antennas: The third chapter reviews the concepts of fractal dimension and its relationship with Rényi entropy, as well as describes the fractal structure behind Sierpinski Gasket and Hilbert antennas.
- Measuring the Fractal nature of observed patterns: The Chapter 5 and 6 include a practical application of the box-counting method in determining the fractal nature of rings of Saturn and the occurrence of specific words in text.
- Fractal analysis applications to digital imaging: Chapters 6 and 7 describe two examples of fractal analysis applications to digital imaging. Chapter 6 introduces the reader to used of Higuchi method for determining the fractal properties of objects represented by digital images. Chapter 7 evaluates colour fractal dimension and lacunarity as video quality metrics.
- Fractal time series analysis: Chapters 8, 9, and 10 overview the different fractal time-series analysis methods. Chapter 8 summarizes the evolution of different methods from Mandelbrot's similarity dimension to variational box-counting methods. Chapter 9 offers a tutorial to adaptive fractal analysis. Chapter 10 reviews the current mono- and multi-fractal,

as well as time- and frequency-domain time series analysis.

- Examples of fractal time series applications: Chapters 11, 12, and 13 describe three cases of fractal time series applications: the characterization of remotely sensed forested landscapes, the generation of natural-looking radar echoes on coastlines, and the study of multi-fractal behaviour of corroded steel surfaces.
- L-systems as fractal models of fracture networks: Chapters 14 and 15 introduce the readers to Lindenmayer systems (L-systems) which can be utilized to model the fractal geometry of rock and hydraulic fractures.
- Multi-fractal analysis and its applications to weighted complex networks: Chapters 16 and 17 describe multi-fractal applications to weighted complex networks and overviews several algorithms such as the box-counting, edge-covering box counting, rank-driven, ball-covering, compact-box-burning, fixed-size box-counting and sandbox algorithm.

# 1

# *Introduction*

**Olga Moreira**

Mandelbrot introduced the idea of using self-similar shapes as the basis to model the regularities and capture the intricate patterns such as the coastline of Britain (Mandelbrot, 1967; 1983). Fractal structures are self-similar and scale-invariant. The same small-scale shape also appears in the large-scale structure. Self-similar fractals are abundant in nature such as snowflake, broccoli, fern leaves, bronchial and pulmonary vascular trees (e.g. Glenny et al., 1991).

Fractal structures are characterized by the Hausdorff dimension (Balka et al., 2015) also known as the "*Fractal Dimension"*. A non-integer dimension that is essentially a measure of "roughness". For instance, the coastline of Britain 1.21 while the coastline of Norway is 1.52. This means the coastline of Norway is more intricate (or rougher) than that of Britain. An advantage of the self-similarity property is that fractal dimension will remain constant regardless of units or scales of measure (see Chapter 2). A fractal structure can be tested for self-similarity by using, for instance, box-counting method (e.g. Grassberger, 1993). The fractal dimension is evaluated from the slope of the log-log plot of the number of boxes versus scaling factor. A good description of the box-counting method is included in chapter 3 and example of applications is included in chapter 4.

Another advantage is that self-similar fractals can be computer-generated using a simple recursive function (e.g. Shiffman, 2012) which reduces time

complexity. Examining self-similar and recursive structures such as the Koch snowflake (see, for instance, chapter 2 and 3), one can deduce that its perimeter is infinite but not the area. The area Koch snowflake will remain the same. This made the design of fractal antennas possible. Fractal antennas maximize the effective length of self-similar shape and broaden their multi-band characteristics.

In practice, some fractal structure present a certain the degree of randomness. Statistical fractals do not exhibit self-similarity, only self-affinity. Their statistical properties are repeated but are resized by independent quantities in the two orthogonal dimensions. Statistical self-affine fractal are characterized by the Hurst exponent which used as a measure of long-term memory of time series. The fractal dimension is evaluated from the slope of the log-log plot of the variance or power spectrum. A good description of fractal time series is included in chapter 8, 9 and 10. Fractal time series analysis has important applications to main research fields including physiology (see Glenny, 1991; Stadnitski, 2012).

Fractal analysis is constantly evolving, broadening its range of applications, including the evaluation and modelling of L-systems and complex networks (see chapters 14 to 17).

## REFERENCES

1. Balka, R., Buczolich, Z., &Elekes, M. (2015). A new fractal dimension: The topological Hausdorff dimension. Advances in Mathematics, 274, 881-927.
2. Glenny, R. W., Robertson, H. T., Yamashiro, S., &Bassingthwaighte, J. B. (1991). Applications of fractal analysis to physiology. Journal of Applied Physiology, 70(6), 2351-2367.
3. Gonzato, G., Mulargia, F., &Marzocchi, W. (1998). Practical application of fractal analysis: problems and solutions. Geophysical Journal International, 132(2), 275-282.
4. Grassberger, P. (1993). On efficient box counting algorithms. International Journal of Modern Physics C, 4(03), 515-523.
5. Mandelbrot, B. (1967). How long is the coast of Britain? Statistical self-similarity and fractional dimension. science, 156(3775), 636-638.
6. Mandelbrot, B. B. (1983). The fractal geometry of nature (Vol. 173, p. 51). New York: WH freeman.
7. Shiffman, D (2012). Chapter 8. Fractals. In: The Nature of Code ISBN-10: 0985930802
8. Stadnitski, T. (2012). Measuring fractality. Frontiers in physiology, 3, 127.

# 2

# *Definition of Fractal Topography to Essential Understanding of Scale-Invariance*

**Yi Jin[1,2], YingWu[1], Hui Li[1], Mengyu Zhao[1]&Jienan Pan[1,2]**

[1]School of Resources and Environment, Henan Polytechnic University, Jiaozuo, 454003, China
[2]Collaborative Innovation Center of Coalbed Methane and Shale Gas for Central Plains Economic Region, Henan Province, Jiaozuo, 454003, China

## ABSTRACT

Fractal behavior is scale-invariant and widely characterized by fractal dimension. However, the cor-respondence between them is that fractal behavior uniquely determines a fractal dimension while a fractal dimension can be related to many possible fractal behaviors. Therefore, fractal behavior is independent of the fractal generator and its geometries, spatial pattern, and statistical properties in addition to scale. To mathematically describe fractal behavior, we propose a novel concept of *fractal topography* defined by two scale-invariant parameters, scaling lacunarity ($P$) and scaling coverage ($F$). The scaling lacunarity is defined as the scale ratio between

**Citation:** (APA): Jin, Y., Wu, Y., Li, H., Zhao, M., & Pan, J. (2017). Definition of fractal topography to essential understanding of scale-invariance. Scientific reports, 7, 46672, DOI: 10.1038/srep46672.

two successive fractal generators, whereas the scaling coverage is defined as the number ratio between them. Consequently, a strictly scale-invariant definition for self-similar fractals can be derived as $D = \log F / \log P$. To reflect the direction-dependence of fractal behaviors, we introduce another parameter $H_{xy}$, a general Hurst exponent, which is analytically expressed by $H_{xy} = \log P_x / \log P_y$ where $P_x$ and $P_y$ are the scaling lacunarities in the $x$ and $y$ directions, respectively. Thus, a unified definition of fractal dimension is proposed for arbitrary self-similar and self-affine fractals by averaging the fractal dimensions of all directions in a $d$-dimensional space, which $D = \sum_{i=1}^{d} (H_{xi}/d) \log F / \log P_x$. Our definitions provide a theoretical, mechanistic basis for understanding the essentials of the scale-invariant property that reduces the complexity of modeling fractals.

## INTRODUCTION

Fractals were originally introduced by Mandelbrot1 to describe the fractal behaviors of similar geometries in disordered and irregular objects such as the natural coastlines1,2,3, phenomena in natural and artificial materials 4,5,6, porous media7,8,9,10, biological structures11, rough surfaces12,13,14,15, as well as novel application of factuality to complex networks and brain systems16,17,18.

The unique property of fractals is that they are independent of the unit of measurement 3 and follow a scaling law in the form

$$M(l) \propto l^{D} \tag{1}$$

where $M$ can be the length of a line or the area of a surface or the volume of an object, and $D$ is the fractal dimension. Eq. (1) implies the property of self-similarity, which means that the value of $D$ from Eq. (1) remains constant over a range of length scales $l$.

Fractal dimension extends the concept of "dimension", because it can be a fraction, rather than an integer as in conventional Euclidean space, indicating the degree of complexity of fractal behaviors. Fractal theory now serves as a powerful, perhaps fundamental, tool for characterizing scale-invariance in many fields[19,20,21,22,23,24,25,26,27].

In practical applications, $D$ can be obtained by a number-size approach or one of its variants, as demonstrated in Eq. (2)

$$N(G(l)) \propto l^{-D} = cl^{-D} \tag{2}$$

where $N(G(l))$ is the number of similar objects of $G$ with characteristic linear dimension $l$ and $c$ is a constant proportionality. $D$ can be determined by the slope of the relationship between log $l$ and log$N(G(l))$

$$D = -\log_l \frac{N(G(l))}{c} \tag{3}$$

However, the number-size relationship is not a definition, but rather a method for determining the implied fractal dimension. Reexamining fractal theory, $D$ is a parameter uniquely determined by the fractal behavior of a similar object (scaling object or fractal generator) in a fractal object, not a parameter that determines such behavior. Different fractal generators following the same fractal behavior will result in the same fractal dimension, while the same fractal generator with different fractal behaviors will lead to different fractal dimensions.

As the variants of the Sierpinski gasket in Fig. 1 show, the fractals in rows 1 and 2 are constructed by different fractal generators, but they share the same fractal dimension, log2/log3, per the number-size relationship (Equation (3)) because their fractal behaviors are the same. The fractal generators for the fractals in rows 2–4 are the same; however, they follow diverse fractal behaviors, resulting in different fractal dimensions (log2/log3, log8/log3, and log5/log6, respectively).

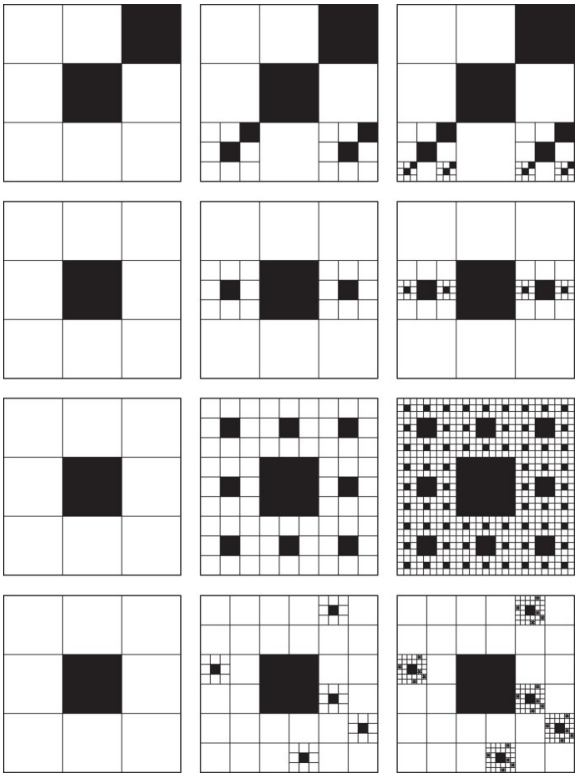

**Figure 1:** Fractals constructed by different fractal generators with the same fractal behaviors or by the same fractal generators with different fractal behaviors.

From left to right in each row, the subfigures demonstrate the construction of fractals with greater detail. Left: the fractal generator is scaled to the characteristic dimension of a fractal object $l_0$. Center: following a fractal behavior, a simple fractal is constructed. Right: based on the fractal generator and following the fractal behavior, a more complex fractal is obtained in a scale-invariant manner.

These examples imply that the definition of fractal behavior must satisfy three key requirements: it must be (1) independent of the fractal generator, (2) not constrained by the geometries, spatial patterns, or statistical properties of the fractal generator, and (3) scale-invariant. The number-size relationship does not suffice to preserve fractal behavior information, which hinders the essential understanding of fractal properties and strictly constrains their applications.

## METHODS AND DISCUSSION

To provide a theoretical, mechanistic basis for understanding the property of scale-invariance, we must mathematically define it per the key requirements we have previously laid out. The first one is **what parameters determine fractal behavior?** For convenience, we call what defines fractal behavior *fractal topography* not only because of the scale and size background, but also that natural structures are often hierarchical, for example, with a sponge-like topology28.

To demonstrate fractal topography, it suffices to exhibit structure in a fractal object using a variant of the Sierpinski gasket. As shown in Fig. 2, there are two scale-invariant parameters that determine the fractal behavior of fractal generator $G$: the ratio of the sizes of two successive scaling objects ($l_i/l_{i+1}$) and the ratio of their number ($N(G(l_{i+1}))/N(G(l_i))$).

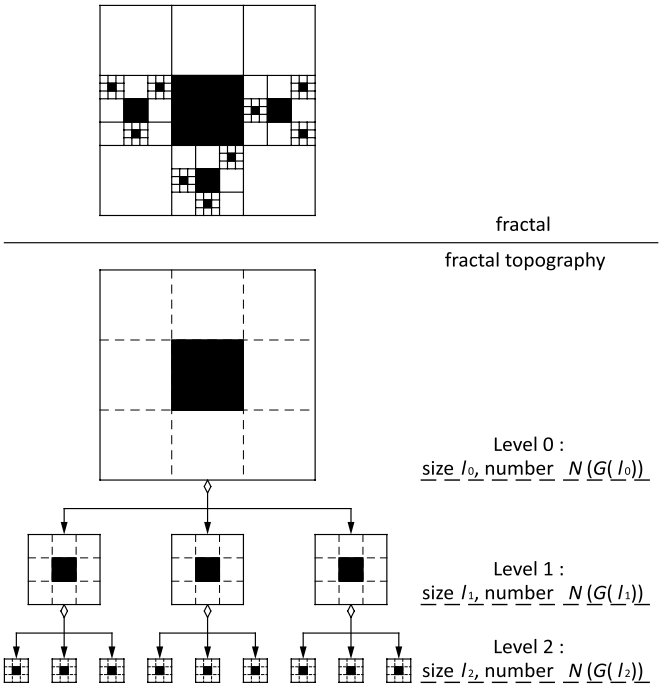


**Figure 2**: A fractal and its topography for a variant of the Sierpinski gasket.

Fractal topographic information is actually implied in the number-size relationship. For convenience, to mathematically define fractal topography, we first propose two notations:

***Scaling lacunarity (P):*** The unit ratio between two successive fractal generators $G(l_i)$ and $G(l_{i+1})$, with the characteristic dimensions $l_i$ and $l_{i+1}$ in a fractal object, as

$$P = \frac{l_i}{l_{i+1}} \tag{4}$$

***Scaling coverage (F):*** The numeric ratio between two successive fractal generators $G(l_i)$ and $G(l_{i+1})$ in a fractal object, yields:

$$F = \frac{N(G(l_{i+1}))}{N(G(l_i))} \tag{5}$$

Apparently, $P$ and $F$ uniquely determine the fractal behavior of the scaling object in a fractal. These two parameters are dimensionless and scale-invariant, because no matter how we compress or stretch the fractal space, $P$ and $F$ will not be altered. Taking the properties independent of a fractal generator and its constraints together, demonstrated in Fig. 1, fractal topography is defined by $\Omega(P, F)$ in this report.

The above discussion answers the question of how to define fractal behavior, but **how does fractal behavior uniquely determine fractal dimension?**

According to Eq. (2), the number of scaling objects of characteristic dimension $l_i$ yields

$$N(G(l_i)) = cl_i^{-D} \tag{6}$$

while the number of the successive objects $N(G(l_i/P))$ satisfies

$$N\left(G\left(\frac{l_i}{P}\right)\right) = c\left(\frac{l_i}{P}\right)^{-D} \tag{7}$$

Taking Eqs (4), (5), (6) and (7) into account, we obtain the relationship between the scaling lacunarity and the scaling coverage

$$F = \frac{N\left(G\left(\frac{l_i}{P}\right)\right)}{N(G(l_i))} = P^D \tag{8}$$

Consequently, a scale-invariant definition of fractal dimension is obtained:

$$D = \frac{\log F}{\log P} \tag{9}$$

Eq. (9) indicates that the fractal dimension $D$ is the exponent of the power-law relationship between $P$ and $F$, a dependent parameter determined uniquely by $P$ and $F$. Compared with Eq. (3), Eq. (9) preserves fractal topography information and defines fractal dimension in a strictly scale-invariant manner, other than what is implied in the number-size relationship.

To verify Eq. (9), some classic fractals, the Koch curve, Sierpinski carpet, Sierpinski gasket, and Menger Sponge (Fig. 3, here the Menger Sponge not demonstrated), are used to validate it and check its generality.

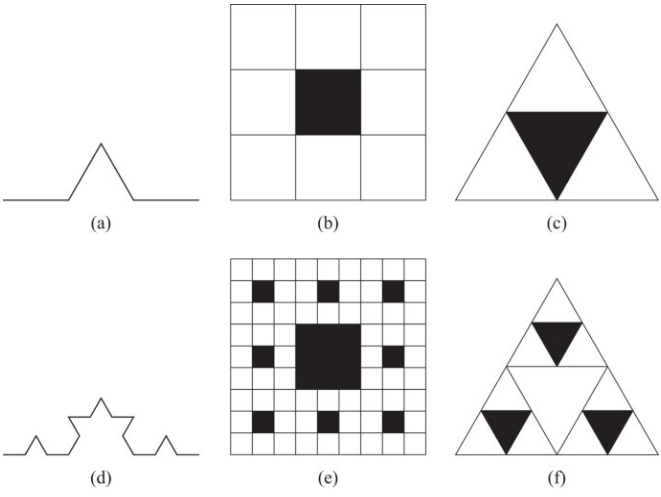


**Figure 3:** Fractals to demonstrate the validity of Eq. (9).

(a–c) are the initiators of scaling objects of the Koch curve, Sierpinski carpet, and Sierpinski gasket, respectively. For convenience, we denote them as fractal generators. At the next step, each potential subpart is replaced by a reduced replicate of the generator and the fractals are obtained.

For a Koch curve, at the stage $n=0$, $N(G(l_0))=1$ (Fig. 3(a)); at the next stage, $N(G(l_1))=4$ and $l_1=l_0/3$ (Fig. 3(b)). Following the definitions of scaling lacunarity and scaling coverage, $P=l_0/l_1=3$ and $F=N(G(l_1))/N(G(l_0))=4$. Therefore, the fractal dimension of the Koch curve $D=\log 4/\log 3=1.2618$. The parameters defining and characterizing the fractal topographies of different classic fractals are listed in Table 1. The results are consistent with their theoretical values3.

**Table 1:**The fractal topography information of classic fractals and their fractal dimensions calculated by Eq. (9)

| **Fractals** | ***P*** | ***F*** | ***D*** |
|---|---|---|---|
| Koch curve | 3 | 4 | 1.2618 |
| Sierpinski carpet | 3 | 8 | 1.8927 |
| Sierpinski gasket | 2 | 3 | 1.5842 |
| Menger Sponge | 3 | 26 | 2.9656 |

Eq. (9) indicates that:

- $P$ and $F$ are the intrinsic and basic properties of fractal behavior. $P$ controls scaling behavior while $F$ determines the degree of space filled by a fractal generator, and together they quantitatively define the topography of a fractal;
- fractal topography uniquely determines fractal dimension, while a fractal dimension can be associated with different fractal topographies/fractal behaviors. For example, the fractal topography with $P$ and $F$ of $a$ and $b$ shares the same fractal dimension with those of $a^{\beta}$and $b^{\beta}$for an arbitrary choice of β
- scaling lacunarity and scaling coverage are real scale-invariant dimensionless parameters different from the scale $l$ and number $N(G(l))$, and they are also independent of the fractal generator $G(l_0)$ and its geometries, spatial patterns, and statistical properties.

In Fig. 3, the maximum scaling coverages $F_{max}$ are 4 (Koch curve), 8 (Sierpinski carpet), and 3 (Sierpinski gasket) at the minimium scaling lacunarities $P_{min}$ of 3, 3, and 2, respectively. However, $F$ can be fixed to be a value in the series $\{0, 1, \cdots, F_{max}\}$, and can even be a fraction in $[0, F_{max}]$. For simplicity and without loss of generality, $F$ and $P$ are set to integers for discussion in this report. Using the Koch curve for explanation, $F$ can be assigned to be 0, 1, 2, 3, and 4 while $P$ is set to be 3. These fractal dimensions are $\log 0/\log 3 \to -\infty$[29], $\log 1/\log 3$, $\log 2/\log 3$, $\log 3/\log 3$ and $\log 4/\log 3$, respectively. Meanwhile, the scaling lacunarity can also be chosen to be larger than $P_{min}$. As the fractal in row 4 of Fig. 1, the scaling lacunarity is 6, which is greater than the minimum scaling lacunarity determined by the geometry of the fractal generator.

The definition of the fractal dimension by Eq. (9) is not new and ideas about topography can be found in many previous works4-9, and can be even tracked back to its original introduction1. For convenience of description, we call the fractal topography of $\Omega\{F_{max}, P\}$ the fully-filling scheme, otherwise the partially-filling scheme, where $F_{max}$ represents the maximum scaling coverage at a scaling lacunarity of $P$.

In 1967, Mandelbrot defined fractal dimension as $D = \log N/\log \frac{1}{l}$ with a number-size approach, implying the idea of fractal topography. In his demonstration of self-similar curves, $1/(1/4)=l_0/l_1$ which is the scaling lacunarity $P$, and $N=N(G(l_1))/1=N(G(l_1))/N(G(l_0))$ characterizes the scaling coverage. If this were not the case, for example, when $l_0$ was set to 1/3, 1/2, or any different scale, the calculation results would not be unique; it is only when the scale is "sufficiently fine" that $N(l)/\log \frac{1}{l}$ would tend to the limit of $D$ and become independent of scale. And the description of scale-invariant phenomena Mandelbrot proposed is very special, because fractal behavior characterized by $D$ was heavily dependent on the fractal generators, which means the scaling lacunarity was set to $P_{min}$ while the scaling coverage was set to $F_{max}$.

In the application of fractal theory in porous media modeling, Perrier and Bird9 pointed out the limitations in understanding fractal behavior and proposed a more general filling mode, namely the partially-filling scheme noted before. However, the scaling lacunarity was not broken away from the constraint of fractal generators to be an independent parameter, which means that $P$ was fixed to $P_{min}$. Turcotte4 had proposed a calculation model for $D$, $\log(N_{i+1}/N_i)/\log(l_i/l_{i+1})$, which is exactly the same topographic definition of fractal dimension as Eq. (9). Unfortunately, the physical meanings of the expressions $l_i/l_{i+1}$ and $N_{i+1}/N_i$ were not defined and left the quantitative description of fractal topography elusive, obscuring an essential understanding of scale-invariant properties.

Based on $\Omega(P, F)$, together with the fractal generator $G$ and its scaling range $[l_{min}, l_{max}]$, a self-similar fractal object is uniquely defined as $F_{sim}\{\Omega(P, F), G, [l_{min}, l_{max}]\}$, which facilitates the modeling of fractal objects, as Fig. 4 demonstrates.

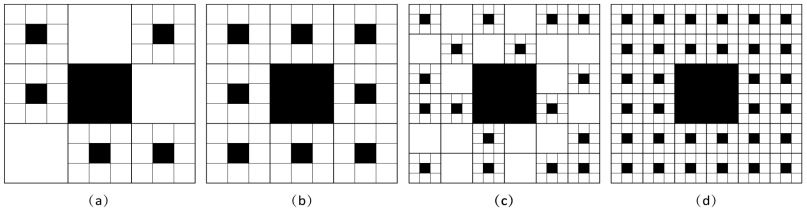


**Figure 4:** Fractals sharing the same fractal generator but different fractal topographies $\Omega(F, P)$.

The scaling lacunarities of (a)–(d) are 3, 3, 6, and 6, respectively, while the scaling coverages are 5, 8, 17, and 32. According to Eq. (9), the fractal dimensions of (a–d) are log5/log3, log8/log3, log17/log6, and log32/log6, respectively.

However, except for the self-similarity, the scale-invariant property might be direction-dependent in a fractal object. Then, **can we unify the definition of fractal dimension for arbitrary fractals?**

Self-affine fractals are objects with scale-invariant and direction-dependent properties30. In nature, vertical cross sections are often examples of this type13,31. A formal definition of a self-affine fractal in a two-dimensional $xy$-space is that $G(\zeta x, \zeta^H y)$ is statistically similar to $G(x, y)$, where $\zeta$ is a scaling factor and $H$ is the Hurst exponent. Based on the scaling lacunarity definition, $G(\zeta x, \zeta^H y)$ can be written into $G(x/P_x, y/P_y)$; and by replacing $\zeta$ by $1/P_x$, $G(\zeta x, \zeta^H y)$ takes the form of $G(x/P_x, y/P_x^H)$. Consequently, we obtain the relationship between $P_x$ and $P_y$ as:

$$P_y = P_x^H \tag{10}$$

where $P_x$ and $P_y$ are the scaling lacunarities in the $x$ and $y$ directions respectively. Therefore, the Hurst exponent is scale-invariantly defined by

$$H = \frac{\log P_y}{\log P_x} \tag{11}$$

Eq. (11) indicates that the Hurst exponent is a scale-invariant parameter that characterizes the power-law relationship between scaling lacunarities in two different directions. However, the results of Eq. (11) are not constrained in the range of [0, 1]. To clarify the distinction, we call this exponent the general Hurst exponent and express it as $H_{xy} = \log P_x / \log P_y$.

In a $d$-dimensional space, the fractal dimension in the $i$th direction is denoted by $D_i$ for convenience. According to the additive law[3,32], the fractal dimension $D$ is the average of the direction-dependent fractal dimensions, which yields $D = \sum_{i=1}^{d} D_i/d$. Taking Eq. (9), (11), and the general Hurst exponent together, the fractal dimension of a self-affine fractal is expressed by

$$D = \frac{\sum_{i=1}^{d} H_{xi}}{d} \frac{\log\ F}{\log\ P_x} \qquad (12)$$

To be consistent with the value range of the Hurst exponent, [0, 1], we denote the maximum scaling lacunarity in all directions of a fractal object by $P_{\max}$. According to Eq. (11), the Hurst exponent $H_i$ in the $i$th direction yields $\log P_i/\log P_{\max}$. Therefore, the general definition of arbitrary fractals is then rearranged into

$$D = \frac{\sum_{i=1}^{d} H_i^{-1}}{d} \frac{\log\ F}{\log\ P_{\max}} \qquad (13)$$

If all $P_i$ are the same, $H_i = 1$ are all satisfied. Thus, Eq. (13) is same as Eq. (9), which characterizes self-similar fractal behaviors. Otherwise, it depicts the direction-dependent fractal behavior of self-affine fractal objects. Obviously, Eq. (9) is only a special case of the general definition of fractal dimension (Equation (13)) to characterize fractal behaviors.

## CONCLUSION

Based on the theoretical, mechanistic basis for understanding the nature of fractal behaviors, two parameters are proposed to define the fractal topography that uniquely determine fractal behavior and dimension. These two parameters, scaling lacunarity and scaling coverage, are independent of the fractal generator and the scale and they are intrinsic properties of a fractal topography. However, owing to anisotropic origins, fractal topography may appear direction-dependent, meaning that the scaling lacunarities are different in different directions. In this study, we find that the physical meaning of the Hurst exponent is a scale-invariant exponent that characterizes the power-law relationship of scaling lacunarities in two different directions. Consequently, a unified definition of fractal dimension for arbitrary fractals is proposed by averaging the fractal dimensions of all directions in a strictly scale-invariant manner.

Apparently, Eq. (13) unifies the definition of fractal dimension for arbitrary fractals, including self-samenesses, self-similarites and self-affinities, due to the proposal of fractal topography. In addition to that, fractal topography provides an essential understanding of fractal behavior that eases the implementation and reduces the modeling complexity of disordered and irregular fractal objects, as demonstrated in some cases of two-dimensional porous media in Fig. 5. Although our definitions are derived in view of regular geometries, their practical application is straightforward in a statistical form.

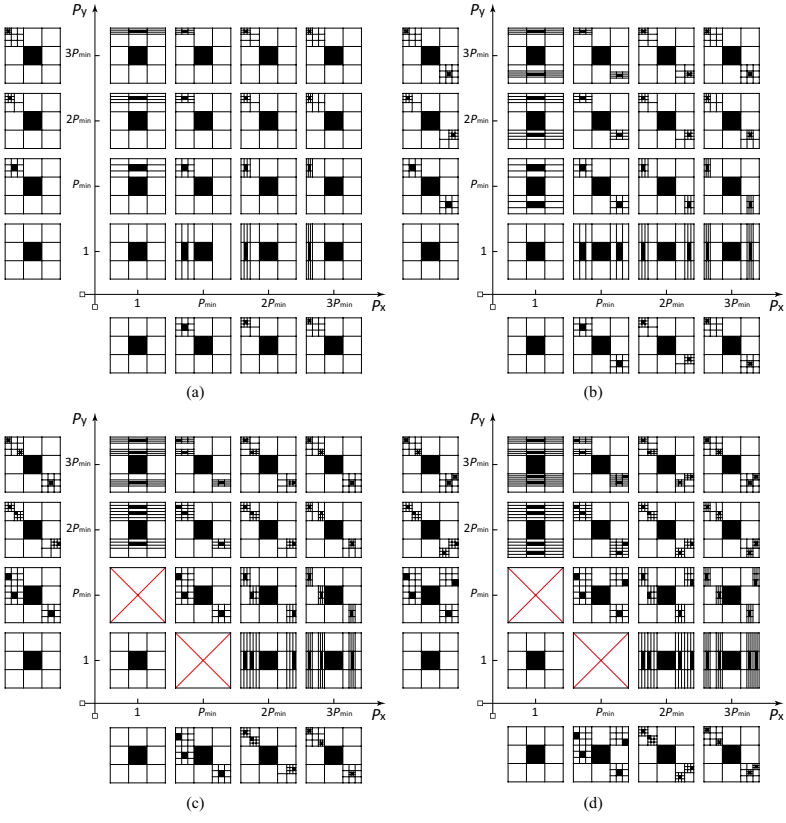


**Figure 5:** Construction of self-same, self-similar, and self-affine objects following different fractal topographies.

All the fractals generated from the same generator but with different scaling lacunarities $P$ and scaling coverages $F$. When $P_x = P_y = 1$, the generated objects are self-same; while $P_x = P_y \neq 1$, the generated objects are self-similar;

else the generated objects are self-affines. The scaling coverages $F$ in (a)–(d) are 1–4, respectively. In each subfigure, as $P_x/P_y$ deviates further from 1, the anisotropy of the fractal increases.

## ACKNOWLEDGEMENTS

This work was supported by the National Natural Science Foundation of China (Grant Nos. 41102093, 41472128), CBM Union Foundation of Shanxi Province, China (Grant Nos. 2012012002, 2015012010), the Program for Science & Technology Innovation Talents in Universities of Henan Province, China (Grant No. 16HASTIT023), and the Program for Innovative Research Team (in Science and Technology) in University of Henan Province, China (Grant No. 17IRTSTHN025).

## REFERENCES


1. Mandelbrot, B. B. How long is the coast of britain? statistical self-similarity and fractional dimension. *Science* 156, 636–8 (1967).
2. Mandelbrot, B. B. Stochastic models for the earth's relief, the shape and the fractal dimension of the coastlines, and the number-area rule for islands. *Proc. Natl. Acad. Sci.* 72, 3825–8 (1975).
3. Mandelbrot, B. B. *The fractal geometry of nature* (Macmillan, New York, 1983).
4. Turcotte, D. L. *Fractals and Choas in Geology and Geophysics* (Cambridge University Press, New York, 1997).
5. Bejan, A. &Lorente, S. Constructal theory of generation of configuration in nature and engineering. *J. Appl. Phys.* 100, 041301 (2006).
6. Cheng, Q. M. Singularity theory and methods for mapping geochemical anomalies caused by buried sources and for predicting undiscovered mineral deposits in covered areas. *J. Geochem. Explor.* 122, 55–70 (2012).
7. Krohn, C. E. & Thompson, A. H. Fractal sandstone pores: Automated measurements using scanningelectron- microscope images. *Phys. Rev. B.* 33, 06366 (1986).
8. Smidt, J. M. &Monro, D. M. Fractal modeling applied to reservoir characterization and flow simulation. *Fractals* 6, 401–408 (1998).
9. Perrier, E., Bird, N. &Rieu, M. Generalizing the fractal model of soil structure: the pore-solid fractal approach. *Geoderma* 88, 137–164 (1999).
10. Jin, Y., Zhu, Y. B., Li, X., Zheng, J. L. & Dong, J. B. Scaling invariant effects on the permeability of fractal porous media. *Transport Porous Med.* 109, 433–453 (2015).
11. West, G. B., Brown, J. H. &Enquist, B. J. A general model for the origin of allometric scaling laws in biology. *Science* 276, 122–6 (1997).
12. Brown, S. R. &Scholz, C. H. Broad bandwidth study of the topography of natural rock surfaces. *J. Geophys. Res.* 90, 12512–12575 (1985).
13. Dubuc, B., Quiniou, J. F., Roquescarmes, C., Tricot, C. &Zucker, S. W. Evaluating the fractal dimension of profiles. *Phys. Rev. A* 39, 1500–1512 (1989).
14. Buzio, R., Boragno, C., Biscarini, F., De Mongeot, F. B. &Valbusa, U. The contact mechanics of fractal surfaces. *Nat. Mater.* 2, 233–236

(2003).

15. Jin, Y., Dong, J. B., Zhang, X. Y., Li, X. & Wu, Y. Scale and size effects on fluid flow through self-affine rough fractures. *Int. J. Heat Mass Tran.* 105, 443–451 (2017).
16. Song, C., Makse, H. A. &Gallos, L. K. Scaling of degree correlations and its influence on diffusion in scale-free networks. *Phys. Rev. Lett.* 100, 248701 (2008).
17. Galvao, V. et al. Modularity map of the network of human cell differentiation. *Proceedings of the National Academy of Sciences* 107, 5750–5755 (2010).
18. Gallos, L., Sigman, M. &Makse, H. The conundrum of functional brain networks: Small-world efficiency or fractal modularity. *Frontiers in Physiology* 3, 123 (2012).
19. Ma, D., Stoica, A. D. & Wang, X. L. Power-law scaling and fractal nature of medium-range order in metallic glasses. *Nat. Mater.* 8, 30–34 (2009).
20. Jin, Y., Song, H. B., Hu, B., Zhu, Y. B. &Zheng, J. L. Lattice boltzmann simulation of fluid flow through coal reservoir's fractal pore structure. *Sci. China Earth Sci.* 56, 1519–1530 (2013).
21. Wang, B. Y. et al. Derivation of permeability-pore relationship for fractal porous reservoirs using series-parallel flow resistance model and lattice boltzmann method. *Fractals* 22, 1440005 (2014).
22. Dingal, P. C. D. P. et al. Fractal heterogeneity in minimal matrix models of scars modulates stiff-niche stem-cell responses via nuclear exit of a mechanorepressor. *Nat. Mater.* 14, 951–60 (2015).
23. Zheng, X. et al. Multiscale metallic metamaterials. *Nat. Mater.* 15, 1100–1106 (2016).
24. Ding, D., Zhao, Y., Feng, H., Si, B. & Hill, R. L. A user-friendly modified pore-solid fractal model. *Sci. Rep.* 6, 39029 (2016).
25. Namazi, H. &Kulish, V. V. Fractal based analysis of the influence of odorants on heart activity. *Sci. Rep.* 6, 38555 (2016).
26. Cheng, Q. Fractal density and singularity analysis of heat flow over ocean ridges. *Sci. Rep.* 6, 19167 (2016).
27. Jin, Y., Li, X., Zhao, M., Liu, X. & Li, H. A mathematical model of fluid flow in tight porous media based on fractal assumptions. *Int. J. Heat Mass Tran.* 108, Part A, 1078–1088 (2017).

28. Carpinteri, A. &Pugno, N. Are scaling laws on strength of solids related to mechanics or to geometry? *Nat. Mater.* 4, 421–423 (2005).
29. Ghanbarian-Alavijeh, B. & Hunt, A. G. Comments on "more general capillary pressure and relative permeability models from fractal geometry" by kewen li. *J. Contam. Hydrol.* 140–141, 21–23 (2012).
30. Mandelbrot, B. B. Self-affine fractals and fractal dimension. *Phys. Scripta* 32, 257–260 (1985).
31. Dubuc, B., Zucker, S. W., Tricot, C., Quiniou, J. F. &Wehbi, D. Evaluating the fractal dimension of surfaces. *Proc. R. Soc. London, Ser. A* 425, 113–127 (1989).
32. Sreenivasan, K. R. Fractals and multifractals in fluid turbulence. *Annu. Rev. Fluid Mech.* 23, 539–604 (1991).

# 3

# *Entropy and Fractal Antennas*

**Emanuel Guariglia** [1,2]

[1]Department of Physics "E. R. Caianiello", University of Salerno, Via Giovanni Paolo II, 84084 Fisciano, Italy
[2]Division of Applied Mathematics, Mälardalen University, 721 23 Västerås, Sweden

## ABSTRACT

The entropies of Shannon, Rényi and Kolmogorov are analyzed and compared together with their main properties. The entropy of some particular antennas with a pre-fractal shape, also called fractal antennas, is studied. In particular, their entropy is linked with the fractal geometrical shape and the physical performance.

**Keywords:** Shannon entropy; Rényi entropy; Kolmogorov entropy; fractal dimension; box-counting dimension; iterated function system; fractal antenna; generalized fractal dimension

**Citation:**:Guariglia, E. (2016). Entropy and fractal antennas. Entropy, 18(3), 84. DOI: 10.3390/e18030084.

# INTRODUCTION

Classically, the concept of entropy arises from the analysis of physical problems in statistical physics and thermodynamics. Since the beginning, it was a measure of uncertainty in a physical system, and based on this, C.E. Shannon [1] proposed to extend this concept for the analysis of complexity in signals, thus giving rise to the emerging information theory [2]. Several year later than Shannon, A. Rényi showed that a valid measure of entropy has to be defined in accordance with a measure of diversity [3]. A step forward in this direction was given by A. Kolmogorov (1958), who used the concept of entropy to define a fundamental measure for chaotic evolution and loss of information in the course of time [4].

Indeed, this entropy is an extension of a known concept in information entropy (for time-dependent processes), which is used to characterize dynamical systems between regular, chaotic and purely random evolution.

Chaotic motions and, in particular, attractors can be also described by iterative maps, which belong to the fundamental methods of fractal geometry.

Chaos, complexity and fractals have many common features, and recently, they have attracted the interest of scholars for their application in science and engineering.

Fractal sets are abstract objects that cannot be physically implemented. However, some related geometries known as pre-fractals have been shown to be very useful in engineering and applied science [5,6]. In particular, some fractal models have been used to design some fractal antenna with very special properties: about one-tenth of a wavelength (p. 231, [**7**]) and a pre-fractal geometrical configuration.

An antenna is a complex device, characterized by different parameters (resonant frequency, gain, directivity, radiation pattern, *etcetera*), which define the performance of the radiator. The chaoticity of the fractal antenna will be studied in the following by an entropy measure based on the computation of the fractal dimension, according to the analysis of a radiating structure given by [8,9].

Since the Rényi entropy $H_\alpha$ and generalized fractal dimension $D_\alpha$ are connected by a well-known relation (see Equation (25)), in this paper, the quantity $D_\alpha$ was used to compute the Rényi entropy $H_\alpha$ of a pre-fractal structure and to describe the electromagnetic behavior of an antenna together with the corresponding performance.

The results of Best [10,11] show how antenna geometry alone (pre-fractal or otherwise) is not a significant factor to determine the performance of small antennas. Yet, this may be a good clue.

In the literature, there are only a few articles about how the self-similarity property of a pre-fractal radiator can influence its performance (see again [8,9]).

In order to investigate in this direction, the values of Rényi entropy $H_\alpha$ through Equation (25) for the classical Sierpinski gasket were determined. The quantity $D_\alpha$ was numerically estimated (see Paragraph 4.3).

## CONCEPT OF ENTROPY

There are basically three definitions of entropy in this article. The Kolmogorov entropy *K*, which measures the chaoticity of a dynamical system (Chapter 6, [12]), can be estimated as the Rényi entropy $H_\alpha$. In information theory, the Shannon entropy is a special case of Rényi entropy for α=1.

### Definition 1

(Shannon entropy)**.** *The Shannon entropy* [1,13] *of a discrete-type RV X is defined as:*

$$H(X) \triangleq -\sum_{i=1}^{N} p_i \log_b p_i \qquad (1)$$

*where N is the number of possible states and* $p_i$ *is the probability of the event* $\{X=x_i\}$*, and it is assumed* $p_i>0$*; the most common used values are* b=2 *and* b=e.

This entropy may be defined in a simple way for a continuous-type RV, as well [13]. Yet, this is not the scope of this article. As is well known, Shannon entropy satisfies different properties, which will not be treated herein [14].

Moreover, it is possible to show that it represents the measure of uncertainty about a suitable partition [13].

A first generalization of this kind of entropy is the so-called Rényi entropy [3,15]: it represents one family of functionals to describe the uncertainty or randomness of a given system.

## Definition 2

(Rényi entropy)**.** *Let α be a positive real number. The Rényi entropy of order α is defined as* [**3**]*:*

$$H_\alpha(X) \triangleq \begin{cases} \dfrac{1}{1-\alpha}\log_b \sum_{i=1}^{N} p_i^\alpha & \alpha > 0,\ \alpha \neq 1 \\ H(X) & \alpha = 1 \end{cases} \tag{2}$$

*where X is discrete-type RV and* $p_i>0$ *is the probability of the event* $\{X=x_i\}$*, and the most common used values are the same as the Shannon entropy.*

If the events $\{X=x_i\}$ are equiprobable, then $H_\alpha$ is maximal and $H_\alpha(X)=\log_b N$ for every $\alpha>0$, *i.e.*, the so-called Hartley entropy $H_0 = \log_b \sum_{i=1}^{N} p_i^0 = \log_b N$ [16]. It is clear that they do not depend on the probability, but only on the number of events with non-zero probability.

In order to understand the meaning of the last definition, it is necessary to observe that at α=1, the quantity:

$$\frac{1}{1-\alpha}\log_b \sum_{i=1}^{N} p_i^\alpha$$

generates the indeterminate form $\frac{0}{0}$. By L'Hôpital's rule [**17**], it is easy to show that:

$$\lim_{\alpha\to 1} \frac{1}{1-\alpha}\log_b \sum_{i=1}^{N} p_i^\alpha = -\sum_{i=1}^{N} p_i \log_b p_i \tag{3}$$

*i.e.*, the Shannon entropy, so $\lim_{\alpha\to 1} H_\alpha(X) = H_1(X) = H(X)$, as shown in Figure 1.

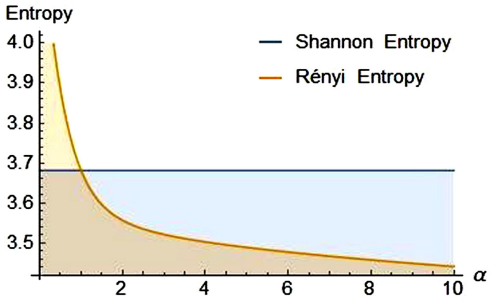


**Figure 1:** Rényi and Shannon entropies for a binomial distribution with N = 20: they converge for α→1, in accord with Equation (3). The computation of both entropies was done for b=2.

Therefore, the Rényi entropy may be considered as a generalization of the Shannon entropy. It can be shown that the Rényi entropies decrease as a function of α [3].

Let $x(t) = [x_1(t), ..., x_d(t)]$ be the trajectory of a dynamical system on a strange attractor. Let the *d*-dimensional phase space be partitioned into boxes of size $l^d$ and sampled at the discrete time intervals τ. Let $p_{i_0,...,i_n}$, be the joint probability that the trajectory x(t=0) is in the box $i_0$, x(t=τ) is in the box $i_1$, ..., and x(t=nτ) is in the box $i_n$ [18,19]; for example:

$$p_{i_0,...,i_n} = P\{x(t=0) \in i_0;\ x(t=\tau) \in i_1;\ ...;\ x(t=n\tau) \in i_n\} \tag{4}$$

According to Equation (1), the quantity:

$$K_n = -\sum_{i_0,...,i_n} p_{i_0,...,i_n} \log p_{i_0,...,i_n} \tag{5}$$

gives the expected amount of information needed to locate the system on a special trajectory $i_0^*, ..., i_n^*$, *i.e.*, if it is known *a priori* that our system was in $i_0^*, ..., i_n^*$, then $K_{n+1} - K_n$ is the necessary information to predict in which box $i_{n+1}^*$ this system will be included. Using the language of information theory, this means that $K_{n+1} - K_n$ measures the loss of information for the system from *n* to n+1 (Chapter 6, [12]). Therefore:

$$\sum_{n=0}^{N-1}(K_{n+1}-K_n) = K_N - \cancel{K_{N-1}} + \cancel{K_{N-1}} - \cancel{K_{N-2}} + \ldots + \cancel{K_1} - K_0$$
$$= K_N - K_0 = -\sum_{i_0,\ldots,i_N} p_{i_0,\ldots,i_N}\log p_{i_0,\ldots,i_N} + p_{i_0}\log p_{i_0}$$
$$= -\sum_{i_0,\ldots,i_{N-1}} p_{i_0,\ldots,i_{N-1}}\log p_{i_0,\ldots,i_{N-1}}$$

The definition of this new kind of entropy will be provided at this point.

## Definition 3

(Kolmogorov entropy)**.** *The Kolmogorov entropy K is defined as* [**19**]*:*

$$K \triangleq \lim_{\tau\to 0}\lim_{l\to 0}\lim_{N\to\infty}\frac{1}{N\tau}\sum_{n=0}^{N-1}(K_{n+1}-K_n)$$
$$= -\lim_{\tau\to 0}\lim_{l\to 0}\lim_{N\to\infty}\frac{1}{N\tau}\sum_{i_0,\ldots,i_{N-1}} p_{i_0,\ldots,i_{N-1}}\log p_{i_0,\ldots,i_{N-1}} \qquad (6)$$

where l and τ have the same meaning as above.

From this definition, it can be seen immediately that it is nothing other than the average rate of loss of information. *K* is independent of the particular partition (thanks to the limit l→0). Figure 2 reveals how *K* represents a measure of chaos: indeed (Chapter 6, [12]):

$$K = \begin{cases} \infty & \text{for random systems} \\ C > 0 & \text{for chaotic-deterministic systems} \\ 0 & \text{for regular motion} \end{cases} \qquad (7)$$

where the definition of a random system can be found in Chapter 3 of [20]. By describing the chaos in a dynamic system, the Kolmogorov entropy is expected to be strongly connected with the Lyapunov exponent $\lambda$; see [21]. For more information about the theoretical aspects of entropy, its generalizations and entropy-like measures, which can be used to measure the complexity of a system, see [22,23,24,25,26].

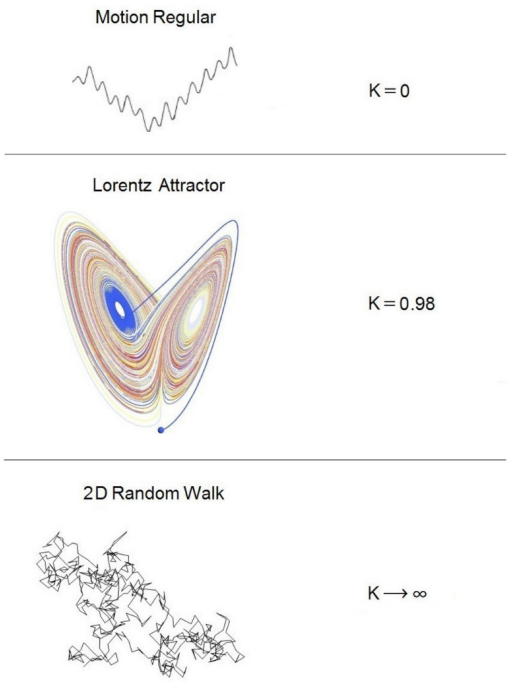


**Figure 2:** Kolmogorov entropy for 1D-regular, chaotic-deterministic and random systems. The attractor is the classical Lorentz attractor [27] with σ=10, R=28, b=8/3 and initial values x(0)=z(0)=0, y(0)=1, while the random motion is given by a 2D-random walk from −1−j to 1+j of 500 elements in which *j* is the imaginary unit.

## REMARKS ON FRACTAL GEOMETRY

A fractal is characterized by the property that each enlargement of this set reveals further details, so it has a structure that is too irregular to be described by a classic mathematical theory (even if a fractal can often be described recursively). Furthermore:

- it is self-similar, *i.e.*, each very small portion of it is exactly or approximately similar to itself (this property has to be understood in the statistical or approximated sense, because a random element can be introduced in the construction of the fractal);
- it is a space-filling curve [**28**].

## Hausdorff–Besicovitch and Box-Counting Dimensions

Among the different definitions of fractal dimensions in use, the Hausdorff–Besicovitch dimension is probably the most important, even if it is not usually used for experimental procedures to find the fractal dimensions of real objects.

Fractal dimensions are very important because they provide a measure of the degree to which new details are revealed at different scales. For example, the fractal dimension of the coastline of Great Britain is about 1.21.2 (Chapter 2, [29]). In order to define the Hausdorff–Besicovitch dimension, some remarks on fractal geometry are given [5,6].

### Theorem 4

(See Figure 3). *If* $n \in \mathbb{Z}^+$ *and A is a bounded subset of Euclidean metric space* $\mathbb{R}^n$*, then there exists a unique number* $D_H \in [0,n]$*, such that:*

$$\mathcal{M}_s(A) = \begin{cases} \infty & \text{if } s < D_H \text{ and } s \in [0,\infty) \\ 0 & \text{if } s > D_H \text{ and } s \in [0,\infty) \end{cases} \tag{8}$$

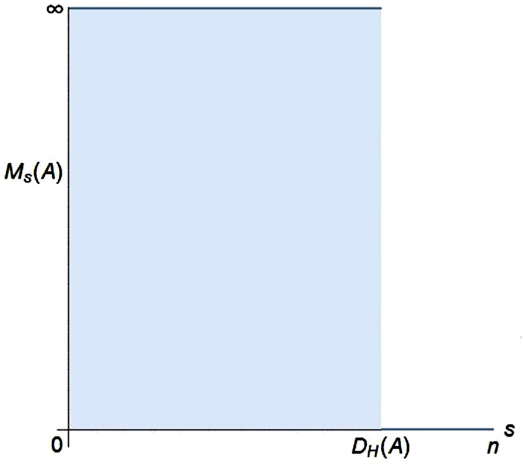


**Figure 3:** Graph of the $M_s(A)$, where *A* is a bounded subset of the Euclidean metric space $\mathbb{R}^n$. It takes only two possible values, and the Hausdorff–Besicovitch dimension of *A* is given by the value of *s* in which there is the jump from ∞ to zero.

## Proof.

See Chapter 3 in [**6**].

## Definition 5

(Hausdorff–Besicovitch dimension)**.** *Under the hypotheses of Theorem* (4)*, the correspondent real number* $D_H$ *present in Equation* (8) *is called the Hausdorff–Besicovitch dimension of A, and it is generally indicated with* $D_H(A)$.

From this last definition, it follows that the Hausdorff–Besicovitch dimension of a bounded subset $A \in \mathbb{R}^n$ is a non-negative number $D_H$, such that:

$$\mathcal{M}_s(A) = \begin{cases} \infty & \text{if } 0 \leq s < D_H(A) \\ 0 & \text{if } s > D_H(A) \end{cases} \tag{9}$$

Therefore, the Hausdorff measure of *A*, *i.e.*, $M_s(A)$, might be equal to zero, infinity or such that $0<M_s(A)<\infty$. In Figure 3, the plot of $M_s(A)$ is presented as a function of *s*, which shows us that $D_H(\cdot)$ is the critical value of the variable *s* in the jump of $M_s(A)$ from $\infty$ to zero.

At this point, the definition of the fractal set can be provided. It is to be recalled that $D_T(A) \leq D_H(A)$, where $D_T(A)$ represents the topological dimension of the bounded subset *A* of $\mathbb{R}^n$ (p. 3, [30]).

## Definition 6

(Fractal set)**.** *A bounded subset* $A \in \mathbb{R}^n$ *is fractal (in the sense of Mandelbrot) if it holds that* $D_T(A)<D_H(A)$*, where the difference* $D_H(A)-D_T(A)$ *is called the fractal degree of A.*

The Hausdorff–Besicovitch dimension is not particularly useful in engineering or applied sciences, because its calculation is not very easy, so another definition of the fractal dimension more suitable to compute the fractal dimension for problems of mathematical modeling was introduced [6,31].

## Definition 7

(Box-counting dimension)**.** *Let* (X,d) *be a metric space and* $A \in H(X)$*, where* H(X) *denotes the space of non-empty compact subsets of X.*

*Let* $N_\delta(A)$, $\forall\delta>0$ *be the smallest number of closed balls of radius* $\beta$ *needed to cover A. The lower and upper box-counting dimensions of A, denoted* $D_{UB}(A)$ *and* $D_{LB}(A)$*, respectively, are defined as:*

$$D_{UB}(A) \triangleq \lim_{\delta\to 0} \sup \frac{\log N_\delta(A)}{\log(1/\delta)}$$

$$D_{LB}(A) \triangleq \lim_{\delta\to 0} \inf \frac{\log N_\delta(A)}{\log(1/\delta)}$$

*When* $D_{UB}(A)=D_{LB}(A)$*, the following limit exists and is called the box-counting dimension of A, denoted* $DB(A)$*:*

$$D_B(A) \triangleq \lim_{\delta\to 0} \left\{ \frac{\log N_\delta(A)}{\log(1/\delta)} \right\} = -\lim_{\delta\to 0} \left\{ \frac{\log N_\delta(A)}{\log \delta} \right\} \tag{10}$$

The box-counting dimension of an object does not exactly have to be equal to the Hausdorff–Besicovitch dimension, even though they can be really close at times. This new definition of the fractal dimension is given by the minimum number of objects needed to cover the fractal set.

In Figure 4, it is shown how the box-counting dimension works to compute the length of England's coastline: looking at the first iterations, the meaning of the adjective box-counting is clear.

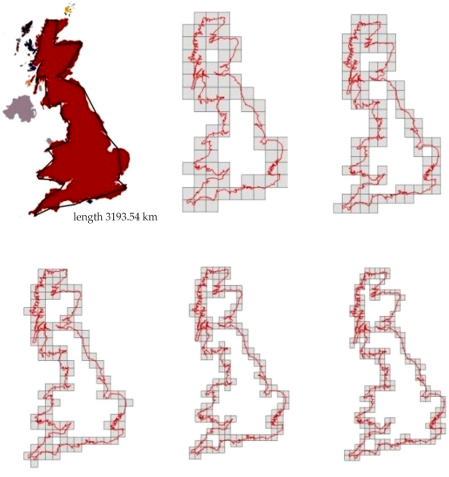


Figure 4: Here, the first steps of the box-counting procedure about England's coastline are represented.

In general, the limit in Equation (10) might not exist; hence, the box-counting and Hausdorff–Besicovitch dimensions are linked by the following relation: $D_H(A) \leq D_{LB}(A) \leq D_{UB}(A)$ (Chapter 3, [6]).

## Iterated Function System and Pre-Fractals

It is to be recalled that a contraction on a metric space (X,d) is a transformation $f:X \rightarrow X$, such that:

$$d(f(x), f(y)) \leq s\, d(x, y), \quad \forall x, y \in X \tag{11}$$

where the number *s*, called the contractivity factor for *f*, belongs to (0,1).

The famous contraction mapping theorem states that every contraction *f* on a complete metric space (X,d) has exactly one fixed point $x_f \in X$, and the sequence of iterations $\{f^n(x)\}n \geq 0$ converges to $x_f$, $\forall x \in X$ (pp. 76–77, [5]).

Clearly any contraction is continuous. If the equality holds in Equation (**11**), *f* is called a contracting similarity, because it transforms sets into geometrically similar sets.

It is now time to give the definition of an important procedure concerning fractals.

## Definition 8

(Iterated function system)**.** *The iterated function system (IFS) is a couple* {X,F}*, where* $F:H(X) \rightarrow H(X)$ *is defined through a finite family of contractions* $\{S_i\}_{i=1}^{m}$ *on the complete metric space* (X,d)*, with* $m \geq 2$*, and* H(X) *denotes again the space of non-empty compact subsets of X. Moreover, the set* $A \in H(X)$ *is called the attractor (or sometimes invariant set) for the IFS if:*

$$A = F(A) = \bigcup_{i=1}^{m} S_i(A) \tag{12}$$

Technically speaking, the operator *F* given by Equation (12) is called the Hutchinson operator associated with the IFS $\{S_1, S_2, ..., S_m\}$ [5,32]. From the definition above, it is clear that the attractor for the IFS is also its unique fixed point. This is the fundamental property of an IFS, because this attractor is often a fractal. An IFS has a unique (non-empty compact) attractor (Chapter 9, [6]), but its introduction brings with it two main problems: the first one

shows the way to represent a given set as the attractor of some IFS, while the second is to reconstruct the IFS starting from its attractor (p. 126, [6]).

Both of these two problems can often be solved by inspection, especially if $F$ has a self-similar structure (see Figure 5).

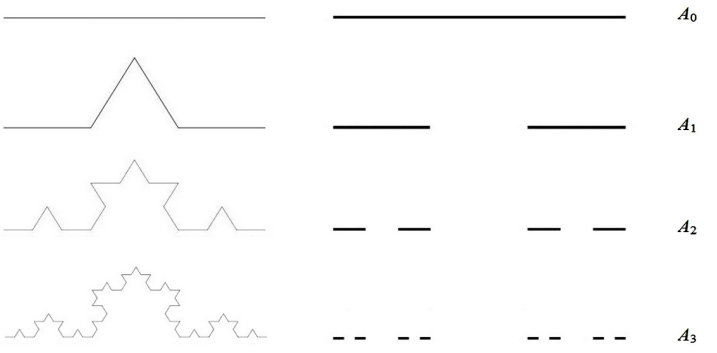


**Figure 5:** Here, the von Kock curve (on the left) and the middle third Cantor set (on the right) are shown: $A_0$ is the initiator of length equal to one in both cases; in the generator $A_1$ for the von Kock curve, the middle third of the unit interval is replaced by the other two sides of an equilateral triangle, while that of the middle third Cantor set is obtained removing the middle third of the interval.

For the majority of the fractals suitable for an application in antenna theory, the thesis of the Moran–Hutchinson theorem (pp. 130–132, [6]) holds true, so:

$$\sum_{j=1}^{m} c_j^s = 1 \tag{13}$$

where $A$ is the attractor of the IFS with contraction factors $c_1, ..., c_m$ and $s = D_H(A) = D_B(A)$.

This theorem provides us the possibility to compute the fractal dimension of many self-similarity fractals. Indeed, let us consider the von Koch curve and the middle third Cantor set (see Figure 5): for the first one, it is:

$$4\left(\frac{1}{3}\right)^s = 1 \Rightarrow s_{koch} = \frac{\log 4}{\log 3} \approx 1.26186 \tag{14}$$

while for the other set, we get:

$$2\left(\frac{1}{3}\right)^{s} = 1 \Rightarrow s_{cant} = \frac{\log 2}{\log 3} \approx 0.63093 \tag{15}$$

IFS can be applied to all self-similarity structures, especially for the simulation of real objects with fractal properties, like fractal antennas.

It is well known that fractals are only mathematical abstractions (because it is impossible to iterate indefinitely in the real word). In addition, numerical simulations show how the fractal modeling in antenna theory provides substantial advantages within a certain value of the iteration m∗m* (typically, for fractal antennas, it is not greater than six). Beyond this value, the benefits are negligible. It is clear that all self-similar structures in nature are nothing other than fractals arrested at a prefixed iteration, *i.e.*, pre-fractals (geometrical objects characterized by a finite number of fractal iterations).

## FRACTAL ANTENNAS

In order to minimize the antenna size holding a high radiation efficiency, a fractal approach to model its geometrical configuration can be considered.

The two fundamental properties of a fractal (*i.e.*, self-similarity and space-filling) allow fractal antennas to have an efficient miniaturization and multiband characteristics.

The well-known log-periodic antennas, introduced by DuHamel and Isbell around the 1950s and closely paralleling the independent-frequency concept [7], might be considered the first fractal antenna of history. Another example of a self-similar antenna discovered in the same period is the spiral antenna (see Figure 6).

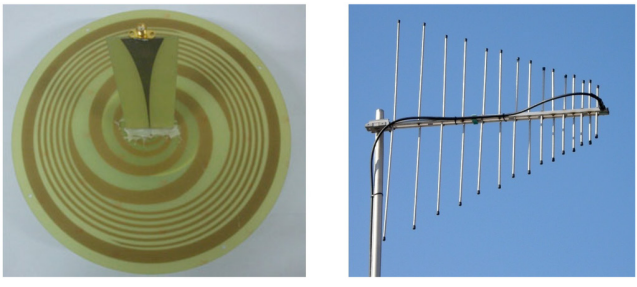

**Figure 6:** Archimedean spiral antenna (on the left) and commercial log-periodic dipole antenna of 16 elements (on the right) [7].

However, their true origin may be traced back to 1988, when Nathan L. Cohen, a Boston University radio astronomer, published a paper about this new type of antenna [33].

Fractal antennas have not only a large effective length, but also a simple matching circuit, thanks to the contours of their geometrical shape, which is able to generate a capacity or an inductance. For instance, a quarter-wavelength monopole may be transformed into a smaller antenna using the von Koch curve (see Figure 5).

A big part of the research on fractal antennas has been done by *Fractal Antenna Systems Inc.*, an American company founded by Cohen.

Carles Puente Baliarda (Polytechnic University of Catalonia) was the first to treat these antennas as multiband antennas. In 1998, he won the award of "innovative IT products with evident market potential" due to his pioneering research in fractal antennas (for a total of € 200,000), while he and his company (*Fractus S.A.*) were the finalists for the European Inventor Award 2014, showing the great potentials of these antennas.

In 2011, 9.79.7 billion fractal-based antenna units were supplied worldwide (a report by BCC Research).

## Sierpinski Gasket and Hilbert Antenna

The Sierpinski triangle *T* can be constructed from an equilateral triangle by the removal of inverted equilateral triangles (see **Figure 7**). It is a fractal and attractive fixed set. Considering Figure 7, it is:

$$\sum_{j=1}^{3} c_j^s = 3\left(\frac{1}{2}\right)^s = 1 \tag{16}$$

since all of the contraction factors $c_1$, $c_2$, $c_3$ are equal to $\frac{1}{2}$. Therefore:

$$s = D_H(T) = D_B(T) = \frac{\log 3}{\log 2} \approx 1.58496 \tag{17}$$

This fractal may be also generated by an IFS (Chapter 9, [6]).

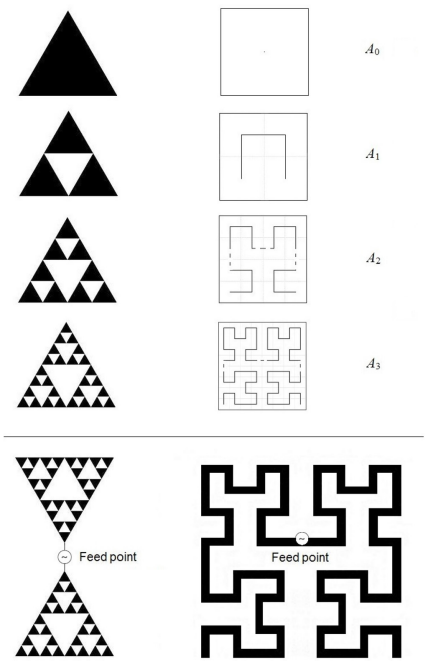


**Figure 7:** A Sierpinski triangle (on the left) and a Hilbert curve (on the right) are shown: as in Figure 5, $A_0$ is the initiator, and $A_1$ is the generator. The Sierpinski triangle is constructed using the iterated function system (IFS), while the other construction is that of David Hilbert. The two relative antennas are shown below with their feed points.

There exist different versions of the Sierpinski triangle. The shape can be modified in many ways, and they are often used in engineering and applied sciences.

The Sierpinski (gasket) antenna belongs to the class of multiband fractal antennas based on the Sierpinski triangle. The classical Sierpinski dipole is shown in Figure 7. It is probably a fractal antenna with more applications, from wireless communication systems (GSM, UMTS and WLAN) through RF MEMS (radio frequency microelectromechanical system) to get to space probe design and ANN (artificial neural network) theory [34,35].

The famous Hilbert curve is a continuous fractal space-filling curve, *i.e.*, it fills the plane without leaving any gaps. Hilbert introduced it as a modification of the Peano curve [28].

There are important differences between these two curves. Indeed, it is not possible to construct the Hilbert curve *H* through the IFS (while for the

other one, this procedure is applicable). The reason is that the steps in the Hilbert curve's construction are not self-similar, *i.e.*, they are not divisible in a number of parts similar to the initial figure.

The original construction of the Hilbert curve is extraordinarily elegant: it starts with a square $A_0$, while in the first step (see Figure 7), the curve $A_1$ connects the centers of the quadrants by three line segments (having a size of one). In the second step, four copies (reduced by 1/2) of this initial stage are made and placed into the quarters (see again Figure 7). In this way, the first copy is clockwise rotated and the last one counter-clockwise rotated by 90 degrees. After this, the start and end points of these four curves are connected using three line segments (of a size of 1/2), and we call the resulting curve $A_2$.

In the third iteration, the scaling is done again by 1/2, and four copies are placed into the quadrants of the square (as in the first step). They are again connected by three line segments (of a size of 1/4) obtaining $A_3$, and so on.

In Figure 7, it can be noticed that each successive stage consists of four copies of the previous one, connected with additional line segments. Therefore, the curve is scaled down by the ratio $\frac{1}{2}$, and four copies are made; so:

$$\sum_{j=1}^{4} c_j^s = 4\left(\frac{1}{2}\right)^s = 1 \tag{18}$$

hence:

$$\left(\frac{1}{2}\right)^s = \frac{1}{4} \Rightarrow s = D_H(H) = D_B(H) = 2 \tag{19}$$

Naturally, the topological dimension of $H$ is one, since it consists only of line segments. Therefore, the Hilbert curve is a fractal for all intents and purposes.

An alternative procedure to IFS is that of the so-called L-systems [36].

In Figure 7, a Hilbert dipole is also shown, where the feed source point is placed at the point of symmetry for these two pre-fractals.

The Hilbert antenna is especially used in spatial communications, like RF MEMS design [37] and, generally speaking, in each (telecommunication) system where the space available for the antenna is limited [38].

## The Results of Best and HRC Conditions

A fractal approach is not the only way to miniaturize an antenna; indeed, there exist few particular non-fractal modifications of the classical von Koch dipole that could have the same performance [10].

In addition, it is clear that fractal geometry does not uniquely translate the electromagnetic behavior of the antenna. The geometrical configuration alone (fractal or non-fractal) could not be the only significant factor that determines the resonant behavior of wire antennas: indeed, a fractal configuration does not represent alone a guarantee of the highest antenna efficiency [11].

The same applies to the loop antennas. It is well known that the main advantage of the fractal loop antennas is that they have a high radiation resistance on a "small" physical area. In Figure 8 (top side), three examples of non-fractal antennas are shown. They offer similar or, in some cases, improved performance over their fractal-antenna counterparts, like the Minkowski antenna. The reason is that the radiation resistance of an electrically-small loop, given by [10]:

$$R_r \approx 31,200 \left( \frac{Area_{loop}}{\lambda^2} \right)^2 \Omega \tag{20}$$

where $\lambda$ is the working wavelength, is generally not valid for a loop antenna with complex geometry. However, there are few small non-fractal loop antennas with similar or better performance than their fractal counterparts (see Figure 8, top side).

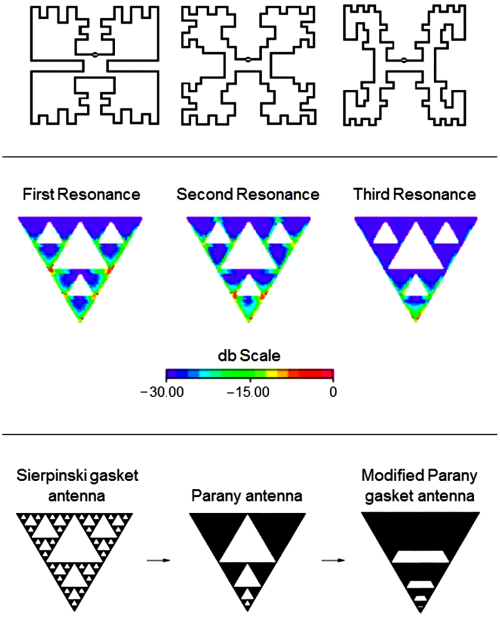


**Figure 8:** Examples of non-fractal antennas that offer similar performance over their fractal counterparts. Three different non-fractal antennas are presented above: they outperform their fractal counterparts, while the current distribution on the Sierpinski gasket antenna at the first three resonance frequencies is shown in the middle of the page. The modified Parany antenna (starting from the classical Sierpinski gasket antenna) is represented below.

In order to investigate the significance of self-similarity in determining the multiband behavior of the fractal antennas, Steven R. Best has presented a comparison of the multiband behavior of the Sierpinski gasket and several modified gaskets where the major portions of the self-similar structure were modified or eliminated [11].

His numerical simulations reveal that many of the self-similar fractal gap structures can be eliminated from the Sierpinski gasket, without modifying its multiband behavior.

Best showed how the total self-similar fractal gap structure is not the primary factor that determines the multiband behavior, because the Sierpinski gasket and modified Parany gasket antenna have the same behavior [11]. Therefore, for all of the Sierpinski-based antennas, the multiband behavior depends on the small isosceles trapezia located in the center of the modified Parany gasket antenna, as shown in Figure 8 (bottom side).

It would seem that some non-fractal geometries could be a good substitute for their fractal counterparts, but this is manifestly untrue.

Indeed, the results obtained by Best represent only a very few special cases, and these antennas do not belong to a family of radiators. Furthermore, the so-called *HCR conditions* can be considered [39] (they provide a necessary and sufficient condition for all frequency independent antennas). This criterion reveals that an antenna satisfies this property if and only if the radiating structure is both self-similar and origin symmetric about a point. It is clear that some non-fractal radiators might belong to this second one, potentially giving them the same performance of a fractal antenna that is non-symmetric about a point.

## The Entropy of a Fractal Antenna

In addition to the box-counting dimension, another convenient way to estimate the fractal dimension is the so-called generalized fractal dimension (or Rényi dimension) $D_\alpha$, given by [40]:

$$D_\alpha(X) \triangleq \begin{cases} \dfrac{1}{\alpha-1}\lim\limits_{\delta\to 0}\dfrac{\log_b \sum\limits_{i=1}^{N} p_i^\alpha}{\log_b \delta} & \alpha > 0,\ \alpha \neq 1 \\ \lim\limits_{\delta\to 0}\dfrac{\sum\limits_{i=1}^{N} p_i \log_b p_i}{\log_b \delta} & \alpha = 1 \end{cases} \tag{21}$$

In this definition, N=N(δ) is the total number of boxes with $p_i>0$, where also here, the most commonly-used values are b=2 and b=e.

Considering the definition of Rényi entropy Equation (7), it is clear that:

$$D_\alpha = -\lim_{\delta\to 0}\frac{H_\alpha(\delta)}{\log_b \delta} \tag{22}$$

As α→0,

$$D_0 = \lim_{\delta\to 0}\frac{\log_b \sum\limits_{i=1}^{N} 1}{\log_b\left(\frac{1}{\delta}\right)} = \lim_{\delta\to 0}\frac{\log_b N}{\log_b\left(\frac{1}{\delta}\right)} \tag{23}$$

which is nothing but the fractal dimension. The numerator of the last equation is simply the Hartley entropy. It can be shown similarly, as for the definition of Rényi entropy, that

$$\lim_{\alpha \to 1} D_\alpha(X) = D_1(X)$$

Therefore, the dimension $D_\alpha$ is a generalization of $D_1$, which is called the information dimension. Indeed, $D_1$ characterizes the information required for the determination of the point location in some cell *i*.

According to Equation (**21**), it also follows that:

$$D_2 = \lim_{\delta \to 0} \frac{\log_b \sum_{i=1}^{N} p_i^2}{\log_b \delta} \tag{24}$$

This quantity is called the correlation dimension, because it is very useful to detect chaotic behavior.

Taking still into account Equation (21), α is clearly a nonincreasing function of *α*, *i.e.*, $D_\alpha \geq D_{\alpha'}$ at $\alpha' > \alpha$: in particular, $D_0 \geq D_1 \geq D_2$.

Therefore, the generalized fractal dimension $D_\alpha$ provides a direct measurement of the fractal properties of an object. Several values of the momentum order *α* correspond to well-known generalized dimensions.

Equation (22) cannot be applied practically, and it is only possible to get an approximation fixing a small value of *δ*, but strictly greater than zero. Therefore, in applied sciences and engineering, Equation (**22**) becomes:

$$H_\alpha = - D_\alpha \log_b \delta = D_\alpha \log_b \epsilon \tag{25}$$

where $H_\alpha = H_\alpha(\delta)$).

This equation shows us that the entropy of a region of size *δ* is a function of the box-counting fractal dimension $\epsilon = 1/\delta$: the entropies of analyzed regions (with size *δ*) can be calculated from the three spatial dimensions through Equation (25) [16].

Right now, the Rényi entropy has to be computed for the geometric configuration of each fractal antenna. It is easy to create an algorithm for its computation using Equation (25). This procedure consists of the classical algorithm for numerical estimating DαDα of affine RIFS-invariant measures; see [41,42]. The Rényi entropy will be computed through Equation (25), considering the logarithm of the cell size (see Figure 9 below).

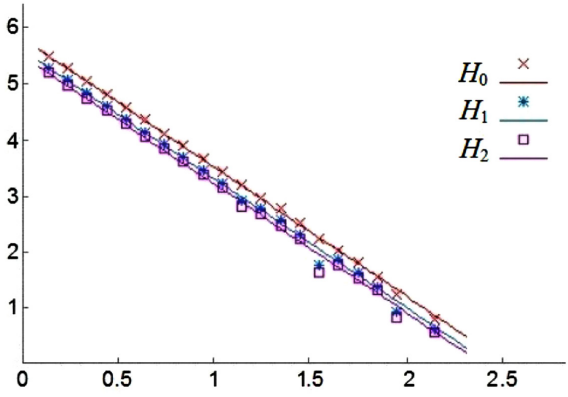


**Figure 9:** The Rényi entropy $H_\alpha$ of a Sierpinski gasket (Figure 7) with α=0,1,2: the plot shows us that Hartley entropy $H_0$ is an upper to both Shannon entropy $H_1$ and collision entropy H2H2. The main limit of this procedure is clearly the precision of the triangulation.

With this procedure, it is possible to compute the entropy for a fractal radiator, but it must be completely modified for each class of fractal antennas.

However, the general definition of entropy for a small antenna, in order to better understand how the chaoticness of the structure may affect its performance, remains an open problem.

## CONCLUSIONS

The main fractals used in antenna theory have been examined, and the explanation as to how the Rényi entropy can be computed through the generalized fractal dimension of a set has been provided. Therefore, the entropy of a fractal antenna can be calculated accordingly, in which the input data are essentially the complexity of the shape, as described in this article for the Sierpinski gasket antenna. The numerical estimation of the generalized fractal dimension $D_\alpha$ (see [41]) is based both on an integration technique over the fractal measures and a triangulation method. It yields good results for the range $\alpha \geq 0$ in an efficient and robust manner. Clearly, the computation of $D_\alpha$ requires the aid of the box-counting algorithm. Furthermore, the developed code is general enough to be used on arbitrary geometrical shapes; hence, this algorithm may be applied both for other fractal antennas and for quantum dynamical systems in order to evaluate their chaoticness.

## REFERENCES


1. Shannon, C.E. A mathematical theory of communication. *Bell Sys. Tech. J.* 1948, *27*, 379–423, 623–656.
2. Garrido, A. Classifying entropy measures. *Symmetry* 2011, *3*, 487–502.
3. Rényi, A. On measures of information and entropy. In Proceedings of the Fourth Berkeley Symposium on Mathematics, Statistics and Probability, Berkeley, CA, USA, 20 June–30 July 1960; Volume 1, pp. 547–561.
4. Kolmogorov, A.N. A new metric invariant of transient dynamical systems and automorphisms in Lebesgue spaces. *Dokl. Akad. Nauk SSSR (NS)* 1958, *119*, 861–864.
5. Barnsley, M.F. *Fractals Everywhere: New edition*; Cambridge University Press: San Diego, CA, USA, 2012.
6. Falconer, K.J. *Fractal geometry: Mathematical Foundations and Applications*; John Wiley & Sons: Hoboken, NJ, USA, 2003.
7. Balanis, C.A. *Antenna Theory: Analysis and Design*; John Wiley & Sons: Hoboken, NJ, USA, 2005.
8. Ram, R.J.; Sporer, R.; Blank, H.-S.; Maccarini, P.; Chang, H.-C.; York, R.A. Chaos in microwave antenna arrays. *IEEE MTT-S Int. Microw. Symp. Dig.* 1996, *3*, 1875–1878.
9. Valdivia, J.A. The Physics of High Altitude Lightning. Ph.D. Thesis, The University of Maryland, College Park, MD, USA, 1997; pp. 48–50.
10. Best, S.R. A Discussion on the Significance of Geometry in Determining the Resonant Behavior of Fractal and Other Non-Euclidean Wire Antennas. *IEEE Antennas Propag. Mag.* 2003, *45*, 9–28.
11. Best, S.R. Operating Band Comparison of the PerturbatedSierpinski and Modified Parany Gasket Antennas. *IEEE Antennas Wirel. Propag. Lett.* 2002, *1*, 35–38.
12. Schuster, H.G.; Just, W. *Deterministic Chaos: An Introduction*; Wiley-VCH: Weinheim, Germany, 2005.
13. Papoulis, A.; Pillai, S.U. *Probability, Random Variables and Stochastic Processes*; McGraw-Hill: New York, NY, USA, 2002; Chapter 14.
14. Csiszár, I. Axiomatic characterization of information measures. *Entropy* 2008, *10*, 261–273.
15. Takens, F.; Verbitski, E. Generalized entropies: Rényi and correlation

integral approach. *Nonlinearity* 1998, *11*, 771–782.

16. Zmenskal, O.; Dzik, P.; Vesely, M. Entropy of fractal systems. *Comput. Math. Appl.* 2013, *66*, 135–146.
17. Marsden, J.E.; Hoffman, M.J. *Elementary Classical Analysis*; W. H. Freeman and Company: San Francisco, CA, USA, 1993.
18. Amigó, J.M.; Keller, K.; Unakafova, V.A. On entropy, entropy-like quantities, and applications. *Discret. Contin. Dyn. Syst. B* 2015, *20*, 3301–3343.
19. Zanette, D.H. Generalized Kolmogorov entropy in the dynamics of the multifractal generation. *Physica A* 1996, *223*, 87–98.
20. Bhattacharya, R.; Majumdar, M. *Random Dynamical Systems: Theory and Applications*; Cambridge University Press: New York, NY, USA, 2007.
21. Pesin, Y.B. Lyapunov characteristic exponents and smooth ergodic theory. *Uspeki Mat. Nauk* 1977, *32*, 55–112.
22. Falniowski, F. On the connections of generalized entropies with Shannon and Kolmogorov-Sinai entropies. *Entropy* 2014, *11*, 3732–3753.
23. Crutchfield, J.P.; Feldman, D.P. Regularities unseen, randomness observed: Levels of entropy convergence. *Chaos* 2003, *13*, 25–54.
24. Ferenczi, S. Measure-theoretic complexity of ergodic systems. *Isr. J. Math.* 1997, *100*, 189–207.
25. Blanchard, F.; Host, B.; Maass, A. Topological complexity. *Ergod. Theory Dyn. Syst.* 2000, *20*, 641–662.
26. Galatolo, S. Global and local complexity in weakly chaotic systems. *Discret. Contin. Dyn. Syst.* 2003, *9*, 1607–1624.
27. Farmer, D.; Crutchfield, J.; Froehling, H.; Packard, N.; Shaw, R. Power spectra and mixing properties of strange attractors. *Ann. N. Y. Acad. Sci.* 1980, *375*, 453–472.
28. Tricot, C. *Curves and Fractal Dimension*; Springer: New York, NY, USA, 1995.
29. Mandelbrot, B.B. *The Fractal Geometry of Nature*; W. H. Freeman and Company: New York, NY, USA, 1982.
30. Hata, M.; Kigami, J.; Yamaguti, M. *Mathematics of Fractals*; American Mathematical Society: Providence, RI, USA, 1997.
31. Addison, P.S. *Fractal and Chaos: An Illustrated Course*; Institute of

Physics Publishing: London, UK, 1997.

32. Hutchinson, J.E. Fractals and self similarity. *Indiana Univ. Math. J.* 1981, *30*, 713–747.
33. Cohen, N.L. Fractal's New Era in Military Antennas Design. Available online: http://defenseelectronicsmag.com/site-files/defenseelectronicsmag.com/files/archive/rfdesign.com/mag/508RFDSF1.pdf (accessed on 4 March 2016).
34. Hwang, K.C. A Modified Sierpinski Fractal Antenna for Multiband Application. *IEEE Antennas Wirel. Propag. Lett.* 2007, *6*, 357–360.
35. Puente-Baliarda, C.; Romeu, J.; Pous, R.; Cardama, A. On the behavior of the Sierpinski multiband fractal antenna. *IEEE Antennas Propag.* 1998, *46*, 517–524.
36. Peitgen, H.; Jürgens, H.; Saupe, D. *Chaos and Fractal: New Frontiers in Science*; Springer: New York, NY, USA, 2004.
37. Vinoy, K.J.; Varadan, V.K. Design of reconfigurable fractal antennas and RF-MEMS for spaced-based communication systems. *Smart Mater. Struct.* 2001, *10*, 1211–1223.
38. Krzysztofik, W.J. Fractal Geometry in Electromagnetics Applications—From Antenna to Metamaterials. *Microw. Rev.* 2013, *19*, 3–14.
39. Hohlfeld, R.G.; Cohen, N.L. Self-Similarity and the Geometric Requirements for Frequency Independence in Antennae. *Fractals* 1999, *7*, 79–84.
40. Sheluhin, O.I.; Smolskiy, S.M.; Osin, A.V. *Self-Similar Processes in Telecommunications*; John Wiley & Sons: Chichester, UK, 2007.
41. Martyn, T. A method for numerical estimation of generalized Rényi dimensions of affine Recurrent IFS invariant measures. In *Thinking in Patterns: Fractals and Related Phenomena in Nature*; Novak, M.N., Ed.; World Scientific Publishing: Singapore, Singapore, 2004; pp. 79–90.
42. Słomczyński, W.; Kwapień, J.; Życzkowski, K. Entropy computing via integration over fractal measures. *Chaos* 2000, *10*, 180–188.

# 4

# *Edges of Saturn's Rings are Fractal*

**Jun Li[1] and Martin Ostoja-Starzewski[2]**

[1] Division of Engineering and Applied Science, California Institute of Technology, 91125 Pasadena, CA, USA
[2] Department of Mechanical Science & Engineering, Institute for Condensed Matter Theory and Beckman Institute, University of Illinois at Urbana-Champaign, 61801 Urbana, IL, USA

## ABSTRACT

The images recently sent by the Cassini spacecraft mission (on the NASA website http://saturn.jpl.nasa.gov/photos/halloffame/) show the complex and beautiful rings of Saturn. Over the past few decades, various conjectures were advanced that Saturn's rings are Cantor-like sets, although no convincing fractal analysis of actual images has ever appeared. Here we focus on four images sent by the Cassini spacecraft mission (slide #42 "Mapping Clumps in Saturn's Rings", slide #54 "Scattered Sunshine", slide #66 taken two weeks before the planet's Augus't 200'9 equinox, and

**Citation:** Li, J., &Ostoja-Starzewski, M. (2015). Edges of Saturn's rings are fractal. SpringerPlus, 4(1), 158.).

slide #68 showing edge waves raised by Daphnis on the Keeler Gap) and one image from the Voyager 2' mission in 1981. Using three box-counting methods, we determine the fractal dimension of edges of rings seen here to be consistently about 1.63 ~ 1.78. This clarifies in what sense Saturn's rings are fractal.

## BACKGROUND

The images recently sent by the Cassini spacecraft mission (available on the NASA website http://saturn.jpl.nasa.gov/photos/halloffame/) show the complex and beautiful rings of Saturn. Beginning with (Mandelbrot, 1982; Avron and Simon, 1981; Fridman and Gorkavyi, 1994), there have been conjectures that radial cross-sections of Saturn's rings are Cantor sets, but, to the best of our knowledge, no convincing fractal analyses of actual images ever appeared. Of the 87 Cassini images, in Figure 1 (a) we reproduce slide #42 bearing the title "Mapping Clumps in Saturn's Rings," in Figure 1 (b) the slide #54 titled "Scattered Sunshine," in Figure 1 (c) we reproduce slide #66 taken two weeks before the planet's August 2009 equinox, and in Figure 1 (d) slide #68 showing edge waves raised by Daphnis on the Keeler Gap. The first of these is a false-color image of Saturn's main rings made by combining data from multiple star occultations using the Cassini ultraviolet imaging spectrograph. In the second of these, Saturn's icy rings shine in scattered sunlight, from about 15° above the ring plane. In the third image, a part of the Cassini Division, between the B and the A rings, appears at the top of the image, showing ringlets in the inner division, while in the fourth Daphnis cruises through the Keeler Gap, raising edge waves in the ring material as it passes. The first two photographs show the curved geometry of Saturn's main rings with a low opening angle, while the latter two reflect the details of a part of the rings. Finally, in Figure 1 (e), we reproduce the image sent by 'Voyager 2' spacecraft in 1981 (http://solarsystem.nasa.gov/planets/images/inset-saturn-rings-large.jpg). The selected set of images represent Saturn's rings from a variety of view angles and regions.

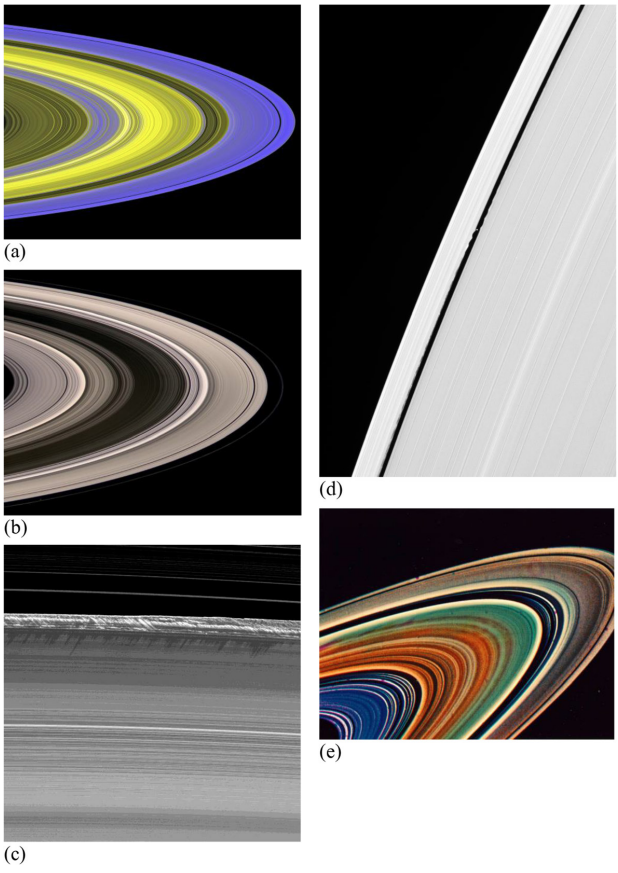


**Figure 1:** (a,b,c,d,e): The original images of the Cassini and Voyager missions.

## RESULTS AND DISCUSSION

As is well known (Mandelbrot, 1982), the fractal dimension $D$ comes from estimation of the slope of log($n$)-log($r$) in $n \propto r^{-D}$, where $n$ is the number of boxes with size $r$ needed to cover the region of interest. The local slopes of log($n$)-log($r$) are also acquired to determine optimal cut-offs of box sizes. The cut-offs are specified where the local slope varies strongly. The log($n$)-log($r$) plots of the three box counting methods for images of Figure 1 (a), (d), and (e) are shown in Figures 2, 3 and 4, respectively. Since the plots for Figures 1 (b) and (c) are very similar to the others, they are not shown here in order to save space. Note that, for modified box counting, $r$ denotes

the ratio of image size to box size, unlike power 2 or divider box counting, where *r* is the box size.

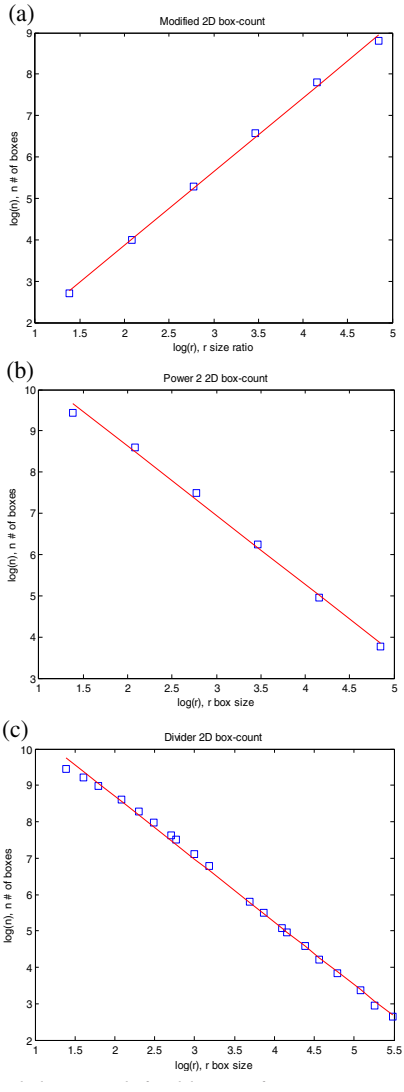


**Figure 2**: Results of box counting method to estimate the fractal dimension of image (a) in Figure 1 : (a) Modified box counting; (b) Power 2 box counting; (c) Divider box counting.

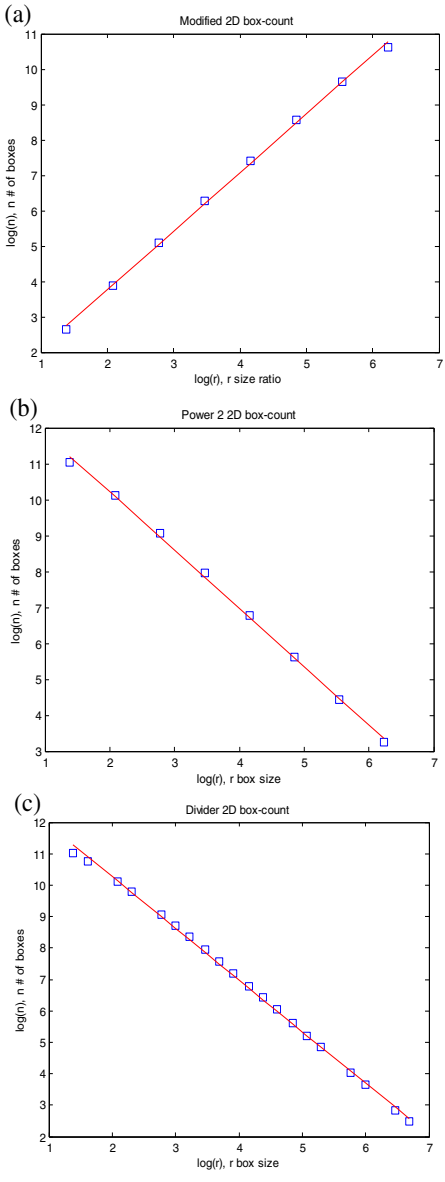


**Figure 3**: Results of box counting method to estimate the fractal dimension of image (d) in Figure 1 : (a) Modified box counting; (b) Power 2 box counting; (c) Divider box counting.

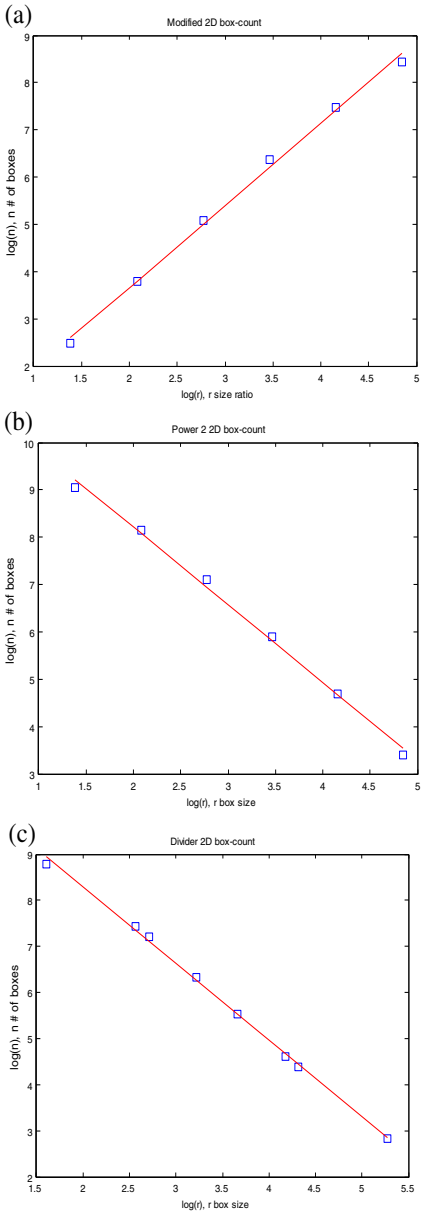


**Figure 4:** Box counting method to estimate the fractal dimension of image (e) in Figure 1 : (a) Modified box counting; (b) Power 2 box counting; (c) Divider box counting.

Note that these images were projections of Saturn's rings from different angles and regions. Following the arguments presented in (Maggi 2008; Meakin 1998), given the fact that the rings' thickness is extremely small compared to their radii, the projection onto the plane of the photograph does not affect the fractal dimension. Besides, the self-similarity of fractals indicates that the fractal dimension of a part is same as that of the whole. Overall, the box counting results of all images are given in Table 1.

**Table 1:** Box counting results

| Image sources | Modified box counting | Power 2 box counting | Divider box counting |
|---|---|---|---|
| Figure 1. (a) | 1.63 | 1.65 | 1.66 |
| Figure 1. (b) | 1.64 | 1.65 | 1.71 |
| Figure 1. (c) | 1.78 | 1.71 | 1.76 |
| Figure 1. (d) | 1.64 | 1.74 | 1.66 |
| Figure 1. (e) | 1.67 | 1.72 | 1.77 |

## CONCLUSIONS

All the images analyzed in this paper yield fractal dimensions in the range 1.63 to 1.78. This is a consistent estimate of the fractal dimension of the rings' edges, regardless of the various image sources we utilized. Indeed, the fact that the rings' edges are fractal provides one more hint to developing models of the intricate mechanics and physics governing these structures of granular matter. Interestingly, somewhat related studies (Feitzinger and Galinski 1987; de la Fuente and de la Fuente 2006a, b) found average fractal dimension ~1.7 for the projected fractal dimension of the distribution of star-forming sites (HII regions) in a sample of 19 spiral galaxies.

## METHODS

Using the box counting method, we determine the fractal dimension of edges of those rings. First, various edge detection methods are performed and compared to optimally identify ring boundaries: 'Sobel', 'Robert', 'Laplacian of Gaussian', 'Canny' and 'Zero-Cross' edge functions in the Matlab Image Processing Toolbox. Furthermore, the morphology operation functions of 'bridge', 'close', 'thicken', 'thin' and 'skel' are employed to connect some isolated pixels and also remove redundant pixels on the boundaries from

consideration of physical reality. It was found that the option of 'Laplacian of Gaussian' edge function with 'close' and 'thin' morphology operation produced optimal appearance of ring boundaries. The resulting edge images are displayed in Figure 5 (a-e), respectively, for the five original images we displayed in Figure 1 (a-e).

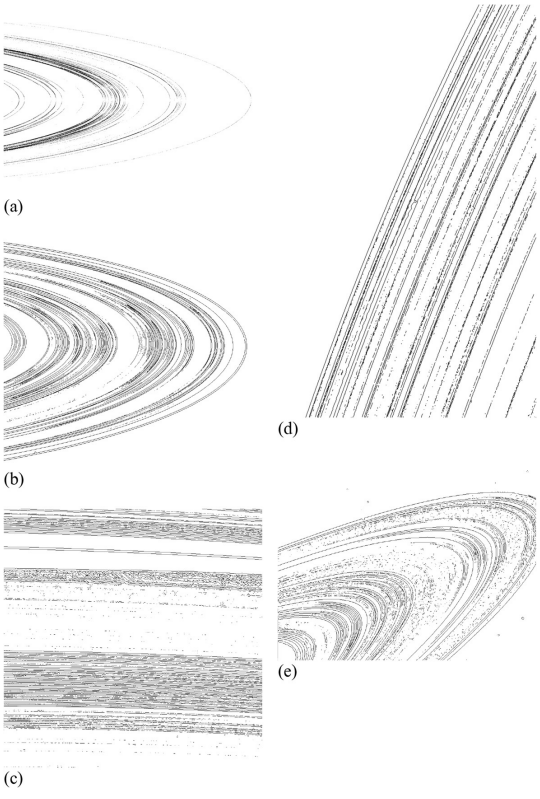


**Figure 5**:(a,b,c,d,e): Images processed, respectively, from Figure 1 (a,b,c,d,e) to capture the ring edges.

We perform three box counting methods to estimate fractal dimensions of the above processed black-white images of Saturn rings, so as to take into account the influences of the sizes and shapes of covering boxes:

- Modified box counting using boxes with shape being self-similar to the global image. This method is well suited for generally rectangular images (Xu and Lacidogna 2011), where the boxes

are rectangles self-similar to the whole image. The selection of the ratio of image size to box size is in powers of 2 for optimal log($n$)-log($r$) regression. When the ratio does not give an integer box size, the box size was chosen to be the closest integer at that ratio.

- Power 2 box counting using boxes with sizes as powers of 2, possessing optimal log($n$)-log($r$) regression. Here the partial boarder effects are evident generally when the image size was not powers of 2. In this case the image was embedded in an empty image with size being powers of 2 closest to the original image size. The box counting was then performed on the 'enlarged' image.
- Divider box counting using boxes with sizes being the dividers of the image size. Subsequent box size may be too close for log($n$)-log($r$) regression, while the border effects can be eliminated.

In particular the cut-offs of box sizes are considered by examining the local slopes of log($n$)-log($r$). Figure 6 shows an example of the local slope of log($n$)-log($r$) for power 2 box counting applied to Figure 1 (a) with $r=2$ to $r=b/2$, where $b$ denotes the image size (after extended to powers of 2). The fine box size $r=2$ tends to be below the average spacing of ring particles, whereas the very coarse box count ($r=b/2$) usually fails to capture structural details. The lower and upper cut-offs of box sizes are then 4 and b/4.

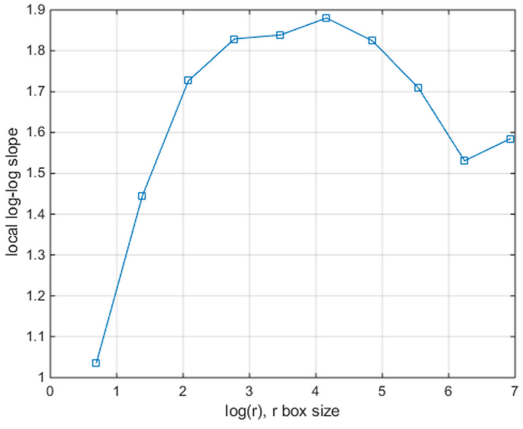


**Figure 6**: An example of the local slope of log(n)-log(r) for power 2 box counting applied to Figure 1 (a) with r=2 to r=b/2, where b denotes the image size (extended to powers of 2).

## ACKNOWLEDGMENT

This work was made possible by the NSF support under the grant CMMI-1030940.

## REFERENCES

1. Avron JE, Simon B (1981) Almost periodic Hill's equation and the rings of Saturn. Phys Rev Lett 46(17):1166–8
2. de la Fuente MR, de la Fuente MC (2006a) The fractal dimensions of the spatial distribution of young open clusters in the solar neighbourhood. AstronAstrophys 452:163–8, Doi:10.1051/0004-6361:20054552
3. de la Fuente MR, de la Fuente MC (2006b) Multifractality in a ring of of star formation: the case of Arp 220. AstronAstrophys 454:473–80, Doi:10.1051/0004-6361:20054776
4. Feitzinger JV, Galinski T (1987) The fractal dimension of star-forming sites in galaxies. AstronAstrophys 179:249–54
5. Fridman AM, Gorkavyi NN (1994) Physics of Planetary Rings. Springer, Berlin
6. Maggi F (2008) Projection of compact fractal sets: application to diffusion-limited and cluster-cluster aggregates. NonlinProcGeophys 15:695–9
7. Mandelbrot BB (1982) The Fractal Geometry of Nature. W.H. Freeman & Co, New York
8. Meakin P (1998) Fractals, scaling and growth far from equilibrium. Cambridge University Press, Cambridge, England
9. Xu J, Lacidogna G (2011) A modified box-counting method to estimate the fractal dimensions. ApplMech Mater 58:1756–61

# 5

# *The Fractal Patterns of Words in a Text: A Method for Automatic Keyword Extraction*

**ElhamNajafi, Amir H. Darooneh**

Department of Physics, University of Zanjan, Zanjan, Iran

## ABSTRACT

A text can be considered as a one dimensional array of words. The locations of each word type in this array form a fractal pattern with certain fractal dimension. We observe that important words responsible for conveying the meaning of a text have dimensions considerably different from one, while the fractal dimensions of unimportant words are close to one. We introduce an index quantifying the importance of the words in a given text using their fractal dimensions and then ranking them according to their importance. This index measures the difference between the fractal pattern of a word in the original text relative to a shuffled version. Because the shuffled text is meaningless (i.e., words have no importance), the difference between the original and shuffled text can be used to ascertain degree of fractality. The

**Citation:** Najafi, E., &Darooneh, A. H. (2015). The fractal patterns of words in a text: a method for automatic keyword extraction. PloS one, 10(6). DOI: journal.pone.0130617

degree of fractality may be used for automatic keyword detection. Words with the degree of fractality higher than a threshold value are assumed to be the retrieved keywords of the text. We measure the efficiency of our method for keywords extraction, making a comparison between our proposed method and two other well-known methods of automatic keyword extraction.

## INTRODUCTION

Language is the human capability for communication via vocal or visual signs. Language can be regarded as a complex system [1], where words are constituents which interact with each other to form particular patterns. Such patterns represent human thoughts, feelings, will, and knowledge which are called meaning. Human language is unique among other communication systems, because there are a lots of words to express the immaterial and intellectual concepts. In addition, the existence of synonymy, polysemy and so on increases its complexity. Texts, as the written form of language, inherit its complexity. A text can be partially understood through regularities in spatial distribution of words and their frequencies. Research has shown that regularity in a text can be expressed as a power law relationship. One of the most well-known power laws is Zipf's law, which shows that if we rank the words in a text from the most common to the least, the frequency of each word is inversely proportional to its rank [2]. A related law, Heaps' law, shows another universal feature of texts: the number of distinct words in a text (i.e., number of word types), changes with the text size (i.e., the number of tokens) in the form of a power law [3]. Another level of regularity is evident only through the pattern of words throughout a text. A text is not just a random collection of words; we can only call this collection a text if it has meaning. In other words, the words in a text must be placed in a specific order to impart meaning. Many power laws cannot capture this fact: any random shuffling process drastically destroys the meaning of a text, but Zipf's law remains unchanged and Heaps' law changes only very slightly [4].

The particular arrangement of words in a specific order arises for two reasons. First, grammatical rules determine where words should be placed within a sentence and specify the position of verbs, nouns, adverbs, and other parts of speech. Grammatical rules make short range correlations between the sequences of words in a sentence. Secondly, a text derives meaning from how the words are arranged throughout. This ordering is

called semantic ordering, and acts across the whole range of the text, hence the long-range correlation can be seen between the positions of any word. The broad meaning of a text also means that different word types have different importance in a text. We can distinguish between two kinds of content words in a text: those which are related to the subject of the text (i.e., the important words), and all others that are irrelevant to it. For a text in cosmology, words like universe, space, big-bang, and inflation are important words. Other words such as is, fact, happening, etc., are irrelevant to the topic of the text. Finding an index for quantifying the importance of words in a given text is crucial to detecting keywords automatically, and provides a very useful starting point for text summarization, document categorization, machine translation and other matters related to automatic information retrieval. Automating these processes is of increasing importance given the increasing size of available information yet limited man-power.

In the current paper, we use the concept of fractal to assign an importance value to every word in a given text. A fractal is a mathematical object (e.g., a set of points in Euclidean space) that has repeating patterns at every scales, it means at any magnification there is a smaller piece of the object that is similar to the whole; this property is called self-similarity. The fractal dimension shows how detail of a fractal pattern changes with scale. It is used as an index of complexity. The fractal dimension of a set is equal or less than the topological dimension of space that the set is embedded in it. We claim that the positions of a word type within the text array form a fractal pattern with a specified dimension that is a positive value less than or equal to one. Based on this fact, an index is presented for ranking the vocabulary words of a given text. The difference between the pattern of a word in the original text versus a randomly shuffled version shows its importance: words with a greater differential between the original and shuffled texts are more important. We compare this approach with other more well-known methods of keyword extraction.

In the following section we review previous research reporting a kind of fractal structure in texts, in order to show that our method is novel. Then we review some basic ideas for keyword extraction which are useful for understanding the different principles currently at work in the field. Finally, we describe our method and how it could be evaluated, and report the results for a sample book.

# BACKGROUND AND RELATED WORKS

## Fractal Structures in Texts

In 1980 G. Altmann made a formula for quantifying of the Menzerath's law [5]. Menzerath-Altmann law says there is a relation between size of a construct and size of its constituents. A system like a language has different levels or constructs, such as syllables, words, syntactic constructions, clauses, sentences and semantic constructs. According to Menzerath-Altmann law, when the size of a construct increases, the size of its constituents decreases, and this holds at every level. Thus, a certain kind of self-similarity exists for each level [6, 7]. Fractal dimension can be calculated for each level. The fractal dimension of a given text is the average value of fractal dimension of levels [8].

For quantitative calculations, texts are usually mapped into time series. A text can be considered as a one dimensional array where elements can be either characters, words or sentences. Ausloos built two time series by replacing each word in the text by their length or frequency [9, 10]. He quantified the complexity in a written text by examining the fractal pattern of its corresponding length and frequency time series, discovering that resulting fractal patterns may be used as an authorship indicator. Furthermore, these length and frequency time series also gave indications of the semantic complexity of the text.

Eftekhari worked on letters instead of words as the constituents of a text, finding that if letter types in a text are ranked from the most common to the least, the frequency of each letter type would be inversely proportional to its rank [11] (i.e., simillar to Zipf's law). If frequency of letter types is plotted versus their ranks in a double logarithmic scale, a straight line is obtained. He called the slope of this line Zipf's dimension. He also suggested a method for calculating fractal dimension of texts, declaring that if letter types are ranked in alphabetical order and frequency of letter types is plotted against their ranks, the slope of such a diagram would be fractal dimension of the literature. Nevertheless, since the data which is used is too disperse he used the so-defined fractal dimension. He also showed that texts exhibit changes in fractal dimension similar to corresponding Zipf's dimension which vary according to the text's size.

## Principles for Keyword Extraction

The first method based on Zipf's analysis of word frequency for keyword extraction was proposed by Luhn [12]. He plotted the Zipf diagram of words, then eliminated words with high and low frequencies, and declared that the words remaining in the mid-range frequencies are the most important words of a text. There are some problems with this method; it omits some important words which have very low frequencies, and may also mistakenly take some common words with mid-range frequencies as keywords. To overcome this deficiency, Ortuño et al. proposed a method based on the concept that important words form clusters [13]. They used standard deviation of distance between consecutive occurrences of a particular word as a measure of word clustering. Words with large standard deviations tend to form clusters and so are more important. Carpena et al. improved this method and introduced the C Value for measuring the importance of words [14] based on their clustering distributions (we review this method in the appendix section in contrast to our own). Another method based on clustering was proposed by Zhou and Slater [15]. They used the density fluctuations of words as a measure of clustering. The method was useful to reduce significance of common words. Mihalcea and Tarau used a method based on the graph theory for detecting the keywords [16]. The text is regarded as a graph with word types nodes with edges occuring between two words where they are adjacent in the text. To extract keywords they introduced the concept of TextRank, calculated similarly to PageRank which is used in the Google search engine for ranking the web pages. TextRank works by counting the number and weight of links to a node to determine importance of the node. The more important nodes are likely to receive more links from other nodes. Words with higher values of TextRank are more important. Herrera and Pury suggested an entropic method for word ranking based on the relative frequency of words in each part of the text [17] (this method is also reviewed in the appendix in contrast to our own). Mehri and Darooneh used several entropic metrics to extract keywords [18]. In particular, they found that cumulative distribution of distances between consecutive occurrences of a word type follows:

$$P = [1 + (q-1)\beta x]^{\frac{1}{1-q}} \quad \textbf{(1)}$$

where x is distance between consecutive occurrences of a word type, $\beta$ is a constant, and q is a positive value. They ranked words according to q value. The value of q in the case of important words is larger than the case of common words [19].

# METHODS

## The Degree of Fractality

Text is a certain arrangement of words in one dimensional array that carries a meaning. Any random shuffling of the words across the text significantly reduces its meaning, hence the ordering of the words is important for representation of the meaning. In other words, the meaning shows a kind of regularity in a text. This regularity also manifests itself in pattern of occurrences of each word in the text array. If we consider the text array as a one dimensional space, the spatial pattern of occurrences of any vocabulary word will form a fractal set or simply a fractal. We can assign a fractal dimension to any word in a given text using the practical method of Box Counting. Using this method, the fractal dimension of a word is generally between 0 and 1.

In Box-Counting the space is divided into boxes. Each box that contains a component of the fractal set is called a filled box. The fractal law is a power law relationship between the number of filled boxes and the box-size [20].

To calculate the fractal dimension of a word by box-counting method, the text array is divided into boxes of size s, we place each s consecutive words in a box. The number of such boxes is $N_s = N/s$ where N is the length of the text. If the considered word appears in one of the boxes, that box is a filled box, $N_b(s)$ stands for the number of filled boxes. A power law relationship exists between the number of filled boxes and the box size s as follows,

$$N_b(s) \propto s^{-D} \quad \textbf{(2)}$$

D is the fractal dimension of the word. Fractal dimension is obtained by measuring the slope of log-log plot of $N_b(s)$ versus s. It is worth noting that here the box size is an integer number, and in practice, we expect to see the power law behavior for the large box sizes.

As we noted earlier, the fractal dimension for any word is between 0 and 1. When all occurrences of a word are distributed uniformly across the text, all of the boxes have the same probability of containing a token of the word. Therefore, in this particular case, the number of filled boxes has the maximum possible value. In other cases, some of the boxes may contain more than one occurrence; this results in some of the other boxes remaining empty, and the number of filled boxes is less than this limiting value.

In a shuffled text, all of the words are distributed uniformly. For small scales, when the number of boxes is greater than the frequency of a word type, the number of filled boxes is expected to be approximately equal to the frequency of the word type. By increasing the box size, the number of filled boxes will be decreased. In large scales, the fact that the number of filled boxes is maximum makes the slope of the log-log plot of $N_b(s)$ versus s close to one; the upper limit for slope. The following equation indicates our conjecture on the number of filled boxes for a word in the shuffled text against the box size, consistent with the above facts.

$$N_b^{sh.}(s,\omega) = \frac{M}{1 + \left(\frac{M-1}{N-1}\right)(s-1)} \qquad \textbf{(3)}$$

where M is frequency of the word ω.

The fractal dimension is the slope of the line of best fit on the log-log plot of the number of filled boxes against the box size. In practice, the choice of the fitting range is very important and definitely has influence on the value of the fractal dimension. Unfortunately, there is no way to automatically choose the most appropriate fitting range. Instead of the fractal dimension, we propose an index which is used to quantify the fractality of the word pattern in another way. The degree of fractality is defined as,

$$d_f(\omega) = \sum_s \log\left(\frac{N_b^{sh.}(s,\omega)}{N_b(s,\omega)}\right) \qquad \textbf{(4)}$$

where ω is a particular word. The degree of fractality, $d_f$, measures the difference between the pattern of occurrences of a word in the original and shuffled text. We use the logarithm in the definition of this index to avoid domination of the values for small box sizes. The degree of fractality is a suitable quantity for ranking the words of a text. In computing the degree of fractality, we only need to find the number of filled boxes for any scale. Unlike the process of computation of the fractal dimension, data regression is not required. Moreover, we are not faced with the problem of determining the fitting range for each word. The larger value for the degree of fractality means the distribution pattern of a word has more differences with the uniform distribution.

## Evaluation of the Method

The degree of fractality gives an importance value for every word type in a given text. Using this value, we are able to list the words from greatest to least importance. The top-ranked words of the list are assumed as keywords.

A comparison with a manually created list of keywords allows for an approximate evaluation of the efficiency of our method. It is important to know how the list of the relevant keywords is prepared for a given book. In our experience we assume that the manually created glossary of a book is a good candidate for providing the relevant keywords of the book. The glossary of a book should be prepared by author or some experts of the field thus it is reliable to be selected as our reference data.

The following two issues are important when we have comparison between the list of relevant and retrieved keywords. First, it is important to compute how many words are common in the two lists if both of them have the same size. Second, what fraction of the retrieved list should be selected to include all the relevant keywords? In binary classification analysis, recall and precision are two metrics which consider the above issues respectively. The recall and precision are calculated as follows according to Herrera and Pury's suggestion [17]. These are well-known metrics for evaluation of keyword extraction methods.

$$R = \frac{N_c}{N_{gloss}} \tag{5}$$

$$P = \frac{N_{gloss}}{N_{last}} \tag{6}$$

Where $N_{gloss}$ is the size of list of relevant keywords (glossary), $N_c$ is the number of common keywords in two lists, which have the rank less than $N_{gloss}$ and $N_{last}$ stands for the last position of relevant keywords in the list of retrieved words. It is worth noting again that these metrics cannot precisely determine the accuracy of the keyword detection methods. According to our experience, they depend on the data processed (selected book, its genre) and on how the list of relevant keywords is prepared.

There is another method for calculating recall and precision that is suggested by Mehri and Darooneh [18]. In this method words with degree of fractality higher than a threshold value are selected as retrieved keywords. The threshold value is choosen such that some percentage of ranked list of

words is selected as the retrieved keywords in each step. Then, number of keywords which is the same between glossary and this new list is counted. Recall and precision are calculated as follows.

$$R = \frac{N_c}{N_{gloss}} \quad (7)$$

$$P = \frac{N_c}{N_{ret}} \quad (8)$$

Again, $N_{gloss}$ is the size of glossary and $N_c$ is the number of keywords which are the same between glossary and selected percentage of retrieved list. $N_{ret}$ is the size of the retrieved list to the whole vocabulary size in percent.

## RESULTS

### Universal Properties of Texts

To explain more details, we apply our method to On The Origin of Species by Charles Darwin [21]. The book is about evolution of populations through a process of natural selection. A digital copy of this text is freely available on Project Gutenberg [22]. We only keep the main body of the text and leave the others (e.g., contents, index). No other preprocessing tasks are performed except deletion of the non-alphabetic characters. The book has a total of 191740 tokens and contains 8842 distinct word types. We examined two famous regularities of texts for this book, the Zipf's and Heaps' law. Fig 1 shows Zipf's law for the book; frequency of each word type is plotted against word rank on a double-logarithmic scale. A straight line is obtained with a slope of −1.01. Fig 2 shows Heap's law for the book; size of vocabulary is plotted versus size of text on a double-logarithmic scale. A straight line is obtained with a slope of 0.73.

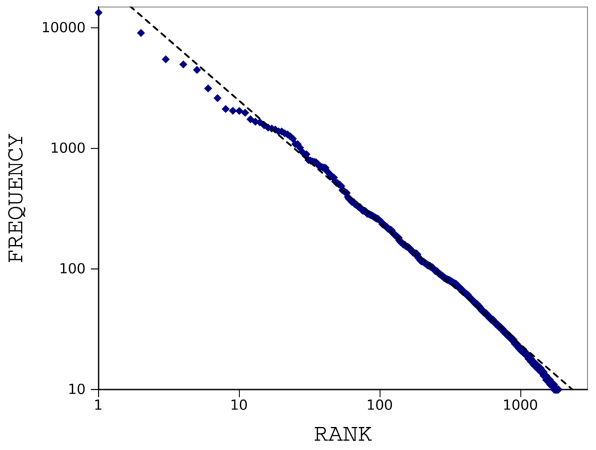


**Figure 1:** Zipf's law for the book The Origin of Species.

Frequency of each word is inversely proportional to its rank in form of power law. The Zipf curve follows a straight line with a slope of −1.01 when plotted on a double-logarithmic scale.

https://doi.org/10.1371/journal.pone.0130617.g001

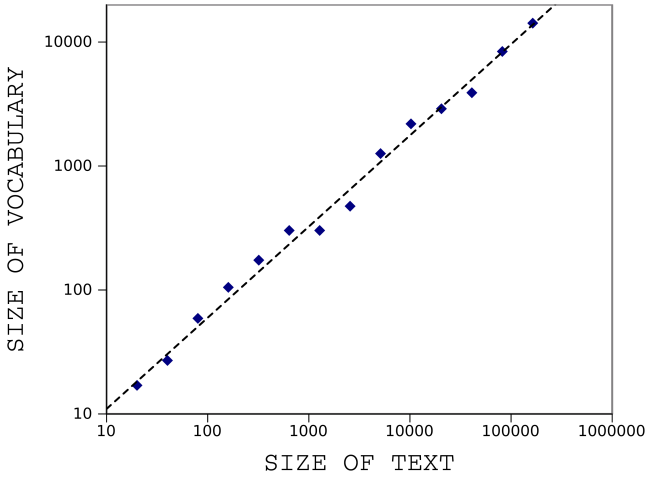


**Figure 2:** Heap's law for the book The Origin of Species.

Size of vocabulary increases as size of text increases, in form of power law. The Heap curve follows a straight line with a slope of 0.73 when plotted on a double-logarithmic scale.

https://doi.org/10.1371/journal.pone.0130617.g002

As outlined earlier the spatial distribution or pattern of ocurrences of any word in a given text exhibits self-similarity. The box counting is a practical procedure for measuring this property. In this procedure, the text is divided into boxes of size s, that varies from 1 to the text size. s = 1 means each box contains only one word, s = 2 means each box contains two words, and so on. A box is called filled if it contains some instances of the considered word. We chose powers of 2 for our box sizes. As an example Fig 3 illustrates division of a small part of our sample book into boxes with size 2, 4 and 8. In this example the appears in 3, 3, and 2 boxes for s = 2, 4, and 8 respectively.

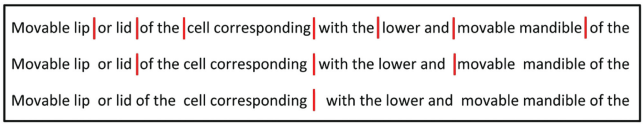


**Figure 3:** Schematic of how an instance text is devided into boxes.

The number of words that is placed in a box, is the box-size. Box-Size for first row is equal to 2 and for the second and third rows are 4 and 8 respectively.

https://doi.org/10.1371/journal.pone.0130617.g003

Distribution of a word is self-similar if we see the same pattern for the word in all scales (in all s). In Fig 4 the distribution of hybrid, one of the vocabulary words in our sample book is shown in three different scales s = 1, s = 256 and s = 1024. As is seen in this figure, distribution of hybrid is the same in these scales.

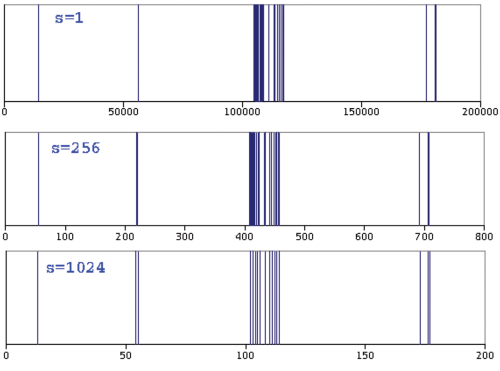


**Figure 4:** Spatial distribution of HYBRID in the book, The Origin of Species **for three different scales.**

As seen, distributions in all scales, s = 1, s = 256 and s = 1024, are statistically the same. They have similar clusters.

https://doi.org/10.1371/journal.pone.0130617.g004

## Ranking the Words and Keyword Detection

All words have a self-similar pattern in the text, but with different fractal dimensions. If the word is uniformly distributed along the text its fractal dimension is close to one. For words which are clustered in text the fractal dimension is substantially less than one. Fig 5 shows distribution of two words of the instance book, hybrid and rarely. Both of them have the same frequency M = 45. Occurrences of hybrid form a cluster in the text while rarely has uniform distribution.

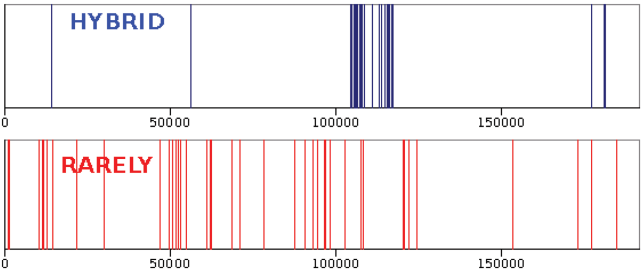


**Figure 5:** Spatial distribution of two words, HYBRID and RARELY, in the book, The Origin of Species.

According to subject of the book, hybrid is an important and the rarely is an irrelevant word, both of them have the same frequency equal to 45. rarely is distributed in the text, uniformly but,hybrid is clustered.

https://doi.org/10.1371/journal.pone.0130617.g005

In Fig 6 we compute the fractal dimension for these words. hybrid has dimension 0.4 and dimension of rarely is 0.8. We also plot the results for other pair of words, cell and actually with 28 occurrences in the book for both of them. cell is clustered as same as hybrid and actually has uniform pattern like rarely.

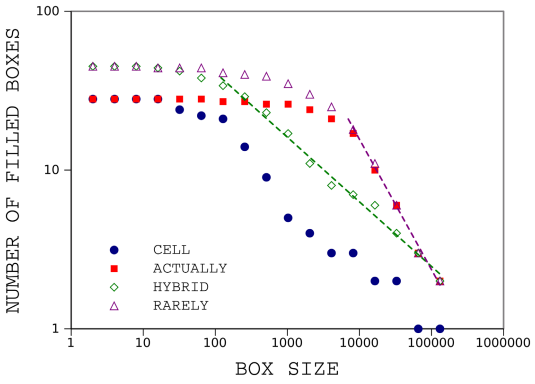


**Figure 6:** Results of box counting for, HYBRID and RARELY.

The dashed line and dash dotted line demonstrate the power law regression. The fractal dimension is about 0.4 for hybrid and is close to 0.8 for rarely. The box counting result of cell and actually is also showed. The fractal dimension is about 0.4 for cell and is close to 0.8 for actually.

https://doi.org/10.1371/journal.pone.0130617.g006

In the shuffled text all words are distributed more uniformly and clustered words do not occur. Fig 7 illustrates the result of box counting for hybrid in our sample book and its shuffled version. Our conjecture on the number of filled boxes in the shuffled text is also plotted, showing that our conjecture has good agreement with the shuffled data.

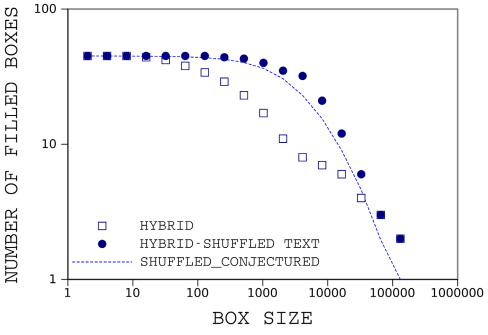


**Figure 7:** Results of box counting for distribution of HYBRID in the original and shuffled text.

hybrid is an important word in the book, The Origin of Species. So, there is a considerable difference between box-counting of this word in the original and shuffled text.

https://doi.org/10.1371/journal.pone.0130617.g007

The patterns of words that have uniform distributions change only slightly after the shuffling process, indicating that the words uniformly distributed in the original text are unimportant. The difference between patterns of a word in the original and shuffled text can be considered an indication of its importance. The degree of fractality which is defined in Eq 4 measures this difference. Fig 8 shows the degree of fractality for two words, hybrid and cell. It is clear from this figure that cell is more important than hybrid. The degree of fractality of hybrid is 8.21 and is 12.71 in the case of cell. Now we can rank all of the words according to the degree of fractality. Table 1 reports the list of twenty top-ranked words and also the first twenty frequent words for comparison. According to the subject of the book, words such as, slaves, illegitimate, saliva, and pedicellariae are important words. They also have higher degree of fractality in comparison with other words. The irrelevant words like, the, of, and, and in have lower degree of fractality, though they are very frequent in the book. It is useful to point out that function words have the lowest degree of fractality overall, but unimportant content words still have lower fractality than important keywords.

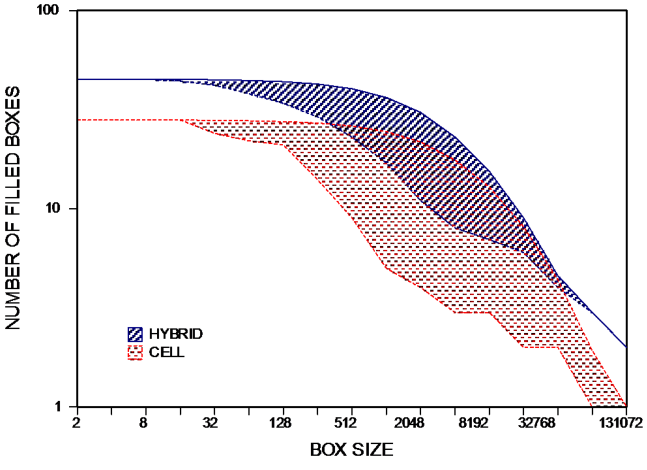


**Figure 8:** Area which is bounded between two curves for CELL and HYBRID in the box counting diagram.

The curves correspond to box counting result for these two words in the original and shuffled text. The area corresponds to cell is bigger than the case of hybrid. cell is more important than hybrid in the book The Origin of Species.

https://doi.org/10.1371/journal.pone.0130617.g008

**Table 1:** List of the twenty top-ranked words according to degree of fractality (left) and the first twenty frequent words (right) from the book The Origin of Species

Words with high degree of fractality are important words according to subject of the book and common words have low degree of fractality. The string un which is placed in the second row of list of top-ranked words is a French determinant which appears four times in a single sentence. So, it is highly clustered and has high value of fractality. Because we do not perform any pre-processing to eliminate foreign words, this word appears in the list.

https://doi.org/10.1371/journal.pone.0130617.t001

| Words | Frequency | Fractality | Words | Frequency | Fractality |
|---|---|---|---|---|---|
| slaves | 34 | 17.42 | the | 13368 | 2.54 |
| un | 4 | 16.70 | of | 9071 | 2.67 |
| illegitimate | 21 | 16.52 | and | 5482 | 2.79 |
| saliva | 5 | 16.42 | in | 4973 | 2.97 |
| pedicellariae | 15 | 16.03 | to | 4477 | 2.79 |
| floated | 18 | 15.98 | a | 3143 | 2.71 |
| pupae | 13 | 15.72 | that | 2612 | 2.77 |
| wax | 42 | 15.65 | as | 2122 | 3.16 |
| vibracula | 12 | 15.54 | have | 2051 | 2.79 |
| masters | 17 | 15.52 | be | 2045 | 2.78 |
| avicularia | 13 | 15.28 | is | 1975 | 2.80 |
| dried | 9 | 15.11 | species | 1745 | 2.42 |
| movable | 10 | 15.10 | by | 1665 | 2.82 |
| segment | 5 | 15.04 | which | 1646 | 2.76 |
| caudicle | 6 | 14.59 | are | 1556 | 2.69 |
| neuters | 12 | 14.93 | or | 1489 | 3.22 |
| cuckoo | 32 | 14.89 | it | 1462 | 3.04 |
| lamellae | 20 | 14.67 | on | 1432 | 3.12 |
| dun | 8 | 14.60 | with | 1383 | 3.02 |
| bucket | 7 | 14.59 | for | 1381 | 2.98 |

doi:10.1371/journal.pone.0130617.t001

For small texts, word frequency becomes increasingly important. For taking into account the effect of frequency, we multiply log(M) by the degree of fractality, causing the most changes in degree of fractality rank in the middle of the list, while words at the top of the list have a small change in their rank. Other choices may change the rank of the words in all parts of the list significantly. Table 2 presents another retrieved list of words according to this Combined Measure. Now, words like slaves, wax, hybrids, and instincts are placed in the top. In this new ranking list, the word, hybrid, changes its place from 321 to 48, the word, rarely also moves from 2203 rank to 1011.

**Table 2:** List of the twenty top-ranked words according to Combined Measure from the book The Origin of Species

These words are important according to the subject of the book. The word, f is related to some classification of species such as f8, f10, f14, … and some proper names. f is kept because non-alphabetical characters are removed in our method.

https://doi.org/10.1371/journal.pone.0130617.t002

| Words | Frequency | Fractality | Combined Measure |
|---|---|---|---|
| slaves | 34 | 17.42 | 26.68 |
| wax | 42 | 15.65 | 25.40 |
| hybrids | 135 | 10.89 | 23.20 |
| instincts | 87 | 11.85 | 23.00 |
| sterility | 100 | 11.27 | 22.53 |
| cuckoo | 32 | 14.89 | 22.40 |
| illegitimate | 21 | 16.52 | 21.85 |
| floated | 18 | 15.98 | 20.07 |
| instinct | 63 | 10.62 | 19.11 |
| masters | 17 | 15.52 | 19.10 |
| lamellae | 20 | 14.67 | 19.09 |
| pedicellariae | 15 | 16.03 | 18.85 |
| cell | 28 | 12.71 | 18.39 |
| nest | 55 | 10.23 | 17.80 |
| f | 46 | 10.62 | 17.66 |
| pupae | 13 | 15.72 | 17.51 |
| cells | 58 | 9.84 | 17.36 |
| fertility | 80 | 9.08 | 17.27 |
| spheres | 19 | 13.46 | 17.22 |
| clover | 15 | 14.55 | 17.11 |

doi:10.1371/journal.pone.0130617.t002

In addition to the degree of fractality, there exist several methods that assign an importance value to any word in a given text. We can list the words in descending order of their importance. In this list the words that are placed in the top ranks are assumed to be keywords. By choosing a threshold value we can identify the list of keywords. In the following section we evaluate our proposed method for the keyword detection task.

## Evaluation of Our Method

The best way to evaluate the efficiency of our approach to keyword detection is comparing its results with other methods. We use two metrics in this comparison: precision and recall. These tell us to what extent the retrieved list of keywords conforms to the manually selected list as described in the previous section. In this work, we would like to compare our method with two efficient methods in keyword extraction, the C Value [14] and Entropy [17]. These methods are selected according to our experience. We found that C Value has the maximum amount of recall compared with other methods and

entropy has maximum amount of precision compared with others [18, 23] (these methods are reviewed in further detail in the appendix). To do the assessment we use the glossary written by W. S. Dallas [24]. Note that the choice of glossary has the potential to considerably alter the result of comparisons.

Two points are relevant before proceeding to the comparison. First, the glossary of the book contains not only words, but also some phrases. To deal with multi-word keywords of the glossary we separate them into single words. For example we convert the phrase ganoid fishes to two separate words ganoid and fishes in the glossary. Second, in any method, a value is assigned to each vocabulary word, then we can sort the words from the highest value to the lowest. We give rank 1 to the first word in the sorted list, the second word takes rank 2 and so on. Unlike in Zipfian ranking, this ranking process allows for rank ties; in other words, if some words have the same assigned value, they should have the same rank. As an example, in Table 3 the words forward and months have equal values. In this case we assign them equal rank (2128) and the next word in the list will have rank 2130. There are two approaches for calculating recall and precision.

**Table 3:** List of ten words and their ranks from the book The Origin of Species

Words with equal Combined Measures take equal ranks.

https://doi.org/10.1371/journal.pone.0130617.t003

| Words | Combined Measure | rank |
|---|---|---|
| forward | 3.31199 | 2128 |
| months | 3.31199 | 2128 |
| saved | 3.31115 | 2130 |
| treat | 3.31115 | 2130 |
| observers | 3.30809 | 2132 |
| gone | 3.30749 | 2133 |
| inferiority | 3.30647 | 2134 |
| agree | 3.30564 | 2135 |
| icebergs | 3.30447 | 2136 |
| laying | 3.30447 | 2136 |
| really | 3.30164 | 2138 |

doi:10.1371/journal.pone.0130617.t003

In Herrera and Puri approach [17], they do not indicate any threshold. After ranking words according to an importance index, the last word of the glossary in the ranked list is found. Then, the number of words from the ranked list which include all the glossary words are selected as keywords. In this approach, they introduce a cut-off frequency; they keep only the words with frequencies greater or equal to the cut-off frequency both in ranked list and in the glossary and omit all other words with lower frequencies. For

example cut-off frequency equal to 2 means only words with frequencies more than 1 are kept and other words are omitted. The number of words from ranked list and from the glossary for various choices of cut-off frequency are written in Table 4. In Fig 9, the recall and precision are plotted against the cut-off frequency. According to Fig 9, recall for Combined Measure is higher than other methods for cut-off frequencies greater than 5. This means that the proposed fractal method is superior to the others as a method for keyword extraction. The precision of Combined Measure is higher than C Value for all cut-off frequencies.

**Table 4:** Number of vocabulary words and number of glossary words for various cut-off frequencies

$N_v$ and $N_g$ are the number of vocabulary words from the book and number of glossary words for each cut-off frequency, respectively.

https://doi.org/10.1371/journal.pone.0130617.t004

| | Cut-off Frequency | | | | | | | | | |
|---|---|---|---|---|---|---|---|---|---|---|
| | 1 | 2 | 3 | 4 | 5 | 6 | 7 | 8 | 9 | 10 |
| $N_v$ | 8842 | 5351 | 4092 | 3428 | 2957 | 2624 | 2352 | 2141 | 1968 | 1855 |
| $N_g$ | 229 | 157 | 126 | 109 | 89 | 79 | 72 | 65 | 57 | 54 |

doi:10.1371/journal.pone.0130617.t004

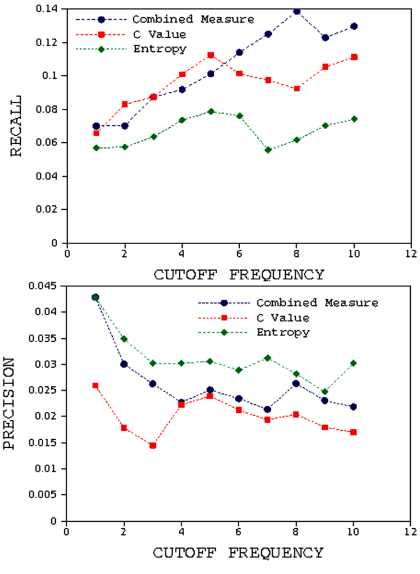


**Figure 9:** Results of calculating Recall and Precision with Herrera and Purri approach for the book The Origin of Species **for 10 cut-off frequencies.**

The fractal method has the highest value of Recall in all frequencies and higher value of Precision than C Value method.

https://doi.org/10.1371/journal.pone.0130617.g009

If we rank the words according to their fractality we will find a power law relationship between the fractality of a word and its rank. Therefore, it is rational to choose the words with rank lesser than a specific value as the retrieved keywords list instead of using the fractality threshold. In Mehri and Darooneh approach [18], after ordering words due to their fractality, a percentage of words from the top of the ranked list are selected as keywords. In the first step, the top 2 percent of the ranked list are selected as keywords (the first 2 percent of 8842). In the next step, the top 4 percent of the list are selected as keywords, and so on. Also, in this approach all of the glossary words are selected as relevant keywords in all steps. In Fig 10, the recall and precision are plotted using Mehri and Darooneh approach. According to this figure recall for fractality for our method is higher than other methods for all retrieved list fractions. The precision of fractality for our method is higher than others for retrieved list fractions of more than 4 percent.

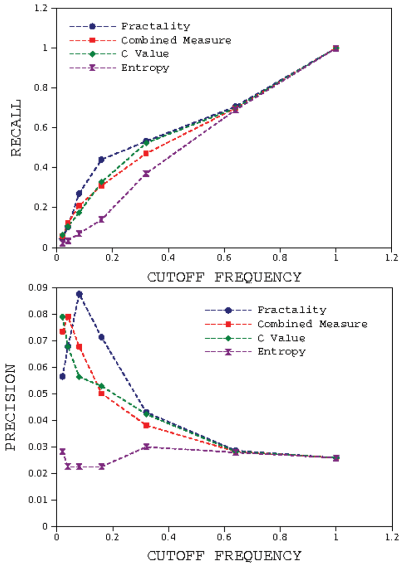


**Figure 10:** Results of calculating Recall and Precision with Mehri and Darooneh approach for the book The Origin of Species.

The fractal method has the highest value of Recall and precision in all vocabulary fractions.

https://doi.org/10.1371/journal.pone.0130617.g010

The validity of our method also extends to other books. The First Three Minutes by Steven Weinberg [25] and A Brief History of Time by Stephen Hawking [26]. The value of recall for our method is higher than for C Value and entropy. The precision value obtained is higher than other methods for cut-off frequencies of more than 9 for Weinberg's book, and more than 8 in the case of Hawking's book.

## CONCLUSION

The pattern of occurrences of a word in a text can be considered as a fractal object with dimension between 1 and 0. We found that words related to the subject of the text have non-uniform spatial distributions and their dimensions are considerably less than one. In contrast, the irrelevant words are distributed uniformly with a dimension close to one. We introduced the concept of degree of fractality which measures the difference between distribution pattern of a word in the original text and randomly shuffled version. While in the shuffled texts all of the words are uniformly distributed across the text, the original text exhibits clustering of important words in particular. We used the degree of fractality in combination with a function of frequency for ranking words in The Origin of Species by Charles Darwin. The top words in the ranked list of the words was selected as the retrieved keywords of the text. The retrieved list of keywords was checked against the glossary of the book. For this checking we used two metrics: precision and recall, which are defined in the context of the binary classification analysis. Compared with two other representative methods in this area, the Entropy and C Value, our approach is more effective as a method for automatic keyword extraction.

Future work should aim to examine the effectiveness of our method in keyword detection for smaller texts. This method could also be applied to key-phrase extraction. Finally, the general framework behind our method could be extended to explore the hidden secrets of genome, for instance by developing a way for data mining non-coding DNA.

# APPENDIX. DESCRIPTION OF RELATED METHODS OF WORD RANKING

## A C Value

The C Value method is based on noticing distribution of the words in a text and word clustering [14]. To quantify the clustering of a word the parameter σ (the standard deviation of the normalized distance between consecutive occurrence of a word) is defined by

$$\sigma = \sqrt{< s^2 > - < s >^2}, \tag{9}$$

Where s is the normalized distance between consecutive occurrences, s = d/ < d >, and < d > is the average distance between occurrences. σ can be normalized with respect to standard deviation of the distance between consecutive occurrences of words in a random text, which has a geometrical spatial distribution of word types, $\sigma_{geo} = \sqrt{1 - P}$ . Where p = M/N is the probability of occurrence of a word type with frequency equal to M in a text with total N words,

$$\sigma_{nor} = \frac{\sigma}{\sigma_{geo}}, \tag{10}$$

$$C(\sigma_{nor}, M) = \frac{\sigma_{nor} - < \sigma_{nor}(M) >}{sd(\sigma_{nor})(M)}, \tag{11}$$

Where $< \sigma_{nor} >= \frac{2M-1}{2M+1}$ and $sd(\sigma_{nor}) = \frac{1}{\sqrt{M}(1+2.8M^{-0.865})}$ are the mean value of the normalized standard deviation and standard deviation of the distribution of $\sigma_{nor}$ in a random text, respectively. C = 0 means the word is distributed randomly in a text and C > 0 means the word forms cluster.

## B Entropy

Entropy is another parameter used to rank the words of a text [17]. For this purpose a text with N words is devided into P parts. The ith part contains $N_i$ words which $\sum_{i=1}^{P} N_i = N$. So the ralative frequency of occurrence of the word type ω in the part i is $f_i(\omega) = \frac{M_i(\omega)}{M(\omega)}$, where $M_i(\omega)$ and $M(\omega)$ are the frequency of word type ω in the ith part and in the whole text, respectively, where $\sum_{i=1}^{P} M_i = M$. With this explanation the probability measure over the partitions can be defined as

$$p_i(\omega) = \frac{f_i(\omega)}{\sum_{j=1}^{P} f_j(\omega)}. \quad (12)$$

The following relation is the Shannon's information entropy for a discrete distribution $p_i(\omega)$

$$S(\omega) = \frac{-1}{Ln(P)} \sum_{i=1}^{P} p_i(\omega) Ln(p_i(\omega)). \quad (13)$$

There is a problem with this relation; it is zero for words with frequency equal to 1. To take into account the effect of frequency, the following relation seems to be a better choice

$$E_{nor}(\omega) = \frac{M(\omega)[1 - S(\omega)]}{E_{ran}(\omega)} \quad (14)$$

where $E_{ran}(\omega) = \frac{P-1}{2ln(P)}$ is the entropy of the word type ω in a random text.

## ACKNOWLEDGMENTS

We acknowledge valuable comments from referees which substantially improved the paper.

## AUTHOR CONTRIBUTIONS

Conceived and designed the experiments: EN AHD. Performed the experiments: EN AHD. Analyzed the data: EN AHD. Contributed reagents/materials/analysis tools: EN AHD. Wrote the paper: EN AHD.

## REFERENCES


1. Larsen-Freeman D, Cameron L. Complex Systems and Applied Linguistics. Oxford: Oxford University Press; 2008.
2. Zipf GK. Human Behavior and the Principle of Least Effort: An introduction to Human Ecology. Cambridge: Addison-Wesley Press; 1949.
3. Heaps HS. Information Retrieval: Computational and Theoretical Aspects. New York: Academic Press; 1978.
4. Sano Y, Takayasu H, Takayasu M. Progress of Theoretical Physics, Supplement No. 194. 2012: 202–209.
5. Altmann G. Prolegomena to Menzerath's law. Glottometrika 2. 1980: 110.
6. Hrebíček L. Fractals in Language. Journal of Quantitative Linguistics, 1(1). 1994: 82–86.
7. Andres J. On a conjecture about the fractal structure of language. Journal of Quantitative Linguistics, 17(2). 2010: 101–122.
8. Andres J, Benešová M, Kubá L, Vrbková J. Methodological Note on the Fractal Analysis of Texts. Journal of Quantitative Linguistics, 19(1). 2012: 1–31.
9. Ausloos M. Generalized Hurst exponent and multifractal function of original and translated texts mapped into frequency and length time series. Phys. Rev. E, 86. 2012: 031108.
10. Ausloos M. Measuring complexity with multifractals in texts. Translation effects. Chaos, Solitons and Fractals, 45. 2012: 13491357.
11. Eftekhari A. Fractal Geometry of Literature: First Attempt to Shakespear's Works. Journal of Quantitative Linguistics, 13. 2006: 177–193.
12. Luhn HP. The Automatic Creation of Literature Abstracts. IBM Journal of Research and Development, 2. 1958: 159–165.
13. Ortuño M, Carpena P, Bernaola-Galvan P, Munoz E, Somoza AM. Keyword detection in natural languages and DNA. Europhysics Letters 57. 2002: 759–764.
14. Carpena P, Bernaola-Galvan P, Hackenberg M, Coronado AV, Oliver JL. Level statistics of words: Finding keywords in literary texts and symbolic sequences. Physical Review E 79. 2009: 035102.
15. Zhou H, Slater GW. A metric to search for relevant words. Physica A

329. 2003: 309–327.

16. Mihalcea R, Tarau P. TextRank: Bringing Order into Texts. Proceedings of conference on Empirical Methods in Natural Language Processing (EMNLP). 2004: 404–411.
17. Herrera JP, Pury PA. Statistical keyword detection in literary corpora. Eur. Phys. J. B 63. 2008: 135.
18. Mehri A, Darooneh AH. The role of entropy in word ranking. Physica A 390. 2011: 3157–3163.
19. Mehri A, Darooneh AH. Keyword extraction by nonextensivity measure. Physical Review E 83. 2011: 056106.
20. Gouyet JF. Physics and fractal structures. New york: Masson Springer; 1996.
21. Darwin C. On the Origin of Species by Means of Natural Selection, or the Preservation of Favoured Races in the Struggle for Life. Nature. London: John Murray 5; 1859.
22. http://www. gutenberg. org/files/22764/
23. KordDelsame K. Ranking the Words in a Text by C Value method. MSc. Thesis (in persian). University of Zanjan. 2012.
24. http://literature. org/authors/darwin-charles/the-origin-of-species/glossary. html
25. Weinberg S. The First Three Minutes. Cambridge: Pegasus Press; 1949.
26. Hawking S. A Brief History of Time. Bantam Books; 1988.

# 6

# *Higuchi Dimension of Digital Images*

**Helmut Ahammer**

Institute of Biophysics, Centre of Physiological Medicine, Medical University of Graz, Graz, Austria

## ABSTRACT

There exist several methods for calculating the fractal dimension of objects represented as 2D digital images. For example, Box counting, Minkowski dilation or Fourier analysis can be employed. However, there appear to be some limitations. It is not possible to calculate only the fractal dimension of an irregular region of interest in an image or to perform the calculations in a particular direction along a line on an arbitrary angle through the image. The calculations must be made for the whole image. In this paper, a new method to overcome these limitations is proposed. 2D images are appropriately prepared in order to apply 1D signal analyses, originally developed to investigate nonlinear time series. The Higuchi dimension of these 1D signals is calculated using Higuchi's algorithm, and it is shown that both regions of interests and directional dependencies can be evaluated independently of the whole picture. A thorough validation of the proposed

**Citation:** Ahammer, H. (2011). Higuchi dimension of digital images. PLoS One, 6(9). DOI: 10.1371/journal.pone.0024796.

technique and a comparison of the new method to the Fourier dimension, a common two dimensional method for digital images, are given. The main result is that Higuchi's algorithm allows a direction dependent as well as direction independent analysis. Actual values for the fractal dimensions are reliable and an effective treatment of regions of interests is possible. Moreover, the proposed method is not restricted to Higuchi's algorithm, as any 1D method of analysis, can be applied.

## INTRODUCTION

Digital images are increasingly utilized to represent data in all kinds of sciences. They can be used for visual or graphical purposes only or for a closer investigation of an object via image processing techniques. If the objects in an image are not geometrically regular—which is often the case for natural objects such as landscapes, animals or cells—both the interpretation and the classification can be important. For these tasks, determining the fractal dimensions of 2D digital images has been very successful in recent years [1]–[5]. The methods involved include the well known Box counting method or the Minkowski dilation method [3]. It is also possible to use gray value statistics [6], differential box counting [7], a variation method [8], a blanket method [9] or frequency analysis [10]–[12]. Despite the effectiveness of these methods, they have some serious limitations. Very often the object of interest does not fill the digital image entirely, but instead is surrounded by a background, e.g., a light microscopic image of a single cell surrounded by culture medium, an electron microscopic image of a cell nucleus surrounded by stroma or a histological image of a special tissue surrounded by neighbouring tissue. In all these cases, it would be necessary to calculate the properties or fractal dimensions only for the regions of interest, without incorporating any information from the background. Furthermore, it is not possible to calculate the fractal dimension of a specific line or curve through an image. Such a line or curve can be considered to be nothing more than a long region of interest without a width or with a width of one pixel.

The present work proposes a new method to overcome these limitations by using 1D signal analysis methods. 2D images are either projected onto 1D signals or several image rows, columns, radial lines or spirals are extracted in order to gather a batch of 1D signals. Projection leads to a loss of information, but has the advantage of drastically decreased computational requirements. Extraction of rows and/or columns does not imply a loss of

information, and the fractal dimension of the whole image can be calculated very precisely.

Theoretically, an extracted 1D signal of an image is an intersection of the gray value surface with a two dimensional plane and therefore, the intersection theorem for fractals [13] can be applied:

$$D_{1D} \geq D_{2D} + D_{Plane} - E, \tag{1}$$

with $D_{1D}$ the fractal dimension of the 1D signal, $D_{2D}$ the fractal dimension of the gray value surface in a three dimensional Euclidian space E=3, and a plane with $D_{Plane} = 2$. Usually the greater than relation can be replaced by equality. Then, the fractal dimension range $\{D_{2D} | 2 < D_{2D} \leq 3\}$ of the surface yields an expected fractal dimension range of $\{D_{1D} | 1 < D_{1D} \leq 2\}$ for the 1D signal or profile. Projection in this context is a data reduction by summing up the grey values along an axis. For this sort of projection the projection slice theorem is valid, which is commonly applied for inverse problems, such as computed tomography. A single projection integrates the original data, unavoidably yielding a loss of high frequency components. Nevertheless, it is feasible to calculate quantitative parameters describing the data set, e.g. the fractal dimension. It turned out that projection yields in many cases quite similar, mainly a little lower values compared to extraction methods, but, in some cases, it can lead to false values, which is described and elaborated thoroughly in the result and discussion sections.

One dimensional data is commonly a time series of data points, which can be examined by a very wide range of excellent linear as well as nonlinear methods. While there exist a huge range of methods concerning 1D signal processing and signal analyses (e.g. 1D filtering algorithms), this study is focused on nonlinear methods studying fractal dimensions of objects. These 1D nonlinear analyses are mainly performed in the investigation of nonlinear dynamical systems [14]–[16], bifurcations [17] or even critical transitions [18]. The range of possible methods includes phase space analysis, attractor analysis, Fourier methods, the Higuchi method [19] and others.

Despite of the effectiveness of these 1D methods, there have been only very limited efforts to expand these methods to 2D in the past. There are a few exceptions [20]–[22], but because of their rarity, there is a very high potential for improving and expanding the classical 2D methods. This

work intends to pursue these promising approaches. The proposed methods include some generally applicable techniques, which can be adapted very easily to actual problems.

# METHODS

## Digital Images

Several digital gray level images were generated in order to test the calculations of the images' Higuchi dimensions. The varying gray level surface of a 2D image can be interpreted as a 3D landscape in a three dimensional embedding space. The following images were constructed (Figure 1A): An image with constant gray value, an image with a cosine shaped variance of gray levels in the horizontal direction and a constant gray value in vertical direction, three images with varying gray levels but predefined fractal dimensions, and finally an image with random gray values.

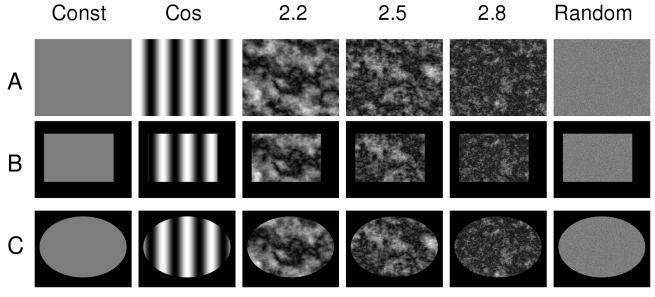


**Figure 1:** Six sample images.

A An image with constant gray value, an image with cosine shaped varying gray levels in the horizontal direction and constant gray value in the vertical direction, three images with varying gray levels but distinct predefined fractal dimensions and finally an image with random gray values. B Same six images as in A, but with a rectangular region of interest (ROI). C Same six images as in A, but with an elliptical ROI.

The fractal gray level landscapes were constructed using an inverse Fourier method described in [23]. Briefly, an artificial, randomly distributed Fourier power spectrum is constructed. The value of the desired fractal dimension, $D_F$, is taken to calculate the slope $\beta = 8 - 2D_F$. Then, β is used to create a corresponding power spectrum. Applying the inverse Fourier

transformation with arbitrary phase values gives a gray value surface with the desired fractal dimension $D_F$.

Two artificial regions of interest (ROI) were constructed, one rectangular and one elliptical, by setting all pixel values outside of the ROI to zero. These images can be seen in Figure 1B&C. The actual shapes of the ROIs were chosen with unsymmetrical distances to the image border in order to simulate an actual case.

All images had an identical resolution of 1300×1030 pixels, which is high enough for the calculations intended [24] and resemble a commonly used image size. The images were saved as 8 bit gray level images in tiff format.

The images were constructed with IDL (Interactive Data Language, ITT Industries Inc., Boulder, USA).

## Construction of 1D Data Sequences

There is not a standard procedure for constructing 1D data point series out of 2D digital images. At first glance, a reduction of order seems to inevitably cause a loss of information. But this loss does not always occur without exception. The amount of lost information is strongly dependent on the actual reduction process. In practice, there exist a huge number of possibilities to extract 1D signals out of 2D images. Extractions of rows or columns, along radial lines, spirals or arbitrary curves or stitching together rows or columns, to name but a few, are possible. In fact, the proposed method of calculating fractal dimensions is not restricted to any special type of extraction and therefore, exemplarily the following extraction algorithms were chosen for this study:

- The gray values are projected vertically to the x-axis and horizontally to the y-axis. This projection resembles the summing up of gray values, and two 1D signals are constructed.
- Every horizontal row and every vertical column of the image is extracted and taken as a separate 1D signal. This approach leads to ($n$+$m$)-many signals, with $n$ the number of image columns and $m$ the number of image rows.
- Radial lines through the centre of the image with a subsequent angle difference of 1° are extracted. Therefore, 180 signals cover the range from 0 to 2π.

- An Archimedean spiral starting at the centre of the image and turning 10 times through the image is extracted.

The evaluation time is considerably low for method (i) and only marginally higher for (iv). The time for (ii) is ($n$+$m$)/2 times and for (iii) 90 times higher than the time for (i). On a standard PC (for the images with a resolution of 1300×1030 pixels), the calculations (including the display of graphical user interfaces and the display of every single regression plot) using method (i) took <0.15 minutes, whereas for method (ii) they took about 200 minutes and for method (iii) about 15 minutes per image. Parallelization of the algorithms, especially for method (ii) and (iii) would be possible, because the individual 1D signals can be independently processed.

The results of the individual signals can also be grouped together by calculating mean values. Therefore, it is possible to get distinct mean values for the x- and/or y-direction or one single value for the whole image.

All the images were additionally investigated and examined with two different ROIs: a rectangular and an elliptical shape. Outside of the ROI, the gray values were set to zero, so each of the 1D signals showed both leading and tailing zeros. Zero gray values were interpreted as being the background. Obviously, the fractal dimension calculations strongly depended on these leading and tailing zeros, and it was not possible to neglect this influence. In order to examine this influence, the calculations were carried out in two ways. First, the calculations were straightforwardly carried out by including the zeros (inclusive background), and second, the calculations were carried out after both the leading and the tailing zeroes were excluded (exclusive background).

## Higuchi Dimension

The Higuchi dimension, $D_H$, is a measure of irregularity and is calculated for time series directly in the time domain [19]. The calculations are carried out without phase space constructions. Several lengths, $L(d)$, of the signal or curve are calculated, and a double logarithmic plot, $\ln L(d)$ versus $\ln d$, is used to estimate the actual dimension value. The assumption is that a fractal signal scales according to the following:

$$L(d) \propto d^{D_H} \qquad (2)$$

The discrete data point series $S : x(1), x(2), x(3),....., x(N)$, with $N$ the total number of data points, must consist of values or observations at regular

intervals. From this single data point series, $d$ new data point series $S_m(d)$, with $m = 1, 2, \ldots . d$, where $m$ is the initial time and $d$ a time interval, are constructed.

$$S_m(d) : x(m),\ x(m+d),\ x(m+2d), \ldots\ldots\ldots x\left(m + \lfloor \frac{N-m}{d} \rfloor d\right) \tag{3}$$

For each $S_m(d)$, the lengths $L_m(d)$ are calculated as follows.

$$L_m(d) = \frac{1}{d}\left\{\left(\sum_{i=1}^{\left[\frac{N-m}{d}\right]} |x(m+id) - x(m+(i-1)d)|\right)\frac{N-1}{\lfloor \frac{N-m}{d} \rfloor d}\right\}, \tag{4}$$

where $m$ and $d$ are integers and $\lfloor\rfloor$ denotes the floor function. The lengths $L_m(d)$ are the normalized sums of the differences of the values, with a distance of $d$ and a starting point $m$. For each $d$, the mean $L(d)$ is calculated as follows.

$$L(d) = \frac{1}{d}\sum_{i=1}^{d} L_m(d) \tag{5}$$

Finally, the slope of a linear regression of a double logarithmic plot of $\ln L(d)$ and $\ln d$ gives the Higuchi dimension, $D_H$. The maximal interval $d_{\max}$ was determined by plotting several regressions with subsequently increasing $d_{\max}$. For each individual regression, the coefficient of determination $R^2$ was calculated. The saturation point, where $R^2$ did not increase significantly was taken for the maximal $d$. Actually, $L(d)$ was calculated for $d = 1, 2, 3 \ldots . 89$, and the best linear regression (again by checking $R^2$) in the double logarithmic plot was gained for the range $d = 20, 21, 22 \ldots . 89$. This range of $d$ resulted in the best estimations of the theoretical dimension values.

The values of the Higuchi dimension, $D_H$, of a 1D curve $S$ always fall in the closed interval [1], [2]. There is one exception, when all the data point values have a constant value. In that case, all the differences in the summation of $L_m(d)$ are all zero, resulting in $D_H = 0$ A simple curve, such as a sine or cosine function, has a dimension $D_H = 1$. The other extreme is a randomly distributed curve with $D_H = 2$. The dimension for fractals lies between 1 and 2.

## Fourier Dimension

Frequency analysis, and in particular the FFT (Fast Fourier Transformation), is widely applied in image processing, and the fractal dimension $D_F$, also called the "Fourier dimension," is related to the power spectrum of a 2D image. The power spectrum is given by:

$$P(k_x,k_y) = c\left|\vec{k}\right|^{-\beta}, \tag{6}$$

with $\left|\vec{k}\right| = \sqrt{{k_x}^2 + {k_y}^2}$, and c is a constant.

$\beta$ can be examined by fitting the function in Equation (6) to the calculated two dimensional power spectrum. By taking the logarithm, the least squares approximation gives:

$$\beta = \frac{N\sum_{ij}\ln|k_{ij}|\,\ln P_{ij} - \sum_{ij}\ln|k_{ij}|\,\sum_{ij}\ln P_{ij}}{N\sum_{ij}(\ln|k_{ij}|)^2 - \left(\sum_{ij}\ln|k_{ij}|\right)^2}, \tag{7}$$

with N the number of data points and *i* and *j* the indices in the horizontal and vertical directions respectively.

The fractal dimension, $D_F$, of 2D images, having a topological dimension $D_t = 2$, can be estimated with the following equation:

$$D_F = \frac{8-\beta}{2}. \tag{8}$$

The range of possible values is between 2 and 3.

The calculations were carried out with IDL (Interactive Data Language, ITT Industries Inc., Boulder, USA).

Both dimensions, the Fourier dimension as well as the Higuchi dimension depend on the construction of a power law of distinct quantities. Although these quantities are not identical, the power law reflects the intrinsic nonlinear relation of these distinct quantities. Therefore, the slopes of the linear fits give estimates rather than exact values for the fractal dimension.

# RESULTS

The dimension values of distinct images were examined according to each of the individual methods. Firstly, projection, extraction of rows, columns, radial lines or spirals was carried out to get 1D signals for the calculation of the Higuchi dimension. For comparison, the images were used to calculate the Fourier dimension. The slopes of the linear regressions of double logarithmic plots were determined, and the estimated values of the fractal dimensions were calculated by linear regressions.

## Linear Regressions

Sample double logarithmic plots and linear regressions can be seen in Figure 2. The linear regressions of the Higuchi method of the images in Figure 1A can be seen in Figure 2A. A close inspection shows a slight tendency for two linear regions, so the actual linear regression was restricted to the second region for values between 20 to 89. This restriction gave the best absolute values, e.g., a sinusoidal shape should have $D_H = 1$, while a random shape should have $D_H = 2$. The linear regressions fit the data very well, with coefficients of determination $R^2$ higher than 0.993.

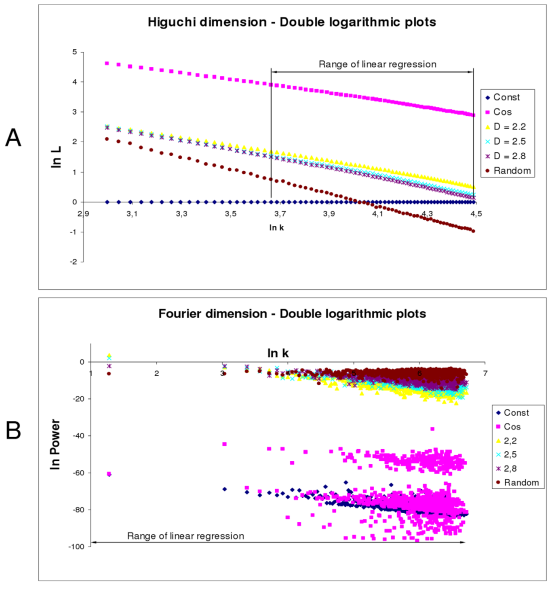


**Figure 2:** Double logarithmic plots of the Higuchi and Fourier dimension.

The individual ranges of linear regressions are depicted. A The slopes of the Higuchi dimension show a slight tendency for two linear regions. Thus, the range of linear regression was limited to the second linear region in order to gain the best absolute dimension values. The linear regression fit the data very well, with coefficients of determination $R^2$ higher than 0.993. B The plot data of the Fourier dimension are highly dispersed. The coefficients of determination $R^2$ were about 0.332. The highest value was 0.664.

The linear regressions of the Fourier method can be seen in Figure 2B. Obviously, compared to the Higuchi method, the plot data is highly dispersed, and the linear regressions did not fit the data very well. The coefficients of determination $R^2$ were worse than for the Higuchi method at approximately 0.332. The highest value was only 0.664.

## Fractal Dimensions of Fractal Shapes

As a first comparison of the Higuchi dimension analysis to the Fourier dimension analysis, gray value images, featuring a fractal surface and predefined certain fractal dimensions, were investigated. The predefined fractal dimensions were D=2.2, D=2.5 and D=2.8, representing low, medium and high fractal dimensions, respectively.

Figure 3 and 4 show the results, and the abscissa values are the predefined fractal dimensions. For every predefined fractal dimension, 100 different images were investigated. The error bars depict the calculated standard deviations. Figure 3 shows the Higuchi dimension results for methods (i), (ii), (iii) and (iv), respectively. Figure 4 shows the results for the Fourier dimension analysis.

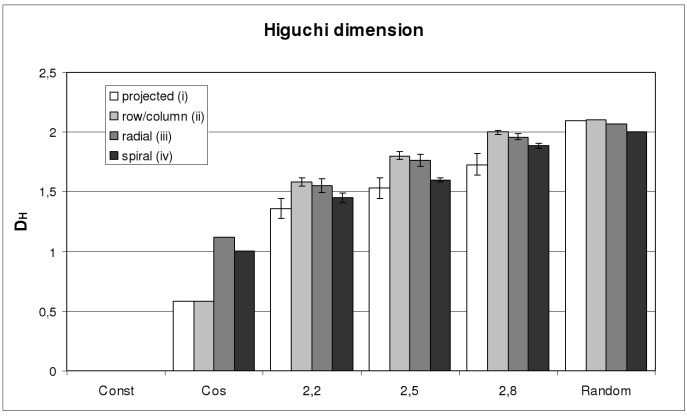


**Figure 3:** Higuchi dimensions of fractal and non-fractal images.

Higuchi dimensions for an image with a constant gray value, an image with a cosine shaped gray value course in the x-direction, three images with predefined fractal dimensions (D=2.2, 2.5, 2.8) and an image with random gray values. The legend depicts the distinct 2D to 1D methods (i)–(iv). (i) projection and averaging the values for the x- and y-direction. (ii) examining every row and column and calculations of averages. (iii) 180 radial lines through the centre of the image and calculations of averages and (iv) spirals through the image and calculations of averages.

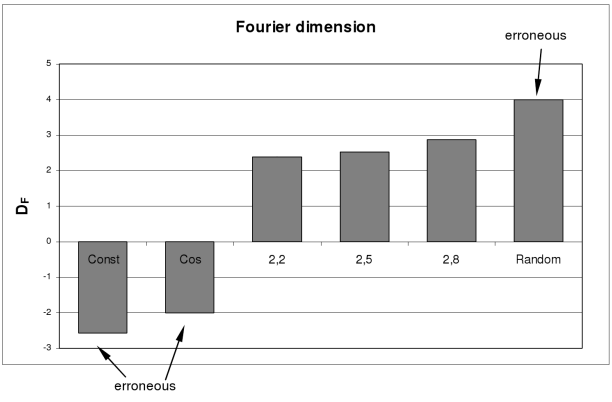


**Figure 4:** Fourier dimensions of fractal and non-fractal images.

Fourier dimensions for an image with a constant gray value, an image with a cosine shaped gray value course in the x-direction, three images with predefined fractal dimensions (D=2.2, 2.5, 2.8) and an image with random gray values. Inaccurate as well as erroneous values are emphasized with arrows.

The values of the Higuchi dimension analysis show a continuous increase and very low levels of errors. The values for the projection method (i) were slightly smaller than for method (ii). Method (ii) and (iii) yielded quite similar values. Again method (iv) yielded marginally smaller values but not so much as method (i). As mentioned in the method section, a single value for an image was calculated.

In contrast, the values of the Fourier dimension (Figure 4) show very clearly that there are some very bad estimates. The values for fractal dimensions from 2.5 and 2.8 are estimated quite well, but the calculation for the lower value of 2.2 shows a very poor estimate.

## Fractal Dimensions of Non Fractal Shapes

The results for an image with a constant gray value, an image with a cosine shaped gray value course in the x-direction can be seen on the left side of Figures 3 and 4. The result for an image with random gray values can be seen on the right side of Figures 3 and 4.

In accordance with the theory, the constant gray value image has an estimated Higuchi dimension of zero for all four methods (i), (ii), (iii) and (iv). Furthermore, the cosine shaped varying image in the x-direction and constant values in y-direction has a Higuchi dimension of one in the x-direction and a Higuchi dimension of zero in y-direction. The average value of approximately 0.5 for methods (i) and (ii) can be seen in Figure 3. Methods (iii) and (iv) yielded a value around 1, as can be seen in Figure 3, too. Finally, the Higuchi dimension of the random image correctly shows the highest values of all.

Contrary to these positive findings for the Higuchi dimension analysis, the Fourier dimension analysis led to quite erroneous values for the non fractal images, which can be seen in Figure 4. The negative values obtained for the constant image and the cosine image are simply incorrect. The Fourier dimension $D_F = 4$ of the random dimension should instead be 3 and is therefore far too large.

## Influence of ROI

The influence of ROIs on the calculations of fractal dimensions is evident, because all the pixels outside of the ROI are zero, representing a black background. If these zeros were included in the calculations, they would definitely alter the results. Therefore, the exclusion of these pixels seems to be mandatory. Exclusion seems to be an easy way of avoiding these problems, but unfortunately this exclusion is not possible for every ROI. In fact, exclusion is only possible for a rectangular ROI, because the image inside the ROI can be extracted as a new image. For all other arbitrary shaped ROIs, there will always be some zero pixels. The influence of background effects was not examined for the Fourier dimension, due to the bad results presented so far. At this stage of development, it appears to be unnecessary to attempt to adapt the Fourier method to give reliable results, especially for ROIs. On the other hand, the Higuchi method offers great potential to overcome these ROI influences very easily. It is possible to exclude background (zeroes) prior to the dimension calculations, and the results thereby gained are shown in Tables 1 and 2 for projection method

(i) and extraction method (ii), respectively. The first two rows show the "correct" values without ROIs, where an exclusion of background does not alter the results, due to an absence of zero background values.

**Table 1:** ROI influences on Higuchi Dimension using projection method (i)

| ROI | Backgr. | Const | Cos | D=2.2 | D=2.5 | D=2.8 | Random |
|---|---|---|---|---|---|---|---|
| - | Incl. | 0 | 0.59 | 1.36 | 1.53 | 1.73 | 2.09 |
| - | Excl. | 0 | 0.59 | 1.36 | 1.53 | 1.73 | 2.09 |
| Rect. | Incl. | 1.09[h] | 1.14[h] | 1.19[l] | 1.32[l] | 1.45[l] | 1.26[l] |
| Rect. | Excl. | 0 | 0.59 | 1.40 | 1.68 | 1.90 | 2.16 |
| Ellipse | Incl. | 1.29[h] | 1.23[h] | 1.37[l] | 1.46[l] | 1.52[l] | 1.37[l] |
| Ellipse | Excl. | 0 | 1.48[h] | 1.40 | 1.59 | 1.74 | 2.14 |

[h]value is too low.

[l]value is too high.

**Table 2:** ROI influences on Higuchi Dimension using every row and column extraction method (ii)

| ROI | Backgr. | Const | Cos | D=2.2 | D=2.5 | D=2.8 | Random |
|---|---|---|---|---|---|---|---|
| - | Incl. | 0 | 0.59 | 1.58 | 1.80 | 1.99 | 2.10 |
| - | Excl. | 0 | 0.59 | 1.58 | 1.80 | 1.99 | 2.10 |
| Rect. | Incl. | 0.74[h] | 0.75[h] | 0.95[l] | 1.11[l] | 1.22[l] | 1.28[l] |
| Rect. | Excl. | 0 | 0.59 | 1.64 | 1.90 | 2.07 | 2.16 |
| Ellipse | Incl. | 1.14[h] | 1.04[h] | 1.23[l] | 1.41[l] | 1.55[l] | 1.64[l] |
| Ellipse | Excl. | 0 | 0.56 | 1.51 | 1.76 | 1.97 | 2.10 |

[h]value is too low.

[l]value is too high.

The rectangular ROI caused following distortions in case of including background (third row in the tables) compared to the "correct" values (first/second row in the tables). For the constant image, projection method (i) (Table 1) showed a far too high Higuchi dimension $D_H$ of approximately 1 instead of $D_H$=0. Extraction method (ii) (Table 2) led to a Higuchi dimension value estimation of 0.74. Almost identical values were gained for the cosine shaped image. The values for the predefined fractal images ($D$=2.2, 2.5, 2.8) are drastically lowered, which is a clear consequence of the leading and tailing zeroes. Effectively, the values represent a mixture of both fractal dimensions ($D$=2.2, 2.5, 2.8 and 0). Decreased values can also be seen for

the random image. Overall, the influence of a rectangular ROI is very drastic and cannot be neglected. On the other hand, exclusion of the background (fourth row in the tables) compensated the ROI effects very well. The values for the non-fractal images are now nearly correct. Only the values for the fractal images and the random image are marginally higher.

The elliptical ROI caused distortions in case of including background (fifth row in the tables) compared to the "correct" values (first/second row in the tables), which are quite similar to the rectangular case. The details are not really of interest, because an arbitrary ROI would lead to an arbitrary background, influencing the results in an individual manner. More important is the question of whether it is possible to restore the values by eliminating the background. In contrast to a rectangular ROI, the background influence can not be eliminated in the same manner, especially for method (i) (sixth row in Table 1). A data point of the projection is only zero when and where all image pixels along the projection direction are zero. In fact, this condition holds only for pixels outside the surrounding rectangle of the ellipse. The areas inside the corners of the surrounding rectangle have zero values, and therefore the projection sums include these zero values, which evidently alter the determinations of the Higuchi dimension. Again, the elimination of the background resembled, with a high degree of conformity, the "correct" values.

Finally, using the extracted signals according to method (ii) (sixth row in Table 2), it was again possible to restore the values for the Higuchi dimension.

## DISCUSSION

There are several accepted methods for determining the fractal properties of objects represented by digital images. The unavoidable drawback of digital images is the limited resolution. A pixel of an image is the smallest element, while the size of the image is the largest element of an image. Nevertheless, fractal analysis of digital images has been very successful in the past and can give reliable results with a high degree of validity [24], [25]. In contrary, this study showed that the Fourier method, which is commonly well suited for gray value images, performed rather poorly if solely regions of interests should be evaluated. The problem of the Fourier method is that it cannot be restricted to regions of interests at all. The discrete Fourier transformation of digital images is calculated with sums of all the elements in the individual

rows and columns. A spatial data restriction is not compatible with discrete Fourier transformation.

In this study, an extension of the classical methods (e.g. Fourier dimension) for digital images has been proposed. This extension includes the use of fractal signal analysis and incorporates a time series evaluation method, developed for the determination and investigation of chaotic dynamical systems. The 2D digital images must be transformed into 1D signals, and the resulting gray level signal can be treated as if it were a time series signal.

The fractal dimensions of the 1D signals were calculated using the Higuchi method. Prior investigations included quite complex methods, such as phase space reconstructions. Especially, Mattfeld [20] proposed a method of stitching together 10 consecutive binary images of 510×510 pixels. The fraction of cells within 510 pixel long column perpendicular to the long axis gave the values for an 1D function. Despite the overall complexity, calculations were restricted to binary images. Contrary, calculations for the Higuchi method do not require a very high computational effort and can be implemented very fast for grey value images, without the need of image segmentation. Klonowski et al. [21] have already implemented the projection method according to (i) but comparisons to other extraction methods or the restriction to region of interests were not given.

In this study four 2D to 1D transformations have been thoroughly examined. The projection method (i) yields two 1D signals, which yield two values for the fractal dimension of one image: one for the x-axis and another for the y-axis. If the object in the digital image should be characterized by a single fractal dimension, an average of both values can be calculated. This average reflects the fractal dimension of the whole image, eliminating possible directional dependencies. For radially symmetric objects like fractal landscapes, both values are nearly identical. For other images, such as the image with a cosine shape in the x-direction and constant shape in y-direction, both values are different.

Therefore, the calculation of two directionally dependent fractal dimensions allows the distinguishing of directional dependencies, which cannot be resolved by classical 2D methods at all. In addition to this advantage, it is always possible to average the two different values and get a value identical to the classical methods.

The projection of the images according to method (i) naturally causes a reduction of information. Hence, only global characteristics of the object

under investigation are examined. The actual values have been slightly lower than the real values. If fine details cannot be ignored, it is possible to avoid the projection by extracting every row and/or column and by calculating the corresponding means, according to method (ii). The computational effort is higher, but every individual value of every pixel is incorporated. Again, the method has the advantage of calculating directional dependencies, as well as the possibility of getting a single average value for the whole image. Orientation independent analyses can be carried out by using the extraction method (iii) or (iv). The calculation effort is lower than for method (ii), but the results are quite reliable. Particularly, the spiral extraction method gives a rotationally independent result without the need of calculating averages.

Moreover, the proposed methods can be applied to regions of interests only. By eliminating the leading and tailing zeros, it has been shown that the proposed 1D method estimates the fractal dimension very well. For arbitrary shapes of the regions of interests, it turned out, that the projection method according to method (i) should be avoided, because there is the possibility of summing up some zero values that are spatially located outside the ROI, but inside the surrounding rectangle. In these cases, it is necessary to use the extraction methods according to (ii) or (iii).

Despite the effectiveness of the proposed 1D extraction method, especially compared to the Fourier method, the limitation is obviously the indirect determination of fractal dimensions $D_{2D}$ of two dimensional objects. In principle, for any one dimensional algorithm, $D_{2D}$ could be determined by adding 1 to $D_{1D}$,

$$D_{2D} = D_{1D} + 1, \tag{9}$$

but this may not be valid for every object, fractal or 2D to 1D extraction method. Considering practical aspects of recalculating $D_{2D}$ from $D_{1D}$, the influence of ROIs, especially for the case of projection, can be investigated by the following generalization:

$$D_{2D} = D_{1D} + c, \tag{10}$$

$c$ being an experimentally derived constant. Since a ROI is a subset of the whole image, the fractal dimension of a ROI image (as far as discussed in this study) should be equal to the fractal dimension of the whole image. If at least one typical test image without any ROI is available, $D_{2D}$ can be estimated with equation (9). If several typical test images are available (which is often the case), the mean could be calculated. Applying several typical ROIs on

this test image or these test images yields $c$, by using equation (10). If $c$ is known, the dimension $D_{2D}$ of a single image under investigation with a ROI can be calculated with equation (10).

## CONCLUSION

The fractal dimensions of objects in a digital image have been investigated by classical 2D methods, such as Box counting or Fourier methods, for a long time. Despite providing many reliable results, these methods have several restrictions, such as direction independence and the impossibility to restrict calculations to regions of interests. These shortcomings are especially problematic because the restriction to regions of interests is a very common task for biomedical images.

To overcome these limitations, this study proposes the transformation of 2D image data to 1D data series and the application of time series analyzing methods. The Higuchi dimension was calculated, and it has been possible to show that the proposed method is able to overcome the aforementioned shortcomings of classical 2D methods. It is possible to obtain directionally dependent fractal dimensions and, moreover, this approach can handle regions of interests very well.

The transformations to 1D signals have been carried out by four methods, but could be extended in future studies. Moreover, there is the great advantage that any conceivable 1D method, initially developed for time series analyses, can be adapted to investigate the spatial gray level information of digital images. In particular, it is intended to apply this method, as an example, to histological images of intraepithelial neoplasia, where a directional examination was not possible before. Prior quantitative examinations included the spatial shape and structure of nuclei [26], but it was not possible to consider their directional distribution throughout the epithelium. In addition, the possibility of restriction to regions of interests will decrease calculation errors and improve classification results. This method will certainly help the pathologist solve a long time diagnosis problem.

## REFERENCES


1. Fuseler JW, Bedenbaugh A, Yekkala K, Baudino TA. Fractal and image analysis of the microvasculature in normal intestinal submucosa and intestinal polyps in $apc^{Min/+\ Mice}$. MicroscMicroanal. 2010;16:73–79.
2. Xiaa Y, Fenga F, Zhaob R, Zhang Y. Multifractal signature estimation for textured image segmentation. Pattern RecognLett. 2010;31(2):163–169.
3. Ahammer H, DeVaney TTJ. The influence of edge detection algorithms on the estimation of the fractal dimension of binary digital images. Chaos. 2004;14:183–188.
4. Ahammer H, DeVaney TTJ, Tritthart HA. Fractal dimension of K1735 mouse melanoma clones and spheroid invasion in vitro. EurBiophys J. 2001;30:494–499.
5. Ahammer H, Helige C, Dohr G, Weiss-Fuchs U, Juch H. Fractal dimension of the choriocarcinoma cell invasion front. Physica D. 2008;237:446–453.
6. Pentland A. Fractal-based description of natural scenes. IEEE Trans. Pattern Anal Mach Intell. 1984;6:661–674.
7. Chaudhuri BB, Sarkar N. Texture segmentation using fractal dimension. IEEE Trans. Pattern Anal Mach Intell. 1995;17:72–77.
8. Dubuc B, Roques-Carmes C, Tricot C, Zucker SW. The variation method: a technique to estimate the fractal dimension of surfaces. SPIE Visual Commun Image Process. 1987;II845:241–248.
9. Peleg S, Naor J, Hartley R, Avnir D. Multiple resolution texture analysis and classification. IEEE Trans Pattern Anal Mach Intell. 1984;6:518–523.
10. Ahammer H, DeVaney TTJ, Tritthart HA. Fractal dimension for a cancer invasion model. Fractals. 2001;9:61–76.
11. Anguiano E, Pancorbo M, Aguilar M. Fractal characterization by frequency analysis. I Surfaces J Microsc. 1993;172:223–232.
12. Aguilar M, Anguiano E, Pancorbo M. Fractal characterization by frequency analysis. II. A new method. J Microsc. 1993;172:233–238.
13. Falconer K. Fractal Geometry 2nd ed. Chichester: John Wiley & Sons; 2003.
14. Fraser AM. Reconstructing attractors from scalar time-series - A comparison of singular system and redundancy criteria. Physica

D. 1989;34:391–404.

15. Grassberger P, Procaccia I. Characterization of strange attractors. Phys Rev Lett. 1983;50:346–349.
16. Broomhead DS, King GP. Extracting qualitative dynamics from experimental data. Physica D. 1986;20:217–236.
17. Yalcinkaya T. Bifurcation to strange nonchaotic attractors. Phys Rev E. 1997;56:1623–1630.
18. Scheffer M, Bascompte J, Brock WA, Brovkin V, Carpenter SR, Dakos V, Held H, vanNes EH, Rietkerk M, Sugihara G. Early-warning signals for critical transitions. Nature. 2009;461(7260):53–59.
19. Higuchi T. Approach to an irregular time-series on the basis of the fractal theory. Physica D. 1988;31:277–283.
20. Mattfeldt T. Nonlinear deterministic analysis of tissue texture: A stereological study on mastopathic and mammary cancer tissue using chaos theory. J Microsc. 1997;185:47–66.
21. Klonowski W, Olejarczyk E, Stepien R. A new simple fractal method for nanomaterials science and nanosensors. Mater Sci-Poland. 2005;23:607–612.
22. Sullivan R, Holden T, Tremberger G, Cheung E, Branch C, Burrero J, Surpris G, Quintana S, Rameau A, Gadura N, Yao H, Subramaniam R, Schneider P, Rotenberg SA, Marchese P, Flamhlolz A, Lieberman D, Cheung T. Fractal dimension of breast cancer cell migration in a wound healing assay. International Journal of Biological and Life Sciences. 2010;6(3):170–175.
23. Turner MJ, Blackledge JM, Andrews PR. Fractal Geometry in Digital Imaging. San Diego: Academic Press; 1998.
24. Ahammer H, DeVaney TTJ, Tritthart HA. How much resolution is enough? - Influence of downscaling the pixel resolution of digital images on the generalised dimensions. Physica D. 2003;181:147–156.
25. Ahammer H, DeVaney TTJ. The influence of noise on the generalized dimensions. Chaos SolitonFract. 2005;25:707–717.
26. Ahammer H, Kroepfl JM, Hackl C, Sedivy R. Fractal dimension and image statistics of anal intraepithelial neoplasia. Chaos SolitonFract. 2011;44:86–92.

# 7

# *Towards Video Quality Metrics Based on Colour Fractal Geometry*

**Mihai Ivanovici[1], Noel Richard, ¨ [2], and Christine Fernandez-Maloigne[2]**

[1]MIV Imaging Venture Laboratory, Department of Electronics and Computers, Faculty of Electrical Engineering and Computer Science, "Transilvania" University, Str. Politehnicii nr. 1, 500019 Bras¸ov, Romania
[2]XLIM-SIC UMR CNRS 6172, Signals, Images and Communications Laboratory, University of Poitiers, Poitiers, Bat. SP2MI, ˆ T´el´eport 2, Bvd. Marie et Pierre Currie, BP 30179, 86962 FuturoscopeChasseneuilCedex, France

## ABSTRACT

Vision is a complex process that integrates multiple aspects of an image: spatial frequencies, topology and colour. Unfortunately, so far, all these elements were independently took into consideration for the development of image and video quality metrics, therefore we propose an approach that blends together all of them. Our approach allows for the analysis of the complexity of colour images in the RGB colour space, based on the probabilistic algorithm for calculating the fractal dimension and lacunarity. Given that all the existing fractal approaches are defined only for gray-scale images, we extend them to the colour domain. We show how these two colour fractal features capture the multiple aspects that characterize the

**Citation:** Ivanovici, M., Richard, N., & Fernandez-Maloigne, C. (2010). Towards video quality metrics based on colour fractal geometry. EURASIP Journal on Image and Video Processing, 2010, 1-18. DOI: 10.1155/2010/308035

degradation of the video signal, based on the hypothesis that the quality degradation perceived by the user is directly proportional to the modification of the fractal complexity. We claim that the two colour fractal measures can objectively assess the quality of the video signal and they can be used as metrics for the user-perceived video quality degradation and we validated them through experimental results obtained for an MPEG-4 video streaming application; finally, the results are compared against the ones given by unanimously-accepted metrics and subjective tests.

## VIDEO QUALITY METRICS

There is a plethora of metrics for the assessment of image and video quality [1]. They used to be: (i) *full reference* or *reference based*, when both the video sequence at the transmitter and the video sequence at the receiver are available, then the sequence at receiver is compared to the original sequence at transmitter, and (ii) *no reference* or *without reference*, when the video sequence at the transmitter is not available; therefore, only the video sequence at the receiver is being analyzed. Recently a third class of metrics emerged: the so-called "reduced-reference" [2, 3] which are based on the sequence at the receiver and on some features extracted from the original signal at the transmitter. This is the case of the fractal measures we propose.

For the quality assessment of an image or a video sequence, the metrics can be also divided into *subjective* and *objective*. During the last decade, several quality measures, both subjective and objective, have been proposed, especially for the assessment of the quality of an image after lossy compression, image rendering on screen or for digital cinema [4]. Most of them use models of the human visual system to express the image perception as a specific pass-band filter (to be more precise, a pass-band filter for the achromatic vision and a low pass-filter for the chromatic one) [5]. In this paper we explore a well-known property of the human visual system, that is, to be "sensitive" to the visual complexity of the image. We use fractal features—thus a multiscale approach—to estimate this complexity. In addition, we rely on the hypothesis that the fractal geometry is capable of characterizing the image complexity in its whole—the space—frequency complexity and the colour content–-thus the complexity of the image reflected in a certain colour space, and any of the aspects of the image degradation, like a more spread power spectrum and local discontinuities of the natural correlation of the image.

The most complex metrics are based on models of the human visual system, but some of them are now classical signal fidelity metrics like the signal-to-noise ratio (SNR) and its variant peak SNR (PSNR), the mean-squared error (MSE) and root MSE (RMSE) which are simply distance measures. These simple measures are unable to capture the degradation of the video signal from a user perspective [6]. On the other hand, the subjective video quality measurements are time consuming and must meet complex requirements (see the ITU-T recommendations [7–10]) regarding the conditions of the experiments, such as viewing distance and room lighting. However, the objective metrics are usually preferred, because they can be implemented as algorithms and are human-error free.

The Video Quality Experts Group (VQEG) (http://www.vqeg.org/) is the main organization dealing with the perceptual quality of the video signal and they reported on the existing metrics and measurement algorithms [11]. A survey of video-quality metrics based on models of the human vision system can be found in [12] and several no-reference blockiness metrics are studied and compared in [13]. A more recent state-of-the-art of the perceptual criteria for image quality evaluation can be found in [14]. OPTICOM (http://www.opticom.de/) is the author of one metric for video quality evaluation called "Perceptual Evaluation of Video Quality" (PEVQ), which is a reference-based metric used to measure the quality degradation in case of any video application running in mobile or IP-based networks. The PEVQ Analyzer [15] measures several parameters in order to characterize the degradation: brightness, contrast, PSNR, jerkiness, blur, blockiness, and so forth. Some of the first articles that proposed quality metrics inspired by the human perception [16, 17] drew also the attention on some of the drawbacks of the MSE and the importance of subjective tests. Among the unanimously accepted metrics for the quantification of the user-perceived degradation are the ones proposed by Winkler use image attributes like sharpness and colourfulness [18–20]. In [21], the authors propose a no-reference quality metric also based on the contrast, but taking into account the human perception, and in [22], the hue feature is exploited. Wang proposes in [23] a metric based on the structural similarity between the original image and the degraded one. The structural similarity (SSIM) unifies in its expression several aspects: the similarity of the local patch luminances, contrast, and structure. This metric was followed by a more complex one, based on wavelets, as an extension of SSIM to the complex wavelet domain, inspired by the pattern recognition capabilities of the human visual system [24].

Together with Wang, Rajashekar is the author of one of the latest image quality metric based on an adaptive spatiochromatic signal decomposition [25, 26]. The method constructs a set of spatiochromatic function basis for the approximation of several distortions due to changes in lighting, imaging, and viewing conditions. Wavelets are also used by Chandler and Hemami to develop a visual signal-to-noise ratio (VSNR) metric [27] based on their recent psychophysical findings [28–30]. Related to the wavelets, a multiresolution model based on the natural scene statistics is used in [31].

Most of the existing metrics for the video quality are used to quantify the degradation introduced by the compression algorithm itself, as a consequence of the reduced bit rate. We are interested in objectively assessing the degradation in video quality caused by the packet loss at network level [32]. In our experiments, we identified two kinds of degradation: (i) the degradation that affects the sequence, that is, the temporal component of the signal and (ii) the degradation that affects the frames, that is, the spatial component. Given the way the majority of the video frames are degraded (see Figure 1), the most useful metric would be the blockiness, which objectively quantifies the impairments. To quantify the degradation of a single video frame, one could simply measure the affected area in number of pixels of number of $8 \times 8$ blocks or an appropriate perceptual metric, able to quantify the degradation from a human perspective. Apart from blockiness, the degraded frames are «dirty», that is, many blocks containing other information than they should. Therefore, a metric able to quantify the *dirtiness* would be useful.

(a) Original video frame, CFD = 3.14 (b) Degraded video frame, CFD = 3.31 (c) Absolute difference, CFD = 3.072

**Figure 1**: One original video frame from the "football" video sequence (a), the corresponding degraded received video frame (b), and the absolute difference (c).

The degradation that affects the video frames is in fact a mixture of several impairments, including blockiness and the sudden occurrence of new colours. The modifications of the image content reflect both in the

colour histograms—a larger spread of the histogram due to the presence of new colours—and the spectral representation of the luminance and chrominance (high frequencies due to blockiness). Given all the above considerations, we believe that metrics like blur, contrast, brightness, and even blockiness lose their meaning, and they are not able to reflect the degradation; therefore, they cannot be applied for such degraded video frames. Metrics able to capture all the aspects of the degradation that reflect the colour spread–-the amount of new colours occurring in the degraded video frames would be more appropriate. We, therefore, consider that the approaches based on multiscale analysis and image complexity are more adapted to the video-quality assessment. Fractal analysis-based approaches offer the possibility to synthesize into just one measure adapted to the human visual system, all the relevant features for the quality of an image (e.g., colourfulness and sharpness) instead of analyzing all image characteristics independently and then to find a way to combine the intermediate results. Due to its multiscale nature, the fractal analysis is in accordance with the spirit of all multiresolution wavelet-based approaches mentioned before, which unfortunately work only for gray-scale images. Therefore, one of the advantages of our approach would be the fact that it also takes into account the colour information. In addition, the fractal measures are invariant to any linear transformation like translation and rotation.

Our choice is also justified by the way that humans perceive the fractal complexity. In a study on human perception conducted on fractal pictures [33], the authors conclude that "the hypothesis on the applicability and fulfillment of Weber-Fechner law for the perception of time, complexity and subjective attractiveness was confirmed". Their tests aimed at correlating the human perception of time, complexity, and aesthetic attractiveness with the fractal dimension and the Lyapunov exponent, based on the hypothesis that the perception of fractal objects may reveal insights of the human perceptual process. In [34], the most attractive fractals appeared to be the ones with the fractal dimension comprised between 1.1 and 1.5. According to [35], "the prevalence of fractals in our natural environment has motivated a number of studies to investigate the relationship between a pattern's fractal character and its visual properties", for example, [36, 37]. The authors of [35] investigate the visual appeal as a function of the fractal dimension, and they establish three intervals: [1.1–1.2] low preference, [1.3–1.5] high preference, and [1.6–1.9] low preference. Pentland finds in this psychophysical studies [38, 39] that for the one-dimensional fractional

Brownian motion and the two-dimensional Brodatz textures, the correlation between the fractal dimension and the perceived roughness is more than 0.9.

Last but not least, the very essence of the word "complex" of Latin-etymology—meaning "twisted together", designating a system composed of closely connected components—emphasizes the presence of multiple components that interact with each other, generating an emergent property [40].

## FRACTAL ANALYSIS

The fractal geometry introduced by Mandelbrot in 1983 to describe self-similar sets called fractals [41] is generally used to characterize natural objects that are impossible to describe by using the classical (Euclidian) geometry. The fractal dimension and lacunarity are the two most-known and widely used fractal analysis tools. The fractal dimension characterizes the complexity of a fractal set, by indicating how much space is filled, while the lacunarity is a mass distribution function indicating how the space is occupied [42]. These two fractal properties are successfully used to discriminate between different structures exhibiting a fractal-like appearance [43–45], for classification and segmentation, due to their invariance to scale, rotation, or translation. The fractal geometry proved to be of a great interest for the digital image processing and analysis in an extremely wide area of applications, like finance [46], medicine [44, 47, 48], and art [49].

There exist several different mathematical expressions for the fractal dimension, but the box-counting is the most popular due to the simplest algorithmic formulation, compared to the original Hausdorff definition expressed for continuous functions [50]. The box-counting definition of the fractal dimension is $D_{\text{box}} = -\log N(\delta)/\log \delta$, where $N(\delta)$ is the number of boxes of size $\delta$ needed to completely cover the fractal set. The first practical approach belongs to Mandelbrot, but that was followed by the elegant probability measure of Voss [51, 52]. On a parallel research path, Allain and Cloitre [53] and Plotnick et al. [54] developed their approach as a version of the basic box-counting algorithm. All the other approaches for the computation of the fractal dimension, like $\delta$-parallel body method [55] (a.k.a. covering-blanket approach, Minkowsky sausage, or morphological covers) or fuzzy [56] are more complex from a point of view of implementation and more difficult to extend to a multidimensional colour space. However, we proposed in [57] a colour extension of the covering blanket approach based

on a probabilistic morphology. On the other hand, despite the large number of algorithmic approaches for the computation of the fractal dimension and lacunarity, only few of them offer the theoretical background that links them to the Hausdorff dimension.

However, such tools were developed long time ago for grey-scale small-size images, but due to the evolution of the acquisition techniques the spatial resolution significantly increased and, in addition, the world of images became coloured. The very few existing approaches for the computation of fractal measures for colour images are restricted to a marginal colour analysis, or they transform a gray-scale problem in false colour [48]. In the following section, we briefly present our colour extension of the existing probabilistic algorithm by Voss [51], fully described in [58], which were validated on synthetic colour fractal images [59] and used to characterize the colour textures representing psoriatic lesions, in the context of a medical application in dermatology [60]. Then, we show how the colour fractal dimension and lacunarity can be used to characterize the degradation of the video signal for a video streaming application. Without loss of generality, we present the results we obtain in the case of an MPEG-4 video-streaming application.

## COLOUR FRACTAL DIMENSION AND LACUNARITY

The existing approaches for the estimation of the fractal dimension, especially the box-counting-like approaches, consider the gray-scale image a set of points S in an Euclidian space of dimension E. In the probabilistic algorithm defined by Voss [51] upon the proposal from Mandelbrot [41], the spatial arrangement of the set is characterized by the probability matrix $P(m,\delta)$, the probability of having m points inside a cube of size $\delta$ (called *box*), centered in an arbitrary point of the set S. In other words, $P(m,\delta)$ is the probability that the signal «visited» the box of size $\delta$. The matrix is normalized so that $\sum_{m=1}^{N} P(m,\delta) = 1,\ \text{for all}\ \delta \in R^{+}$, where N is the maximum number of pixels that are included in a box of size $\delta$. Given the total number of points in the image is M, the number of boxes that contain m points is $(M/m)P(m,\delta)$. Thus, the total number of boxes needed to cover the image is

$$\langle N(\delta)\rangle = \sum_{m=1}^{N} \frac{M}{m} P(m,\delta) = M \sum_{m=1}^{N} \frac{1}{m} P(m,\delta). \quad (1)$$

Consequently $N(\delta) = \sum_{m=1}^{N}(1/m)P(m,\delta)$ is proportional to $\delta^{-D}$, where D is the fractal dimension to be estimated.

If a gray-scale image is considered to be a discrete surface $z = f(x,y)$, where z is the luminance in every (x,y) point of the space, then a colour image is a hyper-surface in a 3-dimensional colour space. Thus, we deal with a 5-dimensional hyper-space where each pixel is a 5-dimensional vector. We use RGB for the representation of colours due to its cubical organization, even though it is not a Euclidian uniform space. The classical algorithm of Voss uses boxes of variable size $\delta$ centered in the each pixel of the image and counts how many pixels fall inside that box. We generalize this by counting the pixels for which the Minkowski infinity norm distance to the center of the hyper-cube is smaller than $\delta$. Practically, for a certain square of size $\delta$ in the (x,y) plane, we count the number of pixels that fall inside a 3-dimensional RGB $(r \pm \delta/2, g \pm \delta/2, b \pm \delta/2,)$ cube of size $\delta$, centered in the current pixel $(r,g,b)$—the colour of the current pixel. The theoretical development and validation on synthetic colour fractal images can be found in [58].

Even from the very beginning, when Mandelbrot introduced the fractal geometry, he was aware of the fact that the fractal dimension itself is not sufficient to fully capture the complexity of nondeterministic objects; therefore, he defined the lacunarity $\Lambda$ as a complementary metric. Later on, Voss expressed it based on the probabilities $P(m,\delta)$ and using the first and second order moments of the measure distribution (2). Following the previous considerations, the lacunarity can be therefore defined and computed for colour images as well. See also [61] for a complete view of the definition and the interpretation of lacunarity for synthetic and natural colour fractal images

$$\Lambda(\delta) = \frac{M^2(\delta) - (M(\delta))^2}{(M(\delta))^2}, \tag{2}$$

where

$$M(\delta) = \sum_{m=1}^{N} mP(m,\delta),$$

$$M^2(\delta) = \sum_{m=1}^{N} m^2P(m,\delta). \tag{3}$$

The lacunarity characterizes the topological organisation of a fractal object, an image in our particular case, being a scale-dependent measure of spatial heterogeneity. Images with small lacunarity are more homogeneous with respect to the size distribution and spatial arrangement of gaps. On the other hand, images with larger lacunarity are more heterogeneous. In addition, lacunarity must be taken into consideration after inspecting the fractal dimension: in a similar manner with the Hue-saturation couple in colour image analysis, the lacunarity becomes of greater importance when complexity, that is, the fractal dimension, increases.

## APPROACH ARGUMENTATION AND VALIDATION

In Figure 1, we present two video frames: one from the original video sequence and the corresponding degraded video frames from the sequence at the receiver, along with the pseudoimage representing the absolute difference between the former two. The computed colour fractal dimensions are 3.14, 3.31, and 3.072, respectively. One can see that the larger fractal dimension reflects the increased complexity of the degraded video frame. The increased complexity comes from the blockiness effect, as well as from the dirtiness and the augmented colour content (see also the 3D histograms in Figure 3).

The corresponding lacunarity curves are depicted in Figure 2. One can see that the curve for Figure 1(b) is placed highly above the curve for the Figure 1(a) indicating a more lacunar and heterogeneous image. Surprisingly enough, the difference Figure 1(c) has a very similar lacunarity to the one of the original image, but the difference pseudoimage is more lacunar than the original for small values of $\delta$: $\delta \leq 10$–-indicating that the degradation mainly takes place in blocks of $8 \times 8$ pixels–-while for larger values of $\delta$ it is less lacunar–-more uniform, clearly seen, and justified by the smaller variations of colours. The complexity revealed by the lacunarity curves is in accordance with the fractal dimension: the original unaffected video frame being a less lacunar image than the degraded one.

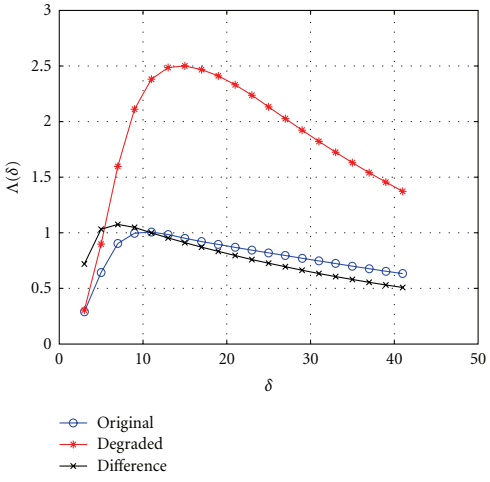


**Figure 2**: Lacunarity curves for the images in Figure 1 (also for images 10.1, 10.2, and 10.3 in Figure 10 , resp.).

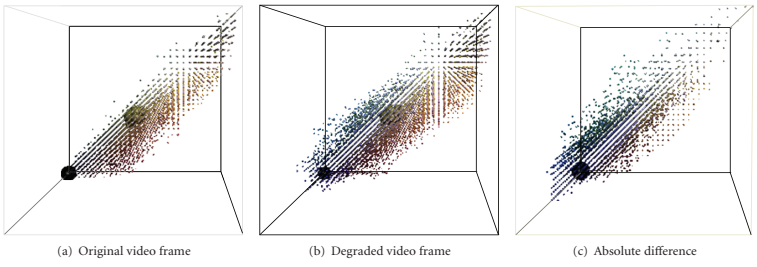


**Figure 3**: The 3D histograms for the two-video frames.

Because the lacunarity is a measure of how the space is occupied, we present in Figure 3 the 3D histograms in the RGB colour space, as a visual justification. One can see that the histogram of the degraded video frame is more spread than the one of the original video frame, indicating a more rich image from the point of view of its colour content.

For the quantification of the spread of the 3D histograms, we computed the co-occurrence matrices for the three images in Figure 1. This choice is justified by the fact that in the case of a random fractal the fractal dimension is proportional to the variance of the increments [51]. Therefore, we computed the co-occurrence matrices for a neighborhood distance of one pixel, on the horizontal direction. In this way, the computed co-occurrence

is a measure of the correlation between pixels. In Figure 4, for the two video frames we show the three overlayed co-occurrence matrices, one for each RGB component. The results indicate that the variance of the values is larger for the degraded video frames, indicating a smaller correlation between the neighbour pixels. The lack of correlation is the natural consequence of the sum of impairments that affect the degraded frame. As shown in [59], that the co-ocurrence matrix shape is linked to the fractal dimension of the signal or image. These two points of view—the 3D histograms and the co-occurrence matrices—are a first validity proof and justification for a fractal approach.

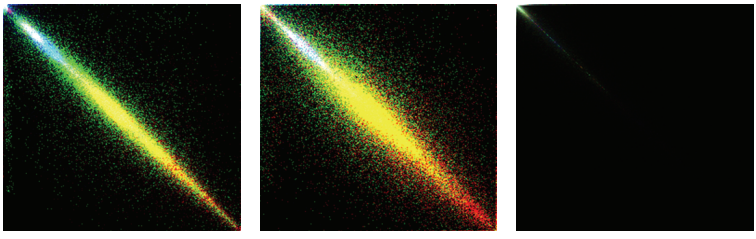

(a) Original video frame (b) Degraded video frame (c) Absolute difference

**Figure 4**: The overlayed co-occurrence matrices.

For an even further investigation and argumentation, we analyze the video frames from the point of view of their spectral fluctuations. Random function or signal complexity can be defined based on its power-density spectrum: for a random fractal signal v(t), the power-density function varies upon a power law in $1/f^{\beta}$. So, the Fourier transform $V(f,T)$ computed on T time samples of v(t) allows to express the spectral density function $S_V(f)$ as

$$S_V(f) \propto T\,|\,V(f,T)\,|^2 \quad \text{as } T \longrightarrow \infty. \tag{4}$$

The link between the power law of $\beta$ and the fractal dimension D is defined by the relation (5) from [51], where E is the dimension of the Euclidian space representing the topological dimension of the signal (e.g., E=1 for a one-dimensional signal and E=2 for an image) and H is the Hurst factor, which indicates the complexity of the fractal object. H is comprised between 0 and 1 and intimately connected to the fractal dimension. A value of H close to 0 indicates a very complex object, while a value close to 1 indicates a «simpler» object, that is, a smoother signal

$$D = E + 1 - H = E + \frac{3 - \beta}{2}. \tag{5}$$

Given that it is almost impossible to estimate the impact of the artifacts in the spatial domain, without any reference (original video signal), in the frequence domain is clearly enough that the artifacts induce very high frequencies and a specific modification of the spectrum which could be close to a complexity induced by a fractal model.

In Figure 5, we show the 2D FFT of the two video frames, for each colour plane, and in Figures 6, 7, and 8 the horizontal and vertical slices of the spectra, corresponding to the spatial frequencies v=0 and u=0, respectively. One can clearly note that the marginal analysis (plane by plane) is not able to reflect the entire colour degradation that affects the video signal, but the degradation induces a complexity fluctuation that is, well captured by the fractal dimension. So, it is yet another proof that justifies the use of a colour estimation of degradation by means of colour fractal geometry.

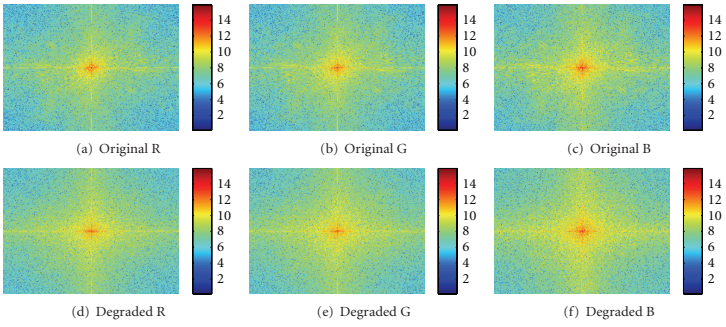


**Figure 5**: 2D FFT of the two video frames, per plane.

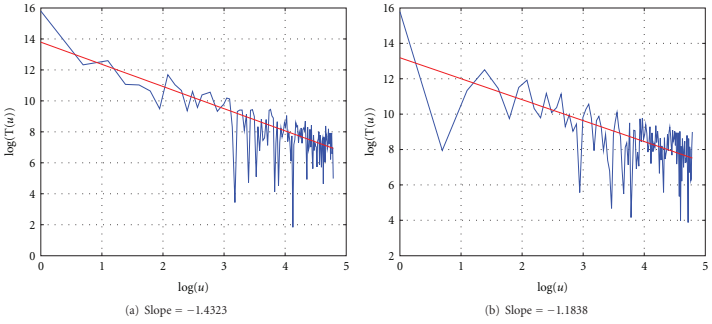

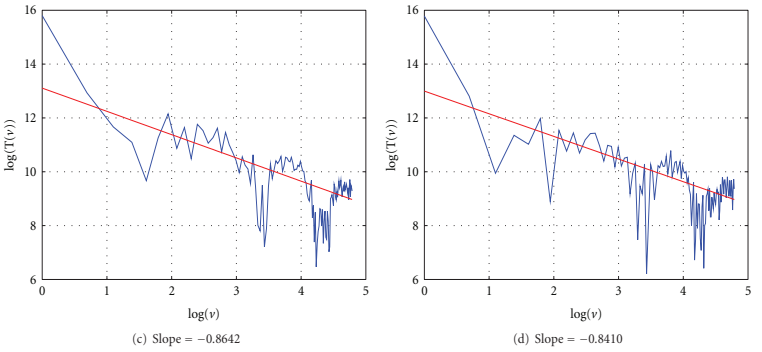


**Figure 6**: *T(u* ) (top) and *T(v* ) (bottom) for the red plane, for the original (left) and degraded (right) video frames.

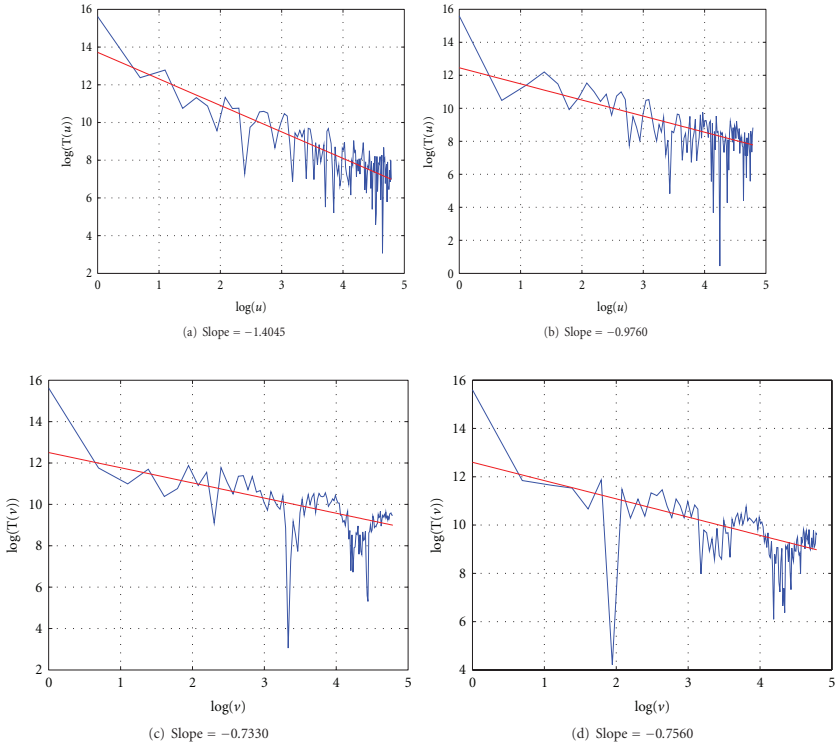


**Figure 7**: *T(u* ) (top) and *T(v* ) (bottom) for the green plane, for the original (left) and degraded (right) video frames.

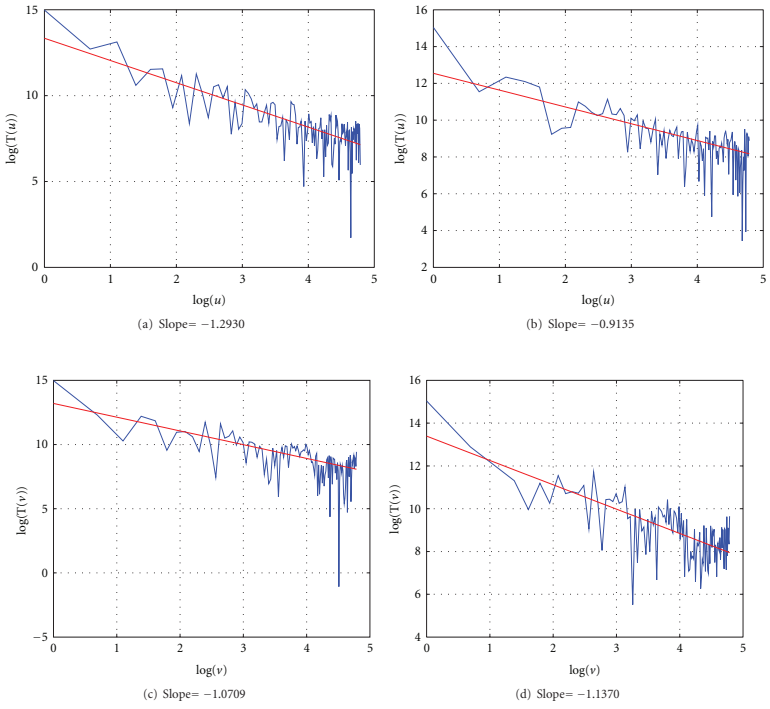


**Figure 8**: *T(u* ) (top) and *T(v* ) (bottom) for the blue plane, for the original (left) and degraded (right) video frames.

The order of complexity of our approach, for an image of size $N^2$ is $O(N^2M)$, where M represents the results of the sum $3^2+5^2+7^2+\cdots+m_{\max}^2$, $m_{\max}$ being the maximum hypercube size–- 41 in our case. Given that the sum of the squares of the first $n$ odd natural numbers is

$$1^2 + 3^2 + 5^2 + \cdots + (2n-1)^2 = \frac{n(2n-1)(2n+1)}{3}, \tag{6}$$

then

$$M = \frac{n(2n-1)(2n+1)}{3} - 1, \tag{7}$$

where $n = m_{\max}/2$.

In addition, due to the complexity of the colour Fourier transform based on Quaternionic approaches, our approach is the more suitable at this moment for a real-time implementation. For an image of size $N^2$, the complexity of

a parallel implementation of our approach would be $O(N^2)$, while for a 2D Fast Fourier Transform the best case is of $O(N^2 \log N)$ complexity.

In Figure 9(a), we depict the block diagram that illustrates the use of the colour fractal dimension and lacunarity as video-quality metrics in a reduced reference scenario. At the source, the two fractal measures are computed for each video frame and sent along with the coded video frames over the network. At destination, the same fractal measures are computed for the received video frames and compared with the references.

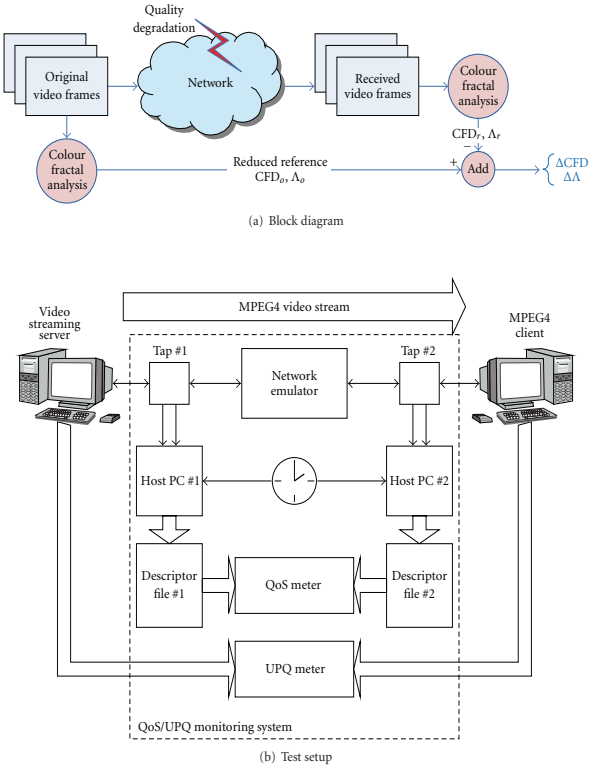


**Figure 9**: The block diagram and the test setup. Block diagramTest setup.

## EXPERIMENTAL RESULTS

From the plethora of IP-based video application, we chose an MPEG-4 streaming application. Streaming applications usually use RTP (Real-Time Protocol) over UDP; therefore, the traffic generated by such an application

is inelastic and doesnot adapt to the network conditions. In addition, neither UDP itself or the video streaming application implement a retransmission mechanism. Therefore, the video streaming applications are very sensitive to packet loss: any lost packet in the network will cause missing bits of information in the MPEG video stream.

Given that packet loss is the major issue for an MPEG-4 video streaming application, in our experiments the induced packet loss percentage varied from 0% to 1.3%. Above this threshold, the application cannot longer function (i.e., the connection established between the client and the server breaks), and tests cannot be performed. The test setup is depicted in Figure 9(b): the MPEG-4 streaming server we used was the Helix streaming server from Real Networks (http://www.realnetworks.com/) and the MPEG-4 client was mpeg4ip (http://mpeg4ip.sourceforge.net/). We modified the source code of the client to record the received video sequence as individual frames in bitmap format. We ran the tests using three widely used video sequences: "football", "female", and "train", MPEG-4 coded. The video sequences were 10 seconds long, with 250 frames, each of $320 \times 240$ size. The average transmission rate was approximately 1 Mb/s, which was a constrained from using a trial version of the MPEG-4 video streaming server–-however it represents a realistic scenario.

The monitoring system we designed and implemented uses two Fast Ethernet network taps to "sniff" the application traffic on the links between two Linux PCs that run the video streaming server and client. The traffic is further recorded as packet descriptors by the four programmable Alteon UTP (Unshielded Twisted Pair) and NICs (Network Interface Card), two for each tap, in order to mirror the full-duplex traffic. From each packet, all the information required for the computation of the network quality of service (QoS) parameters is extracted and stored in the local memory as packet descriptors. The host PCs, that control the programmable NICs, periodically collect this information and store it in descriptor files. These traffic traces are analyzed in order to accurately quantify the quality degradation induced by the network emulator: one-way delay, jitter, and packet loss, as instantaneous or average values, as well as histograms. In parallel, the video signal is recorded for the offline processing. Since the two measurements described above are correlated from the point of view of time, the effects of the measured network degradation on the quality of the video signal can be estimated by the module denoted user-perceived quality (UPQ) meter. More results and details about the experimental setup are to be found in [62–64].

In Figure 10, one may see three type of degradation that occurs in our tests: *important* or *severe* degradation (top); *less-affected* frames (middle) and *special* or green degraded frames (bottom). The difference $\Delta CFD$ between the colour fractal dimension of the degraded and the original corresponding video frame will be considerable for the first two images that exhibit an important degradation–-that is, almost the entire image is affected by severe blockiness, and the scene cannot be understood. $\Delta CFD$ will be small, but still positive for less affected images (the football players may no longer be identifiable, but the rest of the scene is unchanged). For the «green» images the colour fractal dimension is smaller than the one of the corresponding original frames, therefore, the $\Delta CFD$ will be negative.

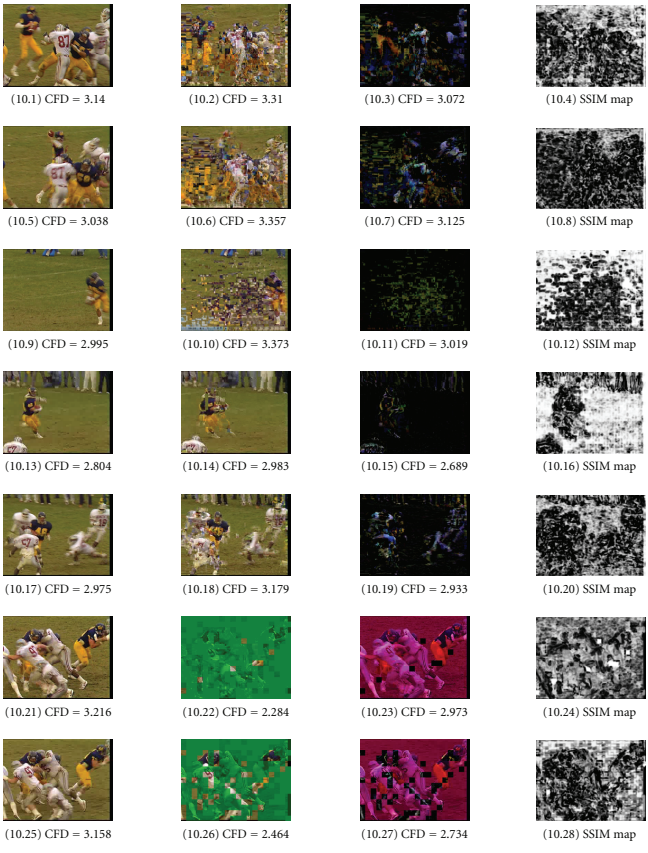


**Figure 10**: Original video frames (1st column) from the "football" sequence, degraded frames exhibiting different levels of degradation (2nd column), absolute differences (3rd column), and the SSIM map [ 23 ] (4th column).

The corresponding lacunarity curves are depicted in Figure 11–-the blue curve for the original video frame, the red curve for the degraded video frame, and the black one for the absolute difference pseudoimage. The largest lacunarity is for the most affected video frames, as expected. From a human perception point of view, the colourlacunarity curves are able to reveal the correct ranking, as well as the colour fractal dimension.

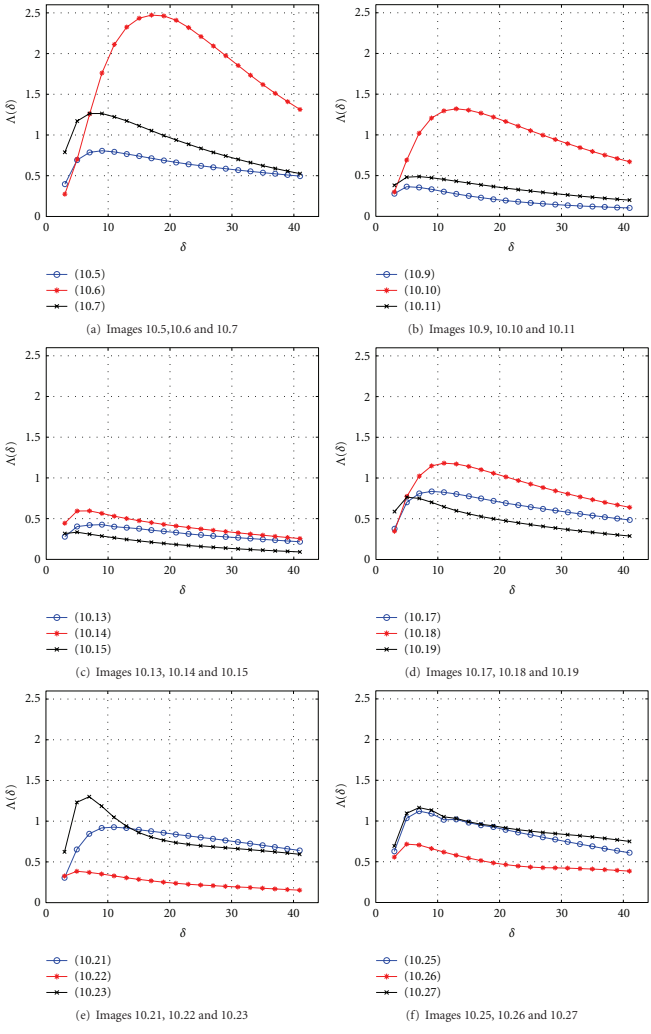


Figure 11: Corresponding colourlacunarity curves for the images in Figure 10.

In order to analyse the degradation in time, in Figure 12 the evolution of the colour fractal dimension in time is depicted. One can see that the original

"football" sequence is characterized by a large variation in the complexity of the image, due to the fact that the scene changes and also due to the high dynamicity. Therefore, the variation of the colour fractal dimension due to degradation is almost insignificant. In addition, due to the lost video frames, the two curves will get more and more desynchronized in time, which makes the analysis more difficult. However, it is possible to create a reference-based metric by using the colour fractal dimension (note the grey zones that indicate a slight increase of the fractal dimension due to quality degradation).

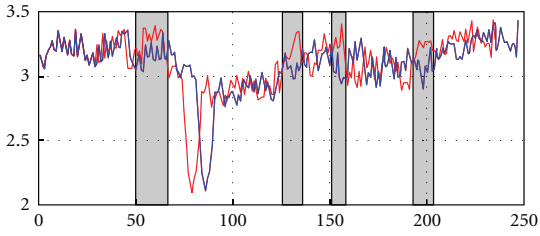


**Figure 12**: The colour fractal dimension as a function of time, blue-original, red-received, for the "football" video sequence.

One can note that for the original "football" video sequence the colourlacunarity has also an important variation (see Figure 13) from frame to frame, but its values are comprised between 0 and 1.5. For the degraded video sequence (b), we can see that the lacunarity skyrockets up to 3.0 for the interval of video frames affected by important degradation (the first interval market with grey). The less important degradation (the next greyed intervals) can only be detected if we take as reference the lacunarity of the original video sequence. In order to implement a no-reference metric, lacunarity $\geq 1.5$ can indicate the severe degradation.

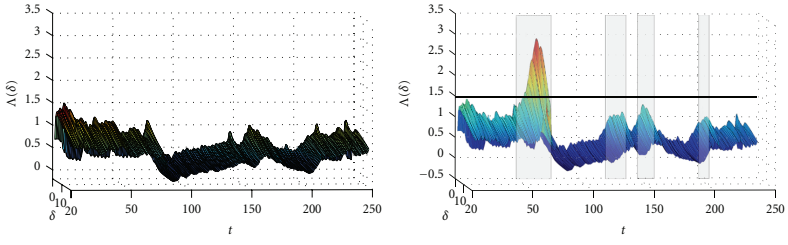


**Figure 13**: The colourlacunarity curves versus time for the "football" sequence. Original video seqDegraded video seq.

We analyzed two more video sequences: “female” and “train” (Figure 14). The corresponding colour fractal dimension as a function of time are depicted in Figure 15. The lacunarity curves are presented in Figure 16.

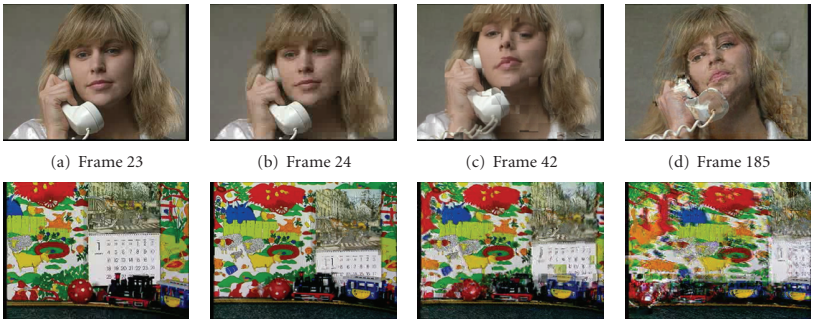

(a) Frame 23 (b) Frame 24 (c) Frame 42 (d) Frame 185

(e) Frame 0 (f) Frame 77 (g) Frame 105 (h) Frame 192

**Figure 14**: Frames from “female” (top row) and “train” (bottom row) video sequence.

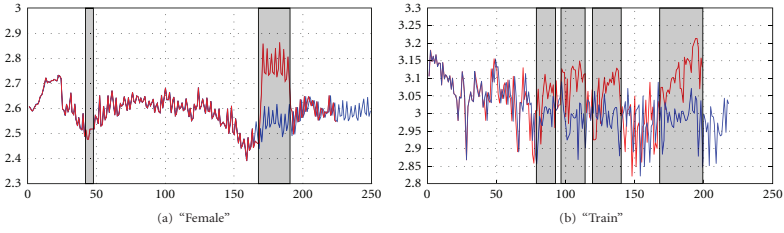

(a) “Female” (b) “Train”

**Figure 15**: The colour fractal dimension as a function of time (blue-original, red-received/degraded) for the “female” and “train” video seq.”Female””Train”.

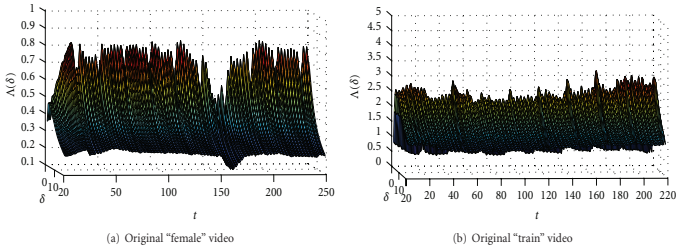

(a) Original “female” video (b) Original “train” video

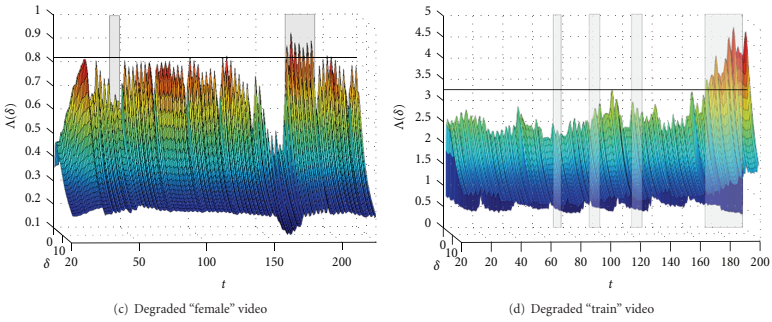


**Figure 16**: The colourlacunarity curves versus time for "female" and "train".

For the "female" and the "train" video sequences, one may note another interesting characteristic of the lacunarity curves, which exhibit a certain periodicity in time (see Figure 17). The explanation is the fact that from time to time the video signal is affected by a not-so-severe blockiness due to the encoding mechanisms only. This is not visible on the "train" video sequence, due to the high-complexity content of the image scene, but it can be easily seen on the "female" video sequence–-an example is depicted in Figure 14(b).

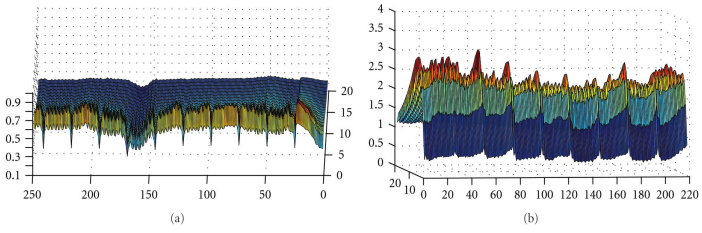


**Figure 17**: Periodicity of the lacunarity in time for the "female" (a) and "train" (b) video sequences.

## COMPARISON

In this section, we present a comparison with some of the metrics mentioned in the introduction: SNR, PSNR, MSE, SSIM, and VSNR. For the computation of the SSIM we used the Matlab code (http://www.ece.uwaterloo.ca/~z70wang/research/ssim/) provided by the author of the metric proposed in [23] and for VSNR the Matlab implementation available (http://foulard.ece.cornell.edu/dmc27/vsnr/vsnr.html) provided by the authors of

[27]. For colour images, the MSE (8), SNR (9), and PSNR (10) metrics are often computed independently for the red, green, and blue (RGB) colour channels and averaged together in order to compute the final distortion. We chose to compute these classical signal fidelity measures in the RGB colour space, despite of the very well-known fact that the RGB space is not perceptually uniform–-to be consistent with the definition of the colour fractal approach, which was developed based on the RGB colour space. We are aware of the fact that metrics like SNR and MSE could perform better in a perceptual colour space (e.g., CIELAB) and in addition we envisage a further development of the colour fractal approach in Lab and HSV

$$\mathrm{MSE} = \frac{1}{MN}\sum_{i=1}^{M}\sum_{j=1}^{N}[o(i,j) - d(i,j)]^2, \tag{8}$$

$$\mathrm{SNR} = 10\log_{10}\left[\frac{(1/MN)\sum_{i=1}^{M}\sum_{j=1}^{N}o(i,j)^2}{\mathrm{MSE}}\right], \tag{9}$$

where $o(i,j)$ is the original image, $d(i,j)$ is the degraded image, both of them of size $M \times N$

$$\mathrm{PSNR} = 10\log_{10}\left[\frac{I_{\max}^2}{\mathrm{MSE}}\right], \tag{10}$$

where $I_{\max}$ is the maximum intensity level, that is, 255 for an image.

In Table 1, we show the results we obtain for the images in Figure 10, when we compute the difference between the colour fractal dimension of the degraded video frame and the colour fractal dimension of the original video frame, along with the various metrics mentioned above. The values of $\Delta\mathrm{CFD}$ are very well correlated to SNR, PSNR, and MSE, and well correlated to VSNR, but they are not at all correlated to SSIM. However, for the minimum visible degradation—images 10.13 and 10.14 for which $\Delta\mathrm{CFD} = 0.178$ is small—the SSIM indicates the largest similarity, as well as PSNR, and VSNR has also a large value. For the largest visible degradation—images 10.21, 10.22, 10.25, and 10.26—the VSNR well captures it, while SSIM does not reach its minimum values.

**Table 1:**Comparison between the $\Delta CFD$ **and** SNR, PSNR, MSE, SSIM, and VSNR

| Images | ΔCFD | SNR [dB] | PSNR [dB] | MSE | SSIM | VSNR |
|---|---|---|---|---|---|---|
| 10.1, 10.2 | 0.17 | −11.9025 | 12.3316 | 0.0585 | 0.3907 | 2.1754 |
| 10.5, 10.6 | 0.319 | −11.1911 | 13.0221 | 0.0499 | 0.226 | 1.4855 |
| 10.9, 10.10 | 0.378 | −5.3733 | 18.8619 | 0.0130 | 0.5199 | −1.5415 |
| 10.13, 10.14 | 0.178 | −4.4426 | 19.7353 | 0.0106 | 0.6199 | 5.7999 |
| 10.17, 10.18 | 0.205 | −9.8929 | 14.3382 | 0.0368 | 0.2868 | 3.8740 |
| 10.21, 10.22 | −0.932 | −20.0039 | 4.2135 | 0.3790 | 0.4158 | 6.4629 |
| 10.25, 10.26 | −0.694 | −18.9250 | 5.2437 | 0.2990 | 0.3717 | 6.2717 |

We plan to perform a further comparison between the metrics on larger databases of test images. In addition, we have to mention the fact that the SSIM and VSNR were mainly used to assess the quality degradation induced by the image compression algorithms, case in which the image degradation is not as violent as in our experiments. Therefore the right way to compare our method against all the existing approaches is not straightforward and, definitely, not amongst the goals of the current paper.

In addition, in Table 2 we show a comparison of our approach against the SNR, PSNR, MSE, SSIM, and VSNR from the point of view of the required algorithmical complexity. We are assuming an image of size $N^2$.

Table 2:Complexity of approaches

| Approach | CFD | SNR | PSNR | MSE | SSIM | VSNR |
|---|---|---|---|---|---|---|
| Complexity | $O(N^2M)$ | $O(N^2)$ | $O(N^2)$ | $O(N^2)$ | $O(cN^2)$ | $O(N^2)$ |

The constant c for the complexity of SSIM approach is given by the size of the window for computing the local mean and variance—$8 \times 8$—and the $11 \times 11$ circular-symmetric Gaussian weighting function that is, used when computing the map of local SSIM values. The maximum complexity bounds in case of VSNR is clearly given by the complexity of the discrete wavelet transform (DWT) that is, used. It is known that an efficient implementation of DWT is $O(N^2)$. The following relationship is evident: c<M; however, the complexity of a parallel implementation of our approach would be in $O(N^2)$.

## SUBJECTIVE TESTS

The original hypothesis was that the quality perceived is directly proportional to the fractal complexity of an image. In order to validate from a subjective point of view the approach we proposed for the assessment of the video quality, we performed several subjective tests, on different video frames from video sequences—sport videos of football matches, in particular. The

aim of the experiments was to prove that the complexity of colour fractal images is in accordance with the human perception; therefore, the colour fractal analysis-based tools are appropriate for the development of video quality metrics.

We ran our experiments on a set of 27 individuals, guided by the general recommendations from [7]. In the experiment, we used video frames—original and degraded—from the standard test "football" video sequence. Pairs of images were presented, thus the experiments were *reference-based*. After presenting the minimum and the maximum degradation that may affect the video frames, the individuals were asked to grade the perceived degradation with a score comprised between 0 and 5, according to the levels of degradation presented in Table 3, in accordance with the quality levels specified by the ITU.

**Table 3:**Levels of perceived image degradation

| | |
|---|---|
| 0 | No degradation at all |
| 1 | imperceptible |
| 2 | perceptible, but not annoying |
| 3 | slightly annoying |
| 4 | annoying |
| 5 | very annoying |

For the images in Figure 10, the mean opinion score and the standard deviation, $\sigma_{MOS}$, computed based on the 27 responses are presented in Table 4, as well as the colour fractal dimension (CFD) and its variation, $\Delta CFD$.

**Table 4:**The MOS and standard deviation

| Image | (10.2) | (10.6) | (10.10) | (10.14) | (10.18) | (10.22) | (10.26) |
|---|---|---|---|---|---|---|---|
| MOS | 4.6296 | 4.2963 | 4.1852 | 2.2222 | 2.1111 | 5.0000 | 3.4444 |
| $\sigma_{MOS}$ | 0.4921 | 0.6688 | 0.6815 | 0.6980 | 0.8006 | 0 | 0.8006 |
| $\Delta CFD$ | 0.17 | 0.319 | 0.378 | 0.178 | 0.205 | −0.932 | −0.694 |
| CFD | 3.31 | 3.357 | 3.373 | 2.983 | 3.179 | 2.284 | 2.464 |

If we exclude the images 10.22 and 10.26, for which the estimated colour fractal dimension variation is negative because of the important degradation and lack of information, the correlation coefficient between the MOS and $\Delta CFD$ is 0.8523. Despite of the fact that these results must be extended to

a bigger image set, the approach creates a new perspective on the perception of colour image complexity. If we take into account the two images, 10.22 and 10.26, the correlation between mean score and estimated colour fractal complexity is 0.4857. This result, induced by the negative value for the colour fractal complexity variation, may lead to new developments for colour fractal measures. Clearly enough, the perceived complexity of those images is lower than the one of the others.

We conclude that the fractal dimension reflects the perceived visual complexity of the degraded images, as long as the degradation is not extreme and $\Delta CFD$ is not negative. We plan to run more subjective experiments in order to augment the pertinence of the results from a statistical point of view and to propose a better colour fractal estimator to deal with this minor numerical inconsistency.

## CONCLUSIONS

We conclude that the colourlacunarity itself can be used as a no-reference metric to detect the important degradation of the video signal at the receiver. The colour fractal dimension and lacunarity can be definitely used as a reference-based metrics, but this is usually impossible in a real environment setup when the original signal is not available at the receiver. The colour fractal dimension is not enough to be used as a stand-alone metric but in a reduced-reference scenario, the fractal features we propose—the colour fractal dimension and the colourlacunarity–-can be used to objectively assess any degradation of the received video signal and, given that they are correlated to the human perception, they can be used for the development of quality of experience metrics. An important aspect, which represents an invaluable advantage, is the robustness of the fractal measures to any modification of the video signal during the broadcast, like translation, rotation, mirroring or even cropping (e.g., when the image format is changed from 6:9 to 3:4).

For the computation of the two metrics we propose a colour extension of the classical probabilistic algorithm designed by Voss. We show that our approach is able to capture the relative complexity of the video frames and the sum of aspects that characterize the degradation of an image, thus the colour fractal dimension and lacunarity can be used to characterize and objectively assess the degradation of the video signal. To support our approach and conclusions, we also investigated the 3D histograms, the co-occurrence

matrices and the power density functions of the original and degraded video frames. In addition, we present the results of our subjective tests. Given that the fractal features are well correlated to the perceived complexity by the human visual system, they are of great interest as objective metrics in a video quality analysis tool set.

Our choice of using the RGB colour space perfectly suits the probabilistic approach, and the extension from cubes to hypercubes was natural and intuitive. We are aware of the fact that the RGB colour space may not be the best choice when designing an image analysis algorithm from the point of view of the human visual system and given that a perceptual objective metric is desired, we plan to further develop our colour fractal metrics by using other colour spaces, for example, Lab or HSL, capable of better capturing and reflecting the human perception of colours, but with a higher computational cost.

## REFERENCES


1. Fernandez-Maloigne C: Fundamental study for evaluating image quality. *Proceedings of the Annual Meeting of TTLA, December 2008, Taiwan*
2. Yamada T, Miyamoto Y, Serizawa M, Harasaki H: Reduced-reference based video quality metrics using representative-luminance values. *Image Communication* 2009,24(7):525-547.
3. Oelbaum T, Diepold K: Building a reduced reference video quality metric with very low overhead using multivariate data analysis. *Proceedings of the 4th International Conference on Cybernetics and Information Technologies, Systems and Applications (CITSA '07), 2007*
4. Fernandez-Maloigne C, Larabi MC, Anciaux G: Comparison of subjective assessment protocols for digital cinema applications. *Proceedings of the 1st International Workshop on Quality of Multimedia Experience (QoMEX '09), July 2009, San Diego, Calif, USA*
5. Rosselll V, Larabl M-C, Fernandez-Malolgne C: Objective quality measurement based on anisotropic contrast perception. *Proceedings of the 4th European Conference on Colour in Graphics, Imaging, and Vision (CGIV '08), June 2008* 108-111.
6. Wang Z, Bovik AC: Mean squared error: love it or leave it? A new look at Signal Fidelity Measures. *IEEE Signal Processing Magazine* 2009,26(1):98-117.
7. ITU-R Recommendation BT.500 : *Subjective quality assessment methods of televisionpictures*. International Telecommunications Union; 1998.
8. ITU-T Recommendation P.910 : *Subjective video quality assessment methods formultimedia applications*. International Telecommunications Union; 1996.
9. ITU-R Recommendation J.140 : *Subjective assessment of picture quality in digitalcable television systems*. International Telecommunications Union; 1998.
10. ITU-T Recommendation J.143 : *User requirements for objective perceptual videoquality measurements in digital cable television*. International Telecommunica-tions Union; 2000.
11. Video Quality Experts Group : The validation of objective models of video quality assessment. Final report, 2004
12. van den Branden Lambrecht CJ: Survey of image and video quality

metricsbased on vision models. presentation, August 1997

13. Winkler S, Sharma A, McNally D: Perceptual video quality and blockiness metrics for multimedia streaming applications. *Proceedings of the 4th International Symposium on Wireless Personal Multimedia Communications, September 2001* 553-556.
14. Pappas TN, Safranek RJ, Chen J: Perceptual criteria for image quality evaluation. In *Handbook of Image and Video Processing*. 2nd edition. Academic Press, San Diego, Calif, USA; 2000:669-686.
15. OPTICOM GmbH Germany : Pevq—advanced perceptual evaluation of videoquality. white paper, 2005
16. Teo PC, Heeger DJ: Perceptual image distortion. *Proceedings of IEEE International Conference of Image Processing, 1994* 982-986.
17. Karunasekera SA, Kingsbury NG: A distortion measure for blocking artifacts in images based on human visual sensitivity. *IEEE Transactions on Image Processing* 1995,4(6):713-724. 10.1109/83.388074
18. Winkler S: Visual fidelity and perceived quality: towards comprehensive metrics. *Human Vision and Electronic Imaging, January 2001, Proceedings of SPIE* 4299: 114-125.
19. Winkler S: Issues in vision modeling for perceptual video quality assessment. *Signal Processing* 1999,78(2):231-252. 10.1016/S0165-1684(99)00062-6
20. Winkler S: *Digital Video Quality: Vision Models and Metrics*. John Wiley &Sons, New York, NY, USA; 2005.
21. Bringier B, Richard N, Larabi MC, Fernandez-Maloigne C: No-reference perceptual quality assessment of colour image. *Proceedings of the 14th European Signal ProcessingConference (EUSIPCO '06), September 2006, Florence, Italy*
22. Quintard L, Larabi M-C, Fernandez-Maloigne C: No-reference metric based on the color feature: application to quality assessment of displays. *Proceedings of the 4th European Conference on Colour in Graphics, Imaging, and Vision (CGIV '08), June 2008* 98-103.
23. Wang Z, Bovik AC, Sheikh HR, Simoncelli EP: Image quality assessment: from error visibility to structural similarity. *IEEE Transactions on Image Processing* 2004,13(4):600-612. 10.1109/TIP.2003.819861
24. Sampat MP, Wang Z, Gupta S, Bovik AC, Markey MK: Complex wavelet structural similarity: a new image similarity index. *IEEE*

*Transactions on Image Processing* 2009,18(11):2385-2401.

25. Rajashekar U, Wang Z, Simoncelli EP: Quantifying color image distortions based on adaptive spatio-chromatic signal decompositions. *Proceedings of IEEE International Conference on Image Processing (ICIP '09), November 2009, Cairo, Egypt* 2213-2216.
26. Rajashekar U, Wang Z, Simoncelli EP: Perceptual quality assessment of color images using adaptive signal representation. *Human Vision and Electronic Imaging XV, January 2010, San Jose, Calif, USA, Proceedings of SPIE* 7527:
27. Chandler DM, Hemami SS: VSNR: a wavelet-based visual signal-to-noise ratio for natural images. *IEEE Transactions on Image Processing* 2007,16(9):2284-2298.
28. Chandler DM, Lim KH, Hemami SS: Effects of spatial correlations and global precedence on the visual fidelity of distorted images. *Human Vision and Electronic Imaging XI, January 2006, San Jose, Calif, USA, Proceedings of SPIE* 6057:
29. Chandler DM, Hemami SS: Effects of natural images on the detectability of simple and compound wavelet subband quantization distortions. *Journal of the Optical Society of America A* 2003,20(7):1164-1180. 10.1364/JOSAA.20.001164
30. Chandler DM, Hemami SS: Suprathreshold image compression based on contrast allocation and global precedence. *Human Vision and Electronic Imaging VIII, January 2003, Santa Clara, Calif, USA, Proceedings of SPIE* 5007: 73-86.
31. Sheikh HR, Bovik AC, Cormack L: No-reference quality assessment using natural scene statistics: JPEG2000. *IEEE Transactions on Image Processing* 2005,14(11):1918-1927.
32. Malkowski M, Claßen D: Performance of video telephony services in UMTS using live measurements and network emulation. *Wireless Personal Communications* 2008,46(1):19-32. 10.1007/s11277-007-9353-5
33. Mitina OV, Abraham FD: The use of fractals for the study of the psychology of perception: psychophysics and personality factors, a brief report. *International Journal of Modern Physics C* 2003,14(8):1047-1060. 10.1142/S0129183103005182
34. Sprott JC: Automatic generation of strange attractors. *Computers and*

*Graphics* 1993,17(3):325-332. 10.1016/0097-8493(93)90082-K

35. Taylor RP, Spehar B, Wise JA, Clifford CWG, Newell BR, Hagerhall CM, Purcell T, Martin TP: Perceptual and physiological responses to the visual complexity of fractal patterns. *Nonlinear Dynamics, Psychology, and Life Sciences* 2005,9(1):89-114.
36. Knill DC, Field D, Kersten D: Human discrimination of fractal images. *Journal of the Optical Society of America A* 1990,7(6):1113-1123. 10.1364/JOSAA.7.001113
37. Cutting JE, Garvin JJ: Fractal curves and complexity. *Perception and Psychophysics* 1987,42(4):365-370. 10.3758/BF03203093
38. Pentland AP: Fractal-based description of natural scenes. *IEEE Transactions on Pattern Analysis and Machine Intelligence* 1984,6(6):661-674.
39. Pentland AP: On perceiving 3-d shape and texture. *Proceedings of the Symposium on Computational Models in Human Vision, 1986, Rochester, NY, USA*
40. Ghosh K, Bhaumik K: Complexity in human perception of brightness: a historical review on the evolution of the philosophy of visual perception. *OnLine Journal of Biological Sciences* 2010,10(1):17-35. 10.3844/ojbsci.2010.17.35
41. Mandelbrot BB: *The Fractal Geometry of Nature*. W.H. Freeman and Co, New York, NY, USA; 1982.
42. Tolle CR, McJunkin TR, Rohrbaugh DT, LaViolette RA: Lacunarity definition for ramified data sets based on optimal cover. *Physica D* 2003,179(3-4):129-152. 10.1016/S0167-2789(03)00029-0
43. Chen W-S, Yuan S-Y, Hsiao H, Hsieh C-M: Algorithms to estimating fractal dimension of textured images. *Proceedings of IEEE Interntional Conference on Acoustics, Speech, and Signal Processing (ICASSP '01), May 2001* 1541-1544.
44. Lee W-L, Chen Y-C, Hsieh K-S: Ultrasonic liver tissues classification by fractal feature vector based on M-band wavelet transform. *IEEE Transactions on Medical Imaging* 2003,22(3):382-392. 10.1109/TMI.2003.809593
45. Frazer GW, Wulder MA, Niemann KO: Simulation and quantification of the fine-scale spatial pattern and heterogeneity of forest canopy structure: a lacunarity-based method designed for analysis of continuous canopy heights. *Forest Ecology and Management* 2005,214(1–3):65-

90.

46. Peters EE: *Fractal Market Analysis: Applying Chaos Theory to Investmentand Economics*. John Wiley & Sons, New York, NY, USA; 1952.
47. Nonnenmacher TF, Losa GA, Weibel ER: *Fractals in Biology and Medicine*. Birkhäuser, New York, NY, USA; 1994.
48. Manousaki AG, Manios AG, Tsompanaki EI, Tosca AD: Use of color texture in determining the nature of melanocytic skin lesions—a qualitative and quantitative approach. *Computers in Biology and Medicine* 2006,36(4):419-427. 10.1016/j.compbiomed.2005.01.004
49. Taylor RP, Spehar B, Clifford CWG, Newell BR: The visual complexity of pollock's dripped fractals. *Proceedings of the International Conference of Complex Systems, 2002*
50. Falconer K: *Fractal Geometry, Mathematical Foundations and Applications*. John Wiley & Sons, New York, NY, USA; 1990.
51. Voss R: Random fractals: characterization and measurement. In *Scaling Phenomena in Disordered Systems*. Plenum Press, New York, NY, USA; 1985:1-11.
52. Keller JM, Chen S, Crownover RM: Texture description and segmentation through fractal geometry. *Computer Vision, Graphics and Image Processing* 1989,45(2):150-166. 10.1016/0734-189X(89)90130-8
53. Allain C, Cloitre M: Characterizing the lacunarity of random and deterministic fractal sets. *Physical Review A* 1991,44(6):3552-3558. 10.1103/PhysRevA.44.3552
54. Plotnick RE, Gardner RH, Hargrove WW, Prestegaard K, Perlmutter M: Lacunarity analysis: a general technique for the analysis of spatial patterns. *Physical Review E* 1996,53(5):5461-5468. 10.1103/PhysRevE.53.5461
55. Maragos P, Sun F: Measuring the fractal dimension of signals: morphological covers and iterative optimization. *IEEE Transactions on Signal Processing* 1993,41(1):108-121. 10.1109/TSP.1993.193131
56. Pedrycz W, Bargiela A: Fuzzy fractal dimensions and fuzzy modeling. *Information Sciences* 2003, 153: 199-216.
57. Ivanovici M, Richard N: Colour covering blanket. *Proceedings of the International Conference on Image Processing, Computer Vision and Pattern Recognition, July 2010, Las Vegas, Nev, USA*

58. Ivanovici M, Richard N: Fractal dimension of colour fractal images. *IEEE Transactions on Image Processing*. Inrevision

59. Ivanovici M, Richard N: Colour fractal image generation. *Proceedings of the International Conference on Image Processing, Computer Vision and Pattern Recognition, July 2009, Las Vegas, Nev, USA* 93-96.

60. Ivanovici M, Richard N, Decean H: Fractal dimension and lacunarity of psoriatic lesions—a colour approach. *Proceedings of the 2nd WSEAS International Conference on Biomedical Electronics and Biomedical Informatics (BEBI '09), August 2009, Moskow, Russia* 199-202.

61. Ivanovici M, Richard N: The lacunarity of colour fractal images. *Proceedings of the International Conference on Image Processing (ICIP '09), November 2009, Cairo, Egypt* 453-456.

62. Ivanovici M: Objective performance evaluation for mpeg-4 video streaming applications. *Scientific Bulletin of University "POLTEHNICA" Bucharest C* 2005,67(3):55-64.

63. Ivanovici M, Beuran R: User-perceived quality assessment for multimedia applications. *Proceedings of the 10th International Conference on Optimization of Electricaland Electronic Equipment (OPTIM '06), Ma 2006* 55-60.

64. Ivanovici M, Beuran R: Correlating quality of experience and quality of service for network applications. In *Quality of Service Architectures for Wireless Networks: Performance Metrics and Management*. IGI-Global; 2010:326-351.

# 8

# *Fractal Analysis of Time-Series Data Sets: Methods and Challenges*

**Ian Pilgrim and Richard P. Taylor**

University of Oregon, Eugene, Oregon, USA

## ABSTRACT

Many methods exist for quantifying the fractal characteristics of a structure via a fractal dimension. As a traditional example, a fractal dimension of a spatial fractal structure may be quantified via a box-counting fractal analysis that probes a manner in which the structure fills space. However, such spatial analyses generally are not well-suited for the analysis of so-called "time-series" fractals, which may exhibit exact or statistical self-affinity but which inherently lack well-defined spatial characteristics. In this chapter, we introduce and investigate a variety of fractal analysis techniques directed to time-series structures. We investigate the fidelity of such techniques by applying each technique to sets of computer-generated time-series data sets with well-defined fractal characteristics. Additionally, we investigate the inherent challenges in quantifying fractal characteristics (and indeed of verifying the presence of such fractal characteristics) in time-series traces modeled to resemble physical data sets.

**Citation:** Pilgrim, I., & Taylor, R. P. (2018). Fractal Analysis of Time-Series Data Sets: Methods and Challenges. In Fractal Analysis. IntechOpen.DOI: 10.5772/intechopen.81958

**Keywords:** fractal, spatial fractal, time-series fractal, fractal analysis, fractal dimension, self-similarity, self-affinity, topological dimension, embedding dimension, similarity dimension, box-counting dimension, covering dimension, variational box-counting, Hurst exponent, variance method, Dubuc variation method, adaptive fractal analysis, power-law noise, Brownian motion, fractional Brownian motion

## INTRODUCTION

In this chapter, we explore a species of fractals known as "time-series" fractals. Such structures generally may be conceived (and visualized) as functions of independent variables whose plots exhibit shapes and patterns that are evocative of the more familiar spatial fractals. However, lacking well-defined spatial characteristics, time-series fractals call for analytical tools that depart from those of the world of spatial fractals. To lay the foundation for a discussion of such analytical tools, we begin with an overview of fractal structures and traditional fractal analysis techniques. We then introduce time-series fractals and investigate the unique analytical tools necessitated by such structures. Finally, we investigate the relative fidelity of these analytical tools, as well as the shortcomings inherent in performing fractal analysis on time-series fractals of limited length and/or fine-scale detail.

## MOTIVATING THE FRACTAL DIMENSION

Mathematician Benoit B. Mandelbrot often is credited with introducing the notion of a fractional, or fractal, dimension in his 1967 paper, "How long is the coast of Britain?" [1]. In fact, however, the curious nature of coastline measurements had been discussed by Lewis Fry Richardson 6 years prior in the *General Systems Yearbook* [2]. Richardson, a pacifist and mathematician, sought to investigate the hypothesis that the likelihood that war would erupt between a pair of neighboring nations is related to the length of the nations' shared border. As Richardson and Mandelbrot note, such a hypothesis is difficult to evaluate, since individual records of the

length of Britain's west coast varied by up to a factor of three. Indeed, as the precision of such measurements increases—that is, by decreasing the length of the "ruler" used to trace the profile—the measured total length appears to increase as well. This quality reflects the fact that the outline of the British coastline is an example of a "self-similar" structure—that is, a structure that exhibits the same statistical qualities, or even the exact details, across a wide range of length scales. In light of this apparent fundamental indeterminacy, Mandelbrot posits that familiar geometrical metrics such as length are inadequate for describing the complexity found in nature.

Recognizing Richardson's prior investigations, Mandelbrot notes that Richardson had indeed produced an empirical relation between a measured coast length L and the smallest unit of measurement G : $L(G)=MG^{1-D}$ , where M is a positive constant and $D\geq 1$ —but observes that "unfortunately it attracted no attention" [1]. In Ref. [1], building upon Richardson's observations, Mandelbrot introduces the formalism of a fractional, or fractal[1], dimension to quantify the nature of such shapes.

Following Mandelbrot's example, to generalize the concept of a geometrical dimension, we may begin by examining the scaling behavior of such trivially self-similar objects as a line, a square, and a cube. For example, consider a line segment of length L , which can be separated into NN non-overlapping subsets of length L/N , each of which is identical to the whole segment but for a scaling factor $r(N)=1/N$ . Analogously, a square with side length L may be decomposed into $N^2$ facsimiles of side length L/N , each of which is scaled down from the original by a factor $r(N)=N^{-1/2}$ , and a cube of side length L can be decomposed into $N^3$ facsimiles of side length L/N with corresponding scaling ratio $r(N)=N^{-1/3}$ ; see Figure 1. To generalize this pattern, we may observe that the scaling ratio r(N) follows the relationship $r(N)=N^{-1/D}$ . In this relationship, $D=-\log(N)/\log(r(N))$ is known as the *similarity dimension* of the structure in question.

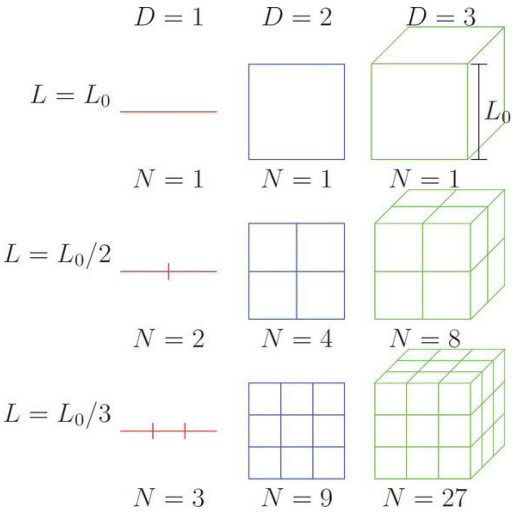


**Figure 1:** A line, a square, and a cube are examples of trivially self-similar Euclidian shapes. A Euclidian shape in D dimensions may be said to contain N = $(L / L_0)^{-D}$ exact copies of itself scaled by a factor of $L / L_0$. Image provided by R.D. Montgomery.

Applying the concept of a similarity dimension to less trivial shapes is straightforward in the case of exactly self-similar structures, such as structures that are constructed via iteration of a generating pattern. As an example, consider the Koch curve, illustrated in Figure 2. The Koch curve is constructed as follows: Beginning with a line segment of unity length, replace the middle third of the segment with an equilateral triangle whose base has a length of 1/3 and overlies the original line segment, then remove this overlapping base segment. The resulting figure thus consists of four line segments, each of which has a length of 1/3. Iterating this process for each new line segment yields a sequence of figures that exhibit increasingly fine structure, with the limiting state of this series exhibiting exact self-similarity, in the sense that a nontrivial subset of the shape is exactly identical to the whole. This exact self-similarity is illustrated in Figure 2, which shows that the full Koch curve may be described as being formed from four exact copies of itself, each scaled down by a factor of 1/3. Thus, we can apply the above relation to find that the Koch curve has a similarity dimension of $D=-\log(4)/\log(1/3)\approx 1.26$.

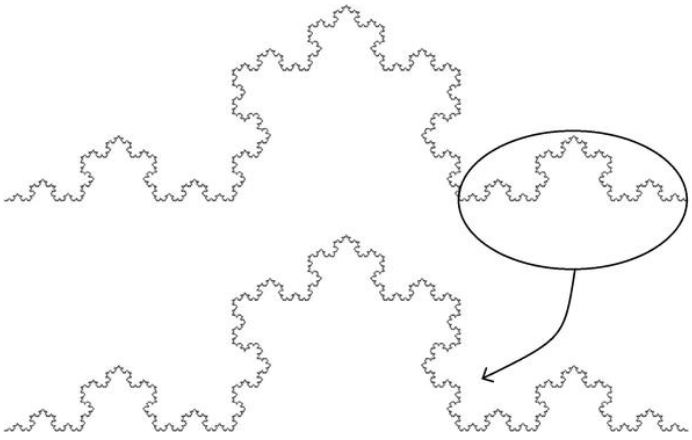

**Figure 2:** The Koch curve is an example of an exact self-similar figure with a non-integer similarity dimension.

The similarity dimension described above represents but one example of a plurality of dimensions that can be defined and calculated for a given figure. Indeed, the utility of the similarity dimension is limited by the fact that it applies only to figures that exhibit exact self-similarity; by contrast, the complexity witnessed in natural systems such as coastlines generally exhibits self-similarity only in the statistical sense. As an example, Figure 3 illustrates a structure that exhibits statistical self-similarity. Specifically, Figure 3 illustrates an example of a modified Koch curve formed by randomizing the orientations of the line segments as the structure is generated.

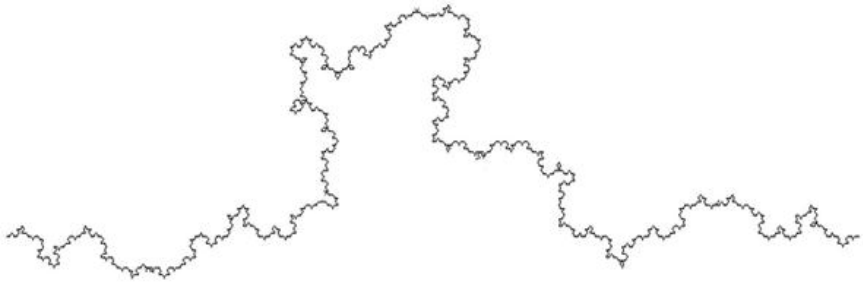

**Figure 3:** Introducing randomness into the generating algorithm of the Koch curve produces a statistically self-similar fractal structure.

As a tool for quantifying the nature of such fractal structures that do not exhibit exact self-similarity, we now turn to the (roughly self-explanatory)

"box-counting dimension," also known as the "covering dimension." Given a structure that extends in two dimensions[2], the box-counting dimension may be determined as follows: First, superimpose a square grid with individual boxes of size $\ell \times \ell$ over the figure in question, and count the number of boxes $N(\ell)$ within which some portion of the figure in question is present (see Figure 4). Next, repeat this procedure while varying the box size $\ell$ and construct a plot of $\log(N(\ell))$vs$\log(1/\ell)$ ; for a self-similar structure, the data should follow a linear trend with a gradient equal to the box-counting dimension *D*. Such a plot is generally known as a scaling plot.

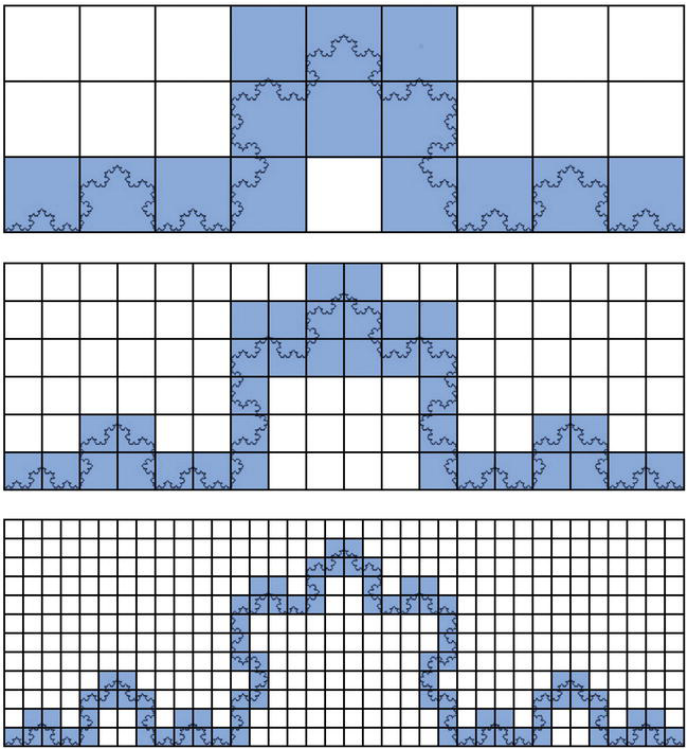

**Figure 4:** Applying the box-counting method to the Koch curve. The number of boxes of side length $\ell$ occupied by some portion of the curve follows $N(\ell) \propto \ell^{-D}$, where D is the box-counting dimension of the curve.

The box-counting method also may be described in more geometrically intuitive terms. For example, and as shown in Figure 4, one may observe that the set of all occupied boxes at a given length scale $\ell\ell$ collectively serves as an approximation of the total structure as "observed" at the length scale $\ell$ . Stated differently, the set of $\ell \times \ell$ boxes that overlap some portion of the base

structure may be seen as representing a snapshot of the base structure as viewed at a resolution corresponding to the length $\ell$ . In general, however, the set of boxes covering the base structure cannot be expected to represent the geometric details of the structure at any length scale. For example, as shown in Figure 4, is evident that the incompatibility of the straight edges of the square boxes and the jagged boundary of the Koch curve leads to a markedly crude representation of the structure at all length scales, as each occupied box will always contain details that cannot be fully represented by that box.

While the box-counting method of estimating fractal dimension is conceptually straightforward, some care must be taken to preserve the utility of the method. For example, one must select an appropriate range of box sizes $\ell\ell$ over which to examine the scaling trend, given that any observed fractal scaling trend will not persist over all possible length scales. That is, for any finite structure, it is possible to encompass the structure in a box of size $L \times L$ , for an appropriate value of $L$ . In such a case, applying the box-counting method with boxes of size $\ell \geq L$ will always return a value $N(\ell)=1$ —only one box can be filled when the box size contains the entire structure—thus resulting in an apparent fractal dimension of zero. As another example, when considering a range of box sizes $\ell \lesssim L$ , nearly all such boxes will be counted as filled, and the box count $N(\ell)$ will scale as the square of the inverse box size $1/\ell$ . In this case, the box-counting method will return an apparent fractal dimension of $D=2$ , and we may say that the pattern "looks two-dimensional" when examined at this coarse scale. When dealing with patterns found in nature, the opposite extreme of possible length scales merits consideration as well. For a mathematically-generated fractal figure, such as a figure that exhibits structure at arbitrarily fine length scales, the box-counting method may be applied with arbitrarily small box sizes $\ell$ . However, naturally occurring fractal structures invariably exhibit a smallest length scale to which a scaling trend may extend. For example, while the scaling trend certainly must cease at the molecular and atomic scales, such fractal scaling behavior generally diverges at length scales many times larger than this. In such cases, applying the box-counting method at length scales $\ell$ smaller than a smallest feature size observed in the structure yields a number of filled boxes $N(\ell)$ that scales linearly with the inverse box size $1/\ell$ ; thus, the figure "looks one-dimensional" to the box-counting analysis at these scales.

Such conditions necessitate careful determination of the appropriate range of length scales over which to assess fractal scaling behavior. This determination may be made empirically, such as by observing the range of length scales over which the scaling plot is sufficiently linear. Alternatively, this determination may be made by convention, such as may be based on statistical arguments. In practice, it is generally not known *a priori* whether a structure under consideration should even be expected to *be* a fractal, and hence whether it should be expected to produce a scaling plot with a linear trend between cutoffs defined by appropriate physical and/or measurement limitations. Accordingly, it is preferred to adopt conventions with some degree of universality and that do not presuppose the existence of the fractal scaling behavior under investigation. More specifically, it is common to adopt the following conventions, noting that the ranges may be bounded by physical and/or measurement limitations. The coarse-scale analysis cutoff generally corresponds to a limit of the range of length scales measured, which in turn generally is related to the coarse-scale size of the structure itself. This limit is conventionally set at $\ell = L/5$ , where L is the side length of the smallest square that may circumscribe the structure, thus guaranteeing that the grid includes no fewer than 25 boxes. Turning to the fine scale, the physical limit is determined by the smallest (nontrivial) feature size that is observed in the structure, while the fine-scale measurement limit is conventionally chosen to satisfy the requirement that each box contains no fewer than five data points. In practice, the more restrictive of these two limits is chosen (i.e., the larger of the physical fine-scale limit and the fine-scale measurement limit).

As a further consideration in optimizing the performance of the box-counting method, one must select the position and orientation of the box grid relative to the structure in question. To the extent that the box-counting method seeks to probe an inherent quality of a structure, the observed fractal dimension should not be affected by a spatial translation or rotation of the grid with respect to the structure, since the structure itself has no preferred orientation. However, consider the case shown in Figure 5, in which the box-counting method is applied to a fractal profile. In the box-counting scheme discussed above, all boxes that contain any portion of the structure under examination are counted toward the total; applying this to the structure of Figure 5, we find that 35 boxes are filled using this box size $\ell$ . Suppose, however, that one is able to reposition the boxes semi-independently of

one another, by translating a set of adjacent ℓ×ℓ boxes within each column of width ℓ . Doing so, we find that a careful repositioning of the boxes within these columns results in the box count N(ℓ) dropping to 29. This apparent inconsistency serves to motivate a refinement of the box-counting analysis as described above. Specifically, the "variational box-counting method" includes shifting the boxes in columns as described above so as to minimize the number of ℓ×ℓ boxes needed to entirely cover the figure in question. The variational box-counting method thus serves to eliminate some of the apparent ambiguity of the traditional box-counting method. Of course, some ambiguity still remains in this amended method, given that the rotational orientation of the columns relative to the examined structure remains arbitrary. To eliminate this residual ambiguity, one may repeat the above-described variational method at a variety of rotational orientations of the grid with respect to the figure and choose the angle that minimizes N(ℓ) for each value of ℓ . However, in practical applications, incorporating this additional variation does not significantly affect the measured dimensions.

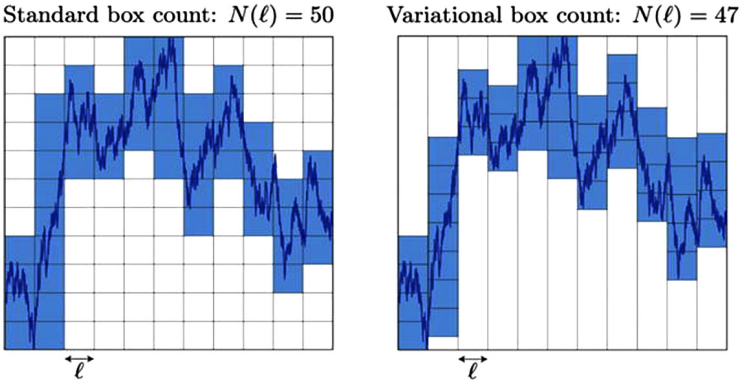


**Figure 5:** An example of applying the variational box-counting method. When the boxes are constrained in a grid (left), we find a box count N (ℓ) = 50 ; however, when the ℓ × ℓ boxes are allowed to shift vertically within columns of width ℓ (right), the measured box count N (ℓ) drops to 47.

## TIME-SERIES FRACTAL STRUCTURES

The fractal structures discussed above generally represent examples of spatial fractal structures—that is, structures with spatial extent and whose fractal characteristics are embodied in their spatial form. However, many

observable structures and phenomena exhibit fractal behavior while lacking spatial form. Another important class of structures to which fractal analysis may be directed is that of "time-series" structures—that is, structures that may be represented as a single-valued function of a single independent variable. As suggested by their name, a time-series structure may refer to some variable quantity—say, stock market prices, or atmospheric pressure—that fluctuates in time, but for the purposes of this work we intend for the term to refer to any data set or plot consisting of a dependent variable that may be represented as a single-valued function of an independent variable.

As with the spatial structures considered above, a time-series structure may exhibit fractal scaling properties in either a statistical or an exact sense, which may be quantified using the formalism of fractal dimensions. Unfortunately, the box-counting methods described above for measuring a fractal dimension are ill-suited to time-series structures. Simply put, this limitation arises from the fact that box-counting methods assess the fractal dimension of shapes that extend in space, while the spatial "shape" of a time-series structure is inherently undefined. That is, since the two axes of a plot representing a time-series data set generally represent variables with distinct units, the geometric aspect ratio of such a plot is fundamentally undefined.

As an example, consider the data set displayed in Figure 6, which plots the daily closing price of a certain technology stock over a period of roughly 16 years. Specifically, Figure 6 illustrates three representations of the same data set, with the respective $y$-axis of each illustration scaled by a distinct factor. In qualitative terms, one may be tempted to conclude that the data in the top panel appear the most linear and that the data in the bottom panel appear the most space-filling. Accordingly, given that a box-counting fractal analysis technique essentially assesses the space-filling properties of a structure, applying a box-counting analysis to each plot would yield distinct results for each plot.

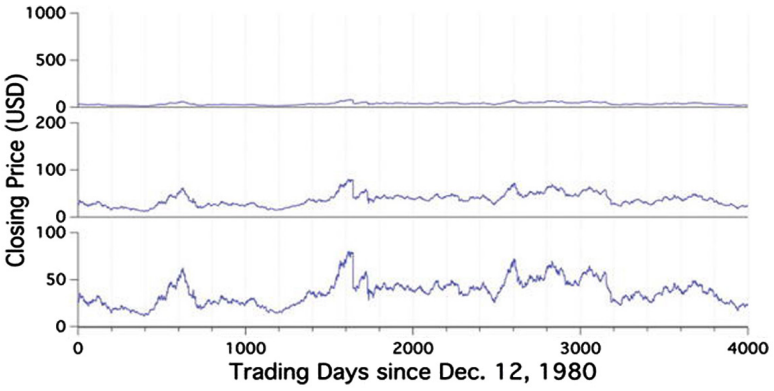


**Figure 6:** Daily closing prices for a single stock from December 1980 to October 1996. Each of the three plots displays the same data, but the y-axis of each plot is scaled by a distinct factor. A box-counting fractal analysis would return unique results for each plot, despite each plot representing the same data set.

The difficulty here lies in the fact that a box-counting fractal analysis necessarily treats a figure as a spatial entity whose orthogonal dimensions have the same units. By contrast, a time-series trace such as the one displayed in Figure 6 lacks this property, but may still exhibit fractal characteristics in the form of either statistical or exact self-affinity. As discussed above, exact and statistical self-similarity describe structures whose precise details or statistical properties (respectively) are repeated as its orthogonal dimensions are rescaled by a similar factor. By contrast, exact and statistical self-affinity refer to structures whose precise details or statistical properties (respectively) are repeated as its two orthogonal dimensions are resized by independent quantities [4].

Due to the incommensurability of the orthogonal axes defining a time-series trace, such structures cannot exhibit self-similarity, only self-affinity. As an example, Figure 7 displays the data set shown in Figure 6 alongside a subset of the data set. When this subset is appropriately rescaled in each of the $x$- and $y$-axis, the resulting plot shares the general statistical properties of the original trace, and hence exhibits statistical self-affinity.

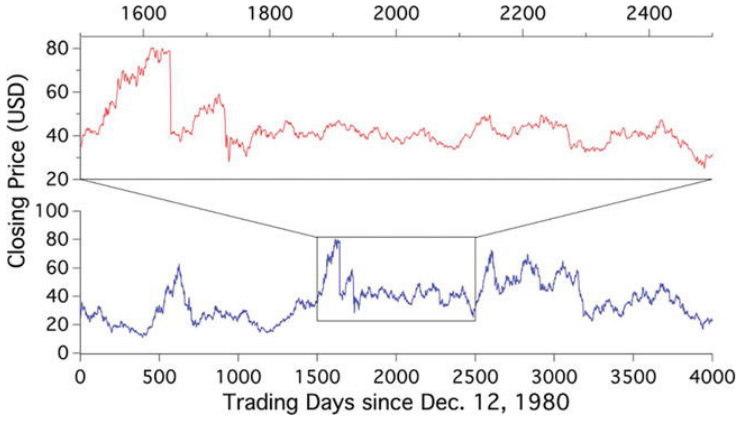


**Figure 7:** Statistical self-affinity in a fractal time-series trace. Choosing a subset of the stock price data shown in Figure 6 and rescaling the x- and y-axes yields a trace that shares statistical properties with the original.

It also is possible, albeit less common, for a time-series trace to exhibit *exact* self-affinity. As an example, Figure 8 illustrates three experimentally measured data sets in which rescaling the *x*- and *y*-axes of the traces by carefully chosen factors produces structures that share the characteristics of the original traces [5].

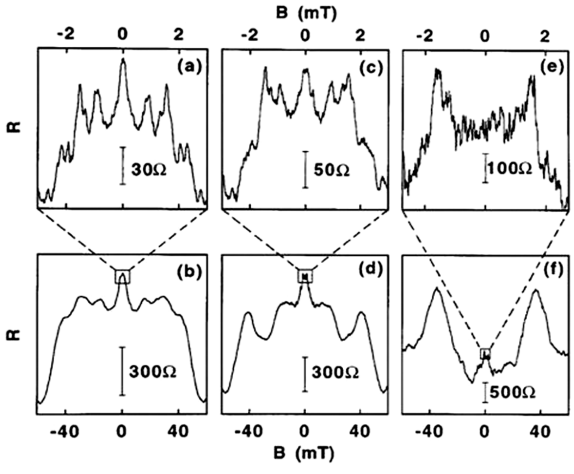


**Figure 8:** Magnetoresistance fluctuations (MCF) recorded in an electron billiard device can represent examples of exact self-affinity in time-series structures. Each of the three columns in this figure represents a single MCF observed at a coarse scale (bottom) and a fine scale (top). From [5].

## FRACTAL ANALYSIS OF TIME-SERIES TRACES: BEYOND BOX-COUNTING

As discussed above, when applying a box-counting method to a time-series structure, the measured scaling properties of the structure will depend on the aspect ratio with which the data are presented, which is in turn an arbitrary choice. Accordingly, applying a box-counting method to a time-series trace will return a fractal dimension that is essentially arbitrary. Thus, it is necessary to develop fractal analysis techniques that are insensitive to such artificial geometric parameters. In the following, we survey a sampling of such techniques proposed in the literature.

Returning to the example of Figure 5, above, this figure in fact illustrates the variational box-counting method as applied to fractal profile in the form of a time-series fractal. Indeed, fractal analyses of such time-series fractal structures have traditionally been performed using the variational box-counting method [6, 7], which does offer performance improvements over the traditional fixed-grid box-counting method. Nonetheless, the variational box-counting method still suffers from a fatal flaw. To see why this is so, consider the plots shown in Figure 9.

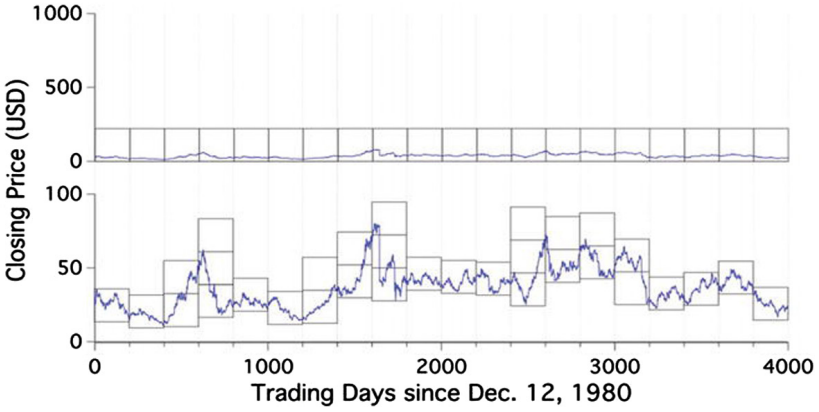


**Figure 9:** Visualizing a variational box-counting method applied to the stock price data of Figures 6 and 7 with a "resolution" of $\ell = 200$ trading days. Displaying the data with a price range of 0–100 USD yields a box count of 37. Displaying the data with a price range of 0–1000 USD yields a box count of 20.

Figure 9 illustrates the stock price data of Figures 6 and 7 represented in two plots with the price axes respectively scaled by two different factors, as well as a visualization of a variational box-count method applied at a "length"

scale $\ell$=200 trading days. When the prices shown range from 0–100 USD (top of Figure 9), we find that a minimum of 37 boxes are needed to entirely cover the trace. However, when the price range is expanded to 0–1000 USD (effectively increasing the domain: range aspect ratio of the data; bottom of Figure 9), the number of boxes needed to cover the trace falls to 20. Indeed, the number of boxes $N(\ell)$ needed to cover the "compressed" plot will be proportional to $1/\ell$ for all values of $\ell\ell$ such that the boxes are "taller" than the range of values found within any of its $L/\ell$ columns. That is, as long as each box is "taller" than the vertical extent of the trace within each column, the trace will "look" one-dimensional.

Of course, the fundamental issue is that the concept of an $\ell\times\ell$ "box" on a time-series trace is meaningless, since the enclosed "area" has units of (in this case) days times dollars. While it is entirely reasonable to overlay a spatial figure with boxes of a well-defined area in the case of a box-counting analysis of a spatial fractal, the concept of a square drawn on a plot with incompatible and independently scalable axes is ill-defined. In some cases, this inadequacy is resolved by adopting conventions that eliminate such ambiguity. For example, a time-series trace may be normalized in its *x*- and *y*-axes such that the domain and range of the plot each run from 0 to 1, and the structure may be analyzed via a box-counting analysis that utilizes a square grid that just circumscribes the trace. While such a normalization convention may provide a consistent method for investigating the relative scaling properties among a set of related time-series traces, the absolute values of the dimensions produced by such analyses would remain essentially arbitrary.

Developing a fractal analysis technique that is appropriate for time-series structures generally amounts to taking one of two approaches: (1) to treat the time-series structure as a geometric figure without a well-defined aspect ratio, or (2) to treat the time-series structure as an ordered record of a process that exhibits a quantifiable degree of randomness. Following the latter approach, Harold Edwin Hurst introduced a formalism for quantifying the nature of self-affine time-series structures in a 1951 paper on the long-term storage capacity of water reservoirs [8].

In Ref. [8], Hurst introduces the concept of the "Hurst exponent" $H$, which may be understood as quantifying the character of the randomness exhibited in a time-series structure via an autocorrelation measurement. Specifically, a Hurst exponent of $H=0.5$ describes a process that is purely random, such that the value of the trace at time $t_i$ is entirely independent of the value at time $t_j$, $i\neq j$. By contrast, Hurst exponents in the range $0.5<H<1$ represent

traces exhibiting positive autocorrelations, while Hurst exponents in the range $0<H<0.5$ represent traces exhibiting negative autocorrelations. Intuitively speaking, a positive autocorrelation may be understood as representing a trace in which a "high" value (say, relative to the mean) is more likely than not to be followed by additional "high" values, while a negative autocorrelation may be understood as representing a trace in which "high" and "low" values alternate at short time scales; see Figure 10.

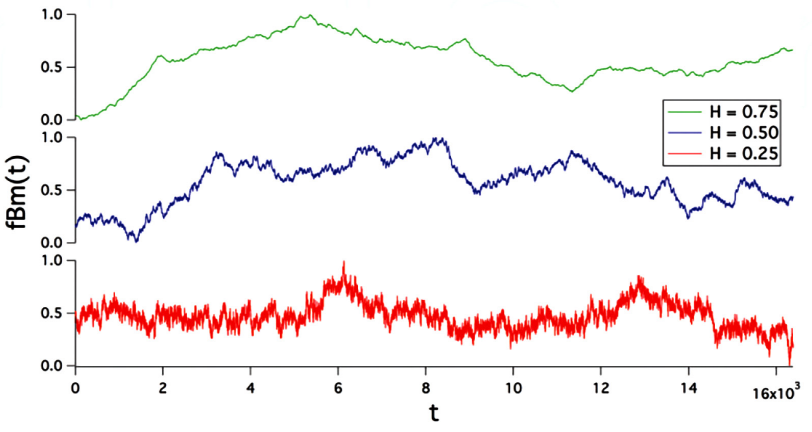


**Figure 10:** Examples of time-series traces characterized by Hurst exponents of (bottom to top) H = 0.25, 0.50, and 0.75. A trace with H = 0.5 represents purely random process, whereas traces with H = 0.25 and H = 0.75 represent processes whose subsequent increments are negatively and positively correlated, respectively.

The Hurst exponent of a data set may be calculated by examining the scaling properties of a "rescaled range" of the data, as follows. Consider a data set $\{x_t\}(t=1,2,3,\ldots,T)$, and let $\{x_i,x_i+1,\ldots,x_{i+\tau}\},\tau\leq T,i=1,2,3,\ldots,T-\tau$ represent any sequence of $\tau+1$ points within the data set. The rescaled range $(R/S)$ statistic is then defined as:

$$\left(\frac{R}{S}\right)_\tau = \frac{1}{s_\tau}\left[\sup_{i\leq t\leq i+\tau}\sum_{k=i}^{t}(x_k-\bar{x}_{i,\tau}) - \inf_{i\leq t\leq i+\tau}\sum_{k=i}^{t}(x_k-\bar{x}_{i,\tau})\right], \quad (1)$$

where

$$\bar{x}_{i,\tau} = (1/\tau)\sum_{t=i}^{\tau} x_t \quad (2)$$

is the sample mean and

$$s_{i,\tau} = \left[ (1/\tau) \sum_{t=i}^{\tau} (x_t - \overline{x}_{i,\tau})^2 \right]^{1/2} \quad (3)$$

is the sample standard deviation. The quantity

$$\left\langle \left( \frac{R}{S} \right)_{\tau} \right\rangle_i \quad (4)$$

is then proportional to $\tau^H$ , such that the gradient of a plot of $\log\left(\langle (R/S)_\tau \rangle_i\right)$ is equal to the Hurst exponent *H*.

The Hurst exponent also may be described as a measure of long-range correlations within a data set, such that measuring these correlations as a function of interval width may provide another measurement of the Hurst exponent. As an example of such an analysis, the "variance method"[3] calculates the scaling properties of the trace's autocorrelation as a function of time interval[4] via calculation of the quantity

$$V(\Delta t) = \left\langle [x_{t+\Delta t} - x_t]^2 \right\rangle_t \quad (5)$$

for a range of values of Δt . This quantity is then related to the Hurst exponent as $V(\Delta t) \propto \Delta t^{2H}$ such that a plot of log(V(Δt))vslog(Δt) is expected to be linear (within an appropriate range of values of Δt ) with slope. 2*H*. In practice, however, the variance method is found to produce a poor estimate of Hurst exponent.

As another means of quantifying the fractal properties of time-series traces, we now turn our attention to a method proposed by Benoit Dubuc in a 1989 paper [9] on the fractal dimension of profiles. Dubuc's proposed "variation method"[5] is conceptually similar to the variational box-counting method described above, but improves upon this method by resolving the fundamental arbitrariness of drawings boxes on a time-series trace. In short, Dubuc's variation method probes the "space-filling" characteristics of a time-series trace through measurement of the scaling behavior of the amplitude of the trace within an ϵϵ neighborhood as ϵϵ is varied.

In practical terms, Dubuc's variation method may be implemented is as follows: Consider a time-series data set $\{x_t\}(t=1,2,3,\ldots,T)$. For a given value of ϵ , define the functions uϵ(t) and bϵ(t) as follows:

$$u_\epsilon(t) = \sup_{t' \in R_\epsilon(t)} x_{t'},$$
$$b_\epsilon(t) = \inf_{t' \in R_\epsilon(t)} x_{t'}, \quad (6)$$

where

$$R_\epsilon(t) = \{s : |t - s| \leq \epsilon \text{ and } s \in [1, T]\}. \quad (7)$$

That is, for a given value of ϵ and for each point $t_i$ in the trace, examine the set of points $\{x_{t'}\}$ within ϵ data points of $t_i$, and let $u\epsilon(t_i)$ and $b\epsilon(t_i)$ be (respectively) the maximum and minimum values of $x_{t'}$ found in this range. Thus, uϵ(t) and bϵ(t) may be understood as traces that represent (respectively) the upper and lower envelopes of oscillation of a trace at a particular scale set by ϵ. At large values of ϵ, the traces uϵ(t) and bϵ(t) will be slowly varying relative to the variation present in the original data set; reducing the value of ϵ will produce traces uϵ(t) and bϵ(t) that each resemble the original data set with increasing fidelity (see Figure 11).

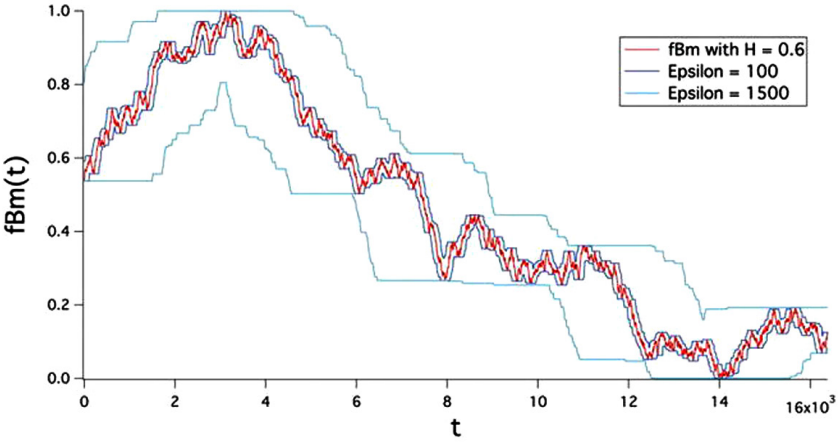


**Figure 11:** Visualizing the application of Dubuc's variation method at two distinct values of ϵ. The trace under consideration is a fractional Brownian motion (fBm), whose properties are discussed below.

Having constructed the traces uϵ(t) and bϵ(t), we then define vϵ(t)=uϵ(t)−bϵ(t) and calculate

$$V(\epsilon) = \frac{1}{\epsilon^2} \sum_t v_\epsilon(t). \quad (8)$$

Conceptually, V(ϵ) may be regarded as representing the (crucially, not necessarily integer) number of ϵ×ϵ "boxes" whose total "area" would be equal to that of the envelope bounded by uϵ(t) and bϵ(t) . Of course, the concept of "area" is ill-defined in this context, but this is of no concern, given that we have not implied a geometrical relationship between the *x* and *y* dimensions. In continued analogy with spatial box-counting analyses, the fractal dimension of the trace is then determined via the relationship $V(\epsilon) \propto (1/\epsilon)^D$ , such that a plot of log(V(ϵ))vslog(1/ϵ) is expected to follow a linear trend (within an appropriate range of values of ϵ ) with a slope corresponding to the fractal dimension *D*.

As a final means of quantifying the fractal properties of time-series traces, we consider a technique known as "adaptive fractal analysis" (AFA) [10]. Similar to Dubuc's variation method, AFA may be broadly described as investigating the geometrical properties of a time-series trace (in contrast to the aforementioned analyses that are best understood as probing numerical correlations). For example, and as discussed above, Dubuc's variation method may be described as quantifying the generalized "area" needed to cover a time-series trace as analyzed at different characteristic time scales; in the case of AFA, approximations to the time-series trace are generated at varying resolutions, and the fidelity of such approximations is recorded as the resolution is varied. The AFA algorithm may be executed as follows: Again, consider a time-series data set x(t)(t=1,2,3,…,T). Next, choose a window with a width equal to an odd integer w=2n+1,w<T, and partition the data set into overlapping subsets of length *w* such that each pair of adjacent subsets overlap by n+1 data points. Within each window, the linear best-fit line to the data within that window is calculated, resulting in a series of disconnected straight lines. That is, the series of disconnected best-fit lines overlap in pairs such that each index in the domain of the original data set is matched with respective points on each of two subset fit lines (with the exception of the *n* data points at either end of the trace). Next, these best-fit lines are "stitched" together to form a single, smoothly continuous curve in the following manner: Label the windows that span the trace with consecutive integers, and label the windows' corresponding best-fit lines as $y^{(j)}(l)(l=1,2,\ldots,n+1)$. Then, within each window *j*, construct the curve

$$y^{(w)}(l) = w_1 y^{(j)}(l+n) + w_2 y^{(j+1)}(l), \tag{9}$$

l=1,2,…,n+1 , where w1=(1−(l−1)/n) and $w_2$=(l−1)/n. Conceptually, each value $y^{(w)}(l)$ may be thought of as representing the weighted average of

the values of the two best-fit lines with values at that index, weighted so as to be inversely proportional to the distance between that index and the midpoint of the window. Repeating this procedure across all windows produces a trace $y^{(w)}(t)$ that is continuous and differentiable, and that may be understood as representing an approximation to the trace x(t) at a length scale, or "resolution," defined by *w* (see Figure 12).

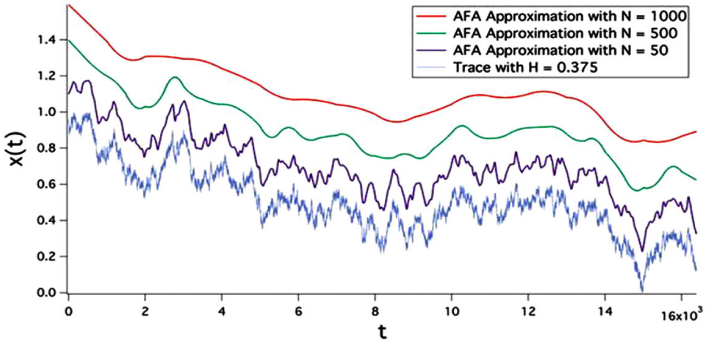


**Figure 12:** Examples of applying the procedure of AFA at several values of N (corresponding to the window width w discussed in the text). The light blue trace (bottom) is a 16,384-point fractal trace with H = 0.375 , while the red (top), green (second from top), and purple (third from top) traces represent approximations produced by the AFA technique at N = 1000 , N = 500 , and N = 50 , respectively. Traces are vertically offset for clarity. Note that smaller values of N yield approximations that are increasingly similar to the trace under consideration.

As *w* is decreased, y(w)(t) becomes a better approximation to x(t)xt ; the scaling behavior of this fidelity as *w* is varied is used to determine the Hurst exponent. Specifically,

$$F(w) = \left[\frac{1}{T}\sum_{i=1}^{T}\left(y^{(w)}(t_i) - x(t_i)\right)^2\right]^{1/2} \propto w^H, \tag{10}$$

such that a plot of log(F(w))vslog(w) will be linear (over an appropriate range) with slope *H*.

## EVALUATING FRACTAL ANALYSIS TECHNIQUES

Each of the fractal analysis techniques discussed above is best understood as providing an *estimate* of the fractal dimension or Hurst exponent that

characterizes a given time-series data set. The sections that follow present a method for evaluating the fidelity of these estimates that was developed and applied by the authors to the fractal analysis techniques under consideration. To objectively and quantifiably evaluate the fidelity of each of these techniques, it is desirable to investigate the accuracy of each technique when applied to traces with known Hurst exponents/fractal dimensions. To introduce a method for producing such "control" traces, we begin with a general discussion of noise traces.

A noise trace, as an example of a time-series structure, may be described as a single-valued function of a single independent variable. A variety of methods exist for quantifying the statistical properties of noise traces. For example, in addition to the aforementioned measurements of space-filling characteristics and long-range correlations, a spectral analysis of a noise trace may offer a natural quantification of the trace's statistical properties.

Power-law noise represents a significant and broad class of noise traces. Specifically, a power-law noise trace has a power spectral density given by $P(f) \propto 1/f^{\beta}$ . A noise trace characterized by $\beta=0$ thus represents noise whose spectral power density is a constant across all frequencies, while $\beta=1$ corresponds to the " 1/f noise" that characterizes many natural systems, and $\beta=2$ is known as "brown noise." In principle, $\beta\beta$ can assume any value; however, we begin our investigation by considering the $\beta=2$ case.

A "brown noise" trace characterized by $\beta=2$ is so termed owing to its relation to Brownian motion, which describes the net motion of a particle whose individual steps are random and independent. Brownian motion generally may refer to a process extending in any number of dimensions; however, we restrict our attention to brown noises that may be understood as a time-dependent plot of the position of a particle undergoing Brownian motion along one dimension. (As used herein, "Brownian motion" and "brown noise" will be used interchangeably to describe a Brownian motion in one dimension.) Given that a Brownian motion may be described as the cumulative sum of a series of random, independent steps, it is straightforward to generate a Brownian motion trace as a cumulative integral of a white noise trace. For our purposes, we define a white noise trace as a series of values with zero mean taken from a normal distribution (i.e., a Gaussian noise trace; see Figure 13). As a result, a brown noise trace is characterized by a Hurst exponent of $H=0.5$ .

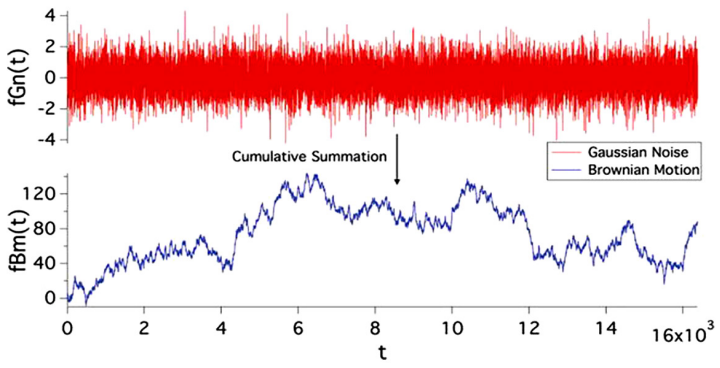


**Figure 13:** The cumulative sum of Gaussian white noise results in Brownian motion.

Relaxing the restriction that the Gaussian noise trace consists of statistically independent increments permits consecutive increments to be positively or negatively correlated, such that the plot formed by the cumulative sum of the noise trace may be characterized by a Hurst exponent that deviates from H=0.5 . Such a trace is termed a "fractional Brownian motion" (fBm). Mandelbrot and Van Ness [11] provide a formalism for quantifying the properties of such structures as follows: Consider a conventional Brownian motion trace $B(t,\omega)$ , where tt denotes time and ω represents the particular realization of the random function that generated the specific Brownian motion. The data set $B(t,\omega)$ is thus a function whose increments $B(t_2,\omega)-B(t_1,\omega)$ have a mean of zero and a variance of $|t_2-t_1|$ , and whose non-overlapping increments $B(t_2,\omega)-B(t_1,\omega)$ and $B(t_4,\omega)-B(t_3,\omega)$ are statistically independent. A "reduced fractional Brownian motion" $BH(t,\omega)$ , then, is further characterized by the parameter H , 0<H<1 , and satisfies

$$B_H(0,\omega)=b_0,$$

$$B_H(t,\omega)-B_H(0,\omega)=\frac{1}{\Gamma\left(H+\frac{1}{2}\right)}\left\{\int_{-\infty}^{0}\left[(t-s)^{H-1/2}-(-s)^{H-1/2}\right]dB(s,\omega)\right.$$

$$\left.+\int_0^t(t-s)^{H-1/2}dB(s\omega)\right\}. \qquad (11)$$

A fractional Brownian motion trace is thus self-affine in the sense that

$$\{B_H(t_0+\tau,\omega)-B_H(t_0,\omega)\}\triangleq\{h^{-H}[B_H(t_0+h\tau,\omega)-B_H(t_0,\omega)]\}, \qquad (12)$$

where

$$\{X(t,\omega)\}\triangleq\{Y(t,\omega)\} \qquad (13)$$

denotes that the two random functions $X(t,\omega)$ and $Y(t,\omega)$ have identical finite joint distribution functions [11]. Thus, on average, when an interval on an fBm trace is expanded by a factor of h , the difference of the values at the endpoints of the interval $B_H(t_0+h\tau,\omega)-B_H(t_0,\omega)$ increases by a factor of $h^H$ . This property represents an example of statistical self-affinity, in which the observed statistical properties within the intervals are preserved when the x and y axes are scaled by distinct factors (specifically, h and $h^H$ , respectively).

Quantifying self-affinity using the formalism of the Hurst exponent motivates drawing a parallel between the Hurst exponent and the fractal dimension, as follows. Following the argument of Ref. [4], consider an fBm trace $V_H(t)$ that extends over a total time span $\Delta t=1$ and a total vertical range $\Delta V_H=1$ . Dividing the time span into *n* increments of width 1/n , we expect the vertical range of the portion of the trace within each interval to scale as $\Delta t^H=1/n^H$ (see Figure 14). Accordingly, on average, the portion of $V_H(t)$ present in a given interval may be covered by $\Delta V_H/\Delta t=(1/n^H)/(1/n)=n/n^H$ square boxes of side length 1/n . Thus, the total number of square boxes of side length 1/n needed in order to cover the entire trace is expected to be $n(n/n^H)=n^{2-H}$ . If we recall that the spatial box-counting method relates number of square boxes of side length $\ell$ needed to cover a trace to the fractal dimension of the trace as $N(\ell)\propto(1/\ell)^{D_F}$ , we may conclude that[6] $D_F=2-H$ .

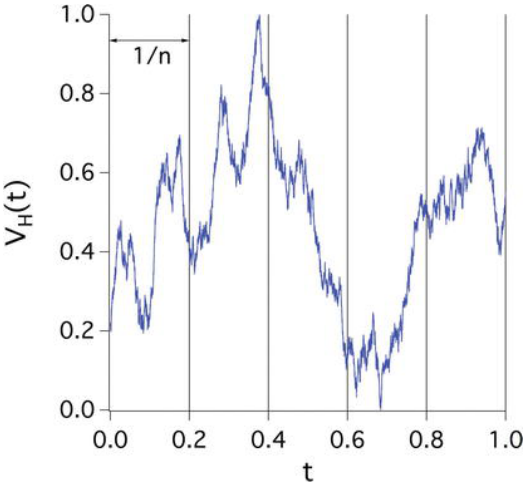


**Figure 14:** Deriving a relationship between the Hurst exponent and fractal dimension. A Brownian motion trace V H t ( H = 0.5 ) is normalized in both dimensions to be circumscribed inside a unit square, and subsequently is divided into n intervals of width 1/n. The self-affinity of an fBm trace leads to an

estimation of the number of square boxes needed to cover the trace at a given length scale, motivating a relationship between H and $D_F$. See text for details.

The relationship $D_F=2-H$ is appealing in its simplicity, and indeed is frequently found in the literature; however, Ref. [4] is quick to acknowledge the inherent difficulty in assigning a fractal dimension to a self-affine structure, given that such a construction is predicated upon assigning an arbitrary rescaling relationship between incompatible coordinates. Mandelbrot, too, notes the apparent relation $D_F=2-H$ [12] and clarifies that this relation holds in the fine-scale limit. This disparity serves to highlight a general distinction between the Hurst exponent and the fractal dimension as descriptors of a time-series trace. Specifically, the Hurst exponent may be understood as a descriptor of *global* correlations, while the fractal dimension may be understood as describing a trace's *local fine-scale structure* [13].

## RELATIONSHIP BETWEEN FRACTAL DIMENSION AND SPECTRAL EXPONENT

We may continue this exercise of comparing our various statistical parameters by considering the spectral exponent ββ as a means of quantifying the nature of a fractal trace. In practice, it is impractical to utilize a spectral analysis to evaluate the fractal properties of a time-series structure, due to the imprecision (relative to the aforementioned fractal analysis techniques) of applying a power law best-fit curve to characterize a spectral decomposition of a trace. Nevertheless, we may investigate the relationship that exists between the spectral exponent $\beta$ , the fractal dimension $D_F$ , and the Hurst exponent H , so long as we recognize the imprecisions of these comparisons. In particular, the spectral exponent $\beta$ typically is said to relate to the Hurst exponent as $\beta=2H+1$ , implying the relationship $D_F=(5-\beta)/2$ . This relationship may be derived by observing that the two-point autocorrelation function

$$G_V(\tau) = \langle V(t)V(t+\tau)\rangle - \langle V(t)\rangle^2 \propto \tau^{\beta-1} \tag{14}$$

for a trace V(t) is related to the quantity $\langle|V(t_\tau)-V(t)|^2\rangle$ as

$$\left\langle |V(t_\tau) - V(t)|^2 \right\rangle = 2\left[\left\langle V^2 \right\rangle - G_V(\tau)\right]; \tag{15}$$

comparing this result to the aforementioned relationship

$$\left\langle |V(t+\tau) - V(t)|^2 \right\rangle \propto \tau^{2H} \tag{16}$$

leads to the expression $\beta-1=2H$ [14]. However, systematic study [15] demonstrates that such a relationship is generally not very robust. Indeed, it is straightforward to test this robustness: In analogy to the investigation performed in Ref. [15], we investigated the relationship between spectral exponent and fractal dimension by generating a set of 20 noise traces, each with a length of 16,384 points and with a $\beta$ value between 0 and 2. Applying each of the previously discussed time-series fractal analysis techniques to each of these traces produced a corresponding set of fractal dimensions (for the variational box-counting analysis and Dubuc's variation analysis) or Hurst exponents (for the variance analysis); these data are shown in Figure 15, with the Hurst exponents "converted" to fractal dimensions via $D_F=2-H$ . Plotting these measured parameters as a function of the well-defined spectral exponent used to generate each trace, we see that the relationship $D_F=(5-\beta)/2$ breaks down for $D_F$ close to 1 or 2.

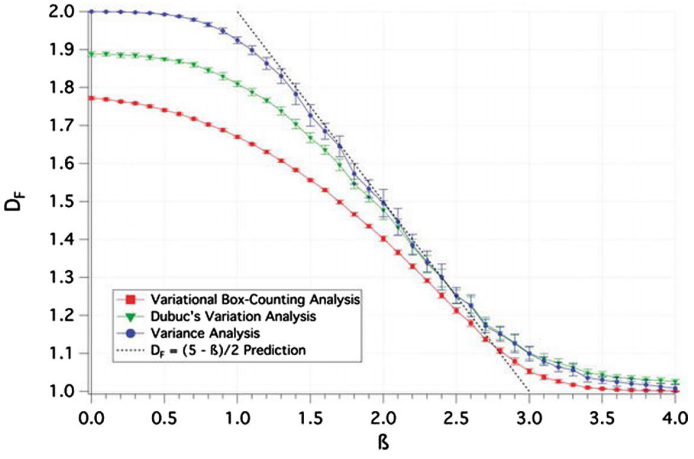


**Figure 15:** Measured fractal dimensions of colored noise traces generated with well-defined power spectral densities $\beta$ . Each data point represents the average value of $D_F$ measured with the respective fractal analysis method for the set of 20 traces at the corresponding value of $\beta$ . Each error bar represents one standard deviation from the mean value of $D_F$ recorded for each set of 20 traces. Lines connecting the data points are provided as a guide to the eye. The dashed line corresponds to the relationship $D_F = 5 - \beta / 2$ .

## GENERATING FRACTIONAL BROWNIAN MOTIONS AND CHARACTERIZING FRACTAL ANALYSIS TECHNIQUES

The framework of the investigation summarized in Figure 15 may be applied to a more thorough investigation of the fidelity of each fractal analysis technique discussed above. That is, if we generate afBm trace with a well-defined Hurst exponent and subject such a trace to the analysis techniques under consideration, we may evaluate the robustness of each analysis technique. In so doing, we may evaluate not only the fidelity of each analysis method, but also may explore how the analysis methods (individually and/or collectively) respond to less-idealized data sets. That is, by generating fBm traces with well-defined Hurst exponents and modifying the traces to better resemble real-world data sets, we may gain insight into how best to interpret our analytical results of experimentally derived data. Specifically, in addition to testing these analysis techniques on "full-size" 16,384-point fBm traces (with 16,384 arbitrarily chosen as a "sufficiently large" number), we additionally tested these analyses on traces of reduced length and/or reduced spectral content, which may better represent experimentally measured data sets.

A variety of methods exist for generating a fractional Brownian motion trace that exhibits a well-defined predetermined Hurst exponent. Examples of such methods include random midpoint displacement, Fourier filtering of white noise traces, and the summation of independent jumps [14]. This chapter considers randomly generated fBm traces that were created using a MATLAB program that generates a fractional Gaussian noise trace with the desired Hurst exponent via a Fourier transform and subsequently computes the cumulative sum of the noise trace to yield a fractional Brownian motion trace with a specified well-defined Hurst exponent.

While such computer-generated fBm traces are accurately described as exhibiting a well-defined Hurst exponent, the inherently finite nature of these traces precludes the traces from being fully "fractal." That is, as with any natural structure with finite extent, the generated fBm traces necessarily exhibit a fine-scale resolution limit (owing to the point-wise granularity of the traces) as well as a coarse-scale size limit (owing to the finite total length of the traces). With this in mind, we must be content to forge ahead with the simplifying assumption that the effects of these particular limitations on our estimates of the underlying fractal scaling properties are negligible when considering a computer-generated fBm trace whose total length exceeds

its step increment by several orders of magnitude. Accordingly, for the purposes of this analysis, we assume that an fBm trace generated with a predetermined Hurst exponent " $H_{in}$ " and with a total length well in excess of its resolution limit is a suitable representative of a pure fractal structure characterized by $H_{in}$ . Thus, we assume that such a trace may fairly be used as a control against which the fidelity of the above-mentioned analysis techniques may be evaluated.

The procedure for evaluating each of these analysis techniques is thus as follows: We first generated a set of 50 16,384-point fBm traces as well as 50 512-point fBm traces at each of 39 input Hurst exponents $H_{in}$ between 0.025 and 0.975. In this manner, we sought to evaluate not only the fidelity of each fractal analysis technique in returning the expected results for the longer 16,384-point traces, but also the effect of performing the same analyses on data sets of limited length. Next, we applied each analysis technique under consideration to each of these traces, returning either a measured Hurst exponent $H_{out}$ or a measured fractal dimension $D_{out}$ . In the case of the Dubuc variation analysis, which returns a measured fractal dimension, this value was "converted"[7] to a Hurst exponent via the relation $H_{out}=2-D_{out}$ . Having extracted these values of $H_{out}$ for each sample fBm trace and for each analysis technique, we produced a plot of $H_{out}$ vs $H_{in}$ representing all fBm traces analyzed with each analysis technique; these results are displayed in Figures 16 and 17 for randomly-generated fBm traces with lengths of 16,384 points and 512 points, respectively. In each of Figures 16 and 17, each data point represents the average $H_{out}$ value measured via the corresponding analysis method. Each corresponding logarithmic scaling plot was fit to a straight line between a fine-scale cutoff of five data points and a coarse-scale cutoff of 1/5 of the full length of the trace. Each error bar represents one standard deviation in the measured values averaged to yield the corresponding data point. The dashed black line represents the ideal relationship $H_{out}=H_{in}$ ; that is, data points representing traces whose measured $H_{out}$ values exactly match their generating $H_{in}$ values would fall on this line.

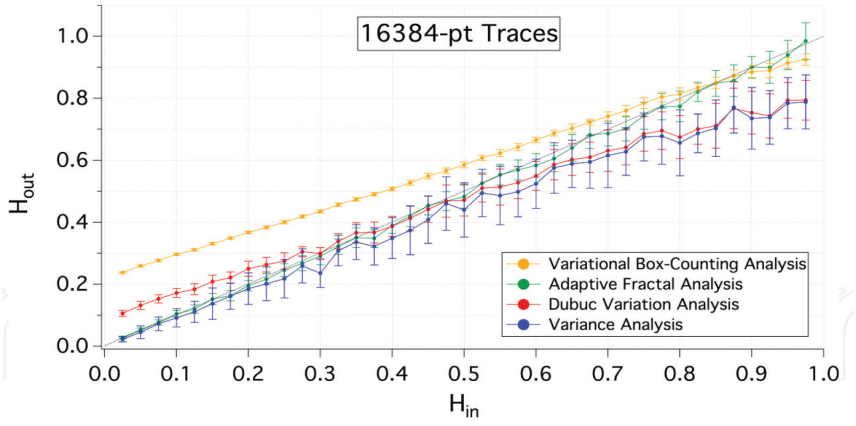


**Figure 16:** Plotting H out vs. H in for randomly-generated-16,384-point fBm traces as measured by the variational box-counting method (yellow), adaptive fractal analysis (green), Dubuc's variation analysis (red), and the variance analysis (blue).

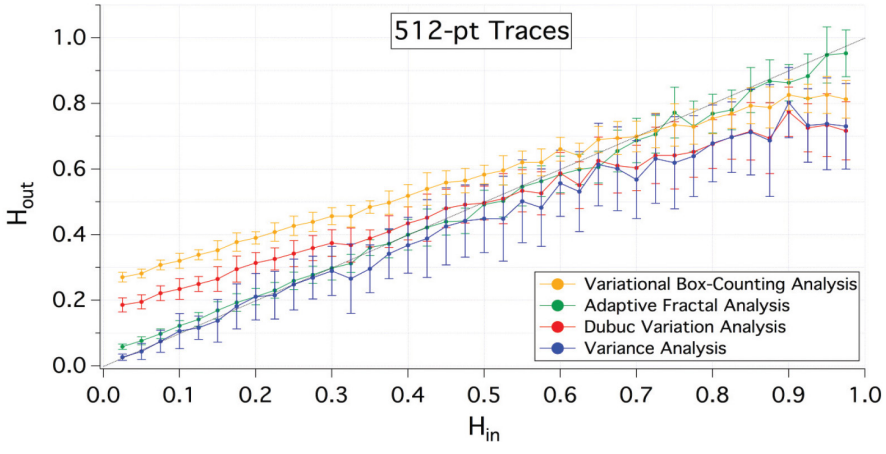


**Figure 17:** Plotting H out vs. H in for randomly-generated 512-point fBm traces as measured by the variational box-counting method (yellow), adaptive fractal analysis (green), Dubuc's variation analysis (red), and the variance analysis (blue).

In the ideal case of a perfectly fractal fBm trace subjected to an analysis technique that produces a precise and accurate value of the Hurst exponent, a plot of $H_{out}$ vs. $H_{in}$ is expected to be linear with unity slope. Based on the

results of the analyses summarized in Figures 16 and 17, our results may be summarized as follows: the variational box-counting method tends to over-estimate H except in the case of high H values; the variance analysis tends to under-estimate *H*; the Dubuc variation analysis performs well only for H~0.5 ; and AFA provides an accurate estimate of *H* throughout the range of *H* values. In the case of the shorter, 512-point traces, the deviations from the ideal relationship $H_{out}$ vs. $H_{in}$ are more pronounced. Additionally, the precision of the estimated *H* values for these shorter traces suffers as well, as seen in the relatively large error bars on the data points corresponding to the shorter traces.

We also investigated the effect on the measured *H* values resulting from another common deviation from ideal fractal behavior. Specifically, in experimentally measured time-series data sets, the smallest-scale measured features often are significantly larger than the resolution limit of the trace. Such is very often the case for experimentally measured data sets that are asserted to represent fractal behavior, in which the finest-scale features may exhibit a characteristic scale that is well over an order of magnitude larger than the point-wise resolution of the trace. To probe the effect of this limitation on a fractal analysis of such a trace, we repeated the above technique on a set of randomly-generated 512-point fBm traces that had been spectrally filtered via Fourier transforms to exhibit a well-defined minimum feature size (i.e., a well-defined maximum frequency component). Specifically, each trace was subjected to a Fourier filter that eliminates all frequency components corresponding to periods shorter than 10 data points, such that the resultant traces have a minimum feature size of 10 points. Figure 22 illustrates a characteristic result of this filtering procedure by comparing the original and Fourier filtered versions of an fBm trace with $H_{in}$=0.5 .

Performing a fractal analysis of time-series traces with limited spectral content requires a reassessment of the length scales over which one expects to observe the fractal scaling properties. Whereas our analysis of fBm traces whose spectral content extended to the resolution limit of the traces examined scaling properties to a minimum length scale of five data points, we now cannot expect to see such scaling properties at length scales smaller than our minimum feature size of 10 data points. Given this well-defined minimum feature size, it may be tempting to set our fine-scale analysis cutoff at 10 data points and expect to observe the desired scaling properties at all length scales greater than this. In practice, however, the effect of such spectral filtering is manifest in a fractal analysis even at length scales significantly greater than that of the minimum feature size.

The results of passing the 512-point Fourier filtered fBm traces through the fractal analysis techniques under consideration are displayed in Figures 19 and 20, which illustrate the results obtained when applying fine-scale cutoffs of 10 data points (i.e., the traces' minimum feature size) and 20 data points, respectively. In each of Figures 19 and 20, each data point represents the average $H_{out}$ value measured via the corresponding analysis technique using the aforementioned cutoffs at the fine scale limit and 1/5 of the entire trace as the coarse scale cutoff limit. Each error bar represents one standard deviation in the measured values that were averaged to yield the corresponding data point. The dashed black line represents the ideal relation $H_{out}=H_{in}$ , as discussed above.

Examples of the logarithmic scaling plots that yielded the data summarized in Figures 16–17 and 19–20 are provided in Figures 21–24. For purposes of illustration, each of these figures shows the logarithmic scaling plots produced by applying the corresponding fractal analysis technique to the specific pair of fBm traces illustrated in Figure 18. That is, each fractal analysis technique under consideration quantifies the fractal characteristic of the input trace by determining the slope of a best-fit line to a log–log scaling plot; Figures 21–24 provide examples of these logarithmic scaling plots.

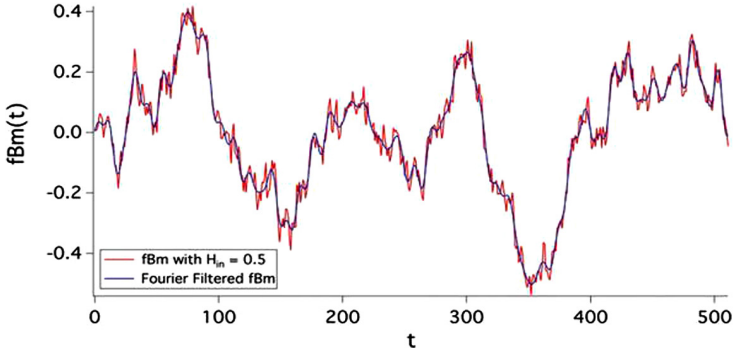


**Figure 18:** Comparison of a 512-point fBm trace with H in = 0.5 before (red) and after (blue) Fourier filtering to a minimum feature size of 10 points.

In each of Figures 21–24, the vertical dashed lines indicate the cutoffs between which the scaling plot is fitted with a straight line whose slope is measured to determine $H_{out}$ . For both traces in each of these figures, the coarse-scale analysis cutoff corresponds to the location of the line labeled

"1/5 of trace." The fine-scale analysis cutoff for the raw trace (red points) corresponds to the location of the line labeled "5 points" (corresponding to the data in Figure 17), while the fine-scale analysis cutoff for the filtered trace (blue points) may be chosen as 10 data points (corresponding to the data in Figure 19) or 20 data points (corresponding to the data in Figure 20), as represented by respective dashed vertical lines in Figures 21–24.

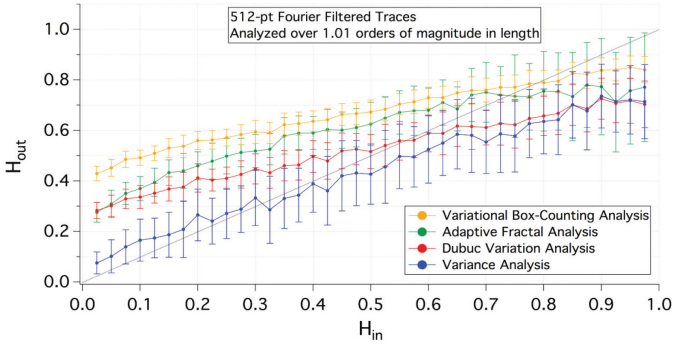


**Figure 19:** Summarizing the fidelity of four fractal analysis methods in measuring the H value for randomly-generated 512-point fBm traces with a minimum feature size of 10 points. The scaling properties were observed over 1.01 orders of magnitude in length scale.

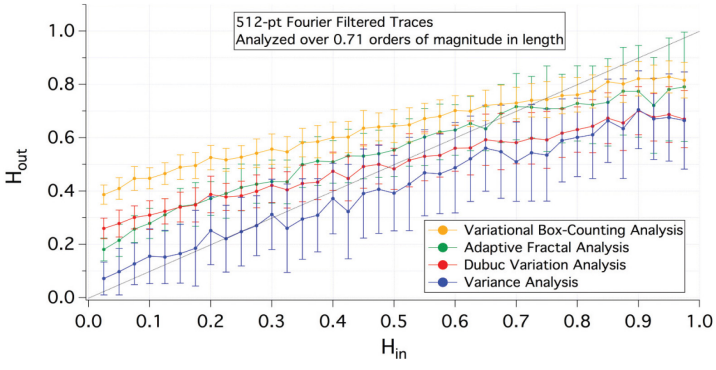


**Figure 20:** Summarizing the fidelity of four fractal analysis methods in measuring the H value for randomly-generated 512-point fBm traces with a minimum feature size of 10 points. The scaling properties were observed over 0.71 orders of magnitude in length scale.

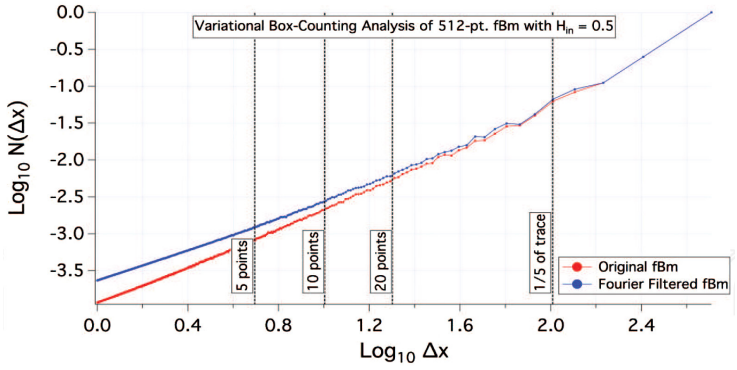


**Figure 21:** Comparison of scaling plots produced by the variational box-counting method applied to a 512-point fBm trace with H in = 0.5 before (red) and after (blue) Fourier filtering to a minimum feature size of 10 points.

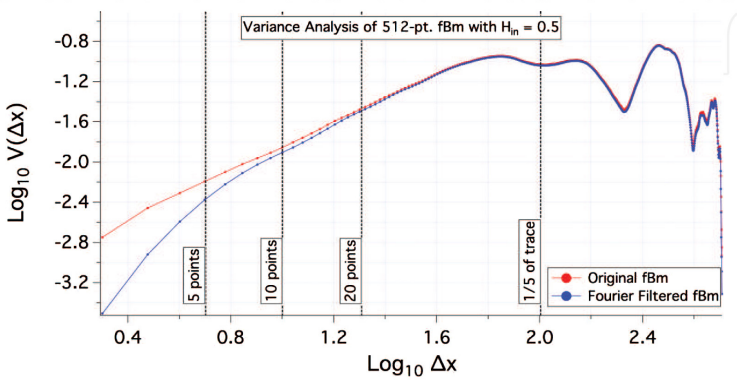


**Figure 22:** Comparison of scaling plots produced by the variance method applied to a 512-point fBm trace with H in = 0.5 before (red) and after (blue) Fourier filtering to a minimum feature size of 10 points.

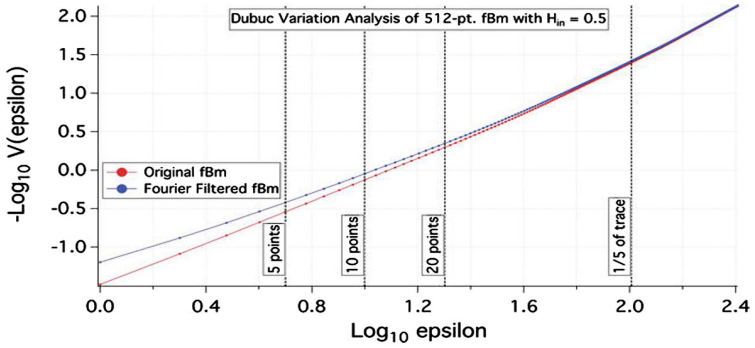


**Figure 23:** Comparison of scaling plots produced by the Dubuc variation method applied to a 512-point fBm trace with H in = 0.5 before (red) and after (blue) Fourier filtering to a minimum feature size of 10 points.

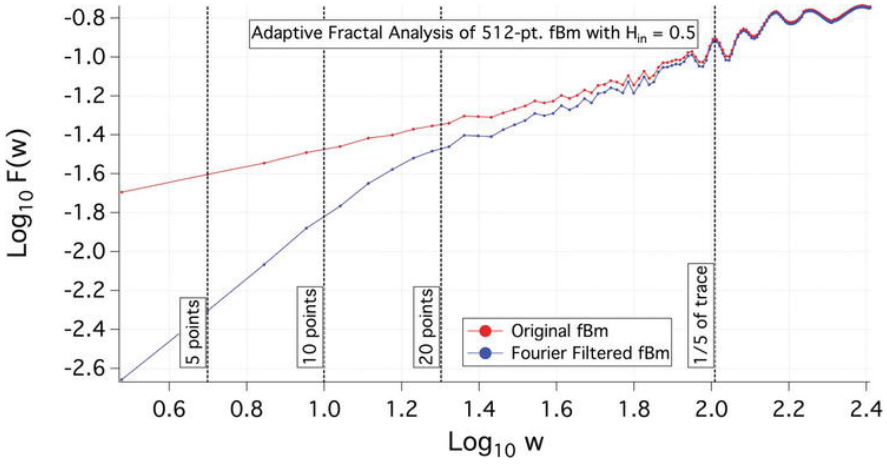


**Figure 24:** Comparison of scaling plots produced by the adaptive fractal analysis method applied to a 512-point fBm trace with H in = 0.5 before (red) and after (blue) Fourier filtering to a minimum feature size of 10 points.

## CONCLUSIONS

Contrasting the trends displayed in Figures 19 and 20 with those displayed in Figures 16 and 17 highlights the inherent challenge in assessing the fractal properties of time-series structures that suffer from limited total length and/or limited resolution/spectral content. Indeed, accommodating the impact of

a minimum feature size that is significantly in excess of the trace's resolution limit generally necessitates restricting a fractal analysis to length scales larger still than even this observed minimum feature size. This in turn often restricts an analysis of scaling properties to a consideration of relatively few orders of magnitude in length. For example, performing a fractal analysis of a 512-point Fourier filtered trace using analysis cutoffs corresponding to 10 data points and 1/5 of the trace length corresponds to an analysis of the scaling behavior over barely more than one order of magnitude in length scale; attempting to increase the accuracy of the measurement by raising the fine-scale cutoff to 20 data points further reduces the scaling range to 0.71 orders of magnitude.

Moreover, Figures 21–24 demonstrate the difficulty in identifying an appropriate fine-scale cutoff for fractal analysis of a time-series trace, even when the minimum feature size found in the trace is easily identifiable and/or well-defined. The examples of Figures 21–24 further highlight an important distinction between the application of fractal analysis techniques to spatial and time-series fractals. In the case of spatial fractals, it often is reasonable to expect to observe fractal scaling behavior between the length scales corresponding to physical constraints (and in particular at length scales sufficiently far from these cutoffs). By contrast, and as seen in Figures 21–24, the effect of imposing (or observing) a finite minimum feature size on a time-series trace is evident at *all* scales, not just at those smaller than the minimum observed period. Accordingly, and as further illustrated in Figures 21–24, this effect may impact the slope of a best-fit line to a logarithmic scaling plot (and, hence, the measured fractal dimension) even when this slope is evaluated between cutoffs that are expected to compensate for the fine-scale limitation.

In light of these results, one must take care when applying these analysis techniques to data sets limited in length or spectral content, as it may be difficult to make a compelling argument for the empirical presence of fractal behavior when examining such a narrow range of length scales. Nevertheless, it is instructive to examine the behavior of fractal analysis applied to known fractal structures such as fBm traces that have been artificially subjected to such constraints. For example, one may argue that an fBm trace that is Fourier filtered to exhibit a coarser minimum feature size is analogous to a natural structure or phenomenon that has been subjected to exterior influences such as weathering effects or measurement limits: both may be considered examples of structures that are legitimately generated via processes associated with fractal behavior, but whose true fractal nature

has been obfuscated by secondary considerations. In the eyes of the authors, such effects do not necessarily render the resulting structures "less fractal" than their idealized counterparts. Nevertheless, such effects demand careful consideration when choosing an analysis method and an acknowledgment of the inherent limitations thereof.

## ACKNOWLEDGMENTS

The authors wish to thank Drs. Adam Micolich, Rick Montgomery, Billy Scannell, and Matthew Fairbanks for fruitful discussions. Generous support for this work was provided by the WM Keck Foundation.

### Notes

- Though Mandelbrot discusses the concept of fractional dimension in this 1967 paper, he did not introduce the term "fractal" until 1975 [3].
- While the box-counting method is typically applied to structures embedded in two dimensions, it is straightforward to generalize the technique to higher- or lower-dimensional systems.
- Not to be confused with the variational box-counting method.
- In all discussions of time-series traces, we refer to the independent variable as "time" as a matter of convention unless otherwise specified. Additionally, as a matter of convention, we refer to an interval of the independent variable as a "length" unless otherwise specified.
- Not to be confused with the variational box-counting method or the variance method.
- Note that this relation only applies to time-series fractals, since the notion of a Hurst exponent is undefined for spatial fractals.
- As discussed above, such a conversion is at best an approximation. Nonetheless, utilizing this conversion serves as a self-consistent means of evaluating the response of this analysis technique when applied to fBm traces of a known Hurst exponent, as well as deviations from this behavior.

## REFERENCES


1. Mandelbrot B. How long is the coast of Britain? Statistical self-similarity and fractal dimension. Science. 1967; 156(3775):636-638. DOI: 10.1126/ science.156.3775.636
2. Richardson LF. The problem of contiguity: An appendix to statistic of deadly quarrels. In: General Systems Yearbook. Ann Arbor: The Society for General Systems Theory; 1961;6:139
3. Mandelbrot B. The Fractal Geometry of Nature. New York: W. H. Freeman and Co; 1982
4. Voss RF. Characterization and measurement of random fractals. PhysicaScripta. 1986;T13:27-32. DOI: 10.1088/0031-8949/1986/ T13/004
5. Taylor RP, Newbury R, Sachrajda AS, Feng Y, Coleridge PT, Dettmann C, et al. Self-similar magnetoresistance of a semiconductor sinai billiard. Physical Review Letters. 1997;78(10):1952-1955. DOI: 10.1103/PhysRevLett.78.1952
6. Micolich AP. Fractal magnetoconductance fluctuations in mesoscopic semiconductor billiards thesis.. Sydney: University of New South Wales; 2000
7. Micolich AP, Taylor RP, Davies AG, Bird JP, Newbury R, Fromhold TM, et al. Evolution of fractal patterns during a classical-quantum transition. Physical Review Letters. 2001;87: 036802. DOI: 10.1103/ PhysRevLett.87.036802
8. Hurst HE. Long-term storage capacity of reservoirs. Transactions of the American Society of Civil Engineers. 1951;116:770-808
9. Dubuc B, Quiniou JF, RoquesCarmes C, Tricot C. Evaluating the fractal dimension of profiles. Physical Review A. 1989;39(3):1500-1512. DOI: 10.1103/PhysRevA.39.1500
10. Riley MA, Bonnette S, Kuznetsov N, Wallot S, Gao J. A tutorial introduction to adaptive fractal analysis. Frontiers in Physiology. 2012;3(371). DOI: 10.3389/ fphys.2012.00371
11. Mandelbrot B, Van Ness JW. Fractional Brownian motions, fractional noises and applications. SIAM Review. 1968;10(4):422-437. DOI: 10.1137/ 1010093
12. Mandelbrot B. Self-affine fractals and fractal dimension. PhysicaScripta. 1985;32:257-260. DOI: 10.1088/ 0031-8949/32/4/001

13. Gneiting T, Schlather M. Stochastic models that separate fractal dimension and the hurst effect. SIAM Review. 2004;46:269. DOI: 10.1137/ S0036144501394387

14. Barnsley MF, Devaney RL, Mandelbrot B, Peitgen HO, Saupe D, Voss RF. The Science of Fractal Images. New York Inc: Springer-Verlag; 1988

15. Labate D, Canavero F, De Marchi A. A comparison of fractal dimension and spectrum coefficient characterization of 1/fα noise. Metrologia. 1994;31(51). DOI: 10.1088/0026-1394/31/1/011s

# 9

# *A Tutorial Introduction to Adaptive Fractal Analysis*

**Michael A. Riley[1], Scott Bonnette[1], Nikita Kuznetsov[1], Sebastian Wallot[2] and Jianbo Gao[3,4]**

[1] Department of Psychology, Center for Cognition, Action, and Perception, University of Cincinnati, Cincinnati, OH, USA
[2]MINDLab, Aarhus University, Aarhus, Denmark
[3] PMB Intelligence, LLC, West Lafayette, IN, USA
[4]BME, School of Life Sciences and Technology, Xi An Jiao Tong University, Xian, PR China

## ABSTRACT

The authors present a tutorial description of adaptive fractal analysis (AFA). AFA utilizes an adaptive detrending algorithm to extract globally smooth trend signals from the data and then analyzes the scaling of the residuals to the fit as a function of the time scale at which the fit is computed. The authors present applications to synthetic mathematical signals to verify the accuracy of AFA and demonstrate the basic steps of the analysis. The authors then present results from applying AFA to time series from a cognitive psychology experiment on repeated estimation of durations of time to illustrate some of the complexities of real-world data. AFA shows promise in dealing with

**Citation:** Riley, M. A., Bonnette, S., Kuznetsov, N., Wallot, S., &Gao, J. (2012). A tutorial introduction to adaptive fractal analysis. Frontiers in physiology, 3, 371.DOI: 10.3389/fphys.2012.00371

many types of signals, but like any fractal analysis method there are special challenges and considerations to take into account, such as determining the presence of linear scaling regions.

**Keywords:** adaptive fractal analysis, time series analysis, fractal physiology, biosignal processing, non-linear analysis

# INTRODUCTION

*Adaptive fractal analysis* (AFA; Hu et al., 2009; Gao et al., 2010, 2011) is a relatively new fractal analysis method that may hold promise in dealing with many types of real-world data. In this paper we present a step-by-step tutorial approach to using AFA. We begin by reviewing some basic principles of fractal processes that will be helpful for our presentation of AFA. We then discuss AFA and provide a guide for implementing it. We conclude with an analysis of some synthetic signals and of some real data from an experiment in human cognition.

## Fractal Processes

Many physiological and behavioral processes exhibit fractal dynamics. This means the measured patterns of change over time—the behavioral time series—exhibit certain properties, including *self-similarity* and *scaling* (Lebovitch and Shehadeh, 2005). Self-similarity means that the patterns of fluctuations at faster time scales mimics the patterns of fluctuations at slower time scales. Scaling means that measures of the patterns (such as the amount of variability present) depend on the resolution or the time scale at which the measurements have been taken. Many fractal analyses, including AFA, focus explicitly on how a measure of variability scales with the size of a time window over which the measure is calculated. Gao et al. (2007) provided a succinct and comprehensive treatment of various fractal analysis methods.

When conducting fractal analysis of a time series it is important to understand the concepts of *fractional Gaussian noise* (fGn) and *fractional Brownian motion* (fBm), and the differences between the two. fGn is a stationary, long-memory process, whereas fBm is a non-stationary, long-memory process (Mandelbrot and van Ness, 1968; Beran, 1994; Mandelbrot, 1997). Roughly speaking, stationary processes fluctuate by a relatively constant degree around a mean value that remains relatively constant over time, whereas for a non-stationary process the statistical

moments of the process (e.g., mean and variance) are time-dependent. "Long-memory" means that the processes exhibit statistical dependencies (correlations) over very long time scales, as opposed to a process for which only adjacent or nearly adjacent data points are correlated with each other. Figure Figure11 depicts sample time series of fBm and fGn processes.

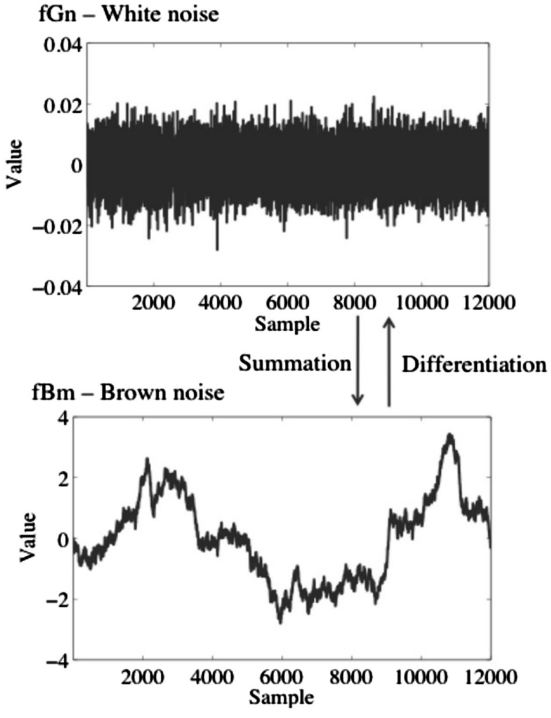


**Figure 1:** Top: A time series of white noise, afGn process. Bottom: a time series of brown noise, afBm process. A brown noise process can be obtained by successively summing data points in the white noise process.

fGn and fBm are, nominally, dichotomous types of signals. While this is true in an important sense, fGn and fBm are nonetheless related. The increments of afBm process (created by differencing the signal, i.e., subtracting each value in the time series from the prior value) form a fGn signal [see Eke et al. (2000), for a detailed description of the fGn-fBm dichotomy]. Stated differently, successively summing the data points in afGn time series will produce a fBm time series. As described below, fGn and fBm require different treatment when using fractal methods to analyze

their temporal structure, and the results of a fractal analysis on these two different types of signals will necessarily have different interpretations.

A parameter called the Hurst exponent, *H*, provides a way to quantify the "memory" or serial correlation in a time series. The exact meaning of *H* depends on whether a signal is fGn or fBm. *H* values indicate the correlation structure of afGn signal, but for a fBm signal the *H* values refer to the correlation structure of the increments obtained by differencing the time series (Cannon et al., 1997). It is therefore necessary to carefully classify a signal as fGn or fBm (or some other kind of signal) before proceeding with fractal analysis of the signal.

With that caveat noted, different *H* values indicate different types of long-memory. Actually, $H = 0.5$ indicates the absence of long-memory (i.e., the process is random—it possesses no memory meaning that data points are uncorrelated with each other) or possesses only short-memory (correlations across very small scales only). This can be considered a null hypothesis of sorts when conducting a fractal analysis; one is often interested in determining whether the data possess some sort of temporal structure rather than being just a truly random, uncorrelated process.

A finding of $0 < H < 0.5$ indicates an anti-correlated or *anti-persistent* process for cases of fGn and fBm, respectively. This means that increases in the signal (for fGn) or in the increments of the signal (for fBm) are likely to be followed by decreases (and decreases are likely to be followed by increases)—a negative long-range correlation. In contrast, $0.5 < H < 1$ indicates a correlated process for fGn or what is termed a *persistent* process for fBm. In this case, increases in the signal (for fGn) or in the increments of the signal (for fBm) are likely to be followed by further increases, and decreases are likely to be followed by decreases (i.e., a positive long-range correlation). Anti-persistent and persistent processes contain structure that distinguishes them from truly random sequences of data.

To reiterate the point made earlier, and as Eke et al. (2000) carefully explained, an important first step in any type of fractal analysis is to determine the basic type of signal one has measured, i.e., whether the signal is fGn or fBm (see also Cannon et al., 1997). Simply plotting the time series can sometimes help the user make a first-pass determination about whether a pre-processing stage of integrating the data is required. Integration is required only if the data are a stationary, noisy increment process (such as fGn; Figure 1). Integration is not advised if the data are a non-stationary

random-walk process (such as fBm; Figure 1). The consequences of this choice are important; *H* estimates can be artificially inflated by integration of a signal which should not be integrated, for example, whereas a lack of integration when it should be performed could suggest the appearance of multiple scaling regions separated by a cross-over point when only one scaling region actually exists (see Delignieìres et al., 2003).

Of course, it is often the case that a plot of the time series cannot be easily classified as an increment or random-walk process based on its appearance alone. Eke et al. (2000) presented a strategy for determining the signal type, termed the signal summation conversion (SSC) method, in the context of a broader approach to analyzing physiological signals that might exhibit fractal dynamics. The method essentially involves comparison of results obtained when the signal is integrated versus not integrated. If *H* values for the non-integrated data approach or exceed a value of 1, then integration of the signal is generally not recommended. *H* values for non-integrated and integrated time series generated by an ideal fBm process should differ by a value of 1; if the difference is considerably greater or less than 1 further scrutiny of the data is required, because in that case the data may not fit within the fBm-fGn framework (Gao et al., 2006; Kuznetsov et al., 2012).

## Adaptive Fractal Analysis

AFA is similar in some regards to detrended fluctuation analysis (DFA; Peng et al., 1994), and many aspects of AFA will be familiar for readers who already understand DFA. We point out some of these similarities in our presentation of AFA to help those readers, although familiarity with DFA is not required. Because of these similarities, AFA shares many of the same advantages as DFA over other fractal methods, such as the fact that *H* estimated by DFA and AFA do not saturate at 1 as is the case for other methods (Gao et al., 2006).

But despite the similarities between the methods, there are important differences which provide AFA with some advantages over DFA. For example, AFA can deal with arbitrary, strong non-linear trends while DFA cannot (Hu et al., 2009; Gao et al., 2011), AFA has better resolution of fractal scaling behavior for short time series (Gao et al., 2012), AFA has a direct interpretation in terms of spectral energy while DFA does not (Gao et al., 2011), and there is a simple proof of why AFA yields the correct *H* while such a proof is not available for DFA [see Equations 6 and 7 in Gao et al. (2011)].

It is important to note that like many other analyses used to quantify fractal scaling AFA cannot be used independently to assert that a process is or is not a fractal process. Because there are non-fractal processes that can falsely give the appearance of fractal scaling and long-range correlations, it is desirable to use other methods for this purpose (e.g., Wagenmakers et al., 2004; Delignieìres et al., 2005; Farrell et al., 2006; Torre et al., 2007).

The first step in AFA is to identify a globally smooth trend signal that is created by patching together local polynomial fits to the time series. This is one of the primary differences between DFA and AFA; DFA does not involve the creation of this globally smooth trend, and instead relies on discontinuous, piece-wise linear fits. Basically, creating a globally smooth trend signal means that one tries to recreate local features of the data using simple polynomial functions. An example is shown in Figure 2. Small segments of the time series can be approximated reasonably well by adjusting the parameters of a polynomial regression model.

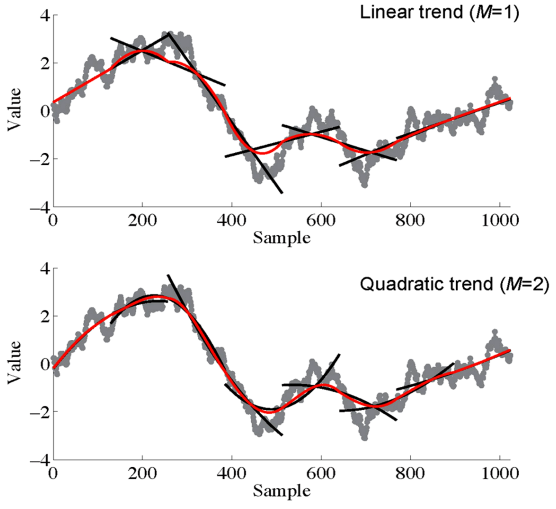


**Figure 2:** An illustration of the process of identifying a globally smooth trend signal. Linear (Top; $M = 1$) or polynomial (Bottom; $M = 2$) trends are fit to pieces of the signal of length $w$ (257 in this case). These fits are shown as black lines superimposed on the original data series (gray curves). The local fits are then stitched together (see Equation 1) to create a smooth global trend signal, depicted in red. Notice that when the end of the series is encountered only half of the data points in that window are used for the trend without smoothing.

We can now express these ideas in more precise terms [see also Tung et al. (2011), who provided a thorough description of the detrending scheme

that forms the basis of AFA]. The goal of this step of the analysis is to create a global trend—a synthetic time series $v(i)$, $i = 1, 2, \ldots, N$, where $N$ is the length of the original time series. We denote the original time series as $u(i)$. Determination of the global trend is achieved by partitioning the original data $u(i)$ into windows of length $w = 2n + 1$, with the windows overlapping by $n + 1$ points. Since setting $w$ (a process we describe below) determines the value of $n$ [i.e., $n = (w-1)/2$], $n$ is not a free parameter that must be chosen.

Within each window the best fitting polynomial of order $M$ is identified. This is done through standard least-squares regression—the coefficients of the polynomial model are adjusted until the polynomial fits the data with the least amount of residual error. Increasing the order $M$ can usually enhance the quality of the fit, but one must be cautious about over-fitting the data. Typically $M$ should be 1 or 2—i.e., a linear or quadratic function. The goal is not to fit every squiggle or variation in $u(i)$ with the polynomial model, but simply to capture any relatively global trends in the data while leaving enough residual variability to analyze further. Presently, there are no validated, objective criteria for selecting $M$, so careful exploration of different $M$ values may be required when analyzing a given time series.

The local fits then have to be "stitched" together in such a way that they provide a smooth global fit to the time series. Without this stitching, the local polynomial fits would be disconnected with each other, as is the case for DFA. The stitching and the resulting smooth trend signal thus represents a major distinction between DFA and AFA. The fit to overlapping regions is created by taking a weighted combination of the fits of two adjacent regions to ensure that the concatenation of the local fits is smooth [mathematically, this means that $v(i)$ is continuous and differentiable], according to

$$y^{(c)}(l) = w_1 y^{(i)}(l + n) + w_2 y^{(i+1)}(l), \quad l = 1, 2, \ldots, n + 1 \qquad (1)$$

where $w_1 = \left(1 - \frac{l-1}{n}\right)$ and $w_2 = \frac{l-1}{n}$. According to this scheme, the weights decrease linearly with the distance between the point and the center of the segment. This ensures symmetry and effectively eliminates any jumps or discontinuities around the boundaries of neighboring regions. In fact, the scheme ensures that the fitting is continuous everywhere, is smooth at the non-boundary points, and has the right- and left-derivatives at the boundary. By choosing the parameters of each local fit to maximize the goodness of fit in each case, and then applying Equation 1 to stitch the local fits together, the global fit will be the best (smoothest) fit to the overall time series. Fur-

thermore, this fitting scheme will work with any arbitrary signal without any a priori knowledge of the trends in the data.

The next step is to detrend the data by removing the global trend signal that was just created. We remove the trend because are interested in how the variance of the residuals of the fit—the more fine-grained fluctuations in the original time series $u(i)$—scale with $w$, as described below. This type of detrending is very different than simply removing a linear (or higher-order) fit to the original time series prior to data analysis (cf. Di Matteo et al., 2003); the detrending method in AFA (and DFA) is done locally over windows of varying length $w$ but not to the entire time series as a whole. The residuals of the fit of the data to the trend signal are identified by subtracting the global trend from the original time series—we compute $u(i) - v(i)$. (This is similar to the detrending step performed in DFA, except that as noted for DFA the local linear fits are not smoothly stitched together to create a globally smooth trend signal, but rather are discontinuous with respect to one another.)

These steps that have been described are then repeated for a range of $w$ values (i.e., for a range of time scales). Thus, one must choose a minimum and maximum $w$, as well as the size of the time steps (i.e., increases in $w$) used for the analysis. It is perhaps best to begin with the smallest and largest possible $w$ values, i.e., $w = 3$ samples and $w = N/2$ samples (or $N/2 + 1$ if the time series has an even number of samples) where $N$ is the length of the time series. However, as discussed by Cannon et al. (1997), exclusion of some of the smaller and larger window sizes can increase the reliability of $H$ estimates. This may be a helpful step when analyzing signals that show a single scaling region over some intermediate range of time scales, and where issues such as measurement noise or insufficient time series length could cause an apparent breakdown of scaling at smaller and larger time scales, respectively. However, one should first ensure that the regions under consideration for exclusion do not themselves contain distinct types of fractal scaling (i.e., that the signal contains multiple scaling regions) to avoid loss of information about the signal. In light of such considerations, we used a $w$ range of 3 to ($2^9 + 1 =$) 513 samples for the analyses reported here. Any further adjustments to the $w$ range can be determined after the next step in the analysis, when one plots $\log_2 F(w)$ as a function of $\log_2 w$, as we describe below in our analyses of sample data (and see Kuznetsov et al., 2012). Typically it is sufficient to use a step size of 1, although there may be occasions when a smaller step size is desired to obtain better resolution for identifying linear scaling relations in the plot. In our experience, a step

size of less than 0.5 typically does not provide useful new information, but this is an issue that should be explored for each unique data set.

The next step is to examine the relation between the variance of the magnitude of the residuals, $F(w)$, and the window size, $w$. For a fractal process, the variance of the residuals scales with $w$ (i.e., is proportional to $w$ raised to the power $H$) according to

$$F(w) = \left[ \frac{1}{N} \sum_{i=1}^{N} (u(i) - v(i))^2 \right]^{1/2} \sim w^H. \tag{2}$$

Fractal scaling can be quantified through the slope (obtained using simple linear regression) of a linear relation in a plot of $\log_2 F(w)$ as a function of $\log_2 w$ (Figure 3). This slope provides an estimate of the Hurst exponent, $H$.

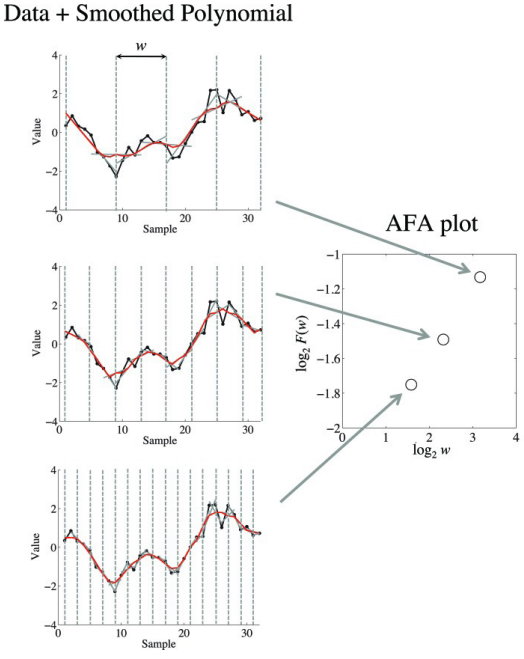


**Figure 3:** On the left is depicted a demonstrations of how the fits to different window sizes $w$ **relate to the AFA plot, shown on the right.** The AFA plot is a plot of $\log_2 F(w)$ (i.e., variance of the residual to the globally smooth trend signal) as a function of $\log_2 w$ (i.e., time scale or window size). A linear relation in this plot captures fractal scaling, and the slope of the line of best fit provides an estimate of the Hurst exponent $H$. For visual simplicity we only depicted non-overlapping window edges with the dotted gray line, while the analysis uses overlapping windows.

It should be noted that two qualitatively different signals (one fGn, the other fBm) could have the same $H$ value. For example, a white noise signal (fGn, so it is integrated prior to analysis) and a brown noise signal (fBm, so it would not be integrated prior to analysis) would both yield $H = 0.5$. Because of this one should use caution performing statistical comparisons of $H$ for signals that may differ in regard to being fGn or fBm, and it is partly for this reason that Eke et al. (2000) emphasize the need to report signal classification along with $H$ values. For clarity, here we distinguish between $H$ for these two processes using the labels $H_{fGn}$ and $H_{fBm}$.

The above steps constitute the basic process of applying AFA. Often one would perform AFA on each time series in an experimental data set to obtain an $H$ value(s) for each, and then submit the set of $H$ values to standard statistical analyses (e.g., $t$-test or analysis of variance) to determine if $H$ changes across experimental conditions or between groups of subjects. That is, $H$ becomes a dependent variable that is analyzed to determine if it changes across levels of some factor.

In the next sections, we apply AFA to known, mathematical fractal processes and then to real-world data obtained from an experiment on human cognition (repeated estimation of the duration of a time interval). The application to known fractal signals demonstrates how AFA is capable of classifying signals in terms of $H$. The application to real-world data reveals the complexities and challenges of using fractal analysis methods to signals that are not idealized fractal processes, like most real signals in the biological, behavioral, and physical sciences. One of these challenges is the matter of deciding how to identify linear scaling regions for AFA (and this challenge applies to other fractal methods, including DFA).

# APPLICATIONS OF AFA

## Application to known Fractal Processes

Here we present applications of AFA to artificially created time series including some well-studied fractal processes. The advantage of doing so is that we can compare the results of AFA to what should be the "right" answers based on a priori, mathematical knowledge of the artificial time series. Consistent with the goal of this paper to serve as a tutorial for using AFA, we do not mean for this to represent a fully comprehensive test of the method, but rather a straightforward, minimal demonstration that the

method correctly identifies these simple "toy" signals. We present results of AFA applied to time series of random, white noise, and two idealized fractal processes known as pink noise and brown noise.

## Synthetic Time Series Properties

The artificial time series were generated using MATLAB (The MathWorks, Inc.; Natick, MA). Ten time series of length $N$ = 10,000 were generated for each of three categories of signals using an inverse Fourier transform (Lennon, 2000): White, pink, and brown noise (see Figure 4). Initially, DFA was used to verify that the synthetic time series we created indeed had the desired mathematical characteristics. The integrated white, integrated pink, and non-integrated brown series were found to have mean (± 1 SD) $H$ values of $H_{\text{fGn}} = 0.49 \pm 0.01$, $H_{\text{fGn}} = 0.97 \pm 0.01$, and $H_{\text{fBm}} = 0.51 \pm 0.01$, respectively. The close correspondence between those results and the theoretical values of $H_{\text{fGn}}$ = 0.5, $H_{\text{fGn}}$ = 1.0, and $H_{\text{fBm}}$ = 0.5, respectively, indicates that the simulations produced accurate simulations of fractal processes. Based on our a priori knowledge of the signals, confirmed by visual inspection of stationarity of the time series and these preliminary checks using DFA, only the white and pink noise time series were integrated prior to AFA. The brown noise time series were not integrated.

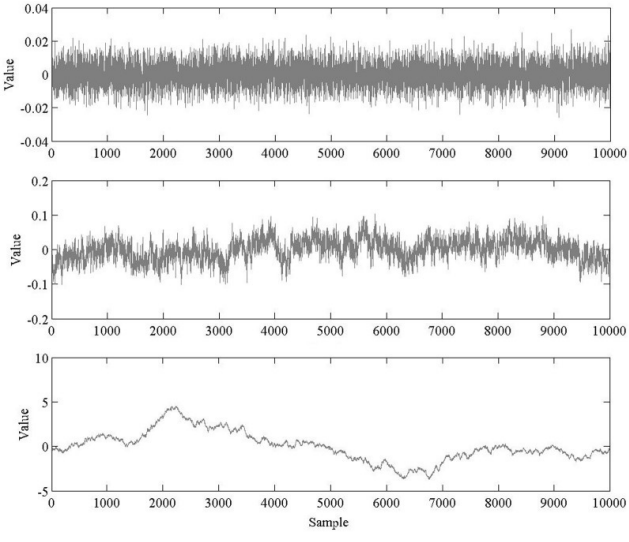


**Figure 4:** Sample time series of white (top), pink (middle), and brown (bottom) noise.

## Data Reduction and Analysis

The AFA steps described above were implemented on the set of 30 synthetic time series. Parameters of window size $w$ = 0.5 and polynomial orders of $M$ = 1 and $M$ = 2 were chosen for the analyses (AFA was performed once with each polynomial order). Sample AFA plots are shown in Figure 5.

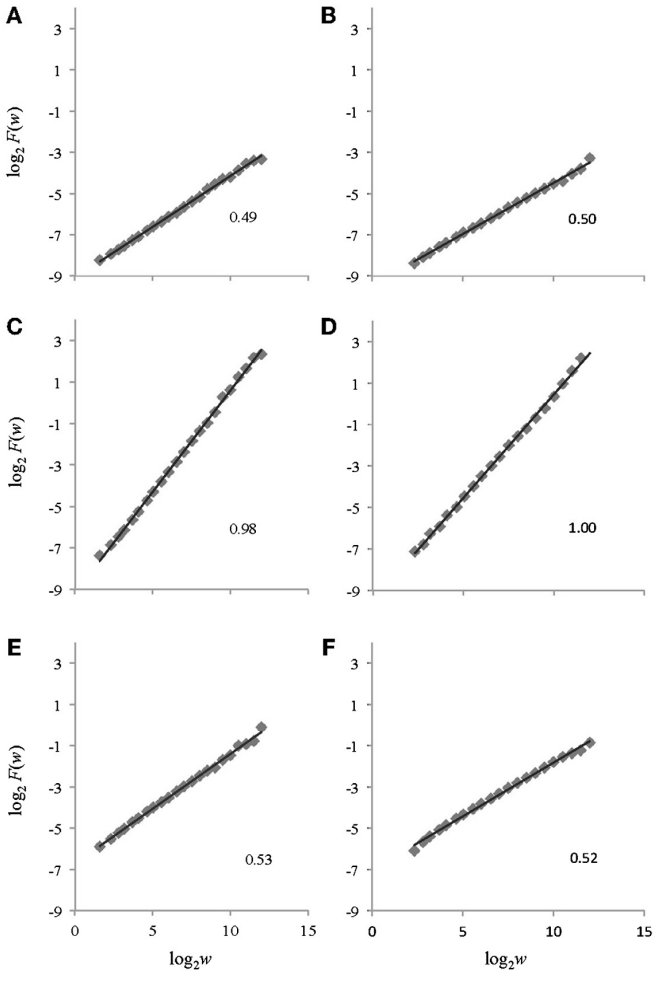


**Figure 5:** Example $\log_2 F(w)$ vs. $\log_2 w$ **plots returned by AFA for the time series** depicted in Figure 4. The plots on the left side (panels A, C, and E) are from AFA using a polynomial order of $M$ = 1 while those on the right side (panels B, D, and F) are from AFA using a polynomial order of $M$ = 2. Plots A and B are for white noise, plots C and D are for pink noise, and plots E and F are for brown

noise. The respective $H_{fGn}$ (A, B, C, and D) and $H_{fBm}$ (E and F) values are shown for each signal.

## Results

For the white noise time series, using polynomial orders of $M = 1$ and $M = 2$, AFA returned mean $H$ values of $H_{fGn} = 0.49 \pm 0.01$ and $H_{fGn} = 0.50 \pm 0.01$, respectively. The pink noise time series were also effectively categorized by AFA in the original time series. A mean $H$ value of $H_{fGn} = 0.98 \pm 0.01$ was obtained using a polynomial order $M = 1$ and a mean value of $H_{fGn} = 0.99 \pm 0.02$ was found using a polynomial order $M = 2$. Lastly, AFA successfully characterized the non-integrated synthetic brown noise time series. Using polynomial orders of $M = 1$ and $M = 2$, AFA returned mean $H_{fBm}$ values of $0.51 \pm 0.02$ and $0.52 \pm 0.01$, respectively.

## Discussion

The application of AFA to the synthetic time series indicated that AFA is able to characterize the types of noise with a similar accuracy as DFA. The obtained $H$ values corresponded very closely to the theoretically expected values and to the values obtained by DFA (presented earlier). The estimates also exhibited high reliability (low SD values). Changing the polynomial order $M$ had very small consequences for these synthetic data; $M = 2$ resulted in slightly better estimates for white and pink noise (and for this polynomial order AFA produced slightly more accurate estimates than did DFA), but slightly worse estimates for brown noise.

## Application to Real-world Data from a Cognitive Psychology Experiment

We analyzed time series produced by a single participant who repeatedly performed a cognitive task (estimating the duration of a temporal interval) over the course of multiple experimental sessions. The task of repeated temporal estimation is frequently used to study the variability of human time estimation (Delignières and Torre, 2010) and was one of the first reported cases of $1/f$ noise in human cognitive behavior (Gilden et al., 1995).

## Experimental Methods

A single female undergraduate student who gave informed consent participated voluntarily in the study which was approved by the Institutional

Review Board at the University of Cincinnati. She was paid $10 per session. The task required the participant to provide repeated estimates of a 1-s time interval. Time estimates were recorded from the presses of the spacebar of a millisecond-accurate keyboard (Apple A1048, Empirisoft). Response times were recorded using the *Psychophysics Toolbox for Matlab* (Brainard, 1997), which recorded the time of each key press during the experiment. We defined one time interval estimate as the time from the beginning of one space bar press to the next one.

At the beginning of each experimental session the participant listened to 20 metronome beats of the 1-s interval to be estimated. The metronome was then turned off, and the participant then immediately began performing the time estimation task. A total of 1050 estimates were produced consecutively in each experimental session, and each session lasted approximately 20 min. There were two experimental conditions that varied with regard to the presence or absence of feedback about the accuracy of the estimates. In the no-feedback condition the participant did not receive any explicit feedback about timing performance. This condition was similar to tasks used previously in continuation tapping experiments (Gilden et al., 1995; Chen et al., 2002; Wagenmakers et al., 2004; Torre and Delignières, 2008). In the feedback condition a computer monitor was used to present feedback specifying the error (in ms) of the most recent estimate on every trial. For example, if the participant hit the space bar 250 ms after 1 s had passed since the previous press, the feedback on the screen would read "250 ms late." The participant first completed 10 no-feedback trials, one per day on consecutive days, and then completed 10 feedback trials (again one per day on consecutive days). For present purposes we focus on just the first and the last trial in each of the two feedback conditions.

## Data Processing and Results

We followed the standard procedure in the literature on temporal estimation to remove all observations less than 300 ms and any observations falling beyond 3 SD from the mean. Such values are likely to originate from accidents such as double-tapping the space bar or not initially pressing the bar hard enough, and a significant number of these kinds of outlying values can have detrimental results. From looking at plots of the data processed in this way (Figure 6), it was clear that the time series of temporal estimates were more similar to fGn than fBm (compare to Figure 1)[1]. Therefore, we integrated our data prior to performing AFA. Then, the same basic steps for AFA described previously were again implemented, but with the following

additional considerations taken into account. We used $M = 1$ (given that using $M = 2$ did not show consistently better results in our analysis of the sample time series) and $\log_2 w$ step sizes of 0.5 (because we wanted to enhance the resolution of the AFA plots to facilitate the identification of linear scaling regions).

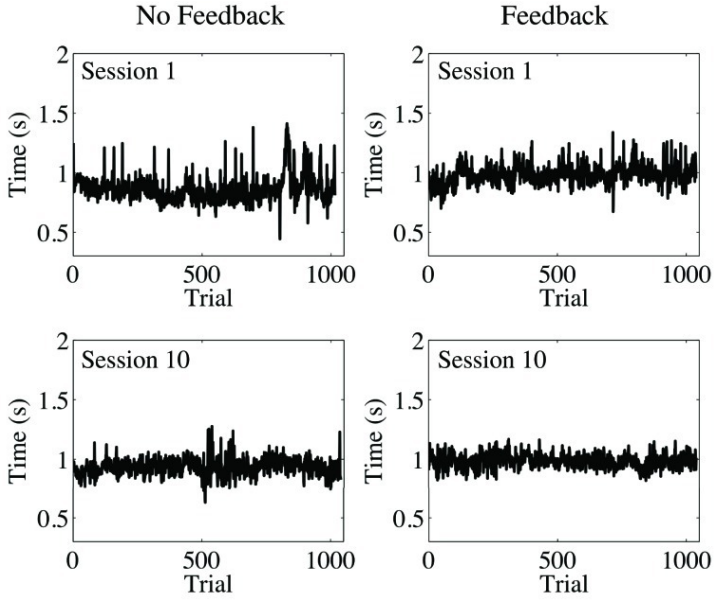


**Figure 6:** Trial series of continuous time estimates with and without accuracy feedback after removing observations faster than 300 ms and beyond 3 SD from the mean. The participant performed the task 10 times in each feedback condition.

When dealing with real-world data, if fractal scaling is present it may be limited to a range of time scales (i.e., $w$ values). If this is not taken into account, it may lead to inaccuracies in the estimation of $H$. Before estimating $H$, then, it was important to visually inspect the plots of $\log_2 F(w)$ as a function of $\log_2 w$ to identify regions where linear scaling might be present. If fractal scaling appears limited, it may be necessary to restrict the range of the linear fit to the plot to exclude regions where linear scaling does not occur. Inclusion of regions where fractal scaling is actually absent can lead to inaccuracies and reduce the reliability of $H$ estimates (Cannon et al., 1997), and may present an unrealistic picture of the degree to which fractal scaling really is a major feature of the signal being analyzed. In practice, it is desirable to make this process as objective and automated as

possible to avoid bias. Elsewhere (Kuznetsov et al., 2012) we have described this issue in more detail, and presented a quantitative procedure designed for this process. For the sake of this tutorial, however, we chose the linear regions visually after inspecting the AFA plots for each trial without the linear fits imposed to examine the possibility of linear scaling.

As often occurs with empirical data (as opposed to pure mathematical fractals), some of our time series yielded slightly curved $\log_2 F(w)$ functions (cf. Di Matteo et al., 2003) and had cut-off edge effects especially at larger time scales ($w > 8$ or 256 estimates). Visual inspection of the AFA plots (see Figure 7) suggested two distinct regions of linear scaling, one for low $w$ (i.e., fast time scales) and a longer region for higher $w$ (i.e., slower time scales), for both feedback conditions and for both the first and last experimental sessions. Such a finding was expected based on previous studies that revealed $H_{fGn} < 0.5$ over the faster scales and $H_{fGn} > 0.5$ at the slower scales (Lemoine et al., 2006; Delignieìres et al., 2008).

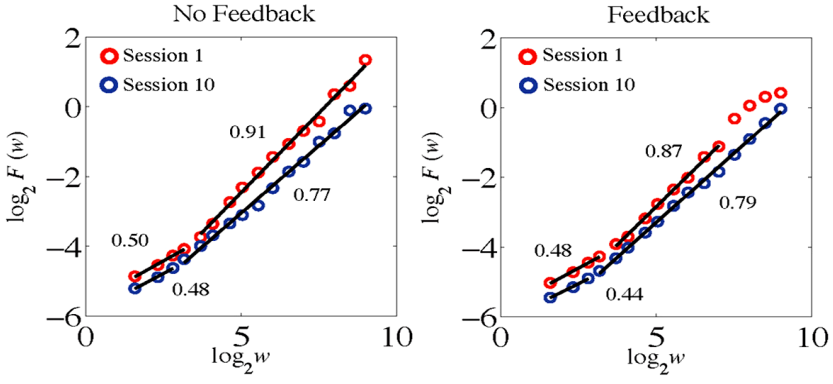


**Figure 7:** AFA plots for the time series of time estimates presented in Figure Figure66. The $H_{fGn}$ values are indicated for each scaling region.

In the first experimental session the fast scaling region for the no-feedback condition spanned windows $\log_2 w$ from 1.58 to 3.17 (in terms of actual number of time estimates this corresponded to a range of 3–9). The $H_{fGn}$ value associated with this region was 0.50, indicating the presence of uncorrelated white noise. The slower scaling region for the no-feedback condition had an $H_{fGn}$ value of 0.91 (indicating a positive correlation at this scale) and spanned windows $\log_2 w$ from 3.17 to 9 (13–513 estimates). On the last trial, after a period of practice, the fast scaling region showed a

tendency to become slightly anti-correlated but was still very close to white noise ($H_{fGn}$ = 0.48) and its length decreased compared to the first session (it now spanned 1.58–2.81 $\log_2 w$, or 3–7 estimates). The slow scaling region increased in length (it now spanned from $\log_2 w$ = 3.17 to 9; 9 to 513 estimates) and became more uncorrelated because its $H_{fGn}$ value decreased to 0.77.

A similar pattern of results was found for performance in the feedback condition (see Figure Figure6,6, right panel). The fast scaling region during the first session spanned windows from 1.58 to 3.17 $\log_2 w$ (in terms of actual number of time estimates this corresponded to a range of 3–9) and had a $H_{fGn}$ = 0.48, indicating uncorrelated white noise dynamics on this scale. One major difference compared to the no-feedback condition was the shorter length of the slow scaling region in the first session, which now spanned values of $\log_2 w$ from 3.17 to 8 (9–257 estimates). Similar to the no-feedback condition, the dynamics at this scale exhibited positive correlation as indexed by $H_{fGn}$ = 0.87. The breakdown at larger $\log_2 w$ is likely due to an initial transient evident in the time series plot for this session—for about the first 100 estimates the participant consistently underestimated the 1-s interval, but then began to estimate it more accurately. Because this only happened during one part of the trial, this affected the slowest scaling region of the AFA plot. At trial number 10, similarly to the no-feedback condition, the fast scaling region showed a tendency to become slightly more anti-correlated but was still very close to white noise ($H_{fGn}$ = 0.44) and its length decreased compared to the first session (it now spanned 1.58–2.81 $\log_2 w$, or 3–7 estimates). The slow scaling region increased in length (it now spanned $\log_2 w$ = 3.17–9; 9–513 estimates) and became less correlated because its $H_{fGn}$ value decreased to 0.79.

## Discussion

Finite, real-world time series are typically more complex than the ideal simulated noises of mathematics. For example, as was apparent in these time series, experimental data can contain multiple scaling regions. Partly, this may be because experimental data contain both the intrinsic dynamics of the process that generated the signal plus the measurement noise inherent in any recording device. Apart from that, the intrinsic dynamics of real-world signals may have singular events and non-stationarities that if severe enough often can complicate many analyses (including AFA). Because of this it is very important to carefully examine the raw data and the corresponding scaling plots before conducing any quantitative analyses.

With regard to the dynamics of cognitive performance in this temporal estimation task, these results provide preliminary evidence of the presence of practice effects in the continuous time estimation task. Practice led to a decrease in the *H* exponent of the slow scaling region, suggesting that the responses became somewhat more uncorrelated at this scale with practice. Of course our preliminary results have to be interpreted with caution because they are based on single participant and there are individual differences in the slow scaling region *H* values in this task (Torre et al., 2011). The differences between feedback conditions at the fast time scales were not expected because previous literature reported anti-correlated dynamics at this scale (Lemoine et al., 2006; Delignieìres et al., 2008). Feedback clearly resulted in an increased tendency for anti-correlated, corrective dynamics at faster time scales because participants were displayed their performance with regard to the benchmark 1 s time. They appeared to use that information to correct performance on a trial-by trial-basis. In the no-feedback condition, this information was not readily available, which led to essentially random performance at the fast time scales.

## GENERAL DISCUSSION

We applied AFA to known fractal signals and to real-world data from an experiment in human cognitive psychology that involved the repeated reproduction of a time interval. AFA recovered the *H* values of the known mathematical signals with high accuracy. This was generally true for both $M = 1$ and $M = 2$. The choice of polynomial order did not have a very large effect, although $M = 2$ yielded slightly better results for the white and pink noise signals but slightly worse results for the brown noise signal. Linear scaling was well defined over a single region for these signals.

Application of AFA to the experimental data revealed some of the complexities in applying fractal analyses to real data, particularly the issue of identification of linear scaling regions. We determined the scaling regions visually and then fit lines to them to obtain estimates of *H*. Often this is sufficient, but it is not an objective process and it could be subject to bias in an experiment that involves testing a particular hypothesis or an initial effort to classify a previously unanalyzed type of signal. If visual selection of the scaling region is used, it should be done by multiple observers (so that inter-rater reliability can be computed) who are blind to the experimental conditions and study hypotheses (to avoid bias). In Kuznetsov et al. (2012) we present an objective, quantitative technique based on model-selection

methods that could be used to identify scaling regions, but more work remains to be done on this issue.

For the experimental time series we analyzed two linear scaling regions were apparent rather than one. Consistent with previous results using other analysis methods including spectral analysis (Lemoine et al., 2006; Delignieìres et al., 2008), these regions showed distinct slopes. The faster time scale yielded lower $H_{fGn}$ and were basically random white noise processes (especially for the no-feedback condition) with a slight tendency toward exhibiting anti-correlated fluctuations. The longer time scale yielded higher $H_{fGn}$ values consistent with a correlated process that was close to idealized pink-noise. The presence of feedback had some influence on the structure of the fluctuations of the repeated temporal estimates, as did the practice afforded by performance on consecutive experimental sessions. One of these effects was that linear scaling for the slower time scale broke down at larger $w$ for the first session in the no-feedback condition, but spanned the entire upper range of $w$ for the last session. These results show that AFA may be sensitive to experimental manipulations that affect the temporal structure of data series both with regard to the estimated $H$ values and the range of $w$ over which fractal scaling occurs.

Besides the issue of identifying linear scaling region, AFA requires several other choices such as the step size for the window size $w$. Typically 0.5 or 1 $\log_2 w$ are used, with smaller values providing greater resolution in the AFA plot. In principle this choice should have little impact on $H$ estimates, and would not seriously impact computation time except perhaps for extremely long time series. It could, however, have a strong impact on the ability to identify linear scaling regions, especially with regard to resolving the existence of linear scaling regions at faster time scales. The choice of polynomial order $M$ for the local fits is also important, especially for signals that may have oscillatory or non-linear trends as higher-order polynomials may be more effective at extracting those trends. Typical choices of 1 or 2 seemed to provide about the same accuracy in estimates of $H$ for the known signals we analyzed.

Other factors that impact the ability to identify linear scaling include the sampling rate and the trial length, which, respectively, will affect the ability to resolve faster and slower time scales. These are important choices. A very high sampling rate might indicate the appearance of scaling at very fast time scales, but if those time scales are not physically realistic, one should be cautious about interpreting them. Increasing trial length may help reveal or

resolve scaling over very long time scales, which may be very important when dealing with apparently non-stationary time series.

Ideally, AFA should be used in conjunction with other methods, and converging results should be sought. But because AFA but has several advantages over similar methods such as DFA (Gao et al., 2011) the results may not always agree, so care should be taken in interpreting the results. Like all fractal analysis methods, AFA requires careful consideration of signal properties, parameter settings, and interpretation of results, and should not be applied blindly to unfamiliar signals. It is particularly important to plot and carefully inspect the time series and the AFA plots to ensure that the apparent signal properties match with the obtained results. In addition, as we noted previously the appearance of linear scaling regions in an AFA plot is not a definitive test for fractal scaling. When used carefully AFA may provide another useful tool for analyzing signals that may exhibit fractal dynamics.

## ACKNOWLEDGMENTS

Supported by NSF grants CMMI 1031958 (JianboGao) and BCS 0926662 (Michael A. Riley).

### Footnotes

[1]Following suggestions by Cannon et al. (1997) and Eke et al. (2000), we performed spectral analyses on the data to provide a more objective classification of our time series as fGn or fBm. The spectral exponents ranged from 0.48 to 0.75, indicating the signals were consistent with fGn.

## REFERENCES


1. Beran J. (1994). Statistics for Long-Memory Processes. Boca Raton, FL: CRC Press
2. Brainard D. H. (1997). The psychophysics toolbox. Spat. Vis. 10, 433–436 10.1163/156856897X00357
3. Cannon M. J., Percival D. B., Caccia D. C., Raymond G. M., Bassingthwaighte J. B. (1997). Evaluating scaled windowed variance methods for estimating the Hurst coefficient of time series. Physica A 241, 606–626
4. Chen Y., Repp B., Patel A. (2002). Spectral decomposition of variability in synchronization and continuation tapping: comparisons between auditory and visual pacing and feedback coditions. Hum. Mov. Sci. 21, 515–532 10.1016/S0167-9457(02)00138-0
5. Delignieìres D., Deschamps T., Legros A, Caillou N. (2003). A methodological note on non-linear time series analysis: is Collins and De Luca (1993)'s open- and closed-loop model a statistical artifact? J. Mot. Behav. 35, 86–96 10.1080/00222890309602124
6. Delignières D., Torre K. (2011): Event-based and emergent timing: dichotomy or continuum? A reply to Repp and Steinman (2010). J. Mot. Behav. 43, 311–318 10.1080/00222895.2011.588274
7. Delignieìres D., Torre K., Lemoine L. (2005). Methodological issues in the application of monofractal analyses in psychological and behavioral research. Nonlinear Dynamics Psychol. Life Sci. 9, 451–477
8. Delignieìres D., Torre K., Lemoine L. (2008). Fractal models for event-based and dynamical timer. Acta Psychol. 127, 382–397
9. Di Matteo T., Aste T., Dacorogna M. M. (2003). Scaling behaviors in differently developed markets. Physica A 324, 183–188
10. Eke H. A., Bassingthwaighte P. J., Raymond G., Percival D., Cannon M., Balla I., Ikrényi C. (2000). Physiological time series: distinguishing fractal noises from motions. Pflügers Arch. 439, 403–415 10.1007/s004240050957
11. Farrell S., Wagenmakers E.-J., Ratcliff R. (2006). 1/*f* noise in human cognition: is it ubiquitous, and what does it mean? Psychon. Bull. Rev. 13, 737–741
12. Gao J. B., Cao Y. H., Tung W. W., Hu J. (2007). Multiscale Analysis of Complex Time Series: Integration of Chaos and Random Fractal Theory, and Beyond. Hoboken, NJ: Wiley Interscience

13. Gao J. B., Hu J., Mao X., Perc M. (2012). Culturomics meets random fractal theory: insights into long-range correlations of social and natural phenomena over the past two centuries. J. R. Soc. Interface 9, 1956–1964
14. Gao J. B., Hu J., Tung W. W. (2011). Facilitating joint chaos and fractal analysis of biosignals through nonlinear adaptive filtering. PLoS ONE 6:e24331 10.1371/journal.pone.0024331
15. Gao J. B., Hu J., Tung W. W., Cao Y. H., Sarshar N., Roychowdhury V. P. (2006). Assessment of long range correlation in time series: how to avoid pitfalls. Phys. Rev. E 73, 016117 10.1103/PhysRevE.73.016117
16. Gao J. B., Sultan H., Hu J., Tung W. W. (2010). Denoising nonlinear time series by adaptive filtering and wavelet shrinkage: a comparison. IEEE Signal Process. Lett. 17, 237–240
17. Gilden D. L., Thornton T., Mallon M. (1995). 1/f noise in human cognition. Science 267, 1837–1839 10.1126/science.7892611
18. Hu J., Gao J. B., Wang X. S. (2009). Multifractal analysis of sunspot time series: the effects of the 11-year cycle and Fourier truncation. J. Stat. Mech. P02066.
19. Kuznetsov N., Bonnette S., Gao J., Riley M. A. (2012). Adaptive fractal analysis reveals limits to fractal scaling in center of pressure trajectories. Ann. Biomed. Eng. [Epub ahead of print]. 10.1007/s10439-012-0646-9
20. Lebovitch L. S., Shehadeh L. A. (2005). Introduction to fractals, in Tutorials in contemporary nonlinear methods for the behavioral sciences, eds Riley M. A., Van Orden G. C. 178–266 Retrieved June 28 2012, from http://www.nsf.gov/sbe/bcs/pac/nmbs/nmbs.jsp
21. Lemoine L., Torre K., Delignières D. (2006). Testing for the presence of 1/f noise in continuation tapping data. Can. J. Exp. Psychol. 60, 247–257
22. Lennon J. L. (2000). Red-shifts and red herrings in geographical ecology. Ecography 23, 101–113
23. Mandelbrot B. B. (1997). Fractals and Scaling in Finance. New York, NY: Springer-Verlag
24. Mandelbrot B. B., van Ness J. W. (1968). Fractional Brownian motions, fractional noises and applications. SIAM Rev. 10, 422–437
25. Peng C. K., Buldyrev S. V., Havlin S., Simons S. M., Stanley H. E., Goldberger A. L. (1994). Mosaic organization of DNA

nucleotides. Phys. Rev. E 49, 1685–1689 10.1103/PhysRevE.49.1685

26. Torre K., Balasubramaniam R., Rheaume N., Lemoine L., Zelaznik H. (2011). Long-range correlation properties in motor timing are individual and task specific. Psychon. Bull. Rev. 18, 339–346 10.3758/s13423-011-0049-1
27. Torre K., Delignières D. (2008). Unraveling the finding of 1/f noise in self-paced and synchronized tapping: a unifying mechanistic model. Biol. Cybern. 99, 159–170 10.1007/s00422-008-0247-8
28. Torre K., Delignières D., Lemoine L. (2007). $1/f^{\beta}$ fluctuations in bimanual coordination: an additional challenge for modeling. Exp. Brain Res. 183, 225–234 10.1007/s00221-007-1035-8
29. Tung W. W., Gao J. B., Hu J., Yang L. (2011). Recovering chaotic signals in heavy noise environments. Phys. Rev. E 83, 046210 10.1103/PhysRevE.83.046210
30. Wagenmakers E. J., Farrel S., Ratcliff R. (2004). Estimation and interpretation of 1/f-noise in human cognition. Psychon. Bull. Rev. 11, 579–615

# 10

# *Pitfalls in Fractal Time Series Analysis: fMRI BOLD as an Exemplary Case*

**Andras Eke[1,2], Peter Herman[2] , Basavaraju G. Sanganahalli [2] , Fahmeed Hyder [2,3], Peter Mukli [1] and Zoltan Nagy [1]**

[1] Institute of Human Physiology and Clinical Experimental Research, Semmelweis University, Budapest, Hungary
[2] Diagnostic Radiology, Yale University, New Haven, CT, USA
[3]Biomedical Engineering, Yale University, New Haven, CT, USA

## ABSTRACT

This article will be positioned on our previous work demonstrating the importance of adhering to a carefully selected set of criteria when choosing the suitable method from those available ensuring its adequate performance when applied to real temporal signals, such as fMRI BOLD, to evaluate one important facet of their behavior, fractality. Earlier, we have reviewed on a range of monofractal tools and evaluated their performance. Given the advance in the fractal field, in this article we will discuss the most widely used implementations of multifractal analyses, too. Our recommended flowchart for the fractal characterization of spontaneous, low frequency fluctuations in fMRI BOLD will be used as the framework for this article

**Citation:** Eke, A., Herman, P., Sanganahalli, B. G., Hyder, F., Mukli, P., & Nagy, Z. (2012). Pitfalls in fractal time series analysis: fMRI BOLD as an exemplary case. Frontiers in physiology, 3, 417. DOI: 10.3389/fphys.2012.00417.

to make certain that it will provide a hands-on experience for the reader in handling the perplexed issues of fractal analysis. The reason why this particular signal modality and its fractal analysis has been chosen was due to its high impact on today's neuroscience given it had powerfully emerged as a new way of interpreting the complex functioning of the brain (see "intrinsic activity"). The reader will first be presented with the basic concepts of mono and multifractal time series analyses, followed by some of the most relevant implementations, characterization by numerical approaches. The notion of the dichotomy of fractional Gaussian noise and fractional Brownian motion signal classes and their impact on fractal time series analyses will be thoroughly discussed as the central theme of our application strategy. Sources of pitfalls and way how to avoid them will be identified followed by a demonstration on fractal studies of fMRI BOLD taken from the literature and that of our own in an attempt to consolidate the best practice in fractal analysis of empirical fMRI BOLD signals mapped throughout the brain as an exemplary case of potentially wide interest.

**Keywords:** fractals, monofractals, multifractals, time series analysis, numerical testing, fMRI BOLD, brain

## INTRODUCTION

Fractality (Mandelbrot, 1967, 1980, 1985; Bassingthwaighte et al., 1994; Gouyet, 1996; Eke et al., 2002), – in addition to deterministic chaos, modularity, self-organized criticality, "small word" network-connectivity – by now has established itself as one of the fundaments of complexity science (Phelan, 2001) impacting many areas including the analysis of brain imaging data such as fMRI BOLD (Zarahn et al., 1997; Thurner et al., 2003; Maxim et al., 2005; Raichle and Mintun, 2006; Fox et al., 2007; Razavi et al., 2008; Wink et al., 2008; Bullmore et al., 2009; Herman et al., 2009, 2011; Ciuciu et al., 2012).

The interest in fractal analysis accelerated the development of the new paradigm beyond a rate when the new – essentially mathematical or physical (i.e., statistical mechanics) – knowledge could be consolidated, their tools thoroughly evaluated and tested before being put to wide-spread use in various fields of science; typically beyond the frontiers of mathematics. The lack of an in-depth understanding of the implications of the methods when applied to empirical data, often generated conflicting results, but also prompted efforts at making up for this deficiency. Early, with the migration

of the fractal concept from mathematics to various fields of science like physiology, the groups of Bassingthwaighte (Bassingthwaighte, 1988; Bassingthwaighte et al., 1994) and Eke et al. (1997) realized the need to adopt a systematic approach in developing needed analytical and testing frameworks to characterize and evaluate various monofractal time series methods (Bassingthwaighte and Raymond, 1994, 1995; Caccia et al., 1997; Eke et al., 2000, 2002). Eke and coworkers demonstrated that conscious and precise monofractal time series analysis could only be done when one has an a priori concept of the nature of the observed signals. They introduced the dichotomous fractional Gaussian noise (fGn) /fractional Brownian motion (fBm) model of Mandelbrot and Ness (1968) as the basis of monofractal time series analysis (Eke et al., 2000, 2002) and offered a strategy for choosing tools according to a proven selection criteria (Eke et al., 2000). Given the continuing advance in the fractal field and in sync with the increasing awareness to avoid potential pitfalls and misinterpretation of results in various forms of fractal analyses (Delignieres et al., 2005; Gao et al., 2007; Delignieres and Torre, 2009; Marmelat and Delignieres, 2011; Ciuciu et al., 2012), in this article we apply our evaluation strategy to multifractal tools, and characterize their most widely used implementations. Our motivation in doing so stems from the potentials of fMRI BOLD multifractal analysis in revealing the physiological underpinnings of activation-related change in scaling properties in the brain (Shimizu et al., 2004).

fMRI BOLD (Ogawa et al., 1990, 1993b; Kwong et al., 1992; Bandettini, 1993) has been selected as an exemplary empirical signal in our demonstrations, because its impact on contemporary neuroscience (Fox and Raichle, 2007). The human brain represents the most complex form of the matter (Cramer, 1993) whose inner workings can only be revealed if signals reflecting on neuronal activities are recorded at high spatio-temporal resolution. One of the most powerful methods, which can record spatially registered temporal signals from the brain, is magnetic resonance imaging (MRI; Lauterbur, 1973). The MRI scanner can non-invasively record a paramagnetic signal (referred to as blood oxygen level dependent, BOLD; Ogawa et al., 1990, 1993a) that can be interpreted as the signature of the functioning brain via its metabolic activity continuously modulating the blood content, blood flow, and oxygen level of the blood within the scanned tissue elements (voxels). Recently, a rapidly increasing volume of experimental data has demonstrated that BOLD is a complex signal, whose fractality – if properly evaluated – can reveal fundamental properties of the

brain among them the so called “intrinsic or default mode” of operation that appears complementing the stimulus-response paradigm in the understanding the brain in a powerful way (Raichle et al., 2001). We hope, our paper could contribute to this major effort from the angle of consolidating some relevant issues concerning fractal analysis of fMRI BOLD.

## CONCEPT OF FRACTAL TIME SERIES ANALYSES

### Monofractals

All fractals are self-similar structures (mathematical fractals in an exact, natural fractals in a statistical sense), with their fractal dimension falling between the Euclidian and topologic dimensions (Mandelbrot, 1983; Eke et al., 2002). When self-similarity is anisotropic, the structure is referred to as self-affine; a feature, which applies to fractal time series (Mandelbrot, 1985; Barabási and Vicsek, 1991; Eke et al., 2002), too. Statistical fractals cannot be described comprehensively by descriptive statistical measures, as mean and variance, because these do depend on the scale of observation in a power law fashion:

$$\frac{\mu_2}{\mu_1} = \left(\frac{s_2}{s_1}\right)^{\varepsilon}, \tag{1}$$

where $\mu_1$, $\mu_2$ are descriptive statistical measures, and $s_1$, $s_2$ are scales within the scaling range where self-affinity is present, and $\varepsilon$ is the power law scaling exponent. From this definition a universal scale-free measure of fractals can be derived:

$$D = -\lim_{s \to 0} \left( \inf \frac{\log (N(s))}{\log (s)} \right). \tag{2}$$

D is called capacity dimension (Barnsley, 1988; Liebovitch and Tóth, 1989; Bassingthwaighte et al., 1994), which is related but not identical to the Hausdorff dimension (Hausdorff, 1918; Mandelbrot, 1967), s is scale and N(s) is the minimum number of circles with size s needed to cover the fractal object to quantify its capacity on the embedding dimensional space (it corresponds to $\mu$ in Eq. 1). For fractal time series, the power law scaling exponent $\varepsilon$ is typically calculated in the time domain as the Hurst exponent (H), or in the frequency domain as the spectral index ($\beta$). H and D relate (Bassingthwaighte et al., 1994) as:

$$H = 2 - D. \quad (3)$$

Further, β can also be obtained from H as (H − 1)/2 for fGn and (H + 1)/2 for fBm processes (Eke et al., 2000).

## Multifractals

While D does not vary along a monofractal time series, it is heterogeneously distributed along the length of a multifractal signal.

This phenomenon gave rise to the term "singular behavior," as self-affinity can be expressed by differing power law scaling along a multifractal time series, $X_i$ as:

$$X_{i+\Delta i} - X_i \propto |\Delta i|^{h(i)}, \quad (4)$$

where h is the Hölder exponent defining the degree of singularity at time point, i. Calculating the fractal dimension for each subsets of $X_i$ of the same h, one obtains the singularity spectrum, D(h) (Mandelbrot spectrum), which describes the distribution of singularities (Frisch and Parisi, 1985; Falconer, 1990; Turiel et al., 2006).

$$D(h) = \frac{\log(\rho(h)/\rho(h_{\max}))}{\log s_{\min}}, \quad (5)$$

where $h_{max}$ is the Hölder exponent corresponding to maximal fractal dimension, $s_{min}$ is the finest scale corresponding to Hölder trajectory, and ρ(h) is the distribution of singularities.

The singular behavior of a multifractal is a local property. Separation of the singularities can be difficult, given the finite sampling frequency of the signal of interest (Mallat, 1999). Thus, in contrast with monofractality, a direct evaluation of multifractality is a demanding task in terms of the amount of data and the computational efforts needed, which can still not guarantee precise results under all circumstance.

With the aid of different moments of appropriate measure, μ, a set of equations can be established to obtain the singularity spectrum, which is a common framework exploited by multifractal analysis methods referred to as multifractal formalism (Frisch and Parisi, 1985; Mandelbrot, 1986; Barabási and Vicsek, 1991; Muzy et al., 1993). Using a set of different moment orders, one can determine the scaling behavior of $\mu^q$, yielding the generalized Hurst exponent, H(q) (Barunik and Kristoufek, 2010; See Figure 1):

$$\langle \mu^q(s) \rangle \propto s^{q \cdot H(q)}. \qquad (6)$$

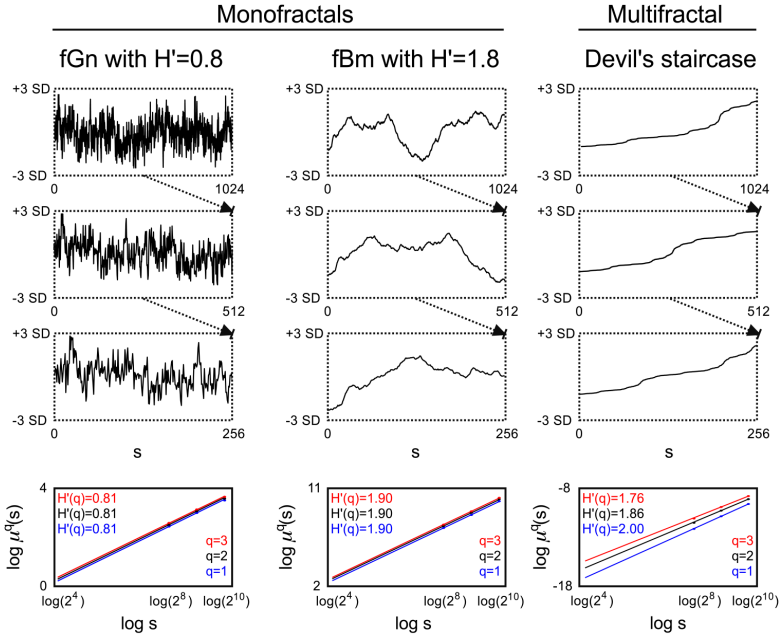


**Figure 1:** Monofractal and multifractal temporal scaling. Three kinds of fractals are shown to demonstrate scale-free property of these structures: a stationary monofractal (fractional Gaussian noise), a non-stationary monofractal (fractional Brownian motion), and a multifractal (Devil's staircase with weight factors $p_1 = p_3 = 0.2$, $p_2 = 0.6$). Every fractal is self-similar: fGn and fBm in a statistical sense (as in empirical structures and processes where fractality is manifested in equal distributions, only) and Devil's staircase in an exact manner (as self-similar structuring in mathematical, i.e., ideal fractals is exact). For fractals, descriptive statistical measures [for example mean, variance, fluctuation ($F_q$) etc.] depend on the corresponding scale in a power law fashion. Thus as a scale-free descriptor, the extended Hurst exponent (H′) is calculated as a slope of regression line between the logarithms of the scale (s) and $F_q$ (For an explanation of H′, see main text). The obtained slopes for different magnifications of the time series [here with the order of q = (1, 2, 3), which is the order of moment of the used measure] are the same for monofractals and different for multifractals, demonstrating that power law scaling behavior is a global property of monofractals, while it is a local property of multifractals. Accordingly, note that slopes in the bottom left and middle panel are the same, while in the right panel they indeed differ. For further details, see main text.

On the right side of Eq. 4 Δi corresponds to scale, s, on the right side of Eq. 6. Using the partition function – introduced in context of Wavelet Transform Modulus Maxima (WTMM) method – singularities are analyzed globally for estimating the (multi)scaling exponent (Mallat, 1999):

$$Z(s,q) = \sum_{k=1}^{N(s)} \mu_i^q(s) \tag{7}$$

$$\tau(q) = \lim_{s\to 0} \inf \frac{\log Z(s,q)}{\log s}, \tag{8}$$

where τ(q) can be also expressed from H(q) (Kantelhardt et al., 2002) as:

$$\tau(q) = q \cdot H(q) - D_T, \tag{9}$$

where $D_T$ is the topological dimension, which equals 1 for time series.

The generalized fractal dimension can also describe the scale-free features of a multifractal time series:

$$D(q) = \frac{\tau(q)}{q-1} = \frac{q \cdot h(q) - 1}{q-1}. \tag{10}$$

The singularity spectrum, D(h), can be derived from τ(q) with Legendre transform (Figure (Figure2),2), via taking

$$h = \tau'(q), \tag{11}$$

the slope of the tangent line taken at q for τ(q), and yielding

$$D(h) = \inf_q (qh - \tau(q)), \tag{12}$$

that when evaluated gives the negative of the intercept at q=0 for the tangent line (See Figure 2).

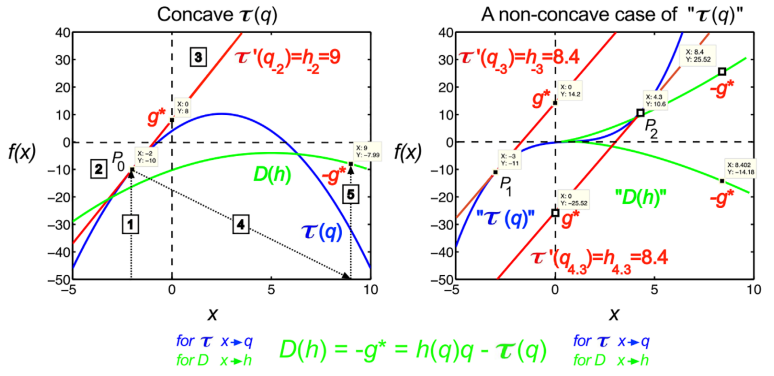


**Figure 2:** Legendre transform. It is known that singularity spectrum, D(h), has a concave shape, and provided that τ(q) is also a concave function, they can be explicitly transformed into each other via the Legendre transform (Bacry et al., 1993). Legendre transform takes a function, in our case τ(q) and produces a function of a different variable, D(h). The Legendre transform is its own inverse and uses minimization as the basis of the transformation process according to Eq. 12. If minimization cannot be achieved, the transformation would fail. On the left a real (concave), on the right a non-concave case for τ(q) is shown. A simple concave function, $f(x)=-x^2+5x+4$ (shown in blue) is used for modeling τ(q). If f(x) is differentiable, hence a tangent line (shown in red) can be taken at point of $P_0$ $(q_0, \tau_0)$ with a slope $\tau'(q)$, then $g^*(q_0)$ is the y-intercept, $(0, g^*)$, and $-g^*$ is the value of the Legendre transform (See Eq. 11). Maximization at $(q_0, \tau_0)$ is valid since for any other point on the blue curve, a line drawn through that point with the same slope as the red line will yield a $\tau_0$-intercept below the point $(0, g^*)$, showing that $g^*$ is indeed obtained as a boundary value (maximum), thus the transformation for D(h) would also yield a single boundary value (minimum) on the green curve as $D(h)=-g^*=\tau'(q)q-\tau(q)$. Steps of the transformation process are shown (1) select q, (2) read τ(q), (3) take a tangent line at (q, τ) and determine its slope, $h=\tau'(q)$, (4) select h, (5) determine D(h) using the above equation; repeat for the set. On the right side, a non-concave function is shown (blue) for demonstrating a case, when due to the non-concave shape of τ(q) the shape of the transformed function, D(h), does not yield a realistic singularity spectrum given that in this case the transform by failing on minimization is poorly behaved yielding ambiguous values.

Natural signals have a singularity spectrum over a bounded set of Hölder exponents, whose width is defined by $[h_{-\infty}, h_{+\infty}]$ (Figure 3).

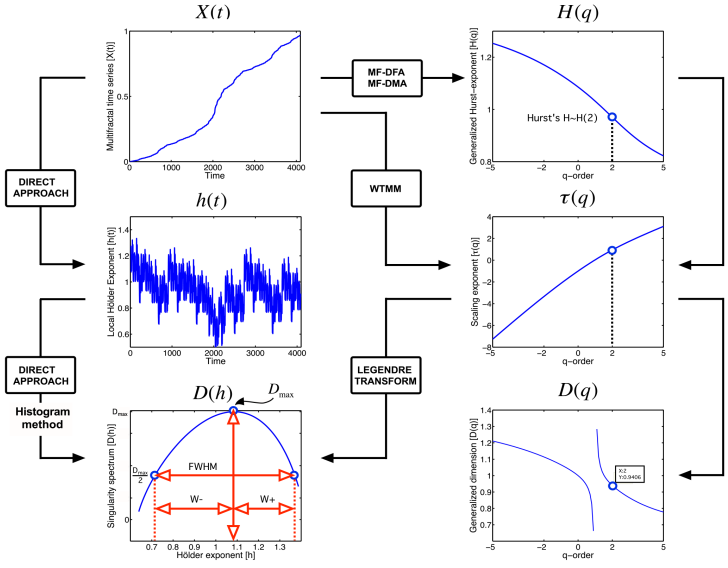


**Figure 3:** Approaches to multifractal analyses. Direct approach of multifractal analysis means exploiting the local power law scaling behavior to obtain local Hölder exponents (Eq. 4), from which the Mandelbrot spectrum is calculated with histogram method (Falconer, 1990; Eq. 5). Indirect approaches shown here (MF-DFA, multifractal detrended fluctuation analysis; MF-DMA, multifractal detrended moving average; WTMM, Wavelet Transform Modulus Maxima) estimates the scaling exponent, τ as a function of q. It is worth to note, that this is carried out differently for MF-DFA, MF-DMA (Eq. 9), and for WTMM (Eq. 8). From τ(q), the Mandelbrot spectrum can be obtained with the application of the Legendre transform, while its relation to generalized fractal dimension D(q) is given by Eq. 10. Singularity spectrum, D(h), is an important endpoint of the analysis. The spectrum is concave and has a nearly parabolic shape with a maximum identified by the capacity dimension at q=0 (Mallat, 1999; Shimizu et al., 2004; Ihlen, 2012). Please note that some of its measures (FWHM, $D_{max}$, W+, W−) can be used to calculate meaningful combined parameters (such as Pc, and W in Eqs 13 and 14, respectively) with potential in correlating with key features of fMRI BOLD time series.

A combination parameter, $P_c$, can be calculated (definitions on Figure 3) to facilitate the separation of time series characteristics (Shimizu et al., 2004), which can aid the exploration of the physiological underpinnings, too.

$$P_c = \frac{h_{\max}}{D_{\max}} \cdot FWHM. \qquad (13)$$

A similar parameter is W (Wink et al., 2008) calculated as

$$W = \frac{W+}{W-}. \tag{14}$$

## IMPLEMENTATION OF FRACTAL TIME SERIES ANALYSES

Implementation of concepts in reliable algorithms is a critical task, as stationary and non-stationary signals require different methods when analyzed for their fractality. For a stationary signal the probability distribution of signal segments is independent of the (temporal) position of the segment and segment length, which translates into constant descriptive statistical measures such as mean, variance, correlation structure etc. over time (Eke et al., 2000, 2002).

Accordingly, signals can be seen as realizations of one of two temporal processes: fBm, and fGn (Eke et al., 2000). The fBm signal is non-stationary with stationary increments. An fBm signal, $X_i$, is self-similar in that its sampled segment $X_{i,n}$ of length n is equal in distribution with a longer segment $X_{i,sn}$ of length sn when the latter is rescaled (multiplied) by $s^{-H}$. This means that every statistical measure, $m_n$, of an fBm time series of length n is proportional to $n^H$

$$X_{i,n} \propto s^{-H} X_{i,sn}, \tag{15}$$

$$m_n \propto pn^H, \ \textit{which yields} \ \log \ m_n \propto \log p + H \log n, \tag{16}$$

where H is the Hurst exponent. H ranges between 0 and 1. Increments $Y_i = X_i - X_{i-1}$ of a non-stationary fBm signal yield a stationary fGn signal and vice versa, cumulative summation of an fGn signal results in an fBm signal. Note that most methods listed below that have been developed to analyze statistical fractal processes share the philosophy of Eq. 15 in that in their own ways all attempt to capture the power law scaling in the various statistical measures of the evaluated time series (Eke et al., 2002).

### Monofractal Methods

Here we focus on widely used monofractal methods selected from those in the literature.

## Time Domain Methods

### *Detrended fluctuation analysis*

The method of Peng et al. (1994) begins with the signal summed and the mean subtracted

$$Y_j = \sum_{i=1}^{j} X_i - \langle X \rangle \,. \tag{17}$$

Then the local trend $Y_{j,n}$ is estimated in non-overlapping windows of equal length n, using least-square fit on the data. For a given window size n the fluctuation is determined as the variance upon the local trend:

$$F_n = \sqrt{\frac{1}{N}\sum_{j=1}^{N}(Y_j - Y_{j,n})^2}, \tag{18}$$

For fBm processes of length N with non-overlapping windows of size n the fluctuation depends on the window size n in a power law fashion:

$$F_n \propto pn^{\alpha}, \text{ and} \tag{19}$$

$$\alpha = \lim_{n \to 0} \frac{\log F_n}{\log n}. \tag{20}$$

If $X_i$ is an fGn signal then $Y_j$ will be an fBm signal. $F_n$ then is equivalent to $m_n$ of Eq. 16 yielding $F_n \propto pn^H$ therefore in this case $\alpha = H$. If $X_i$ is an fBm signal then $Y_j$ will be a summed fBm signal. Then $F_n \propto pn^{H+1}$, where $\alpha = H + 1$ (Peng et al., 1994).

### *Signal summation conversion method*

This method was first introduced by Eke et al. (2000) for enhancing signal classification as a variant of the scaled windowed variance (SWV) analysis of Mandelbrot (1985) as further developed by Peng et al. (1994).

Fluctuations of a parameter over time can be characterized by calculating the standard deviation

$$SD_n = \sqrt{\frac{1}{N-1}\sum_{i=1}^{N}(X_i - \langle X \rangle)^2}. \quad (21)$$

For fBm processes of length N when divided into non-overlapping windows of size n as Eq. 21 predicts the standard deviation within the window, $s_n$, depends on the window size n in a power law fashion:

$$SD_n \propto pn^H, \quad (22)$$

and

$$H = \lim_{n \to 0} \frac{\log SD_n}{\log n}. \quad (23)$$

In practice $SD_n$'s calculated for each segment of length n of the time series are averaged for the signal at each window size. The standard method applies no trend correction. Trend in the signal seen within a given window can be corrected either by subtracting a linearly estimated trend (line detrended version) or the values of a line bridging the first and last values of the signal (bridge detrended version; Cannon et al., 1997). This method can only be applied to fBm signals or cumulatively summed fGn signals.

The signal summation conversion (SSC) method was first used for enhanced signal classification according to the dichotomous fGn/fBm model (Eke et al., 2000). There are two steps: (1) calculate from $X_i$ its cumulative sum (this converts an fGn to an fBm or converts an fBm to its cumulant), and (2) use the bdSWV method to calculate from the cumulant series $\hat{H}'$. The interpretation of $\hat{H}'$ is that when $0 < \hat{H}' \leq 1$, then $X_i$ is an fGn with $\hat{H}'$. Alternatively, when $\hat{H}' > 1$, then the cumulant series is identified as an fBm signal of $\hat{H} = \hat{H}' - 1$. As seen, in order to keep $\hat{H}'$ scaled within the [0,1] range, in the original version of the method in the fBm case 1 was subtracted from the estimate of H. Given that the SSC method handles fGn and fBm signals alike, we eliminate this step and report values as $0 < \hat{H}' < 1$ for fGn and $1 < \hat{H}' < 2$ for fBm signals referring $\hat{H}'$ as the "extended" Hurst exponent. This way, the mere value of the Hurst exponent would reflect on signal class, the focus of fractal time series analysis strategy. Also the use of $\hat{H}'$ would greatly facilitate reviewing the results of numerical performance analyses.

Real-time implementations of SSC and Detrended Fluctuation Analysis (DFA) methods have been recently reported (Hartmann et al., 2012).

## Frequency Domain Method

Fractal analysis can also be done in the frequency domain using methods such as the power spectral density (PSD) analysis (Fougere, 1985; Weitkunat, 1991; Eke et al., 2000).

### *Power Spectral Density Analysis ($^{low}PSD_{w,e}$)*

A time series can be represented as a sum of cosine wave components of different frequencies:

$$X_i = \sum_{n=0}^{N/2} A_n \cos\left[\omega_n t_i + \varphi_n\right] = \sum_{n=0}^{N/2} A_n \cos\left[\frac{2\pi n}{N} i + \varphi_n\right], \tag{24}$$

where $A_n$ is the amplitude and $\Phi_n$ is the phase of the cosine-component with $\omega_n$ angular frequency. The commonly used sample frequency is $f_n = \omega_n/2\pi$. The $A_n(f_n)$, $\Phi_n(f_n)$, and A2n(fn) functions are termed amplitude, phase, and power spectrum of the signal, respectively. These spectra can be determined by an effective computational technique, the fast Fourier transform (FFT). The power spectrum (periodogram, PSD) of a fractal process is a power law relationship

$$A_n^2 \propto p\omega_n^{-\beta}, \text{ or} \left|A(f)\right|^2 \propto 1/f^{\beta} \text{ which yields } \beta = \lim_{n\to 0} \frac{\log A_n^2}{\log f_n}, \tag{25}$$

where β is termed spectral index. The power law relationship expresses the idea that as one doubles the frequency the power changes by the same fraction ($2^{-\beta}$) regardless of the chosen frequency, i.e., the ratio is independent of where one is on the frequency scale.

The signal has to be preprocessed before applying the FFT (subtraction of mean, windowing, and endmatching, i.e., bridge detrending). Discarding the high power frequency estimates improves the precision of the estimates of β (Fougere, 1985; Eke et al., 2000). Eke et al. (2000) introduced this version denoted as $^{low}PSD_{w,e}$ as a fractal analytical tool.

## Time-Frequency Domain Method

Fractal wavelet analysis uses a waveform of limited duration with an average value of zero for variable-sized windowing allowing an equally precise characterization of low and high frequency dynamics in the signal. The

wavelet analysis breaks up a signal into shifted and stretched versions of the original wavelet. In other words, instead of a time-frequency domain it rather uses a time-scale domain, which is extremely useful not only in monofractal but multifractal analysis, too. One such way to estimate H is by the averaged wavelet coefficient (AWC) method (Simonsen and Hansen, 1998). The most commonly used analyzing wavelet is the second derivative of a standard normalized Gaussian function, which is:

$$\psi(t) = \frac{d^2}{dt^2} e^{-\frac{t^2}{2}}. \tag{26}$$

The scaled and translated version of the analyzing wavelet is given by

$$\psi_{a;b}(t) = \psi\left(\frac{t-b}{a}\right), \tag{27}$$

where the scale parameter is a, and the translation parameter b.

The wavelet transformation is essentially a convolution operation in the time domain:

$$W_\psi[X](a,b) = \frac{1}{a}\int_{-\infty}^{+\infty} X(t)\cdot\psi_{a;b}dt. \tag{28}$$

From Eq. 16, one can easily derive how the self-affinity of an fBm signal X(t) determines its continuous wavelet transform (CWT) coefficients:

$$W[X](sa,sb) = {}_d s^{\frac{1}{2}+H} W[X](a,b). \tag{29}$$

The AWC method is based on Eq. 29 (Simonsen and Hansen, 1998) and can be applied to fBm signals or to cumulatively summed fGn signals.

## Multifractal Methods

Three analysis methods are described here; all use different statistical moments (termed q-th order) of the selected measure to evaluate the signal's multifractality. Despite of certain inherent drawbacks, these methods are widely used in the literature, and can obtain reliable results if their use is proper with limitations considered.

## Time Domain Methods

Below, the Multifractal DFA (MF-DFA; Kantelhardt et al., 2002) and the recently published Multifractal Detrended Moving **A**verage (MF-DMA; Gu and Zhou, 2010) will be reviewed. We will focus on MF-DMA, but since it is similar to MF-DFA, their differences will be pointed out, too. They rely on a measure of fluctuation, F, as in their monofractal variant (Peng et al., 1994), and differ in calculating the q-th order moments of the fluctuation function.

- Step 1 – calculating signal profile, $Y_j$, by cumulative summation. It is essentially the same as in Eq. 17, however note that in DFA methods, the mean of the whole signal is subtracted before summation, while in DMA methods this is carried out locally in step 3.
- Step 2 – calculating the moving average function, $\tilde{Y}_j$.

$$\tilde{Y}_j = \frac{1}{n} \cdot \sum_{k=-[(n-1)\theta]}^{[(n-1)(1-\theta)]} y_{t-k} \tag{30}$$

For further details, see Figure 4.

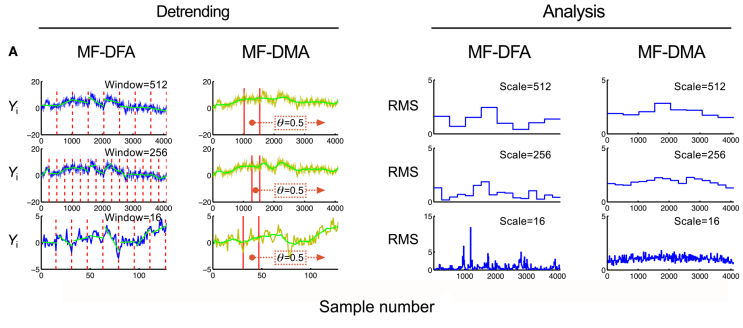


**Figure 4:** Detrending scheme and fluctuation analysis for MF-DFA and MF-DMA methods. The detrending strategy for MF-DFA (A) is that the signal is divided into a set of non-overlapping windows of different sizes, and a local low-order polynomial (typically linear) fit (shown in green) is removed from each window's data. In contrast, MF-DMA (B) removes the moving average point-by-point calculated in different window sizes around the processed point with a position given by θ. This parameter describes the delay between the moving average function and the original signal. Its value is taken from [0, 1] interval, 0 meaning only from signal values on the left ("backward," past),

in contrast with 1 meaning that only signal values to the right ("forward," future) are used for calculating $\tilde{Y}_j$. The centrally positioned sliding window corresponds to the case of $\theta=0.5$ balancing contributions from the past and the future to the reference point. The approaches of MF-DFA and MF-DMA thus ought to yield different detrended signals, whose calculated moments (C,D) and Eqs 33 and 34 obtained by the analysis should also be somewhat different.

- Step 3 – detrending by moving average: By subtracting $\tilde{Y}_t$ a residual signal, $\varepsilon_t$, is obtained:

$$\varepsilon_t = Y_t - \tilde{Y}_t, \tag{31}$$

where $n-[(n-1)\cdot\theta]\leq t\leq N-[(n-1)\cdot\theta]$.

This fundamental step of the DMA methods is essentially different from the detrending step of DFA methods (See Figure 4).

- Step 4 – calculation of fluctuation measure. The signal is split into $N_n=[N/n-1]$ number of windows (See Figure 4), $\varepsilon(v)$, where v refers to the index of a given window. The fluctuating process is characterized by $F_v(n)$, which is given as a function of window size, n:

$$F_v^2(n) = \frac{1}{n}\cdot\sum_{t=1}^{n}\varepsilon_t^2(v). \tag{32}$$

- Step 5 – calculation of q-th order moments of the fluctuation function.

$$F_q(n) = \left(\frac{1}{N_n}\cdot\sum_{v=1}^{N_n}F_v^q(n)\right)^{1/q}. \tag{33}$$

For q=2, the algorithm reduces to the monofractal DMA method. For the special case q=0, $F_q(n)$ can be obtained as a limit value that can be expressed in a closed form:

$$\log[F_0(n)] = \frac{1}{N_n}\cdot\sum_{v=1}^{N_n}\log[F_v(n)]. \tag{34}$$

Relation of the q-th order moment of the fluctuation measure and H(q) follows a power law:

$$F_q(n)\propto n^{H(q)}. \tag{35}$$

Thus H(q) can be estimated as the slope of the least-square fitted regression line between log n and log $[F_q(n)]$. Finally, Mandelbrot spectrum

is obtained with subsequent application of multifractal formalism equations (Eqs 9–12) yielding multifractal features τ(q), D(h).

## Time-Frequency Domain Methods

Wavelet analysis methods can be used to estimate the singularity spectrum of a multifractal signal by exploiting the multifractal formalism (Muzy et al., 1991, 1993, 1994; Mallat and Hwang, 1992; Bacry et al., 1993; Arneodo et al., 1995, 1998; Mallat, 1999; Figure 5). Wavelet transform modulus maxima (WTMM) has strong theoretical basis and has been widely used in natural sciences to assess multifractality.

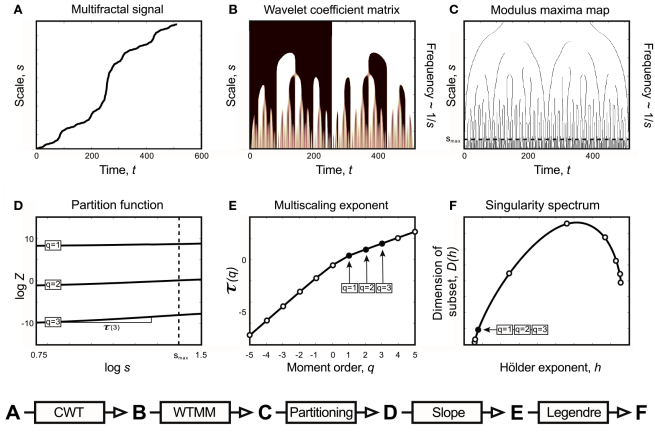


**Figure 5:** Relations of Continuous Wavelet Transform operation, Wavelet Transform Modulus Maxima method, and multifractal formalism to obtain singularity spectrum of an ideal multifractal. Devil's staircase with weight factors $p_1 = p_3 = 0.2$, $p_2 = 0.6$ was used to model an ideal multifractal time series (A). The wavelet coefficient matrix (B) is obtained by continuous wavelet transform in the time-scale space. Modulus maxima map (C) containing the maxima lines across the scales defined by CWT. We call modulus maximum of the wavelet transform $|W_\psi[X](t, s_0)|$; any point $(t_0, s_0)$, which corresponds to a local maximum of the modulus of $|W_\psi[X](t, s_0)|$ is considered as a function of t. For a given scale, it means that $|W_\psi[X](t_0, s_0)| > |W_\psi[X](t, s_0)|$ for all t in the neighborhood right of $t_0$, and $|W_\psi[X](t_0, s_0)| \geq |W_\psi[X](t, s_0)|$ for all t in the neighborhood left of $t_0$. Local maxima are chained, and in the subsequent calculations only maxima chains propagating to the finest scales are used (Mallat, 1999). Chaining local maxima is important, because it is proven that their distribution along multiple scales identifies and measures local singularities, which is tightly linked to the singularity spectrum. The moment-based partition function (D) separates

singularities of various strength as coded in (B,C) as follows. Z is obtained for the range [$s_{min}$, s] as the sum of moments of the wavelet coefficients belonging to those along a set of maxima lines at s [shown as circles in (C)]. This definition corresponds to a "scale-adapted" partition with wavelets at different sizes. A moment-based set of Z are plotted in a log-log representation as shown in (D). Notice that these log Z(log s) functions are lines representing the power law behavior of the multifractal signal within the scaling range shown. Therefore when the slope of each and every log Z(log s) lines are plotted as a function of moment order, q, it yields τ(q) (E). From τ(q) via Legendre transform the singularity spectrum, D(h) (F), is obtained (See Chapter 2, Figure 3).

- Step 1 – continuous wavelet transformation: This step is essentially the same as described previously in Eqs 26–28 yielding a matrix of wavelet coefficients (Figure 5B):

$$W \equiv [w(i_t, i_s)], \tag{36}$$

where $w(i_t, i_s)=|W_\psi[X](t, s)|$, $i_s$ is the scaling index, where $s=s_{min}$, …, $s_{max}$ and $i_t=1, 2, \ldots, N$, where t is the sampling time of each successive data point.

- Step 2 – chaining local maxima: The term modulus maxima describes any point $(t_0, s_0)$ where $|W_\psi=[X](t, s)|$ is a local maximum at $t=t_0$:

$$\frac{\partial W_\psi [X] (t_0, s_0)}{\partial t} = 0. \tag{37}$$

This local maximum is strict in terms of its relation to $t_0$ in its immediate vicinity. These local maxima are to be chained by interconnection to form a local maxima line in the space-scale plane (t, s) (See Figure 5C).

- Step 3 – calculating partition function. With the aid of partition function (Eq. 7, Figure Figure5D),5D), singular behavior of the multifractal time series can be isolated. Wavelet coefficients along maxima chains are considered as μ measures.

$$Z(s, q) = \sum_{\ell \in L(s)} |w(i_s, i_t)|^q. \tag{38}$$

Summation is executed along maxima chains (ℓ), the set of all maxima lines is marked by L(s).

- Step 4 – calculating singularity spectra and parameters of multifractality. The following step is to determine the multiscaling

exponent, $\tau(q)$ by $H(q)$, and then using Eqs 10–12 to give full quantification of the multifractal nature.

## CHARACTERIZATION OF METHODS

Before the application of fractal analysis methods, their behavior should be thoroughly evaluated on a large set of signals with known scale-free structure and broad representation (Bassingthwaighte and Raymond, 1994, 1995; Caccia et al., 1997; Cannon et al., 1997; Eke et al., 2000, 2002; Turiel et al., 2006). Signal classification, estimating performance in terms of precision and limitations of the methods should be clarified during characterization. The capability of multifractal analysis to distinguish between mono- and multifractal processes should also be evaluated.

Stationarity of a signal is an important property for pairing with a compatible fractal analysis tool (see Table 2 in Eke et al., 2002). In addition, all methods have some degree of inherent bias and variance in their estimates of the scaling exponent bearing great importance due to their influence on the results, which can be misinterpreted as a consequence of this effect. The goal of performance analysis is therefore to characterize the reliability of selected fractal tools in estimating fractal parameters on synthesized time series. This should be carried out at least for a range of signal sizes and structures similar to the empirical dataset, so that the reliability of fractal estimates could be accurately determined. Extensive results obtained with our monofractal framework have been reported elsewhere (Eke et al., 2000, 2002), but for the sake of comparison it will be briefly described. Our multifractal testing framework is aimed to demonstrate relevant features of MF-DFA and MF-DMA method, utilizing the equations described in Section "Implementation of Fractal Time Series Analyses."

### Testing Framework for Multifractal Tools on Monofractals

Monofractal signals of known autocorrelation (AC) structure can be synthesized based on their power law scaling. The method of Davies and Harte (1987) (DHM for short) produces an exact fGn signal using its special correlation structure, which is a consequence of the power law scaling of the related fBm signal in the time domain (Eq. 19). It is important, that different realizations can be generated with DHM at a given signal length and Hurst exponent, which consists of a statistical distribution of similarly structured and sized monofractals. The next question is how to define meaningful end-points for the tests? For ideal monofractals with a given length and

true H, Mean Square Error (MSE) is a good descriptor: it can be calculated for each set of series of known H and particular signal length, N (Eke et al., 2002). It carries a combined information about bias and variance, as MSE = bias$^2$ + variance.

Interpreting the multifaceted results of numerical experiments is a complex task. It can be facilitated if they are plotted in a properly selected set of independent variable with impact shown in intensity-coded representations (Figure 6; Eke et al., 2002). Precision index is determined as the ratio of results falling in the interval of [$H_{true} - H_{dev}$, $H_{true} + H_{dev}$], where $H_{dev}$ is an arbitrarily chosen value referring to the tolerable degree of deviation.

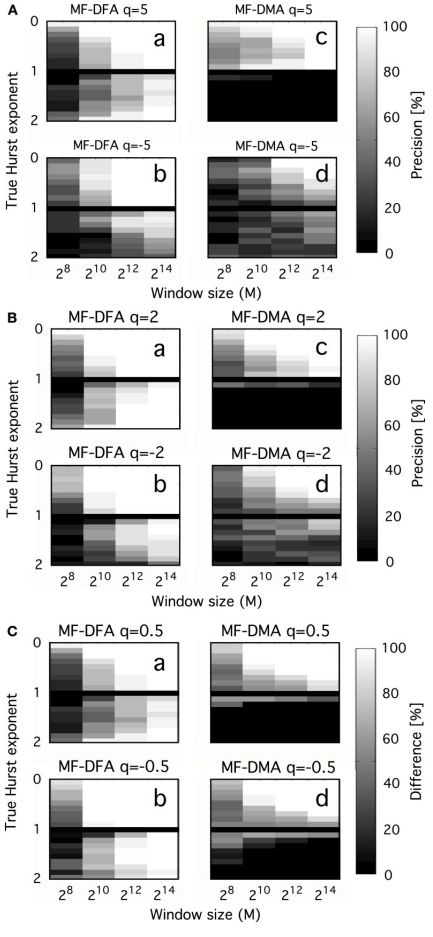


**Figure 6:** Precision as a function of moment order, signal length, and Hurst exponent. Precision of MF-DFA [left side of (A–C)] and MF-DMA [right side of (A–C)] as a function of q, $H_{true}$, N. fGn and fBm signals were generated

by DHM with length of $2^8$, $2^{10}$, $2^{12}$, $2^{14}$, and $H_{true}$ increased from 0.1 to 1.9 in steps of 0.1, skipping $H_{true}=1$ (corresponding to 1/f boundary seen as the black horizontal line in the middle). Estimation of the generalized Hurst exponent should not depend on q, as monofractal's H(q) is a theoretically constant function scattering around $H_{true}$ across different order of moments. The intensity-coded precision index is proportional to the number of estimates of H falling into the range of $H_{true}\pm0.1$, with lighter areas indicating more precise estimation. Calculation of this measure is based on 20 realizations for each q, $H_{true}$, N. (A) Performance of methods for $q=\pm5$. (B) Performance of methods for $q=\pm2$. (C) Performance of methods for $q=\pm0.5$. Besides the clear dependence of precision on $H_{true}$ and N, influence of moment order is also evident, given that the lightest areas corresponding to the most reliable estimates tend to increase in parallel with moment order approaching 0 [Note the trend from (A–C)]. The lower half of the plots indicates that MF-DFA is applicable for signals of both types, while MF-DMA is reliable only on fGn signals. This result is further supported by the paper of Gao et al. (2006), who demonstrated a saturation of DMA at 1 for H when the true extended Hurst exponent exceeds 1 (thus it is non-stationary).

In the monofractal testing framework, we used DHM-signals to evaluate the performance of MF-DMA (Gu and Zhou, 2010) and MF-DFA (Gu and Zhou, 2006), by the code obtained from http://rce.ecust.edu.cn/index.php/en/research/129-multifractalanalysis. It was implemented in Matlab, in accordance with Eqs 17 and 30–35. As seen in Figure 6, precision of MF-DFA and MF-DMA depends on N, H, and the order of moment.

In order to compare the methods in distinguishing multifractality, end-points should be defined reflecting the narrow or wide distribution of Hölder exponents. We select a valid endpoint $\Delta h$ proposed by Grech and Pamula (2012), which is the difference of Hölder exponents corresponding to $q=-15$ and $q=+15$ (Figure 7).

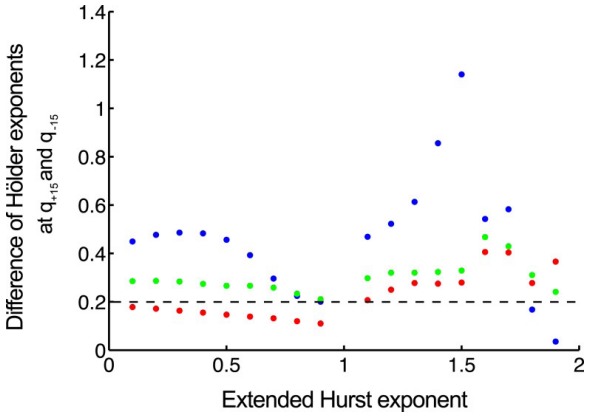


**Figure 7:** Separating monofractals from multifractals. Δh values obtained by MF-DFA (as difference of Hölder exponents at q = +15 and q = −15) are shown for monofractals with length of $2^{10}$ (blue), $2^{12}$ (green), $2^{14}$ (red). It is clearly shown that longer signals are characterized by lower Δh, and its value below 0.2 means that true multifractality is unlikely present (Grech and Pamula, 2012). Signals were created by DHM at extended Hurst exponents of 0–1.9 with a step of 0.1.

## Testing Approaches for Multifractal Tools on Multifractals

Extending the dichotomous model of fGn/fBm signals (introduced in context of monofractals; Mandelbrot and Ness, 1968; Eke et al., 2000) toward multifractal time series is reasonable as it can account for essential features of natural processes exhibiting local power law scaling. Description of an algorithm creating multifractional Brownian motion (mBm) and multifractional Gaussian noise (mGn) can be found here (Hosking, 1984), while implementation of such code can be found on the net (URL1: http://fraclab.saclay.inria.fr/, URL2: www.ntnu.edu/inm/geri/software). Given that these algorithms require Hölder trajectories as inputs, multifractality cannot be defined exactly on a finite set, which is a common problem of such synthesis methods. Selecting a set of meaningful trajectories is a challenging task: it should resemble those of empirical processes and meet the analytical criteria of the selected algorithms (such criteria are mentioned in Concept of Fractal Time Series Analyses).

On the contrary, iterative cascades defined with analytic functions are not influenced by the perplexity of definitions associated with multifractality outlined in the previous paragraph, given that their value at every real point of the theoretical singularity spectrum is known. Due to their simplicity, binomial cascades (Kantelhardt et al., 2002; Makowiec et al., 2012) and Devil's staircases (Mandelbrot, 1983; Faghfouri and Kinsner, 2005) are common examples of theoretical multifractals used for testing purposes. A major drawback of this approach is that these mathematical objects do not account for features in empirical datasets, but can still be useful in comparing reported results.

The most extensive test of multifractal algorithms which used a testing framework of signals synthesized according to the model introduced by Benzi et al. (1993) was reported by Turiel et al. (2006). Briefly, it is a wavelet-based method for constructing a signal with predefined properties of multifractal structuring with explicit relation to its singularity spectrum. Since the latter can be manipulated, the features of the resulting multifractal signal could be better controlled. The philosophy of this approach is very similar to that of Davies and Harte (1987) in that a family of multifractal signals of identical singularity spectra can be generated by incorporating predefined distributions (log-Poisson or log-Normal) giving rise to controlled variability of realizations. Additionally, using log-Poisson distribution would yield multifractals with a bounded set of Hölder exponents in that being similar to those of empirical multifractals. To conclude, this testing framework should merit further investigation.

## ANALYTICAL STRATEGY

In this article we expand our previously published monofractal analytical strategy to incorporate some fundamental issues associated with multifractal analyses keeping how these can be applied to BOLD time series in focus. Progress along the steps of the perplexed fractal analysis should be guided by a consolidated – preferably model-based– view on the issues involved (See Figure 8).

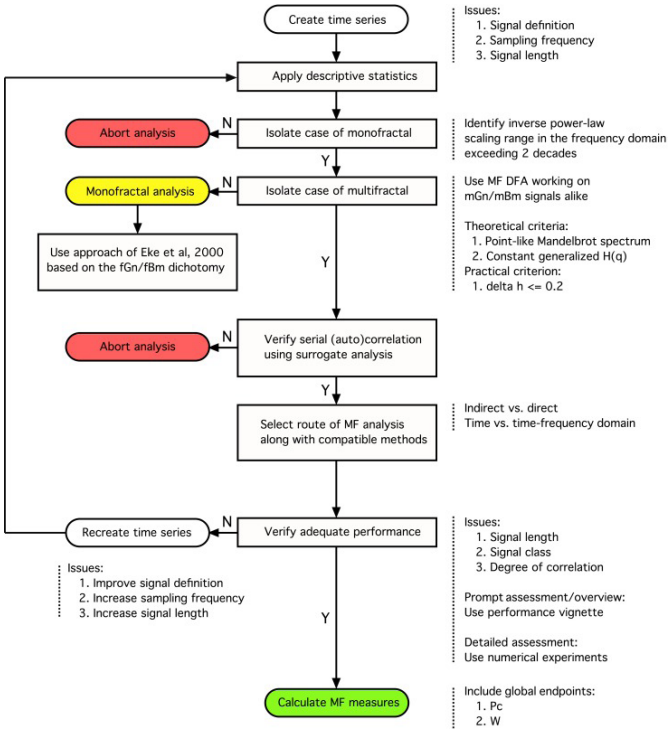


**Figure 8:** Analytical strategy for fractal time series analysis. Toward obtaining a reliable (multi)fractal parameter, which is the purpose of the analysis, the first step to take is to collect a high definition dataset representing the temporal signal, X(t), ensuring adequate definition. Provided that quality-controlled, adequate length of signal, $X_i$, was acquired at a sufficient frequency sampling X(t) (Eke et al., 2002), scale-free processes can be characterized in terms of either a single global or a distribution of many local scaling exponents, the former pertinent to a monofractal, the latter to a multifractal signal, respectively (Figure 1). A detailed flowchart of our monofractal analytical strategy has been reported earlier (Eke et al., 2000, 2002), hence only some of its introductory elements are incorporated here. The signal-to-noise ratio – as part of signal definition – is a source of concern in preprocessing the signal. Ensuring the domination of the underlying physiological processes over inherent noise is a critical issue, which – if not dealt with properly – will have a detrimental effect on the correlation structure of the signal. Endogenous filtering algorithms of the manufacturers of MRI scanners could be operating in potentially relevant frequency ranges of fractal analysis aimed at trend or noise removal (Jezzard and Song, 1996). In case of BOLD signals, this problem may prove hard to track as the system noise may cause a temporally (i.e., serially) correlated error in the measurement

(Zarahn et al., 1997). This may alter the autocorrelation structure of the signal with embedded physiological content (Herman et al., 2011). Various aspects of temporal smoothing have been discussed in Friston et al. (2000). To conclude, scale-free properties of the signal must be preserved during steps carried out before fractal analysis, otherwise the physiologically relevant internal structuring of the BOLD signal cannot possibly be revealed (Herman et al., 2011). Once a multifractal has been isolated by a class-independent method, such as MF-DFA, we can only assume that the multifractal structuring of the signal is due to serial correlation. As autocorrelation structure of the signal can reflect a broad probability distribution, surrogate analysis is needed on a shuffled signal – which destroys this correlation – to ensure that the origin of the scale-invariance is due to genuine autocorrelation in the signal (Kantelhardt:2002]). The null-hypothesis (the signal is not multifractal) is rejected if multifractal measures determined for the raw and surrogate sets are different. This procedure is similar to verifying the presence of deterministic chaos (Herman:2006]). Attention should be given to select the scaling range properly: involving the finest and coarsest scales in calculating H(q) would greatly impair its estimate. The range of moments should be selected such that sufficient range of singularity spectrum is revealed, allowing for the calculation of scalar multifractal descriptors such as $P_c$. Next, one has to decide as to which path of the detailed multifractal analysis to choose (indirect vs. direct or time vs. time-frequency domain)? Each of these paths would have advantageous and disadvantageous contributions to the final results to consider. The methods of analysis must be selected compatible to the path taken. Once methods have been chosen, their performance (precision) ought to be evaluated. With adequate performance verified, the multifractal analyses can then be followed by attempts to find physiological correlates for the estimates of (multi)fractal parameters.

A fundamental question should be answered whether it is worthy at all to take on the demanding task of fractal analysis? This can only be answered if one characterizes the signal in details according to the guideline shown in Figure 8 using tools of descriptive statistics and careful testing; first for the presence of monofractal and later that of multifractal scale-free features. At this end, we present here a new tool for an instantaneous and easy-to-do performance analysis (called “performance vignette”), which can facilitate this process and does not require special knowledge needed to carry out detailed numerical experiments on synthesized signals (Figure 9). The latter, however, cannot be omitted when full documentation of any particular fractal tool’s performance is needed. In that the vignette has been designed for prompt selection, overview, and comparison of various methods; not for their detailed analysis.

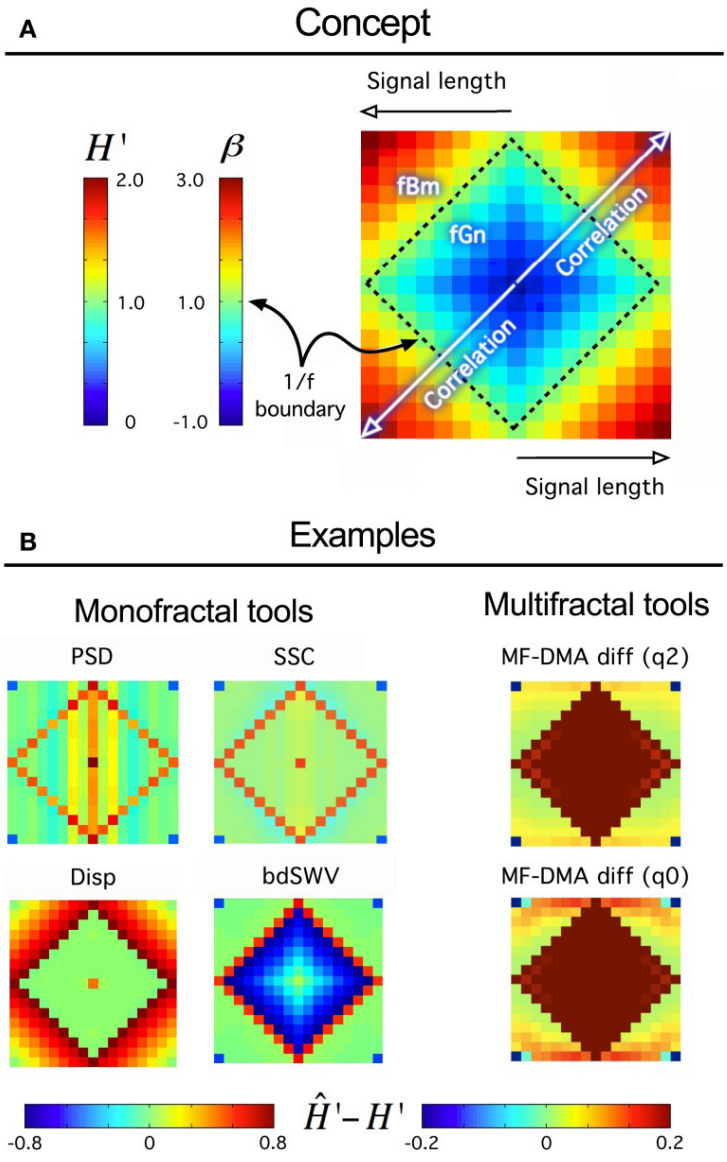


**Figure 9:** Fractal tool performance vignette. It provides a quick assessment of any fractal time series tool's performance. As such can be useful as a method of standardization and/or comparison of various algorithms. Technically, a vignette is created as any given fractal time series method evaluates a volume of synthesized time series for a particular fractal parameter. The results are converted to extended H′ as $H' = H_{fGn}$, $H' = H_{fBm} + 1$ using a conversion table between H and other fractal parameters (Eke et al., 2002). The signals are generated for a range

of length, L [$L_{min}$, $L_{max}$] in increments of ΔL, and for the full range of the fGn/fBm dichotomy at β or H′ at given increments of the exponent, ΔH' by the DHM method (Davies and Harte, 1987; Eke et al., 2000). The volume is created from these signals arranged in a square raster, which will correspond to one of four identical quadrants of the vignette. Once the analysis by a fractal tool has been carried out the results are plotted in a square array as shown in (A) such a way that fGn signals occupy a square created by the four identical quadrants. The 1/f boundary separating the fGn from the fBm range can be easily identified as plotted with a midscale color. Warmer colors indicate over-, cooler colors underestimation of the scaling exponent at the particular signal length or degree of correlation. When applied to class-independent or dependent methods (B), like PSD, SSC (B, upper half) or Disp (dispersional analysis) and bdSWV (bridge detrended Scaled Window Variance) (B, lower half), respectively, an immediate conclusion on signal performance can be drawn: PSD and SSC can be used for fGn and fBm signals alike (except in the vicinity of the 1/f boundary) and SSC is more precise. Disp (Bassingthwaighte and Raymond, 1995; Eke et al., 2000, 2002) and bdSWV (Eke et al., 2000, 2002), two class-dependent methods of excellent performance (note the midscale colored area in the fGn and fBm domains, respectively) do show up accordingly. The vignette is applicable to indicate the performance of multifractal methods, too. The monofractal H can be determined in two ways: in case of $q=2$ from $\tau(q)$, and in case of $q=0$ from $h_{max}$ in the singularity spectrum.

We sustain our recommendation that proper class-dependent or class-independent methods should be chosen.

We feel, that calculating global measures of multifractal scaling, such as $P_c$ (Shimizu et al., 2004) or W (Wink et al., 2008), can help consolidating experimental findings in large fMRI BOLD volumes across many subjects and experimental paradigms. Based on our tests, we conclude that straightforward recommendations for multifractal analysis for the purpose of fMRI BOLD time series analysis needs further investigations.

# PITFALLS

## Sources of Error

Problems emerging from inadequate signal definition (measurement sensitivity, length, sampling frequency)

### *Measurement sensitivity*

The precondition of a reliable fMRI time series analysis is that the BOLD signal has adequate definition in terms of being a true-to-life representation of the underlying biology it samples. In particular, the fMRI BOLD measurement is aimed at detecting the contrast around blood filled compartments in magnetic susceptibility of blood and the surrounding medium in a uniform high field (Ogawa and Lee, 1990). A contrast develops from tissue water relaxation rate being affected by the paramagnetic vs. diamagnetic state of hemoglobin. The contrast increases with decreasing oxygenation of blood, a feature that renders the technique capable of detecting the combined effect of neuronal metabolism coupled via hemodynamics throughout the brain (Smith et al., 2002). As Ogawa and Lee (1990) demonstrated, the BOLD contrast increases with the strength of the main magnetic field, $B_0$ (i.e., due to the sensitivity of the relaxation rate).

In his early paper (Lauterbur, 1973), Lauterbur gave clear evidence of the fact that resolution of magnetic resonance signals will strongly depend on $B_0$. Newer generations of scanners with continuously improved performance were constructed utilizing this relation by incorporating magnets of increased strength (in case of human scanners from, i.e., 1.5–7T, in small animal scanners due to the smaller brain size with strength in the 4–17.2T range). Bullmore et al. (2001) showed indeed, that the performance of some statistical method and their results depended on the magnetic field used (1.5 vs. 3T); calling for caution and continuous reevaluation the methods in the given MRI settings.

In order to confirm the impact of $B_0$ on the sensitivity on the definition of the BOLD signal fluctuations, we have compared the spectral index (ß) of resting-state BOLD fluctuations in vivo to those post mortem and in a phantom in 4, 9.4, and 11.7T in anesthetized rats (Figure 10). What we have learned from this study was that in contrast with amplitude-wise optical measurements of cerebral oxygenation and hemodynamics such as near infrared spectroscopy (Eke et al., 2006), due to the contrast-detecting foundations of fMRI, signal definition cannot be characterized by comparing fluctuation ranges in vivo vs. post mortem. After death deoxyhemoglobin molecules are still present in the MRI voxels post-sacrifice and thus generate susceptibility-induced magnetic field gradients that would impact diffusion of tissue water molecules (Herman et al., 2011), a process that can generate fluctuating BOLD contrast without ongoing physiology. What matters is that in vivo the blood gets oxygenated and via the combined impact of

neuronal metabolism, blood flow, and blood volume, the internal structuring of the BOLD contrast signal will change from close to random to a more correlated level as indicated by β, which is in vivo significantly higher than post mortem. Increasing field strength enhances this effect and yields a more articulated topology of β throughout the brain. Conversely, low field measurements favor the dominance of instrument noise in addition to being less sensitive in detecting the BOLD contrast. The inference of these preliminary data is that, given the BOLD contrast (and presumably even the spatial resolution) of our animal imaging, a 1.5T human scanner may not be of sufficient sensitivity to detect BOLD fluctuations at adequate definition for a reliable monofractal analysis, not to mention multifractal analysis known to require a much higher signal definition for an optimal performance that can be achieved in higher field scanners (Ciuciu et al., 2012).

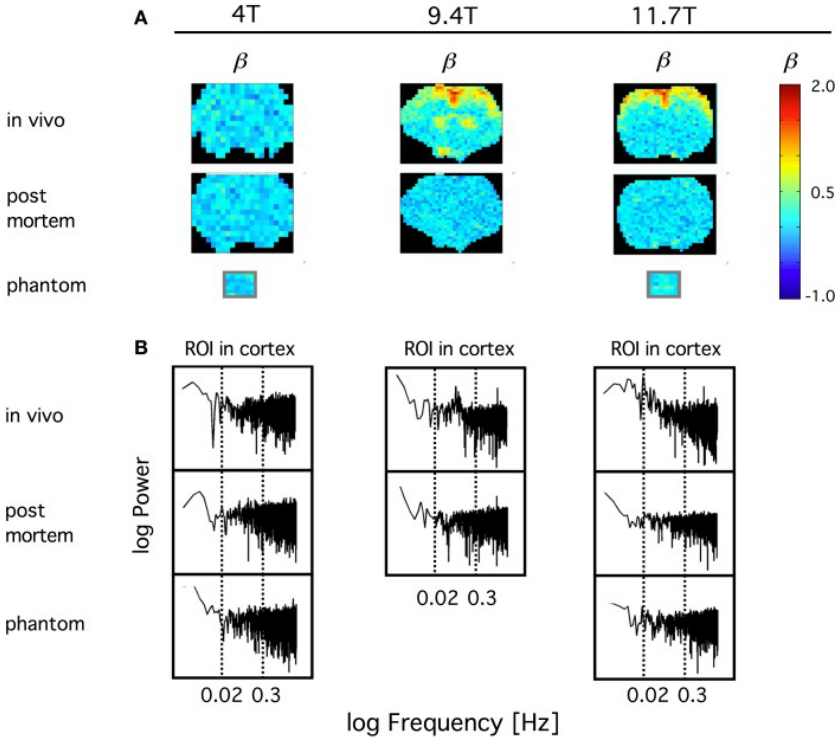


**Figure 10:** Definition of spontaneous BOLD fluctuations critically depends on main field strength. Exemplary coronal scans are shown obtained in anesthetized rat in MR scanner applying 4, 9.4, and 11.7T main external field. All fMRI data were collected at 5 Hz in length of 4096 ($2^{12}$) images with gradient echo planar imaging (EPI) sequence using $^{1}$H surface coils (Hyder et

al., 1995). (A) shows in vivo and post mortem maps of spectral index, β. β was calculated from the spectra of the voxel-wise BOLD time series by the PSD method for a restricted range of fluctuation frequency (0.02–0.3 Hz) found to exhibit inverse power law relationship [fractality; indicated by vertical dashed lines on the PSD plots in (B)]. In order to achieve a suitable contrast for the topology, β are color coded within the fGn range (from 0 to 1). Hence voxel data with $\beta > 1$ indicating the presence of fBm type fluctuations are displayed saturated (in red). β maps for water phantoms placed in the isocenter are also shown for comparison. Note, that the fractal pattern of internal structuring of the spontaneous BOLD signal cannot be captured at adequate definition at 4T as opposed to 11.7T, where the rate of scale-free rise of power toward low frequencies are thus the highest at about the same region of interest (ROI) located in the brain cortex. This dependence translates into an articulate in vivo topology with increasing $B_0$. Also note that in vivo 4T cannot yield a clear topology of β when compared to post mortem, and that the well defined topology achieved at higher fields vanished post mortem indicating the link between β and the underlying physiology.

While the use of fMRI is typically qualitative where the baseline is conveniently differenced away to reveal focal area(s) of interest (Shulman et al., 2007), this practice would not interfere with fractal time series analysis, given that scaling exponent is invariant to mean subtraction.

## *Length and Sampling Frequency*

A signal is a sampled presentation of the underlying process, which generates it. Hence the sampling frequency must influence the extent the signal captures the true dynamics of the process, which is in the focus of fractal analysis irrespective if its analyzed in the time (in form of fluctuations) or in the frequency domain (in form of power distribution across the frequency scale). The sampling frequency should preferably be selected at least a magnitude higher than the highest frequency of the observed dynamics we would aim to capture.

The relationship between length and frequency can best be overviewed in the frequency domain along with the frequency components and aliasing artifact of the spectrum as seen in Figure 12 of Eke et al. (2002). Note, that the dynamics of interest can be best captured hence analyzed if the signal length is long; the sampling frequency is high, because it will provide a spectrum of many components with a weak artifactual impact of aliasing. Herman et al. (2011) have recently demonstrated this relationship on resting-state BOLD time series and concluded that lower frequency dynamics are

better sampled by longer BOLD signals, whereas a high sampling rate is needed to capture dynamics in a wide bandwidth signal (See Figure 3 in Herman et al., 2011). In other words, inadequately low frequency is more detrimental to the result of fractal analysis than somewhat truncated signal.

Due to the discrete representation within the bounded temporal resolution of the signal, the precision of its fractal analysis increases with its length as demonstrated on simulated signals of known (true) fractal measures by the bias and variance of its estimates. The minimum length at which reasonable results can be expected depends not only on signal length but on the method of analysis and the degree of long-range correlation in the signal (as characterized by its H); an issue that has been explored in details for monofractal time series by the groups of Bassingthwaighte and Raymond (1994, 1995); Eke et al. (2000, 2002); Delignieres et al. (2006), and for multifractal methods by Turiel et al. (2006).

Multifractal analysis can be considered as an extension of monofractal analysis, which is explicitly true for moment-based methods: while in case of monofractals a scale-free measure is obtained at $q=2$, the procedure for multifractals uses a set of different q-order moments. Think of q as a magnifier glass: different details of the investigated scale-free structure can be revealed at different magnification. However, if signal definition is poor due to short length or small sampling frequency, estimates of D(h) will become imprecise at large $\pm q$ (Figure 6). Since the order of q needed to obtain characteristic points of the singularity spectrum usually falls beyond $q=\pm 2$, a longer time series is required to guarantee the needed resolution in this range. Hence, dependence of precision on signal length in case of multifractals is a more complicated issue, where the effect of spectral characteristics interacts with that of signal length (Turiel et al., 2006).

A reasonable conclusion is that the recommended minimum length for a reliable multifractal analysis ought to be longer than that found earlier for monofractal series (Eke et al., 2002; Delignieres et al., 2006).

## Problem of Signal Class (fGn vs. fBm)

In fractal analysis, signal classification is a central issue (Eke et al., 2000) and should be regarded as a mandatory step when a tool is to be chosen from the class-dependent group. Living with the relative convenience of using a class-independent method does not render signal classification unnecessary given the great importance of proper interpretation of the findings that can be enhanced by knowing signal class.

Recently, Herman et al. (2011) found in the rat brain using monofractal analysis (PSD) that a significant population of fMRI BOLD signal fell into the non-stationary range of β. These non-stationary signals potentially interfere with resting-state connectivity studies using spatio-temporal volumes of fMRI BOLD. It is even more so, if SSC is used for signal classification (Figure 11) and analysis (Figure 12) shifting the histogram of H′ to the right.

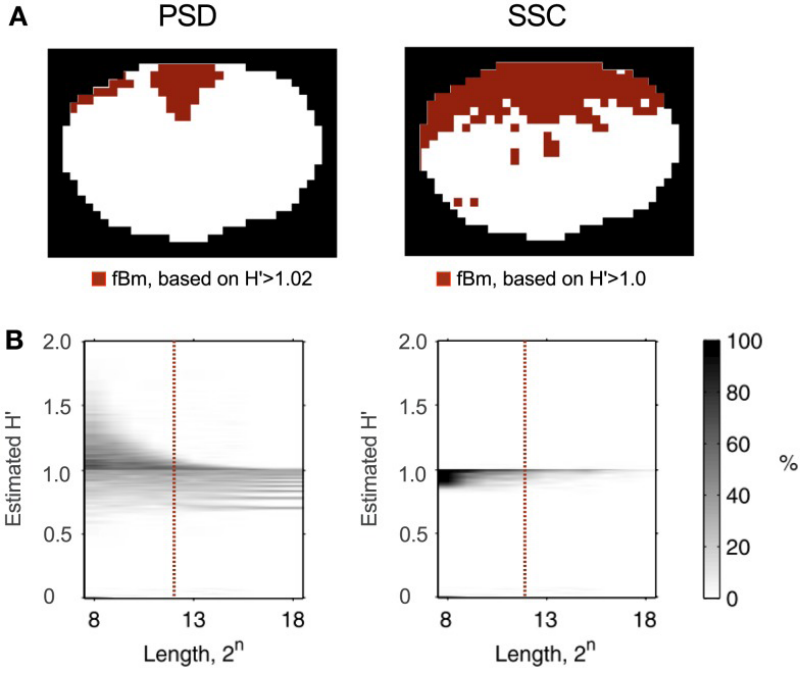


**Figure 11:** Classifying rat fMRI BOLD data. Signal classification was performed on the 11.7T BOLD dataset shown in Figure 10 by the PSD and SSC methods (A) previous tested in this capacity by Eke et al. (2002); misclassification rates for PSD and SSC are shown in the plots of (B) the lower panel. Because SSC is a much better classification tool, than PSD is, the classification topology will be drastically different for these two methods. The ROI's corresponding to voxel-wise signals identified by SSC as non-stationary indeed do clearly delineate the anatomical boundaries of the brain cortex, while those by the PSD only the spots of highest β.

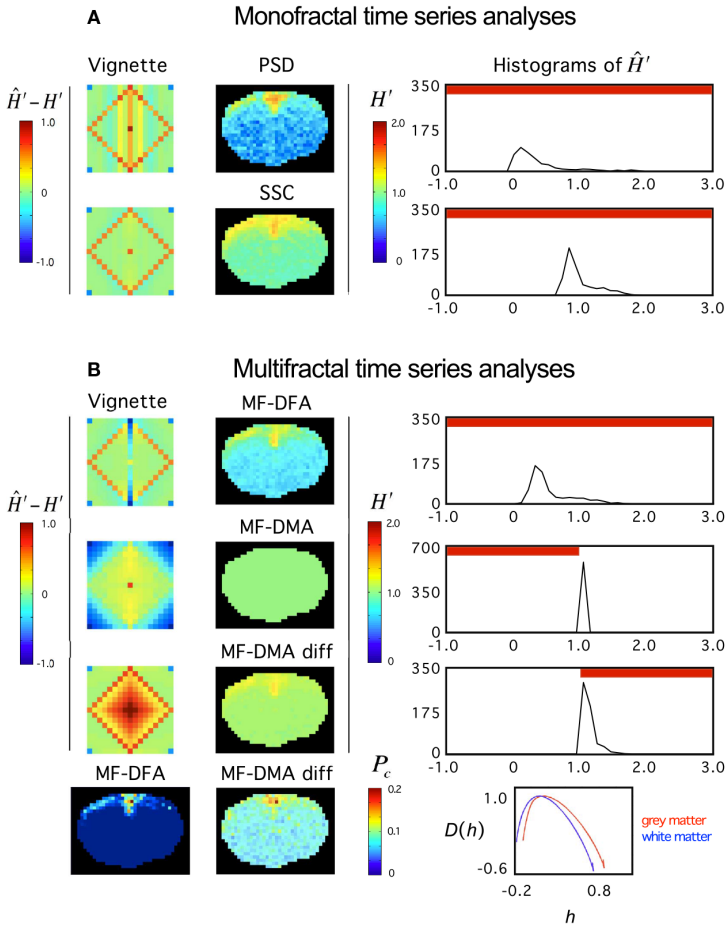


**Figure 12:** Fractal analyses of rat fMRI BOLD data. The 11.7T BOLD dataset shown in Figure 10 was analyzed monofractally (A) in the frequency domain by PSD, in the time domain by SSC, and multifractally (B) in the time domain by MF-DFA and MF-DMA methods. Estimates of spectral index were converted to extended Hurst exponent, H′. Our tool performance vignette is displayed next to the methods. Histograms of H′ computed from the fractal image data by SSC are shown. The vignette data reconfirms that SSC is superior over PSD as a monofractal tool. Due to the downward bias of PSD in the anticorrelated fGn range, H′ are significantly underestimated. Because SSC's estimates are unbiased, the SSC topology should be considered realistic, which translates into a right shift of the SSC H′ histogram relative to that of PSD's. Based on the vignette pattern, among the multifractal tools, MF-DFA works quite well on fGn and fBm signals, alike, while MF-DMA with fair performance in the fGn range

but closer to the 1/f boundary, and fails on fBm signals of the set. For reasons mentioned above, the estimates of SSC should be taken as precise. Given that most values in the fGn range fall into the range of complete uncertainty of the MF-DMA (See Figure 6 at q=2) and that MF-DMA cannot handle fBm signals, all estimates ends up being 1.0. Differencing the signals (including those of the vignette) changed the situation dramatically. As seen on the vignette, the originally fBm signals would be mapped into the fGn range that can be handled by MF-DMA very well. Actually better than the original fGn signals where slight overestimation is seen. This kind of behavior of MF-DMA may have inference with the findings of Gao et al. (2006). Also note, that the double differenced fGn signals end up being overestimated. These effects are worth to investigate in order to characterize the impact of the fGn/fBm dichotomy on the performance of these time domain multifractal tools when signals are being converted between the two classes. $P_c$ – as a global multifractal measure – captures a topology similarly to the monofractal estimates. The corresponding singularity spectra do separate with the likelihood that the underlying multifractalities indeed differ.

For multifractals the problem and proposed solution is generally the same, but the impact of the fGn/fBm dichotomy on the multifractal measures is not a trivial issue. Our preliminary results reported here (Figure 12) are steps in this direction, but this issue calls for continuing efforts in the future. It seems that at least stationarity vs. non-stationarity is a valuable piece of information for selecting a concise model of multifractals.

## Distinguishing Monofractals from Multifractals

Multifractal analysis of an exact monofractal rendered at ideal resolution (in infinite length, sampled at infinite frequency, at infinite sensitivity of detection) would yield a constant H(q), a linear dependence of $\tau$ on q and a point-like Mandelbrot spectrum with its Hölder exponent ($h_{max}$) equal with its Hurst exponent.

Due to the finite and discrete nature of the signal, the singular behavior of a suspected scale-free process cannot be quantified perfectly. As a consequence, the homogeneity of a monofractal's singularities cannot be captured by a multifractal analysis. The reason being is that due to numerical background noise (Grech and Pamula, 2012) – resulting from factors mentioned above – it would always smear the point-like singularity spectrum into one mimicking that of a multifractal. This is confirmed by the apparent uncertainties associated with the estimates of H(q) obtained at various moments in our simulations. All in all, multifractal analyses have been conceived in a manner that tends to view a monofractal as a multifractal.

In order to avoid false interpretation of the data, time series should be produced at the highest possible definition to ameliorate this effect and criteria should also be set up to distinguish the two entities in the signal to be analyzed. Numerical simulation has been demonstrated as a useful tool to work out a parameter that can be used to substantiate a monofractal/multifractal classification (Grech and Pamula, 2012; Figure 6).

## Trends and Noises

Empirical time series are typically non-linear, non-stationary and can be contaminated by noise and other signal components foreign to the fractal analysis of the system under observation. Trend is deterministic in its character and of typically low frequency in contrast with noise, which has a completely random structuring in a higher frequency range. Monofractal analysis methods are quite robust with respect of noise, thus in case of monofractals do not require preprocessing (Bassingthwaighte and Raymond, 1995). When uncorrelated noise is added to a multifractal process, the shape of its singularity spectrum will also be preserved (Figliola et al., 2010). However with correlated noise present, – known to impact fMRI BOLD time series – preprocessing should be considered (Friston et al., 2000), and if carried out, it should be done with an appropriate adaptive filter (Gao et al., 2010, 2011; Tung et al., 2011).

In case of wavelet-based methods, a polynomial trend can be removed based on the analyzing wavelet's properties. However, if the trend has a different character (i.e., trigonometric or exponential), or it has more vanishing moments than that of the analyzing wavelet, the estimation of singularity spectrum will be impaired (See theorem 6.10 in Mallat's book; Mallat, 1999).

Various detrending schemes have been developed to enhance performance of fluctuation analysis (FA) on detrended signals, which has been compared (Bashan et al., 2008). The most common trend removal is based on fitting a low-degree polynomial to local segments of the signal such as employed in DFA (Figure 4). In particular, DFA's trend removal is credited for being very effective, however – as recently reported (Bryce and Sprague, 2012) – it can become inadequate if the trend ends up having a character different from the coded algorithm, which scenario cannot at all be excluded. A further problem is that the signal arbitrarily divided into analyzing window of different sizes in which trend removal is carried out based on a priori assumption (e.g., polynomial). This problem is exaggerated as by using partitioning of the

signal into a set of non-overlapping windows and performing detrending in a window-based manner would not guarantee that the trend in each and every window would be identical with the assumed one. This is especially true for small windows, where trend tends to deviate from that in larger windows. Contrary to expectations, this critical finite size effect is always present, thus this pitfall can only be avoided if explicit detrending is applied by using adaptive methods (Gao et al., 2011).

To conclude, the recently reported uncontrollable bias to the results of DFA (Bryce and Sprague, 2012) raised major concern as to the reliability of FA with this detrending scheme. Thus if DFA is to be used, it should be done with special care taken in the application of more adaptive detrending analyses.

Finally, empirical mode decomposition (EMD) is a promising adaptive approach, one of whose feature is the ability to estimate trend explicitly. It also creates an opportunity to combine EMD with other fractal analysis methods like those based on FA to achieve a more reliable scale-free method (Qian et al., 2011).

## Problems of Moment-based Methods

Using moment-based methods to estimate the Mandelbrot spectrum is a common approach with some drawbacks. Due to the discretized nature of the signal under analysis, small fluctuations cannot be resolved perfectly and therefore the Hölder exponents become biased in the range of their large negative moments (corresponding to the right tail of the singularity spectrum; Turiel et al., 2006). All moment-based methods are influenced by the linearization of the right tail thus yielding biased estimates of the negative statistical moments of the measure, μ (Turiel et al., 2006). This type of error cannot be eliminated with increasing the signal's length (Turiel et al., 2006). In case of large fluctuations in the signal, numerical limitations become problematic when calculating large positive moments.

Problems associated with moment-based methods can be summarized as follows. Firstly, a carefully selected set of different order (q) statistical moments of μ should be calculated. Selecting too large negative and positive moments would lead to imprecise generalized Hurst exponent [H(q)] or multiscaling exponent (Figure 6; Ihlen, 2012). A sufficient range of q is needed, however, in order to characterize the global singular behavior of the studied time series. This is especially important in the evaluation of the spectrum, but from a practical point of view, the spectrum width at half

maximum is sufficient to obtain $P_c$, or W+/W−, that are frequently used lumped parameters in describing multifractal fMRI BOLD signals, too (Shimizu et al., 2004; Wink et al., 2008). In summary, precise estimation of singularity strength is needed at characteristic points of the spectrum: around its maximum (i.e., at $q \approx 0$) and at its half maximum a dense definition is recommended. Thus, the optimal selection depends on the signal character and needs to be analyzed with several sets of q. In general, estimating spectrum between $q = -5$ and $q = 5$ is sufficient in biomedical applications, as proposed by Lashermes and Abry (2004). Secondly, methods implementing direct estimation of singularity spectra can be applied (Figure 3). One typical example is the gradient modulus wavelet projection (GMWP) method, which turned out to be superior to all other tested methods (WTMM, too) in terms of precision as reported by Turiel et al. (2006). It was shown that direct approaches can give quite good results in spite of the numerical challenges imposed by calculating the Hölder exponents (h) locally and without the need of using statistical moments and Legendre transform (Turiel et al., 2006). Strategies including the latter two approaches are widely used and can be considered reasonably, but not exclusively reliable in terms of their handling the numerical difficulties associated with multifractal analysis.

## Problems of Wavelet Transform Modulus Maxima Methods

In case of monofractals, the average wavelet coefficient method is the most effective and the easiest to implement (Simonsen and Hansen, 1998; Eke et al., 2002). It can be used for fBm and cumulatively summed fGn signals.

There are other issues related to this method, whose nature can be numerical on the one hand and theoretical on the other. For example, the first and last points of the signal exhibits artifactual scaling, improperly selected scales would impair the results considerably, etc. A well-selected analyzing wavelet also ensures reliable results, which is also proven for certain indirectly calculated partition functions (via Boltzmann weights; Kestener and Arneodo, 2003). The effect of the modifications addressing these issues is discussed in Faghfouri and Kinsner (2005) and a detailed test of WTMM is reported by Turiel et al. (2006).

Due to the difficulties in the reliable application of WTMM, other methods were developed in the field, the most promising one being the Wavelet Leader method (Lashermes et al., 2005; Serrano and Figliola, 2009), which has recently been applied to human fMRI BOLD signals (Ciuciu et al., 2012). As refinements of WTMM, the wavelet leader is beyond the scope of this review, the reader is referred to the cited references.

## Identifying the Spectral Extent of Monofractality within a Signal

Verifying the presence of self-similarity, as one of the fundamental properties of monofractals is a key element of the analytical strategy of fractal time series analysis (Eke et al., 2000; Figure 8). It should be present within a sufficiently wide scaling range. In case of exact (mathematical) fractals the scaling range is unbounded. In natural fractal time series however it is typically restricted to a set of continuous temporal scales as demonstrated by Eke et al. (2006) for fluctuating cerebral blood volume in humans and Herman et al. (2011) for resting-state fMRI BOLD signals in rat. As shown in the frequency domain by spectral analysis, in both species, scale-free structuring of the signal was present across a range of frequencies well below the Nyquist frequency (half of the sampling frequency). It was characterized by a systematically and self-similarly increasing power toward lower frequencies that could be modeled by Eq. 25 yielding a spectral index of $\beta > 0$, which is an indication of serial correlation between the temporal events (long-term memory). Above this range, the fluctuations were found random with $\beta \approx 0$ meaning that subsequent temporal events were not correlated. The separation of these ranges therefore is crucial because failing to do so would cause a bias in the estimate of $\beta$.

For fractal time series analysis a proper scaling range should be selected where fluctuations are scale-invariant. Optimization of the sampling process, as well as the regression analysis on log-log representations of measures vs. scales yielding the scaling exponent is essential (Eke et al., 2002). In case of time domain methods such as DFA, DMA, and AFA as well introduced by Gao et al. (2011), optimizing the goodness-of-fit of the regression analysis is an example. Detailed recommendations as to how to deal with this problem can be found elsewhere (Peng et al., 1994; Cannon et al., 1997; Eke et al., 2002; Gao et al., 2006). When a signal's spectrum contains other than monofractal components, it may prove difficult to select a monofractal scaling range even by isolating local scaling ranges and fitting local slopes for the spectral index. This procedure should be carefully carried out given that local ranges may end up containing inadequately few spectral estimates for a reliable fitting of the trendline. When the aim is to assess the topology of the measure, this criterion can be relaxed (Herman et al., 2011).

Faghfouri and Kinsner (2005) reported that improper selection of scaling range has a detrimental effect on the results of WTMM. Different scales correspond to different window sizes in MF-DFA and MF-DMA method,

and discarding the smallest and largest window sizes was even suggested by Peng et al. (1994) for the original DFA. Cannon et al. (1997) and Gao et al. (2006) suggested an optimization for the appropriate range of analyzing window sizes (i.e., scales). While this can be regarded as best practice in carrying out MF-DFA, some degree of bias is still introduced to the results arising mainly from the smallest window sizes (Bryce and Sprague, 2012).

### Dualism in Multifractal Formalism

Amongst the indirect, moment-based methods, WTMM uses a different approach to obtain the singularity spectrum than MF-DFA and MF-DMA. Convergence of this dualism is very unlikely, as the relationship of exponents in MF-DFA to the multifractal formalism is reported to be valid only in special cases (Yu and Qi, 2011). The seminal paper of MF-DFA Kantelhardt et al. (2002) established a relationship between the generalized Hurst exponent and multiscaling exponent. The validity of this equation was reported to be valid only if $H = 1$ (Yu and Qi, 2011), and thus another derivation for $\tau(q)$ was proposed. In addition, singularity spectra reported with MF-DFA – as it follows from the Legendre transform of $\tau(q)$ (Eq. 9) – always reaches their maxima at 1, while this does not hold for wavelet methods. In our opinion, revision of results obtained with MF-DFA may be necessary along with consolidating the multifractal formalism published in the field, using the original papers as a starting point of reinvestigation (Frisch and Parisi, 1985; Mandelbrot, 1986; Barabási and Vicsek, 1991; Muzy et al., 1993; Arneodo et al., 1998).

## DEMONSTRATION

Scrutinizing relevant data in selected previous works recognized as having proven or potential impact on the development of the field will likely demonstrate some typical pitfalls.

### Significance of System Noise in the Interpretation of fMRI BOLD Fluctuations

Zarahn et al. (1997) demonstrated early in a careful analysis on spatially unsmoothed empirical human fMRI BOLD data (collected under null-hypothesis conditions) that the examined datasets showed a disproportionate power at lower frequencies resembling of 1/f type noise. In spite of the very detailed analysis, these authors treated the 1/f character as a semi-quantitative

feature of fMRI noise and accepted its validity over a decaying exponential model as the form of the frequency domain description of the observed intrinsic serial, or autocorrelation. The spectral index, β, however was not reported but can be reconstructed from the power slope by converting the semilog plot of power vs. frequency in their Figure 3D panel to a log-log plot compatible to $|A(f)|^2 \propto 1/f^{\beta}$ model. A β value of ~3.3 is yielded, which is exceedingly higher than the values of $0.6 < \beta < 1.2$ reported recently for an extensive 3T dataset by He (2011). This precludes the possibility that the collected resting-state 1.5T BOLD dataset would have been of physiological origin. Our recently reported results for the rat brain with $-0.5 < \beta < 1.5$ reconfirms this assertion (Herman et al., 2011). In fact, Zarahn et al. (1997) wished to determine if the 1/f component of the noise observed in human subjects was necessarily due to physiological cause, but had to reject this hypothesis because they found no evidencing data to support this hypothesis. Zarahn et al. (1997) felt the AC structure (in the time domain, which is equivalent to the inverse power law relationship in the frequency domain) may not be the same for datasets acquired in different magnets, not to mention the impact of using various fMRI scanning schemes (Zarahn et al., 1997). Accordingly, and in light of our rat data for magnets 4, 9.4, and 11.7T, a less than optimal field strength could have led to a signal definition inadequate to capture the $1/f^{\beta}$ type structuring of the BOLD signal of biological origin that must have been embedded in the human datasets Zarahn et al. (1997) but got overridden by system noise. Most recently, Herman et al. (2011) and He (2011) referred to the early study of Zarahn et al. (1997) as one demonstrating the impact of system noise on fMRI data, while Fox et al. (2007) and Fox and Raichle (2007) as the first demonstration of 1/f type BOLD noise with the implication that the 1/f pattern implied fluctuations of biological origin.

## Significance of the General $1/f^{\beta}$ vs. the Strict1/f Model in the Interpretation of fMRI BOLD Noise Data

Fox et al. (2007) reported on the impact of intrinsic BOLD fluctuations within cortical systems on inter-trial variability in human behavior (response time). In conjecture of the notion that the variability of human behavior often displays a specific 1/f frequency distribution with greater power at lower frequencies, they remark "This observation is interesting given that spontaneous BOLD fluctuations also show 1/f power spectrum (Figure S4). While the 1/f nature of BOLD fluctuations has been noted previously (Zarahn et al., 1997), we show that the slope is significantly between −0.5

and −1.5 (i.e., 1/f) and that this is significantly different from the frequency distribution of BOLD fluctuations observed in a water phantom," and in their Figure S4 conclude that "the slope of the best fit regression line (red) is −0.74, close to the −1 slope characteristic of 1/f signals." This interpretation of the findings implies that the spontaneous BOLD fluctuations can be adequately described by the "strict" 1/f model, where the spectral index, β, in $1/f^{\beta}$ – known as the "general" inverse power law model – is treated as a constant of 1, not a variable carrying information on the underlying physiology. Incidentally, studies of Gilden and coworkers (using a non-fMRI approach) have indeed demonstrated (Gilden et al., 1995; Gilden, 2001; Gilden and Hancock, 2007) that response time exhibits variations that could not be modeled by a strict 1/f spectrum but by one incorporating a varying scaling exponent (Gilden, 2009).

Scrutinizing the data of Figure S4 can offer an alternative interpretation as follows. In terms of the hardware, the use of 3T magnet must have ensured adequate signal definition for the study. In their Figure S4, spectral slopes were reported in a lumped manner, in that power at each and every frequency were averaged for the 17 human subjects first (thus creating frequency groups), and then mean slopes along with their statistical variation were plotted for the frequency groups. The mean slope of −0.74 (of thee lumped spectrum) was obtained by regression analysis. This treatment of the data implies that the $|A(f)|^2 \propto 1/f^{\beta}$ model (Mandelbrot and Ness, 1968; Eke et al., 2000, 2002) was a priori rejected otherwise the slope should have been determined for each and every subject in the group across the range of observed frequencies and their associated power estimates (of the true spectrum) first, followed by the statistical analysis for the mean and variance within the group of 17 subjects, for the following reasons. The spectral index is found by fitting a linear model of $|A(f)|^2 \propto 1/f^{\beta}$ across spectral estimates for a range of frequencies. In our opinion when it comes to provide the mean spectral index, it is indeed reasonable (Gilden and Hancock, 2007; Gilden, 2009) to come up with statistics on the fractal estimates for a group of time series data first by obtaining the estimates, proper. Averaging spectral estimates at any particular frequencies and assembling an average spectrum from them tend to abolish the fractal correlation structure for any particular time series and develop one for which the underlying time series is indeed missing. Because the transformation between the two treatments is not linear, the true mean slope of the scale-free analysis cannot be readily reconstructed from the reported slope of the means. Nevertheless, if we regard its value as an approximation and convert it to β, which being less than 1 warrants

the use of $H' = (\beta_{fGn} + 1)/2$, one would yield a value of $\beta = 0.77$ and $H' = 0.87$, respectively.

A recent review by Fox and Raichle (2007) offers an impressive overview and insight of how to delineate cooperative areas (or systems) in the brain based on functional connectivity that emerges from spatial cross-correlation maps of regional fluctuating BOLD signals in the resting brain (Biswal et al., 1995). These authors place the spontaneous activity of the brain as captured in BOLD fluctuations in spatio-temporal domains of fMRI data in the focus of the review emphasizing that itis a fingerprint of a newly recognized mode of functional operation of the brain referred to as default or intrinsic mode (Fox and Raichle, 2007). They argue that the ongoing investigation of this novel aspect of the mode of brain's operation using fractal analysis of resting-state fMRI BOLD may lead to a deeper and better understanding of the way the brain – on the expense of very high baseline energy production and consumption by glucose and oxidative metabolism – maintains a mode capable of selecting and mobilizing these systems in order to respond to a task adequately (Hyder et al., 2006). One has to add that the default or intrinsic mode of operation has been demonstrated and investigated in overwhelming proportions by connectivity analyses based on cross-correlating BOLD voxel-wise signals as opposed on AC of single voxel-wise BOLD time series.

Fox and Raichle (2007) emphasize "spontaneous BOLD follows a 1/f distribution, meaning that there is an increasing power in the low frequencies." In their furthering on the nature of this 1/f type distribution they refer to the studies of Zarahn et al. (1997) and Fox et al. (2007) in the context it was described above (Fox et al., 2007) reaching the same conclusion, in that the characteristic model of human spontaneous BOLD is the 1/f (meaning the "strict") model. We would like to suggest that the notion of 1/f distribution having a regression slope of close to −1 on the log-log PSD plot is somewhat misleading.

In an attempt to consolidate this issue, we suggest that the data be fitted to a model in the form of $1/f^{\beta}$, where β is a variable (Eke et al., 2000, 2002) responding to states of physiology (Thurner et al., 2003; He, 2011) of characteristic topology (Thurner et al., 2003; Herman et al., 2011) in the brain, not a constant of 1. A potential advantage of this model is that by regarding β as a scaling exponent the distribution can then be described to be scale-free (or fractal).

Significance of the $1/f^{\beta}$ model and the dichotomous fGn/fBm analytical strategy in analyzing scaling laws and persistence in human brain activity

As seen above, from the modeling point of view the issue of a reliable description of the autoregressive signal structuring of spontaneous BOLD, is fundamental and critical in resting-state. If it is done properly, it can lend a solid basis for assessing changes in the scaling properties in response to changing activity of the brain. The study of Thurner et al. (2003) was probably the first to demonstrate that spontaneous BOLD in the brain was scale-free and that the scaling exponent of inactive and active voxels during sensory stimulation differed. At the time of the publication of their study, the monofractal analytical strategy of Eke et al. (2000, 2002) based on the dichotomous fGn/fBm model of Mandelbrot and Ness (1968) did not yet reached the fMRI BOLD community, hence Thurner et al. (2003) did not rely on it, either. In this section we will demonstrate the implications of this circumstance in terms of the validity and conclusions of their study. We will do it in a detailed, didactical manner so that our reader should gain a hands-on experience with the perplexed nature of the issue.

Subtracting the mean from the raw fMRI signal precedes the analysis proper, $\bar{I}\vec{x}(t)$, yielding $I\vec{x}(t)$ in Eq. 39,

$$I^{\vec{x}}(t) = \bar{I}^{\vec{x}}(t) - \left\langle \bar{I}^{\vec{x}}(t) \right\rangle_t, \tag{39}$$

which step is compatible with (D)FA (Eke et al., 2000).

Subsequently, in Eq. 40, the temporal correlation function, $C\vec{x}(\tau)$, is calculated

$$C^{\vec{x}}(\tau) = \left\langle I^{\vec{x}}(t) I^{\vec{x}}(t+\tau) \right\rangle = \frac{1}{N-\tau} \sum_{t=1}^{N-\tau} I^{\vec{x}}(t) I^{\vec{x}}(t+\tau). \tag{40}$$

In fact in this step of the analysis the covariance was calculated given that a division by variance was missing. Hence, it is slightly misleading to regard Eq. 40 as the temporal (or auto) correlation (see Eke et al., 2000, Eq. 2). Only, if assumed that the signal is fGn, whose variance is known to be constant over time, the covariance function can be taken as equivalent to the AC function. Because the authors have not tested and proven the signal's class was indeed fGn (Eke et al., 2000), there is no basis for the validity of this assertion.

In Eq. 41, the signal is summed yielding $X\vec{x}\,n(\tau)$, in order to eliminate problems in calculating the AC function due to noise, non-stationarity trends, etc.

$$X_n^{\vec{x}}(\tau) = \sum_{t=1}^{n} I^{\vec{x}}(t) \tag{41}$$

This form of the signal is further referred to as "voxel-profile."

Note, that the signal remains in this summed form for the rest of the analysis (i.e., analyzed as fBm). As a consequence, spectral analysis later in the study was applied to a summed – hence processed – signal and the results were thus reported for this and not the raw fMRI signal, which circumstance prevented reaching a clear conclusion.

Furthermore, the authors indicated that the temporal correlation function would characterize persistence. It seems the two terms (correlation vs. persistence) are used as synonyms of one another whereas they are not interchangeable terms: persistence is a property of fBm, while correlation is that of an fGn signal (Eke et al., 2000). Please note, as the raw signal has been summed, the covariance here characterized persistence that was not present in the raw fMRI signal.

In the next step (Eq. 42), the AC function is approximated by a power law function with γ as its exponent

$$C^{\vec{x}}(\tau) \sim \tau^{-\gamma}, \cdots 0 < \gamma < 1. \tag{42}$$

Based on the equation of the AC function using the Hurst exponent, H, γ must be proportional to 2H (Eke et al., 2000, Eq. 15).

Subsequently, as a part of a FA of the authors (cited in their Reference 19 as unpublished results of their own), the statistics ($Fx^{\vec{}}$ (τ), standard deviation) was calculated for the AC function in Eq. 43

$$F^{\vec{x}}(\tau) = \left\langle \left( X_{n+\tau}^{\vec{x}} - X_n^{\vec{x}} \right)^2 \right\rangle_n^{1/2}. \tag{43}$$

In the left side of Eq. 44, a general power law was applied to the fluctuation from Eq. 43 as $Fx^{\vec{}}$ (τ)~τα

$$F^{\vec{x}}(\tau) \sim \tau^{\alpha},\ \alpha = 1 - \gamma/2. \tag{44}$$

(Note, as the fluctuations have not been detrended, this method is not the DFA of Peng et al., 1994 but strongly related to it).

Consider the scaling exponent, α, on the left side of Eq. 44. According to Peng et al. (1994) and Eke et al. (2002) α=H only if the raw signa l,$\vec{Ix}$ (t), is an fGn. However, because at this point the summed raw signal, $\vec{Xx}$ n(τ), is the object of the analysis, α and H should relate to each other as α=H+1. Given that the signal was summed in Eq. 41 leading up to Eq. 43, and the values for "outside the brain" were reported as α≈0.5, and for "inside the brain" as 0.5<α<1, α must have been improperly calculated because α cannot possibly yield a value of 0.5 for a summed signal given that H scales between 0 and 1 and for an fBm series α=H+1 holds. The reported value of 0.5<α<1 can be regarded correct only for $\vec{Ix}$ (t), the raw fMRI signal, which therefore had to be an fGn process. On the other hand, the reported values 2<β<3 are correct for the $\vec{Xx}$ n signal, only (for reasons given later). Hence the reported α and β values lacking an indication of their respective signal class ended up being ambiguous.

Next, consider the right side of Eq. 44, which expresses α by using γ introduced earlier. We just pointed out that the raw fMRI signal must have been an fGn with α≡H. Consequently, α can be substituted for H in Eq. 44 as H=1−γ/2 and γ expressed as

$$\gamma = 2 - 2H. \tag{45}$$

The authors referring to power law decays in the correlations relate the spectral index, β, to γ as

$$\beta = 3 - \gamma, \tag{46}$$

and further to α as

$$\beta = 2\alpha + 1.$$

Note, that these relations between β, γ, and α in principle do depend on signal class that was not reported.

Now, let us substitute γ as expressed in Eq. 45 into Eq. 46

$$\beta = 3 - 2 + 2H = 1 + 2H,$$

then express H

$$H = \frac{\beta - 1}{2}. \tag{47}$$

As shown by Eke et al. (2000), Figure 2; in Eke et al. (2002), Table 1, based on the dichotomous fGn/fBm model, Eq. 47 would have equivocally identified the case of an fBm signal. As pointed out earlier, the raw fMRI signal was summed before the actual fractal analysis. Consequently, the

relationship $\beta = 3 - \gamma$ ends up holding only if the raw fMRI signal was an fGn process. This is therefore the second piece of evidence suggesting that the class of the raw fMRI signal must have been fGn. Nevertheless, the relationship $\beta = 2\alpha + 1$ could not hold concomitantly for reasons that follow. In an earlier paper of the group (Thurner et al., 2003), the authors stated "The relationship is ambiguous, however, since some authors use the formula $\alpha = 2H + 1$ for all values of $\alpha$, while others use $\alpha = 2H - 1$ for $\alpha < 1$ to restrict H to range (0,1). In this paper, we avoid this confusion by considering $\alpha$ directly instead of H." The fGn/fBm model (Eke et al., 2002) helps resolving this issue as neither of these relationships between $\alpha$ and H holds because if $\alpha$ is calculated with the signal class recognized and determined, the relationship between $\alpha$ and H is equivocally $\alpha = H_{fGn}$ and $\alpha = H_{fBm} + 1$. Based on the fGn/fBm model, the relationship between $\beta$ and $\alpha$ given in Eq. 46 as $\beta = 2\alpha + 1$ needs to be revised, too, to is correct form of $\beta = 2\alpha - 1$ (See Table 1 in Eke et al., 2002).

Thurner et al. (2003) concluded: "Outside the brain and in non-active brain regions voxel-profile activity is well described by classical Brownian motion (random walk model, $\alpha \sim 0.5$ and $\beta \sim 2$)." Recall, the "voxel-profile" is not the raw fMRI signal (intensity signal, $\vec{Ix}(t)$, most probably an fGn), but its summed form, $\vec{Xx}\, n(\tau)$, an fBm.

Our conclusion on the above analysis by Thurner et al. (2003) is as follows: (i) $\alpha$ was improperly calculated by the authors' FA method because $\alpha \sim 0.5$ cannot possibly be valid for an fBm signal given that $\alpha_{fBm} > 1$ (Peng et al., 1994), (ii) $\beta \sim 2$ is only formally valid given that it was calculated based on Eq. 46 from an improperly calculated $\alpha$ and by using an arbitrary relationship between $\alpha$ and $\beta$. The subsequent and opposite effects of these rendered the value of $\beta$ to $\beta \sim 2$.

When the results of Thurner et al. (2003) are interpreted according to the analytical strategy of Eke et al. (2000) based on the dichotomous fGn/fBm model of Mandelbrot and Ness (1968), the reported values of Thurner et al. can be converted for their fMRI "voxel-profile" data $\vec{Xx}\, n$ to $\alpha_{fBm} \sim 1.5$, $\beta_{fBm} \sim 2$, $H_{fBm} \sim 0.5$ or for the raw fMRI intensity signal $\vec{Ix}(t)$ to $\alpha_{fGn} \sim 0.5$, $\beta_{fGn} \sim 0$, $H_{fGn} \sim 0.5$. This interpretation of the data reported for humans by Thurner et al. (2003) is fully compatible with the current findings by He (2011) on the human and by Herman et al. (2009, 2011) on the rat brain.

### Multifractal Analyses on Rat fMRI BOLD Data

Exemplary analysis on empirical BOLD data is presented on the 11.7T coronal scan shown in Figure 10 to demonstrate the inner workings of these methods when applied to empirical data, and point to potential artifacts, too (See Figure 12). For monofractal analysis, we recommend using monofractal SSC for it gives unbiased estimates across the full range of the fGn/fBm dichotomy. For this reason, the topology is well defined and not as noisy as on the PSD maps. MF-DFA, due to its inferior performance in the strongly correlated fGn range (See Figure 6 at q=2), failed with this particular BOLD dataset. Also note, that the histograms obtained for the same datasets evaluated by these different methods do differ indicating that method's performance were different. Proper interpretation of the data therefore assumes an in-depth understanding of the implication of method's performance on the analysis. $P_c$ and most certainly W seems a promising parameter to map from the BOLD temporal datasets. Their proper statistical analyses along with those of singularity spectra for different anatomical locations in the brain should be a direction of future research.

## PHYSIOLOGICAL CORRELATES OF FRACTAL MEASURES OF FMRI BOLD TIME SERIES

Eke and colleagues suggested and demonstrated that β should be regarded as a variable responding to physiology (Eke et al., 1997, 2000, 2002, 2006; Eke and Herman, 1999; Herman and Eke, 2006; Herman et al., 2009, 2011).

Soon, Bullmore et al. (2001) suggested treating 1/f type fMRI BOLD time series as realizations of fBm processes for the purpose of facilitating their statistical analysis using pre-whitening strategies. For this reason, signal classification did not emerge as an issue to address. Then Thurner et al. (2003) demonstrated that human resting-state fMRI BOLD is not only a scale-free signal, but do respond to stimulation of the brain. Their analysis yielded this conclusion in a somewhat arbitrary manner in that the importance of the fGn/fBm dichotomy was not recognized at the time that led to flaws in the calculation of the scaling exponent as demonstrated above. Hu et al. (2008) and Lee et al. (2008) also reported that H obtained by DFA can discriminate activation from noise in fMRI BOLD signal.

In later studies dealing with the complexity of resting-state and task-related fluctuations of fMRI BOLD, the issue of signal class has gradually

shifted into the focus (Maxim et al., 2005; Wink et al., 2008; Bullmore et al., 2009; He, 2011; Ciuciu et al., 2012).

Recently Herman et al. (2011) found in the rat brain using PSD that a significant population of fMRI BOLD signal fell into the non-stationary range of β. The inference of this finding is the potential interference of non-stationary signals with resting-state connectivity studies using spatio-temporal volumes of fMRI BOLD. It is even more so, if SSC is used for signal classification (Figure 11) and analysis (Figure 12) shifting the population histogram of H′ to the right.

The β value converted from the reported human spectral slopes by Fox et al. (2007) (see above) fits very well within the range of human data reported most recently by He (2011) for the same instrument (3T Siemens Allegra MR scanner). He (2011) adopting the dichotomous monofractal analytical strategy of Eke et al. (2002) demonstrated that β of spontaneous BOLD obtained for multiple regions of the human brain correlates with brain glucose metabolism, a fundamental functional parameter offering grounds for the assertion that that β itself is a functional parameter. Herman et al. (2011) using the same analytical strategy (Eke et al., 2000, 2002) on resting-state rat BOLD datasets showed that β maps capture a gray vs. white matter topology speaking for the correlation of β and functional activity of the brain regions being higher in the gray than in the white matter.

With near infrared spectroscopy, – recommended by Fox and Raichle (2007) as a cost-effective, mobile measurement alternative of fMRI to capture resting-state hemodynamic fluctuations in the brain – a $1/f^{\beta}$ temporal distribution of cerebral blood volume (one of the determinant of BOLD) was found in humans, with an age and gender dependence on β (Eke et al., 2006). Furthermore, β determined from heart rate variability time series was found to differ between healthy and unhealthy individuals (Makikallio et al., 2001).

The above physiological correlates seem to have opened a new perspective in basic and clinical neurosciences (Hausdorff et al., 1997) by recognizing β as an experimental variable and applying adequate tools for its reliable assessment (Pilgram and Kaplan, 1998; Eke et al., 2000, 2002; Bullmore et al., 2009; He, 2011) with multifractal analyses as a dynamically expanding perspective (Ciuciu et al., 2012; Ihlen, 2012), too.

We propose that the inter-regional spatial cross-correlation (connectivity) as a means of revealing spatial organization in the brain be supplemented by

a temporal AC analysis of extended BOLD signal time series by mapping β as an index of temporal organization of the brain's spontaneous activity.

## ACKNOWLEDGMENTS

The authors thank the technicians, scientists, and engineers at MRRC (mrrc.yale.edu), and QNMR (qnmr.yale.edu). This work was supported by grants from the National Institutes of Health (R01 MH-067528 and P30 NS-52519 to Fahmeed Hyder) and from the Hungarian Scientific Research Found (OTKA grants I/3 2040, T 016953, T 034122, NIH Grants TW00442, and RR1243 to Andras Eke). Dr. Peter Mukli has been supported by the Semmelweis University Magister Project (TÁMOP-4.2.2/B-10/1-2010–0013).

## REFERENCES

1. Arneodo A., Audit B., Bacry E., Manneville S., Muzy J. F., Roux S. G. (1998). Thermodynamics of fractal signals based on wavelet analysis: application to fully developed turbulence data and DNA sequences. Physica A 254, 24–4510.1016/S0378-4371(98)00002-8
2. Arneodo A., Bacry E., Muzy J. F. (1995). The thermodynamics of fractals revisited with wavelets. Physica A 213, 232–27510.1016/0378-4371(94)00163-N
3. Bacry E., Muzy J. F., Arneodo A. (1993). Singularity spectrum of fractal signals from wavelet analysis – exact results. J. Stat. Phys. 70, 635–67410.1007/BF01053588
4. Bandettini P. A. (1993). "MRI studies of brain activation: temporal characteristic," in Proceedings of the First Annual Meeting of the International Society of Magnetic Resonance in Medicine (Dallas: Society of Magnetic Resonance in Medicine), 143–151
5. Barabási A. L., Vicsek T. (1991). Multifractality of self-affine fractals. Phys. Rev. A 44, 2730–273310.1103/PhysRevA.44.2730
6. Barnsley M. F. (1988). Fractals Everywhere. Boston: Academic Press
7. Barunik J., Kristoufek L. (2010). On Hurst exponent estimation under heavy-tailed distributions. Physica A 389, 3844–385510.1016/j.physa.2010.05.025
8. Bashan A., Bartsch R., Kantelhardt J. W., Havlin S. (2008). Comparison of detrending methods for fluctuation analysis. Physica A 387, 5080–509010.1016/j.physa.2008.04.023
9. Bassingthwaighte J. B. (1988). Physiological heterogeneity: fractals link determinism and randomness in structures and functions. News Physiol. Sci. 3, 5–10
10. Bassingthwaighte J. B., Liebovitch L. S., West B. J. (1994). Fractal Physiology. New York: Published for the American Physiological Society by Oxford University Press
11. Bassingthwaighte J. B., Raymond G. M. (1994). Evaluating rescaled range analysis for time series. Ann. Biomed. Eng. 22, 432–44410.1007/BF02368250
12. Bassingthwaighte J. B., Raymond G. M. (1995). Evaluation of the dispersional analysis method for fractal time series. Ann. Biomed. Eng. 23, 491–50510.1007/BF02584449

13. Benzi R., Biferale L., Crisanti A., Paladin G., Vergassola M., Vulpiani A. (1993). A random process for the construction of multiaffine fields. Physica D 65, 352–35810.1016/0167-2789(93)90060-E

14. Biswal B., Yetkin F. Z., Haughton V. M., Hyde J. S. (1995). Functional connectivity in the motor cortex of resting human brain using echo-planar MRI. Magn. Reson. Med. 34, 537–54110.1002/mrm.1910340409

15. Bryce R. M., Sprague K. B. (2012). Revisiting detrended fluctuation analysis. Sci. Rep. 2, 1–610.1038/srep00315

16. Bullmore E., Barnes A., Bassett D. S., Fornito A., Kitzbichler M., Meunier D., et al. (2009). Generic aspects of complexity in brain imaging data and other biological systems. Neuroimage 47, 1125–113410.1016/j.neuroimage.2009.05.032

17. Bullmore E., Long C., Suckling J., Fadili J., Calvert G., Zelaya F., et al. (2001). Colored noise and computational inference in neurophysiological (fMRI) time series analysis: resampling methods in time and wavelet domains. Hum. Brain Mapp. 12, 61–7810.1002/1097-0193(200102)12:2<61::AID-HBM1004>3.0.CO;2-W

18. Caccia D. C., Percival D., Cannon M. J., Raymond G., Bassingthwaighte J. B. (1997). Analyzing exact fractal time series: evaluating dispersional analysis and rescaled range methods. Physica A 246, 609–63210.1016/S0378-4371(97)00363-4

19. Cannon M. J., Percival D. B., Caccia D. C., Raymond G. M., Bassingthwaighte J. B. (1997). Evaluating scaled windowed variance methods for estimating the Hurst coefficient of time series. Physica A 241, 606–62610.1016/S0378-4371(97)00252-5

20. Ciuciu P., Varoquaux G., Abry P., Sadaghiani S., Kleinschmidt A. (2012). Scale-free and multifractal time dynamics of fMRI signals during rest and task. Front. Physiol. 3:186.10.3389/fphys.2012.00186

21. Cramer F. (1993). Chaos and Order. New York: VCH Verlagsgesellschaft

22. Davies R. B., Harte D. S. (1987). Test for Hurst effect. Biometrika 74, 95–10110.1093/biomet/74.1.33

23. Delignieres D., Ramdani S., Lemoine L., Torre K., Fortes M., Ninot G. (2006). Fractal analyses for 'short' time series: a re-assessment of classical methods. J. Math. Psychol. 50, 525–54410.1016/j.jmp.2006.07.004

24. Delignieres D., Torre K. (2009). Fractal dynamics of human gait: a reassessment of the 1996 data of Hausdorff et al. J. Appl. Physiol. 106, 1272–127910.1152/japplphysiol.90757.2008

25. Delignieres D., Torre K., Lemoine L. (2005). Methodological issues in the application of monofractal analyses in psychological and behavioral research. Nonlinear Dynamics Psychol. Life Sci. 9, 435–461

26. Eke A., Herman P. (1999). Fractal analysis of spontaneous fluctuations in human cerebral hemoglobin content and its oxygenation level recorded by NIRS. Adv. Exp. Med. Biol. 471, 49–5510.1007/978-1-4615-4717-4_7

27. Eke A., Herman P., Bassingthwaighte J. B., Raymond G. M., Balla I., Ikrenyi C. (1997). Temporal fluctuations in regional red blood cell flux in the rat brain cortex is a fractal process. Adv. Exp. Med. Biol. 428, 703–70910.1007/978-1-4615-5399-1_98

28. Eke A., Herman P., Bassingthwaighte J. B., Raymond G. M., Percival D. B., Cannon M., et al. (2000). Physiological time series: distinguishing fractal noises from motions. Pflugers Arch. 439, 403–41510.1007/s004240050957

29. Eke A., Herman P., Hajnal M. (2006). Fractal and noisy CBV dynamics in humans: influence of age and gender. J. Cereb. Blood Flow Metab. 26, 891–89810.1038/sj.jcbfm.9600243

30. Eke A., Herman P., Kocsis L., Kozak L. R. (2002). Fractal characterization of complexity in temporal physiological signals. Physiol. Meas. 23, R1–R3810.1088/0967-3334/23/1/301

31. Faghfouri A., Kinsner W. (2005). "Local and global analysis of multifractal singularity spectrum through wavelets," in Canadian Conference on Electrical and Computer Engineering 2005, Saskatoon, 2163–2169

32. Falconer K. J. (1990). Fractal Geometry: Mathematical Foundations and Applications. Chichester: Wiley

33. Figliola A., Serrano E., Paccosi G., Rosenblatt M. (2010). About the effectiveness of different methods for the estimation of the multifractal spectrum of natural series. Int. J. Bifurcat. Chaos 20, 331–33910.1142/S0218127410025788

34. Fougere P. F. (1985). On the accuracy of spectrum analysis of red noise processes using maximum entropy and periodogram methods: simulation studies and application to geographical data. J. Geogr.

Res. 90, 4355–4366

35. Fox M. D., Raichle M. E. (2007). Spontaneous fluctuations in brain activity observed with functional magnetic resonance imaging. Nat. Rev. Neurosci. 8, 700–71110.1038/nrn2201
36. Fox M. D., Snyder A. Z., Vincent J. L., Raichle M. E. (2007). Intrinsic fluctuations within cortical systems account for inter-trial variability in human behavior. Neuron 56, 171–18410.1016/j.neuron.2007.08.023
37. Frisch U., Parisi G. (1985). "Turbulence and predictability in geophysical fluid dynamics and climate dynamics," in Fully Developed Turbulence and Intermittency Appendix: On the Singularity Structure of Fully Developed Structure, eds Ghil M., Benzi R., Parisi G. (Amsterdam: North-Holland; ), 823
38. Friston K. J., Josephs O., Zarahn E., Holmes A. P., Rouquette S., Poline J. B. (2000). To smooth or not to smooth? Bias and efficiency in fMRI time-series analysis. Neuroimage 12, 196–20810.1006/nimg.2000.0609
39. Gao J., Hu J., Tung W.-W. (2011). Facilitating joint chaos and fractal analysis of biosignals through nonlinear adaptive filtering. PLoS ONE 6, e24331.10.1371/journal.pone.0024331
40. Gao J., Hu J., Tung W. W., Cao Y., Sarshar N., Roychowdhury V. P. (2006). Assessment of long-range correlation in time series: how to avoid pitfalls. Phys. Rev. E Stat. Nonlin. Soft Matter Phys. 73, 016117.10.1103/PhysRevE.73.036602
41. Gao J., Sultan H., Hu J., Tung W. W. (2010). Denoising nonlinear time series by adaptive filtering and wavelet shrinkage: a comparison. IEEE Signal Process. Lett. 17, 3.10.1109/LSP.2010.2050174
42. Gao J. B., Cao Y., Tung W.-W., Hu J. (2007). Multiscale Analysis of Complex Time Series – Integration of Chaos and Random Fractal Theory, and Beyond. Hoboken, NJ: Wiley Interscience
43. Gilden D. L. (2001). Cognitive emissions of 1/f noise. Psychol. Rev. 108, 33–5610.1037/0033-295X.108.1.33
44. Gilden D. L. (2009). Global model analysis of cognitive variability. Cogn. Sci. 33, 1441–146710.1111/j.1551-6709.2009.01060.x
45. Gilden D. L., Hancock H. (2007). Response variability in attention-deficit disorders. Psychol. Sci. 18, 796–80210.1111/j.1467-9280.2007.01982.x

46. Gilden D. L., Thornton T., Mallon M. W. (1995). 1/f Noise in human cognition. Science 267, 1837–183910.1126/science.7892611
47. Gouyet J. F. (1996). Physics and Fractal Structure. Paris: Masson
48. Grech D., Pamula G. (2012). Multifractal background noise of monofractal signals. Acta Phys. Pol. A 121, B34–B39
49. Gu G. F., Zhou W. X. (2006). Detrended fluctuation analysis for fractals and multifractals in higher dimensions. Phys. Rev. E Stat. Nonlin. Soft Matter Phys. 74, 1–710.1103/PhysRevE.74.061104
50. Gu G.-F., Zhou W.-X. (2010). Detrending moving average algorithm for multifractals. Phys. Rev. E Stat. Nonlin. Soft Matter Phys. 82, 1–1210.1103/PhysRevE.82.011136
51. Hartmann A., Mukli P., Nagy Z., Kocsis L., Herman P., Eke A. (2012). Real-time fractal signal processing in the time domain. Physica A 392, 89–10210.1016/j.physa.2012.08.002
52. Hausdorff F. (1918). Dimension und äuß eres Maß. Math. Ann. 79, 157–17910.1007/BF01457179
53. Hausdorff J. M., Mitchell S. L., Firtion R. E., Peng C. K., Cudkowicz M. E., Wei J. Y., et al. (1997). Altered fractal dynamics of gait: reduced stride-interval correlations with aging and Huntington's disease. J. Appl. Physiol. 82, 262–269
54. He B. J. (2011). Scale-free properties of the functional magnetic resonance imaging signal during rest and task. J. Neurosci. 31, 13786–1379510.1523/JNEUROSCI.2111-11.2011
55. Herman P., Eke A. (2006). Nonlinear analysis of blood cell flux fluctuations in the rat brain cortex during stepwise hypotension challenge. J. Cereb. Blood Flow Metab. 26, 1189–119710.1038/sj.jcbfm.9600165
56. Herman P., Kocsis L., Eke A. (2009). Fractal characterization of complexity in dynamic signals: application to cerebral hemodynamics. Methods Mol. Biol. 489, 23–4010.1007/978-1-59745-543-5_2
57. Herman P., Sanganahalli B. G., Hyder F., Eke A. (2011). Fractal analysis of spontaneous fluctuations of the BOLD signal in rat brain. Neuroimage 58, 1060–106910.1016/j.neuroimage.2011.06.082
58. Hosking J. R. M. (1984). Modeling persistence in hydrological time series using fractional differencing. Water Resour. Res. 20, 1898–190810.1029/WR020i012p01898

59. Hu J., Lee J. M., Gao J., White K. D., Crosson B. (2008). Assessing a signal model and identifying brain activity from fMRI data by a detrending-based fractal analysis. Brain Struct. Funct. 212, 417–42610.1007/s00429-007-0166-9

60. Hyder F., Patel A. B., Gjedde A., Rothman D. L., Behar K. L., Shulman R. G. (2006). Neuronal-glial glucose oxidation and glutamatergic-GABAergic function. J. Cereb. Blood Flow Metab. 26, 865–87710.1038/sj.jcbfm.9600263

61. Hyder F., Rothman D. L., Blamire A. M. (1995). Image reconstruction of sequentially sampled echo-planar data. Magn. Reson. Imaging 13, 97–10310.1016/0730-725X(94)00068-E

62. Ihlen E. A. F. (2012). Introduction to multifractal detrended fluctuation analysis in matlab. Front. Physiol. 3:141.10.3389/fphys.2012.00141

63. Jezzard P., Song A. W. (1996). Technical foundations and pitfalls of clinical fMRI. Neuroimage 4, S63–S7510.1006/nimg.1996.0056

64. Kantelhardt J. W., Zschiegner S. A., Koscielny-Bunde E., Havlin S., Bunde A., Stanley H. E. (2002). Multifractal detrended fluctuation analysis of nonstationary time series. Physica A 316, 87–11410.1016/S0378-4371(02)01383-3

65. Kestener P., Arneodo A. (2003). Three-dimensional wavelet-based multifractal method: the need for revisiting the multifractal description of turbulence dissipation data. Phys. Rev. Lett. 91, 194501.10.1103/PhysRevLett.91.194501

66. Kwong K. K., Belliveau J. W., Chesler D. A., Goldberg I. E., Weisskoff R. M., Poncelet B. P., et al. (1992). Dynamic magnetic resonance imaging of human brain activity during primary sensory stimulation. Proc. Natl. Acad. Sci. U.S.A. 89, 5675–567910.1073/pnas.89.12.5675

67. Lashermes B., Abry P. (2004). New insight in the estimation of scaling exponents. Int. J. Wavelets Multi. 2, 497–52310.1142/S0219691304000597

68. Lashermes B., Jaffard S., Abry P. (2005). "Wavelet leader based multifractal analysis," in IEEE International Conference on Acoustics, Speech, and Signal Processing, ICASSP ′05. IV (Philadelphia: Institute of Electrical and Electronics Engineers, IEEE), 161–164

69. Lauterbur P. C. (1973). Image formation by induced local interactions: examples employing nuclear magnetic resonance. Nature 242, 190–19110.1038/242190a0

70. Lee J. M., Hu J., Gao J., Crosson B., Peck K. K., Wierenga C. E., et al. (2008). Discriminating brain activity from task-related artifacts in functional MRI: fractal scaling analysis simulation and application. Neuroimage 40, 197–21210.1016/j.neuroimage.2007.11.019

71. Liebovitch L. S., Tóth T. (1989). A fast algorithm to determine fractal dimensions by box counting. Phys. Lett. A 141, 386–39010.1016/0375-9601(89)90854-2

72. Makikallio T. H., Huikuri H. V., Hintze U., Videbaek J., Mitrani R. D., Castellanos A., et al. (2001). Fractal analysis and time- and frequency-domain measures of heart rate variability as predictors of mortality in patients with heart failure. Am. J. Cardiol. 87, 178–18210.1016/S0002-9149(00)01312-6

73. Makowiec D., Rynkiewicz A., Wdowczyk-Szulc J., Zarczynska-Buchowiecka M. (2012). On reading multifractal spectra. Multifractal age for healthy aging humans by analysis of cardiac interbeat time intervals. Acta Phys. Pol B 5, 159–17010.5506/APhysPolBSupp.5.159

74. Mallat S. (1999). A Wavelet Tour in Signal Processing. San Diego: Academic Press

75. Mallat S., Hwang W. L. (1992). Singularity detection and processing with wavelets. IEEE Trans. Inf. Theory 38, 617–64310.1109/18.119727

76. Mandelbrot B. B. (1967). How long is the coast of Britain? Statistical self-similarity and fractional dimension. Science 155, 636–63810.1126/science.156.3775.636

77. Mandelbrot B. B. (1980). Fractal aspects of the iteration of z → Λ (1- z) for complex l and z. Ann. N. Y. Acad. Sci. 357, 249–25910.1111/j.1749-6632.1980.tb29690.x

78. Mandelbrot B. B. (1983). The Fractal Geometry of Nature. New York: W. H. Freeman and Co

79. Mandelbrot B. B. (1985). Self-affine fractals and fractal dimension. Phys. Scripta 32, 257–26010.1088/0031-8949/32/4/001

80. Mandelbrot B. B. (1986). “Fractals and multifractals: noise, turbulence and non-fractal patterns in Physics,” in On Growth and Form: Fractal and Non-Fractal Pattern in Physics, eds Stanley H. E., Ostrowski N. (Dordrecht: Nijhof; ), 279

81. Mandelbrot B. B., Ness J. W. V. (1968). Fractional Brownian motion, fractional noises and applications. SIAM Rev. Soc. Ind. Appl. Math. 10,

422–437

82. Marmelat V., Delignieres D. (2011). Complexity, coordination, and health: avoiding pitfalls and erroneous interpretations in fractal analyses. Medicina (Kaunas) 47, 393–398
83. Maxim V., Sendur L., Fadili J., Suckling J., Gould R., Howard R., et al. (2005). Fractional Gaussian noise, functional MRI and Alzheimer's disease. Neuroimage 25, 141–15810.1016/j.neuroimage.2004.10.044
84. Muzy J. F., Bacry E., Arneodo A. (1991). Wavelets and multifractal formalism for singular signals: application to turbulence data. Phys. Rev. Lett. 67, 3515–351810.1103/PhysRevLett.67.3515
85. Muzy J. F., Bacry E., Arneodo A. (1993). Multifractal formalism for fractal signals – the structure-function approach versus the wavelet-transform modulus-maxima method. Phys. Rev. E Stat. Phys. Plasmas Fluids Relat. Interdiscip. Topics 47, 875–88410.1103/PhysRevE.47.875
86. Muzy J. F., Bacry E., Arneodo A. (1994). The multifractal formalism revisited with wavelets. Int. J. Bifurcat. Chaos 4, 245–30210.1142/S0218127494000204
87. Ogawa S., Lee T. M. (1990). Magnetic resonance imaging of blood vessels at high fields. Magn. Reson. Med. 16, 9–1810.1002/mrm.1910160103
88. Ogawa S., Lee T. M., Kay A. R., Tank D. W. (1990). Brain magnetic resonance imaging with contrast dependent on blood oxygenation. Proc. Natl. Acad. Sci. U.S.A. 87, 9868–987210.1073/pnas.87.24.9868
89. Ogawa S., Menon R. S., Tank D. W., Kim S., Merkle H., Ellermann J. M., et al. (1993a). Functional brain mapping by blood oxygenation level-dependent contrast magnetic resonance imaging – a comparison of signal characteristics with a biophysical model. Biophys. J. 64, 803–81210.1016/S0006-3495(93)81441-3
90. Ogawa S., Lee T. M., Barrere B. (1993b). The sensitivity of magnetic resonance image signals of a rat brain to changes in the cerebral venous blood oxygenation. Magn. Reson. Med. 29, 205–21010.1002/mrm.1910290208
91. Peng C.-K., Buldyrev S. V., Havlin S., Simons M., Stanley H. E., Goldberger A. L. (1994). Mosaic organization of DNA nucleotides. Phys. Rev. E Stat. Phys. Plasmas Fluids Relat. Interdiscip. Topics 49, 1685–168910.1103/PhysRevE.49.R1796
92. Phelan S. E. (2001). What is complexity science, really? Emergence 3,

120–13610.1207/S15327000EM0301_08

93. Pilgram B., Kaplan D. T. (1998). A comparison of estimators for 1/f noise. Physica D 114, 108–12210.1016/S0167-2789(97)00188-7
94. Qian X. Y., Gu G. F., Zhou W. X. (2011). Modified detrended fluctuation analysis based on empirical mode decomposition for the characterization of anti-persistent processes. Physica A 390, 4388–439510.1016/j.physa.2011.07.008
95. Raichle M. E., MacLeod A. M., Snyder A. Z., Powers W. J., Gusnard D. A., Shulman G. L. (2001). A default mode of brain function. Proc. Natl. Acad. Sci. U.S.A. 98, 676–68210.1073/pnas.98.2.676
96. Raichle M. E., Mintun M. A. (2006). Brain work and brain imaging. Annu. Rev. Neurosci. 29, 449–47610.1146/annurev.neuro.29.051605.112819
97. Razavi M., Eaton B., Paradiso S., Mina M., Hudetz A. G., Bolinger L. (2008). Source of low-frequency fluctuations in functional MRI signal. J. Magn. Reson. Imaging 27, 891–89710.1002/jmri.21283
98. Serrano E., Figliola A. (2009). Wavelet leaders: a new method to estimate the multifractal singularity spectra. Physica A 388, 2793–280510.1016/j.physa.2009.03.043
99. Shimizu Y., Barth M., Windischberger C., Moser E., Thurner S. (2004). Wavelet-based multifractal analysis of fMRI time series. Neuroimage 22, 1195–120210.1016/j.neuroimage.2004.03.007
100. Shulman R. G., Rothman D. L., Hyder F. (2007). A BOLD search for baseline. Neuroimage 36, 277–28110.1016/j.neuroimage.2006.11.035
101. Simonsen I., Hansen A. (1998). Determination of the Hurst Exponent by use of wavelet transforms. Phys. Rev. E Stat. Nonlin. Soft Matter Phys. 58, 79–8710.1103/PhysRevE.58.2779
102. Smith A. J., Blumenfeld H., Behar K. L., Rothman D. L., Shulman R. G., Hyder F. (2002). Cerebral energetics and spiking frequency: the neurophysiological basis of fMRI. Proc. Natl. Acad. Sci. U.S.A. 99, 10765–1077010.1073/pnas.122612899
103. Thurner S., Windischberger C., Moser E., Walla P., Barth M. (2003). Scaling laws and persistence in human brain activity. Physica A 326, 511–52110.1016/S0378-4371(03)00279-6
104. Tung W., Gao J., Hu J., Yang L. (2011). Detecting chaos in heavy-noise environments. Phys. Rev. E Stat. Nonlin. Soft Matter Phys. 83, 046210.10.1103/PhysRevE.83.038601

105. Turiel A., Pérez-Vicente C. J., Grazzini J. (2006). Numerical methods for the estimation of multifractal singularity spectra on sampled data: a comparative study. J. Comput. Phys. 216, 362–39010.1016/j.jcp.2005.12.004

106. Weitkunat R. (1991). Digital Biosignal Processing. New York: Elsevier Science Inc

107. Wink A., Bullmore E., Barnes A., Bernard F., Suckling J. (2008). Monofractal and multifractal dynamics of low frequency endogenous brain oscillations in functional MRI. Hum. Brain Mapp. 29, 791–80110.1002/hbm.20593

108. Yu L., Qi D. W. (2011). Applying multifractal spectrum combined with fractal discrete Brownian motion model to wood defects recognition. Wood Sci. Technol. 45, 511–51910.1007/s00226-010-0341-7

109. Zarahn E., Aguirre G. K., D'Esposito M. (1997). Empirical analyses of BOLD fMRI statistics. I. Spatially unsmoothed data collected under null-hypothesis conditions. Neuroimage 5, 179–19710.1006/nimg.1997.0263

# 11

# *Characterization of Forested Landscapes from Remotely Sensed Data Using Fractals and Spatial Autocorrelation*

**Mohammad Z. Al-Hamdan,[1] James F. Cruise,[2] Douglas L. Rickman,[3] and Dale A. Quattrochi[3]**

[1]Universities Space Research Association at NASA Marshall Space Flight Center, National Space Science and Technology Center, NASA Global Hydrology and Climate Center, Huntsville, AL 35805, USA
[2]Civil and Environmental Engineering Department, University of Alabama in Huntsville, Huntsville, AL 35899, USA
[3]Earth Science Office at NASA Marshall Space Flight Center, National Space Science and Technology Center, NASA Global Hydrology and Climate Center, Huntsville, AL 35805, USA

## ABSTRACT

The characterization of forested landscapes is frequently required in civil engineering practice. In this study, some spatial analysis techniques are presented that might be employed with Landsat TM data to analyze forest structure characteristics. A case study is presented wherein fractal dimensions (FDs), along with a simple spatial autocorrelation technique (Moran's I), were related to stand density parameters of the Oakmulgee National Forest located in the southeastern United States (Alabama). The results indicate that

**Citation:** Al-Hamdan, M. Z., Cruise, J. F., Rickman, D. L., &Quattrochi, D. A. (2012). Characterization of Forested Landscapes from Remotely Sensed Data Using Fractals and Spatial Autocorrelation. Advances in Civil Engineering, 2012, 1–14., DOI: 10.1155/2012/945613

when smaller trees do not dominate the landscape (<50%), forested areas can be differentiated according to breast sizes and thus important flood plain characteristics such as ratio of obstructed area to total area can be estimated from remotely sensed data using the studied indices. This would facilitate the estimation of hydraulic roughness coefficients for computation of flood profiles needed for bridge design. FD and Moran's I remained fairly constant around the values of 2.7 and 0.9 (resp.) for samples with either greater than 50% saplings or less than 50% sawtimber and with ranges of 2.7–2.9 and 0.6–0.9 as the saplings decreased or the sawtimber increased. Those indices can also distinguish hardwood and softwood species facilitating forested landscapes mapping for preliminary environmental impact analysis.

## INTRODUCTION

The characterization of forested landscapes is frequently required in civil engineering practice. Examples include estimation of quantities for clearing prior to construction projects, environmental impact analysis, and characterization of hydraulic roughness for flood plain studies. Increasingly, professionals are considering the use of remotely sensed data to aid in these estimations. In 2003, the Federal Highway Administration funded a project, conducted jointly by Mississippi State University and the University of Alabama in Huntsville, AL, USA. to evaluate the efficacy of using remotely sensed data in the planning and environmental impact analysis of transportation systems. Since transportation lines (both road and rails) frequently must traverse forested areas, one major focus of the project was the use of remotely sensed data to characterize these landscapes.

The specific transportation needs that directed the project were to characterize the hydraulic roughness of flood plains for bridge design and environmental impact analysis. Recent studies have confirmed the importance of rigid, unsubmerged vegetation in determining flow depths and velocities in shallow flow situations such as commonly encountered in wide flood plains [1–4]. The studies highlight the importance of stand density (ratio of obstructed area to total area) and trunk diameter. Musleh and Cruise [1] showed the relationship between these variables and classical hydraulic roughness parameters such as Manning's n and the Darcy f factor. Accurate land cover and species identification are also important aspects of environmental impact analysis, particularly in identification of wetlands under the forest canopy.

Several sources of remotely sensed data are currently available that might be useful for forest characterization purposes. The data can be from satellite or aircraft platforms and can be from either passive or active instruments. A large amount of research has been performed using active remotely sensed data, particularly airborne radar to estimate forest parameters [5–11]. Most passive remotely sensed data are much more easily accessible and cost effective than are active data. A significant amount of research has been performed on forest biomass estimation using passive instruments, particularly radiometric data [12–24]. However, studies that employ passive radiometric data (e.g., Landsat Thematic Mapper (TM), NOAA Advanced Very High-Resolution Radiometer (AVHRR), or the Moderate-Resolution Imaging Spectroradiometer (MODIS)) usually focus on the estimation of indirect measurement of biomass or canopy coverage such as the Leaf Area Index (LAI) or Normalized Difference Vegetation Index (NDVI). Thus, it would be of great benefit if passive radiometer data could be employed to characterize forest structure such as stand density and trunk size.

In this study, some spatial analysis techniques are presented that might be employed with Landsat TM data to analyze forest structure characteristics. The spectral characteristics (7 bands) and spatial resolution (30 m) of TM data make it very suitable for use in the analysis of even moderate-sized forested areas. In an earlier paper by Al-Hamdan et al. [25], the authors examined the impact of spatial and spectral resolution of remotely sensed data on the spatial indices that might be used for landscape characterization. That study concluded that Landsat TM might possess the ideal attributes for this purpose. A case study is now presented wherein fractal dimensions, along with a simple spatial correlation technique, were related to stand density parameters of the Oakmulgee National Forest located in the southeastern United States (Alabama).

## FRACTAL ANALYSIS AND SPATIAL AUTOCORRELATION METHODS

One of the most essential issues in interpretation and analysis of remotely sensed data is the observation and measurement scale [26]. Scale is crucial to the characterization of geospatial data because many environmental processes and patterns are scale-dependent [27]. Recently developed spatial analysis approaches from a variety of science disciplines offer the possibility of highly efficient statistical characterization, analysis, and identification of

spatial data in remotely sensed images. Spatial autocorrelation and fractal measurement are methods that have been developed to characterize the scaling property of spatial data [28]. Although the fractal technique and other textural analyses have been applied extensively [29–42], its use as a spatial technique for characterizing remote sensing images needs to be evaluated more in terms of its utility to help characterize forest growth characteristics such as stand sizes [25, 26, 43, 44], as demonstrated in this study.

## Fractals

Classical geometry cannot provide tools for analysis of the forms of most spatial patterns of nature because they are so irregular and fragmented [44]. Fractal geometry was developed as a mathematical basis for characterizing complex natural patterns [45]. In classical geometry, a point has an integer topological dimension of zero, a line has one dimension, an area has two dimensions, and a volume has three dimensions [26, 44]. However, the fractal dimension (FD) is a noninteger value that exceeds the Euclidean topological dimension [44, 45]. The FD can vary between zero and one, between one and two, or between two and three; for a point pattern, a curve, or a surface, respectively [26, 44]. As the geometrical complexity of a perfectly flat two-dimensional surface (FD=2.0) increases so that it begins to fill a volume, the FD values approach 3.0 [44].

The foundation for fractal analysis is self-similarity, which can be defined as a property of a curve or surface where each part is indistinguishable from the whole [26, 44–46]. In order to define the theoretical FD, the degree of self-similarity is used and expressed as a self-similarity ratio [26, 44, 45]. Thus, the FD of a curve can be defined as [26, 44]

$$\mathrm{FD} = \frac{\log(N_s)}{\log\left(1/r_f\right)}, \tag{1}$$

where $N_s$ is the number of similar copies and $r_f$ is the scale reduction factor. Measuring the length of the curve using various step sizes by a procedure called the walking-divider method [46] is a common way to estimate the FD value of a curve (e.g., a coastline) [26, 44]. In the case of irregular curves, the length increases as the measurement interval decreases, and a linear regression can capture such an inverse relationship between total line length and step size [26, 44, 47]:

$$\log(L) = C + B\log(S_s), \tag{2}$$

where L is the line length, $S_s$ is the step size, B is the slope of the regression, and C is a constant. For the case of a curve, FD can then be calculated by

$$\mathrm{FD} = 1 - B. \tag{3}$$

For a raster-based remotely sensed image (surface), FD can be estimated in a similar approach using a method that is called the isarithm method [44], which was evolved from Goodchild [46], Shelberg et al. [48], and Lam and De Cola [49]. With the isarithm method, a mean FD from individual FD values of gray-scale contours is computed [26]. For each isarithm brightness value and each step size, the algorithm classifies each pixel below the isarithm value as white and each pixel above this value as black [26, 44]. Each neighboring pixel along the rows or columns is then compared to determine whether the pairs are both black or both white; if they are not of the same color, then an isarithm lies between the two neighboring pixels. The total number of boundary pixels is used to approximate the length of each isarithm line [26, 47]. A linear regression is performed using the logarithms of the total length of the boundary and the step size. The regression slope B is used to determine the FD of the isarithm line [26, 44], where

$$\mathrm{FD} = 2 - B. \tag{4}$$

Equation (4) differs from (3) because as a flat surface grows more complex, FD increases from a value of 2.0 and approaches 3.0 as the surface begins to fill a volume [26]. The final FD of the surface is the average of the FD values for those isarithms having a coefficient of determination "$R^2$" greater than or equal to 0.9 [26, 44, 47, 50].

It has been shown in many previous forestry research studies [51–60] that there is a significant positive relationship between crown width and the Diameter at Breast Height (DBH) for both hardwood and softwood species. Thus, an increase in the stand diameter implies an increase in the crown width and vice versa. As illustrated in Figure 1 [25], if continuous small crown trees are covering two adjacent remotely sensed pixels of a similar area, the result is two homogenous surfaces. Thus, the integration of the brightness levels within each pixel (i.e., pixel value) will be similar in magnitude. If the pixel values do not vary significantly, the result is less complexity in terms of fractals (smaller FD) and more homogeneity in terms of autocorrelation [25]. On the other hand, if the pixels are covered with large crown trees,

the result is nonhomogenous adjacent pixels leading to more complexity in terms of fractals and less homogeneity in terms of autocorrelation [25].

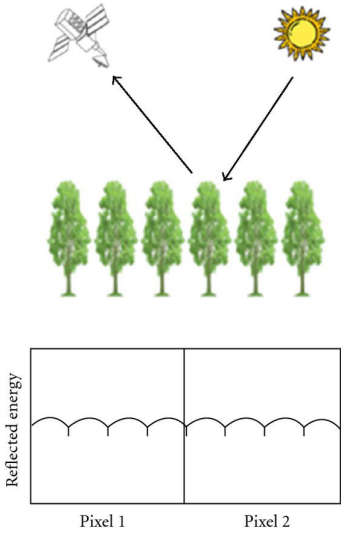


**(a)**

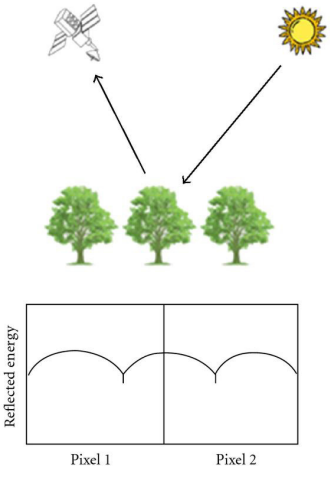


**(b)**

**Figure 1**: Size class effect on remotely sensed data: (a) small crown trees and (b) large crown trees (courtesy of Al-Hamdan et al. [25]).

## Spatial Autocorrelation

Another index that can be used to analyze the spatial autocorrelation of images is Moran's I. Moran's I [61] is an index of spatial autocorrelation which reflects the differing spatial structures of the smooth and rough surfaces [47]. Thus, it is a potential technique in characterizing and estimating measures of forest-related surface roughness based on crown diversity. Moran's I is a spatial correlation statistic and is calculated from the following formula [47]:

$$I(d) = \frac{n \sum_i^n \sum_j^n w_{ij} z_i z_j}{W \sum_i^n z_i^2}, \quad (5)$$

where I(d) is Moran's spatial autocorrelation at distance d, $w_{ij}$ is weight at distance d, so that $w_{ij}$ is 1 if point j is within distance d of point i, otherwise $w_{ij} = 0$, $z_i$ is deviation (i.e., $z_i = x - x_{mean}$ for variable x). W = the sum of all the weights where $i \neq j$.

Moran's I can vary from +1.0 for perfect positive autocorrelation (a clumped pattern) to −1.0 for perfect negative autocorrelation (a checker board pattern) [44]. Moran's I is different from the FD in that the FD is focused on the object shape, size, and the tortuosity of the edges of these objects [47]. Moran's I does not explicitly consider the shapes and sizes of objects once the weights, $w_{ij}$, in (5) are determined [47].

# CASE STUDY

Oakmulgee National Forest is located in central Alabama and encompasses an area of 128,638 ha (317,861 acres) (Figure 2). According to the US Forest Service inventory analysis, there are three size classes present within the forest data sets, namely, sawtimber, poletimber, and saplings. This size classification was based on the diameter at breast height (DBH) of the tree trunk. The DBH values for those classes are greater than 22.86 cm (9.0 in), from 12.7 cm (5.0 in) to 22.6 cm (8.9 in), and from 2.54 cm (1.0 in) to 12.45 cm (4.9 in), respectively. Forest species includes softwood and hardwood trees. Longleaf-slash pine, shortleaf-loblolly, and cypress are examples of softwood trees (Figure 3(a)). White oak, red oak, hickory, sweetgum, ash, and yellow-poplar are examples of hardwood trees (Figure 3(b)). The forest database included digital maps linked to attribute tables containing the stand characteristics (i.e., tree types, sizes, and species) of the forest.

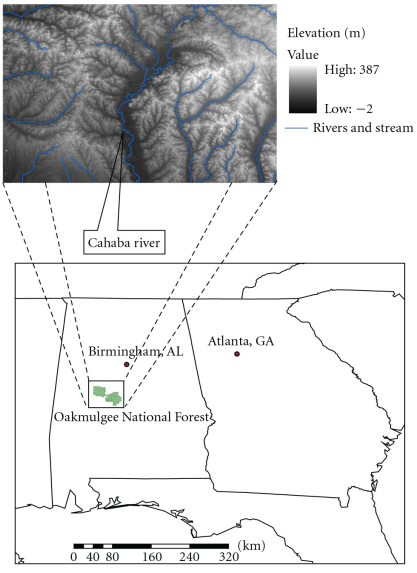


**Figure 2**: Location map of study area.


**Figure 3**: Examples of (a) Softwood trees and (b) Hardwood trees.

Other spatial data were also collected to characterize the region for geoidentification and location purposes. These data included state and county maps, roads, streams, and topographic images (digital line graph

data) that were useful in providing visual locations of points within the forest area. The sources of these data were the Environmental Systems Research Institute (ESRI) and the US Bureau of the Census Topologically Integrated Geographic Encoding and Referencing System (TIGER).

The remote sensing data consisted of Landsat TM images of the forest area taken in summer 1999. The TM instrument records energy reflected in seven bandwidths as shown in Table 1. As shown in the table, the spatial resolution of the Landsat TM images is 30 meters except for band 6 which is 120 meters. For consistency purposes, the data recorded in Band 6 were excluded from these analyses. The source for the Landsat TM images was the EROS Data Center of the United States Geological Survey (USGS). This study focused on a comparison of samples identified from the same Landsat TM scene. Thus, the authors believed that it was not necessary to atmospherically correct the satellite data because any atmospheric effects would prevail for all of the study sites; that is, all samples would have similar atmospheric effects. Additionally, previous work employing spatial statistical techniques in the Image Characterization and Modeling System (ICAMS), particularly fractal analysis of remote sensing data, has implied that there is little influence of atmospheric effects on the overall statistical analysis results [26, 43, 62].

**Table 1**: Landsat Thematic Mapper (TM)

| Bands | Wavelength (micrometers) | Resolution (meters) |
|---|---|---|
| Band 1 | 0.45–0.52 | 30 |
| Band 2 | 0.52–0.60 | 30 |
| Band 3 | 0.63–0.69 | 30 |
| Band 4 | 0.76–0.90 | 30 |
| Band 5 | 1.55–1.75 | 30 |
| Band 6 | 10.40–12.50 | 120 |
| Band 7 | 2.08–2.35 | 30 |

## IMAGE CHARACTERIZATION AND MODELING SYSTEM (ICAMS)

ICAMS is a software module that was developed to measure, characterize, and model multiscale remotely sensed data [62, 63]. It contains a robust set of fractal measurement algorithms embedded in a GIS-type architecture.

It contains a number of spatial measurement methods that can be used to address a variety of significant issues related to scale and fractal analysis.

The main functions of ICAMS are image input, image characterization, specialized functions, and image display and output. The image input subsystem includes basic image processing functions, such as file transformation, georeferencing, image registration, and a variety of image viewing capabilities [62]. The image characterization subsystem provides users with an array of spatial and nonspatial measures for characterizing image data. The non-spatial measures include basic descriptive statistics measures (i.e., mean, mode, median, and variance) and histograms. The spatial measures include fractal analysis [49], variogram analysis [64, 65], spatial autocorrelation indices [66, 67], and textural measures such as local variance [68]. The specialized subsystem of ICAMS provides aggregation routines for aggregating pixels to simulate multiscaled data for scale effect analyses [26]. The image output subsystem contains functions to output original images or derived products in two-dimensional or three-dimensional form. ICAMS provides the ability to calculate the FD of remotely sensed images using the isarithm method [49], variogram [65], and triangular prism methods [69]. Lam et al. [70] found that the isarithm method calculates the FD fairly accurately and more so than the other two methods, thus the isarithm method was used in this study.

## PROCEDURE

The procedure followed in the case study is illustrated in Figure 4. Raster and vector data were collected for the Oakmulgee National Forest as described previously. The raster data (TM images) were then imported into the ER Mapper remote sensing software package in order to trim, locate, and crop the images of the study area and to export the data to the ARCINFO 8.2 GIS package. The relevant vector data (state and county lines, roads, streams, DLG (topographic) data, and National Forest delineations) were also imported into ARCINFO and overlaid onto the raster images. Figure 5 illustrates some attributes of the data set. Samples were collected randomly covering of all parts of the forest. As shown in Figures 2 and 5, the area is bisected by the Cahaba River, so care was taken to obtain a representative number of samples from both sides of the river. In addition, the elevation of the forest ranged from 60 m to 170 m above mean sea level with an average of 130 m. So, again care was taken to obtain samples representative of all topographic conditions so as not to bias the results. Criteria for the selection

of the window (number of pixels in a sample) were based on the resolution, minimum mapping unit size, and nature of the classes (size of the regions, characteristic scale, directionality, and spatial periodicity) to be identified [71]. It is understood that a smaller window size does not convey sufficient spatial or texture information to characterize land surfaces. On the other hand, if the window size is too large, too much information from other surfaces could be included and hence the algorithm might not be efficient. The sample size for this study was chosen to be 100 × 100 pixels based on the average sample size used in the research literature [28, 71]. As shown in Figure 5(e), a total of 52 samples were collected for Oakmulgee National Forest. It can be noted that the sample size in the study area was larger than 30 and hence the distribution of the sample means can be approximated reasonably well by a normal distribution for statistical purposes [72].

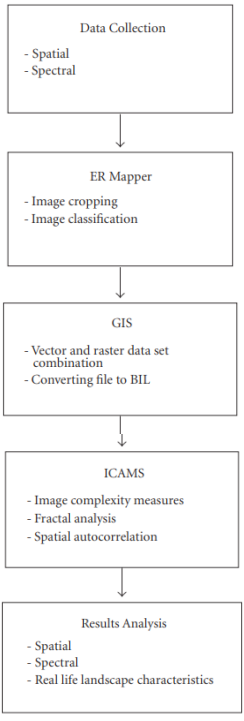


**Figure 4**: Study methodology.

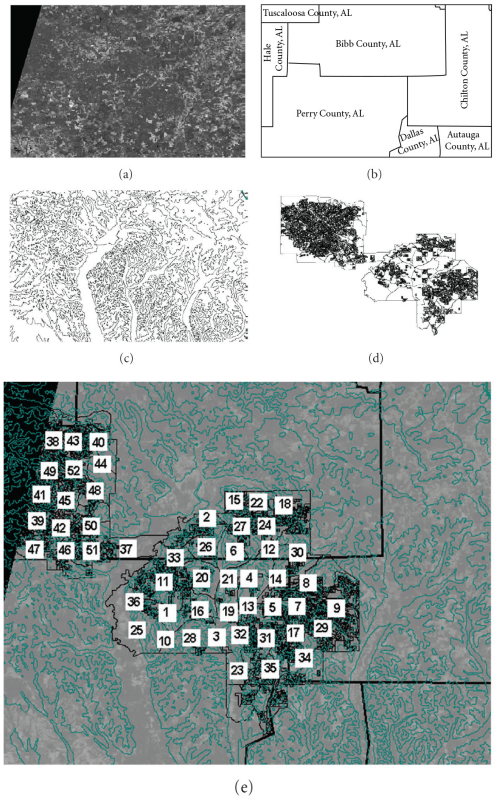


**Figure 5**: Overlaying and sampling process for Oakmulgee National Forest: (a) Landsat TM image, (b) counties, roads, and city locations (c) DLGs, (d) forest stands, and (e) overall layers and samples.

Information was then collected for each sample including size class (sawtimber, poletimber, saplings), species groups (hardwood and softwood), age, and elevation using the national forests vector GIS data obtained from the Forest Service and the digital elevations GIS data obtained from the Earth Resources Observation Systems (EROS) Data Center. For each sample, the percentage of each size class and species group was determined using the digital map of the national forest based on the area covered by each size class and species group in the GIS. Also, the average elevation for each sample was determined using the Digital Line Graph (DLG) data in the GIS. Table 2 shows the *in situ* forest data and the average elevations for all samples collected from all the study area. The raster (TM) data of the area were then imported to the GIS module, ICAMS, where the spatial analytical

techniques of fractals and autocorrelation were conducted and the spatial indices of FD and Moran's I were found. Figure 6 shows an example of two subset images from TM Band 1 and their associated FD and Moran's I. The FD and Moran's I values were found for all bands of Landsat TM and for all 52 samples. The averages of FD and Moran's I for each sample were then calculated using the results of all Landsat TM bands except the thermal Band 6. Finally, the results were analyzed in terms of the relationships between the image complexity indices and the forest characteristics.

**Table 2**: *In situ* forest data of Oakmulgee National Forest, AL, USA

| Sample no. | *Size classes | | | Species | | Evaluation (m) |
|---|---|---|---|---|---|---|
| | Sawtimber (%) | poletimber (%) | Saplings (%) | Hardwood (%) | Softwood (%) | |
| 1 | 65 | 1 | 34 | 26 | 74 | 120 |
| 2 | 85 | 11 | 4 | 50 | 50 | 90 |
| 3 | 83 | 10 | 7 | 43 | 57 | 105 |
| 4 | 83 | 10 | 7 | 43 | 57 | 143 |
| 5 | 74 | 7 | 19 | 38 | 62 | 143 |
| 6 | 77 | 9 | 14 | 41 | 59 | 165 |
| 7 | 79 | 10 | 11 | 36 | 64 | 161 |
| 8 | 70 | 6 | 24 | 31 | 69 | 135 |
| 9 | 77 | 9 | 14 | 41 | 59 | 165 |
| 10 | 27 | 0 | 73 | 22 | 78 | 113 |
| 11 | 82 | 10 | 8 | 36 | 64 | 126 |
| 12 | 70 | 6 | 24 | 30 | 70 | 170 |
| 13 | 77 | 9 | 14 | 36 | 64 | 120 |
| 14 | 94 | 6 | 0 | 75 | 25 | 135 |
| 15 | 60 | 0 | 40 | 24 | 76 | 120 |
| 16 | 86 | 14 | 0 | 49 | 51 | 129 |
| 17 | 86 | 14 | 0 | 52 | 48 | 162 |
| 18 | 69 | 6 | 25 | 33 | 67 | 135 |
| 19 | 80 | 10 | 10 | 41 | 59 | 120 |
| 20 | 86 | 12 | 2 | 47 | 53 | 145 |
| 21 | 95 | 5 | 0 | 77 | 23 | 143 |
| 22 | 49 | 0 | 51 | 0 | 100 | 144 |
| 23 | 86 | 13 | 1 | 44 | 56 | 114 |
| 24 | 74 | 8 | 18 | 39 | 61 | 165 |

| | | | | | | |
|---|---|---|---|---|---|---|
| 25 | 88 | 12 | 0 | 56 | 44 | 90 |
| 26 | 67 | 3 | 30 | 33 | 67 | 165 |
| 27 | 14 | 0 | 86 | 8 | 92 | 156 |
| 28 | 0 | 0 | 100 | 23 | 77 | 140 |
| 29 | 67 | 5 | 28 | 32 | 68 | 154 |
| 30 | 21 | 0 | 79 | 0 | 100 | 150 |
| 31 | 86 | 13 | 1 | 48 | 52 | 135 |
| 32 | 48 | 0 | 52 | 21 | 79 | 144 |
| 33 | 42 | 0 | 58 | 14 | 86 | 105 |
| 34 | 56 | 0 | 44 | 26 | 74 | 120 |
| 35 | 77 | 9 | 14 | 38 | 62 | 128 |
| 36 | 88 | 12 | 0 | 50 | 50 | 98 |
| 37 | 34 | 0 | 66 | 0 | 100 | 60 |
| 38 | 71 | 7 | 22 | 39 | 61 | 150 |
| 39 | 64 | 0 | 36 | 26 | 74 | 146 |
| 40 | 88 | 12 | 0 | 73 | 27 | 123 |
| 41 | 70 | 7 | 23 | 37 | 63 | 143 |
| 42 | 90 | 10 | 0 | 52 | 48 | 105 |
| 43 | 47 | 0 | 53 | 19 | 81 | 135 |
| 44 | 52 | 0 | 48 | 28 | 72 | 110 |
| 45 | 57 | 0 | 43 | 22 | 78 | 125 |
| 46 | 72 | 7 | 21 | 32 | 68 | 115 |
| 47 | 82 | 10 | 8 | 42 | 58 | 110 |
| 48 | 90 | 10 | 0 | 74 | 26 | 126 |
| 49 | 65 | 3 | 32 | 29 | 7 | 143 |
| 50 | 64 | 0 | 36 | 27 | 73 | 114 |
| 51 | 76 | 8 | 16 | 37 | 63 | 115 |
| 52 | 58 | 0 | 42 | 25 | 75 | 120 |

*Sawtimber: diameter at breast height (DBH) > 9 inch, poletimber: DBH = 5–8.9 inch, and saplings: DBH = 1–4.9 inch.

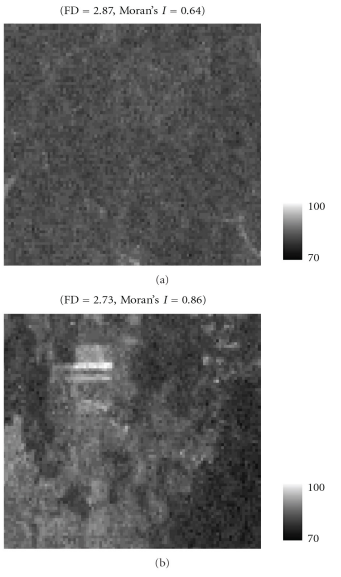


**Figure 6**: Two subset images from TM Band 1 and their associated FD and Moran's .

# RESULTS

## Analysis of Variance (ANOVA) Tests

First, the ability of the spatial complexity indices to distinguish between the different size classes and species groups was examined. ANOVA is a technique that is useful to test for the equality of several means simultaneously. It is a method for splitting the total variation of the data into meaningful components that measure different sources of variation [73]. One-way ANOVA is analysis of variance when there is one independent variable while two-way ANOVA is analysis of variance when there are two independent variables.

To study the effectiveness of remote sensing analytical techniques to distinguish between two size classes (i.e., two independent factors) and also between two species groups, a number of two-way ANOVA tests [73], were conducted using the average spatial analytical indices (i.e., FD, Moran's I) as the dependent factor and the tree size classes or species groups as the independent factor. Rejecting the null hypothesis that the column effects are

equal to zero means rejecting the hypothesis that there is no difference in the percentages of the two size classes or the two species groups. As discussed previously, the average values of FD and Moran's I were computed from the samples using the results of all TM bands except band 6 (thermal infrared).

Two-way ANOVA tests were conducted for two of the size classes at a time. The significance level was chosen to be 0.05 in order to be consistent with the research literature in the areas of remote sensing and land characterization [47, 51, 74, 75]. The first test rejected the null hypothesis of no difference between the percentages of sawtimber and poletimber classes at the 0.05 significance level using the average FD as the dependent variable. Similarly, ANOVA rejected the null hypothesis of the percentage of trees in the sawtimber and saplings size classes using the average FD. ANOVA also rejected the null hypothesis for the percentage of trees in the poletimber and saplings size classes using the average FD at the 0.05 level. Thus, it appears from these results that there is sufficient fidelity in the FD computed from the TM data that one can distinguish between timber size classes with a reasonable degree of statistical confidence.

The same battery of tests was also run using the average Moran's I as the dependent variable with similar results. The two-way ANOVA test results appear to show that Moran's I values computed from TM data can also be employed to distinguish between timber size classes with reasonable statistical confidence.

Two-way ANOVA tests were also conducted using different species (i.e., softwood and hardwood) as the independent factors. The tests rejected the null hypothesis of no difference in percentage of hardwood and softwood trees in the samples using both the FD and Moran's I as dependent variables at the 0.05 significance level.

## Regression Analyses

The FD is plotted against the percentage of forest trees in each class category in Figures 7 through 9. First, the figures demonstrate that the FD has definite boundaries depending on the percentage of trees in the larger (sawtimber) and smaller (saplings) classes. The maximum FD is 2.89 for a sample with a saplings percentage of 0% and sawtimber percentage of 90%. Conversely, the minimum FD was 2.67 for a sample with a sapling percentage of 66% and sawtimber percentage of 34%. The figures also illustrate that the FD

remains fairly constant around the value of 2.7 for samples with either greater than 50% saplings or less than 50% sawtimber. These observations are consistent with the reasoning outlined earlier, that is, trees with smaller crown widths will produce more homogeneous canopies (smaller FD) than will trees with larger crown widths. It appears from these results that when the percentage of smaller trees (saplings) within the forest becomes greater than 50%, then the canopy image becomes so homogeneous that the lower fractal bound is reached. Thus, the FD cannot be determinative for sapling percentages beyond 50%.

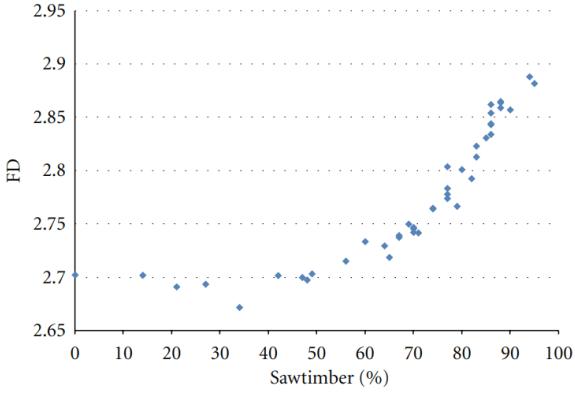


**Figure 7**: FD versus sawtimber.

However, in the region between the boundaries, there appears to be a fairly linear relationship between the FD and the percentage of class category. Samples with greater than 50% saplings or less than 50% sawtimber were excluded from the data set (a total of 10 samples) and linear functions were fitted to the remaining data as shown in Figures 10–12. Both Figures 8 and 11 show that there is considerable more scatter in the poletimber data than is present in the other two classifications. This observation is also consistent with the general concept discussed previously in that the poletimber represents a forest structure that is dominated by neither small trees nor large trees and thus these samples would demonstrate a greater range of image complexity (and greater variation in FD) than would the sawtimber or saplings samples.

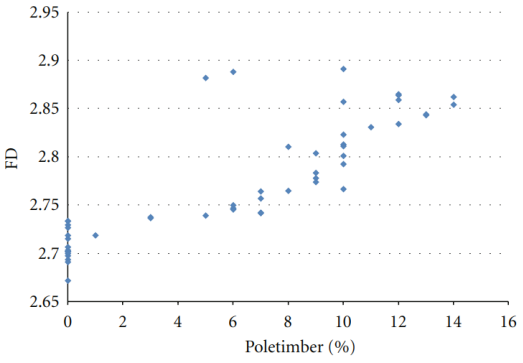


**Figure 8**: FD versus poletimber.

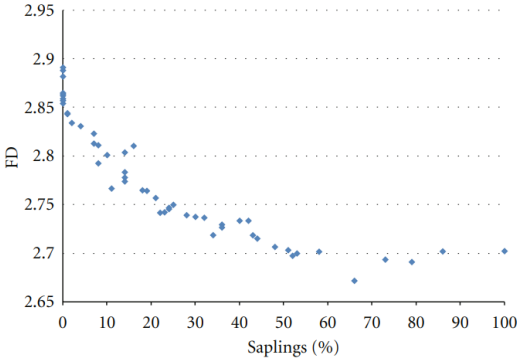


**Figure 9**: FD versus saplings.

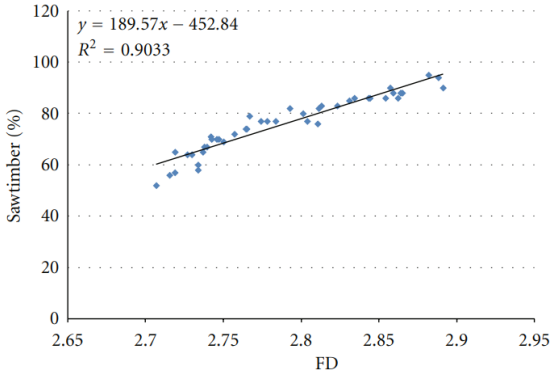


**Figure 10**: FD versus sawtimber (bounds excluded).

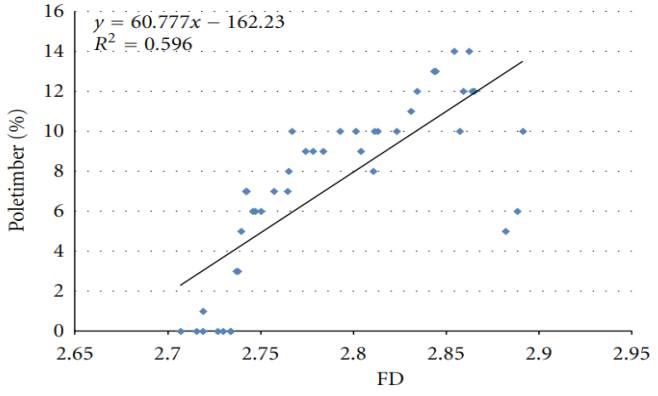


**Figure 11**: FD versus poletimber (bounds excluded).

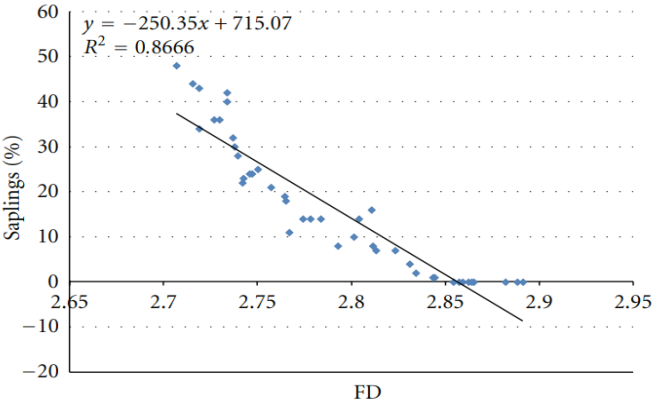


**Figure 12**: FD versus saplings (bounds excluded).

The situation is similar in the case of Moran's I statistic (Figures 13–15). Again, the statistic appears to demonstrate definite bounds with a maximum of about 0.9 for samples with greater than 50% saplings and a minimum of about 0.6 for a sawtimber percentage of 94%. Again, as in the fractals case, there appears to be a fairly linear relationship between Moran's I and the class percentages between the boundaries (Figures 16–18). However, as in the case of fractals, Moran's I cannot be considered a definitive measure of stand density for samples with greater than 50% saplings.

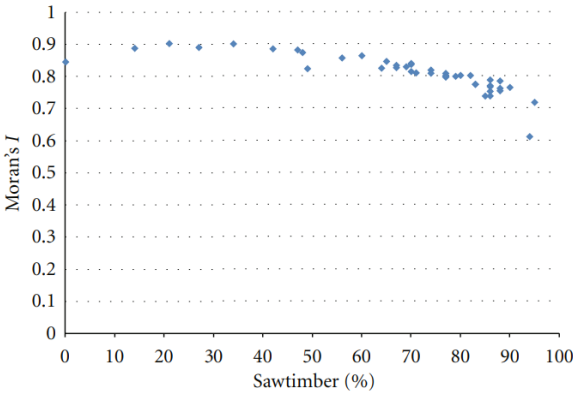


**Figure 13**: Moran's I versus sawtimber.

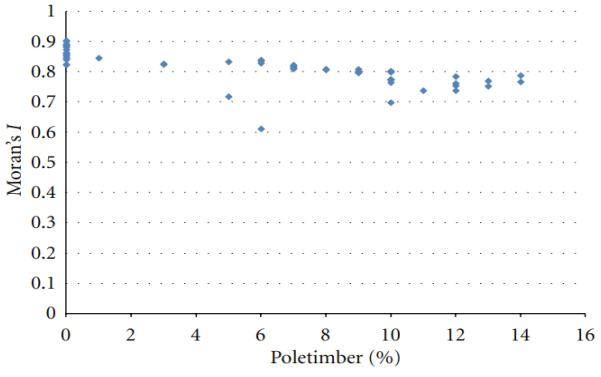


**Figure 14**: Moran's I versus poletimber.

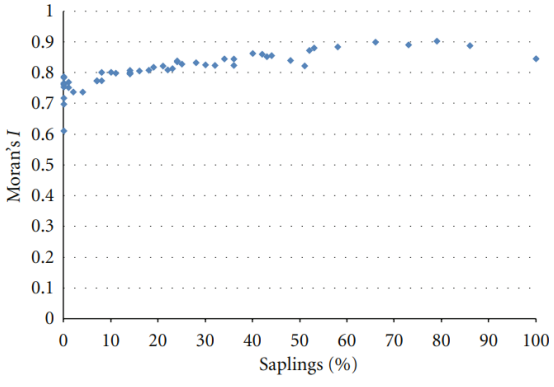


**Figure 15**: Moran's I versus saplings.

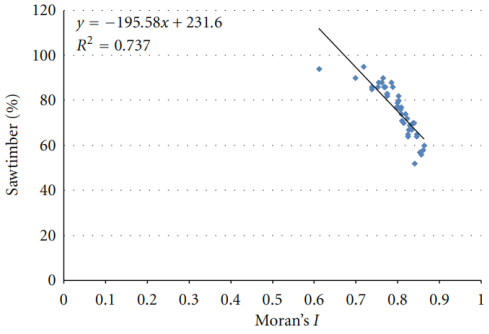


**Figure 16**: Moran's I versus sawtimber (bounds excluded).

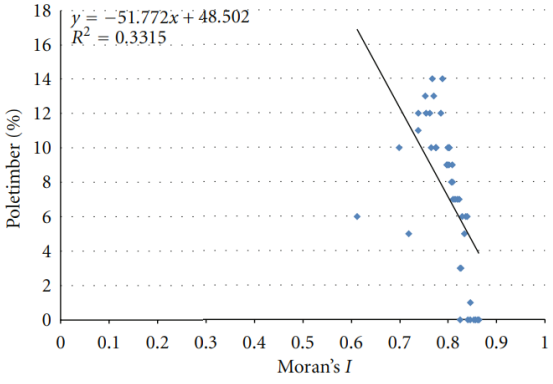


**Figure 17**: Moran's I versus poletimber (bounds excluded).

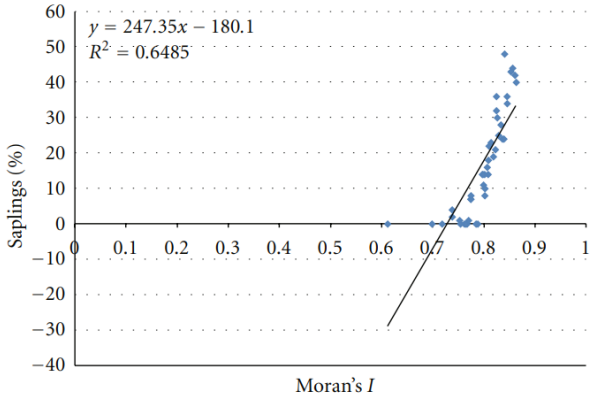


**Figure 18**: Moran's I versus saplings (bounds excluded).

As for the species groups, there appears to be a fairly linear relationship between the FD and the species group percentages as well as between the Moran's I and the species group percentages (Figures 19–22). All the regressions showed an increase (positive slopes) in FD and a decrease (negative slopes) in Moran's I as the hardwood percentages increased while all the regressions showed a decrease (negative slopes) in FD and an increase (positive slopes) in Moran's I as the softwood percentages increased. The explanation is the same as given for the stand sizes case because softwood trees (e.g., Pine trees) are mostly with small crowns, while hardwood trees (e.g., Oak trees) likely have large crowns. As a matter of fact, the species group case had even stronger correlations with the average spatial indices than the DBH case. This can be due to the fact that remote sensing data do not measure DBH directly, but they measure crown reflectivity by satellite sensors. So, for a given species group, the reflectance value recorded by satellite sensors is a function of exposed projection area (canopy closure). The strong relationship between the spatial indices and both types of species groups hardwood and softwood is very important to the potential prediction process of the trunk diameter from the spatial indices, because it suggests that whether the tree is a softwood or a hardwood would not affect the relationship between its trunk size and the spatial indices. In other words, having different species groups would not skew the potential trunk size predictions. Thus, potential forest tree trunk size prediction models would be valid for any species groups.

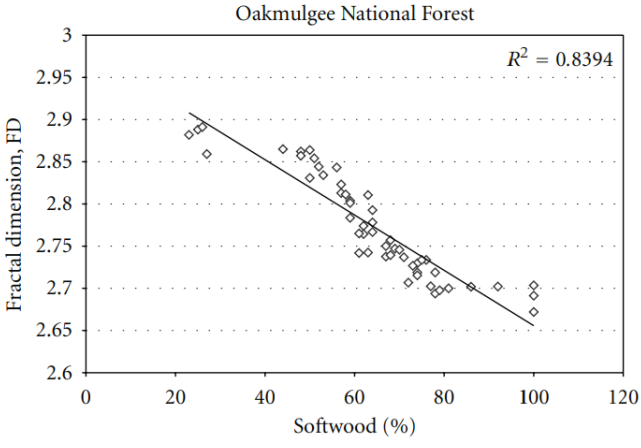


**Figure 19**: FD versus softwood.

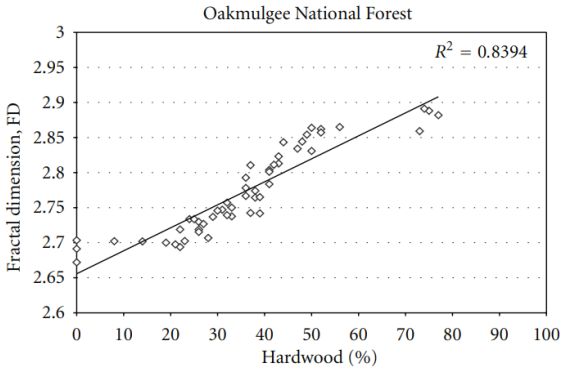


**Figure 20**: FD versus hardwood.

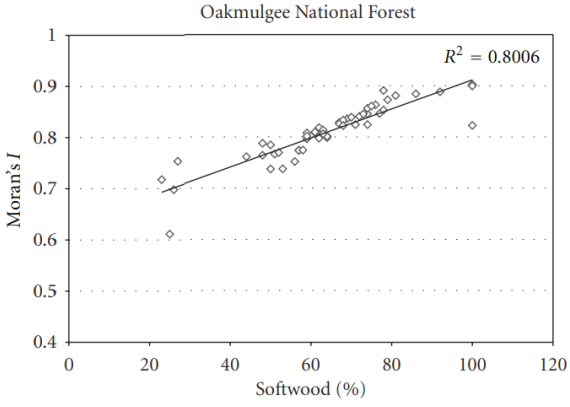


**Figure 21**: Moran's I versus softwood.

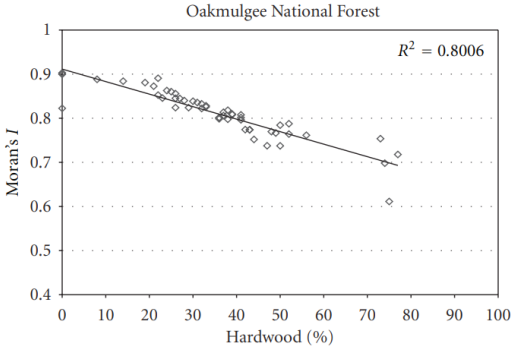


**Figure 22**: Moran's I versus hardwood.

## CONCLUSIONS

The results of the case study presented herein appear to confirm the basic theory pertaining to the application of fractal and spatial analyses to forest canopies. The relationships between image complexity and forest stand characteristics appear to be confirmed up to a point. However, it appears that as the percentage of smaller diameter trees becomes greater, and particularly if it exceeds 50%, then the canopy image obtained from Landsat TM data becomes sufficiently homogeneous so that the spatial indices reach their lower limits and thus are no longer determinative.

It also appears, at least for the Oakmulgee forest, that the relationships between the spatial indices and forest class percentages within the boundaries can reasonably be considered linear. The linear relationship is much more pronounced in the sawtimber and saplings cases than in samples dominated by medium sized trees (poletimber). The large variation in the poletimber data is consistent with the theory of image complexity of forest surfaces as put forth in this work.

From a civil engineering applications perspective, the results indicate that up to a point where smaller trees dominate the landscape, forested areas can be differentiated according to breast sizes and thus important flood plain characteristics such as ratio of obstructed area to total area can be estimated from remotely sensed data. This would facilitate the estimation of hydraulic roughness coefficients (e.g., Manning's n) for computation of flood profiles needed for bridge design. Even in the case where smaller trunks do dominate, then the knowledge of that fact alone would also facilitate the estimation of the required parameters. Likewise, remotely sensed indices such as fractals or Moran's I can distinguish hardwood and softwood species with good accuracy. Thus, forested landscapes can be mapped for preliminary environmental impact analysis.

These results appear to indicate that both fractal dimensions and spatial autocorrelation indices hold promise as means of estimating forest stand characteristics from remotely sensed images. However, additional work is needed to confirm that the boundaries identified for Oakmulgee National Forest and the linear nature of the relationship between image complexity indices and forest characteristics are generally evident in other forests. In addition, the effects of other parameters such as topographic relief and image distortion due to sun angle and cloud cover, for example, need to be examined.

## ACKNOWLEDGMENTS

This work was supported by a grant from the US Department of Transportation "Applications of remote sensing and related spatial technologies to environmental assessments in transportation." The assistance of the project manager, Dr. Roger King of Mississippi State University, and the USDOT program director, Dr. K. Thirumalai is gratefully acknowledged. The authors would also like to thank Dr. Nina Lam of Louisiana State University and Dr. Charles Emerson of Western Michigan University for their assistance.

## REFERENCES

1. F. A. Musleh and J. F. Cruise, "Functional relationships of resistance in wide flood plains with rigid unsubmerged vegetation," *Journal of Hydraulic Engineering*, vol. 132, no. 2, pp. 163–171, 2006.
2. D. S. Rhee, H. Woo, B. A. Kwon, and H. K. Ahn, "Hydraulic resistance of some selected vegetation in open channel flows," *River Research and Applications*, vol. 24, no. 5, pp. 673–687, 2008.
3. D. Poggi, C. Krug, and G. G. Katul, "Hydraulic resistance of submerged rigid vegetation derived from first-order closure models," *Water Resources Research*, vol. 45, no. 10, Article ID W10442, 14 pages, 2009.
4. E. Q. Hui, X. E. Hu, C. B. Jiang, F. K. Ma, and Z. D. Zhu, "A study of drag coefficient related with vegetation based on the flume experiment," *Journal of Hydrodynamics*, vol. 22, no. 3, pp. 329–337, 2010.
5. M. L. R. Sarker and J. E. Nichol, "Biomass estimation using texture measurements of dual polarization SAR data," in *Proceedings of the Remote Sensing and Photogrammetry Society Conference*, May, 2010.
6. R. M. Lucas, A. A. Held, S. R. Phinn, and S. Saatchi, "Tropical forests," in *Remote Sensing for Natural Resource Management and Environmental Monitoring*, S. L. Ustin, Ed., pp. 239–315, John Wiley & Sons, Hoboken, NJ, USA, 2004.
7. J. R. Santos, M. S. PardiLacruz, L. S. Araujo, and M. Keil, "Savanna and tropical rainforest biomass estimation and spatialization using JERS-1 data," *International Journal of Remote Sensing*, vol. 23, no. 7, pp. 1217–1229, 2002.
8. J. R. Santos, C. C. Freitas, L. S. Araujo et al., "Airborne P-band SAR applied to the aboveground biomass studies in the Brazilian tropical rainforest," *Remote Sensing of Environment*, vol. 87, no. 4, pp. 482–493, 2003.
9. J. E. S. Fransson and H. Israelsson, "Estimation of stem volume in boreal forests using ERS-1 C- and JERS-1 L-band SAR data," *International Journal of Remote Sensing*, vol. 20, no. 1, pp. 123–137, 1999.
10. K. J. Ranson and G. Sun, "An evaluation of AIRSAR and SIR-C/X-SAR images for mapping northern forest attributes in Maine, USA," *Remote Sensing of Environment*, vol. 59, no. 2, pp. 203–222, 1997.
11. P. A. Harrell, L. L. Bourgeau-Chavez, E. S. Kasischke, N. H. F. French,

and N. L. Christensen, "Sensitivity of ERS-1 and JERS-1 radar data to biomass and stand structure in Alaskan boreal forest," *Remote Sensing of Environment*, vol. 54, no. 3, pp. 247–260, 1995.

12. J. E. Nichol and M. L. R. Sarker, "Efficiency of texture measurement from two optical sensors from improved biomass estimation," in *Proceedings of the 7th ISPRS TC Symposium—100 Years ISPRS*, W. Wagner and B. Székely, Eds., vol. 38 of *IAPRS*, Vienna, Austria, July, 2010.
13. T. Kajisa, T. Murakami, N. Mizoue, N. Top, and S. Yoshida, "Object-based forest biomass estimation using Landsat ETM+ in Kampong Thom Province, Cambodia," *Journal of Forest Research*, vol. 14, no. 4, pp. 203–211, 2009.
14. D. Lu, "Aboveground biomass estimation using Landsat TM data in the Brazilian Amazon," *International Journal of Remote Sensing*, vol. 26, no. 12, pp. 2509–2525, 2005.
15. A. Baccini, M. A. Friedl, C. E. Woodcock, and R. Warbington, "Forest biomass estimation over regional scales using multisource data," *Geophysical Research Letters*, vol. 31, no. 10, Article ID L10501, 4 pages, 2004.
16. O. N. Krankina, M. E. Harmon, W. B. Cohen, D. R. Oetter, Z. Olga, and M. V. Duane, "Carbon stores, sinks, and sources in forests of northwestern Russia: can we reconcile forest inventories with remote sensing results?" *Climatic Change*, vol. 67, no. 2-3, pp. 257–272, 2004.
17. D. P. Turner, M. Guzy, M. A. Lefsky, W. D. Ritts, S. van Tuyl, and B. E. Law, "Monitoring forest carbon sequestration with remote sensing and carbon cycle modeling," *Environmental Management*, vol. 33, no. 4, pp. 457–466, 2004.
18. G. M. Foody, D. S. Boyd, and M. E. J. Cutler, "Predictive relations of tropical forest biomass from Landsat TM data and their transferability between regions," *Remote Sensing of Environment*, vol. 85, no. 4, pp. 463–474, 2003.
19. Å Rosenqvist, A. Milne, R. Lucas, M. Imhoff, and C. Dobson, "A review of remote sensing technology in support of the Kyoto Protocol," *Environmental Science and Policy*, vol. 6, no. 5, pp. 441–455, 2003.
20. J. Dong, R. K. Kaufmann, R. B. Myneni et al., "Remote sensing

estimates of boreal and temperate forest woody biomass: carbon pools, sources, and sinks," *Remote Sensing of Environment*, vol. 84, no. 3, pp. 393–410, 2003.

21. R. F. Nelson, D. S. Kimes, W. A. Salas, and M. Routhier, "Secondary forest age and tropical forest biomass estimation using thematic mapper imagery," *BioScience*, vol. 50, no. 5, pp. 419–431, 2000.
22. T. Häme, A. Salli, K. Andersson, and A. Lohi, "A new methodology for the estimation of biomass of conifer-dominated boreal forest using NOAA AVHRR data," *International Journal of Remote Sensing*, vol. 18, no. 15, pp. 3211–3243, 1997.
23. G. L. Anderson, J. D. Hanson, and R. J. Haas, "Evaluating landsat thematic mapper derived vegetation indices for estimating above-ground biomass on semiarid rangelands," *Remote Sensing of Environment*, vol. 45, no. 2, pp. 165–175, 1993.
24. P. J. Curran, J. L. Dungan, and H. L. Gholz, "Seasonal LAI in slash pine estimated with landsat TM," *Remote Sensing of Environment*, vol. 39, no. 1, pp. 3–13, 1992.
25. M. Al-Hamdan, J. Cruise, D. Rickman, and D. Quattrochi, "Effects of spatial and spectral resolutions on fractal dimensions in forested landscapes," *Remote Sensing*, vol. 2, no. 3, pp. 611–640, 2010.
26. D. A. Quattrochi, C. W. Emerson, N. S.-N. Lam, and H. L. Qiu, "Fractal characterization of multitemporal remote sensing data," in *Modeling Scale in Geographic Information Science*, N. J. Tate and P. M. Atkinson, Eds., pp. 13–33, John Wiley & Sons, Hoboken, NJ, USA, 2001.
27. M. Goodchild, R. Haining, and S. Wise, "Integrating GIS and spatial data analysis: problems and possibilities," *International Journal of Geographical Information Systems*, vol. 6, no. 5, pp. 407–423, 1992.
28. W. Zhao, *Multiscale analysis for characterization of remotely sensed images*, Ph.D. dissertation, Louisiana State University, Baton Rouge, La, USA, 2001.
29. S. Lovejoy and D. Schertzer, "Generalized scale invariance in the atmosphere and fractal models of rain," *Water Resources Research*, vol. 21, no. 8, pp. 1233–1250, 1985.
30. J. R. Krummel, R. H. Gardner, G. Sugihara, R. V. O'Neill, and P. R. Coleman, "Landscape patterns in a disturbed environment," *Oikos*, vol. 48, no. 3, pp. 321–324, 1987.
31. M. J. MacLennan and P. J. Howarth, "The use of fractal geometry

to identify ranges of scale variance in digital remotely sensed data," in *Proceedings of the 21st International Symposium on Remote Sensing Environment*, Ann Arbor, Mich, USA, October 1987.

32. M. W. Palmer, "Fractal geometry: a tool for describing spatial patterns of plant communities," *Vegetatio*, vol. 75, no. 1-2, pp. 91–102, 1988.
33. W. B. Cohen, T. A. Spies, and G. A. Bradshaw, "Semivariograms of digital imagery for analysis of conifer canopy structure," *Remote Sensing of Environment*, vol. 34, no. 3, pp. 167–178, 1990.
34. B. Zeide, "Fractal geometry in forestry applications," *Forest Ecology and Management*, vol. 46, no. 3-4, pp. 179–188, 1991.
35. N. D. Lorimer, R. G. Haight, and R. A. Leary, "The fractal forest: fractal geometry and applications in forest science," *General Technical Report* NC-170, US Department of Agriculture, Forest Service, North Central Forest Experiment Station, St. Paul, Minn, USA, 1994.
36. B. A. St-Onge and F. Cavayas, "Automated forest structure mapping from high resolution imagery based on directional semivariogram estimates," *Remote Sensing of Environment*, vol. 61, no. 1, pp. 82–95, 1997.
37. B. Barbanis, H. Varvoglis, and C. L. Vozikis, "Imperfect fractal repellers and irregular families of periodic orbits in a 3-D model potential," *Astronomy and Astrophysics*, vol. 344, no. 3, pp. 879–890, 1999.
38. N. Coops and D. Culvenor, "Utilizing local variance of simulated high spatial resolution imagery to predict spatial pattern of forest stands," *Remote Sensing of Environment*, vol. 71, no. 3, pp. 248–260, 2000.
39. J. F. Weishampel, D. L. Urban, and H. H. Shugart, "Semivariograms from a forest transect gap model compared with remotely sensed data," *Journal of Vegetation Science*, vol. 3, no. 4, pp. 521–526, 1992.
40. J. F. Weishampel, J. H. Sloan, J. C. Boutet, and J. R. Godin, "Mesoscale changes in textural pattern of "intact" Peruvian rainforests (1970s–1980s)," *International Journal of Remote Sensing*, vol. 19, no. 5, pp. 1007–1014, 1998.
41. J. F. Weishampel, J. R. Godin, and G. M. Henebry, "Pantropical dynamics of "intact" forest canopy texture," *Global Ecology and Biogeography*, vol. 10, no. 4, pp. 389–397, 2001.
42. J. B. Drake and J. F. Weishampel, "Simulating vertical and horizontal

multifractal patterns of a longleaf pine savanna," *Ecological Modelling*, vol. 145, no. 2-3, pp. 129–142, 2001.

43. C. W. Emerson, N. S.-N. Lam, and D. A. Quattrochi, "A comparison of local variance, fractal dimension, and Moran's *I* as aids to multispectral image classification," *International Journal of Remote Sensing*, vol. 26, no. 8, pp. 1575–1588, 2005.
44. N. S.-N. Lam, H. L. Qiu, D. A. Quattrochi, and C. W. Emerson, "An evaluation of fractal methods for characterizing image complexity," *Cartography and Geographic Information Science*, vol. 29, no. 1, pp. 25–35, 2002.
45. B. B. Mandelbort, *The Fractal Geometry of Nature*, W. H. Freeman, New York, NY, USA, 1983.
46. M. F. Goodchild, "Fractals and the accuracy of geographical measures," *Mathematical Geology*, vol. 12, no. 2, pp. 85–98, 1980.
47. C. W. Emerson, N. S.-N. Lam, and D. A. Quattrochi, "Multi-scale fractal analysis of image texture and pattern," *Photogrammetric Engineering and Remote Sensing*, vol. 65, no. 1, pp. 51–61, 1999.
48. M. C. Shelberg, N. S.-N. Lam, and H. Moellering, "Measuring the fractal dimensions of surfaces," in *Proceedings of the 6th International Symposium on Automated Cartography*, pp. 319–328, Ottawa, Canada, October 1983.
49. N. S.-N. Lam and L. De Cola, Eds., *Fractals in Geography*, Prentice Hall, Englewood Cliffs, NJ, USA, 1993.
50. S. Jaggi, D. A. Quattrochi, and N. S.-N. Lam, "Implementation and operation of three fractal measurement algorithms for analysis of remote-sensing data," *Computers & Geosciences*, vol. 19, no. 6, pp. 745–767, 1993.
51. D. C. Bragg, "A local basal area adjustment for crown width prediction," *Northern Journal of Applied Forestry*, vol. 18, no. 1, pp. 22–28, 2001.
52. D. Oladi, *Developing a framework and methodology for plantation assessment using remotely sensed data*, Ph.D. thesis, University of New Brunswick, New Brunswick, Canada, 1996.
53. J. Guavin, T. Hunt, and R. Tardif, "Edmondstone Applied Forestry Technology Group," Documentation on Growth Phase Model, 1993.
54. W. A. Farr, D. J. Demars, and J. E. Dealy, "Height and crown width related to diameter for open-grown western hemlock and Sitka

spruce," *Canadian Journal of Forest Research*, vol. 19, no. 9, pp. 1203–1207, 1989.

55. P. T. Sprinz and H. E. Burkhart, "Relationships between tree crown, stem, and stand characteristics in unthinned loblolly pine plantation," *Canadian Journal of Forest Research*, vol. 17, pp. 534–538, 1987.
56. E. G. Roberts and R. D. Ross, "Crown area of free-growing loblolly pine and its apparent independence of age and site," *Journal of Forestry*, vol. 63, no. 6, pp. 462–463, 1965.
57. B. C. Wile, "Crown size and stem diameter in red spruce and balsam fir," *Forestry Pub.* 1056, Canada Department of Forestry. Forestry Research Branch, Ontario, Canada, 1964.
58. J. H. Smith and G. R. Baily, "Influence of stocking and stand density on crown widths of douglas fir and lodgepole pine," *Commonwealth Forestry Review*, vol. 43, no. 3, pp. 243–246, 1964.
59. P. E. Vezina, "More about the crown competition factor," Department of Forestry. Forest Research Branch, Contribution No. 505, 1963.
60. C. O. Minor, "Stem-crown diameter relations in southern pine," *Journal of forestry*, vol. 49, no. 7, pp. 490–493, 1951.
61. A. D. Cliff and J. K. Ord, *Spatial Autocorrelation*, Pion Limited, London, UK, 1973.
62. N. S.-N. Lam, D. A. Quattarochi, H.-L. Qiu, and W. Zhao, "Environmental assessment and monitoring with image characterization and modeling system using multi-scale remote sensing data," *Applied Geography Studies*, vol. 2, no. 2, pp. 77–93, 1998.
63. D. A. Quattrochi, N. S.-N. Lam, H. L. Qiu, and W. Zhao, "Image characterization and modeling system (ICAMS): a geographic information system for the characterization and modeling of multiscale remote sensing data," in *Scale in Remote Sensing and GIS*, D. A. Quattroch and M. F. Goodchild, Eds., pp. 295–307, CRC/Lewis Publishers, Boca Raton, Fla, USA, 1997.
64. P. A. Burrough, "Fractals and geostatistical methods in landscape studies," in *Fractals in Geography*, N. S.-N. Lam, L. De Cola et al., Eds., pp. 87–121, Prentice Hall, Englewood Cliffs, NJ, USA, 1993.
65. D. M. Mark and P. B. Aronson, "Scale-dependent fractal dimensions of topographic surfaces: an empirical investigation, with applications in geomorphology and computer mapping," *Mathematical Geology*, vol.

16, no. 7, pp. 671–683, 1984.

66. M. F. Goodchild, *Spatial Autocorrelation, Concepts and Techniques in Modern Geography*, 47, Geo Books, Norwich, UK, 1986.
67. N. S.-N. Lam, M. Fan, and K. B. Liu, "Spatial-temporal spread of the AIDS epidemic, 1982–1990: a correlogram analysis of four regions of the United States," *Geographical Analysis*, vol. 28, no. 2, pp. 93–107, 1996.
68. C. E. Woodcock and A. H. Strahler, "The factor of scale in remote sensing," *Remote Sensing of Environment*, vol. 21, no. 3, pp. 311–332, 1987.
69. K. C. Clarke, "Computation of the fractal dimension of topographic surfaces using the triangular prism surface area method," *Computers & Geosciences*, vol. 12, no. 5, pp. 713–722, 1986.
70. N. S.-N. Lam, H.-L. Qiu, and D. Quattrochi, "An evaluation of fractal surface measurement methods using ICAMS (Image Characterization and Modeling System)," in *Proceedings of the ACSM/ASPRS Annual Convention*, Seattle, Wash, USA, April 1997.
71. S. W. Myint, *Wavelet analysis and classification of urban environment using high-resolution multispectral image data*, Ph.D. dissertation, Louisiana State University, Baton Rouge, La, USA, 2001.
72. R. E. Walpole, R. H. Myers, and S. L. Myers, *Probability and Statistics for Engineers and Scientists*, Macmillan Publishing, New York, NY, USA, 1998.
73. R. E. Walpole, *Introduction to Statistics*, Macmillan Publishing, New York, NY, USA, 1982.
74. M. A. Lefsky, *Lidar remote sensing of canopy height profiles: application to spatial and temporal trends in canopy structure*, Ph.D. thesis, The University of Virginia, Charlottesville, Va, USA, 1997.
75. S. E. Watts, *Determining forest productivity and carbon dyanamics in Southeastern Ohio from remotely-sensed data*, Ph.D. dissertation, The Ohio State University, Columbus, Ohio, USA, 2001.

# 12

# *Application of Fractal Algorithms of Coastline Echo's Generation on Marine Radar Simulator*

**Shuguang Ji[1], Zhang Zhang[2], Hongbiao Yang[1], Dan Liu[3] and Rapinder Sawhney[1]**

[1]University of Tennessee, 37996 Knoxville TN, USA
[2]Tangshan Maritime Safety Administration of People's Republic of China, 100736 Tangshan, China
[3]Department of Audio, Visual and Image Technology, National Police University of China, 100038 Shenyang, China

## ABSTRACT

### Background

Marine radar simulator is a useful approach endorsed by International Maritime Organization (IMO) to train the seafarers on how to operate marine radar equipment and use marine radar equipment for positioning and collision avoidance in laboratory. To fulfill all of the marine radar simulator

**Citation:** Ji, S., Zhang, Z., Yang, H., Liu, D., &Sawhney, R. (2016). Application of fractal algorithms of coastline echo's generation on marine radar simulator. Visualization in Engineering, 4(1), 8.,DOI: 10.1186/s40327-016-0037-7.

training requirements, a high performance simulator is necessary. However, imperfections with currently available marine radar simulators require simulator developers to make improvements.

### Case description

In this study, improved fractal algorithms (random Koch curve, fractional Brownian motion, and Weierstrass-Mandelbrot function) are applied to generate natural-looking radar echoes on a marine radar simulator.

### Discussion and evaluation

From the results of the simulations, we can observe that the structures of the coastline echoes generated by improved fractal algorithms, especially by fractional Brownian motion algorithm, outperform the echoes generated by conventional method in representing a natural coastline feature.

### Conclusions

Based on evaluations from a panel of experienced mariners, we conclude that the coastline echoes simulated by fractal algorithms better represent a natural coastline feature than those generated by conventional methods.

## BACKGROUND

The International Convention on Standards of Training, Certification and Watchkeeping for Seafarers 78/95 (STCW Convention 78/95) of International Maritime Organization (IMO) requires using a marine radar simulator to train seafarers. A marine radar simulator is the only acceptable approach in the laboratory for seafarers to learn how to operate radar equipment and use radar for positioning, navigation, and anti-collision. Upon completing all requirements set forth in the training, the trainee will receive certification for qualifications to work on board. Currently, marine radar simulators are widely used by the members of IMO as one of many useful tools for seafarer education and training (Ali 2006; Organization 2006; Teel et al. 2009; Xiuwen et al. 2010). However, due to the limitation of the simulation technology, the marine radar simulators on the market are unable to replicate the performance of real radar equipment. Taking the simulation of coastline echoes as an example, the coastline echo is generated by raw data, which are acquired from the digitalized chart and consist of a collection of coordinate

points. By connecting two adjacent coordinate points, a straight line is generated to approximate a real coastline echo. This method works well for generating a coastline echo under a large radar range (say 6 nautical miles (NM)). However, when the radar range is adjusted to a smaller radar range (such as 0.25 NM), the shape of coastline echo will lose its natural structure and look quite artificial (Ji et al. 2015; Zhang 2007). In addition, it should take around three seconds for the scan line of the marine radar to rotate a round. By adopting a traditional generation method for the coastline echo under small radar range, the time for the scan line to rotate around is much more likely to exceed three seconds, since extra sampling coordinate points (if available) have to be inserted to generate a high quality coastline echo. Imperfections like the artificial coastline shape and slow rotation of the radar scan line may have negative impacts on the training effectiveness for users (Ji et al. 2015; Zhang 2007). In order to overcome the problems associated with the conventional coastline echo simulation approach, we apply fractal theory to the coastline echo simulation process, since fractal theory is widely used as a graphics tool for generating natural-looking shapes like coastlines, rivers, mountains, and other natural features (Pentland 1984). The simulation results are evaluated and scored by 30 experienced mariners to validate that the coastline echoes generated by fractal algorithms look more natural than those generated by conventional method. Furthermore, an improved fractal algorithm is designed to guarantee the scan line can finish a round of rotation within three seconds, which is difficult to be achieved using the conventional method, especially under a larger radar range.

## LITERATURE REVIEW

The STCW Convention provides required components for seafarer training, which use the radar simulator as a tool of training and assessment. These highlights include (Ali 2006; Organization 2006; Teel et al. 2009): factors affecting performance and accuracy; detection of misrepresentation of information, including false echoes and sea returns; setting up and maintaining displays; range and bearing; plotting techniques and relative motion concepts; identification of critical echoes; course and speed of other ships; time and distance of the closest approach to crossing, meeting or overtaking ships; detecting course and speed changes of other ships; effects on the changes of the own ship's course or speed or both; and application of the International Regulations for Preventing Collisions at Sea. To fulfill all of these training requirements, a high performance marine radar simulator is

needed. In the current marine radar simulator market, the major developing teams include Nautical Software (2016), Bridge Command (2016), Kongsberg Maritime (2016), Landfall (2016), and Dalian Maritime University Institute of Navigational Technology (2016). In addition, some previous research investigates methods to improve the marine radar simulator. For example, Arnold-Bos et al. developed a versatile bistatic and polarimetric marine radar simulator. In their simulator, realistic sea surfaces are generated using the two-scale model on a semi-deterministic basis, so as to incorporate the presence of ship wakes in the simulation (Arnold-Bos et al. 2006). Yin et al. designed a radar simulator using a PC to generate radar echoes and a radar interface board to generate radar signals. Their simulator has a more flexible and realistic operation interface than other simulators (Yin et al. 2007). Zhang et al. put forward a coastline echo intensity algorithm based on RGB and HIS color models and applied this algorithm on the marine radar simulator. The simulation results from this model are consistent with the electronic chart (Zhang et al. 2010).

In this study, we incorporate fractal theory, a branch of non-linear mathematics, to improve coastline echo simulation. The research targets of fractal theory are irregular objects and non-linear systems in the nature. The term "fractal"? was first used by mathematician Benoit Mandelbrot in 1975 to extend the concept of theoretical fractional dimensions to geometric patterns in nature (Mandelbrot 1983). In the 1980s, fractal theory was applied into the signal processing for radar because the echoes reflected into radar system have many fractal patterns (Ji et al. 2015; Zhang 2007). Even though fractal theory has been widely applied in fields such as virtual reality, image processing, and time series analysis, etc. (Ji et al. 2005; Zhang et al. 2005), there are few studies to apply it into the simulation of coastline echo for marine radar simulator. This research aims to close this gap. Partial of findings reported in this article were originally presented at the 94th Transportation Research Board Annual Meeting. We improved the research methodology in Ji et al. (2015) in this article. Especially, a full control of the physical parameters involved fractal function, Weierstrass-Mandelbrot function (WMF), is used to simulate coastline echoes. In addition, a quantitative validation of the simulation results is designed to assess the

fidelity of the simulation outcomes and comprehend possible values of the introduced parameters among the simulation algorithms.

## METHODS

The echo reflection on radar simulator can be classified into three types (Ji et al. 2015; Zhang 2007). A Type I Echo is the echo reflected by artificial architectures such as berth and breakwater. Type I Echoes have regular shape and can be used for positioning because of its clear boundaries and fixed position. A Type II Echo is the echo reflected by rocky coast. Type II Echoes have a realistic pattern as well as fixed position. A Type III Echo is an echo reflected by flat coast such as sand coast. Type III Echoes have a large echo reflection zone and relatively weak reflection. Additionally, the shape and position of a Type III Echo will change with the motion of the waves. This study focuses only on simulation of Type II Coastline Echoes because of its natural fractal features. Three different fractal algorithms are adopted to simulate coastline echoes. A comparison among these three simulation algorithms is included.

### Random Koch Curve Algorithm

The Koch curve was described by Swedish mathematician Helge von Koch in 1904 (Keddam and Takenouti 1988). The curve can be constructed as shown in Fig. 1. First, a straight line is divided into tree equal segments, and an equilateral triangle is raised from the middle third. The resulting line segments are again divided into thirds with an equilateral triangle raised from the middle third of each. This process is repeated through the desired number of iterations (Cross 1994). The length of the Koch curve can be infinite because the total length of the curve increases by one third with each iteration (Baliarda et al. 2000). The dimension of Koch curve is 1.262. This makes us consider Koch curve a candidate to simulate coastlines, since coastlines are fractal curves with dimensions ranging from 1 (very smooth) to 1.5 (very rough)(Aviles and Scholz 1987). From Fig. 1 we can see that the resulting curve is roughly similar to the natural pattern of a coastline.

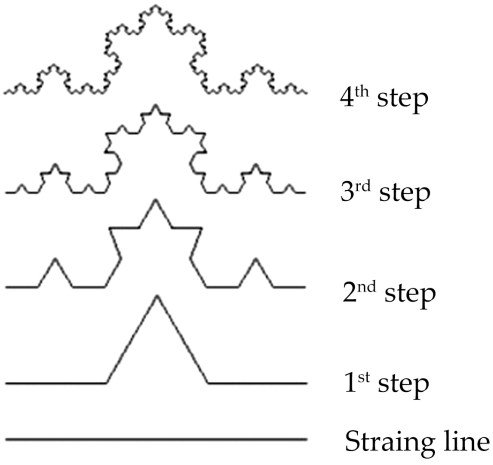


**Figure 1**: Construction of regular Koch curve.

However, the Koch curve generated through this theoretical approach is too regular and symmetric to simulate a coastline echo, since the inlets in real coastlines are similar to each other but not identical. Thus, we incorporate randomness into the regular Koch curve generation process to produce a more natural-looking coastline echo (Ji et al. 2015; Zhang 2007). In order to add randomness into the Koch curve, half of the time, we raise the equilateral triangle from the middle third; half of the time, we bent the equilateral triangle down from the middle third (Filoche and Sapoval 2000). In Fig. 2, Koch curves generated by regular and random methods are compared. When comparing to a naturally forming coastline, the random Koch curve looks more realistic than the regular Koch curve, as the regular Koch curve appears too artificial to exist in a natural environment.

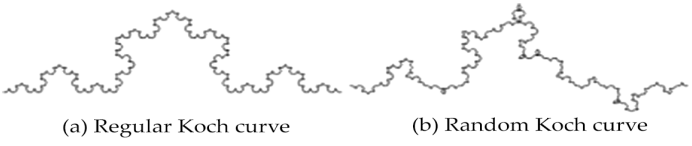


**Figure 2**: Comparison between regular and random Koch curve.

Even though the random Koch curve is an improved method for coastline echo simulation, application of this method without constraints may bring distortion into the simulation process. As long as the distance between two

adjacent sample points is short, the distortion from the simulation of the coastline echo is negligible. However, as the distance between sample points increases, the distortion becomes more noticeable. For example, as shown in Fig. 3, the trend of the simulated coastline echo in the two boxes (shown in Fig. 3 b) is different from the original trend of coastline echo (shown in Fig. 3 a) (Ji et al. 2015; Zhang 2007).

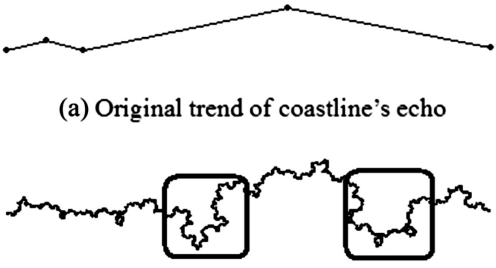


**Figure 3**: Trend distortion from random Koch curve algorithm.

To avoid the above distortion, a control value (c) is introduced into the simulation process (in this study, c =15). Once the distance between two adjacent sample points is shorter than c, the random Koch curve is used directly to simulate the coastline echo between these two adjacent sample points. If this distance is larger than c, several random points are inserted between the sample points to break the original line into smaller segments. Then, the random Koch curve algorithm is applied between new adjacent sample points to simulate the coastline echo. The value c can be adjusted in accordance with computer's performance. We can apply a smaller c value into the random Koch curve algorithm on a high performance computer. As shown in Fig. 4, after adopting a random Koch curve algorithm with a control value, the distortion of the trend of simulated coastline echo is negligible. Also, we notice that there is no obvious improvement between the simulated coastline echoes if the iteration is more than three times based on visual inspection. Therefore, we suggest that three iterations are sufficient for the simulation of the coastline echo by random Koch curve algorithm with control value.

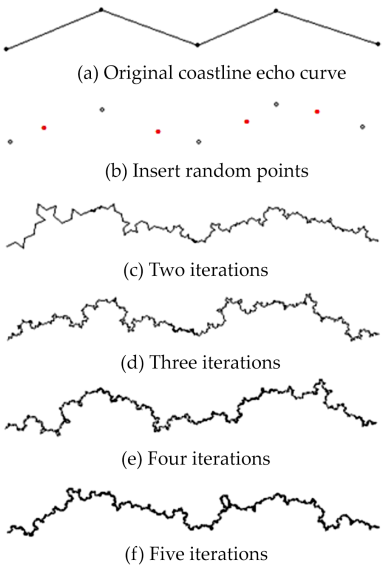


**Figure 4**: Coastline echoes generated by random Koch curve algorithm with control value under different iterations.

## Fractional Brownian MotionAlgorithm

Fractional Brownian Motion (FBM) was introduced by Mandelbrot and van Ness in 1968 (Rostek and Schöbel 2013). We know that Brownian motion, which is also called Wiener process, is a random process (Falconer 2013). If $-\infty<t<\infty$ and $w$ belongs to a set of values of a random function and if the intervals $(t_1,t_2)$ and $(t_3,t_4)$ do not overlap, the ordinary Brownian motion $B(t,w)$ is a real random function with independent Gaussian increments. Therefore, $B(t_2,w)-B(t_1,w)$ has a mean of zero and a variance $|t_2-t_1|$. Also, $B(t_2,w)-B(t_1,w)$ is independent of $B(t_4,w)-B(t_3,w)$. Let $0<H<1$ and $b_0$ be an arbitrary real number. For $t>0$, the random function $B_H(t,w)$ below is called a reduced FBM with Hurst coefficient $H$ and starting value $b_0$ at time 0 (Dieker 2004; Mandelbrot and Van Ness 1968).

$$B_H(t,w)-B_H(0,w)=\frac{1}{\Gamma(H+\frac{1}{2})}\left(\int_{-\infty}^{0}[(t-s)^{H-\frac{1}{2}}-(-s)^{H-\frac{1}{2}}]\,dB(s,w)+\int_{0}^{t}(t-s)^{H-\frac{1}{2}}dB(s,w)\right) \quad (1)$$

where $\Gamma$ represents the Gamma function: $\Gamma(\alpha)=\int_0^\infty x^{\alpha-1}e^{-x}dx$ and $B_H(0,w)=b_0$ (Mandelbrot and Van Ness 1968).

In practice, the random midpoint displacement (RMD) method is used to simulate FBM. By the RMD method, the height of a midpoint between two other points is given by:

$$h_{new} = \frac{1}{2}\left(h_{left} + h_{right}\right) + h_{random} \tag{2}$$

where $h_{random}$ is a random offset. In our simulation, the coordinates of the midpoints are calculated by the formula below (Boyle et al. 2007):

$$x_i^{new} = \frac{1}{2}(x_i + x_{i+1}) + h_i \tag{3}$$

$$y_i^{new} = \frac{1}{2}(y_i + y_{i+1}) + h_i \tag{4}$$

$$h_i = \Delta_i \cdot Gauss(\cdot) = \frac{\sigma}{(2^{2i})^H}\sqrt{1 - 2^{2H-2}} \cdot Gauss(\cdot) \tag{5}$$

where $\sigma$ is the standard deviation of the heights of sample points. $H$ is Hurst index and $G\ a\ u\ s\ s(\cdot)$ is a random number generated by standard normal distribution which has a mean of zero and a standard deviation of one. The curves generated by the RMD method under different Hurst coefficients are shown in Fig. 5. The dimension of a fractal curve generated by RMD method equals to $2-H$ (Huang et al. 1992). As we mentioned above, the dimensions of coastlines range from 1 to 1.5. Therefore, we can select Hurt coefficient in the range of 0.5 and 1 to simulate coastline by RMD method. In this study, Hurst coefficient is set to 0.6.

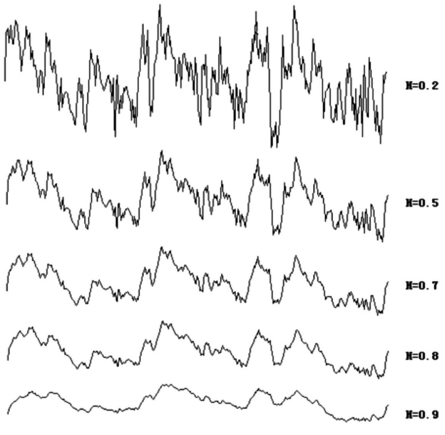


**Figure 5**: The curves generated by FBM algorithm with different Hurst coefficient.

Figure 6 a is the coastline echo generated by the conventional method. The results shown in the other subfigures of Fig. 6 are the coastline echoes generated by FBM method ($H$=0.6) under a different number of iterations. It can be seen that the FBM method works better than the conventional method in terms of coastline echo simulation since more details are provided and the shape is approximate to a real coastline. In addition, we notice that there are no obvious differences between the coastline echoes with more than three iterations via visual inspection. We suggest that three iterations are sufficient for coastline echo simulation by the FBM method as well.

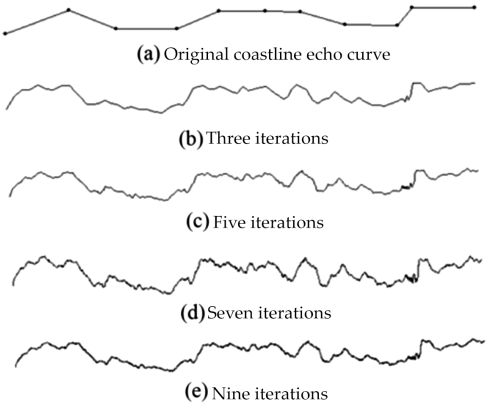


**Figure 6**: Coastline echoes generated by FBM algorithm under different iterations ($H$ =0.6).

## Weierstrass-Mandelbrot Function Algorithm

In 1872, German mathematician Karl Weierstrass devised a function, that is continuous everywhere but differentiable nowhere. This function is called Weierstrass function. The Weierstrass function is defined as:

$$f(t) = \sum_{n=0}^{\infty} a^n cos(b^n \pi t)$$

where $0<a<1$, $b$ is a positive odd integer, and $a\,b>1+1.5\varpi$ (Weierstrass 1967; Zhang et al. 2015). In 1977, Mandelbrot extended the Weierstrass function to the following form,which is called Weierstrass-Mandelbrot function. He also pointed out that the WMF is a fractal and has no smallest scale (Berry

and Lewis 1980; Mandelbrot 1979). WMF has been widely adopted to simulate various phenomena in real world (Harrouni 2008; Ma et al. 2015; Shanhua et al. 2015; Wang et al. 2015; Zhang et al. 2015).

$$W(t) = \sum_{n=-\infty}^{+\infty} \frac{(1 - e^{i\gamma^n t})e^{i\phi_n}}{\gamma^{(2-D)n}}$$

where $D$ is the fractal dimension of the graph of $W(t)$ and $1<D<2$. $\gamma$ is a parameter larger than 1. $\phi_n$ is an arbitrary phase. When $\phi_n=0$, the form of WMF is:

$$W(t) = \sum_{n=-\infty}^{+\infty} \frac{1 - cos(\gamma^n t)}{\gamma^{(2-D)n}}$$

When $\phi_n=n\,\varpi$, the form of WMF becomes:

$$W(t) = \sum_{n=-\infty}^{+\infty} \frac{(-1)^n sin(\gamma^n t)}{\gamma^{(2-D)n}}$$

Without loss of generality, we use $\phi_n=0$ to generate cosine series to simulate the coastline echo (Zhang et al. 2015). By inspecting the simulation results under various combinations of $D$ and $\gamma$, we notice that the fractal dimension $D$ has much larger impact on the fluctuation frequency of the cosine series than parameter $\gamma$. Additionally, in order to keep consistent with the fractal dimension of actual signals, parameter $D$ should be selected between 1 and 1.5, since the fractal dimensions of actual signals range from 1 to 1.5. Therefore, in this study, $\gamma$ and $D$ are set to 1.5 for both. Figure 7 presents the cosine series simulated in Matlab using aforementioned parameters. It can be seen that the cosine series generated by WMF have infinitely complex patterns across different scales. Based on the characteristics and previous applications of fractal theory (Majumdar and Tien 1990; Voss 1988; Yang et al.), the cosine series generated by WMF can be used to simulate the natural pattern of a coastline.

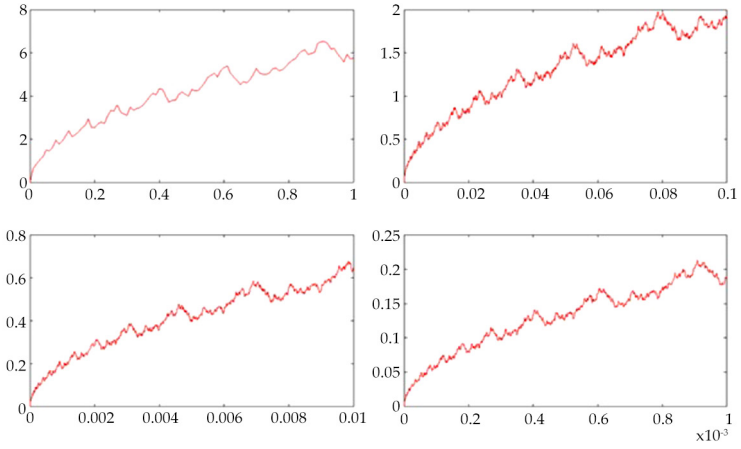


**Figure 7**: Cosine series generated by WMF in different scales ($D$ =1.5,$\gamma$=1.5, $\phi_n$=0).

## Algorithm Improvement

We know that, in the process of simulating coastline echoes using fractal algorithms, a collection of sample or random points will be added in each iteration. As the number of added points increase, the simulation software will consume more computer resources, such as calculation ability and storage space, which may slow down the rotation of scan line, or even result in a buffer overflow. As the radar range increases, the amount of information included in the radar simulation also increases. Typically, increasing iterations and radar range produce a slower rotating scan line or can even result in failure of the simulation. To troubleshoot this issue, we introduce a threshold value (L) into the simulation process. Only when the distance between two adjacent sample points is larger than the threshold value L (in this study $L$ =10), the fractal algorithms will be applied. Otherwise, the conventional simulation method will be used to generate the coastline echo. This is because the conventional simulation method works well enough under large radar ranges. Again, the value L can be adjusted in accordance with computer's performance. We can set L to a smaller value or even zero in the improved algorithm on a high performance computer. For those who are using similar computers as the authors do, $L$ =10 is a good starting point. Figure 8 illustrates the flow chart of improved fractal algorithms for the generation of coastline echo.

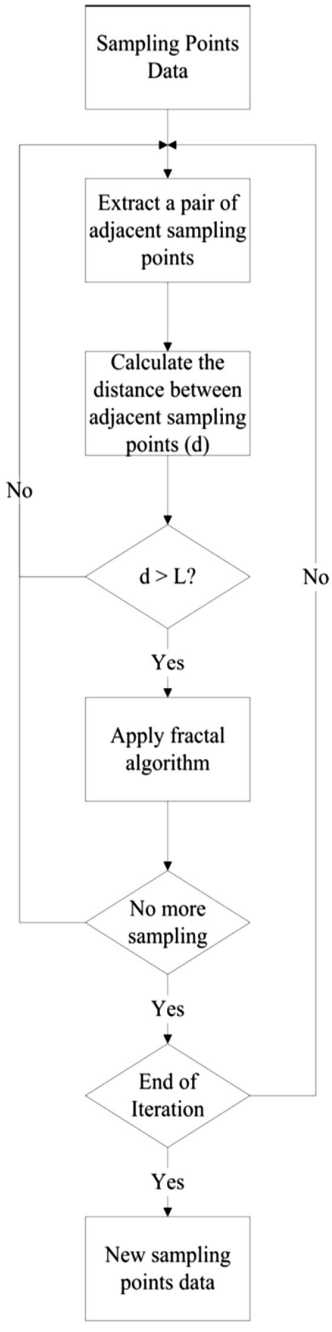


**Figure 8**: Flow chart of improved fractal algorithm.

# RESULT AND DISCUSSION

## Simulation Outcomes on Marine Radar Simulator

The simulation algorithms were implemented in the C++ language and tested on a laptop with an Intel(R) Core (TM) i5-2520M CPU, 2.50 GHz processor, 2 cores, Intel HD Graphics 3000 graphic card, and 8 GB RAM (Windows 7 64-bit). Figure 9 presents a panel of simulation outcomes of the coastline echoes under 0.25 NM radar range using the conventional method and fractal algorithms. All of the fractal algorithms uses three iterations. Figure 9 a shows the coastline echoes generated by conventional method. It can be observed that the simulated coastline echoes by this method is in a regular straight line pattern without the natural features of coastline echoes. In Fig. 9 b, throw in some randomness, we notice that the regularity of simulate coastline echoes starts to fade out. While using FBM method to generate coastline echoes (as shown in Fig. 9 c), the pattern of simulated coastline echoes looks interestingly real. The features of real coastline echoes, such as inlets and promontories can be observed clearly. The coastline echoes simulated by WMF method (as shown in Fig. 9 d) show natural features of coastline echoes as well; however, the natural features of simulated coastline echoes by WMF method are not as obvious as those generated by FBM method. In summary, via visual inspection, we can observe that the structures of the coastline echoes generated by fractal algorithms (Fig. 9 b, c,) outperform the echo generated by conventional method in representing a natural coastline feature (Fig. 9 a).

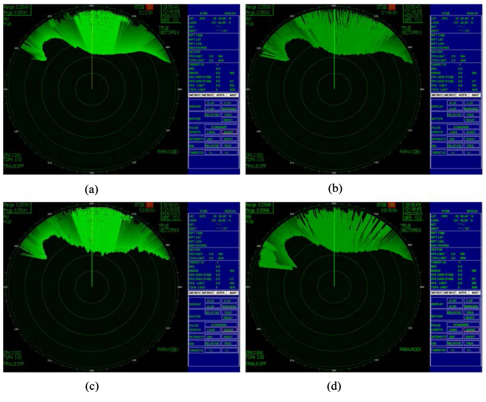


**Figure 9**: Simulation outcomes of coastline echo. a by conventional method, b by random Koch curve algorithm, c by FBM algorithm, and d by WMF algorithm.

To support above conclusion from visual inspection, a survey is designed for a panel of 30 experienced mariners to collect their opinion on the patterns of simulated coastline echoes by conventional method and fractal algorithms. These mariners consist of 17 licensed officers on board (including two captains, two chief mates, three second mates, and ten third mates), five maritime enforcement investigators, and eight researchers in nautical science. The average working years of these mariners are 5.6 years ranging from 1 to 30 years. All the mariners report that they have experience of using radar equipment for positioning and navigation. The coastline echoes generated by different methods are presented to them. They are required to evaluate and score these coastline echoes. To be specific, in the first part of the survey, we provide the mariners three pairs of comparison figures of simulated coastline echoes (conventional method *v.s*. random Koch curve, conventional method *v.s*. FBM, and conventional method *v.s*. WMF). The mariners need to select the best simulation result from each panel based on their own judgements. In the second part of the survey, the mariners are required to score the coastline echoes simulated by conventional methods and three fractal algorithms. Score scale is using a likert scale from 1 to 5, where 1 is "bad" and 5 is "excellent". The evaluation results are summarized in Table 1. For example, comparing the coastline echo simulated by conventional method with the one by FBM, 30 % of the mariners consider the conventional method is better and 70 % of the mariners think otherwise. Regarding the evaluation scores, the median evaluation scores on the coastline echoes generated by conventional method and FBM are 3 points and 4 points respectively. In general, the results of the evaluation from experienced mariners validate the advantages of fractal algorithms in terms of simulation of coastline echoes.

**Table 1:**Summary of evaluations from experience mariners on the simulated coastline echoes by various methods

| **Survey** | **Simulation method** | **Evaluation result** |
|---|---|---|
| Part I | Conventional Method *v.s*. Random Koch Curve | 30 % *v.s*. 70 % |
| | Conventional Method *v.s*. FBM | 30 % *v.s*. 70 % |
| | Conventional Method *v.s*. WMF | 33 % *v.s*. 67 % |
| Part II | Conventional Method | [2.00, 3.00, 4.00] |
| | Random Koch Curve | [3.00, 3.00, 4.00] |
| | FBM | [3.00, 4.00, 4.25] |
| | WMF | [2.00, 3.50, 4.00] |

Note: scores in square bracket are [25 % quantile, median, 75 % quantile]

## Performance Analysis of Improved Fractal Algorithms

According to the time of scan line finishing a rotation in Table 2, the improved fractal algorithms can guarantee the scan line to rotate around in no more than three seconds regardless of whether the radar range is small (say 0.25 NM) or large (say 6 NM) or the number of iterations is many or few. By contrast, the unimproved fractal algorithms can result in significantly slower rotation of scan line or even simulation failure.

**Table 2:**Speed of scan line to rotate a round by different algorithms, iterations, and radar ranges (unit in second/round)

| **Algorithm** | **Iteration** | **Radar range (in NM)** | | | | | | | |
|---|---|---|---|---|---|---|---|---|---|
| | | **6** | **5** | **4** | **3** | **2** | **1** | **0.5** | **0.25** |
| Random Koch Curve | 1 | 3 | 3 | 3 | 3 | 3 | 3 | 3 | 3 |
| | 2 | 12 | 11 | 8 | 6 | 5 | 3 | 3 | 3 |
| | 3 | – | – | – | – | 8 | 7 | 6 | 5 |
| FBM | 1 | 3 | 3 | 3 | 3 | 3 | 3 | 3 | 3 |
| | 2 | 3 | 3 | 3 | 3 | 3 | 3 | 3 | 3 |
| | 3 | 5 | 4 | 3 | 3 | 3 | 3 | 3 | 3 |
| | 4 | 12 | 11 | 8 | 6 | 5 | 5 | 5 | 3 |
| WMF | 1 | 3 | 3 | 3 | 3 | 3 | 3 | 3 | 3 |
| | 2 | 31 | 25 | 11 | 8 | 7 | 5 | 4 | 3 |
| | 3 | – | – | – | – | 14 | 11 | 8 | 6 |
| Improved | 1 | 3 | 3 | 3 | 3 | 3 | 3 | 3 | 3 |
| Random Koch Curve/ | 2 | 3 | 3 | 3 | 3 | 3 | 3 | 3 | 3 |
| FBM/WMF | 3 | 3 | 3 | 3 | 3 | 3 | 3 | 3 | 3 |
| | 4 | 3 | 3 | 3 | 3 | 3 | 3 | 3 | 3 |

Note: " –" means the simulation failed

Moreover, the improved fractal algorithm can still keep a natural-looking pattern and detail of the coastline echoes. Taking an improved FBM algorithm with threshold value (L) as an example, the coastline echoes generated by improved FBM algorithm (Fig. 10 b and c) are still better representations of

a natural coastline echo than the echoes generated by conventional method (Fig. 10 a). Additionally, the natural pattern and Detail of the coastline echo improve as the threshold value (L) decreases.

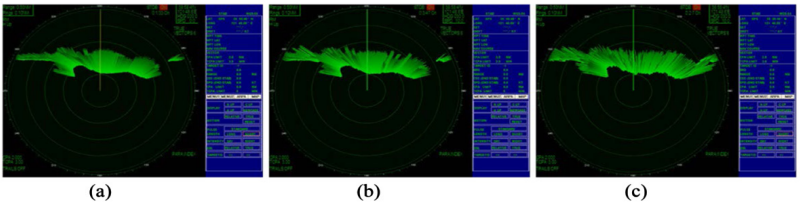


**Figure 10**: Simulation outcomes of coastline echo. a by conventional method, b by improved FBM algorithm with $L$ =10, and c by improved FBM algorithm with $L$ =3.

## Comparison of Three Fractal Algorithms

Based on calculations under the same number of iterations (i) and amount of original sample points of a coastline, the total number of sample points used by a random Koch curve algorithm in the simulation process is $2^i$ times of those used by the FBM and WMF algorithm. Since the number of the sample points can directly affect the rotation speed of the scan line, the FBM and WMF algorithm performs better than the random Koch curve algorithm from this aspect.

In addition, the pattern of the coastline echoes generated by FBM algorithm can be adjusted by Hurst index $H$ conveniently. The pattern of the coastline echoes simulated by WMF algorithm can be adjusted by the different combinations of $D$, $\gamma$, and $\phi_n$ as well. By contrast, the pattern of the coastline echoes generated by a random Koch curve algorithm can be changed very little. According to the simulation outcomes in this study, the coastline echoes generated by the FBM algorithm more closely resemble real coastline echoes than the echoes generated by a random Koch curve and WMF algorithm.

# CONCLUSION

In this paper, fractal algorithms are applied into the simulation of coastline echoes on marine radar simulator. The simulation outcomes from different methods are compared as well. In order to guarantee the rotating speed of

radar scan line, threshold value L is introduced into the simulation process. Based on our evaluation, the improved FBM algorithm is the best choice for the simulation of coastline echoes on marine radar simulators. Natural-looking coastline echoes generated by the algorithms introduced in this study can improve the quality of the training significantly. The fractal algorithms developed in this paper are packaged into a dynamic link library (dll) with well documented application programmable interface (API), which means that the algorithms are decoupled from the simulator program. This brings great benefits and convenience when transplanting the algorithm to other simulators, as long as the simulator is able to load a dll library. Since a dll library is supported by most of Windows based programs, we believe that the adoption of our algorithms on other simulators will be effortless. One limitation of this study is that we only simulated Type II coastline echoes. Another limitation of this study is that we aim at applying the fractal algorithms into the simulation of the coastline echoes in radar simulator rather than finding the best parameters of the fractal algorithms for the simulation. Last but not least, since the authors are unable to collect real data from marine radar on board, a survey method is employed to evaluate the simulation results by fractal algorithm. In the future, simulation of other radar echo types will be considered; how to choose the parameters for the fractal algorithms should be investigated; and a more objective evaluation approach should be designed to evaluate the simulation results.

## REFERENCES


1. Ali, A (2006). Simulator instructor-stcw requirements and reality. *Pomorstvo: Scientific Journal of Maritime Research*, *20*(2), 23–32.
2. Arnold-Bos, A, Martin, A, Khenchaf, A (2006). A versatile bistaticpolarimetric marine radar simulator. In *Radar, 2006 IEEE Conference On*, (pp. 605–612).
3. Aviles, C, &Scholz, C (1987). Fractal analysis applied to characteristic segments. *Journal of Geophysical Research*, *92*(B1), 331–344.
4. Baliarda, C.P, Romeu, J, Cardama, A (2000). The koch monopole: A small fractal antenna. *Antennas and Propagation, IEEE Transactions on*, *48*(11), 1773–1781.
5. Berry, M, & Lewis, Z (1980). On the weierstrass-mandelbrot fractal function. In *Proceedings of the Royal Society of London A: Mathematical, Physical and Engineering Sciences*, (Vol. 370. The Royal Society, pp. 459–484).
6. Boyle, R, Parvin, B, Koracin, D, Paragios, N, Tanveer, S.-M (2007). Advances in visual computing.
7. Bridge Command (2016). Interactive 3D Ship Simulator. https://www.bahookie.org/.
8. Cross, S.S (1994). The application of fractal geometric analysis to microscopic images. *Micron*, *25*(1), 101–113.
9. Dalian Maritime University Institute of Navigational Technology (2016). Marine Radar Simulator. http://nvc.dlmu.edu.cn/list.php?fid=3.
10. Dieker, T. (2004). *Simulation of fractional brownian motion*. The Netherlands: MSc theses, University of Twente, Amsterdam.
11. Falconer, K (2013). Fractals: A very short introduction.
12. Filoche, M, &Sapoval, B (2000). Transfer across random versus deterministic fractal interfaces. *Physical review letters*, *84*(25), 5776.
13. Harrouni, S (2008). Fractal classification of typical meteorological days from global solar irradiance: application to five sites of different climates, 29–54.
14. Huang, S, Oelfke, S, Speck, R (1992). Applicability of fractal characterization and modelling to rock joint profiles. In *International Journal of Rock Mechanics and Mining Sciences &Geomechanics Abstracts*, (Vol. 29. Elsevier, pp. 89–98).

15. Ji, S, Liu, D, Zhang, Z (2005). A review on fractal image compression coding and some improvement measures. In *PDPTA'05*, (pp. 151–156).
16. Ji, S, Zhang, Z, Yang, H, Liu, D, Sawhney, R (2015). Simulation of coastline's echo on marine radar simulator based on fractal theory. In *Transportation Research Board 94th Annual Meeting*.
17. Keddam, M, &Takenouti, H (1988). Impedance of fractal interfaces: new data on the von koch model. *Electrochimicaacta*, *33*(3), 445–448.
18. Kongsberg Maritime (2016). Polaris Ships Bridge Simulator. http://www.km.kongsberg.com/ks/web/nokbg0240.nsf/AllWeb/B2F29B3742D75297C1257315003C3F6F?OpenDocument.
19. Landfall (2016). Marine Radar Simulator. http://www.landfallnavigation.com/radarsimulator.html.
20. Mandelbrot, B.B, & Van Ness, J.W (1968). Fractional brownian motions, fractional noises and applications. *SIAM review*, *10*(4), 422–437.
21. Mandelbrot, B (1979). Fractals: form, chance and dimension. Fractals: form, chance and dimension., by Mandelbrot, BB, *1*, 16+ 365.
22. Mandelbrot, B.B (1983). The fractal geometry of nature, *173*.
23. Majumdar, A, & Tien, C (1990). Fractal characterization and simulation of rough surfaces. *Wear*, *136*(2), 313–327.
24. Ma, C, Yang, J, Zhao, L, Mei, X, Shi, H (2015). Simulation and experimental study on the thermally induced deformations of high-speed spindle system. *Applied Thermal Engineering*, *86*, 251–268.
25. Nautical Software (2016). Marine Radar Simulator. http://www.nauticalsoftware.com/training-software/marine-radar-simulator.html.
26. Organization, I.M (2006). Internatinoal Convention on Standards of Training, Certification and Watchkeeping for Seafarers, 1978, as amended in 2006 London.
27. Pentland, A.P (1984). Fractal-based description of natural scenes. Pattern Analysis and Machine Intelligence, IEEE Transactions on (6), 661–674.
28. Rostek, S, &Schöbel, R (2013). A note on the use of fractional brownian motion for financial modeling. *Economic Modelling*, *30*, 30–35.
29. Shanhua, X, Songbo, R, Youde, W (2015). Three-dimensional surface parameters and multi-fractal spectrum of corroded steel. *PloS one*, *10*(6), 0131361.

30. Teel, S, Sanders, J, Parrott, D.S, Wade, L, Gervais, T, Rovinski, K, Stone, L.C, Murai, K, Hayashi, Y (2009). Evaluation of marine simulator training based on heart rate variability. In *Systems, Man and Cybernetics, 2009. SMC 2009. IEEE International Conference On*. IEEE, (pp. 233–238).
31. Voss, R.F. (1988). *Fractals in Nature: from Characterization to Simulation*: Springer.
32. Wang, J, Wu, C, Liu, C, Wei, J (2015). Fractal simulation on random rough surface. In *2015 International Conference on Automation, Mechanical Control and Computational Engineering*. Atlantis Press.
33. Weierstrass, K (1967). Übercontinuirlichefunktioneneinesreellen arguments, die fürkeinenwerth des letztereneinenbestimmtendifferentialquotientenbesitzen, 1872. Karl WeiertrassMathematischeWerke.
34. Xiuwen, L, Yong, Y, Yicheng, J, Xinyu, Z (2010). Design radar signal interface for navigation radar/arpa simulator using radar display. In *Circuits, Communications and System (PACCS), 2010 Second Pacific-Asia Conference On*, (Vol. 1. IEEE, pp. 442–445).
35. Yin, Y, Liu, X, Li, Z (2007). Key technologies of navigation radar simulator using real radar monitor. *Journal of System Simulation*, *19*(5), 1014–1017.
36. Yang, X, Qin, K, Wu, C, Chen, L. Simulation of coastlines based on cloud fractal.
37. Zhang, Z, Liu, D, Han, Y, Ji, S (2005). Characteristics, Applications and the Prospects of DSP. In *Parallel and Distributed Processing Techniques and Applications*, (pp. 161–165).
38. Zhang, Z. (2007). *Research On The Algorithm Of Generating Coastline Echo In Radar Based On Fractal Theory*. China: Master's thesis, Dalian Maritime University.
39. Zhang, C, Zhang, D, Quan, D (2010). Echo image generation method for marine radar based on opengl modeling and simulation technology. *Journal of Dalian Maritime University*, *3*, 017.
40. Zhang, L, Yu, C, Sun, J (2015). Generalized weierstrass–mandelbrot function model for actual stocks markets indexes with nonlinear characteristics. Fractals, 1550006.

# 13

# *Three-Dimensional Surface Parameters and Multi-Fractal Spectrum of Corroded Steel*

**Xu Shanhua, Ren Songbo, Wang Youde**

School of Civil Engineering, Xi'an University of Architecture and Technology, Xi'an, Shannxi, People's Republic of China

## ABSTRACT

To study multi-fractal behavior of corroded steel surface, a range of fractal surfaces of corroded surfaces of Q235 steel were constructed by using the Weierstrass-Mandelbrot method under a high total accuracy. The multi-fractal spectrum of fractal surface of corroded steel was calculated to study the multi-fractal characteristics of the W-M corroded surface. Based on the shape feature of the multi-fractal spectrum of corroded steel surface, the least squares method was applied to the quadratic fitting of the multi-fractal spectrum of corroded surface. The fitting function was quantitatively analyzed to simplify the calculation of multi-fractal characteristics of corroded surface. The results showed that the multi-fractal spectrum of

**Citation:** hanhua X, Songbo R, Youde W (2015) Three-Dimensional Surface Parameters and Multi-Fractal Spectrum of Corroded Steel. PLoS ONE 10(6.,DOI: 10.1371/journal.pone.0131361.

corroded surface was fitted well with the method using quadratic curve fitting, and the evolution rules and trends were forecasted accurately. The findings can be applied to research on the mechanisms of corroded surface formation of steel and provide a new approach for the establishment of corrosion damage constitutive models of steel.

## INTRODUCTION

A rough surface with self-similarity and scale invariance always has a fractal geometrical property[1–2]. Many studies have been conducted on the morphology characteristics of rough surfaces on the basis of fractal geometry theory. Many types of fractal surfaces have been established and have played important roles in ultra-precision industries[3–6], materials science[7–10], electromagnetic wave scattering[11–13], and many other fields. In addition, in actual projects, the morphology of rough surface often presents variability, i.e., anisotropic and local characteristics in spatial distribution[14,15], which makes the fractal geometry theory difficulty to be applied in practical engineering.

As a common building material, steel, because of air-borne chloride ions, moisture, fugitive dust, etc., is highly susceptible to corrosion damage. The surface of corroded steel becomes gradually roughening from the very beginning of a plane. It well known, the surface of corroded steel is mainly roughened by corrosive pitting among all corrosion results, which is generating considerable interest. For geometric morphology, due to a large number of bumps or potholes (pits) and planar regions (without pits) on corroded surface of steel, the rough surface attacked by the corrosive pitting presents larger discreteness and concave convex feature. And the existing experimental data show that the multi-fractal dimension of a corroded steel surface is between two and three. The existing research results show that the surface attack by corrosive damage is characterized by continuity, non-differentiability and self-affinity, and is of multi-fractal features with a certain measure[16–18]. Thus, the research for the multi-fractal features is a powerful tool for analyzing the randomness and discreteness of the damage mechanism of corroded steel. However, the difficulties in the multi-fractal features analysis of corroded steel surface, such as tedious calculations, make it too complex to be applied to practical projects. Therefore, the present study is trying to use a simplified method to study the multi-fractal characteristics of corroded steel surface.

The Weierstrass-Mandelbrot (W-M) method is a common mathematical model used to construct the fractal surface in engineering. In this study, irregular fractal surface of the corroded steel is tried to be constructed by using the W-M method with specific fractal parameters, and calculate its multi-fractal spectrum. Then, based on the shape feature of the multi-fractal spectrum, the least squares method is applied to quadratic fitting of the multi-fractal spectrum of corroded surfaces. Finally, we conduct quantitatively analysis on the fitting curve to obtain an exact description and accurate analysis of the multi-fractal characteristics of the corroded steel surface.

# MATERIALS AND METHODS

## Material and Specimens

The material used in this study was a Q235 steel, which is a normalized 0.25% low-carbon steel, extensively used in industrial and civil buildings: the matrix consists of a ferritic–pearlitic microstructure with a 20~40μm ferrite grain size, as shown in Fig 1; its basic chemical composition is shown in Table 1. All specimens were cut out from a same steel plate.

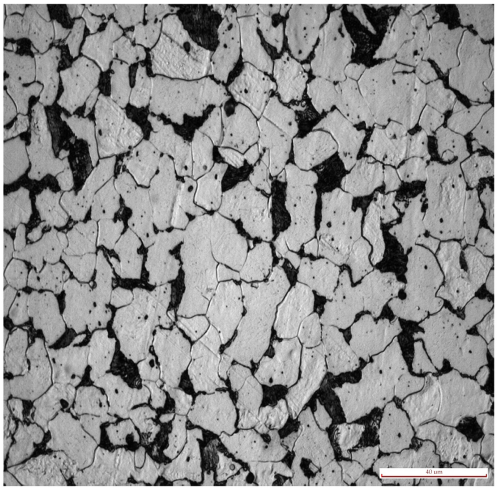

**Figure 1:** Microstructure of Q235 steel material.

White part is ferrite and black part is pearlite.

**Table 1:** Chemical composition of Q235 steel (wt. %)

| C | Si | Mn | P | S | Cr | Ni | Cu | N |
|---|---|---|---|---|---|---|---|---|
| 0.2 | 0.36 | 1.4 | 0.45 | 0.45 | 0.3 | 0.3 | 0.3 | 0.008 |

## Atmospheric Corrosion Experiment

A test sited in Xi'an (latitude 39°45' N, longitude 108°56' E) was selected for the atmospheric corrosion experiment. The test setup of the atmospheric corrosion experiment is shown in Fig 2. During the experimental period, the monthly temperature(T), relative humidity(RH), annual precipitation(P), and rainwater acidity(PH) values were measured to identify the atmospheric corrosive environment. According to GB/T 19292.4–2003[19], the specimens for corrosion were 400 mm in length, 60 mm in width and 8 mm in thickness, installed at 45°in the oblique direction. Table 2 presents the atmospheric corrosion conditions measured depending on the test site. After exposed for 0.5, 1, 2 and 4 years, orderly, the specimens were immersed in HCL solution (12% by volume) at room temperature for removing the corrosion products, cleaned with water, dried with hot air, rinsed in acetone, and then kept in a drying oven until the 3D profile measurement[20].

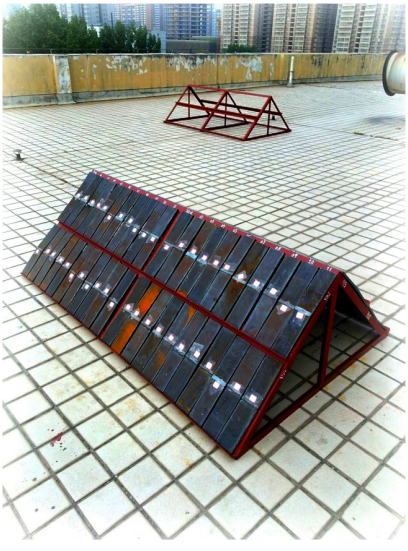

**Figure 2:** Setup of atmospheric exposure test.

**Table 2:** Atmospheric corrosion conditions on the test site

| Exposed period | *T*(*K*) | *RH*(%) | *P*(mm) | *PH* |
|---|---|---|---|---|
| Mar. 2008-Apr. 2009 | 294 | 65 | 1755 | 6.3 |
| Mar. 2009-Apr. 2010 | 294 | 61 | 2186 | 6.7 |
| Mar. 2011-Apr. 2012 | 294 | 63 | 1738 | 6.4 |
| Mar. 2012-Apr. 2013 | 295 | 69 | 2016 | 6.5 |
| May | 294 | 64 | 2106 | 6.6 |

T − the temperature; RH − the relative humidity; P− the annual precipitation; PH− the rainwater acidity.

## 3D Surface Profile Measurements

In order to gain the 3D morphology of the surface of corroded specimens, a non-contact PS50 3D profiler produced by NANOVER Company was used in this study. The 3D profiler was designed with leading edge white light axial chromatism optical pens to obtain nanometer resolution for surface inspection, hi-speed 3D metrology and more precise thickness mapping on a wider range of geometries and materials than any other profiometer[20].The vertical resolution was 0.28μm and the horizontal resolution was 8μm. The setup used for 3D surface morphology measurements is shown in Fig 3A. Each specimen had been detected the corroded surface at a measurement zone of 40 mm×30 mm(along the directions of transverse and longitude, respectively) approximately arranging at the central of specimen, and the scanning step was set to 15μm[20]. The elementary diagram of the measurement area is shown in Fig 3B.

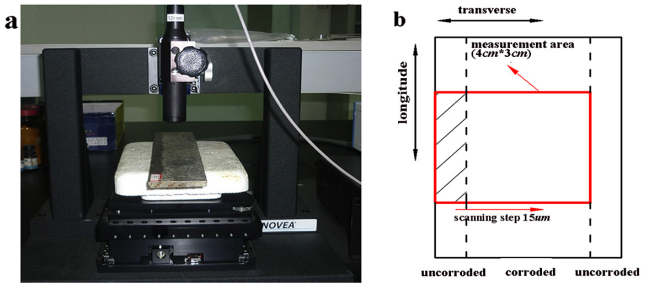


**Figure 3:** Laser focus measurement of the atmospheric exposure test specimen.

(a) Equipment used for measurements; (b) Schematic diagram of the measurement area.

## Surface Morphology and Pitting Characterization

Fig 4 clearly shows the surface morphologies of corroded specimens exposed for 0.5, 1, 2 and 4 years, respectively. The images were draw by Golden Software Surfer 8. The software is a full-function 3D visualization, contouring and surface modeling package that runs under Microsoft windows, which is used extensively for terrain modeling, bathymetric modeling, landscape visualization, surface analysis, contour mapping, watershed and 3D surface mapping, gridding, volumetric, and much more. In this study, the 3D surface mapping was applied to show more detail of the corroded surface. The profiles of the different measurement regions are presented in Fig 4 (S1 Table).

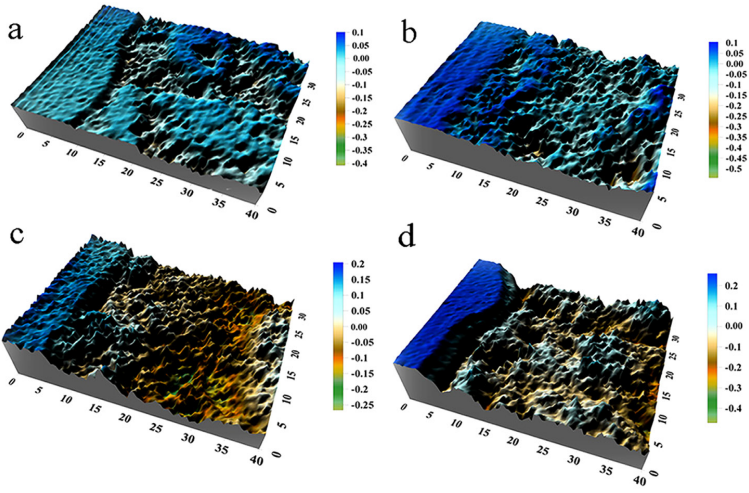


**Figure 4:** Contour of measured corroded surface images.

(a) Surface image of 0.5 year old test specimen; (b) Surface image of 1 year old test specimen; (c) Surface image of 2 years old test specimen; (d) Surface image of 4 years old test specimen.

It is well known, the corrosive attack can produce a network of corrosion on metal surface, which may be treated as a single pit or as two or more adjacent pits. Corrosion damage is also related to the link up of adjacent pits during subsequent exposure time. As shown in Fig 4, at the initial stage of corrosion, a few micro-pits only occurred on some particular locations on the corroded surface of specimens, which made the surface slightly irregular

(shown in Fig 4A). And with the passage of corrosion time, large amounts of pits occurred on the surface and superimposed each other, which made the corroded surface signally irregular and uneven (shown in Fig 4D). Thus it can be seen that roughness and irregular of the corroded surface increased with the increasing exposure.

Although Fig 4 may directly reflect corrosion status of the corroded steel, the quantitative analysis from the angle of mathematics is hard to evaluate. Thus, the engineering application is in urgent need of a method, which can simulate the corroded surface of steel with high-precision and be convenient to quantitatively analyze the simulation.

## RESULTS AND DISCUSSION

### Construction of the Multi-fractal Spectrum of Corroded Steel Surface

In science and engineering, many mathematical models with different multi-fractal characteristics based on the Weierstrass-Mandelbrot(W-M) method were generally used to analyze the surface conditions[21–26]. By using the W-M method, here, we can obtain a fractal surface with respect to an arbitrary surface of corroded steel through setting some specific multi-fractal parameters. For instance, when a fractal dimension (D) was known, the corresponding fractal surface can be obtained by employing the W-M fractal function, and the function is expressed as follows:

$$Z(x,y) = \sum_{n=1}^{\infty} C_n \lambda^{-(3-D)^n} \sin[\lambda^n (x \cos B_n + y \sin B_n) + A_n] \tag{1}$$

Where $C_n$ is the characteristic length scale, i.e., the scaling constant; n is the wave number; $A_n$ and $B_n$, which have uniform distribution in [0, 2π], are independent random number, respectively; D is a multi-fractal dimension between 2 and 3; $\lambda$ is constant greater than 1.

In this study, the fractal surfaces with D value of 2.2, 2.3, 2.5, and 2.8 were constructed by the W–M method ($\lambda$ = 1.3) to simulate the surface of corroded steel exposed for 0.5, 1, 2 and 4 years, respectively. Fig 5 shows the W–M surface with different fractal dimensions which were plotted by the MATLAB software.

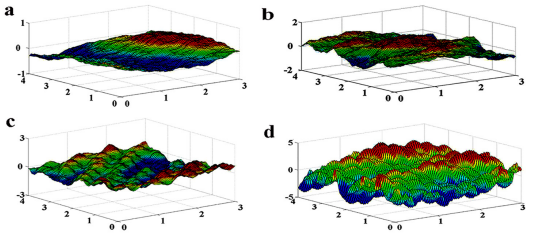


**Figure 5:** Fractal surfaces based on the W–M method.

(a) Fractal surface with D = 2.2; (b) Fractal surface with D = 2.3; (c) Fractal surface with D = 2.5; (d) Fractal surface with D = 2.8.

From Fig 5, it reveals that the fractal surface based on the W–M method was similar with the corresponding surface of corroded steel (shown in Fig 4) in roughness distribution pattern and surface fluctuation trend. Here we evaluated the accuracy of the constructed surface by comparing the measurement data and the theoretical data[27].

$$Thesimulatedprecision = 1-(\frac{\sum|h-h'|}{h})\cdot\frac{1}{n} \qquad (2)$$

where h is the measurement data of practical surface, h ' is the theoretical data of simulated surface, n is the number of date. To obtain the surface height (h or h ') of every point, the calculation principle was defined by using the method shown in Fig 6. Noted that the datum plane used to measure the height of the surface was obtained by least squares.

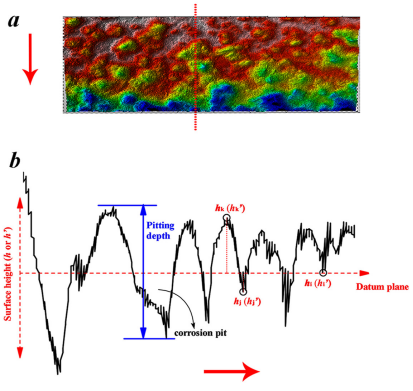


**Figure 6:** Surface profile (a) and the principle to obtain the surface height parameters (b), (red arrow indicates the trend of the profile).

Blue indicates pitting depth, red indicates surface height based on the datum plane.

Table 3 showed the simulation precisions of fractal surfaces for corroded specimens with different corrosion time. And it can be found that the fractal surfaces with D value of 2.2, 2.3, 2.5, and 2.8 had more than 90% accuracy for simulating the corroded surfaces exposed for 0.5, 1, 2 and 4 years, respectively. That is to say, it is effective to simulate the rough surface of corroded steel by the W-M method.

**Table 3:** The simulation precisions of fractal surfaces for corroded specimens with different corrosion time

| Dimension | 2.2 | 2.3 | 2.5 | 2.8 |
|---|---|---|---|---|
| Simulation precision (%) | 98.9 | 97.2 | 94.8 | 91.5 |

## Calculation of the Multi-fractal Spectrum

Many methods can be used to calculate fractal dimension[28–30], among which the multi-fractal dimension approaching to the real value can be obtained by the calculus of variations or the box counting method. Note that the box counting method, possessing the advantage of clear mathematical principle and simple calculation, was used in this study to calculate the multi-fractal parameters of corroded steel surface.

A set of boxes with size of l are used to divide the datum plane of the fractal surface of corroded steel[ 31], make $\varepsilon = l / L$, $L = 512$ and $\varepsilon < 1$, $\nu_i(\varepsilon)$ is distribution probability of the height of corroded surface for the box(i), which can be calculated as follow:

$$\nu_i(\varepsilon) = \frac{h_i}{\sum_{j}^{i} (h_i)_j} \tag{3}$$

In Eq (3), $h_i$ is the height of corroded surface for the box(i), $\sum(h_i)_j$ is the sum of the height for all boxes. When the height distribution is of multi-fractal features, it can be described as:

$$\nu_i(\varepsilon) \sim \varepsilon^{\alpha} \tag{4}$$

$$M_{\alpha}(\varepsilon) \sim \varepsilon^{-f(\alpha)} \tag{5}$$

where α depending upon the box(i) is the singularity of the subset of height probabilities, $M_{\alpha}(\varepsilon)$ refers to the number of boxes having the same height

distribution probability when the size of box is ε, and f(α) is the multi-fractal dimension of subset with the α value. Generally, the value of $M_\alpha(\varepsilon)$ increases with the decreasing of ε[32]. A qth-order partition function applied in statistical physics, $\chi_q(\varepsilon)$, can be described as[33]:

$$\chi_q(\varepsilon) = \sum v_i(\varepsilon)^q = \varepsilon^{\tau(q)} \quad (6)$$

$$\tau(q) = \lim_{\tau \to 0} \left[ \frac{\ln x_q(\varepsilon)}{\ln \varepsilon} \right] \quad (7)$$

where q is the moment order, τ(q) is a non-linear function of q and is known as the mass exponent function.

The singularity strength function α and the singularity spectrum f(α) can be calculated through Legendre transform:

$$\alpha(q) = \tau'(q) = \frac{d\tau(q)}{dq} \quad (8)$$

$$f(\alpha(q)) = q \cdot \alpha(q) - \tau(q) \quad (9)$$

Theoretically, with the increasing of |q|, the values of α(q) and f(α(q)) are closer to their theoretical limit. But in fact, when q reaches an oversized value, the computational workload will be increased significantly, which will lead to running out of memory; when |q| stands on an undersized value, of which the increment can cause obvious variation of f(α). The reason can be considered as that f(α) calculated through undersized |q| is only part of the multi-fractal spectrum, but cannot completely reflect probability distribution of the fractal surface. In practical, it is impossible to take the value of q to be infinite. But generally, the saturation extent of multi-fractal spectrum increases with the increasing of the q[31]; thus, we determined the value of $|q|_{max}$ through that f(α) and α tend to be saturated. In this study, all of the multi-fractal spectrums of corroded surfaces were obtained with $|q|_{max} = 60$.

Through the analysis above, we calculated f(α)~α of the fractal surfaces (D = 2.2, 2.3, 2.5, and 2.8) corresponding to the corroded surfaces exposed for 0.5, 1, 2 and 4 years.

Fig 7 plots the multi-fractal spectrums of the fractal surfaces with different dimensions (S2 Table). It can be seen that the shapes of all spectrums are inverted parabolas, but the difference of shapes among the spectrums is still obvious: the multi-fractal spectrum of corroded surface is plumping with the increasing of fractal dimension, and the spectrum span is also widening. It is well known value of Δα ($\alpha_{max} - \alpha_{min}$) determines the

width of the spectrum, which is the main reason to increase the local indices of the studied variable, i.e., the more the unevenly distributing of surface, the wider the spectrum, the greater the heterogeneity of distribution and vice versa[34]. Thus, the conclusions can also be drawn: the surface of corroded steel unevenly distributes with the increasing of the value of Δα.

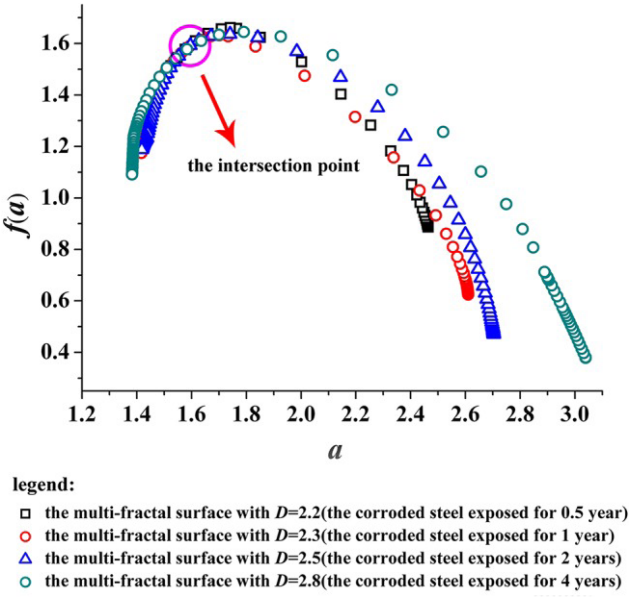


**Figure 7:** Multi-fractal spectrums, f(***α***)~***α***, with D = **2.2, 2.3, 2.5 and 2.8.**

The width of which along α denotes the degree of multi-fractal complexity.

Moreover, when the surface of corroded steel is more rough and irregular, the end position of the corresponding multi-fractal spectrum is lower, which means that the proportion of subsets referring to small probability continues to increase for the corroded surface.

As shown in Fig 7, the intersection point of all multi-fractal spectrums is (1.6, 1.6), which indicating the fractal subset with α = 1.6 (the edge of pits) has a largest proportion on the fractal surface. That is to say the fractal subset with α = 1.6 can determine the sharpness or roughness of the corroded steel surface, distinctly. For the Q235 steel under atmospheric corrosion environment, the corrosion damage mainly manifests corrosive pitting due to the heterogeneous microstructures and chemical composition[35, 36], as shown in Fig 4. Pits occur at some particular locations of the corroded

surface, link up with adjacent pits with the increasing of exposure, and eventually influence the sharpness or roughness of the corroded surface. Thus, it can be seen the effect of atmospheric corrosion on surface condition of Q235 steel can be signally reflected by the development of corrosion pits with the method of multi-fractal.

## Fitting of the Multi-fractal Spectrum of Corroded Steel Surface

It can be known from Eq (8) and (9) that the calculation of multi-fractal spectrum is unable to be represented by using a specific or simple function, which makes the multi-fractal spectrum difficult to take quantitative analysis and to be applied in engineering. To simply formulate the multi-fractal spectrums of corroded surface, we had researched their trend and shape, and the following conclusion can be drawn:

Each multi-fractal spectrum (shown in Fig 7) can be decomposed into a left part and a right part of inverted parabolas and both of the parts are continuously differentiable.

Therefore, we can fit the multi-fractal spectrums of the fractal surfaces (with D = 2.2, 2.3, 2.5, and 2.8) corresponding to the corroded specimens exposed for 0.5, 1, 2 and 4 years by the method of least squares. And the left and right part of the multi-fractal spectrum can be respectively expressed as piecewise functions as follows for satisfying fitting precision in this study [37]:

$$f(\alpha(q)) = A[(\alpha(q)-\alpha_0(q)]^2 + B[(\alpha(q)-\alpha_0(q)] + C \qquad (10)$$

where α is singularity strength by evaluating a probability of subset, $\alpha_0$ is the singularity strength for $D = D_{max}$. A, B, and C are the undetermined coefficients, which can be obtained by a least squares procedure. Herein the absolute value of A is inversely proportional to the value of Δα; the value of C is proportional to the maximum value of f(α).

Generally, the greater value of α can reflect a phenomenon that the probability of corresponding subset is smaller; the lower value of α can reflect a phenomenon that the probability of corresponding subset is bigger. The criterion reflected in multi-fractal spectrum can also be explained that the greater value of α can make the small probability of subset to be

a significant impact on multi-fractal spectrum; on the contrary, the smaller value of α can make the big probability of subset to be a significant impact.

f(α) is a multi-fractal singularity spectrum representing irregularity and complexity of the fractal surface. The extreme values in the distribution of height probability are associated with the low values of f(α), $f(\alpha)_{min}$ and $f(\alpha)_{max}$, in such a way the big and small probability of height subsets are related to the left and right part of the spectrum, respectively.

Making comprehensive analysis of above discussions, the conclusions can be drawn: the greater the value of C, the higher the $f(\alpha)_{max}$, and the higher the $f(\alpha)_{max}$, the more complex and irregular the fractal surface of corroded steel; on the contrary, the smaller the value of C, the lower the $f(\alpha)_{max}$, and the lower the $f(\alpha)_{max}$, the more unobvious the complexity and regularity of corroded surface.

We fit f(α) of the right and left part by employing quadratic functions (red and blue curves shown in Figs Figs88–11) around $\alpha_0$ with least squares method, respectively.

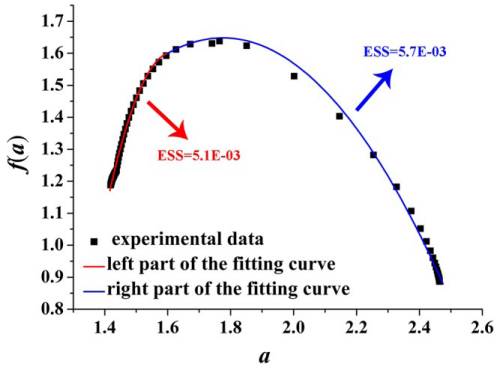


**Figure 8:** Left and right parts of the fitting curve of the multi-fractal spectrum with D = **2.2 (Eq 10).**

ESS is the error sum of square; red indicates the left part of the fitting curve; blue indicates the right part of the fitting curve. D-value of the minimum and maximum value is 1.05.

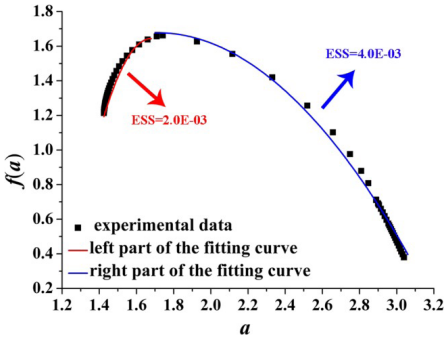


**Figure 11:** Left and right parts of the fitting curve of the multi-fractal spectrum with D = **2.8 (Eq 10).**

ESS is the error sum of square; red indicates the left part of the fitting curve; blue indicates the right part of the fitting curve. D-value of the minimum and maximum value is 1.61.

Fig 8 plots the fitting curve of the multi-fractal spectrum with D = 2.2. The fitting functions of the right and left part curve are expressed as Eq (11) and Eq (12), respectively:

$$f(\alpha) = -1.57(\alpha-1.6)^2 + 0.55(\alpha - 1.6) + 1.6 \quad (11)$$

$$f(\alpha) = -11.0(\alpha-1.6)^2 + 0.31(\alpha - 1.6) + 1.6 \quad (12)$$

Fig 9 plots the fitting curve of the multi-fractal spectrum with D = 2.3. The fitting functions of the right and left part curve are expressed as Eq (13) and Eq (14), respectively:

$$f(\alpha) = -1.4(\alpha-1.6)^2 + 0.5(\alpha - 1.6) + 1.6 \quad (13)$$

$$f(\alpha) = -9.3(\alpha-1.6)^2 + 0.55(\alpha - 1.6) + 1.6 \quad (14)$$

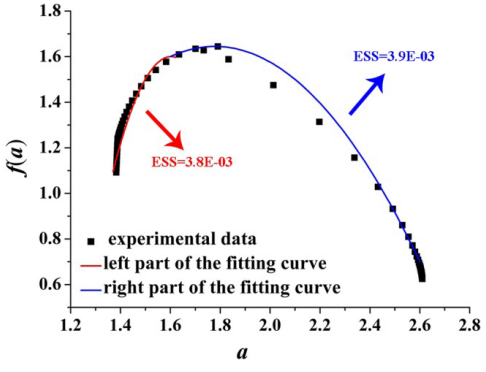


**Figure 9:** Left and right parts of the fitting curve of the multi-fractal spectrum with D = **2.3 (Eq 10).**

ESS is the error sum of square; red indicates the left part of the fitting curve; blue indicates the right part of the fitting curve. D-value of the minimum and maximum value is 1.23.

Fig 10 plots the fitting curve of the multi-fractal spectrum with D = 2.5. The fitting functions of the right and left part curve are expressed as Eq (15) and Eq (16), respectively:

$$f(\alpha) = -1.3(\alpha-1.6)^2 + 0.5(\alpha - 1.6) + 1.6 \quad (15)$$

$$f(\alpha) = -8.0(\alpha-1.6)^2 + 0.6(\alpha - 1.6) + 1.6 \quad (16)$$

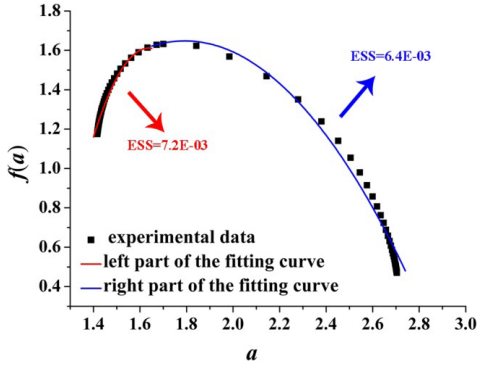


**Figure 10:** Left and right parts of the fitting curve of the multi-fractal spectrum with D = **2.5(Eq 10).**

ESS is the error sum of square; red indicates the left part of the fitting curve; blue indicates the right part of the fitting curve. D-value of the minimum and maximum value is 1.29.

Fig 11 plots the fitting curve of the multi-fractal spectrum with D = 2.8. The fitting functions of the right and left part curve are expressed as Eq (17) and Eq (18), respectively:

$$f(\alpha) = -0.7(\alpha-1.6)^2 + 0.15(\alpha - 1.6) + 1.67 \quad (17)$$

$$f(\alpha) = -7.0(\alpha-1.6)^2 + 1.1(\alpha - 1.6) + 1.6 \quad (18)$$

Figs 8–11 show the fitting curves agreed well with computations which can meet the engineering precision requirements. According to the quantitative analysis of the fitting functions, we can find that the corroded surface of different specimen can be indeed reflected by a specific fitting curve of multi-fractal spectrum.

In multi-fractal spectrum, the left part determines the proportion of big probability subsets (the areas with obvious ups and downs) on the corroded surface; at this moment, the bigger the probability of subsets, the rougher

the corroded surface, and the rougher the corroded surface, the smaller the value of the corresponding α. The right part determines the proportion of small probability subsets (the areas with smaller ups and downs); at this moment, the smaller the probability of subsets, the more smooth the corroded surface, and the smoother the corroded surface, the greater the value of the corresponding α.

Making intuitive observation of each fitting curve in Figs 8–11, |A| of left part curve is more than that of the right part, which explains the phenomenon that the range of the right part of the multi-fractal spectrum is larger than that of the left part. As well known, the larger the range of multi-fractal spectrum, the more the kinds of subsets described by the multi-fractal spectrum. Thus, it can be drawn that the subsets corresponding to the right part of the multi-fractal spectrum play a leading role in description of the multi-fractal spectrum.

Connecting with corrosion process of steel, when the steel surface is attacked by shallower pits in the initial stage of corrosion, |A| of the right part curve fitting the multi-fractal spectrum is larger and the corresponding range is narrower; the kinds of the subsets included in the corroded steel surface must also be less and the surface is almost a plane. With the increasing exposure time, because the pits contact the sub-surface constituent particles causing further corrosion and link up with adjacent pits damaging the corroded surface, |A| of the right part curve fitting the multi-fractal spectrum must be smaller and the corresponding range is wider; the kinds of the subsets including to the surface of corroded steel must also be more and the surface is more irregular and discrete.

Some parameter of the quadratic fitting is shown in Table 4. Making comprehensive analysis of Table 4 and Figs 4 and 5, the following conclusions can be made that with the increasing of Δα from 1.05 to 1.61 or the decreasing of |A| from 11 to 7, the surface of corroded steel is distributing more unevenly and irregularly; with the increasing of Δf(α) from 0.30 to 0.83, the surface will fluctuate more obviously.

**Table 4:** Parameters of the multi-fractal spectrum

| Dimension | $\alpha_{min}$ | $\alpha_{max}$ | $\Delta\alpha$ | $\alpha_0$ | $f(\alpha_{min})$ | $f(\alpha_{max})$ | $f(\alpha)_{max}$ | $\Delta f(\alpha)$ |
|---|---|---|---|---|---|---|---|---|
| 2.2 | 1.42 | 2.46 | 1.05 | 1.60 | 1.19 | 0.89 | 1.60 | 0.30 |
| 2.3 | 1.38 | 2.61 | 1.23 | 1.60 | 1.09 | 0.62 | 1.60 | 0.47 |

| | | | | | | | | |
|---|---|---|---|---|---|---|---|---|
| 2.5 | 1.42 | 2.70 | 1.29 | 1.60 | 1.18 | 0.47 | 1.60 | 0.70 |
| 2.8 | 1.42 | 3.04 | 1.61 | 1.60 | 1.21 | 0.38 | 1.60 | 0.83 |

$\alpha_{min}$ – the minimum value of singularity strength; $\alpha_{max}$ –the maximum value of singularity strength; Δα–D-value of the minimum and maximum value; $\alpha_0$ – the singularity strength for $D_{max}$; $f(\alpha_{min})$–the singularity spectrum for $\alpha_{min}$; $f(\alpha_{max})$– the singularity spectrum for $\alpha_{max}$; $f(\alpha)_{max}$ –the maximum value of singularity spectrum; Δf(α)–D-value of the maximum and minimum spectrum.

It can be seen from the calculation formula of the multi-fractal spectrum, the weighting factor, q, is the slope of the multi-fractal spectrum, which can also be obtained using: $q = \partial f(q(\alpha)) / \partial q(\alpha)$ [38]. For the multi-fractal spectrums mentioned above, whether the right part or the left part, an inequality exists as:

$$\frac{\partial q(\alpha)}{\partial \alpha} = \frac{1}{(\partial \alpha(q(\alpha))/\partial q(\alpha))} = \frac{1}{(\partial^2 \tau(q(\alpha))/\partial^2 q(\alpha))} < 0 \quad (19)$$

According to Eq (19), it can be seen q decreases with the increasing of α. In the left part of the fitting curve, q is a constant positive number; q is a constant negative number in that of the right part. |q| continues to increase with α. When q tends towards the plus infinity, the maximum probability subset has a significant impact on the multi-fractal spectrum, i.e., the corresponding corroded surface is a big bumps or potholes. Whereas q tends towards the minus infinity, the minimum probability subset has a significant impact on the multi-fractal spectrum, i.e., the corresponding corroded surface is similar to be a plane.

According to the analysis and discussion in this study, it can be known which part of subsets of the corroded surface has a decisive influence on shape and trending of the multi-fractal spectrum through mathematical analysis of fitting function of the multi-fractal spectrum. In addition, the overall shape and local characteristics of corroded surface of steel can also be derived by the analysis of fitting expression.

## CONCLUSIONS

In this study, we constructed the fractal surfaces of the corroded steel by using the W-M method and calculated the multi-fractal spectrums. Using the method of least squares to fit the multi-fractal spectrums of the fractal surfaces with D value of 2.2, 2.3, 2.5, and 2.8 corresponding to the surfaces

of corroded specimens exposed for 0.5, 1, 2 and 4 years. Making comparison analysis of the fitting curves and calculated values, the following conclusions can be drawn:

- f(α), between 1 and 2, was the fractal dimension of the subset relating to the singularity strength α, which was a measure of the complexity, irregularity and non-uniformity of the fractal surface. In physical condition, f(α) can intuitively reflect completeness of the fractal surface.
- $\Delta f(\alpha)$, $f(\alpha)_{max}$-$f(\alpha)_{min}$, reflected surface roughness; the higher the value of $\Delta f(\alpha)$, the greater the difference among the subsets of the fractal surface of corroded steel, and the greater the difference among the subsets, the more irregular the fluctuation and distribution of corroded surface. On the contrary, for the fluctuation and distribution to be uniformity, the surface tends towards a plane.
- C, given in the fitting function, can reflect the value of $f(\alpha)_{max}$ in the multi-fractal spectrum. The greater the value of C, the higher the value of $f(\alpha)_{max}$, and the higher the value of $f(\alpha)_{max}$, the more complex and irregular the fractal surface of corroded steel. Whereas, the smaller the value of C, the lower the value of $f(\alpha)_{max}$, and the lower the value of $f(\alpha)_{max}$, the better the completeness of the fractal surface.
- q was constant positive number in the left part of the fitting curve and constant negative number in that of the right part. With the decreasing of q, the smaller probability subset had a significant impact on the multi-fractal spectrum; the description of the fractal surface of corroded steel is more subtle. This means that, with the decreasing of q, the subsets relating to the areas with slight ups and downs had a significant impact on the multi-fractal spectrum, which was conducive to represent more minutely the fractal surface of corroded steel and made the computed result much more close to the real value.

## REFERENCES

1. Schroeder MR. Physics. Fractals, chaos, Power laws: Minutes from an infinite paradise 1st ed. Cambridge: Courier Dover Publication; 2012.
2. Barabási AL. Fractal concepts in surface growth 1st ed London: Cambridge University Press; 1995.
3. Tong XL, Li YH, Lin HS, Qi X. Research on phase-shifting interferometer contrast three-dimensional topography of ultra precision surface. Journal of Electronic Measurement and Instrument. 2009; 23(12): 65–69.
4. Ren MJ, Cheung CF, Kong LB. A task specific uncertainty analysis method for least-squares-based form characterization of ultra-precision freeform surfaces. Measurement Science and Technology. 2012; 23(5): 54005–54014.
5. Lee SR, Li ZG, Wang BG, Chiou HS. An application of the fractal theory in the design of heat sink for precision measurement instrument. Key Engineering Materials. 2005; 295: 717–722.
6. Zong WJ, Sun T, Li D, Chen K, Dong S. Mechanical lapping single crystal diamond. Journal of Harbin Institute of Technology. 2005; 8(3): 285–288.
7. Wan FX, Huang XP, Wu JF, Huang JL. Multi-fractal characteristic of metal material worn surface with plant abrasive. Applied Mechanics and Materials. 2014; 668: 43–47.
8. Kamila AC, Juliana A, Thaís AP, Luis ROH. 3-D reconstruction by extended depth-of-field in failure analysis–Case study II: Fractal analysis of interlaminar fracture in carbon/epoxy composites. Engineering Failure Analysis. 2012; 25: 271–279.
9. Lawrence KD, Ramamoorthy B. Structure function–based fractal characterisation of cylinder bore surfaces using stylus profile data. International Journal of Precision Technology. 2014; 4(1): 19–28.
10. Ţălu Ş, Marković Z, Stach S, Marković BT, Ţălud M. Multifractal characterization of single wall carbon nanotube thin films surface upon exposure to optical parametric oscillator laser irradiation. Applied Surface Science. 2014; 289: 97–106.
11. David B, Erik OS, Kimberly AR, Zachary DN, Andrew ST. Numerical prediction of sound scattering from surfaces with fractal geometry: A preliminary investigation. Ln: Engelhardt PV, Churukian AD, Rebello

NS, editors. The Combined Use of Light and Sound for Imaging and Therapy. POMA 12: 161st Meeting Acoustical Society of America: 2011 May 23–27; Seattle, Washington. New York: American Institute of Physics; 2014. 12. p. 1–9.

12. Eftaxia K, Frangos P, Kapiris P, Polygiannakis J. Kopanas J, Peratzakis A, et al. Review and a model of pre-seismic electromagnetic emissions in terms of fractal electrodynamics. Fractals. 2004; 12(2): 243–273.
13. Chen J, Lo TKY, Leung H, Litva J. The use of fractals for modeling EM waves scattering from rough sea surface. Geoscience and Remote Sensing; IEEE Transactions. 1996; 34(4): 966–972.
14. Oleg VA, Dmitry NB, Alexander VK, Steen GH. Fractal description of rough surfaces. Applied optics. 2002; 41(22): 4620–4629.
15. Gan SY, Zhou Q, Xu XD, Hong YL, Liu Y, Fu SJ. Study on the surface roughness of substrate with multi-fractal spectrum. Microelectronic engineering. 2007; 84(5): 1806–1809.
16. Berry MV, Lewis ZV. On the Weierstrass-Mandelbrot fractal function. Proceedings of the Royal Society of London A; 1980. pp: 459–484.
17. El-Sonbaty IA, Khashaba UA, Selmy AI, Ali AI. Prediction of surface roughness profiles for milled surfaces using an artificial neural network and fractal geometry approach. Journal of Materials Processing Technology. 2008; 200(1): 271–278.
18. Majumdar A, Tien CL. Fractal characterization and simulation of rough surface. Wear. 1990; 136(2): 313–327.
19. Corrosion of metals and alloys-corrosively of atmospheres-Determination of corrosion rate of standard specimens for the evaluation of corrosively. GB/T 19292.4–2003.
20. Xu SH, Wang YD. Estimating the effects of corrosion pits on the fatigue life of steel plate based on the 3D profile. International Journal of Fatigue. 2015; 72: 27–41.
21. Qi DW. Analysis and processing of X-ray image of log with defects based on fractal theory. Ph. D. Thesis, Northeast Forestry University. 2003. Available: http://cdmd.cnki.com.cn/Article/CDMD-10225-2003110997.htm.
22. Jiang Z, Wang H, Fei B. Research into the application of fractal geometry in characterizing machined surfaces. International Journal of Machine Tools and Manufacture. 2001; 41(13): 2179–2185.

23. Liao XY, Lei WY. The geometric precision and performance analysis for matching surface based on fractals. Journal of Chongqing University. 1999; 22(6): 18–23.

24. Mandelbrot BB. Stochastic models for the earth's relief, the shape and the fractal dimension of the coastlines, and the number-area rule for islands. Proceedings of the National Academy of Sciences USA. 1975; 72(10): 3825–3828.

25. Mandelbrot BB. The Fractal Geometry of Nature 1st ed. New York: Macmillan Publishers; 1983.

26. Bora CK, Flater EE, Street MD, Redmond JM, Starr MJ, Carpick RW. Multi-scale roughness and modeling of MEMS interfaces. Tribology Letters. 2005; 19(1): 37–48.

27. Sun HQ, Xie HP. Fractal simulation of rock fracture surface. Rock and Soil Mechanics. 2008;28(2): 347–352.

28. Ni HJ, Huang XL, Ning XB, Huo CY, Liu TB, Ben D. Multi-fractal analysis of resting state fmri series in default mode network: age and gender effects. Chinese Science Bulletin. 2014; 59(25): 3107–3113.

29. Yang XD, He AJ, Zhou Y, Ning XB. Multi-fractal mass exponent spectrum of complex physiological time series. Chinese Science Bulletin. 2010; 55: 1996–2003.

30. Vahedi A, Gorczyca B. Settling velocities of multi-fractal flocs formed in chemical coagulation process. Water Research. 2014; 53: 322–328. doi: 10.1016/j.watres.2014.01.008

31. Sun X, Wu ZQ, Huang Y. Fractal theory and its applications 1st ed. Hefei: China Science and Technology University Press; 2003.

32. Sayyad AJ, Nikooee E, Ayatollahi S, Alamdari A. Investigating wettability alteration due to asphaltene precipitation: Imprints in surface multi-fractal characteristics. Applied Surface Science. 2013; 256(21): 6466–6472.

33. Bird N, Díaz MC, Saa A, Tarquis AM. Tarquis. Fractal and multi-fractal analysis of pore-scale images of soil. Journal of hydrology. 2006; 322: 211–219.

34. Zeleke TB, Si BC. Characterizing scale-dependent spatial relationships betweensoil properties using multi-fractal techniques.Geoderma. 2006; 134: 440–452.

35. Du CW, Li XG, Liang P, Liu ZY, Jia GF, Cheng YF. Effects of microstructure on corrosion of X70 pipe steel in an alkaline soil. Journal

of materials engineering and performance. 2009; 18(2): 216–220.

36. Wang LW, Du CW, Liu ZY, Zeng XX, Li XG. Influences of $Fe_3C$ and pearlite on the electrochemical corrosion behaviors of low carbon ferrite steel. ActeMetallurgicaSinica. 2011; 47(10): 1227–1232.
37. Smirnov VI. A course of higher mathematics 1st ed. London:Pergamon Press; 1964.
38. Cai XQ. The statistics of multi-fractal parameter. Journal of Zhangzhou Teachers College.1997; 3: 109–113.

# 14

# *Application of the Fractal Geometry Theory on Fracture Network Simulation*

**Zhiwei Zhou, Yuliang Su, Wendong Wang & Yi Yan**

China University of Petroleum(East), No. 66, Changjiang West Road, Huangdao District, Qingdao 266580, China

## ABSTRACT

In this paper, we introduce an L-system based on the fractal geometry to study complex fracture networks. Comparing with other simulation models, the fractal fracture could not only maintain the bifurcation of the fracture geometry but also represent the multi-level feature of the complex fracture networks according to its fractal characteristics. Since the fractal geometry is always connected with several controlling parameters, the factors affecting on the fracture propagation can be quantized. With the fractal fractures, further studies on the fracture geometry and the multi-leveled branches are carried out, and the results can be concluded as: (1) when the complex fracture geometry is considered, the influence of the connectivity and complexity of the fracture network on the well performance is hard to ignore, and enhancing the connectivity and complexity of the fracture

**Citation:** Zhou, Z., Su, Y., Wang, W., & Yan, Y. (2017). Application of the fractal geometry theory on fracture network simulation. Journal of Petroleum Exploration and Production Technology, 7(2), 487-496., DOI: 10.1007/s13202-016-0268-0.

network will perform better than making a long but disconnected fracture on the shale gas development; (2) of a multi-leveled fracture network, the main fractures near the horizontal well contributes to the initial production, but the conductivity ratio (conductivity of the secondary fractures versus the conductivity of the main fractures) influences the decline rate, so a high production rate cannot be maintained without an efficient contributing area covered with conductive secondary fractures.

## INTRODUCTION

Duo to the low permeability and porosity, economic development of the shale gas resources always needs a multistage hydraulic fracturing. Different from the traditional bi-wing hydraulic fractures, complex fracture networks are generated near the horizontal wells in the shale gas reservoirs, as monitored by microseismic events (MSE) (Fisher et al. 2002; Maxwell et al. 2002; Daniels et al. 2007). Mine-back experiments and some field observations (Huang and Kunsoo 1993; Mayerhofer 2006) suggest that hydrofractures do not propagate linearly; when the reservoir is rich in natural fractures (NFs), the hydraulic fractures (HFs) may be created multi-branched. And it is mentioned that the complexity of the fracture networks is the main factor differing from the bi-wing fractures that contributes to the well production (Jang et al. 2015).

Considering the complex geometry, width of the branches of the fracture network is smaller than a single bi-wing fracture, the proppant might not be able to transport to the tip of the total fracture network (Xu et al. 2009), and this leads to a multi-level feature of the fracture networks which has a significant influence on the well performance. Analytical methods such as rate transient analysis (RTA) and well logging both show that the critical zone of the stimulated reservoir is smaller than the total area monitored by MSE (Friedrich 2013; Rahimi et al. 2014). The complexity and connectivity are two key parameters of the fracture networks, they relate directly with the well production, and it is obvious that the complexity and connectivity of the fracture network near the horizontal well are higher (Jones et al. 2013; Chen et al. 2016).

For better studying the performance of the fracture networks, analytical and numerical methods are applied. Olsen et al. studied the interactions between HFs and NFs and introduce a method to characterize the propagation of the complex fracture network considering the heterogeneity of the

reservoir and the irregular distribution of natural fractures (Olson 2008; Olson and Arash 2009). Besides the analytical studies, numerical models are developed for further study and engineering simulation. The dual-porosity model, wiremesh model and unconventional fracture model (UFM) are three typical numerical models that can take the main characteristics of the fractures into consideration when simulating a complex fracture network. Dual-porosity model is first introduced by Warren and Root (Warren and Root 1963) to characterize the behavior of naturally fractured reservoirs and now widely applied in fracture modeling (Zimmerman et al. 1993; Du et al. 2010; Cipolla et al. 2010). The stimulated region is regarded as dual porosity or even multi-porosity, and the properties of the grids can be assigned independently. The wiremesh model is consisted of two perpendicular sets of vertical planar fractures, and it quantizes the complicated geological and engineering factors to the parameters controlling the propagation of the wiremesh network (Xu et al. 2009; Xu et al. 2010; Meyer and Lucas 2011). The properties of the planar fractures and their spacing are related to different engineering parameters even MSE, and the mechanical interactions between the fracturing fluid and fracture walls are its main consideration (Xu et al. 2010; Weng et al. 2011). However, the models above cannot display the fracture geometry and that is the reason UFM is developed (Weng et al. 2011; Weng 2015). The UFM mainly studies the interactions between the HFs and NFs and details the propagation of the fracture network within the unstructured grids. It couples the fracture geometry with the factors influencing the propagation such as the orientation of the NFs and the rock deformation.

In fact, of either wiremesh model or the UFM, the main focus is the description on the fracture propagation; the conceptual models mentioned by Jones et al. (2013), Chen et al. 2016), studying the influence of the fracture complexity and connectivity on the typical production curves, fail to consider the fracture bifurcation. So in this paper, we would like to introduce a method based on the fractal geometry theory to characterize the fracture network and to analyze the well performance. The fractal geometry theory was put forward by Mandelbrot (1979) and has been applied to rock mechanics since 1982 (Xie 1993; Wang et al. 2015a, b) utilized the iterated function system (IFS) to study the bifurcation performance of the fracture network. According to the fractal geometry theory, the fracture network we generated can be both bifurcated and multi-leveled, the fracture geometry

can be related to few fractal controlling parameters, and these lead to the main advantages of the model: (1) characterizing the bifurcation feature of the fracture geometry; (2) quantifying the connectivity and complexity of the fracture network for analyzing; and (3) classifying the fractures into different levels to differ the main fractures and secondary fractures.

# FRACTAL FRACTURES BASED ON THE L-SYSTEM

## Characterization of Fractal Fracture Model

L-system is a rewriting system that defines a complex object by replacing parts of the initial object according to rewriting rules, and it simulates development rules and topological structure well (Lindenmayer 1968; Han 2007). The system has the feature of self-adjusting when something bifurcates, and this feature can describe the growth of trees. However, in this paper, we first introduce the L-system into fracture characterization because a fracture also has similar development rules and topological structure as trees and the interaction between HFs and NFs could be regarded as a type of rule-adjusting procession affecting the propagation of the fracture, which coincides with the basement of the L-system.

Four key parameters control the generation of a fractal fracture. They relate closely to the fractal fracture geometry which influences the performance of the production wells:

- The fractal distance ($d$) mainly controls the extending distance of the fractal fractions, it relates closely to the half-length of the fracture obtained by MS monitoring, and the influence of the fractal distance is shown in Fig. 1.

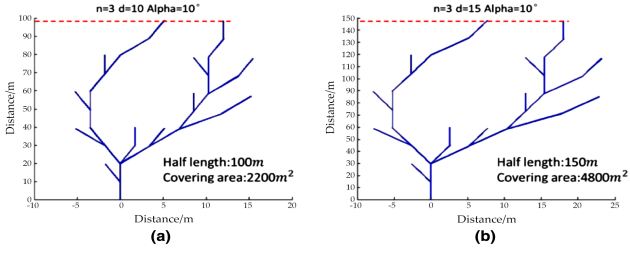


**Figure 1**: Influence of the fractal distance ($d$) on the geometry of the fracture network.

- The deviation angle ($\alpha$) controls the orientation when the fracture deviates or generates a secondary branch; it relates to the area of the stimulated reservoir, and when cooperating with the fractal distance, the size of the fractal fracture network can be adjusted for matching. Figure 2 shows the influence of the deviation angle on the orientation of the branches.

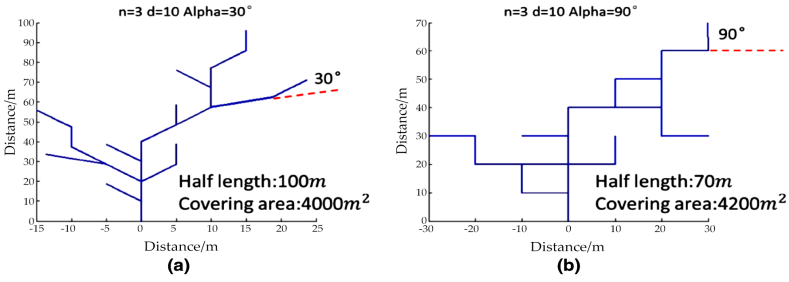


**Figure 2**: Influence of the deviation angle ($\alpha$) on the geometry of the fracture network.

- The number of iterations ($n$) controls the growth of a fractal fracture network. It depends on the complexity of the fracture network or the density of the MS events. This parameter relates to the multi-level feature of the fractal branches: in each iteration, the fractal fractures propagate from the original nodes following the given generating rules to construct part of the network. It is now considered that during the actual stimulating procession, the secondary fractures extend on the basis of the main fractures, so with this similarity, levels of the fractal fractures are also distinguished based on the generating orders according to the iteration times.
- There are rules for controlling the growth of the bifurcation. To account for an irregular propagation mode of a complex fracture network, the rules for controlling are always preset as more than three. In conjunction with the iteration times, the fractal fracture model could model numerous fracture geometries under different conditions. And by adjusting the combination of the growth rules, the value of the fractal distance and deviation angle, the fractal fracture model can generate the best fractal geometry matching the given fracture network.

## Geometry Calibration with L-system

The generating rules preset the basement to match or to generate a fracture pattern. It is recognized that the fracture network is generated from the interaction between HFs and NFs. When a hydraulic fracture interacts with a natural fracture, three cases are concluded to happen as shown in Fig. 3: crossing, terminating or offsetting (Huang et al. 2015a, b). So the generating rules are preset to characterize these three cases, and each case could be differed into different situations if a high matching accuracy is asked for.

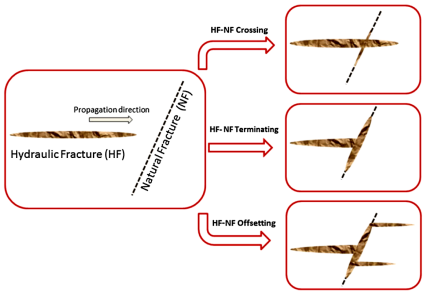


**Figure 3**: Hydraulic and natural fracture interaction scenarios (Huang et al. 2015a, b).

To represent the cases, we may preset the generating rules as shown in Fig. 4. The cases "Crossing" and "Terminating" can be simplified as a straight line, and to represent the case "Offsetting," at least three cases are necessary. The generating rules can be adjusted by changing the length or the deflection angle. But as we have mentioned before, presetting too much generating rules is not necessary since what we want is a fractal fracture geometry with multi-level feature and following the extending tendency of the fracture network.

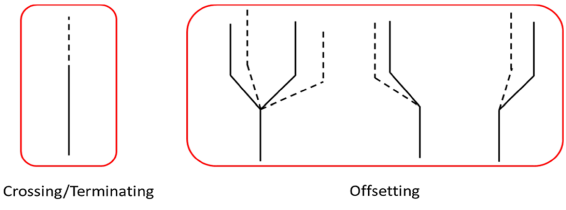


**Figure 4**: Schematic view of the preset generating rules (the *dashed lines* show that the distance and the deflection angle of the rules can be adjusted).

Two simple applications are carried out to illustrate the matching effect of the fractal fractures: Fig. 5a is a typical fracture obtained from the mine-back experiments, the main trunk is first matched with the combination of the generating rules, and by increasing the iteration times, the fractal fractions are generated from the main trunk as shown in Fig. 5c, and the obtained fractal geometry not only follows the extending tendency of the actual fracture but also maintains the fractal characteristics.

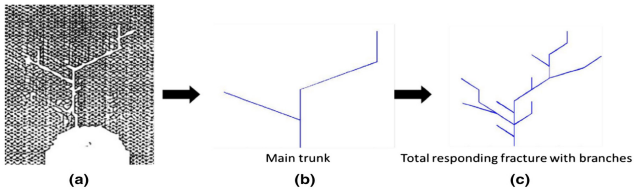


**Figure 5:** Fracture obtained from mine-back experiments and its matching patterns. a Comes from the experiments of Huang and Kunsoo (1993), and b and c are the corresponding fractal fractures obtained in this paper.

To match the fracture geometry in the shale gas reservoirs, the MSE can be introduced as the constraints since it is the most significant and common used information about the fracture network. Figure 6 shows an application of the fractal geometry on characterizing the fracture network according to the MSE, and the green signals are pointed to represent different situations. Taking the total distance between the MSE and the nodes of the fractal pattern as the final optimization object, the fractal pattern is randomly generated by adjusting the fractal distance, the turning angle and the combination of the generating rules until the error limit is reached. The results show that the fractal geometry could also match the propagating tendency of the fracture network calibrated by MSE.

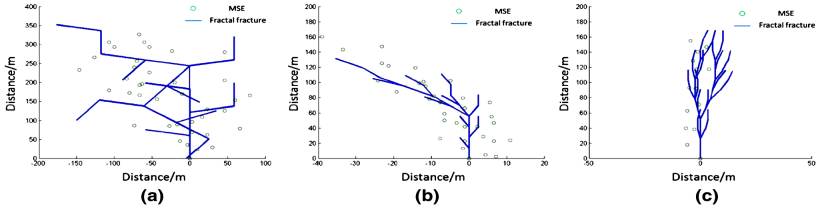


**Figure 6**: Using fractal pattern to match the fracture network calibrated by MSE.

## Simulation Workflow

To convert the fractal geometry to the well performance, we put forward a workflow shown in Fig. 7. The fracture network geometry is generated and discretized into 2D grids to represent the conductive fractures contributing to the production. With this simulation workflow, the fractal fracture geometry can be converted to the conductive fracture network with any simulator, and in this paper, we use E300 simulator of Eclipse for numerical simulation.

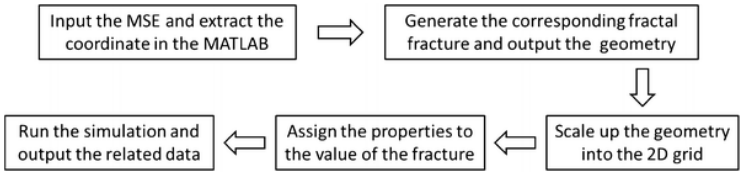


**Figure 7**: Schematic of the fracture simulation workflow.

## Well Performance Analysis based on a Case Study

The fractal fracture model (FFM) could analyze the influence of either individual fractures or the integral fracture geometry on the well production. In this part, we would like to study the influence of the multi-leveled fractures, fracture geometry and conductivity ratio, which are rarely analyzed before, on the well performance based on the fractal fracture model.

The analysis is carried out based on a case study. The simulation data and production data are simplified from a shale gas reservoir of China as listed in Table 1. The fractal controlling parameters and the fractal geometry are obtained by history matching under the limitation of the fracture monitoring data. The fractal fracture geometry of each half-wing is taken as the same, and the matching results are shown in Fig. 8.

**Table 1:**Parameters for the base model for simulation

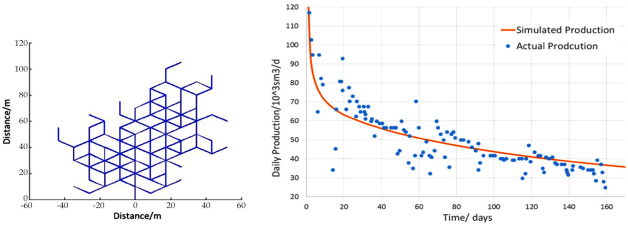


**Figure 8**: Production matching (*right*) and the responding fractal fracture geometry (*left*).

Multi-level feature of Fractal Fracture NetworkAccording to the multi-level feature of the fractal geometry, fractal fracture network has its advantage on classifying the fractures into different levels. Taking the fracture network in Fig. 8 as an example, three more iterations have been done to generate the responding fractal pattern, so the network is divided into 3 levels with their synthesized length and covering area shown in Fig. 9, and the cumulative production of each pattern is also compared.

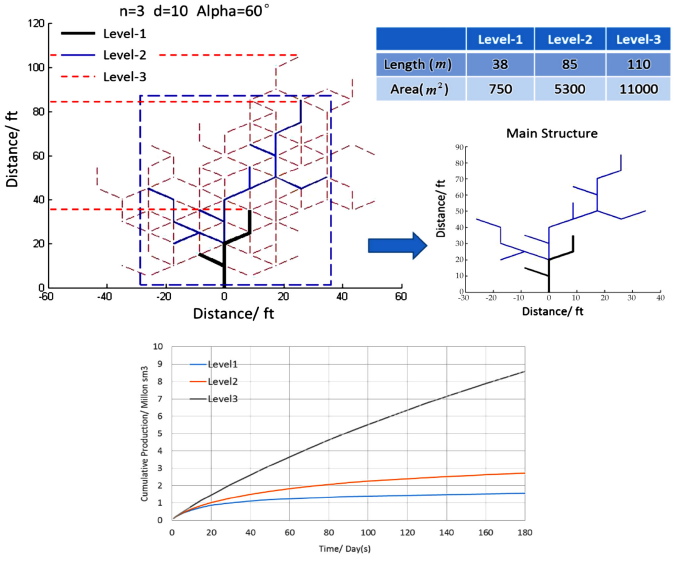


| | Level-1 | Level-2 | Level-3 |
|---|---|---|---|
| Length ($m$) | 38 | 85 | 110 |
| Area($m^2$) | 750 | 5300 | 11000 |

**Figure 9**: Multi-level fractal fracture and the responding cumulative production curves.

The production comparison shows that there is a great enhance on the well production when the fracture network on level 3 is utilized for simulation. However, the growth on the length and the covering area from level 2 to level 3 are both smaller than those from level 1 to level 2. It is assumed that the difference comes from the development on the connectivity and complexity of the fracture network. To demonstrate the assumption, we try to adjust the length and the covering area of other two levels to match level 3 and compare their production data as shown in Fig. 10.

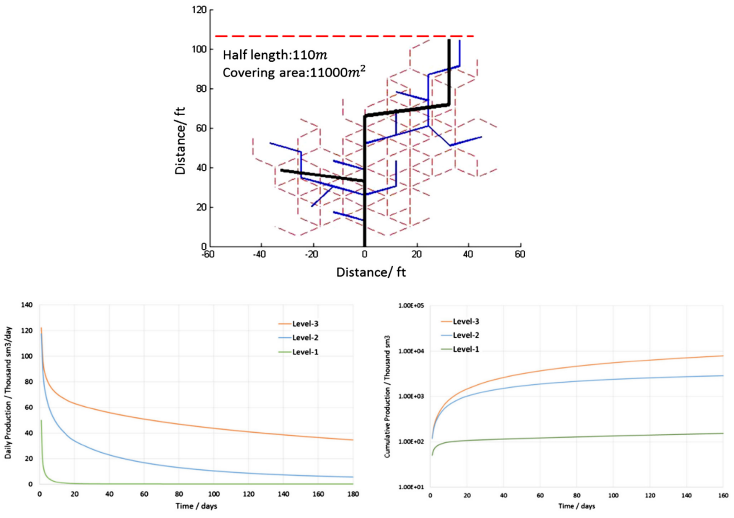


**Figure 10**: Comparison of the production of the fracture network under different complexity and the responding daily production rate and cumulative production curves.

According to the simulation results, daily production rate of level 1 soon goes down and its cumulative production is far smaller than that of the other two. The low complexity of level 1 cannot provide a high production, and it also demonstrates that the bi-wing fracture is hard to fit the fracture modeling in shale gas reservoirs. Daily production rate of level 2 is similar to that of level 3, but it also soon goes down, resulting in the difference on their cumulative production, demonstrating that when the complexity of the fracture network is large enough, it will not influence the initial production rate, but it still influences the decline rate of the production curves.

## Influence of the Fracture Geometry on the Well Production

As we have discussed, the complexity of the fracture network is critical to the well production; however, with the different fractal fracture geometry, how could we evaluate the fracture performance? We generate four fractal fracture networks by combining different generating rules with the same fractal distance and deviation angle as shown in Fig. 9 to run for simulation, and the patterns and the simulated results are compared in Fig. 11 (lines in black are the main structure of the network, and the lines in blue are their fractions).

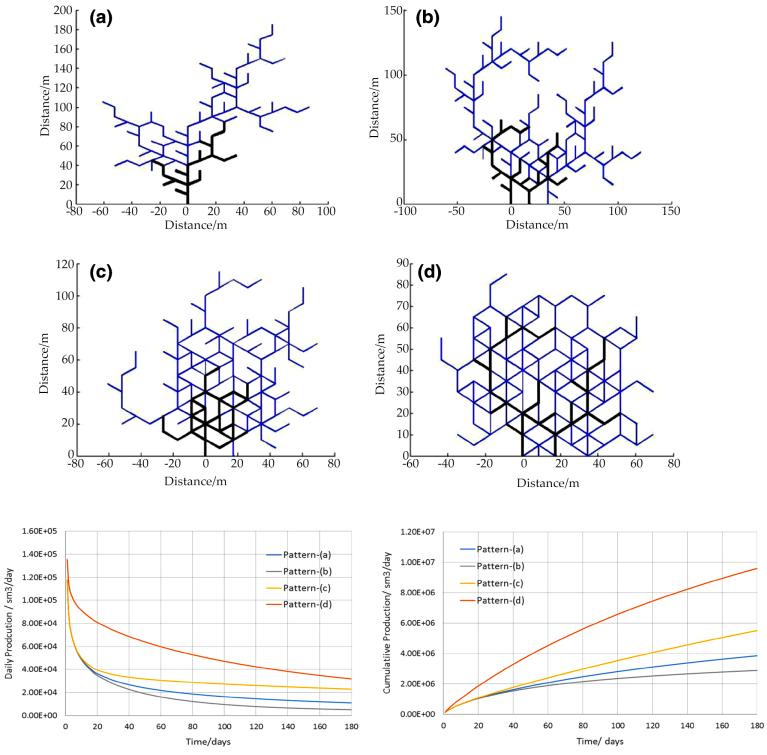


**Figure 11**: Fracture patterns and their production comparison.

Comparing the fracture geometry and production data of patterns (a), (c) and (d), the final production drops with the reduction in the fracture connectivity, although the synthesized length of the fracture increases. So when the complex geometry of the fracture network is considered, the fracture connectivity performs a more critical influence on the well performance than the facture half-length. Combined with the conclusion we drawn before, the efficiency of the fracture network, related to the complexity and connectivity, is a determining factor to the well production, and only considering the increase on the fracture half-length in the shale gas development may contribute little to the final recovery. On the other hand, both pattern (a) and pattern (b) are low in connectivity and production, but the final production of pattern (a) is higher, showing that the synthesized half-length of the fracture network is still positive to the fracture performance.

## Influence of the Conductivity Ratio on the Well Production

In the actual production, the conductivity of the fracture network is proved to be different, and there are several main fractures with higher conductivity and secondary branches with relatively lower value. The conductivity ratio (conductivity of secondary branches versus the main fractures) is also an important factor to determine the fracture performance. To analyze the influence of the conductivity ratio on the well production, we take the main structure in Fig. 9 as the main fractures, and the fractures in level 3 as the secondary branches, the conductivity ratio is given as 1:1–1:100, and the comparison with the actual production is shown in Fig. 12.

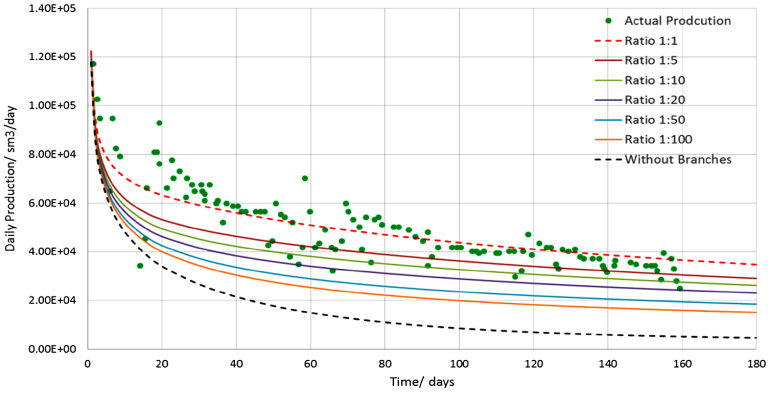


**Figure 12**: Influence of the fracture conductivity ratio on the daily production.

- The initial production is almost the same. Since the pressure wave does not spread to the secondary branches, the main fractures of the network determine the early production.
- With the ratio changes and the conductivity of secondary fractures turns down, the decline rate of the production curves increases. So the decline rate, which is a key factor to maintain the high production rate, is connected directly with the overall effect of fracturing.
- The contribution of the secondary branches maintains a great proportion to the well production, so in the hydraulic fracture network simulation and in the actual fracturing design, only concerning the stimulated results of the main fractures without optimizing the secondary fractures may finally result an inefficient stimulated reservoir area and a low level of production.

## CONCLUSIONS

- In this paper, a novel fracture model based on the fractal geometry is introduced, we detail the fractal controlling parameters and their influence on the fracture geometry, and two simple matching cases present that the fractal fracture could be utilized to match either the rock fractures or the fracture network in the shale gas reservoirs.
- The factors affecting on the fracture propagation can be quantized into several fractal controlling parameters, the fractal fracture can be divided into different levels according to the iteration times, and these are two advantages of the fractal fracture differing from other normal fracture models.
- With the features of the fractal fractures, further studies on the influence of the fracture geometry and the conductivity ratio of the fracture network on the well performance are carried out, and we obtain the following conclusions: (1) considering the complex fracture geometry, the complexity and connectivity of the fracture network perform a obvious influence on the well production, and (2) the secondary fractures also contribute greatly to the fracture performance. The conductivity ratio mainly influences the decline rate, and it is not sensible to concern over the synthesized fracture half-length of the covering area without considering the contributing efficiency of the fracture network during the fracturing design.

## REFERENCES

1. Chen Z, Liao X, Zhao X, Lv S, Zhu L (2016) Asemianalytical approach for obtaining type curves of multiple-fractured horizontal wells with secondary-fracture networks. Soci Pet Eng. doi:10.2118/178913-PA
2. Cipolla CL et al (2010) Reservoir modeling in shale-gas reservoirs. SPE ReservEvalEng 13(04):638–653
3. Daniels JL et al (2007) Contacting more of the barnett shale through an integration of real-time microseismic monitoring, petrophysics, and hydraulic fracture design. In: SPE annual technical conference and exhibition. Society of Petroleum Engineers
4. Du CM et al (2010) Modeling hydraulic fracturing induced fracture networks in shale gas reservoirs as a dual porosity system. In: International oil and gas conference and exhibition in China. Society of Petroleum Engineers
5. Fisher MK et al (2002) Integrating fracture mapping technologies to optimize stimulations in the Barnett Shale. In: SPE annual technical conference and exhibition. Society of Petroleum Engineers
6. Friedrich M (2013) Determining the contributing reservoir volume from hydraulically fractured horizontal wells in the Wolfcamp formation in the Midland Basin. Unconventional resources technology conference (URTEC)
7. Han J (2007) Plant simulation based on fusion of L-system and IFS. Computational science—ICCS 2007, pp 1091–1098
8. Huang J-I, Kunsoo K (1993) Fracture process zone development during hydraulic fracturing. In: International journal of rock mechanics and mining sciences and geomechanics abstracts, vol 30, No. 7. Pergamon
9. Huang J et al (2015a) Natural-hydraulic fracture interaction: microseismic observations and geomechanical predictions. Interpretation 3(3):SU17–SU31
10. Huang J et al (2015b) Natural-hydraulic fracture interaction: microseismic observations and geomechanical predictions. Interpretation 3(3):SU17–SU31
11. Jang Y et al (2015) Modeling multi-stage twisted hydraulic fracture propagation in shale reservoirs considering geomechanical factors. In: SPE eastern regional meeting. Society of Petroleum Engineers
12. Jones JR, Richard V, Wahju D (2013) Fracture complexity impacts on pressure transient responses from horizontal wells completed with

multiple hydraulic fracture stages. In: SPE unconventional resources conference Canada. Society of Petroleum Engineers

13. Lindenmayer A (1968) Mathematical models for cellular interaction in development. J TheorBiol 18:280–315
14. Mandelbrot BB (1979) Fractals: form, chance and dimension. In: Mandelbrot BB (ed) Fractals: form, chance and dimension. WH Freeman & Co., San Francisco, p 1 (16 + 365)
15. Maxwell SC et al (2002) Microseismic imaging of hydraulic fracture complexity in the Barnett shale. In: SPE annual technical conference and exhibition. Society of Petroleum Engineers
16. Mayerhofer MJ et al (2006) Integration of microseismic-fracture-mapping results with numerical fracture network production modeling in the Barnett Shale. In: SPE annual technical conference and exhibition. Society of Petroleum Engineers
17. Meyer BR, Lucas WB (2011) A discrete fracture network model for hydraulically induced fractures-theory, parametric and case studies. In: SPE hydraulic fracturing technology conference. Society of Petroleum Engineers
18. Olson JE (2008) Multi-fracture propagation modeling: Applications to hydraulic fracturing in shales and tight gas sands. The 42nd US rock mechanics symposium (USRMS). American Rock Mechanics Association
19. Olson, JE, Arash DT (2009) Modeling simultaneous growth of multiple hydraulic fractures and their interaction with natural fractures. In: SPE hydraulic fracturing technology conference. Society of Petroleum Engineers
20. Rahimi ZA et al (2014) Correlation of stimulated rock volume from microseismicpointsets to production data-A horn river case study. In: SPE Western North American and Rocky Mountain joint meeting. Society of Petroleum Engineers
21. Wang W et al (2015a) A mathematical model considering complex fractures and fractal flow for pressure transient analysis of fractured horizontal wells in unconventional reservoirs. J Nat Gas SciEng 23:139–147
22. Wang W, Su Y, Zhang X, Sheng G, Ren L (2015b) Analysis of the complex fracture flow in multiple fractured horizontal wells with the fractal tree-like network models. Fractals 23(2):1550014

23. Warren JE, Root PJ (1963) The behavior of naturally fractured reservoirs. Soc Petrol Eng J 3(03):245–255
24. Weng X (2015) Modeling of complex hydraulic fractures in naturally fractured formation. J Unconv Oil Gas Resour 9:114–135
25. Weng X, Kresse O, Cohen CE, Wu R, Gu H (2011) Modeling of hydraulic-fracture-network propagation in a naturally fractured formation. SPE Prod Oper 26(04):368–380
26. Xie H (1993) Fractals in rock mechanics. Crc Press
27. Xu W, Le Calvez JH, Thiercelin MJ (2009) Characterization of hydraulically-induced fracture network using treatment and microseismic data in a tight-gas sand formation: a geomechanical approach. In: SPE tight gas completions conference. Society of Petroleum Engineers
28. Xu W, Thiercelin MJ, Ganguly U, Weng X, Gu H, Onda H, Sun J, Le Calvez J (2010) Wiremesh: a novel shale fracturing simulator. Soc Pet Eng. doi:10.2118/132218-MS
29. Zimmerman RW et al (1993) A numerical dual-porosity model with semianalytical treatment of fracture/matrix flow. Water Resour Res 29(7):2127–2137

# 15

# *Drained Rock Volume Around Hydraulic Fractures in Porous Media: Planar Fractures versus Fractal Networks*

**KiranNandlal& Ruud Weijermars**

Harold Vance Department of Petroleum Engineering, Texas A&M University, 3116 TAMU, College Station, TX 77843-3116, USA

## ABSTRACT

This study applies the Lindenmayer system based on fractal theory to generate synthetic fracture networks in hydraulically fractured wells. The applied flow model is based on complex analysis methods, which can quantify the flow near the fractures, and being gridless, is computationally faster than traditional discrete volume simulations. The representation of hydraulic fractures as fractals is a more realistic representation than planar bi-wing fractures used in most reservoir models. Fluid withdrawal from the reservoir with evenly spaced hydraulic fractures may leave dead zones between planar fractures. Complex fractal networks will drain the reservoir matrix more effectively, due to the mitigation of stagnation flow zones. The flow velocities, pressure response, and drained rock volume (DRV) are visualized for a variety of fractal fracture networks in a single-fracture

**Citation:** Nandlal, K., &Weijermars, R. (2019). Drained rock volume around hydraulic fractures in porous media: planar fractures versus fractal networks. Petroleum Science, 16(5), 1064-1085., DOI: 10.1007/s12182-019-0333-7.

treatment stage. The major advancement of this study is the improved representation of hydraulic fractures as complex fractals rather than restricting to planar fracture geometries. Our models indicate that when the complexity of hydraulic fracture networks increases, this will suppress the occurrence of dead flow zones. In order to increase the DRV and improve ultimate recovery, our flow models suggest that fracture treatment programs must find ways to create more complex fracture networks.

## INTRODUCTION

The massive shift in US oil and gas production, after the Millennium turn, from conventional to unconventional reservoirs, has seen the hydraulic fracturing of production wells become a crucial aspect of completion engineering. The productivity of shale wells is now primarily based on how effectively hydraulic fractures help to provide new pathways for flow toward the wells from the reservoir matrix with ultra-low permeability. A proper understanding of the creation of hydraulic fractures and modeling of fluid flow near these fractures is needed for improvement in both the early well productivity and the ultimate recovery factor. The engineering of hydraulic fractures in unconventional hydrocarbon plays is a rapidly evolving art. Industry has moved to reduce fracture spacing from over 100 ft in 2010, to 50 ft in 2014, and less than 20 ft in 2018. The fracture spacing is designed using estimations of geomechanical rock properties from pilot wells in combination with fracture propagation models.

The earliest attempts to compare hydraulic fracture patterns may be traced back to Warpinski et al. (1994), but today there is still no consensus regarding the relative merits of the various fracture propagation modeling platforms. The American Rock Mechanics Association (ARMA) has recently initiated seven benchmark tests for 20 participating models (Han 2017) with the intent to showcase recognized physics of hydraulic fracturing. Most platforms for modeling hydraulic fracture propagation are based on assumed homogeneous rock properties, which therefore uniquely favor the formation of planar, sub-parallel hydraulic fractures (Parsegov et al. 2018).

Although current fracture diagnostics can rarely resolve the detailed nature of the fractures created during fracture treatment of unconventional hydrocarbon wells (Grechka et al. 2017), recent empirical evidence suggests that deviations from planar fracture geometry may exist. Physical evidence from cores that were sampled from a hydraulically fractured rock volume indicates that the generated fracture density far exceeds the number of

perforation clusters (Raterman et al. 2017). The creation of fracture complexity in terms of deflection, offset, and branching is possible at bedding surfaces and other naturally occurring heterogeneities, with preexisting natural fractures not appearing necessary for the creation of complex, distributed fracture systems. In fact, this finding is not entirely new. Work by Huang and Kim (1993) from mineback and laboratory experiments showed that the common notion that hydraulic fractures are planar in nature and assumed to propagate linearly perpendicularly to the minimum stress in simplified geomechanical models is not always correct. Clearly, empirical evidence suggests that fracture treatment may form fracture networks with branching fractal dimensions initiating from the perforation points (Fig. 1b), rather than planar hydraulic fractures (Fig. 1a). Thus, the practice of representing hydraulic fractures as single-planar, bi-wing cracks in the subsurface may be an overly simplistic representation of what in reality are more complex, fractal structures.

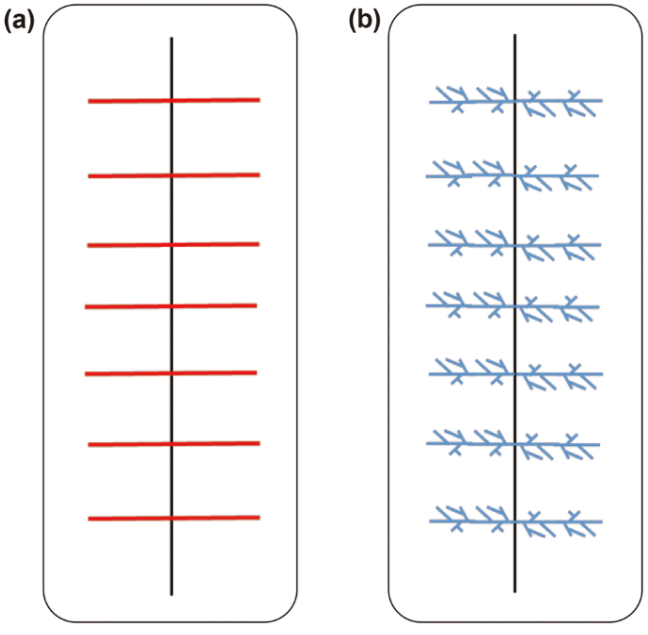


**Figure 1**: a Plan view of idealized planar hydraulic fractures along a horizontal wellbore. b Plan view of bi-wing branched, hydraulic fracture networks.

The likelihood of complex fracture networks being created by the fracture treatment process (rather than mutually sub-parallel planar fractures) is further supported by evidence from microseismic monitoring

(Fisher et al. 2002; Maxwell et al. 2002). In fact, most microseismic clouds generated during fracturing jobs show a poor correlation with the assumed planar, sub-parallel fractures. Therefore, we assume that the creation of complex hydraulic fracture networks may be more representative for many fractured or treated wells, especially those that possess a network of natural fractures due to stress regimes varying over geological time. Such conditions are typical of most unconventional shale plays under exploration and development. Consequently, the use of planar hydraulic fractures for modeling reservoir depletion may not always appropriately account for the actual reservoir attributes. The subsequent use of such over-simplified planar fracture geometries in flow models leads to unreliable calculations of important reservoir attributes such as the drained rock volume (DRV) and flaws in the associated pressure response.

Current fracture representation methods that try to capture fracture complexity include discrete fracture network models and the unconventional fracture model (Weng et al. 2011; Zhou et al. 2012) and are reviewed in Sect. 3.1. These established fracture geometry models use block centered grids typically coupled with finite-difference discretization flow models, including compositional flow models to simulate reservoir performance (Yu et al. 2017). The drawback of these finite-difference schemes is that they can be computationally intensive due to the necessity of fine meshing, especially at the fracture intersections. Other methods to model flow in fractured porous media include semianalytical models to simulate and analyze the pressure change for complex well interference systems (Yu et al. 2016). The suitability of the dual-porosity flow model (Warren and Root 1963) for low permeability reservoirs has been questioned (Cai et al. 2015). Further work has led to the development of triple porosity models to model flow in fractured reservoirs (Sang et al. 2016). Zhou et al. (2012) proposed a semianalytical solution for flow in a complex hydraulic fracture network model, which combined an analytical reservoir solution with a numerical solution on discretized fracture panels. The present study applies the analytical CAM flow model (Weijermars et al. 2016, 2017a, b, 2018), which is computationally efficient, while being able to accurately model the flow near fractal fractures such as those observed in field tests (Raterman et al. 2017).

Planar, sub-parallel hydraulic fractures with a certain spacing will develop dead flow zones between them where no fluid can be moved due to the occurrence of stagnation points surrounded by infinitely slow flow regions in their vicinity (Fig. 2a). Such dead zones suppress well productivity. These

may be remedied by plugging prior perforations and re-fracking into the dead flow zones by placing new perforations midway between the legacy perf zones after prior production wanes (Fig. 2b). However, the existence of dead zones is entirely premised upon the assumption that hydraulic fractures are planar and sub-parallel (Weijermars et al. 2017a, b, 2018).

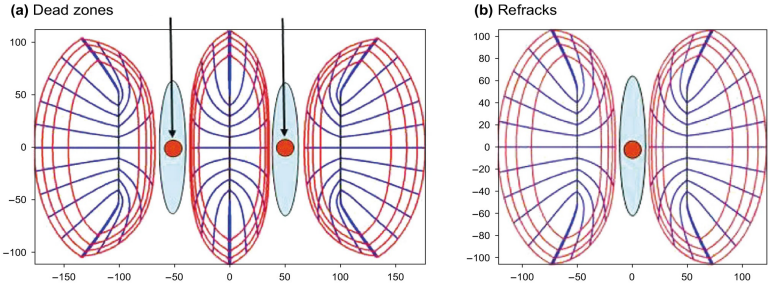


**Figure 2**: a Time-of-flight visualizations showing drained rock volume (DRV, red contours) and dead zones (blue region, around flow stagnation point, red dot) between three parallel, planar hydraulic fractures. b Refracks will tap into the dead zones. Length scale in ft.

The flow analysis in this study uses branched fractals for describing the complex fracture networks that are present in the subsurface. A variety of branched fractal fracture networks are imported into a drainage model based on complex analysis methods (CAM) to determine the flow response and pressure changes in the reservoir, for a given fracture geometry and fracture surface area. The major effect observed due to increasing fractal nature and branching of the fracture network (as outlined later in this study) is that the extent of dead zones between hydraulic fracture stages is suppressed. Instead, a more diffuse network of fractures drains the matrix between the fracture initiation points spaced by the perforation zones. Depending on the geometry of hydraulic fractures, an otherwise non-fractured matrix with negligible spatial variation in permeability can be drained more or less effectively. Future work will need to determine when hydraulic fractures will develop as fractal networks. While the jury is still out on the prominent geometry of hydraulic fractures (planar vs. fractal), the models developed in the present study consider the effect on drained rock volume in a systematic investigation of hydraulic fracture geometry ranging from planar to multi-branched, higher-order fractals. The present study breaks new ground by modeling the flow around fractal fracture networks in porous media. The results have implications for fracture treatment designs required to maximize the drained rock volume.

## *Natural examples of hydraulic fractures*

In addition to the cited examples of hydraulic fractures branching into closely spaced fracture networks (Raterman et al. 2017; Huang and Kim 1993), manifestations of bifurcating fracture networks are commonly known from surface outcrops of hydraulic fractures formed by natural processes. For example, hydrothermal veins invaded and hydraulically fractured Proterozoic rocks from the AravalliSupergroup in the state of Rajasthan, India (Kilaru et al. 2013; McKenzie et al. 2013; Pradhan et al. 2012). These hydraulic fractures formed under high fluid pressures deeper in the crust before being exhumed by tectonic uplift and erosion. Polished slabs containing the naturally created hydraulic fracture networks in Bidasar ophiolites are shown in Fig. 3a. These rocks are exploited as facing stones and quarried near the villages of Bidasar-Charwas, Churu district (Fig. 3b). The quarries are confined to a 0.5-km-wide and 2.5–3.5-km-long belt of open pits dug below the desert plain. The rock in these pits has been described as the Bidasar ophiolite suite (Mukhopadhyay and Bhattacharya 2009).

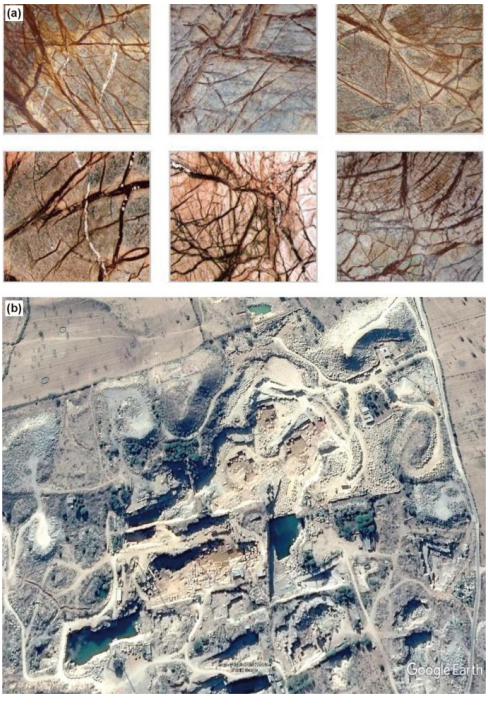


**Figure 3**: a Examples of rock slabs from Bidasar with bifurcating, hydraulic injection veins. Image dimensions about 1 square meter (courtesy Dewan Group). b Satellite image of quarry near Bidasar, Rajasthan, India (roads for

scale). North is down in the above image (Google Earth composite of December 16, 2015).

The precise natural pressure responsible for the injection of the hydraulic veins is unknown, but the pressure has exceeded the strength of the rock and was large enough to open the fractures at several km burial depth, thus being in the order of 100 MPa. The fluid was injected into the fractures as well as into a pervasive system of microcracks connected to the main fractures. Based upon the splaying of the fractures, one may reconstruct the provenance of the fracture propagation (van Harmelen and Weijermars 2018). Local heterogeneities in elastic properties may create conditions favoring the nucleation of fracture bifurcation points. More work is needed to determine the critical conditions required for creating fractal fracture networks in hydraulic fracture treatment programs.

Slabs like those shown in Fig. 3a may serve as a natural analog for flow into hydraulic fractures in shale reservoirs, with the limitation that shale may have different elastic moduli, different petrophysics, grain sizes and most crucially, the fracture aperture width from hydraulic fracturing which is smaller than that in our natural analog presented here. Hydraulic fracture apertures in shale reservoirs are thought to be in the range of 1–5 mm with the majority of created fracture apertures being less than 2 mm (Gale et al. 2014; Zolfaghari et al. 2016; Arshadi et al. 2017). Natural fracture networks created in the rocks of Bidasar due to hydrothermal activity in the earth's crust bears similarity to man-made hydraulic fracture networks that require the use of high pressure fluids and proppants by fleets of pumps and trucks.

We contend that the injection patterns of hydrothermal veins exposed in natural outcrops and in quarries (of rocks exhumed by tectonic processes and subsequent erosion) provide a useful analog for hydraulic fracture networks created when fluid injection is applied to hydrocarbon wells. Figure 4a, b shows an analysis of the principal hydraulic fractures in a rock slab from Bidasar. The corresponding flow front through the main fractures and matrix is modeled in Fig. 4c, d. The simulation does not account for the creation of the fractures, but instead assumes that these have already developed and are subsequently flushed by the hydrothermal injection fluid. For details, see a prior study from our research group (van Harmelen and Weijermars 2018).

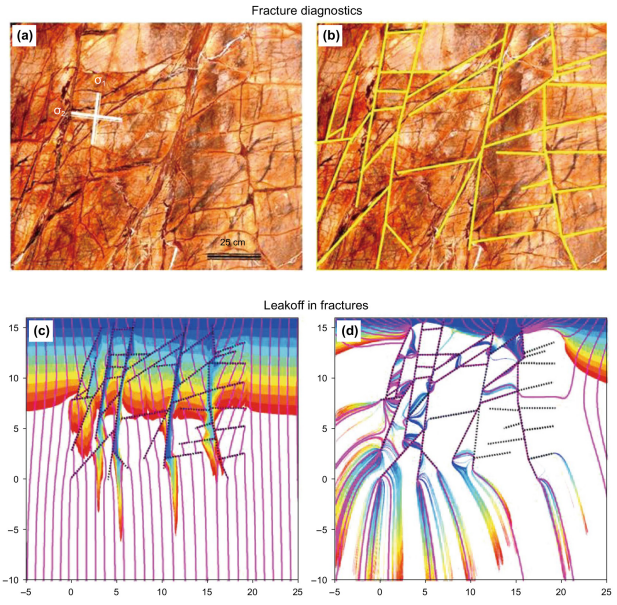


**Figure 4**: After van Harmelen and Weijermars 2018, Fig. 10a, b.

Orthogonal photograph of polished rock slab with injection veins. a Filled fracture veins with interpreted directions of the original largest ($\sigma_1$) and intermediate ($\sigma_2$) principal stress axes. Major veins open first normal to $\sigma_1$ and then normal to $\sigma_2$, which likely swapped with $\sigma_1$ after hydraulic loading of the main veins. b Interpreted principal fracture network (yellow lines). c, d Fluids take by matrix and fractures in model assuming low permeability contrast (c), and high permeability contrast (d). Matrix blocks between the fractures in case d take less fluids than in case c. Rainbow colors give time of flight contours, and fluid injection is from the top. Flow lines are given by magenta streamlines.

# FRACTURES AND FRACTAL THEORY

## Prior Models of Complex Hydraulic Fractures

### *Fracture propagation and fracture flow models*

Various attempts have been made by researchers to develop new models to better represent complex hydraulic fracture network systems, in

both geomechanical fracture propagation models and in production forecasting based on flow models in fractured reservoirs. For example, the geomechanical unconventional fracture model (UFM) was developed to simulate the propagation of complex fractures in formations with preexisting natural fractures (Weng et al. 2011). The UFM simulates the propagation, deformation, and fluid flow in a complex network of fractures. The model seeks to solve a system of equations governing parameters such as fracture deformation, height growth, fluid flow, and proppant transport, while considering the effect of natural fractures by using an analytical crossing model. The Wiremesh model consists of a fracture network with two orthogonal sets of parallel and uniformly spaced fractures (Xu et al. 2010; Meyer and Bazan 2011). Given fracture spacing, mechanical properties of the formation layers and pumping parameters, this shale fracturing simulator can be used to predict the growth of the hydraulic fracture network. Benefits of the Wiremesh model come in the form of increased surface area of the fracture network and mechanical interaction of fractures but are still only an approximation of the network's complexity. Limitations of this model include not being able to directly link preexisting natural fractures to the hydraulic fracture network with regard to the fracture spacing used and that the network geometry is assumed to be elliptical in shape and thus symmetric. These assumptions do not always fit with fracture geometry indicated by microseismic data. Alternative modeling attempts sought to create a complex fracture network by finding a full solution to the coupled elasticity and fluid flow equations using 2D plane strain conditions (Zhang et al. 2007). Other studies presented a complex fracture network capable of predicting the interaction of hydraulic fractures with natural fractures but did not consider fluid flow and proppant transport (Olson and Taleghani 2009).

Flow models of fractured reservoirs have also advanced by upscaling a discrete fracture network (DFN) model into a dual-porosity reservoir model or by enhancing the permeability of stimulated reservoir areas (Zhou et al. 2012). The fundamental discrete fracture network (DFN) solution methodology is based on satisfying continuity, mass conservation, constitutive relationships, and momentum equations (Meyer and Bazan 2011). For fracture representation in this method, each fracture panel had to be manually input with specific fracture parameters thus requiring prior knowledge of hydraulic fracture orientation. The model also assumes the intersection of individual planar fractures to create the complex fracture network with drained area represented by pressure depletion plots. These

DFN are created using stochastic simulations based on probabilistic density functions of geometric parameters of fracture sets relating to fracture density, location, orientation and sizes based on measurements from field outcrops or borehole images. DFN requires an extremely fine grid at the scale of the fractures leading to complicated gridding and for multi-stage wells with large fracture numbers is very computationally expensive.

Recent advancements with DFN have now led to the embedded discrete fracture model (EDFM). EDFM allows for complex fractures to be implemented in conventionally structured matrix grids without using local grid refinement (Yu and Sepehrnoori 2018). EDFM can be thought of as a hybrid approach where the dual-porosity model is used for the smaller- and medium-size fractures, and the DFN is used to model larger fractures (Li and Lee 2008). Advantages of EDFM include the use of a structured grid to represent the matrix and fractures. EDFM was initially used for planar 2D cases but has developed to model in 3D (Moinfar et al. 2014). Though EDFM has overcome some of the problems of the traditional DFM method, it can still be computationally expensive in complexly fractured reservoirs.

### *Fracture Geometry Models*

Beyond the modeling attempts outlined above to recreate and describe complex fracture networks, work has been done by various authors to characterize the created fracture complexity based on field data. Zolfaghari et al. (2016) proposed the use of flowback salinity data to help characterize the fracture network complexity. The shape of the flowback curves is used to define the aperture size distribution (ASD) for a particular well. A narrow ASD is correlated with a simple fracture network, while a wider ASD is believed to match a fracture network that is more dendritic and complex in nature. Zolfaghari et al. (2017) looked at correlating total ions produced from chemical flowback to estimate fracture surface area for two wells that was validated against rate transient analysis (RTA) values. Based on these results, the authors postulated that greater production from one well was due to the larger fracture area calculated. This larger fracture area was attributed to a more complex fracture network in the subsurface, but there was no indication of potential fracture geometry. Another attempt to characterize fracture complexity utilizes tracer flowback data. Li et al. (2016) made use of tracer flowback data to characterize fracture morphology into three general categories. Based on the tracer breakthrough curve (BTC) the hydraulic fractures are roughly classified as microfractures, large fractures, and their mix. These methods allow for qualitative descriptions of the subsurface

fracture network but do not allow for quantitative description in terms of surface area of the complex fracture network in contact with the reservoir matrix or fracture network geometry.

The majority of fracture flow methods attempt to introduce discrete fractures to model explicitly the elastic fracture propagation, subsequent flow and evacuation of fluid from the reservoir. The importance of accounting for fracture network complexity is apparent from production and pressure transient responses (Jones et al. 2013). Properly modeling the complexity of the fracture network is crucial for accurate history matching in these reservoirs. In addition to the discrete fracture models based on geomechanical failure modes, another potential approach to model fracture complexity uses fractal geometry. Fractals have long been used to model naturally occurring phenomena including petroleum reservoir and subsurface properties and equations (Berta et al. 1994; Cossio et al. 2012). Early work by Katz and Thompson (1985) and Pandey et al. (1987) showed that fracture propagation in nature was not irregular and could be represented by various fractal models. Building forward on this work Al-Obaidy et al. (2014) and Wang et al. (2015) approached the fracture network problem by creating branched fractal models to capture fracture network complexity.

## *Fractal Theory*

Fractal theory was first put forth by Mandelbrot (1979) as "*a workable geometric middle ground between the excessive geometric order of Euclid and the geometric chaos of general mathematics*". A fractal was defined by Mandelbrot as a rough or fragmented geometric shape that can be split into parts each of which is a reduced-size copy of the whole. For an object to be termed a fractal, it must possess some non-integer (fractal) dimension (Frame et al. 2012). If this fractal dimension is an integer, we can obtain normal Euclidean geometry such as lines, triangles and regular polygons. Cossio et al. (2012) put into simple terms that a property of a given system can be termed a fractal if its seemingly chaotic, and unpredictable behavior with respect to time and space can be captured in a simple power-law equation. One of the basic principles underlying fractal geometry is the concept of self-similarity at various levels. If one zooms in on the represented object, a natural repetition of patterns and properties can be observed.

The abundance of fractals in our natural environment ranges from the fractal nature of coastlines to the growth and bifurcation of trees and plants. The use of fractals allows one to make mathematical sense from seemingly random and chaotic processes. Early use of fractals in petroleum engineering

began with the work of Katz and Thompson (1985) to represent pore spaces in sandstone cores. The use of fractal theory to represent the pore space was verified by its accurate prediction of the core porosity. We now extend this approach of fractals to model complex hydraulic fracture networks in a reservoir with assumed parameters.

One approach in the fractal theory is to create a fracture network model by using the fractal addition of the Lindenmayer system (Wang et al. 2017). The Lindenmayer system (L-system) is widely used to describe the growth of plants which can be seen to be bifurcating in nature as well as being fractal at some scale. The L-system is a rewriting system that defines a complex object by replacing parts of the initial object according to given rewriting rules which simulate development rules and topological structures well (Lindenmayer 1968; Han 2007). Wang et al. (2017) introduced the L-system into fracture characterization because a fracture has similar development rules to trees. Four key parameters are used to control the generation of the fracture network, and these parameters influence the performance of production wells (Wang et al. 2018):

- Fractal distance ($d$) controls the extending distance of the fractal fractions, (can be thought of as a basic repeating pattern) and closely relates to the half-length of the fractures created.
- Deviation angle ($\alpha$) controls the orientation of the fracture branching once deviation from the base fracture pattern occurs and relates to the area of the stimulated reservoir.
- Number of iterations ($i$) controls the growth complexity of the fracture network or in other words fracture network density. This parameter relates to the multi-level feature of the fractal branches; during each iteration, the fractal fractures will branch from the original nodes following the given generating rules to construct that part of the network.
- Growth of the bifurcation of the fractures and irregular propagation mode of a complex fracture network are subject to fractal rules, which are an implicit means to account for geomechanical heterogeneities (Wang et al. 2015, 2017, 2018).

The branching fractal model used in our study makes use of a simple L-system growth rule, which along with the fractal distance parameter controls the branched hydraulic fracture network's half-length, the deviation angle controls the branched fracture network width span, and the iteration number controls the branching complexity or density. Though the fracture

geometry created using the L-system is seemingly random, we use the branching of the hydraulic fracture in our models to capture and replicate the physical evidence seen in cores recovered from the Hydraulic Fracturing Test Site (HFTS). These cores show that hydraulic fractures "diverge with a projected line of intersection, or branch line, just out of the core" (Raterman et al. 2017). We acknowledge that due to uncertainty in the subsurface, there are infinite possibilities that can be modeled by changing parameters such as branching angle, fracture length, and iteration number. Our current model uses branching angles and other parameters (given in Table 1) that generate a fractal network span and half-length that matches commonly observed values from fracture propagation modeling and microseismic data.

**Table 1:**Parameters used for creation of different fracture geometries

| Fracture model | *F* length, ft | *G* length, ft | Branching angle, degrees | Created fracture half-length $x_f$, ft | Created fractal network span, ft |
|---|---|---|---|---|---|
| Planar | 400 | – | – | 400.0 | – |
| First-generation fractal | 100 | 100 | 10 | 398.5 | 34.70 |
| Second-generation fractal | 40 | 40 | 10 | 398.2 | 69.04 |
| Third-generation fractal | 18 | 15 | 10 | 391.1 | 89.44 |

# FLOW MODELS

## Complex Analysis Method (CAM) Tool

The effect of different fracture networks on drained areas, velocity profiles, and pressure depletion is quantified and visualized using complex analysis methods. Introductions to analytical element method applications to subsurface flow are found in several textbooks (Muskat 1949; Strack 1989; Sato 2015). Hydraulic fractures connected to a well act as line sinks (Weijermars and van Harmelen 2016). For multiple interval sources with time-dependent strength $m_k(t)$, the instantaneous velocity field at time $t$ can be calculated from:

$$V(z,t) = \sum_{k=1}^{N} \frac{m_k(t)}{2\pi L_k} e^{-i\beta_k} \cdot \left(\log\left[e^{-i\beta_k}(z - z_{c,k}) + 0.5L_k\right] - \log\left[e^{-i\beta_k}(z - z_{c,k}) - 0.5L_k\right]\right) \quad \text{[ft/month]}. \tag{1}$$

Traditional applications of CAM in subsurface flow models make use of

integral solutions to model streamlines for steady state flows (Muskat 1949; Strack 1989; Sato 2015). A fundamental expansion of the CAM modeling tool is the application of Eulerian particle tracking of time-dependent flows, which was first explored in Weijermars (2014) and then benchmarked against numerical reservoir simulations in Weijermars et al. (2016).

Most current studies use numerical reservoir simulation to create pressure depletion plots as a proxy for the drained regions in the reservoir after production. CAM can determine the drained rock volume (DRV) by constructing time-of-flight contours to the well based on Eulerian particle tracking taking into account the changing velocity field (Weijermars et al. 2017a, b). This approach provides accurate determinations of the DRV (Parsegov et al. 2018) with the added benefit of identifying flow stagnation zones. Such stagnation zones or "dead zones" are defined as regions of zero flow velocity (Weijermars et al. 2017a, b), which create undrained areas that can be targeted for refracturing (Weijermars and Alves 2018; Weijermars and van Harmelen 2018). Another added advantage of CAM models is their infinite resolution at the fracture scale due to the method being gridless and meshless, resulting also in faster computational times compared to numerical simulations. Modeling flow in fractured porous media using analytical solutions generated with time-stepped CAM models also allows the determination of pressure changes in the reservoir. Pressure depletion plots are calculated by evaluating the real part of the complex potential to quantify the pressure change at any location $z$ at a given time $t$ by:

$$\Delta P(z,t) = -\frac{\phi(z,t)\mu}{k} \qquad \text{[psi]} \tag{2}$$

Here $\phi(z,t)$ is the potential function with pressure scaling based on fluid viscosity $\mu$ and permeability $k$ of the reservoir. The actual pressure field at any given time can be computed from the following expression with $P_0$ accounting for the initial pressure of the reservoir:

$$P(z,t) = P_0 + \Delta P(z,t) = P_0 - \frac{\phi(z,t)\mu}{k} \qquad \text{[psi]} \tag{3}$$

The basic premise of the CAM solution is placing the produced fluid volume back into the reservoir to determine the areas drained and the pressure response corresponding to this fluid placement. From replacing production into the reservoir based on history matching using decline curve analysis, the corresponding pressure depletion is obtained by simply reversing the signs of the values on the pressure scale from positive to negative (Weijermars et al. 2017b). For the pressure depletion plots later in this study, the spatial

pressure change $\Delta P(z,t)$ is shown.

## Flux Allocation and Production Modeling

This study assumes a synthetic production well of 8000 ft horizontal length and 80 transverse fractures with 100-ft spacing between them. This gives a total distance covered by the fractures of 7900 ft, leaving an untreated distance of 100 ft between the heel of the well and the first hydraulic fracture of the treatment plan. The flow simulation starts with a single fracture, using a base case model with a single-planar fracture, expanded with branched iteration models of the fracture geometry. The fracture trees initiating from single perforations are then expanded to multiple fractal systems for fracture stages with variations in complexity to observe the impacts on the DRV, velocity field, and pressure field. By assuming symmetry about the wellbore, we initially look at only one half of the fracture (half-length $x_f$) to determine the effects on the flow velocities and pressure depletion for different fracture geometry models.

Current fracture propagation models that use simple planar fractures have the ability to predict proppant placement density which due to uneven placement can create zones of higher fracture conductivity (Parsegov et al. 2018). Though work has been done on proppant placement in complex fracture networks (Shrivastava and Sharma 2018) as we assume infinite fracture conductivity in our fractal network, uneven proppant placement is not considered in this model.

Production data from a typical Wolfcamp well used in a companion study (Parsegov et al. 2018) were used to produce a history matched type curve based on decline curve analysis. To match the production decline, the Duong decline method was used and found to give a total cumulative production over 30 years that is in line with forecasted EUR for wells in the Wolfberry play, Midland Basin under which the Wolfcamp Formation falls. Forecasts give an ultimate per well recovery estimated at 100,000–140,000 barrels of oil equivalent (Hamlin and Baumgardner 2012). The well used Duong decline parameters resulting in a cumulative production forecast of 102,069 bbls after a productive well life of 30 years.

Flux allocation was proportional to the relative surface areas of each branched fracture. For each successive iteration, the next generation of branches of the fracture network becomes progressively shorter, thereby automatically being allocated less of the overall production. This allocation

method based on fracture length allows for the main fracture branches having the highest allocated flux, while the progressive iterations of the branched network will have less flux allocated. The flux allocation algorithm used is as follows:

$$q_k(t) = Z \cdot S(1 + WOR) \cdot q_{\text{well}}(t) \cdot \left( \frac{h_k L_k}{\sum_k^n h_k L_k} \right) \quad [\text{ft}^3/\text{month}] \tag{4}$$

where $Z$ is a conversion factor of 5.61 to convert from barrels to ft$^3$; $S$ is the prorated factor to scale the total well production, for example scaling for one half-length of one fracture, S=(1/80)×0.5=0.00625.

Once the flux algorithm has been properly calculated, the next step is the creation of the time-dependent strength value to use in the velocity and pressure potential equations. This strength is scaled by reservoir properties such as the formation volume factor ($B$), porosity ($n$) residual oil saturation ($R_o$) (Khanal and Weijermars 2019) and fracture height ($H$) and is given as follows (data used is given in Table 2):

$$m_k(t) = \frac{B \cdot q_k(t)}{H_k \cdot n \cdot (1 - R_o)} \quad [\text{ft}^2/\text{month}]. \tag{5}$$

**Table 2:**Reservoir parameters used for modeling

| Porosity $n$ | Permeability $k$, µD | Water–oil ratio (WOR) | Formation volume factor $B$ | Viscosity $\mu$, cP | Residual oil saturation $R_o$ | Fracture height $H$, ft |
|---|---|---|---|---|---|---|
| 0.05 | 1 | 4.592 | 1.05 | 1 | 0.20 | 75 |

## Drained Rock Volume (DRV)

For the determination of drainage areas, the CAM process utilizes the concept of flow reversal. The produced fluid is essentially placed back into the reservoir at the same rate as produced to determine where the fluid has been drained from. As such, the way in which the hydraulic fractures are represented will have a direct impact on the area which is drained, and the corresponding pressure gradient that drives the fluid flow back into the reservoir. The underlying assumption is that the larger the surface area of the hydraulic fracture the easier the flow into the matrix (and reverse), the narrower will be the width of the region drained around the fracture and thus the lower the pressure needed to achieve a given production rate. A fracture with smaller overall surface area (idealized planar hydraulic fracture, Fig. 5a)

will need to have wider drainage width, whereas for the same production, a greater fracture surface area in contact with the matrix will mean a narrower drainage width (Fig. 5b).

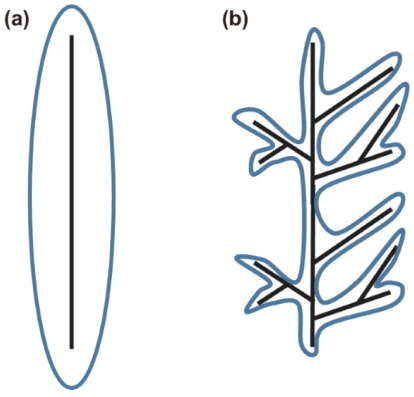


**Figure 5**: a Plan view of drainage area around a planar fracture. b Drainage area around a branched fracture representative of our fracture network.

Initially, we expected that a larger fractal dimension with more surface area would increase the injectivity of the matrix and require lower pressures to evacuate the reservoir fluid. Our models, however, show that once a constant total fluid production is used the overall pressure change remains the same regardless of the fracture network complexity. The models confirm the expectation that more complex fractal networks cause smaller lateral drained areas away from the fractures with greater local pressure variations. The reason for the localized pressure depletion peaks is that denser fracture networks with the same injectivity per fracture length will locally remove more fluid molecules from the matrix, thus resulting in larger pressure depletion locally.

The hydraulic fractal network is created and applied using an effective method of investigation by first modeling a small section of the horizontal wellbore. Because we use the method of fractals, a small sample of the well system should in fact be representative of the much larger drainage behavior of the well. This modeling strategy will also be beneficial in terms of computational and modeling time. Once the flow and pressure response have been determined based on individual fractal networks with increasing complexity, the investigation is extended to multiple fractal networks to investigate the possible effects of flow interference in fractured wells with numerous stages. Using this method both symmetrical and asymmetrical networks are modeled to determine changes in drained areas and flow

response. The impact of fractal network complexity on reduction in flow stagnation zones is investigated to help determine the ideal fracture geometry to increase overall recoveries.

## Model Validation

The analytical solution to flow based on the complex analysis method has been validated against numerical simulators in previous work done. Weijermars et al. (2017a) compared the results of the analytical method for flow in planar fractures modeled as line sinks against a commercial simulator (ECLIPSE) that was augmented with a validated streamline tracing algorithm. This allowed for the comparison of time of flight contours as well as streamline patterns. This validation against the numerical simulator was achieved via a three-step process. Flow simulation in the commercial simulator provided pressure and flow rates on the six faces for each finite cell. These results were then imported into a streamline algorithm to obtain streamline tracing data, which was then imported in Petrel to visualize the actual streamlines. For the simple planar fracture case, the results from the numerical simulator matched well with the analytical complex analysis method proving validation of the complex analysis solution (Fig. 6). Our current model can be thought of as an extension of this validated case where we replace the simple planar fracture by our complex fractal network that comprises numerous line sinks acting within our reservoir. For a more detailed look at the validation, the reader is referred to the work by Weijermars et al. (2017a).

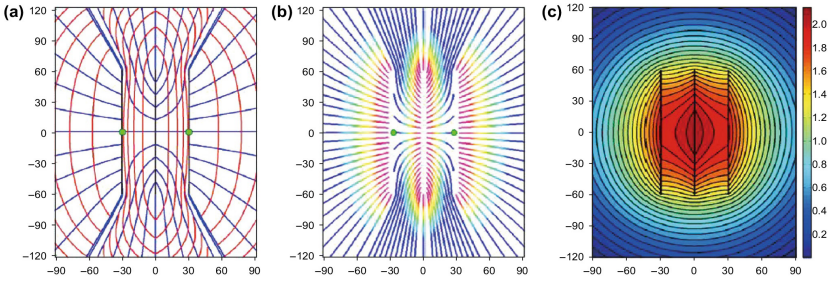


**Figure 6**: Adapted from Weijermars et al. (2017a, b).

Streamlines with drainage contours. a Analytical solutions. Streamlines (blue), time of flight contours (red), stagnation points (green). b Commercial simulator. Streamlines and time of flight contours (rainbow colors). c Analytical pressure field. Fractures represented as black lines.

# RESULTS

## Fractal Network Creation

The Lindenmayer (L-system) rewriting system based on fractals is used to construct numerous branching fractal networks. This system defines a complex object by replacing parts of the initial object according to given rewriting rules. The L-system, combined with information on fractal network geometry, fractal distance ($d$), deviation angle ($\alpha$), and iteration number ($i$), allows the defining of rules for creating the overall network. A systematic workflow to investigate the effect of fractal network complexity is laid out in the subsequent sections.

The network structure is defined by a simple string or axiom using variables '$F$' and '$G$'. Using these variables, branching is represented by the use of square brackets with the '+' and '−' symbols denoting either clockwise or anticlockwise branching angles. The iteration number gives the replacement rules, changing the branching complexity and is referred to as different fractal generations. A simple fractal code written in MATLAB from the M2-TUM group from the TU Munich was modified for our purpose of fractal network generation in 2D (available at http://m2matlabdb.ma.tum.de/author_list.jsp).

Axiom used for generation of the symmetrical fractal networks:

- Symmetrical axiom rule = '$F\,[+G]\,[-G]\,F$'.

Generated fractal networks using the above axiom and geometry parameters from Table 1 are shown below (Fig. 7).

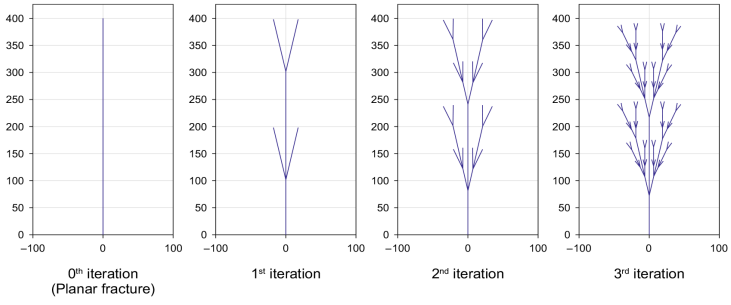


**Figure 7**: Fractal networks created using the axiom rule and fracture geometry properties.

## Drainage by Single Symmetrical Fractal Networks

The first scenario investigated uses symmetrical fractal networks. The L-system with given fractal geometry parameters (Table 1) were incorporated in the CAM model to determine flow and drained rock volume responses for a variety of fractal geometries, ranging from a single-planar fracture to a third-generation symmetrical fractal network (Fig. 8). Moving from the planar fracture geometry towards higher fractal generations, an exponential increase occurs in the fracture surface area. Even a simple branching hydraulic fracture is shown to have a much larger surface area than the planar fracture. Assuming the well production rate is fixed, total drained volume of fluid per fractal network stage stays constant. Higher fractal generations cover a larger areal extent but drain narrower matrix depth, whereas the planar fracture drains broader distances away from the fracture (Figs. 5, 8).

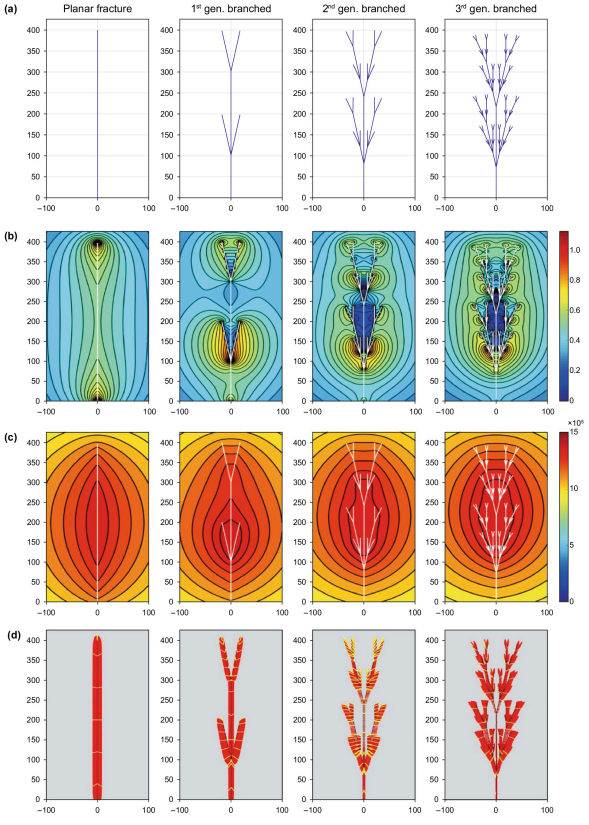


**Figure 8**: a Fracture geometry modeled with planar fracture, first-generation symmetrical fractal network, second-generation, third-generation from left to

right. b Velocity contour plot (ft/month) after 1 month production. c Pressure contour plots (drawdown in psi) after 1 month production. d Drained areas after 30 years production (drained area highlighted in red with tracked streamlines in yellow). Length scale in ft.

The velocity contour plots show that when the fracture geometry evolves from planar to successive branched iterations there is a greater variability of the local velocities (Fig. 8b). As the branching complexity increases, individual fracture segments are spatially clustered close together, leading to small scale interferences resulting in higher flow velocities at the fracture network outer extremities, which is balanced by slower velocities between the branching fractures. The overall pressure change is found to be similar even as fracture complexity increases (Table 3). Pressure change is directly linked to the amount of production from the reservoir which is kept constant for all simulations. What is observed from the pressure depletion plots is that the greatest local pressure response occurs in areas with the highest fracture density (Fig. 8c). Comparing the response from the velocity and pressure plots, the greatest pressure change does not correlate with where fluid flows fastest around the fractures. However, there is a clear correlation between the steepest pressure gradients (regions where the pressure contours are spaced tightest) and the regions of highest flow velocity.

**Table 3:**Comparison of various parameters for different symmetrical fracture geometry

| Fracture model | Maximum velocity, ft/month | Maximum pressure change, psi* | Fracture surface area, $ft^2$ |
|---|---|---|---|
| Planar fracture | 0.9477 | $1.3939 \times 10^6$ | $6.000 \times 10^4$ |
| First-generation fractal | 1.1088 | $1.4547 \times 10^6$ | $10.501 \times 10^4$ |
| Second-generation fractal | 1.0087 | $1.4286 \times 10^6$ | $20.403 \times 10^4$ |
| Third-generation fractal | 1.0979 | $1.5035 \times 10^6$ | $37.040 \times 10^4$ |

*The pressures of an order $10^6$ psi are due to reservoir permeability assumption of 1 μD, and would be a order of $10^3$ psi if 1 mD is assumed

Drained areas are outlined by the time-of-flight contours inferred from particle tracking, based on the production allocation due to the selected fracture strengths (Fig. 8d). Results for a planar fracture geometry show equal drainage around the entire fracture. As more complex fractal networks are simulated, the results show the total drained area stays constant (regardless of fracture complexity as a constant production is used). However, the DRV regions are not distributed equally around the fracture segments in the

network, leading to some small undrained areas between the branches of the fractal network.

## Drainage by Single Asymmetrical Fractal Networks

Previous modeling (Sect. 5.2) assumed the generation of symmetrical fracture branches on both sides of the main branch. Due to the anisotropic nature of rocks, there is a strong possibility that these branches in reality may form asymmetrically due to changing rock properties. Using the L-system, different generations of branched asymmetrical fractures are modeled with the CAM to determine the impacts of asymmetry on flow and drained rock volumes (Fig. 9). The axiom rule for this asymmetrical fractal network is given as:

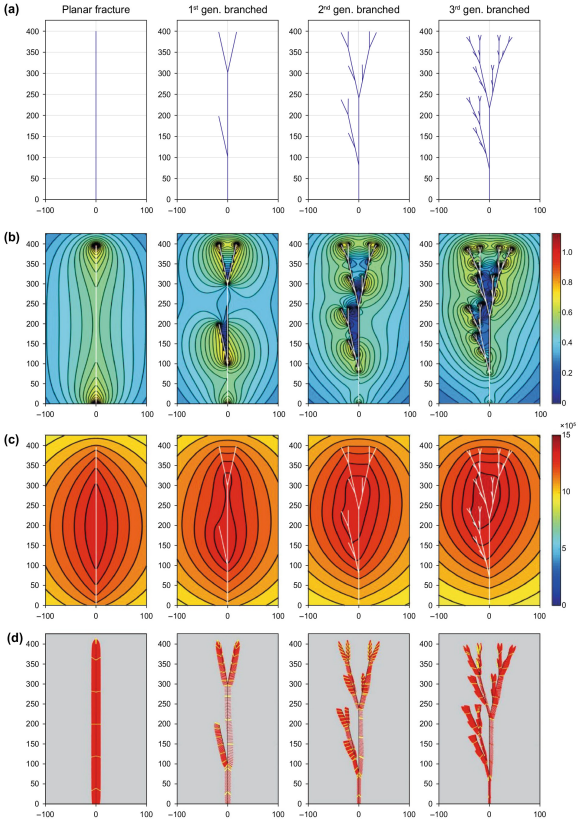


**Figure 9**: a Fracture geometry modeled with planar fracture, asymmetrical first-generation asymmetrical fractal network, second generation, third generation from left to right. b Velocity contour plot (ft/month) after 1 month production.

c Pressure contour plots (drawdown in psi) after 1 month production. d Drained areas after 30 years production (drained area highlighted in red with tracked streamlines in yellow). Length scale in ft.

Axiom used for generation of the asymmetrical fractal network:

- Asymmetrical axiom rule = '$F\ [-G]\ F$'.

Asymmetric fractal networks still effectuate an increase in fracture surface area for successive iterations when compared to a planar fracture but less than for a symmetrical fracture network (Fig. 10). The velocity plots again show greater variability in flow velocities as the fractal network complexity increases with the greatest variation coinciding with the region where fracture density is highest (Fig. 9b). The asymmetrical fractal network shows similarity to the symmetrical fractal network in terms of overall pressure depletion and maximum/minimum flow velocities. The major difference with the asymmetric fractal network is the skewing of the highest pressure depletion contours to the area of highest fracture density (Fig. 9c). The premise that the steepest pressure gradients (areas where the pressure contours are tightest) correlate with areas of highest flow velocity is reinforced from these plots. Drained areas are found to conform to the areas of highest flow velocity (Fig. 9d) with small-scale stagnation areas found in between the highly branched areas as seen before in the symmetrical fracture network models (Fig. 8).

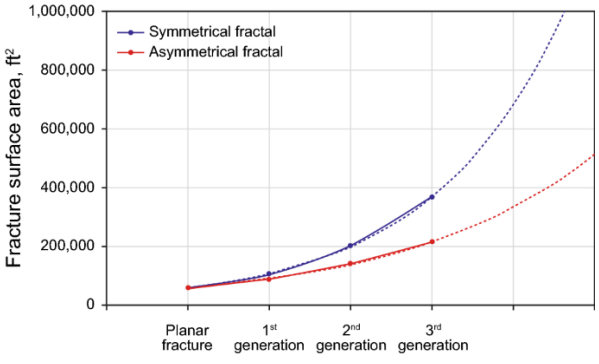


**Figure 10**: Graph of surface area versus fracture geometry type for asymmetrical and symmetrical fractal networks.

## Interference Effects of Multiple Fractal Networks

Simulations in the previous section investigated the effect of moving from a single-planar fracture to more complex symmetrical and asymmetrical branching fractal networks. Modeling of a single fracture is the most logical point to start from but is not truly representative of modern hydraulically fractured wells with multiple perforations per stage and multiple stages, resulting in several hundred fracture initiation points at the perforations. The typical hydraulically fractured well completion in 2017 and beyond can have 50 stages or more. The spacing of the fractures may have a crucial impact on flow interference and thus affects drained areas and estimated ultimate recovery. This section seeks to determine the impact of interference effects on flow velocity, pressure depletion, and drained areas by simulating multiple fracture networks with different fractal network configurations. Using a base case of three planar fractures, comparisons of flow velocity, drained areas, and pressure depletion are made for various combinations of second-generation fractal networks (Fig. 11).

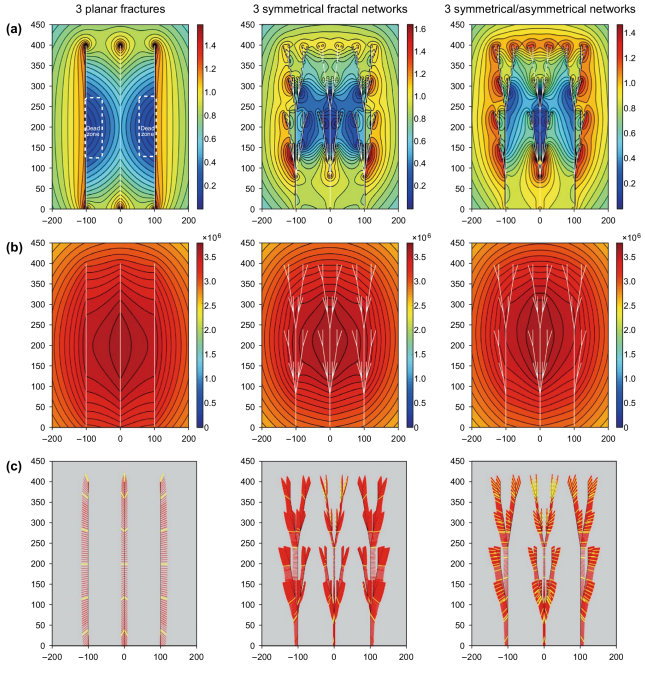


**Figure 11**: a Velocity contour plots (ft/month) after 1 month production. b Pressure contour plots (drawdown in psi) after 1 month production. c Drained areas after 30 years production. Length scale in ft.

The base case models the flow response of three planar fractures and shows that with the given fracture half-length and fracture spacing, extremely low flow velocities occur between the central and outer fractures (Fig. 11a, left column). Flow stagnation zones are identified by velocity lows. These stagnation zones create areas in the reservoir that are left undrained due to the interference effect of the multiple fractures. The only way to drain these areas would be refracturing into the stagnation zones. The pressure depletion plot (Fig. 11b, left column) shows the largest pressure drop occurs between the fractures; however, this coincides with our lowest flow velocities and stagnation zones. This reinforces the idea put forward in Weijermars et al. 2017b that the pressure plots are poor proxies to recognize the reservoir areas drained by the fractures. The drained region after 30 years is visualized by the time-of-flight contours to the fractures (Fig. 11c, left column) and shows the majority of the drained area is at the outer fractures where we also have the highest flow velocities. Flow interference between the fractures creates the stagnation zones that lead to undrained rock volumes.

The second scenario investigates the response to three symmetrical second-generation fractal networks (Fig. 11, center column). Slower velocities are again found between the branched fractal areas but for this case are confined to a smaller area. This in turn means that branched networks create smaller stagnation zones, than with the planar fractures and thus the fractal network should be conducive to drain more of the reservoir space effectively (Fig. 11c, center column). Better drainage coverage from the fractal network means less refractures are needed between the initial fractures. For branching fractal networks, too small a fracture spacing will result in draining the same reservoir areas due to overlapping fractal networks creating an inefficient drainage process.

A third scenario looks at a central symmetrical fractal network flanked by two asymmetrical fractal networks (Fig. 11, right column). Again, the areas of highest velocity occur at the periphery of the fractures with the slowest flow between the fractal networks. From the various simulations, there is a clear correlation between higher fractal network complexity and suppression in the areal extent of flow stagnation zones. Reduction in stagnation zones in turn means more efficient drainage of our rock and smaller undrained areas between fracture stages.

One interesting simulation case uses a symmetrical fractal network followed by two asymmetrical networks that grow away from the first symmetrical network (Fig. 12). This orientation is used to represent the effect

of stress shadowing during sequential hydraulic fracturing from toe to heel. Stress shadowing is the concept that fractures in the subsurface will tend to propagate away from the direction of already fractured rock due to changes in the stress regime (Nagel et al. 2013). The introduction of a poroelastic model to capture stress shadowing is outside of the scope of this work but to recreate this effect we have the first hydraulic fracture network at the toe being symmetrical due to no stress shadowing. The subsequent hydraulic fracture networks towards the heel of the well (Fig. 12) will be influenced by stress shadowing and this is captured by no branching of the fractal network in the direction of the previous hydraulic fracture at the toe leading to an asymmetrical fractal network. Using this fracture geometry to mimic stress shadowing, the area of greatest pressure depletion becomes skewed toward the initial fracture at the toe of the well (Fig. 12b). Comparison of the velocity and pressure plots in Fig. 12 shows the region with the largest pressure drop corresponds to the lowest flow velocities between the first toe fracture and the middle fracture. One would expect when the pressure drop is greater in a localized area, fluid velocity would be higher in that area of the reservoir. The physical explanation for the disparity between the regions with the largest flow rates and faster drainage being shifted with respect to the regions of highest pressure depletion as seen in our CAM model is as follows. Fluid moves fastest where the pressure gradients are steepest. The regions where fluid molecules are actively removed from the reservoir maintain the steepest pressure gradient. Adjacent regions with flow stagnation still will experience wider spacing between their fluid molecules leading to pressure depletion. This concept of the fundamental difference between pressure depletion and actual drained rock volume was first recognized in recent studies (Weijermars et al. 2017b; Weijermars and Alves 2018; Weijermars and van Harmelen 2018), using the same model tools outlined in the present study. Most current models use pressure plots to show drained areas but conclusions from this study show that velocity plots (rarely visualized in other models) give a better indication of actual drained rock volume. The fracture configuration of Fig. 12 results in a less effectively drained area near the initial toe fracture, whereas areas drained by the fractal networks at the heel side with less pressure depletion and higher flow velocities drain a slightly larger area, with a decrease in the size of the stagnation zone.

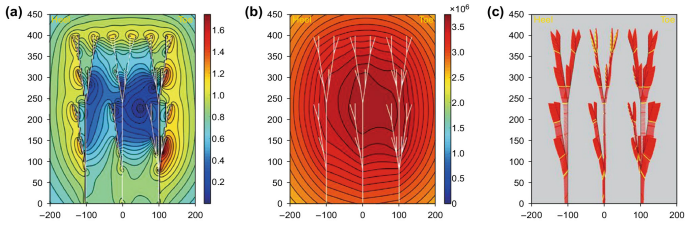


**Figure 12**: a Velocity contour plot for three branched fracture networks (ft/month) after 1 month production. b Pressure contour plots (drawdown in psi) after 1 month production. c Drained areas after 30 years production. Length scale in ft; surface area covered by symmetric/asymmetric three fracture networks is $4.9207 \times 10^5$ ft$^{2.}$

Another configuration investigated was a single-fracture stage with five fractures, each made up by a second-generation symmetrical fractal network (Fig. 13). This simulation mimics today's industry standard of five fracture clusters per stage. Typical fracture distance in horizontal wells can go as low as 20 ft between perforation clusters. For this model, we maintain a fracture cluster spacing of 100 ft as used in previous simulations for ease of comparison and visual resolution. Similar to our base case with three symmetrical second-generation fractal networks (Fig. 11, central column), we again find slower velocities between the branched fractal networks, creating narrower flow stagnation areas. The stagnation regions are smaller than those created by planar fractures. A crucial take away from this simulation is that fracture interference effects, similar to those seen in other models, will occur equally for narrower spaced fractal networks. However, the much smaller fracture spacing used in the most recent well stimulation programs will only increase the intensity of local flow interference. Although more fractures increase the contact area with the matrix, the drained rock volume will not increase linearly with surface area increase due to the effect of increasing flow interference.

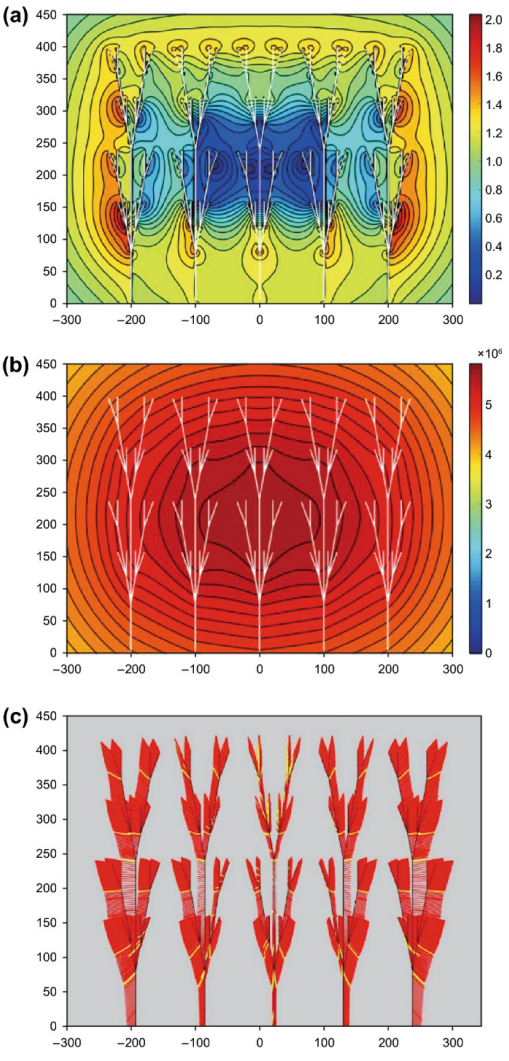


**Figure 13**: a Velocity contour plot for five symmetrical branched fracture networks (ft/month) after 1 month production. b Pressure contour plots (drawdown in psi) after 1 month production. c Drained areas after 30 years production. Length scale in ft; surface area covered by five fracture networks is $1.0201 \times 10^6$ ft$^{2.}$

## Multiple Full-length Fractal Networks

The preceding results all looked at half of the total fracture network length. The reason for this approach was the assumption of symmetry of the

network on both sides of a horizontal wellbore. A final simulation looks at a full fracture length ($2x_f$) for a single-fracture treatment stage with three perforation clusters, each generating fractal fractures (Fig. 14). Results show that the premise of flow symmetry about the wellbore is confirmed, as the velocity plots show contour patterns closely resembling those in Fig. 9b (center column). Flow stagnation points in Fig. 14 are shifted across the reservoir space to a location between the three fractures close to the wellbore, different from those seen in Fig. 11. The overall effect of a more complex fracture network is to reduce the spatial spread of flow stagnation zones, leading to improved efficiency of the DRV near the individual fractures.

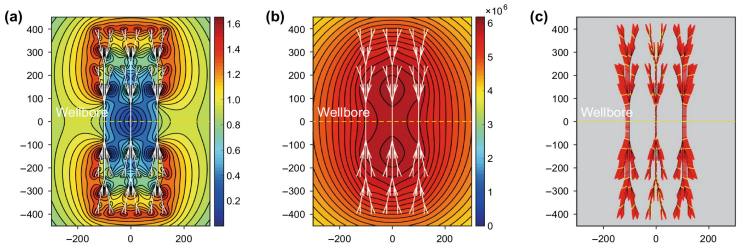


**Figure 14**: a Velocity contour plot for three full ($2x_f$) branched fracture networks (ft/month) after 1 month production. b Pressure contour plots (drawdown in psi) after 1 month production. c Drained areas after 30 years production. Length scale in ft.

## DISCUSSION

The true nature of hydraulic fracture geometries created in the subsurface during fracture treatment programs is still not properly resolved. Most fracture propagation models result in fractures that generate as simple planar features due to ease of modeling and the lack of inclusion of mechanical heterogeneity in such models. Meanwhile, numerous experimental and field observations show that planar fractures are too simple an assumption and they are more likely to exist as branching fracture networks. What is beyond doubt is that differences in the fracture geometry will have a distinct impact on the outcome of production forecasting models and history matching the actual production rates, drained areas and estimated ultimate recovery. Previous analytical solutions have looked at flow into parallel planar fracture arrays (Zhou et al. 2012; Yu et al. 2017) but failed to consider the effect on flow when fracture geometries are non-planar. Our method takes into

account variable fracture geometries and visualizes the flow interference of fractal fracture networks. High-resolution visualizations of velocity and DRV areas are presented, which may substantially contribute to improve our current understanding of the flow process in hydraulically fractured reservoirs. The use of pressure depletion plots as proxies for drained rock volume is unreliable as has been highlighted in prior studies (Weijermars and van Harmelen 2018; Khanal and Weijermars 2019). In low permeability reservoirs, there occurs a distinct mismatch between the depth of pressure investigation and drained rock volume growth (Weijermars and Alves 2018), which is why the determination of the tracking of the time-of-flight of drained fluid to the hydraulic fractures of a well is required to delineate the DRV more accurately.

## Interference Effects

The effect of fracture geometry on flow interference was investigated using a fractal fracture network description in combination with the complex analysis methods (CAM) to model drainage patterns and the resulting DRV near hydraulic fractures. Several series of simulations were conducted to determine the impact on drained areas and flow velocities when the fracture geometry varies, starting from a single-planar fracture and evolving up to third-generation branching fractals. For greater fractal network complexity, the local area drained away from each individual fracture segment becomes smaller as compared to the area of drained regions near a single-planar fracture. The difference occurs because fractals have a larger fracture surface area and we are putting back a constant amount of produced fluid (via the principle of flow reversal) in both the single and fractal models. Consequently, the fractal network shows more variations in flow velocities and pressure depletion peaks as compared to a planar fracture. These extreme changes in velocity lead to uneven drainage by the fracture network with the possibility of small undrained areas due to stagnation points occurring between the branches.

A planar fracture geometry based on our model's fracture spacing and half-length creates stagnation surfaces leading to relatively large undrained areas between the fractures. In contrast, the fractal network geometry shows a reduction in the effect and areal extent of the stagnation zones (as seen from a comparison of the velocity and drained area plots, Fig. 11), due to a decrease in the interference effect on flow. The position of flow separation surfaces separating the drainage regions of individual fractures is controlled by the ratio of the fracture length and fracture spacing (Weijermars et al.

2018). When the fracture spacing is greater than a quarter of the fracture length, the flow stagnation points occur midway between the individual fractures. For complex fractal networks, each fracture branch has a smaller length compared to a single-planar fracture. The smaller fracture branch lengths mean less flow interference will occur for an otherwise constant fracture cluster spacing.

## Pressure Depletion

Results show (Fig. 8c) that when the fracture surface area increases due to the more complex fractal networks, the average reservoir pressure change remains the same. One might expect that a greater fracture surface area to place fluid back into the reservoir model would result in smaller overall pressure changes. However, pressure peaks and lows show a larger spread where the fracture network complexity increases. The local variation in the pressure response is affected mostly by the fracture density. From the pressure plots (Fig. 11b), one can observe that areas with the highest fracture density give pressure contour depletion peaks. The current model uses a pre-fracture matrix permeability of 1 μD giving pressure changes in the magnitude of $10^6$ psi (Fig. 14). When the permeability is changed to an after-fracture permeability of 1 mD, the pressure change magnitude drops to the range of $10^3$ psi, which is in line with field observations. We assume this after-fracture permeability change is due to the creation of a network of microfractures in the rock that is termed the enhanced after-fracture permeability region.

## Model Limitations

One aspect that the current model does not consider is the effect of various fractal iterations on fracture conductivity. Beyond the concept of fracture conductivity decreasing with time due to partial fracture closure following reservoir pressure decline (Daneshy 2005), as we create successive iterations, each new branch will be less conductive due to fracture width reduction and the lesser ability for proppant placement. In the current model, all fractures are given a constant flux, whereas in reality, the shorter distal fracture branches may have a smaller aperture and consequently less proppant placement, which may suppress fluid flux. The use of microproppant to help prop these smaller secondary and microfracture networks can retain fracture conductivity and is a field currently under research (Kim et al. 2018). The impact of fracture closure with time can be looked at in future

work by the addition of a parameter to further decrease strength of flux into the fractal network. Water blockage to flow due to imbibed water during the fracturing job and subsequent soaking period is also not accounted for. Another crucial point is that the current model ensured there was no overlapping of fractal branches either within a stage or by multiple stages. This may not always be true in nature, and with very low current fracture spacing, there is a possibility of these fractal networks crossing. The possible crossing of the fractal networks from sequential fracture clusters can result in communication between stages that is regularly seen in the field (Barree and Miskimins 2015; Li et al. 2016).

### Practical Implications

The impact of fractal fracture geometries on the DRV and stagnation zones is investigated in this study. Our models indicate that when the complexity of hydraulic fracture networks increases, this will suppress the occurrence of dead zones. In order to increase the DRV and boost the associated well productivity (and thus improve ultimate recovery), our models suggest that fracture treatment programs must find ways to create more complex fracture networks. The generation of such complex fracture networks is currently not included in concurrent fracture treatment design models, which limit the fracture development to mutually parallel planes. Because observational evidence from field experiments suggests that hydraulic fractures in hydrocarbon wells range from planar to multi-branched fractals (Huang and Kim 1993; Raterman et al. 2017), fracture treatment propagation models need to be modified to more realistically account for the development of complex fracture geometries that predictably follows from local geomechanical heterogeneities at the grain scale of rocks. The complex fracture geometry and fracture crossing provide a valid alternative explanation for the fact that tracer readings may overlap across fracture stages, which some commercial fracture propagation models presently attribute to the occurrence of longitudinal fractures parallel to the wellbore (Barree and Miskimins 2015).

## CONCLUSIONS

The aim of this project was to more accurately represent the detailed flow patterns and drained rock volume (DRV) in unconventional reservoirs for a range of complex fractal fracture geometries. Such fractal flow models may help reservoir engineers to improve the hydrocarbon recovery rates. The simulations in this work show that the fracture geometry and complexity

have a significant impact on the detailed hydrocarbon migration route near the fractures. Major conclusions realized from our study are as follows:

- A complex fracture network enhances the drained rock volume via two mechanisms. The first is that with more complex networks, the overall fracture surface area increases resulting in larger access to fluid stored in the reservoir matrix rock. The second mechanism is the suppression of stagnant flow zones when the complexity of the hydraulic fracture network increases.
- Hydraulic fracture treatment programs should stimulate the creation of bifurcating fractures as approximated by our fractal model. By reducing stagnant flow regions, the DRV will more effectively drain the reservoir. This will lead to improved drainage between the fractures, which will increase the estimated ultimate recovery from hydrocarbon wells.
- Using CAM, we are able to visualize in high resolution the effects of various fractal network geometries on flow and pressure response in the reservoir. We highlighted the fact that pressure plots, commonly used as proxies for drainage patterns, are poor proxies for the actual DRV. The DRV can be more accurate predicted using streamline tracking and time-of-flight contouring, as shown in our study.
- For planar fractures, stagnation zones in a three-fracture cluster occur close to the outer fractures, typically when the fracture spacing is less than a quarter of the fracture length (Fig. 11, left panel).
- Once fracture complexity is introduced in the form of fractal networks, the effect of the branching fractures leads to suppression of the flow stagnation areas, allowing for more efficient drainage (Fig. 11, center panel). The velocity plots for the fractal networks show a larger spread in the local variation of velocity than for the planar fractures.
- The highest velocities are still found at the periphery of the fractal networks for all cases. However, for asymmetrical fractal networks, there is a tendency for the highest pressure and velocity response to skew toward the areas of highest fracture density (Fig. 11, right panel).
- It will be necessary to determine whether the creation of complex fracture networks in the subsurface is solely dependent on the

reservoir matrix properties (presence of natural fractures or matrix heterogeneities) or if fractal networks can be created by applying specific techniques during the hydraulic fracturing process. This requires the application of better diagnostic tools including the refinement of microseismic techniques to properly define and monitor created fractal network geometry.

- Improved capacity to engineer and model the propagation direction and control the generation of fractal geometries for hydraulic fractures are urgently needed in order to further increase the productivity of hydrocarbon wells by fracture treatment.

## REFERENCES

1. Al-Obaidy RTI, Gringarten AC, Sovetkin V. Modeling of induced hydraulically fractured wells in shale reservoirs using "branched" fractals. In: SPE annual technical conference and exhibition, 27–29 October. Amsterdam; 2014. https://doi.org/10.2118/170822-MS.
2. Arshadi M, Zolfaghari A, Piri M, Al-Muntasheri G, Sayed M. The effect of deformation on two-phase flow through proppant-packed fractured shale samples: a micro-scale experimental investigation. Adv Water Resour. 2017;105:108–31. https://doi.org/10.1016/j.advwatres.2017.04.022.
3. Barree RD, Miskimins JL. Calculation and implications of breakdown pressures in directional wellbore stimulation. In: SPE hydraulic fracturing technology conference, 3–5 February. The Woodlands; 2015. https://doi.org/10.2118/173356-MS.
4. Berta D, Hardy HH, Beier RA. Fractal distributions of reservoir properties and their use in reservoir simulation. In: International petroleum conference and exhibition of Mexico, 10–13 October. Veracruz; 1994. https://doi.org/10.2118/28734-MS.
5. Cai L, Ding D-Y, Wang C, Wu Y-S. Accurate and efficient simulation of fracture–matrix interaction in shale gas reservoirs. Transp Porous Media. 2015;107:305–20. https://doi.org/10.1007/s11242-014-0437-x.
6. Cossio M, Moridis GJ, Blasingame TA. A semi-analytic solution for flow in finite-conductivity vertical fractures using fractal theory. In: SPE annual technical conference and exhibition, 8–10 October. San Antonio; 2012. https://doi.org/10.2118/163057-STU.
7. Daneshy AA. Pressure variations inside the hydraulic fracture and its impact on fracture propagation, conductivity, and screen-out. In: SPE annual technical conference and exhibition, 9–12 October. Dallas; 2005. https://doi.org/10.2118/95355-MS.
8. Fisher MK, Wright CA, Davidson BM, Goodwin AK, Fielder EO, Buckler WS, et al. Integrating fracture mapping technologies to optimize stimulations in the Barnett shale. In: SPE annual technical conference and exhibition, 29 September–2 October. San Antonio; 2002. https://doi.org/10.2118/77441-MS.
9. Frame M, Manna S, Novak M. Fractals: complex geometry, patterns, and scaling in nature and society; 2012. http://www.worldscinet.com/fractals/mkt/aims_scope.shtml. World Scientific Publishing Company

Journal.

10. Gale J, Laubach S, Olson J, Eichhubl P, Fall A. Natural fractures in shale: a review and new observations. AAPG Bull. 2014;98(11):2165–216. https://doi.org/10.1306/08121413151.
11. Grechka V, Li Z, Howell R, Vavrycuk V. Single-well moment tensor inversion of tensile microseismic events. In: 2017 SEG international exposition and annual meeting, 24–29 September. Houston; 2017. SEG-2017-16890707.
12. Hamlin HS, Baumgardner RW. Wolfberry play, Midland Basin, West Texas. New York: AAPG Southwest Section Meeting; 2012.
13. Han G. Highlights from hydraulic fracturing community: from physics to modelling. URTeC 2768686; 2017.
14. Han JS. Plant simulation based on fusion of L-system and IFS. In: Shi Y, van Albada GD, Dongarra J, Sloot PMA, editors. Computational science—ICCS 2007. ICCS 2007. Lecture notes in computer science, vol 4488. Berlin: Springer.
15. Huang J, Kim K. Fracture process zone development during hydraulic fracturing. Int J Rock Mech Min SciGeomechAbstr. 1993;30(7):1295–8. https://doi.org/10.1016/0148-9062(93)90111-P.
16. Jones JR, Volz R, Djasmari W. Fracture complexity impacts on pressure transient responses from horizontal wells completed with multiple hydraulic fracture stages. In: SPE unconventional resources conference Canada, 5–7 November. Calgary; 2013. https://doi.org/10.2118/167120-MS.
17. Katz A, Thompson AH. Fractal sandstone pores: implications for conductivity and pore formation. Phys Rev Lett. 1985;54:1325. https://doi.org/10.1103/PhysRevLett.54.1325.
18. Khanal A, Weijermars R. Pressure depletion and drained rock volume (DRV) near hydraulically fractured parent and child wells (Eagle Ford Formation). J Pet Sci Eng. 2019;172:607–26. https://doi.org/10.1016/j.petrol.2018.09.070.
19. Kilaru S, Goud BK, Rao VK. Crustal structure of the western Indian shield: model based on regional gravity and magnetic data. Geosci Front. 2013;4(06):717–28. https://doi.org/10.1016/j.gsf.2013.02.006.
20. Kim BY, Akkutlu IY, Martysevich V, Dusterhoft R. Laboratory measurement of microproppant placement quality using split core plug permeability under stress. In: SPE hydraulic fracturing technology

conference and exhibition, 23–25 January. The Woodlands; 2018. https://doi.org/10.2118/189832-MS.

21. Li J, Pei Y, Jiang H, Zhao L, Li L, Zhou H, Zhang Z. Tracer flowback based fracture network characterization in hydraulic fracturing. In: Abu Dhabi international petroleum exhibition and conference, 7–10 November. Abu Dhabi; 2016. https://doi.org/10.2118/183444-MS.
22. Li L, Lee SH. Efficient field-scale simulation of black oil in a naturally fractured reservoir through discrete fracture networks and homogenized media. SPE ReservEval Eng. 2008;11(4):750–8. https://doi.org/10.2118/103901-PA.
23. Lindenmayer A. Mathematical methods for cellular interactions in development II. Simple and branching filaments with two-sided inputs. J Theor Biol. 1968;18(3):300–15. https://doi.org/10.1016/0022-5193(68)90080-5.
24. Mandelbrot BB. Fractals: form, chance and dimension. San Francisco: WH Freeman and Co.; 1979. p. 16–365 **(p. 1)**.
25. Maxwell SC, Urbancic TI, Steinsberger N, Zinno R. Microseismic imaging of hydraulic fracture complexity in the Barnett shale. In: SPE annual technical conference and exhibition, 29 September–2 October. San Antonio; 2002. https://doi.org/10.2118/77440-MS.
26. McKenzie NR, Hughes NC, Myrow PM, Banerjee DM, Deb M, Planavsky NJ. New age constraints for the Proterozoic Aravalli-Delhi successions of India and their implications. Precambrian Res. 2013;238:120–8. https://doi.org/10.1016/j.precamres.2013.10.006.
27. Meyer BR, Bazan LW. A discrete fracture network model for hydraulically induced fractures: theory, parametric and case studies. In: SPE hydraulic fracturing technology conference, 24–26 January. The Woodlands; 2011. https://doi.org/10.2118/140514-MS.
28. Moinfar A, Varavei A, Sepehrnoori K, Johns RT. Development of an efficient embedded discrete fracture model for 3D compositional reservoir simulation in fractured reservoirs. SPE J. 2014;19:289–303. https://doi.org/10.2118/154246-PA.
29. Mukhopadhyay S, Bhattacharya AK. Bidasar ophiolite suite in the trans-Aravalli region of Rajasthan: a new discovery of geotectonic significance. Indian J Geosci. 2009;63(4):345–50.
30. Muskat M. Physical principles of oil production. New York: McGraw-Hill; 1949.

31. Nagel N, Zhang F, Sanchez-Nagel M, Lee B, Agharazi A. Stress shadow evaluations for completion design in unconventional plays. In: SPE unconventional resources conference Canada, 5–7 November. Calgary; 2013. https://doi.org/10.2118/167128-MS.
32. Olson JE, Taleghani AD. Modeling simultaneous growth of multiple hydraulic fractures and their interaction with natural fractures. In: SPE hydraulic fracturing technology conference, 19–21 January. The Woodlands; 2009. https://doi.org/10.2118/119739-MS.
33. Pandey CS, Richards LE, Louat N, Dempsey BD, Schwoeble AJ. Fractal characterization of fractured surfaces. Acta Metall. 1987;35(7):1633–7. https://doi.org/10.1016/0001-6160(87)90110-6.
34. Parsegov SG, Nandlal K, Schechter DS, Weijermars R. Physics-driven optimization of drained rock volume for multistage fracturing: field example from the Wolfcamp Formation, Midland Basin. In: Unconventional resources technology conference held in Houston. Texas, 23–25 July 2018. https://doi.org/10.15530/urtec-2018-2879159.
35. Pradhan VR, Meert JG, Pandit MK, Kamenov G, Mondal MEA. Paleomagnetic and geochronological studies of the mafic dyke swarms of Bundelkhand craton, central India: implications for the tectonic evolution and paleogeographic reconstructions. Precambrian Res. 2012;198–199:51–76. https://doi.org/10.1016/j.precamres.2011.11.011.
36. Raterman KT, Farrell HE, Mora OS, Janssen AL, Gomez GA, Busetti S, Warren M. Sampling a stimulated rock volume: an Eagle Ford example. In: Unconventional resources technology conference. Austin, 24–26 July 2017. https://doi.org/10.15530/urtec-2017-2670034.
37. Sato K. Continuum analysis for practical engineering. London: Springer; 2015. p. 300.
38. Sang G, Elsworth D, Miao X, Mao X, Wang J. Numerical study of a stress dependent triple porosity model for shale gas reservoirs accommodating gas diffusion in kerogen. J Nat Gas Sci Eng. 2016;32:423–38. https://doi.org/10.1016/j.jngse.2016.04.044.
39. Shrivastava K, Sharma MM. Proppant transport in complex fracture networks. In: SPE hydraulic fracturing technology conference and exhibition, 23–25 January. The Woodlands; 2018. https://doi.org/10.2118/189895-MS.
40. Strack ODL. Groundwater mechanics. Englewood Cliffs: Prentice-

Hall; 1989.

41. vanHarmelen A, Weijermars R. Complex analytical solutions for flow in hydraulically fractured hydrocarbon reservoirs with and without natural fractures. Appl Math Model. 2018;56:137–57. https://doi.org/10.1016/j.apm.2017.11.027.
42. Wang W, Su Y, Sheng G, Cossio M, Shang Y. A mathematical model considering complex fractures and fractal flow for pressure transient analysis of fractured horizontal wells in unconventional reservoirs. J Nat Gas Sci Eng. 2015;23:139–47. https://doi.org/10.1016/j.jngse.2014.12.011.
43. Wang W, Su Y, Zhou Z, Sheng G, Zhou R, Tang M, et al. Method of characterization of complex fracture network with combination of microseismic using fractal theory. In: SPE/IATMI Asia Pacific oil & gas conference and exhibition, 17–19 October. Jakarta; 2017. https://doi.org/10.2118/186209-MS.
44. Wang WD, Su YL, Zhang Q, Xiang G, Cui SM. Performance-based fractal fracture network model for complex fracture network simulation. Pet Sci. 2018;15:126–34. https://doi.org/10.1007/s12182-017-0202-1.
45. Warren JE, Root PJ. The behavior of naturally fractured reservoirs. Soc Pet Eng J. 1963;1963(3):245–55.
46. Warpinski NR, Moschovidis ZA, Parker CD, Abou-Sayed IS. Comparison study of hydraulic fracturing models—test case: GRI staged field Experiment No. 3 (includes associated paper 28158). SPE Prod Facil. 1994;9:7–16. https://doi.org/10.2118/25890-PA.
47. Weijermars R. Visualization of space competition and plume formation with complex potentials for multiple source flows: some examples and novel application to Chao lava flow (Chile). J Geophys Res. 2014;119(3):2397–414. https://doi.org/10.1002/2013JB010608.
48. Weijermars R, Alves IN. High-resolution visualization of flow velocities near frac-tips and flow interference of multi-fracked Eagle Ford wells, Brazos County, Texas. J Pet Sci Eng. 2018;165:946–61. https://doi.org/10.1016/j.petrol.2018.02.033.
49. Weijermars R, van Harmelen A. Breakdown of doublet recirculation and direct line drives by far-field flow in reservoirs: implications for geothermal and hydrocarbon well placement. Geophys J Int. 2016;206:19–47. https://doi.org/10.1093/gji/ggw135.
50. Weijermars R, van Harmelen A. Shale reservoir drainage visualized

for a Wolfcamp Well (Midland Basin, West Texas, USA). Energies. 2018;11:1665. https://doi.org/10.3390/en11071665.

51. Weijermars R, van Harmelen A, Zuo L. Controlling flood displacement fronts using a parallel analytical streamline simulator. J Pet Sci Eng. 2016;139:23–42. https://doi.org/10.1016/j.petrol.2015.12.002.
52. Weijermars R, van Harmelen A, Zuo L, Alves IN, Yu W. High-resolution visualization of flow interference between frac clusters (part 1): model verification and basic cases. In: SPE/AAPG/SEG unconventional resources technology conference, 24–26 July. Austin; 2017a. SPE URTeC 2670073A.
53. Weijermars R, van Harmelen A, Zuo L. Flow interference between frac clusters (part 2): field example from the Midland Basin (Wolfcamp Formation, Spraberry Trend Field) with implications for hydraulic fracture design. In: SPE/AAPG/SEG unconventional resources technology conference, 24–26 July. Austin; 2017b. SPE URTeC 2670073B.
54. Weijermars R, van Harmelen A, Zuo L, Alves IN, Yu W. Flow interference between hydraulic fractures. SPE ReservEval Eng. 2018;21(4):942–60. https://doi.org/10.2118/194196-PA.
55. Weng X, Kresse O, Cohen CE, Wu R, Gu H. Modeling of hydraulic fracture network propagation in a naturally fractured formation. SPE Prod Oper. 2011;26(4):368–80. https://doi.org/10.2118/140253-PA.
56. Xu W, Thiercelin MJ, Ganguly U, Weng X, Gu H, Onda H, et al. Wiremesh: a novel shale fracturing simulator. In: International oil and gas conference and exhibition in China, 8–10 June. Beijing; 2010. https://doi.org/10.2118/132218-MS.
57. Yu W, Wu K, Zuo L, Tan X, Weijermars R. Physical models for inter-well interference in shale reservoirs: relative impacts of fracture hits and matrix Permeability. In: SPE/AAPG/SEG unconventional resources technology conference, 1–3 August. San Antonio; 2016. https://doi.org/10.15530/URTEC-2016-2457663.
58. Yu W, Xu Y, Weijermars R, Wu K, Sepehrnoori K. Impact of well interference on shale oil production performance: a numerical model for analyzing pressure response of fracture hits with complex geometries. In: SPE hydraulic fracturing technology conference and exhibition, 24–26 January. The Woodlands; 2017. https://doi.org/10.2118/184825-MS.

59. Yu W, Sepehrnoori K. Embedded discrete fracture model (EDFM) for complex fracture geometry. Shale gas and tight oil reservoir simulation (pp. 155–200). Cambridge: Gulf Professional Publishing, an imprint of Elsevier; 2018.
60. Zhang X, Thiercelin MJ, Jeffrey RG. Effects of frictional geological discontinuities on hydraulic fracture propagation. In: SPE hydraulic fracturing technology conference, 29–31 January. College Station; 2007. https://doi.org/10.2118/106111-MS.
61. Zhou W, Banerjee R, Poe BD, Spath J, Thambynayagam M. Semi-analytical production simulation of complex hydraulic fracture network. In: SPE international production and operations conference & exhibition, 14–16 May. Doha; 2012. https://doi.org/10.2118/157367-MS.
62. Zolfaghari A, Ghanbari E, Dehghanpour H, Bearinger D. Fracture characterization using flowback salt-concentration transient. SPE J. 2016;21(1):233–44. https://doi.org/10.2118/168598-PA.
63. Zolfaghari A, Tang Y, He J, Dehghanpour H, Bearinger D, Virues C. Fracture network characterization by analyzing flowback salts: scale-up of experimental data. In: SPE unconventional resources conference, 15–16 February. Calgary; 2017. https://doi.org/10.2118/185078-MS.

# 16

# *Multifractal Analysis of Weighted Networks by a Modified Sandbox Algorithm*

**Yu-Qin Song[1,2], Jin-Long Liu[1], Zu-GuoYu[1,3]&Bao-Gen Li[1]**

[1] Hunan Key Laboratory for Computation and Simulation in Science and Engineering and Key Laboratory of Intelligent Computing and Information Processing of Ministry of Education, Xiangtan University, Xiangtan, Hunan 411105, China
[2] College of Science, Hunan University of technology, Zhuzhou, Hunan 412007, China
[3]School of Mathematical Sciences, Queensland University of Technology, Brisbane, Q4001, Australia

## ABSTRACT

Complex networks have attracted growing attention in many fields. As a generalization of fractal analysis, multifractal analysis (MFA) is a useful way to systematically describe the spatial heterogeneity of both theoretical and experimental fractal patterns. Some algorithms for MFA of unweighted complex networks have been proposed in the past a few years, including the sandbox (SB) algorithm recently employed by our group. In this paper, a modified SB algorithm (we call it SBw algorithm) is proposed for MFA of weighted networks. First, we use the SBw algorithm to study the multifractal

**Citation:** Song, Y. Q., Liu, J. L., Yu, Z. G., & Li, B. G. (2015). Multifractal analysis of weighted networks by a modified sandbox algorithm. Scientific reports, 5, 17628.,DOI: 10.1038/srep17628.

property of two families of weighted fractal networks (WFNs): "Sierpinski" WFNs and "Cantor dust" WFNs. We also discuss how the fractal dimension and generalized fractal dimensions change with the edge-weights of the WFN. From the comparison between the theoretical and numerical fractal dimensions of these networks, we can find that the proposed SBw algorithm is efficient and feasible for MFA of weighted networks. Then, we apply the SBw algorithm to study multifractal properties of some real weighted networks — collaboration networks. It is found that the multifractality exists in these weighted networks and is affected by their edge-weights.

## INTRODUCTION

Complex networks have attracted growing attention in many fields. More and more research works have shown that they connect with many real complex systems and can be used in various fields[1,2,3,4]. Fundamental properties of complex networks, such as the small-world, the scale free and communities, have been studied[5,6]. Song *et al.*[1] found the self-similarity property[7,8,9] of complex networks. Gallos *et al.* gave a review of fractality and self-similarity in complex networks[10]. At the same time, some methods for fractal analysis and how to numerically calculate the fractal dimension of complex networks have been proposed. Especially, the box-counting algorithm[11,12] was generalized and applied to calculate the fractal dimension of complex networks. Subsequently, an improved algorithm was proposed to investigate the fractal scaling property in scale-free networks[13]. In addition, based on the edge-covering box counting, an algorithm was proposed to explore the self-similarity of complex cellular network[14]. A ball-covering approach and an approach defined by the scaling property of the volume were proposed to calculate the fractal dimension of complex networks[15]. Later on, box-covering algorithms for complex networks were further studied[16,17].

Although fractal analysis can describe global properties of complex networks, it is inadequate to describe the complexity of complex networks by a single fractal dimension. For systematically characterizing the spatial heterogeneity of a fractal object, multifractal analysis (MFA) has been introduced[18,19]. MFA has been widely applied in many fields, such as financial modeling[20,21], biological systems[22,23,24,25,26,27,28,29,30,31,32], geophysical systems[33,34,35,36,37,38,39,40] and also complex networks[41,42,43,44,45]. Lee *et al.*[46] mentioned that MFA is the best tool to describe the probability distribution of the clustering coefficient

of a complex network. Some algorithms were proposed for MFA of unweighted complex networks in past a few years[41,42,43,44,45]. Furuya and Yakubo[41] pointed out that a single fractal dimension is not enough to characterize the fractal property of a scale-free network when the network has a multifractal structure. They also introduced a compact-box-burning (CBB) algorithm for MFA of complex networks. Wang *et al.*[42] proposed an improved fixed-size box-counting algorithm to study the multifractal behavior of complex networks. Then this algorithm was improved further by Li *et al.*[43]. They applied the improved fixed-size box-counting algorithm to study multifractal properties of a family of fractal networks proposed by Gallos *et al.*[47]. Recently, Liu *et al.*[45] employed the sandbox (SB) algorithm proposed by Tél *et al.*[48] for MFA of complex networks. The comparison between theoretical and numerical results of some networks showed that the SB algorithm is the most effective and feasible algorithm to study the multifractal behavior of unweighted networks[45].

However, all the algorithms for MFA in refs 41, 42, 43, 44, 45 are just feasible for unweighted networks. Actually, there are many weighted networks in real world[49,50,51], but few works have been done to study the fractal and multifractal properties of the weighted networks. Recently, an improved box-covering algorithm for weighted networks was proposed by Wei *et al.*[52]. They applied the box-covering algorithm for weighted networks (BCANw) to calculate the fractal dimension of the "Sierpinski" weighted fractal network (WFN)[53] and some real weighted networks. But the BCANw algorithm was only designed for calculating the fractal dimension of weighted networks.

In this work, motivated by the idea of BCANw, we propose a modified sandbox algorithm (we call it SBw algorithm) for MFA of weighted networks. First, we use the SBw algorithm to study the multifractal property of two families of weighted fractal networks (WFNs): "Sierpinski" WFNs and "Cantor dust" WFNs introduced by Carletti *et al.*[53]. We also discuss how the fractal dimension and generalized fractal dimensions change with the edge-weights of the WFN. Through the comparison between the theoretical and numerical fractal dimensions of these networks, we check whether the proposed SBw algorithm is efficient and feasible for MFA of weighted networks. Then, we apply the SBw algorithm to study multifractal properties of some real weighted networks — collaboration networks[54].

# RESULTS AND DISCUSSION

## Multifractal Properties of Two Families of Weighted Fractal Networks

In order to show that the SBw algorithm for MFA of weighted network is effective and feasible, we apply our method to study the multifractal behavior of the "Sierpinski" WFNs and the "Cantor dust" WFNs53. These WFNs are constructed by Iterated Function Systems (IFS) 55, whose Hausdorff dimension is completely characterized by two main parameters: the number of copies $s>1$ and the scaling factor $0<f<1$ of the IFS. In this case, the fractal dimension of the fractal weighted network is called the similarity dimension and given by53:

$$d_{fract} = -\frac{\log(s)}{\log(f)}. \quad (1)$$

To construct "Sierpinski" WFNs and "Cantor dust" WFNs53, a single node and a triangle is set as a initial network $G_0$ respectively. The first a few steps to construct them are shown in parts a) and b) of Fig. 1 respectively.

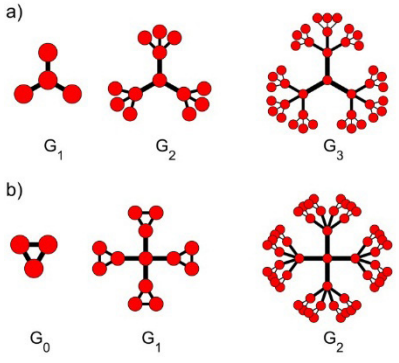


**Figure 1**:(a) The "Sierpinski" weighted fractal networks, s=3, f=1/2 and $G_0$ is composed by a single node. From the left to the right, the 1th generation $G_1$, the 2th generation $G_2$ and the 3th generation $G_3$ are shown. The fractal dimension of the limit network is log(3)/log(2)≈1.5850. (b) The "Cantor dust" weighted fractal networks, s=4, f=1/5 and $G_0$ is a triangle. From the left to the right, the 0th generation $G_0$, the 1th generation $G_1$ and the 2th generation $G_2$ are shown. The fractal dimension of the limit network is log(4)/log(5)≈0.8614.

We first consider two "Sierpinski" WFNs with parameters $s=3$, $f=1/2$ and $s=3$, $f=1/3$ respectively. Considering the limitation of the computing capability of our computer, we construct the 8th generation $G_8$ of these two networks. There are 9841 nodes and 9837 edges in the $G_8$ of these two networks. For the case $s=3$, $f=1/2$, the edge-weights of $G_8$ are equal to 1, 1/2, 1/4, 1/8, 1/16, 1/32, 1/64, 1/128, respectively; the diameter of $G_8$ is less than 4. When we use the SBw algorithm for MFA of $G_8$, radiuses $r$ of sandboxes are set to 1/128, 1/128+1/64, ···, 1+1/2+1/4+1/8+1/16+1/32+1/64+1/128, respectively for this case. We can do similar analysis for $G_8$ of network with $s=3$, $f=1/3$. It is an important step to look for an appropriate range of $r$ (*i.e.*, $r\in[r_{min}, r_{max}]$) for obtaining the generalized fractal dimensions $D(q)$ (defined by equations (6) and (7)) and the mass exponents $\tau(q)$ (defined by equation (5)). In this paper, we set the range of $q$ values from −10 to 10 with a step of 1.

When $q=0$, $D(0)$ is the fractal dimension of a complex network. Now we adopt the SBw algorithm to estimate the fractal dimension of two "Sierpinski" WFNs with parameters $s=3$, $f=1/2$ and $s=3$, $f=1/3$ respectively. We show the linear regression of $\ln(\langle[M(r)]^{q-1}\rangle)$ against $(q-1)\ln(r/d)$ for $q=0$ in Fig. 2. By means of the least square fit, the slope of the reference lines are estimated to be 1.5419 and 1.0169, with standard deviations 0.0309 and 0.0148, respectively. It means that the numerical fractal dimension is $1.5419\pm0.0309$ and $1.0169\pm0.0148$, respectively; they are very close to the theoretical similarity dimension 1.5850 and 1.0 respectively. Hence we can say that the numerical fractal dimension obtained by the SBw algorithm is very close to the theoretical similarity dimension for a "Sierpinski" WFN.

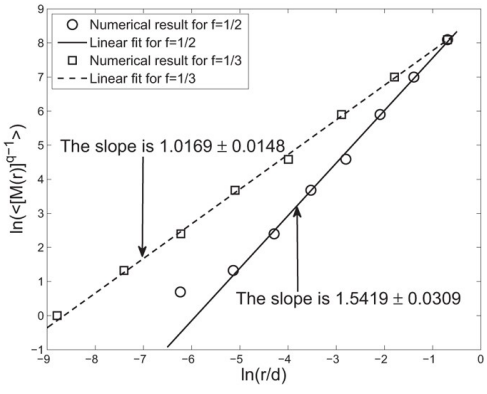


**Figure 2**: Examples of fractal analysis of the "Sierpinski" weighted fractal networks $G_8$ with 9841 nodes.

Here, copy factor $s=3$ and the scaling factor $f=1/2$, 1/3, respectively. By means of the least square fit, the slope of the reference lines are $1.5419\pm0.0309$ and $1.0169\pm0.0148$ respectively. The theoretical result is 1.5850 (for $f=1/2$) and 1.0 (for $f=1/3$), respectively.

To further check the validity of the SBw algorithm, let the copy factor $s$ be 3 and the scaling factor $f$ be any positive real number in the range $0<f<1$. From Equation (1), we can get the relationship between the fractal dimension and the scaling factor $f$ of the "Sierpinski" WFN as:

$$d_{fract} = -\frac{\log(3)}{\log(f)}. \qquad (2)$$

For each value of $f=1/2$, 1/3, 1/4, 1/5, 1/6, 1/7, 1/8, 1/9, we calculate fractal dimensions and their standard deviations of the 8th generation "Sierpinski" WFN $G_8$ by the SBw algorithm. The results are shown in part a) of Fig. 3, where each error bar takes twice length to the standard deviation. This figure shows that the numerical fractal dimensions obtained by the SBw algorithm agree well with the theoretical fractal dimensions of these networks. This figure also shows that the fractal dimension of WFNs is affected by the edge-weight. This result coincides with the conclusion obtained by Wei *et al.*52.

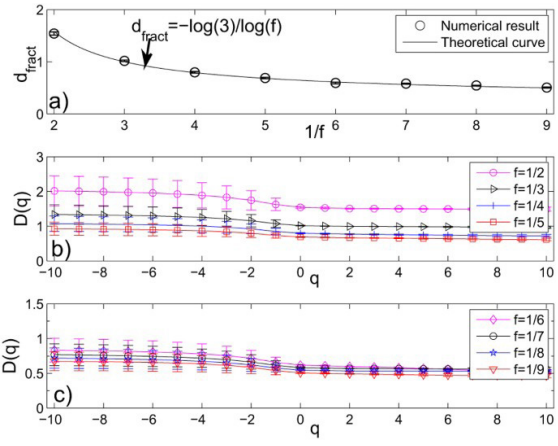


**Figure 3**:(a) The fractal dimensions and their standard deviations of $G_8$ of "Sierpinski" WFNs with parameter $s=3$. The solid curve represents the theoretical $d_{fract}$ given by Eq. (2), circles are the numerical fractal dimensions estimated by the SBw algorithm. (b,c) The generalized fractal dimensions $D(q)$ curves and their standard deviations of the 8th generation $G_8$ of "Sierpinski" WFNs estimated by the SBw algorithm. Here, the parameter $s=3$, $f=1/2$, 1/3, 1/4, 1/5

and 1/6, 1/7, 1/8, 1/9, respectively. Each error bar takes twice length to the standard deviation for all the results.

Hence we can apply the SBw algorithm to calculate the generalized fractal dimensions $D(q)$ and their standard deviations of "Sierpinski" WFNs. In parts b) and c) of Fig. 3, we show the generalized fractal dimensions $D(q)$ of the 8th generation $G_8$ of "Sierpinski" WFNs, with the parameter $s=3$, $f=1/2$, 1/3, 1/4, 1/5 and 1/6, 1/7, 1/8, 1/9 respectively. From these figures, we can see that all the 8th generation $G_8$ of "Sierpinski" WFNs for different $f$ have multifractal property and the multifractal property of these weighted networks is affected by their edge-weights. The result also shows that the generalized fractal dimension $D(q)$ almost decreases with the decrease of the scaling factor $f$ for any $q$.

For "Cantor dust" WFNs, we can only construct the 5th generation networks with $s=4$ and $f=1/2$, 1/3, 1/4, 1/5, 1/6, 1/7, 1/8, 1/9, respectively. We first calculate fractal dimensions and their standard deviations of these WFNs by the SBw algorithm. The results are shown in part a) of Fig. 4. From this figure, we can see that the numerical fractal dimensions obtained by the SBw algorithm are very close to the theoretical fractal dimensions $d_{fract}=-\log(4)/\log(f)$ for these WFNs. Then we apply the SBw algorithm to calculate the generalized fractal dimensions $D(q)$ and their standard deviations of these "Cantor dust" WFNs. We show the numerical results of the 5th generation $G_5$ of "Cantor dust" WFNs in parts b) and c) of Fig. 4. From these figures, we can see that all $D(q)$ curves are nonlinear. It indicates that all these weighted networks have multifractal property. Similar to "Sierpinski" WFNs, the multifractal property of these networks is affected by their edge-weights.

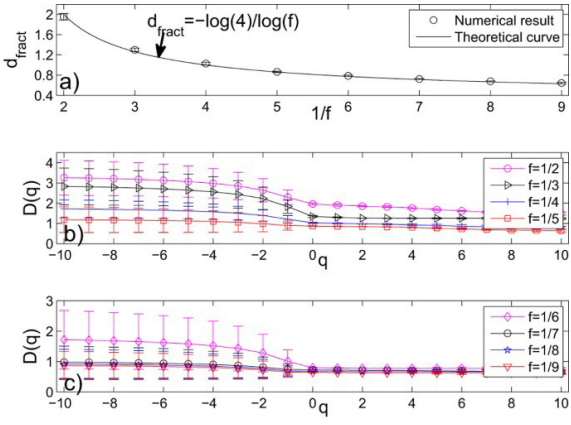


**Figure 4**:(a) The fractal dimensions and their standard deviations of $G_5$ of "Cantor dust" WFNs with parameter $s=4$. The solid curve represent the theo-

retical $d_{fract}$ given by Eq. (1), circles indicate the numerical fractal dimension estimated by the SBw algorithm. (b,c) The generalized fractal dimensions $D(q)$ curves and their standard deviations of $G_5$ of "Cantor dust" WFNs estimated by the SBw algorithm. Here, the parameter $s=4$, $f=1/2$, 1/3, 1/4, 1/5 and 1/6, 1/7, 1/8, 1/9, respectively. Each error bar takes twice length to the standard deviation for all the results.

The multifractal property of "Sierpinski" WFNs and "Cantor dust" WFNs revealed by the SBw algorithm indicates that these model networks are very complicated and cannot be characterized by a single fractal dimension.

## Applications: Multifractal Properties of Three Collaboration Networks

Now we apply the SBw algorithm to study multifractal properties of some real networks. We study three collaboration networks: the high-energy theory collaboration network54, the astrophysics collaboration network54 and the computational geometry collaboration network56.

## HIGH-ENERGY THEORY COLLABORATION NETWORK

This network has 8361 nodes and 15751 edges, the edge-weights are defined as54:

$$w_{ij} = \sum_k \frac{\delta_i^k \delta_j^k}{n_k - 1}, \tag{3}$$

where $n_k$ is the number of co-author in the $k$th paper (excluding single authored papers), $\delta_i^k$ equals to 1 if the $i$th scientist is one of the co-author of the $k$th paper, otherwise it equals to 0. The data contains all components of the network, for a total of 8361 scientists, not just the largest component of 5835 scientists. When two authors share many papers, the weight value is larger, thus the distance is less. So, in Equation(9), $p$ had better be a negative number (e.g. −1 given by Newman54). For different values of $p$, we can calculate the shortest path by Equation(9) and obtain different weighted networks. Then we apply the SBw algorithm to calculate the generalized fractal dimensions $D(q)$ and their standard deviations of the largest component of the network with 5835 nodes. We show the relation between the numerical fractal dimension of the High-energy theory collaboration networks and

values of $p$ in part a) of Fig. 5. From this figure, we can see the value of fractal dimension decreases with the increase of the absolute value of $p$, the values of fractal dimensions are almost symmetric about the vertical axis. We show the numerical results on the generalized fractal dimensions $D(q)$ of the High-energy theory collaboration networks for different values of $p$ in parts b) and c) of Fig. 5. From these figures, we can see that all the High-energy theory collaboration networks for different $p$ have multifractal property and the multifractal property of these weighted networks is affected by the edge-weight. We can also see that the generalized fractal dimensions $D(q)$ almost decrease with the increase of the absolute value of $p$.

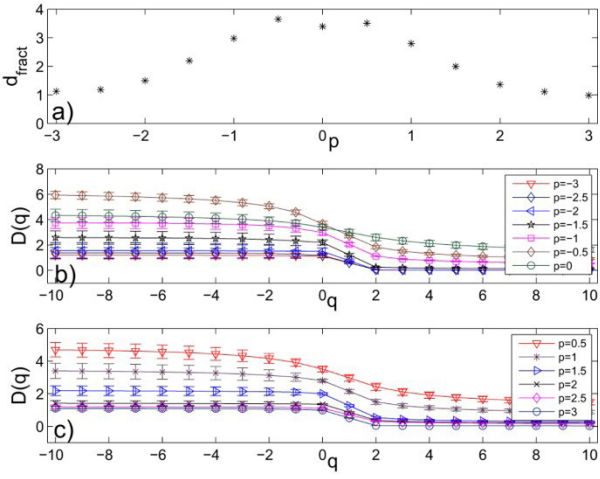


**Figure 5**:(a) The relation between values of the fractal dimension of the High-energy theory collaboration networks and values of $p$. We set the range of the $p$ values from −3 to 3 with a step of 0.5. (b,c) The generalized fractal dimensions $D(q)$ curves and their standard deviations of the the High-energy theory collaboration network by using the SBw algorithm. Here, the range of the $p$ values from −3 to 3 with a step of 0.5. Each error bar takes twice length to the standard deviation for all the results.

## Astrophysics Collaboration Network

This network has 16706 nodes and 121251 edges, the edge-wights is defined as Equation(3). Here, the data contains all components of the network, for a total of 16706 scientists, not just the largest component of 14845 scientists. When two authors share many papers, the weight value is larger, thus the distance is less. So, in Equation(9), $p$ had also better be a negative

number (e.g. −1 given by Newman54). We calculate the shortest path by Equation (9) and obtain some weighted networks with different values of $p$. Then we apply the SBw algorithm to calculate the generalized fractal dimensions $D(q)$ and their standard deviations of the largest component of the network with 14845 nodes. We show the numerical results of the astrophysics collaboration networks in parts a) and b) of Fig. 6. From this figure, we can see that these networks also have multifractal property and the multifractal property of these weighted networks is affected by the edge-weight.

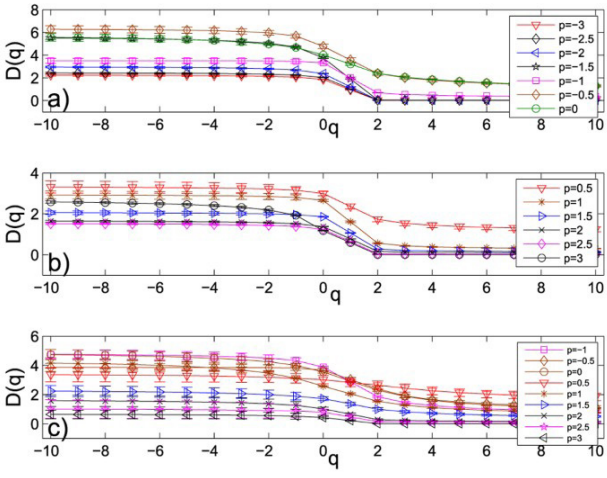


**Figure 6**: The generalized fractal dimensions $D(q)$ curves and their standard deviations of (a,b) the astrophysics collaboration networks and (c) the computational geometry collaboration networks estimated by the SBw algorithm. Here, we set the range of the $p$ values from −1 to 3 with a step of 0.5. Each error bar takes twice length to the standard deviation for all the results.

## Computational Geometry Collaboration Network

The authors collaboration network in computational geometry was produced from the BibTeX bibliography which obtained from the Computational Geometry Database. This network has 7343 nodes and 11898 edges. Two authors are linked with an edge, if and only if they wrote a common paper or book, etc. The value of edge-weight is the number of common works, so the value is one integer, such as 1, 2, 3, ···, etc. The data contains all components of the network, for a total of 7343 scientists, not just the largest component of 3621 scientists. The data can be got from Pajek Data56. When two authors

share many papers, the weight value is larger, thus the distance is less. So, in Equation (9), $p$ had better be a negative number. We calculate the shortest path by Equation (9) and obtain some weighted networks with different values of $p$. Then we apply the SBw algorithm to calculate the generalized fractal dimensions $D(q)$ and their standard deviations of the largest component of the network with 3621 nodes. Because the way to define the weight of this network is different from another two real networks, we can only calculate the generalized fractal dimensions $D(q)$ and their standard deviations of the largest component of the network with 3621 nodes for $p \geq -1$. We show the numerical results of the computational geometry collaboration networks in part c) of Fig. 6. From this figure, we can also see that these networks have multifractal property and the multifractal property of these weighted networks is affected by the edge-weight (but the impact is relatively small).

## CONCLUSIONS

In this paper, a modified sandbox algorithm (we call it SBw algorithm) for MFA of weighted networks is proposed. First, we used the SBw algorithm to study the multifractal property of two families of weighted fractal networks (WFNs): "Sierpinski" WFNs and "Cantor dust" WFNs. We also discussed how the fractal dimension and generalized fractal dimensions change with the edge-weights of the WFN. From the comparison between the theoretical and numerical fractal dimensions of these networks, we can find that the proposed SBw algorithm is efficient and feasible for MFA of weighted networks.

In addition, we applied the SBw algorithm to study the multifractal properties of some real networks — the high-energy theory collaboration network, the astrophysics collaboration network and the computational geometry collaboration network. We found that multifractality exists in these weighted networks and is also affected by their edge-weight. Our result indicates that multifractal property of weighted networks are affected both by their edge weight and their topology structure.

## METHODS

### Multifractal Analysis

The fixed-size box-counting algorithm is one of the most common and effective algorithms to explore multifractal properties of fractal sets19.

For a support set $E$ in a metric space $\Omega$ and a normalized measure $\mu$ (i.e. $0 \leq \mu(\Omega) \leq 1$), we consider the partition sum:

$$Z_\varepsilon(q) = \sum_{\mu(B)} [\mu(B)]^q, \tag{4}$$

where $q \in R$ and the sum runs over all different non-overlapping boxes $B$ which cover the support set $E$ with a given size $\varepsilon$. The mass exponents $\tau(q)$ of the measure $\mu$ is defined as:

$$\tau(q) = \lim_{\varepsilon \to 0} \frac{\ln Z_\varepsilon(q)}{\ln \varepsilon}. \tag{5}$$

The generalized fractal dimension $D(q)$ of the measure $\mu$ is defined as:

$$D(q) = \begin{cases} \dfrac{\tau(q)}{q-1}, & q \neq 1, \\ \lim\limits_{\varepsilon \to 0} \dfrac{Z_{1,\varepsilon}}{\ln \varepsilon}, & q = 1. \end{cases} \tag{6}$$

where $Z_{1,\varepsilon} = \sum_{\mu(b) \neq 0} \mu(B) \ln \mu(B)$. A numerical estimation of the generalized fractal dimension $D(q)$ can be got from the linear regression of $\ln Z_\varepsilon(q)/q-1$ against $\ln\varepsilon$ for $q \neq 1$, $Z_{1,\varepsilon}$ against $\ln\varepsilon$ for $q=1$, respectively.

Tèl *et al.*48 proposed the sandbox (SB) algorithm for MFA of fractal sets which is an extension of the box-counting algorithm19. The generalized fractal dimensions $D(q)$ are defined as48:

$$D(q) = \lim_{r \to 0} \frac{\ln \langle [M(r)/M(0)]^{q-1} \rangle}{\ln(r/d)} \frac{1}{q-1}, \quad q \in R, \tag{7}$$

where $M(r)$ is the number of points in the sandbox with radius $r$, $M(0)$ is the number of all points in the fractal object. It is denoted the brackets $\langle \cdot \rangle$ to take statistical average over randomly chosen centers of the sandboxes. From Equation (7) we can get the relation:

$$\ln(\langle [M(r)]^{q-1} \rangle) \propto D(q)(q-1)\ln(r/d) + (q-1)\ln(M_0). \tag{8}$$

From Equation (8), we can obtain an estimation of the generalized fractal dimension $D(q)$ by the linear regression of $\ln(\langle [M(r)]^{q-1} \rangle)$ against $(q-1)\ln(r/d)$. Then, we can also get the mass exponents $\tau(q)$ through $\tau(q) = (q-1)D(q)$. Specifically, $D(0)$ is the fractal dimension, $D(1)$ is the information dimension, $D(2)$ is the correlation dimension of the fractal object, respectively.

## A Modified Sandbox Algorithm for Multifractal Analysis of Weighted Networks

Recently, our group employed the SB algorithm proposed by Tél *et al.*48 for MFA of unweighted complex networks45. In the SB algorithm45, the radiuses $r$ of the sandbox are set to be integers in the range from 1 to the diameter of the unweighted network. However, in weighted networks, the values of edge-weights could be any real numbers excluding zero and the shortest path is defined by the path between two nodes such that the sum of values of its edge-weights to be minimized in some way57. So, the shortest path between two nodes could be any real numbers excluding zero. In this paper, for weighted networks, we denote the length of shortest path between node $i$ and node $j$ by $d_{ij}$ and $d_{ij}$ is defined as52:

$$d_{ij} = \min\left(w_{ij_1}^p + w_{j_1j_2}^p + \cdots + w_{j_{m-1}j_m}^p + w_{j_mj}^p\right), \tag{9}$$

where $w_{kh}$ means the edge-weight of directly connecting node $k$ and node $h$ in a path, $j_m(m=1, 2, \cdots)$ are IDs of nodes and $p$ is a real number. In particular, when $p$ equal to zero, the length of the shortest path given by Equation(9) is the same as unweighted networks57. If the edge-weight is only a number without obvious physical meaning, we set $p$ equals to 1, such as the "Sierpinski" WFN53. In some real weighted networks, one case is that the bigger edge-weight of between any two nodes is, the less distance is, such as the collaboration networks, where $p<054$; the other case is that the bigger edge-weight of between any two nodes is, the further distance is, such as the real city network and the "Sierpinski" WFN, where $p>0$.

The SB algorithm is unfeasible for MFA of weighted networks because we cannot obtain enough numbers of boxes (even only one sandbox we can obtain when the diameter of the weighted network is less than one). Wei *et al.*52 proposed an improved box-covering algorithm for fractal analysis of weighted network (BCANw). In the present work, motivated by the idea of BCANw, we propose a modified sandbox algorithm (we call it SBw algorithm) for MFA of weighted networks. The SBw algorithm can deal with the multifractal property (hence can also deal with the fractal property) of weighted networks.

Before we apply the SBw algorithm for MFA of weighted networks, we need to calculate the shortest-path distance matrix $D$ of the network and set the range of radiuses $r$ of the sandboxes. The detail is given as:

- A network is mapped to an adjacent matrix $W_{N\times N}$, where $N$ is the total number of nodes in the network. For any given real

numbers $p$, the elements of the adjacent matrix $w_{ij}^{p} \neq 0$ is the edge-weight between directly connecting nodes $i$ and $j$, otherwise $w_{ij}^{p} = 0$. According to the adjacent matrix $W_{N\times N}$, we can calculate the shortest path distance matrix $D$ by applying the Floyd's algorithm58 of Matlab BGL toolbox59;

- For any given real numbers $p$, order the edge-weights $w_{ij}^{p}$ as $w_1 \leq w_2 \leq \cdots \leq w_m$, where $m$ is the number of edge-weights. From the fractal theory, we should look for an appropriate range of radiuses $r$ to perform the least square linear fit and then obtain the generalized fractal dimensions $D(q)$ accurately. We tried choosing the radius $r$ from 0 to diameter $d$ with equal (linearly or logarithmically) intervals. But we found it is hard to look for an appropriate range of radiuses $r$ to perform the least square linear fit and then obtain the generalized fractal dimensions $D(q)$ of weighted complex networks we considered accurately. So the radiuses $r$ of the sandboxes are obtained by accumulating the value of the edge-weights until it is larger than the diameter $d$ of the network. So, we can get the set of radiuses (denoted as $R$), where $R = \{w_1, w_1 + w_2, \cdots, \sum_{i=1}^{k} w_i : \ k \leq m\}$ and $\sum_{i=1}^{K} w_i \leq d < \sum_{i=1}^{K+1} w_i$. Specifically, for any $i$, $j$, if $w_i = w_j = 1$, then the radius set $R$ is the same as the SB algorithm for unweighted network.

In this sense, the SBw algorithm can be applied to calculate the mass exponents $\tau(q)$ and the generalized fractal dimensions $D(q)$ not only for unweighted network but also for weighted networks. Now we propose a modified SB algorithm (SBw) for MFA of weighted network as:

- Initially, ensure that all nodes in the network are not covered and not selected as a center of a sandbox.
- Set every element in the radius set $R$ as the radius $r$ of the sandbox which will be used to cover the nodes, where $R$ is obtained as above. (in the SB algorithm the radius $r$ in the range $r \in [1, d]$, where $d$ is the diameter of the network).
- Rearrange the nodes of the entire network into a random order. Make sure the nodes of the network are randomly chosen as the center of a sandbox.
- According to the size $N$ of networks, choose the first 1000 nodes in a random order as the center of 1000 sandboxes, then for each

sandbox, search all the neighbor nodes which have a distance to the center node within $r$.

- Count the number of nodes in each sandbox of radius $r$, denote the number of nodes in each sandbox of radius $r$ as $M(r)$.
- Calculate the statistical average $\langle [M(r)]^{q-1} \rangle$ of $[M(r)]^{q-1}$ over all 1000 sandboxes of radius $r$.
- For different values in the radius set $R$, repeat steps (2) to (6) to obtain the statistical average $\langle [M(r)]^{q-1} \rangle$ and then use $\langle [M(r)]^{q-1} \rangle$ for linear regression.

## ACKNOWLEDGEMENTS

This work is supported by the National Natural Science Foundation of China (Grant No. 11371016), the Chinese Program for Changjiang Scholars and Innovative Research Team in University (PCSIRT) (Grant No. IRT1179) and the Research Foundation of Education Commission of Hunan Province of China (Grant No. 15C0389).

## REFERENCES


1. Song, C. M., Havlin, S. &Makse, H. A. Self-similarity of complex networks. Nature 433, 392–395 (2005).
2. Newman, M. E. J. Networks: an introduction. Oxford University Press, Oxford (2009).
3. Vidal, M., Cusick, M. E. &Barabasi, A. L. Interactome networks and human disease. Cell 144, 986–998 (2011).
4. Xu, C. J., Zheng, Y., Su, H. S. & Wang, H. Containment control for coupled harmonic oscillators with multiple leaders under directed topology. Int. J. Control. 88**(2)**, 248–255 (2015).
5. Watts, D. J. &Strogatz, S. H. Collective dynamics of small-worldnetworks. Nature 393, 440–442 (1998).
6. Barabasi, A. L. & Albert, R. Emergence of scaling in random networks. Science 286, 509–512 (1999).
7. Mandelbrot, B. B. The Fractal Geometry of Nature. Academic Press, New York (1983).
8. Feder, J. Fractals. Plenum, New York (1988).
9. Falconer, K. J. Techniques in Fractal Geometry. Wiley, New York (1997).
10. Gallos, L. K., Song, C. M., Havlin, S. &Makse, H. A. A review of fractality and self-similarity in complex networks. Physica A 386, 686 (2007).
11. Song, C., Havlin, S. &Makse, H. Origins of fractality in the growth of complex networks. Nat. Phys. 2, 275–281 (2006).
12. Song, C., Gallos, L. K., Havlin, S. &Makse, H. A. How to calculate the fractal dimension of a complex network: the box covering algorithm. J. Stat. Mech.: Theor. Exp. 3, 4673–4680 (2007).
13. Kim, J. S., Goh, K. I., Kahng, B. & Kim, D. A box-covering algorithm for fractal scaling in scale-free networks. Chaos 17, 026116 (2007).
14. Zhou, W. X., Jing, Z. Q. &Sornette, D. Exploring self-similarity of complex cellular networks: The edge-covering method with simulated annealing and -periodic sampling. Physica A 375, 7417–52 (2007).
15. Gao, L., Hu, Y. & Di, Z. Accuracy of the ball-covering approach for fractal dimensions of complex networks and a rank-driven algorithm. Phys. Rev. E 78, 046109 (2008).

16. Ng, H. D., Abderrahmane, H. A., Bates, K. R. &Nikiforakis, N. The growth of fractal dimension of an interface evolution from the interaction of a shock wave with a rectangular block of sf6. Commun. Nonlin. Sci. Numer. Simul. 16, 4158–4162 (2011).
17. Schneider, C. M., Kesselring, T. A., Andrade Jr, J. S. & Herrmann, H. J. Box-covering algorithm for fractal dimension of complex networks. Phys. Rev. E 86, 016707 (2012).
18. Grassberger, P. &Procaccia, I. Characterization of strange attractors. Phys. Rev. Lett. 50, 346–349 (1983).
19. Halsey, T. C., Jensen, M. H., Kadanoff, L. P., Procaccia, I. &Shraiman, B. I. Fractal measures and their singularities: The characterization of strange sets. Phys. Rev. A. 33, 1141–1151 (1986).
20. Canessa, E. Multifractality in time series. J. Phys. A 33, 3637–3651 (2000).
21. Anh, V., Tieng, Q. M. &Tse, Y. K. Cointegration of stochastic multifractals with application to foreign exchange rates. Int. Trans. Oper. Res. 7, 349–363 (2000).
22. Yu, Z. G., Anh, V. & Lau, K. S. Multifractal characterisation of length sequences of coding and noncoding segments in a complete genome. Physica A 301, 351–361 (2001).
23. Yu, Z. G., Anh, V. & Lau, K. S. Measure representation and multifractal analysis of complete genomes. Phys. Rev. E 64, 031903 (2001).
24. Anh, V., Lau, K. & Yu, Z. G. Recognition of an organism from fragments of its complete genome. Phys. Rev. E 66, 031910 (2002).
25. Yu, Z. G., Anh, V. & Lau, K. S. Multifractal and correlation analyses of protein sequences from complete genomes. Phys. Rev. E 68, 021913 (2003).
26. Yu, Z. G., Anh, V. & Lau, K. S. Chaos game representation of protein sequences based on the detailed hp model and their multifractal and correlation analyses. J. Theor. Biol. 226, 341–348 (2004).
27. Zhou, L. Q., Yu, Z. G., Deng, J. Q., Anh, V. & Long, S. C. A fractal method to distinguish coding and non-coding sequences in a complete genome based on a number sequence representation. J. Theor. Biol. 232, 559–567 (2005).
28. Yu, Z. G., Anh, V., Lau, K. S. & Zhou, L. Q. Clustering of protein structures using hydrophobic free energy and solvent accessibility of proteins. Phys. Rev. E 73, 031920 (2006).

29. Yu, Z. G., Xiao, Q. J., Shi, L., Yu, J. W. &Anh, V. Chaos game representation of functional protein sequences and simulation and multifractal analysis of induced measures. Chin. Phys. B 19, 068701 (2010).
30. Han, J. J. & Fu, W. J. Wavelet-based multifractal analysis of dna sequences by using chaos-game representation. Chin. Phys. B 19, 010205 (2010).
31. Zhu, S. M., Yu, Z. G. &Ahn, V. Protein structural classification and family identification by multifractal analysis and wavelet spectrum. Chin. Phys. B 20, 010505 (2011).
32. Zhou, Y. W., Liu, J. L., Yu, Z. G., Zhao, Z. Q. &Anh, V. Multifractal and complex network analysis of protein dynamics. Physica A 416, 010505 (2014).
33. Kantelhardt, J. W. et al. Long-term persistence and multifractality of precipitation and river runoff records. J. Geophys. Res. 111, D01106 (2006).
34. Veneziano, D., Langousis, A. &Furcolo, P. Multifractality and rainfall extremes: A review. Water Resour. Res. 42, W06D15 (2006).
35. Venugopal, V., Roux, S. G., Foufoula-Georgiou, E. &Arneodo, A. Revisiting multifractality of high-resolution temporal rainfall using a wavelet-based formalism. Water Resour. Res. 42, W06D14 (2006).
36. Yu, Z. G., Anh, V., Wanliss, J. A. & Watson, S. M. Chaos game representation of the dst index and prediction of geomagnetic storm events. Chaos, Solitons and Fractals. 31, 736–746 (2007).
37. Zang, B. J. & Shang, P. J. Multifractal analysis of the yellow river flows. Chin. Phys. B 16, 565–569 (2007).
38. Yu, Z. G., Anh, V. &Eastes, R. Multifractal analysis of geomagnetic storm and solar flare indices and their class dependence. J. Geophys. Res. 114, A05214 (2009).
39. Yu, Z. G., Anh, V., Wang, Y., Mao, D. &Wanliss, J. Modeling and simulation of the horizontal component of the geomagnetic field by fractional stochastic differential equations in conjunction with empirical mode decomposition. J. Geophys. Res. 115, A10219 (2010).
40. Yu, Z. G., Anh, V. &Eastes, R. Underlying scaling relationships between solar activity and geomagnetic activity revealed by multifractal analyses. J. Geophys. Res.: Space Physics 119, 7577–7586 (2014).

41. Furuya, S. &Yakubo, K. Multifractality of complex networks. Phys. Rev. E 84, 036118 (2011).
42. Wang, D. L., Yu, Z. G. &Anh, V. Multifractal analysis of complex networks. Chin. Phys. B 21, 080504 (2012).
43. Li, B. G., Yu, Z. G. & Zhou, Y. Fractal and multifractal properties of a family of fractal networks. J. Stat. Mech.: Theor. Exp. 2014, P02020 (2014).
44. Liu, J. L., Yu, Z. G. &Anh, V. Topological properties and fractal analysis of a recurrence network constructed from fractional brownian motions. Phys. Rev. E 89, 032814 (2014).
45. Liu, J. L., Yu, Z. G. &Anh, V. Determination of multifractal dimension of complex network by means of the sandbox algorithm. Chaos 25, 023103 (2015).
46. Lee, C. Y. & Jung, S. H. Statistical self-similar properties of complex networks. Phys. Rev. E 73, 066102 (2006).
47. Gallos, L. K., Song, C. M., Havlin, S. &Makse, H. A. Scaling theory of transport in complex biological networks. Proc. Natl. Acad. Sci. USA. 104, 7746–7751 (2007).
48. Tél, T., Fülöp, A. &Vicsek, T. Determination of fractal dimensions for geometric multifractals. Physica A 159, 155–166 (1989).
49. Bagler, G. Analysis of the airport network of india as a complex weighted network. Physica A 387, 2972–2980 (2008).
50. Hwang, S., Yun, C. K., Lee, D. S. &Kahng, B. Spectral dimensions of hierarchical scale-free networks with weighted shortcuts. Phys. Rev. E 82, 056110 (2010).
51. Cai, G., Yao, Q. & Shao, H. D. Global synchronization of weighted cellular neural network with time-varying coupling delays. Nonlin. Sci. Numer. Simul. 17, 3843–3847 (2012).
52. Wei, D. J. et al. Box-covering algorithm for fractal dimension of weighted networks. Scientific Reports 3, 3049 (2013).
53. Carletti, T. &Righi, S. Weighted fractal networks. Physica A 389, 2134–2142 (2010).
54. Newman, M. E. J. Scientific collaboration networks. ii. shortest paths, weighted networks and centrality. Phys. Rev. E 70, 056131 (2001).
55. Barnsley, M. Fractals everywhere. Academic Press, San Diego (2001).

56. Vladimir, B. & Andrej, M. Pajek datasets. (2006) Available at: http://vlado.fmf.uni-lj.si/pub/networks/data/. (Date of access: 11th October 2015).
57. Newman, M. E. J. Analysis of weighted networks. Phys. Rev. E 389, 2134–2142 (2004).
58. Floyd, R. W. Algorithm 97: Shortestpath. Commun. ACM 5**(6)**, 345 (1962).
59. Gleich, D. F. MatlabBGL: A graph library for matlab based on the boost graph library. (2006) available at: http://dgleich.github.com/matlab-bgl. (Date of access: 11th October 2015).

# 17

# *Reliable Multi-Fractal Characterization of Weighted Complex Networks: Algorithms and Implications*

**YuankunXue& Paul Bogdan**

Ming Hsieh Department of Electrical Engineering, University of Southern California, 90007, CA, USA

## ABSTRACT

Through an elegant geometrical interpretation, the multi-fractal analysis quantifies the spatial and temporal irregularities of the structural and dynamical formation of complex networks. Despite its effectiveness in unweighted networks, the multi-fractal geometry of weighted complex networks, the role of interaction intensity, the influence of the embedding metric spaces and the design of reliable estimation algorithms remain open challenges. To address these challenges, we present a set of reliable multi-fractal estimation algorithms for quantifying the structural complexity and heterogeneity of weighted complex networks. Our methodology uncovers that (i) the weights of complex networks and their underlying metric spaces play a key role in dictating the existence of multi-fractal scaling and (ii) the multi-fractal scaling can be localized in both space and scales. In addition,

**Citation:** Xue, Y., & Bogdan, P. (2017). Reliable multi-fractal characterization of weighted complex networks: algorithms and implications. Scientific reports, 7(1), 1-22., DOI: 10.1038/s41598-017-07209-5.

this multi-fractal characterization framework enables the construction of a scaling-based similarity metric and the identification of community structure of human brain connectome. The detected communities are accurately aligned with the biological brain connectivity patterns. This characterization framework has no constraint on the target network and can thus be leveraged as a basis for both structural and dynamic analysis of networks in a wide spectrum of applications.

## INTRODUCTION

Complex systems consist of heterogeneous agents mutually influenced via interactions of different intensities over multiple spatio-temporal scales. This heterogeneity encompassed in both the participating components and their varying interactions makes complex systems difficult to decipher. To understand and control these complex systems, the network theory provides an effective mathematical modeling framework that enables the encoding of the entities (nodes) of a complex system and their heterogeneous interactions (links) of different strength (weights) into a topological network configuration implicitly embedded in metric spaces, where the distance among nodes is decided both by the structural configuration of the system (topology) and the intrinsic nature of the inter-node couplings (e.g., social affinity, chemical bonds, traffic intensity or neural connectivity strength). In some cases, the properties of the inter-couplings among system components and the corresponding spatial embeddings even play a far more dominant role in regulating the overall system behaviors and dynamics. For instance, the atomic and molecular interactions among a chain of amino acids definitively dictate not only the dynamical spatial conformation of the corresponding protein but also its biological functionality[1, 2]. The disturbance of normal protein interactions can lead to irreversible pathological consequences known as proteopathies like Alzheimer's, Parkinson's[3] and Huntington's disease[4]. Therefore, the study of structural organization, formation and dynamics of the complex systems can benefit from studying their geometrical properties and discovering new relationships between geometrical characteristics and network problems (e.g., community structure identification).

Learning the geometric principles underlying the organization of complex systems modeled by weighted networks facilitates the identification of their fundamental properties. Some of complex networks have been found to be *Small world* or *Ultra-small world*. Small world network model characterizes a graph of size $N$ for which its average path length increases

proportionally to the logarithm of the number of nodes ⟨d⟩∼logN⟨d⟩∼logN. In contrast, the Ultra-small world networks are characterized by smaller shortest path distances that scale as dmin∼loglogNdmin∼loglogN. Albert Barabasi and his colleagues found that the Erdos-Renyi random network model can not explain the formation of densely interconnected hubs or clusters in a family of real networks with degree distribution obeying a power-law5. In contrast to the Erdos-Renyi random network model that leads to a narrow normal degree distribution, the power-law degree distribution of these networks has such a long tail that we cannot reason about the interconnection density of the network given a randomly chosen sample, hence they are *scale-free*.

The discovery of small-world property led to the belief that complex networks are not invariant under a length-scale transformation according to which an exponential dependence holds between the size of the network and its average path length. However, it is found that a variety of real networks exhibit self-repeating patterns at all length scales by applying a renormalization procedure6, 7. This illustrates the concept of *self-similarity*. The coexistence of self-similarity and small-world property in a variety of complex networks is further verified8. These two contradictory properties call for further investigation on the appropriate mathematical model of complex networks and their main features. A phase transition phenomenon is found between the local self-similarity and the global small-world property by studying the stability of nodes by renormalization group theory9.

The uncovered self-similarity in complex networks connects to the important *fractal* and *multi-fractal* geometry domain where a family of objects are distinguished based on their self-repeating patterns and invariability under scale-length operations. Such objects are known as fractal objects. A mono-fractal object obeys a perfect self-repeating law at all scales. When embedded in Euclidean metric space and tiled by equally sized boxes at different scales, it becomes apparent that an important property of fractals is the power-law dependence between the mass distribution $M(r)$ (e.g., the number of points in a box) and the scale factor $r$:

$$M(r) \sim r^{D} \tag{1}$$

In Eq. (1), $D$ is the *fractal dimension* and represents a real-valued number in contrast to the embedded space dimension which is always an integer. Fractal dimension is the major tool for describing the fractal geometry and the heterogeneity of irregular geometric objects that the dimension of its embedded space fails to capture. For instance, in Euclidean geometry, a

straight line and a crooked line share the same geometrical dimension but have very distinct properties. Multi-fractals could be seen as an extension to fractals with increased complexity. They are invariant by translation although a distortion factor $q$ needs to be considered to distinguish the details of different regions of the objects as a consequence of *inhomogenous* mass distribution. Intuitively, multi-fractals are *not* perfect self-repetitions but rich in *localized* variations of detailed geometric configurations. Consequently, a single fractal dimension is *not* sufficient to characterize the irregularity of the geometric shapes as the scaling factor measured across the object could be *different*. As a result, multi-fractal analysis (MFA, see Methods for details) is proposed to capture the localized and heterogenous self-similarity by learning a generalized fractal dimension $D(q)$ under different distortion factors $q$.

MFA has been applied to investigate the underlying geometrical principles in a wide spectrum of applications including signal processing[10,11,12,13], imaging processing[14,15,16], genomics[17, 18], geophysics[19, 20], turbulence analysis[10, 21, 22], network traffic modeling 23 and financial analysis[24,25,26,27]. Irrespective of the effectiveness of MFA in various domains, its application to study the self-similarity of complex networks is *not* straightforward as the Euclidean metric is not well defined in a topological object like the complex network. The box-covering method was introduced28 to calculate the fractal dimension of unweighted complex networks and the authors proved its reducibility to the well-known graph coloring problem, which is NP-hard. However, a single fractal dimension is not a sufficient characterization of self-similarities embedded in the complex network. For instance, how can we distinguish fractal networks that share exactly the same fractal dimension but look entirely different? Fig. 1 shows two fractal networks, namely, *Sierpinski fractal networks and* $(u, v)$*-flower*. Both networks have the exact same fractal dimension of $ln(6)/ln(3) \approx 1.631$ but show distinct structural properties. Apparently, relying on mono-fractal analysis does not allow us to distinguish between these two networks. Another relevant question is how link weights affect the fractality/multi-fractality of the weighted complex network. Link weights play an important role in governing the dimension of the network as there exists a mapping from a weighted network to a network spatially embedded where weights translate to the length of links that affects its dimension[29, 30]. To address this problem, an alternative box-covering method (BCANw) was proposed for the numerical determination of the fractal dimension of weighted complex networks31. Its application has also been extended to

study the inhomogeneity of weighted real-world networks through multi-fractal analysis. Following the same line, a similar study of multi-fractality embedded in weighted networks using the modified sandbox method (SBw) is reported32. However, neither of the two methods considers the impact imposed by the distribution of the link weights. Both algorithms are prone to *intrinsic* estimation bias as a consequence of i) ignoring the skewness of the link weight distribution and ii) the implicit assumption that a global fractal/multi-fractal scaling holds at all scales of the network. Moreover, there is no theoretical foundation to support the design and evaluation of both algorithms in order to analyze the factors that adversely impact their numerical accuracy. All these disadvantages leave room for an erroneous characterization of both the structural and dynamical features of the weighted complex networks.

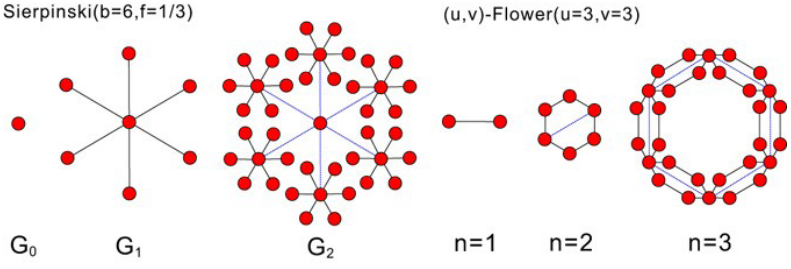


**Figure 1**: Failure of single (dominant) fractal dimension to capture the heterogeneity in detailed configuration of fractal networks. A comparative example shows. (a) Sierpinski fractal network ($s=1/3$, $b=6$) and (b) (u, v)-flower fractal network ($u=3$, $v=3$) share the same fractal dimension (1.631) yet having distinct topological structure.

To overcome these issues, we first analytically study the multi-fractal structure of the Sierpinski fractal network family to set up the theoretical ground for evaluation and comparative analysis of our proposed algorithms. We find that the multi-fractality identified by SBw can be just the side effect of the limited size of the network considered. The analytical discussion of multi-fractality in Sierpinksi family $\mathscr{S}$ provides the theoretical basis on which not only we can quantitatively reason about the existence of multi-fractality/fractality from an asymptotic perspective that numerical approaches will surely fail to offer, but also we can shed some light on the design of numerical algorithms for reliable estimation of multi-fractal spectrum of the complex networks.

To motivate the design of a reliable algorithm which eliminates the disadvantages of BCANw and SBw, we analyze the source of the estimation bias of both algorithms through a set of numerical experiments. We show a compatible growth rule is required to remove the bias, given weighted complex networks of finite resolution. The detailed quantitative error analysis to investigate the source of the intrinsic estimation bias of both algorithms can be found in our Supplementary Material Section 2.

Based on both our theoretical findings and numerical experimental results, we propose the *finite box-covering algorithm for weighted network (FBCw)* and the *finite sandbox algorithm for weighted network (FSBw)* with improved performance. We compare the accuracy of the estimates obtained by FBCw and FSBw with our analytical results of Sierpinski fractal network as well as with those obtained by BCANw and SBw. The comparison shows that the proposed algorithms are not only able to give reliable numerical estimates of fractality with insensitivity to the distribution of link weights, but also are capable of detecting the fractal scaling dependence when it holds within a finite range of scales (i.e., scale-localized).

More importantly, we apply the proposed algorithms to learn the multi-fractal structure of a set of real world weighted networks. We show the link weights play a definitive role in governing the existence of fractality in the network. The investigated weighted networks exhibit a phase transition from self-similar networks to small-world networks when converted to binary networks. Furthermore, we demonstrate that the fractal and multi-fractal scaling behaviors can be *spatially localized* and co-exist in the same network. Learning from our observations on the locality of the scaling behavior of real world weighted networks, we finally propose a network characterization framework based on the localized scaling feature space learned by the construction of scaling feature vectors for each node in the network. The proposed characterization is general and not limited to complex networks that are fractal or multi-fractal. It can be easily interfaced with subsequent analytical tools (e.g., machine learning algorithms) to unveil the intrinsic properties of the weighted complex networks. To illustrate the benefits of our methodology, we apply our algorithms to the network community detection in the human brain connectome. The identified communities are consistent with our biological knowledge.

The following discussion is organized in three parts. In the first part, we present the estimation error of previous numerical algorithms. In the second part of discussion, we compare the performance of BCANw, SBw with the proposed FBCw and FSBw. Finally, we present the multi-fractal analysis

on a set of weighted real world complex network and propose a localized scaling based approach for the characterization of the weighted complex networks. We provide an illustrative application example in network community detection to show its effectiveness.

# RESULTS

## Analysis of Finite Resolution and Link Weight Distribution

### *Estimation error analysis and stairway effect*

The link weights distribution of complex networks largely depend on the growth rule and weights allocation process. For instance, the distribution of link weights of Sierpinski family is shaped by the scaling factor $s$ and growth rule $b$. Interestingly, for small scaling factor $s$, we prove $G_k$ approaches a monofractal that has no explicit dependence on weights distribution (See the proof in Supplementary Material Section 1). Yet this is valid only for a complex network that has *infinite* resolution in the sense that box/sandbox can grow by infinitely small steps (but not continuously) in a network of unbounded range of scales. In most of cases, this does not hold for complex networks and perfect fractals of limited size (e.g., Sierpinski network of limited size). Therefore, when it comes to numerical calculation of the limit in Eqs (13) and (17) using linear regression which is shared by both box-covering and sandbox methods, we are able to show that the box/sandbox should grow in a regulated way that is ***compatible*** with link weights distribution such that the ***stairway*** effect is minimized.

The stairway effect is an immediate consequence of applying box-covering or sandbox methods to weighted complex network of finite resolution to estimate the generalized fractal dimensions using linear regression. For a linear regression that minimizes least square error (LSE) $\sum (y_i - x_i\theta)^2$, stairway effect can be stated as stagnant changes in $y_i$ irrespective of variation of $x_i$ up to a certain range. We show a simple example in Fig. 2 where the output and input observations are made from a linear relation $y = 50 - 0.4x$. The solid line shows the perfect fitting when no staircase is introduced. The two dashed lines correspond to the case where a set of unchanging observations are inserted (i.e., fake observations) between two actual $y$ observations at two different locations (as denoted by $x_i$), creating two pieces of "staircases" in the plot. As a consequence of minimization of LSE, the fitted lines in presence of staircases deviate from

the perfect fitting differently based on the position of the staircases in the plot. We can show the estimation error is proportional to the width of the staircase and the number of fake observations inserted. We have presented the detailed error analysis regarding the stairway effect in our Supplementary Material Section 2.

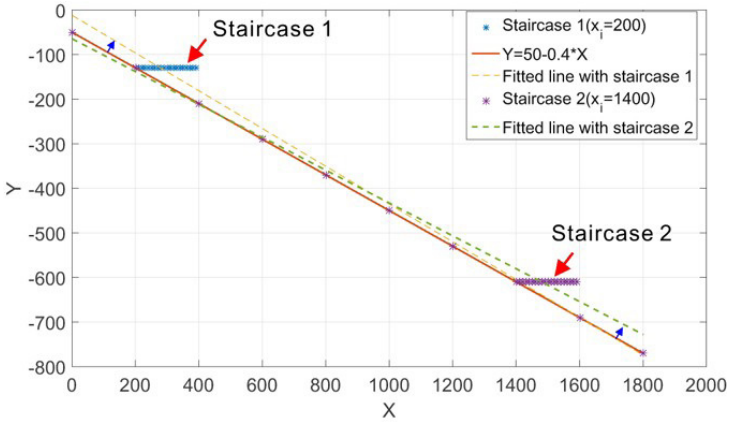


**Figure 2**: A case study of stairway effect. A linear relation $y = 50 - 0.4x$ is observed on a set of input $x$. Two sets of unchanging $y$ observations are manually inserted between two actual measurement to create "stairs". The introduction of such stairs biases the linear regression and causes estimation errors.

## *Finite resolution and compatible growth rule*

The above mentioned insertion of fake observations can be understood as an interpolation or oversampling process when a system with *finite resolution* is measured. For instance in a linear system, except for the case where input and output are decoupled in the system of interest, a staircase will be created in the measurement if the sampling rate is *not compatible* with the changing rate of the output, e.g., sampling rate is much greater than how the system actually changes its state. The changing rate of the system in this example intrinsically determines its "resolution".

Similarly, a fundamental difficulty in extending the use of box-covering or sandbox method for determination of multi-fractality in complex network lies in its finite resolution. For a geometric multi-fractal/fractal object embedded in Euclidean space, the probability measure $\mu$ is well-defined on a continuous interval $(0, L]$ where $L$ is the length of the object. Alternatively stated, it is possible to grow box size continuously and retrieve the estimates

from a linear regression that considers all obtained measurements. However, the distance metric of a complex network is discrete and probability measure $\mu$ is not defined on a continuously spanning $l$ horizon, i.e., for any $l_i$ and $l_{i+1} \in (0, L]$, there exist an infinite subset $L_i = \{l_{i_k} | l_{i_k} \in (l_i, l_{i+1})\}$ on which the probability measure $\mu$ is a constant. In other words, we can not distinguish between any element in this subset based on their associated probability measure, hence the *resolution* is *finite*.

As a consequence, we observe staircases that correspond to the measurements on these subsets $L_i$ if we directly apply box-covering or sandbox method with box size (or equivalently the radius of a sandbox, we use only the term "box size" for short) growing continuously. The presence of staircases, as we discussed earlier, introduces bias into the estimates of generalized fractal dimension. Obviously, we can minimize the stairway effect if we can aptly choose a growth strategy to scale the box size $l$ such that no element in $\cup L_i$ is chosen as the size of a box. We call such strategy, if exists, as *compatible growth rule*.

For unweighted networks, a compatible growth rule can be easily found by increasing the box size in a discrete way, i.e., adding one each time. This is feasible because even though the resolution of an unweighted network is limited yet it is *homogenous* across the network, i.e., distance between any directly connected pair of nodes is identical. However, such property does not hold for a weighted complex network due to the *distribution of link weights*. Searching for a compatible growth rule for box size scaling in a weighted network is much more difficult and sometimes impossible. To give some intuition, let us look at sandbox method. Formally, for a weighted network $G=(V, E)$, let us assume $v_i \in V$ as the center of sandbox and $v_j \in V$ as a random node. Denote $d_{i,j}$ as the shortest path length between $v_i$ and $v_j$. The shortest path distribution $F_{d_{i,j}}(l) = P\{d_{i,j} \leq l\}$ has a discrete support set $L_i = \{l_k | F_{d_{i,j}}(l_k) \neq F_{d_{i,j}}(l_{k'}), \forall k \neq k'\}$ defined by $G$. A compatible growth rule of $v_i$ on $G$ is thus a strictly ordered set $L_{<,v_i} = \{l_1, l_2, \ldots, l_n\}$ where $l_{k+1} > l_k$. Therefore, the compatible sandbox growth rule $L(G)$ on $G$ is defined by $L(G) = \cap_i L_{<,v_i}$ where $v_i$ is the center of the sandbox. It should be noted that it is always possible to find a compatible growth rule for a sandbox centered at a fixed point by growing its size by its *unique* distance to all other nodes. However, there is no guarantee that this growth rule is compatible for another sandbox centered differently. A compatible growth rule requires that the support of path length distribution is shared among all choices

of sandbox centers. Apparently, if the choice of sandbox in Eq. (17) (see FBCw and FSBw description in Methods section) is randomized over all the nodes in an unweighted graph $G$, $L(G) = \{1, 2, 3, \ldots, d_{min}\}$ where $d_{min}$ is the shortest path length of the longest distance between any pair of nodes of $G$. However, it can be practically difficult to find in a weighted network of *rich heterogeneity* such $L(G)$ that i) is shared by a sufficiently large subset of $V$ to be mathematically consistent with the estimate obtained by the box-covering method and ii) provides large set of samples of $l$ to numerically calculate the limit in Eq. (17).

Such heterogeneity connects tightly to the skewness of the underlying *link weight distribution* of $G$ that governs not only the existence of $L(G)$ but also the design of a reliable algorithm to determine the multi-fractality of $G$ when $L(G)$ does not exist. For instance, the unweighted network corresponds to the case where the link distribution is a symmetric delta function, hence the existence of multi-fractality is solely determined by the topological properties of the network. When the link weights are uniformly distributed, the topology of network again determines the multi-fractality of the network. Since the weights are uniformly distributed, $L(G) = \{E[w], 2E[w], \ldots, d_{min} E[w]\}$ is a statistically compatible growth rule. In other cases especially when the distribution is *highly skewed*, a poorly designed algorithm without awareness of link distribution leads to significant estimation errors in Eqs (13) and (17), rendering the basis of multi-fractal analysis questionable. This estimation error can be well-explained by our analytical findings that the incompatible growth rule with presence of a skewed link weight distribution will lead to the stagnant observations in spite of the growing box size of $l$, i.e., the staircase. Wider staircases will produce *underestimated* slope, hence biased estimates of multi-fractality.

Both BCANw and SBw that are previously proposed for numerical determination of multi-fractality in weighted networks fall into this category as they both rely on an incompatible growth rule and do not consider the skewness of link distribution. We show in the following discussion their disadvantages compared to our proposed algorithms. To make fair comparison under the same experimental setting with priorly known ground truth about multi-fractality of the study object, we choose Sierpinski fractal network family as our target network. We conduct comparative error analysis across all four algorithms when applied to estimate the dominant fractal dimension of the target networks.

## Comparative Analysis of Estimation Methods

### *Intrinsic estimation bias of BCANw and SBw*

To corroborate our argument, we first present two numerical experiments where a simple yet incompatible growth rule is applied to both box-covering and sandbox methods when used for determination of the dominant fractal dimension of Sierpinski network $G_5 \in S$ with $b=3$, $s=1/2$ (see Supplementary Material Section 1 for detailed construction of $G_5$). The incompatible growth rule increases the size of the box linearly by accumulating a fixed step length. We show in Fig. 3 the estimated fractal dimension using a box-covering method with this growth rule. The theoretical fractal dimension is $ln(b)/ln(s) \approx 1.585$. As predicted, the staircases are present throughout the scales of $l$ considered. To show its impact on the estimates, we plot the fitted line given by the linear regression on collected measurements and a reference line with the theoretical slope. As one notices in the figure, the staircases drive the estimates to deviate from the theoretical slope. We can make similar observations in Fig. 4 that shows the estimated dominant fractal dimension of the $G_5$ using sandbox method following the same growth rule. The staircases correspond to incompatible choice of box size $l$ from the set $\cup L_i$ for which the probability measure is not defined. As a result, the measure $\mu(B(l))$ remains stagnant irrespective of changes in $l$, introducing estimation errors when linear regression is performed in Eqs (13) and (17) to determine numerically the multi-fractal spectrum.

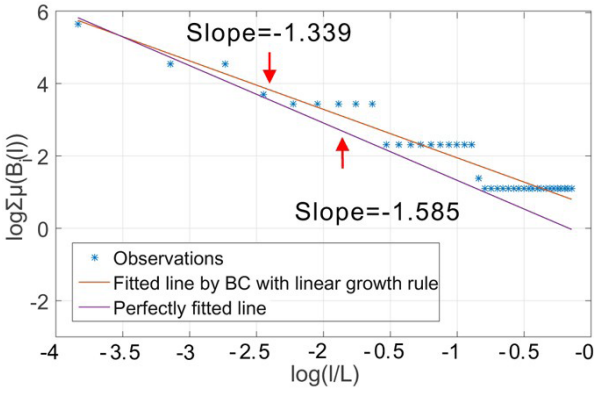


**Figure 3**: Observation of staircase effect in determination of dominant fractal dimension of $G_4$ of Sierpinski fractal network family using box-covering method with an incompatible linear growth rule.

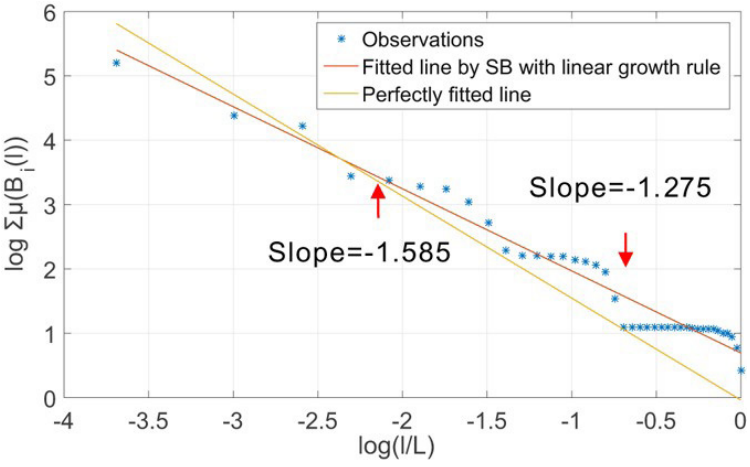


**Figure 4**: Observation of staircase effect in determination of dominant fractal dimension of $G_4$ of Sierpinski fractal network family using sandbox method with an incompatible linear growth rule.

These two simple examples verify our analytical prediction in our analysis of incompatible growth rule when an incompatible growth rule is enforced. In what follows, we show that neither BCANw nor SBw is immune to such incompatible growth rule. Again, we use $G_5$ as a case study to compare with our simple settings of our first set of experiments. In contrast to a linear growth rule, both BCANw and SBw employ a growth rule $L_< = \{w_1, w_1+w_2, \ldots, \sum_i w_i, \forall w_i \in W(G)\}$ where $W(G) = \{w_1, w_2, w_3, \ldots, w_n\}$ is an ordered set of all the weights of $G$ such that $w_k \leq w_{k+1}$ for all choices of $i$. We apply the BCANw and SBw to estimate the dominant fractal dimension of $G_5$. To verify the existence of staircase effect when applying BCANw and SBw, we show two case studies in Figs 5 and 6. As one can notice, accumulating the link weights to grow either the box or sandbox is still not compatible with the Sierpinski fractal network $G_5$. We observe in both experiments that the staircases introduce large bias (1.375 and 1.327 compared to 1.585) in numerical determination of limits in Eqs (13) and (17). The failure to accurately calculate them translates directly to *unreliable estimation* of the *multi-fractal spectrum*.

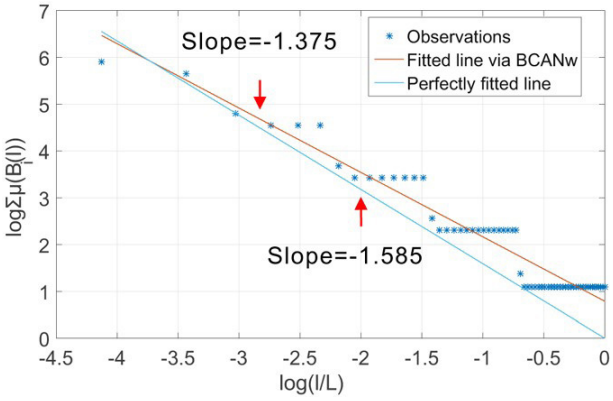


**Figure 5**: Observation of staircase effect in determination of dominant fractal dimension of $G_4$ of Sierpinski fractal network family using BCANw.

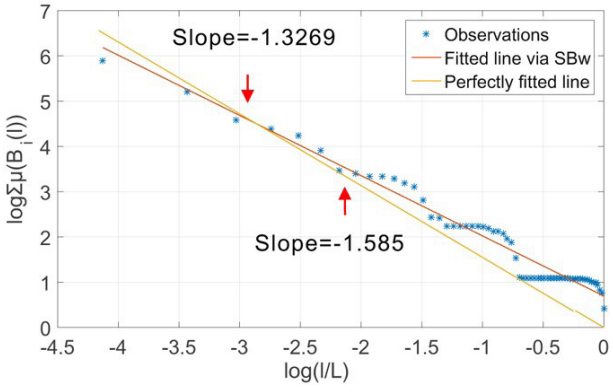


**Figure 6**: Observation of staircase effect in determination of dominant fractal dimension of $G_4$ of Sierpinski fractal network family using SBw.

Moreover, we argue that the estimation errors recognized in Figs 5 and 6 do not come from "infrequent anomalies" of the experiments. Given a fixed size of the network, repeating the experiments using box-covering or averaging the result over an increased set of sandbox centers does not fundamentally compensate the error introduced by BCANw and SBw ignoring finite resolution and link weight distribution of the target network. We performed BCANw with random choice of node coloring order and repeated the experiment by 1000 to 11,000 times with a step length of 200 to obtain the averaged number of boxes to cover the graph to avoid the bias introduced by the deterministic ordering. It should be also noted that the reason we take the average number of boxes comes from the practical

consideration. It represents the average performance of the BCANw when it is computationally impossible to repeat the experiments indefinitely to obtain the minimal number of boxes given large-scale networks. We performed SBw with random choice of the center of sandbox from 5% to 100% of nodes in $G_5$ with a step length of 1.9%. For each step, the results are averaged over 1000 trials. To illustrate the importance of awareness of the finite resolution and link weight distribution on the estimation algorithm, we also performed the proposed FBCw and FSBw with the same settings as BCANw and SBw. The results are plotted in Fig. 7.

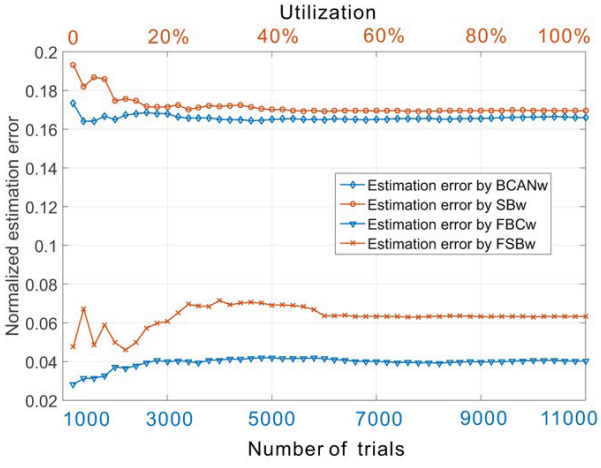


**Figure 7**: Normalized estimation errors of dominant fractal dimension of $G_5$ ($b=3$, $s=1/2$) under different (i) numbers of the repeated trials for box-covering-based methods (BCANw and FBCw) and (ii) utilization of nodes as sandbox center for sandbox-based methods (SBw and FSBw). Averaging the estimations over an increasing number of box-covering trials or nodes used as sandbox centers brings trivial improvement to the intrinsically biased estimation of BCANw and SBw. The proposed FBCw and FSBw provide better accuracy by addressing the finite resolution and the skewness of the link weight distribution of the weighted complex network.

We show the estimation errors of the four algorithms normalized against the theoretical dominant fractal dimension. For box-covering based algorithms (BCANw and FBCw, blue lines), we plot the error against different numbers of trials (1000 to 11000). For sandbox-based algorithms (SBw and FSBw, orange lines), the error is plotted against utilization of total number of nodes used as the candidates for the sandbox center. Several key observations can be made for BCANw and SBw: i) As the averaging

is performed over an increasing number of trials or sandbox centers, the estimation error is improved slightly. For BCANw, this can be understood as the randomization helps remove the bias of the ordering by which we check the nodes to assign box ID. For SBw, the improvement on estimation error is more significant (from 19.3% to 17%) while it eventually approaches that of BCANw. This is well aligned with Eq. (17) in that the randomized choice of sandbox is the necessary condition for the equivalency of sandbox method to box-covering method. ii) Even though the improvements on estimation accuracy are observed for both BCANw and SBw as the averaging helps remove the random bias, they are trivially small. The randomization is not able to fundamentally compensate for the estimation errors introduced by their incompatible growth rules. Therefore, the staircase effect from the case studies presented in Figs 5 and 6 is the *intrinsic estimation bias* of both algorithms. iii) In contrast, the proposed FBCw and FSBw algorithms consistently outperform the BCANw and SBw by a larger margin. The worst-case normalized estimation error of FBCw is less than 4% and that of FSBw is less than 7%.

The experimental results show that the state-of-the-art BCANw and SBw methods are not immune to errors due to the influence of finite resolution and link weight distribution, hence suffering from the intrinsic estimation bias. It should be noted that these biased estimations can be noticed *only if we know the ground truth* of multi-fractality of the interested network. Such ground truth can hardly be reached if i) we have no access to estimation approaches with optimality guarantee (e.g., optimal box-covering or sandbox methods with compatible growth rule) and/or ii) the underlying mechanism that regulates the growth of the network is unknown or changing over time (e.g., non-deterministic). For weighted fractal networks that extend themselves based on simple rules (e.g., Sierpinski fractal family), our theoretical multi-fractal analysis (see Supplementary Material Section 1) shows that it is possible to develop an optimal approach based on which the ground truth (i.e., the theoretical multi-fractality) can be obtained. However, for most of real-world weighted complex networks there is no such ground truth against which we can compare our estimation of multi-fractality and it is practically very difficult to develop algorithms with optimality guarantees. As a consequence, the bias, which is very likely to exist when BCANw and SBw is used, can hardly be identified hence leading us to unreliable conclusions about the target networks and the urgent need for reliable numerical estimation approaches. As a case study, Fig. 7 already showed the advantage of the proposed algorithms in estimating the fractal dimension

of $G_5$. In what follows, we present a more comprehensive set of comparative analysis on the proposed FBCw and FSBw against BCANw and SBw.

## *FBCw and FSBw for weighted complex network of finite resolution*

To further validate the proposed FBCw and FSBw based on the known ground truth about the fractality of the target network, we consider the Sierpinski fractal family with ranged variations in the size of the graph and the skewness of link weight distribution. Formally, the skewness of the distribution is a measure of the *asymmetry* of the probability distribution of a real-valued random variable about its mean. We introduce the Pearson's moment coefficient of skewness $\gamma$ as the measure of the asymmetry in link weight distributions as follows:

$$\gamma = \frac{E[(X-\mu)^3]}{E[(X-\mu)^2]^{3/2}} = \frac{\kappa_3}{\kappa_2^{3/2}} \tag{2}$$

$\kappa_t$ are the $t$-thcumulants. The probability distribution with positive skewness usually has a longer right tail or the mass of the distribution is concentrated on the left of the distribution.

We extensively measured the skewness of link weight distribution of the $G_5$ and $G_8$ under different copy factor ($b=2$ to 8) and scaling factor $s$ ranging from 0.95 to $4.5\times10^{-4}$. We report the results in Fig. 8. We can observe that: i) the skewness of the link weight distribution of Sierpinski fractal network increases as the scaling factor decreases and the size of the network grows. Figure 8(a) shows the skewness of link weight distribution of $G_5$. The smaller scaling factor leads to a less asymmetric distribution. The large copy factor further amplifies this skewness by placing more mass on the left side of distribution (i.e., links with small weights). Similarly, Fig. 8(b) shows a significantly increased skewness in large networks compared to Fig. 8(a). (ii) The skewness of link weight distribution does not increase linearly as the scaling factor decreases. A *transition phenomenon* can be observed as the scaling factor decreases. The skewness grows much slower at large $s$ and seems insensitive to the change of copy factors. This observation suggests some potential underlying *phase transition* of the Sierpinski fractal networks as scaling factor decreases. We show a case study in Supplementary Material Section 3 by associating the scaling factor to the free energy of a multi-fractal and study its first-order discontinuity. We

observe that there exists a critical scaling factor $s$ that describes a transition from a mono-fractal phase to a multi-fractal phase (when considering networks of limited size) of Sierpinski fractal network. (iii) For the same copy factor, the skewness of the link weight distribution tends to converge as the scaling factor decreases. The copy factor $b$ dominantly influences the skewness of the link distribution when the scaling factor is small.

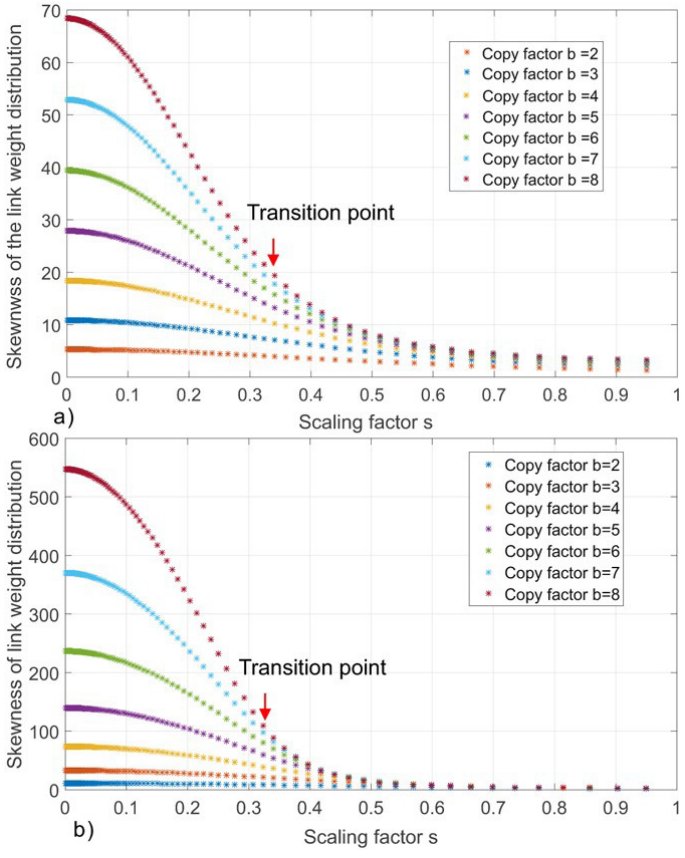


**Figure 8**: Skewness of link weight distribution of Sierpinski fractal network. (a) The skewness of link weight distribution of $G_5$ as function of scaling factor $s$ and copy factor $b=2, 3, 4, 5, 6, 7, 8$. (b) The skewness of link weight distribution of $G_7$ as function of scaling factor $s$ and copy factor $b=2, 3, 4, 5, 6, 7, 8$.

Figure 8 also shows that the skewness of the link distribution of Sierpinski fractal network is affected by the size of the graph, copy factor $b$ and scaling factor $s$. In order to understand how this skewness has impact on the numerical

determination of the multi-fractality and compare our proposed FBCw and FSBw with BCANw and SBw, we present two comparative experiments. In the first experiment, we consider a set of Sierpinski family members ranging from $G_3$ (39 nodes) to $G_8$ (9840 nodes) given the fixed copy factor $b=3$ and scaling factor $s=1/2$. The estimated fractal dimensions are reported in Fig. 9 for BCANw (blue line), SBw (orange line), FBCw (yellow line) and FSBw (magenta line), respectively. For comparison purpose, we also show the theoretical dominant fractal dimension of the target networks with the dashed line. Based on the results in Fig. 9, we can make the following observations:

(i) The proposed FBCw and FSBw are *less sensitive* to the size of target graph compared to BCANw and SBw. The normalized estimation errors of FBCw and FSBw performed on $G_3$ with only 39 nodes are 5.24% (averaged estimated fractal dimension = 1.50) and 6.56% (averaged estimated fractal dimension = 1.48), respectively. In contrast, the estimation errors of BCANw and SBw are 25.6% (1.18) and 22.4% (1.23), respectively. This property of the proposed FBCw and FSBw is very important in practice when used as the basis of multi-fractality analysis on real networks for which we have neither ground truth to reason about the estimation error nor scaling methods to improve the accuracy. It is critical to have algorithms that have no strict constraint on the target network and deliver reliable estimates in various settings.

(ii) As the graph size grows, the accuracy of all four algorithms is improved as a consequence of more observations obtained to perform the linear regression. This is aligned with Eqs (13) and (17) in that the numerical calculation of the limit in both equations is asymptotically equal to the theoretical value given the linear regression performed on a network member $G_\infty$ of the Sierpinski fractal network with unbounded size. However, it should be also noted that the BCANw and SBw still suffer from significant estimation errors compared to the theoretical value in spite of a large-scale target network (e.g., $G_8$). Combined with Fig. 8, one primary influencing factor is the increased skewness of link weight distribution of a larger network that will worsen the performance of box-covering and sandbox algorithms with no compatible growth rule. In contrast, FBCw and FSBw quickly converge to the theoretical value with very small errors.

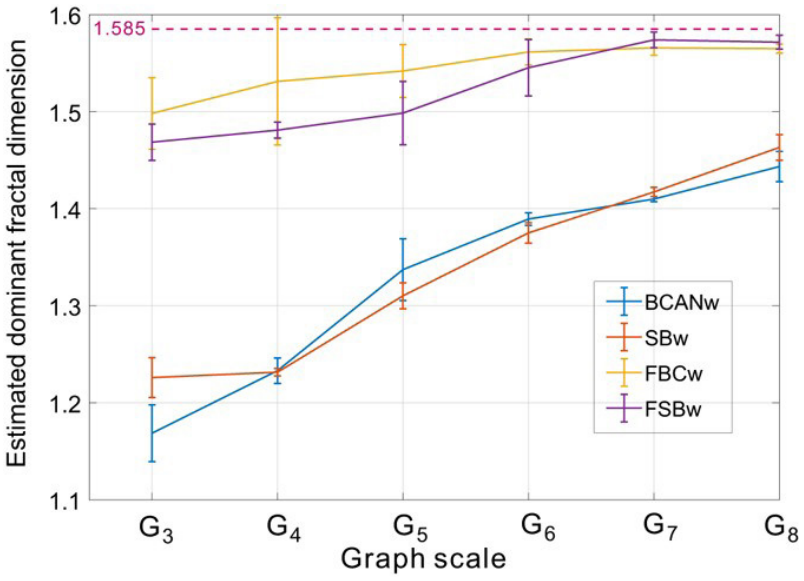


**Figure 9**: Estimated dominant fractal dimension of Sierpinski fractal network family ($G_3$ to $G_8$ with $b=3$ and $s=1/2$) using BCANw, SBw, FBCw and FSBw. As predicted by Eqs (13) and (17), the estimation accuracy is improved as the numerical calculation of the limit by the linear regression is performed over a growing set of observations. However, the increased skewness of link weight distribution prevents BCANw and SBw from approaching the theoretical value as quickly as the proposed FBCw and FSBw do.

To further corroborate our discussion on the adverse impact of skewed link weight distribution on the accuracy of BCANw and SBw, we present the second set of experiments. The experimental setup is motivated by the observation we made in Fig. 8 that the skewness of link weight distribution is dominantly affected by the copy factor $b$. Therefore, we choose a member network from the Sierpinski fractal network family as the seed network. We adopt different values for the copy factor $b$ with a fixed scaling factor $s=1/3$ to generate an array of fractal networks. Then BCANw, SBw and the proposed FBCw and FSBw are employed to estimate the dominant fractal dimensions of all generated networks. Due to the constraint of the computing power, we choose $G_5$ as seed network and the copy factor ranges from 2 (62 nodes) to 8 (37448 nodes). We report in Fig. 10 the normalized estimation error against the corresponding skewness of the distribution $\gamma$ for BCANw (blue line), SBw (orange line), FBCw (yellow line) and FSBw (magenta line),

respectively. Figure 10 can be interpreted as follows. First, by increasing the copy factor one can notice a further skewed link weight distribution. As a result, the estimation accuracy of BCANw and SBw degrades accordingly. The normalized estimation error of BCANw grows from 6.79% ($\gamma$=4.0103, $b$=2) to 15.92% ($\gamma$=20.2235, $b$=8). Similarly, the degradation of estimation accuracy of SBw is worse than BCANw. The error increases from 10.01% to 17.2%. Second, the performance of FBCw and FSBw is not adversely impacted by the increased $\gamma$. Interestingly, the accuracy is improved as the copy factor increases. This improvement is discussed in our first set of experiments as a result of larger set of observations obtained for more reliable calculation of limit in Eqs (13) and (17).

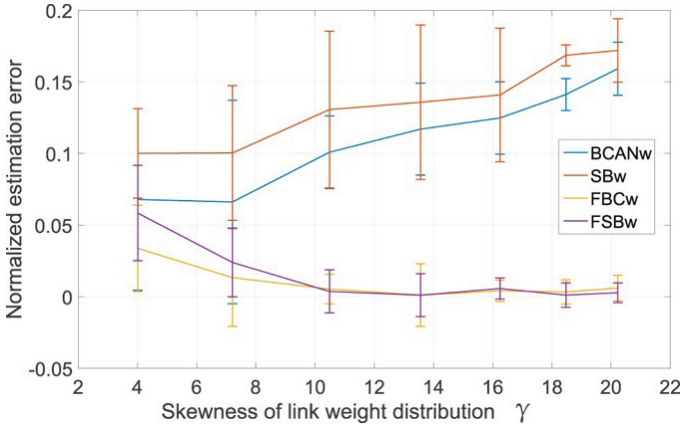


**Figure 10**: Normalized estimation error of BCANw, SBw, FBCw and FSBw under different skewness $\gamma$ of link weight distribution by changing the copy factor $b$ of $G_5$ from 2 to 8. (i) The performance of BCANw and SBw degrade as the $\gamma$ grows. (ii) BCANw and SBw tend to underestimate the dominant fractal dimension which is aligned with our theoretical prediction in analysis of the staircase effect. (iii) The proposed FBCw and FSBw tends to be insensitive to the change of $\gamma$ and benefit from the increased size of the target network.

It is very important to note that both BCANw and SBw *underestimate* the dominant fractal dimension, which is predicted by our analytical findings in estimation errors analysis section. The incompatible growth rule of BCANw and SBw gives rise to the larger set of stagnant observations (i.e., wider staircase) when the skewness is positively higher. A network with higher positive skewness of link weight distribution has more links with smaller weights. SBw grows the sandbox by accumulating the link weights in an ascending order. In presence of highly (and positively)

skewed link weight distribution, it might take a large amount of iterations to grow from $l_i$ to $l_{i'}$ such that the probability measure $\mu(B_i(l_i))$ is not equal to $\mu(B_i(l_{i'}))$. All the observations generated between $l_i$ and $l_{i'}$ become stagnant observations or staircases. The more positively skewed the distribution is, the wider the staircases will be and SBw is more likely to underestimate fractal dimension of the network, which is well aligned with our observations in Fig. 10. For the similar reason, even though BCANw grows the box size by accumulating the unique distance in an ascending order, yet we have seen in Fig. 5 that BCANwcan not eliminate the staircase effect thus it is prone to underestimate the fractal dimensions as the network becomes more skewed in terms of the link weight distribution.

We have validated the proposed FBCw and FSBw by showing we can obtain fractality estimation of better accuracy over the established BCANw and SBw for the weighted complex networks. In the following discussion, we will employ the proposed FSBw and FBCw for numerical identification of multi-fractality in a set of real-world complex networks.

## Multi-fractal Analysis of Real Networks

### *Vision and objectives of the multi-fractal analysis*

Multi-fractality is deeply rooted in the intrinsic heterogeneity of the networks. More specifically, the non-uniformness of the network structure serves as a major source for a spectrum of distinct self-similarities embedded in different regions of the network at a variety of scales. This embedded heterogeneous self-similarities can be identified through the multi-fractal analysis. Intuitively, multi-fractal analysis can be understood as a microscope with an array of distorting filters that pick up a set of distinct scaling behaviors from corresponding parts of the network by changing the distortion factor $q$. A perfect geometric or topological fractal (e.g., fractal networks) shares the same scaling behavior (i.e., the dominant fractal dimension) that is immune to the changes of $q$, suggesting a consistent self-similarity across the network. Such geometric or topological consistency in self-similarity is usually a result of a common underlying growing rule throughout the scales of the network considered (e.g., Sierpinski fractal network). However, such well-preserved growth rule is rarely found (e.g., non-fractal networks) or inconsistent (e.g., coexistence of small-world and fractal properties with phase transitions) in the real-world networks due to the complicated network formation process. This generation process cradles for the intrinsic

heterogeneity in both the structural (e.g., network clusters, communities, hubs) and dynamical (e.g., network control, robustness) aspects of the real-world networks. In the following discussion, we will focus on the structural aspects of a set of weighted real-world networks to answer the following three key research questions:

(i) Whether the multi-fractal scaling behaviors can be observed in the target network and how can they be exploited for betterment of our understanding on the structural properties of real networks?

(ii) What is the contribution of link weight to such scaling behaviors if verified in (i) and how will the change of link weight fundamentally impact the observed multi-fractality?

(iii) How can the identification of the multi-fractality be leveraged to supplement our characterization of the real-world complex networks and provide a novel perspective and a practical probe for unveiling their under-explored structural organization?

To study these questions, we choose two weighted real-world networks. The first weighted network is a scientific collaboration network in astrophysics with 16705 nodes and 111252 edges. Each node represents an author and an edge connects two nodes if they published one or more papers together. The weight between any pair of nodes is determined by,

$$w_{i,j} = \sum_k \frac{\delta_{i,k}\delta_{j,k}}{n_k} \tag{3}$$

$n_k$ is the number of authors of $k$-th paper. $\delta_{i,k} = 1$ only if author $i$ co-authored the $k$-th paper and it is 0 otherwise. The weight quantifies how frequently and closely two authors collaborate. The second weighted network comes from the Budapest Reference Connectome v3.0 which generates the common edges of the connectomes of 1015 vertices, computed from the MRI of the 477 subjects of the Human Connectome Project's 500-subject release. For each edge $e_{i,j}$, the weight $w_{i,j}$ is based on the electrical connectivity of two nodes and calculated by the number of fibers $n$ divided by the average fiber length $l$.

### *Space-localized multi-fractal scaling*

To address the three major research questions, we consider three sets of experiments. In the first set of experiments, we study whether the target weighted networks in two different domains show any fractal or multi-fractal scaling behaviors. Towards this goal, we applied the proposed FBCw to both networks in order to learn the scaling dependence as expected by Eq. (13) when the distorting factor $q$ is varied within a finite range from $-10$ to 10 with a step length of 0.1. A key observation on Eq. (13) is that the role of the distorting factor $q$ connects primarily to the identification of the non-uniformness of the probability measure $\mu(B)$ defined on the support of the weighted networks. Such non-uniformness of the measure and their distinct scaling dependence over the interested scales $l$ arbitrates the existence and properties of the multi-fractality in the target network. If the measure $\mu(B)$ is otherwise uniform at all scales, Eq. (13) will not be affected by the choice of $q$, hence learning only the mono-fractality of the support.

Motivated by such observations, we first look at the weighted collaboration network and report in Fig. 11 the distribution of the measure $\mu(B(l))$ over the partitions (i.e., boxes) of different scales (i.e., size of the box) to give an undistorted overview of the non-uniformness of the measure. Several key observations are due: i) the distribution of the measure $\mu(B(l))$ changes from a near-uniform distribution to a peak shape as the scale increases. Alternatively stated, the probability to find any node in a given box at a specific scale $l$ is also a function of the choice of that box. At almost each scale, there exists a partition that contains the dominant number of nodes. This scaling skewness of the measure strongly suggests the structural heterogeneity of the target network and serves as a necessary condition for the emergence of multi-fractality. ii) The rightmost X-axis boundary of the measure distribution marks the minimal number of partitions of scale $l$ required to cover the target network. By learning the shrinking law of these boundaries, we can have a straightforward way to verify the existence of fractal scaling behavior. More precisely, we can notice that the rightmost boundaries of the measure do not shrink as quickly as an exponential function but following a power law (which is much slower as indicated in Fig. 11). The corroboration of these two observations demonstrates the existence of multi-fractal behavior in the collaboration network.

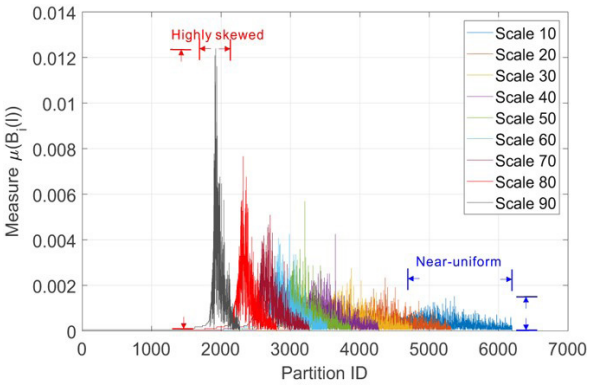


**Figure 11**: Distribution of probability measure as a function of scale of multi-fractal analysis on collaboration network.

To further investigate the mulitfractality of the collaboration network, we performed the follow-up experiment to report the scaling dependence between $\sum \mu(B)^q$ against the normalized box size $l/L$ in a $log-log$ plot under different distorting factors $q$. For ease of visualization and readability, we construct the plots by choosing only the cases when $q$ is integer-valued. The results are plotted in Fig. 12. We can observe that the logarithmic distorted accumulative measure $log(\sum \mu(B)^q)$ has a linear dependence that is almost *immune* to the changes of negative $q$ on the normalized scale $log(l/L)$, suggesting a mono-fractal scaling behavior. However, such linear dependence still holds and is subject to remarkable changes as a function of positive $q$, which is an indicator of the existence of multi-fractality. To understand this, we need to link this observation with Eq. (13). Negative distorting factor $q$ places greater weights to the partitions with smaller measures whereas does the opposite when positively valued. In other words, we are able to learn distinct scaling dependence of different regions of the measure distribution, which again correspond to different parts of the target network. In our case when $q$ is positively valued, the observed multi-fractal scaling dependence corresponds to the partitions of the collaboration network with dominant probability measures. In contrast, the mono-fractal scaling behavior is strongly related to partitions with small probability measures. The two sets of distinct scaling behaviors not only verify the multi-fractal scaling dependence of target network but also suggest a *co-existence* of multi-fractality and mono-fractality in the same network while belonging to different parts of the network. To understand this, we need to look at how the partition is done to tile the target network with box-covering method.

Eq. (13) holds only if the covering is optimal (i.e., with minimal number of boxes, see Definition 5). To achieve this, each box has to be as compact as possible such that it covers the maximal possible number of nodes in a connected component. Such connected components might coincide with regions of the network that are highly clustered such that their scaling follows power-laws characterized by different exponents, hence exhibiting multi-fractal behaviors. In contrast, the non-compact box covers nodes that failed to be reached by nodes in these connected components and demonstrate a shared mono-fractal scaling. In other words, it is the intrinsic variations of the network structure that contribute to the observed co-existence of distinct scaling dependence such that the observed multi-fractal scaling dependence is *space-localized*.

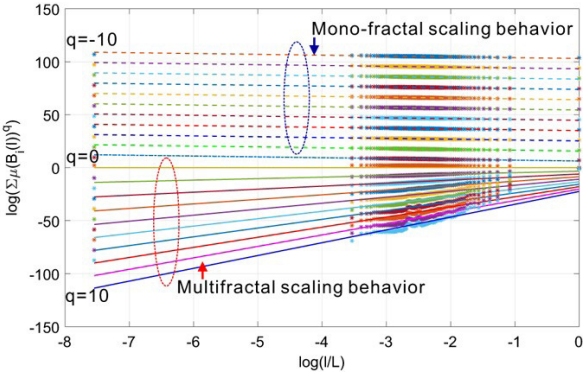


**Figure 12**: Coexistence of multi-fractal and mono-fractal scaling in the collaboration network.

The exact mathematical explanation for the coexistence of mono-fractality and multi-fractality calls for a more sophisticated understanding of the underlying network formation mechanism, which is beyond the scope of this work and remains as a future extension.

## *Scale-localized inconsistent multi-fractality of weighted real networks*

We not only observed the inconsistency of scaling behaviors in different regions of the network, but also we noticed that such scaling is not consistent over the interested scales even when the network exhibits same type of scaling (mono-fractal or multi-fractal) with a fixed $q$. More specifically, we observed the existence of a finite range of scales at which a *localized* scaling behavior holds. To better illustrate this, we have specifically picked cases

when $q = -6$, 0, and 6 and reported the scaling dependence in a $log - log$ plot for each of them. The results are shown in Fig. 13. We use the dashed blue lines to show the range of scales where the fractal scaling appears and the red dashed lines to show outliners. Consequently, we can make the following two observations: (**i**) Fig. 13(a–c) consistently show that the self-similar property does not hold at *all scales* of networks and it might only show up in a finite range of scales. Phase-transition behavior can be observed on boundaries of this range. Moreover, such phase transition phenomenon also holds under a variety of distorting factor $q$. In other words, the multi-fractality of the collaboration network is *scale-localized*. This finding resonates with our claims at the beginning of this section that there is *no* common underlying growth rule for the generation of real networks to produce simple self-repeating structures at all scales of the real networks. As we observed in Figs 12 and 13, the self-similarity is neither spatially consistent across the network nor well-preserved at all scales of the network. (**ii**) In such cases, it is *not* sufficient to have an algorithm that can reliably estimate the scaling dependence *when it exists*. It is also primarily important for the algorithm to *detect* the boundary of scales between which such scaling dependence holds and make a *localized* estimation accordingly. We argue that BCANw ignored such localized fractal scaling by the implicit assumption that *scaling behavior holds at all scales of the complex network*. In contrast, our proposed FBCw is able to locate the phase-transitional scales based on which a reliable estimate is therefore made. To demonstrate this, we performed the BCANw and FBCw on the same network under identical experimental settings. We plotted the fitted linear functions by two algorithms in Fig. 13(a–c). Biased by the implicit assumption that fractal scaling holds at all scales, BCANw tends to average the estimates by considering all the observations, irrespective of their contribution to the fractal scaling behaviors. In comparison, the proposed FBCw detected the locality of multi-fractality and ignored the outliners in the observations not belonging to the range where fractal scaling holds and fit a linear function only to those within it. The difference between the two fitted lines shows the estimation bias of BCANw by assuming a fractal scaling held at all scales.

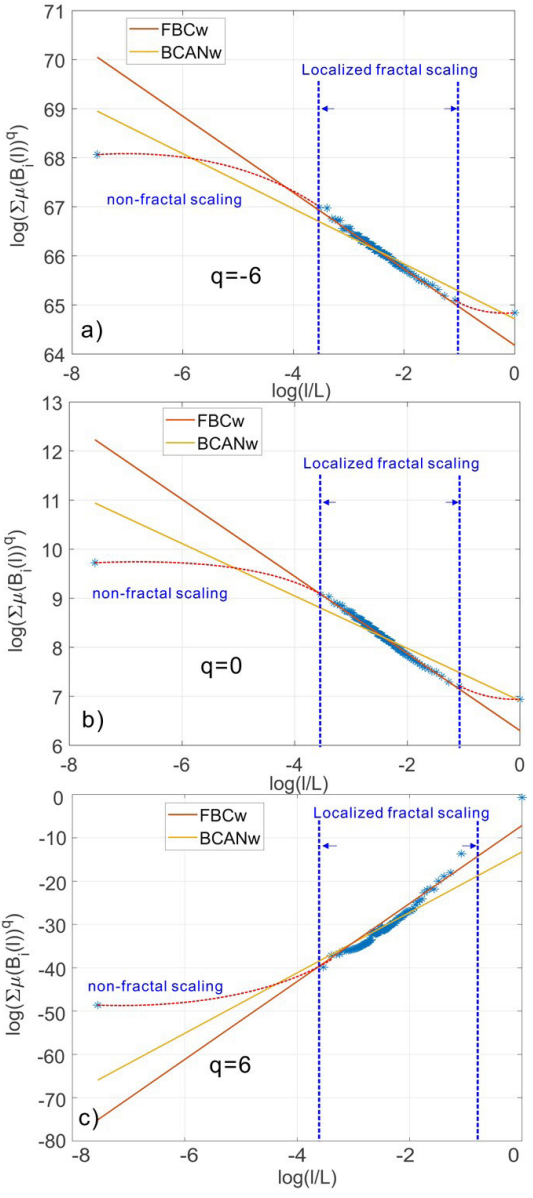


**Figure 13**: The failure of BCANw to capture the localized fractal scaling of collaboration network over a *finite* range of network scales. In the case of real world networks, the self-similar property does not holds at all scales of networks. There might exist a finite range of scales where fractal scaling behavior dominates. Moreover, this phase transition phenomenon consistently holds under all distorting factor $q$, suggesting a *localized* multi-fractality.

We have repeated the above experiments on the Budapest human connectome network and report the results in Figs 14 and 15. Figure 14 depicts the uniform distribution of probability measure of partitions for the Budapest brain network. Similar to our observations on the collaboration network, the distribution of measure shifts from a near-uniform distribution to a peak shaped non-uniform distribution, suggesting the underlying structural heterogeneity of the brain network, which serves as the major source of multi-fractality. By learning the shrinking behavior of the rightmost boundary of the measure distribution as the size of the box increases, one can observe a power-law dependence which is verified by the subfigure in Fig. 14 where we plot the scaling dependence between the accumulative measure $\sum \mu(B)^q$ and the normalized scale $l/L$ in a $log-log$ scale. Figure 14 is well aligned with our findings in the collaboration network. Budapest brain network also exhibits a *localized* fractal scaling over the ranged delimited by a pair of dashed blue lines, suggesting an inconsistent power-law scaling behavior valid only over a finite range of scales. The fractal organization of brain network is well reported in the related literature. However, few prior efforts have identified the localized fractal scaling given a weighted brain network. To study the multi-fractality of the Budapest brain network, we performed the multi-fractal analysis on it and reported the scaling dependence under different choice of distorting factor $q$ in Fig. 15. We can identify the similar co-existence of mono-fractal and multi-fractal scaling as we did in collaboration network. The network regions that correspond to the partition with small measure follow dominantly a near-invariant power-law scaling dependence on the scale of the box. In contrast, the collections of densely connected nodes (e.g., connected components) compactly covered by the box shows a varying power-law dependence as $q$ positively changes. However, a major distinction from the collaboration network is the range of scales where such power-law holds. As one can notice, there exists a scale around $-1$ depicted by the grey dashed line such that the fractal scaling is not respected any more. No linear function could accurately explain the scaling dependence after this scale. This is aligned with our finding in Fig. 14, suggesting a scale-localized fractal scaling behavior that is not globally consistent.

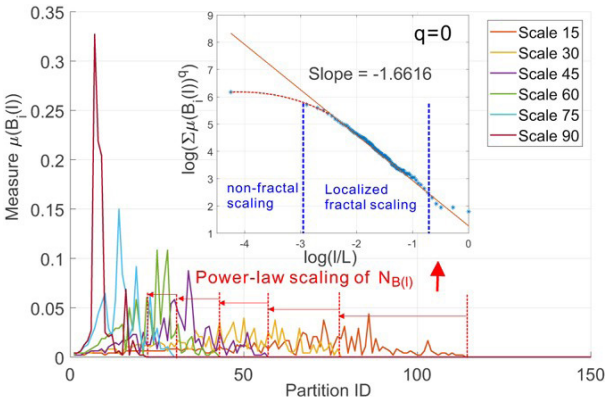


**Figure 14**: Distribution of probability measure as a function of scale of multi-fractal analysis on Budapest connectome network.

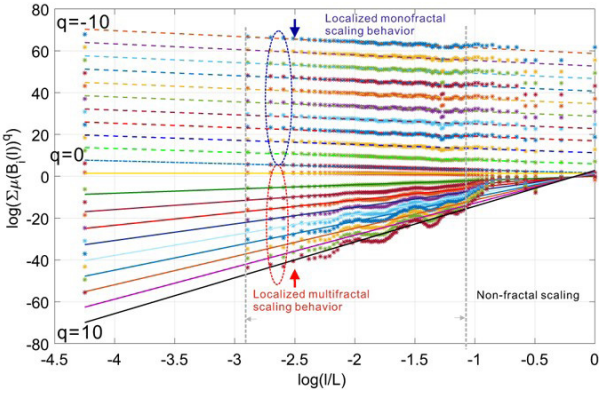


**Figure 15**: Coexistence of localized multi-fractal and mono-fractal scaling in the Budapest connectome network.

## *Link weight to dictate the mulifractality*

In the second set of experiments, we investigate how the link weights could fundamentally influence the underlying multi-fractality in both networks. Towards this end, we transformed both networks into binary (i.e., unweighted) networks by removing the link weight between any pair of connected nodes. From the geometrical perspective, the link weights on the graph perform a scale transformation to the graph by increasing or decreasing the length of the links when spatially embedded while keeping its topological feature intact. By removing the link weights, we are studying existence of the

multi-fractality from a pure topological perspective to understand the role of link weights via comparative analysis. More specifically, we measured the distribution of the probability measure and studied the scaling dependence between minimal number of boxes covering the network and the scale of the box. Figures 16 and 17 summarize the results for collaboration network and Budapest brain network, respectively. Thus, we make the following observations: i) The distribution of probability measure follows a similar changing pattern as the scale of box changes, i.e., from a near-uniform shape to a highly non-uniform shape. This is well aligned with our claims that such non-uniformness is a reflection of structural heterogeneity determined majorly by the topology of the network, which stays intact during our transformation. ii) However, the scaling dependence is fundamentally changed and we observed a total loss of fractal scaling behavior. Instead, the scaling can be well explained by an exponential law, indicating that both the collaboration network and the brain network behave as the well-known *small-world* networks. Compared with their weighted versions, the role of link weight is powerful in dictating the existence of multi-fractality in real networks. Consequently, this finding not only calls for developing new algorithms for estimating reliably the multi-fractal characteristics of weighted complex networks, but also highlights the importance of understanding the structural implications of the identified multi-fractality. This brings us to the following discussion on the third research question of this work.

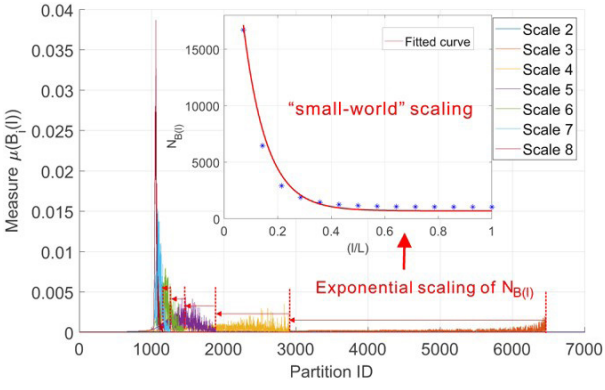


**Figure 16**: The fundamental impact of link weights on the multi-fractality of network. We keep the exactly same structure of the collaboration network but remove all its weights to transform the network into a binary network. We performed the proposed box-covering method to measure the scaling dependence of number of boxes and the distribution of their associated measure. Figure

shows the *loss* of multi-fractality as a result of removal of link weights. Instead, we notice it the scaling dependence is best explained by an exponential law ($a * exp(bx)$, $a = 3.75 * 10^4$, $b = -11.55$) suggesting the unweighted collaboration network becomes a "small-world" network.

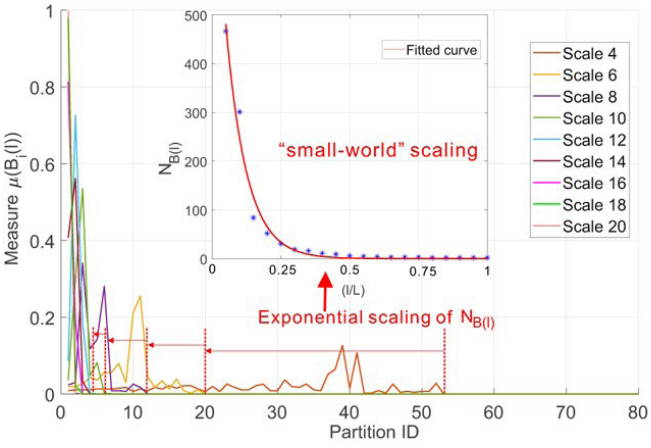


**Figure 17**: The fundamental impact of link weights on the multi-fractality of Budapest connectome network. Figure shows the similar loss of multi-fractality by removing the weights on the links of Budapest connectome. The scaling behavior is best explained by an exponential law ($a * exp(bx)$, $a = 934.7$, $b = -0.664$) indicating that the common brain connectome is a "small-world" if no weights are considered.

## *Localized scaling based network characterization and community detection*

In the third set of experiments, we study how the multi-fractal analysis framework can be employed to characterize the complexity of networks beyond simply reporting whether they follow a multi-fractal/fractal scaling as many previous works did. We use the multi-scale analysis to quantify the global complexity of the network from a microscopic point of view. Based on the analysis, we proposed a general network characterization framework based on the localized scaling feature space constructed by learning the localized scaling feature vector for each node.

We noticed in the first two sets of experiments that a real world network is *complex* in the sense that there exists no common growth rule that governs the evolution of the network generation process consistently in both the scale and space domain. Similar to our two target examples when certain variation

or transformation introduced into the network, the fundamental structural behaviors of the network are subject to remarkable mutations. No single model or characterization is sufficient to fully understand the structural variations and their resulting complexity of the network, hence calling for a set of expressive characterizing strategies that supplement each other to give an unbiased and well-quantified overview of the complex networks. We strongly believe that multi-fractal analysis is a powerful framework to learn the localized scaling behavior and quantify the structural variations of the complex networks.

On one hand, at the microscopic level, the complexity of the network is embedded in the form of different *chemical environments* (i.e., the outer environment surrounding a given node) that each node interacts at *different scales*. More intuitively, the structural variations of the network can be understood as distinct views that a node observes with a lens of variable focal length ranging from the minimal path distance of the network up to its diameter. If all the nodes share the identical viewing experiences with such lens, then the network should have no structural variations like an unweighted lattice which can be fully characterized by its dimension. Otherwise, such microscopic differences in views at a variety of scales, when integrated collectively, translate into the observed structural variations from a global perspective that require multifaceted characterizations.

On the other hand, multi-fractal analysis framework is exactly one of such multi-scale techniques to study and quantify the microscopic proxy of network complexity in terms of structural variations. From the mathematical point of view, Eqs (13) and (17) suggest the structural variations (i.e., structural heterogeneity and link weight distribution) of the networks are the major contributor of the observed scaling behaviors in the complex networks. These variations are distributed in an inhomogeneous way and repeat locally and imperfectly (i.e., space-localized) within a finite range of scales (i.e., scale-localized). Reversely, multi-fractal analysis also provides a way to characterize such structural variation by identifying and quantifying the scaling behaviors (again, not necessarily fractal and/or multi-fractal). More specifically, the proposed SBw method for the weighted complex network is one of such quantifying tools which are able to measure the microscopic differences of the chemical environments for a given node at varied scales by learning its *localized scaling dependence* from where it is located.

This underlying connection between the multi-fractal analysis and the microscopic view of the network complexity leads us to the straightforward

implementation of our proposed localized scaling based network characterization approach. More precisely, we start with a given node $k$ of the network and perform the SBw centered at it with $q=0$ to learn the scaling dependence it experiences as we increase the scale $l$ of the sandbox up to the network diameter $L$. This results in a localized scaling feature vector of tuples $\mathscr{S}_k = [s_{k,1}^{\mathrm{T}}, s_{k,2}^{\mathrm{T}}, \ldots, s_{k,n}^{\mathrm{T}}]^{\mathrm{T}}$, where $s_{k,i} = (logN_k(B(l_i)), log(l_i/L))$. $\mathscr{S}_k$ is populated by the sampled logarithmic scaling dependence between the normalized box scale $l/L$ and the number of nodes covered by the sandbox centered at $k$, hence *localized*. We repeat the process for every node of the network to construct a localized scaling feature space $\mathscr{S}(G) = \{\mathscr{S}_k | k \in \mathcal{N}\}$ for the given network $G$. The localized scaling feature space $\mathscr{S}(G)$ is uniquely spanned by the localized scaling feature vectors of different network nodes. Its structure and properties are determined by the original network. Therefore, $\mathscr{S}(G)$ can be leveraged to characterize the network from a scaling dependence perspective. To the best of our knowledge, this is the first time that the localized scaling behavior of network is proposed as a quantitative profiling approach to characterize the structural characteristics of the complex network.

An immediate application of this profiling approach is an easy integration with unsupervised machine learning algorithms to perform label-free detection of the network communities. The basic assumption is that the nodes sharing the same or similar scaling dependence localized to where they stand in the network should reside in similar chemical environments therefore belonging to the same network community. As a proof of concept, we performed the simple yet effective unsupervised $k$-means clustering algorithm with elbow method for network community detection on the Budapest human connectome and visualized the result in Fig. 18. This community detection approach identifies seven communities (colored differently in Fig. 18). The detection process is totally label-free with no prior knowledge of the functionality and locations of brain components and solely based on localized scaling feature vector of each node. Several key observations are due: i) brain network is symmetric so are the communities detected by the proposed approach, which is aligned with anatomical structure of human brain. ii) The dominant community (purple nodes) detected corresponds to the densely interconnected brain functional cluster formed by left and right Putamen, left and right Caudate, left and right Thalamus together with left and right Hippocampus. This community is consistent with the biological facts. The Putamen and Caudate are anatomically correlated

to form the basal ganglia which is well known to be strongly interconnected with the cerebral cortex, thalamus, and brainstem to perform the control of voluntary motor movements and procedural learning. Thalamus is also manifoldly connected to the Hippocampus via the mammillo-thalamic tract and serves as an important relay station to propagate the sensory and motor signals to the cerebral cortex. This detected community serves as the major bridge between the two hemispheres and connectivity hubs to other functional entities thus sharing the similar chemical environment. iii) It can be noticed that the nodes belonging to the same community might not be necessarily immediate neighbors in contrast to the conventional modularity based communities. This is because the nodes are clustered based on their scaling dependence which is determined by the surrounding chemical environment at different scales. Therefore, it is possible that two nodes that are physically separated share the similar chemical environment to be labeled in the same community. For brain network, such chemical environment is a consequence of biological network evolution process and might have important functional implications that need to be explored in the future. In this sense, the concept of network community has been extended to characterize the node of the network from its relative spatial relation to the rest of the network. We hope the proposed localized scaling based network characterization and community detection can introduce a new research perspective for betterment of our understanding of the real world complex network in different domains.

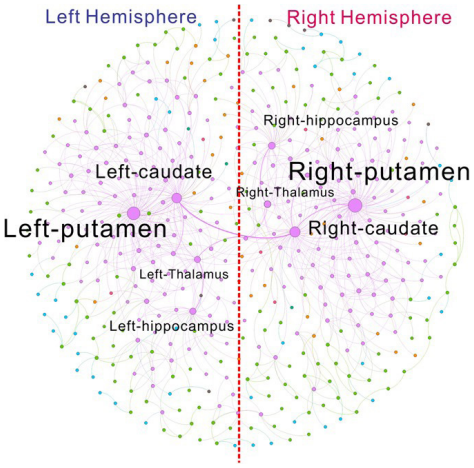


**Figure 18**: An example application of the proposed localized scaling feature space for characterization of weighted complex network. Interfaced with the

unsupervised machine learning based clustering algorithm, the localized scaling based community detection is able to identify the brain network communities consistent with the anatomical facts. The detected communities are not limited to neighboring nodes but based on their relative spatial relations to the rest of network with potential functional implications.

## DISCUSSION

The multi-fractal analysis has been long established to describe physical phenomena and objects by studying statistical scaling laws. The major attraction of its application stems from its capability to characterize the spatial and temporal irregularities that euclidean geometry fails to capture in real world physical systems, by an elegant interpretation of power-law behaviors. Its demonstrated effectiveness in characterizing complex systems motivates us to extend its formalism to the analysis of complex networks. However, the multi-fractality of weighted complex networks, the role of interaction intensity, influence of the underlying metric spaces and the design of reliable multi-fractality estimation algorithms are rarely discussed and remain an open challenge.

In this paper, we provide strong theoretical and experimental evidence for the intrinsic estimation bias of the previously proposed algorithms introduced by the incompatible growth of box scales and the implicit assumption that fractal scaling behaviors, if exist, hold at all scales of the networks. To overcome these disadvantages, we proposed two algorithms that can reliably estimate the multi-fractality of the network based on the critical points that correspond to a power-law scaling such that (i) it avoids box scales that lead to stagnant probability measures (i.e., staircase effect) and (ii) identifies the range of scales where a power-law scaling holds. In addition, we demonstrated that the estimation bias of the previously proposed algorithms deteriorates as a function of link weight distribution skewness and can not be compensated by either repeating the experiments or increasing the size of the networks (irrespective of the fact that it is practically difficult to scale the real world networks without changing its properties). More importantly, our work showed that the estimation can hardly be trusted if it assumes the existence of a scaling law that rules the network formation process throughout the scales. We provide real world weighted network examples where the observed distribution of scaling behaviors is localized in both space (e.g., co-existence of mono- and multi-

fractal scaling dependency) and scales (e.g., power-law scaling valid over a finite range of scales).

Localized scaling behaviors reflect the fact that the network formation process of these networks is neither governed by a self-repeating iteration function system (IFS) that produces simple mono-fractal networks (e.g., Sierpinski fractal networks) nor a distribution of these IFSs throughout the scales of the network, which leads to a multi-fractal scaling behavior described by Eqs (13) and (17). Moreover, the formation of real world complex networks corresponding to different scales are constructed at different time points during the network formation process. The discontinuity of a power-law scaling at different scales therefore suggests that the network formation process is *dynamic* governed by *heterogeneous* forces as opposed to *stationary* models where either a fixed linking probability is assumed throughout the process (e.g., random graph theory) or a static linking policy (e.g., preferential attachment) is governing.

Furthermore, the network formation process and the resulting heterogeneous characteristics of real world networks also can not be fully explained from a pure structural and topological perspective. It is necessary to understand the role of the interaction intensity among the network components, the associated weight assignment process over time (e.g., how the weights change over time) and the metric space implicitly implied by the nature of these interactions (e.g., affinity relations, physical connectivities, causal dependences). We corroborate our argument with strong supporting evidence. More precisely, we identified both theoretically and experimentally two fundamental fractality transition phases that are governed by the intensity of network interactions (i.e., weights) and the embedded metric space defined on these networks:

(i) The scaling of the weights in a network formation process governed by an IFS determines the fractality of the network at a given scale. We reported the theoretical upper bound for the scaling factor $s$ that transforms the network into a mono-fractal network given a) an IFS that leads to a family of Sierpinski fractal networks of unbounded size and b) the box size of an optimal covering method can shrink at same rate as the network grows. We argue that the observed multi-fractality of Sierpinski fractal networks by prior works does not necessarily come from a distribution of fractal scaling behaviors (i.e., multi-fractality) but can result from any deviation from these conditions (e.g., limited

size and network growth rate). As a simple synthetic fractal network as the Sierpinski fractal network is, the weights and their distribution exhibit surprisingly powerful impact on the fractality of the networks. In a set of more realistic experiments, we further showed:

(ii) The weights and the metric space defined on real world networks arbitrate the existence of the fractality. By converting the collaboration network and the human brain connectome into binary networks, we decoupled the metric spaces defined on both networks from the link weights and transformed them to be a function of network topology alone. We demonstrated the removal of observed localized fractal scaling behaviors and an exponential scaling law (i.e., small-world property) takes place after the transformation of both networks. While keeping the topological configuration intact, the redefinition of metric space fundamentally altered the statistical scaling law of both networks.

This observation is not only important for the betterment of our understanding of the formation process of the real networks as the scaling behaviors reveal how the network grows. It is also a primary key to the network dynamics as the scaling behavior of the network plays a key role in governing the flows of the information across the network such as the rumor spreading in social networks or the protein exchange in a gene regulatory network. In these real world networks, the interaction intensity usually changes at a much more frequent pace compared to the changing rate of the network topology. For instance, a traffic network might stay structurally unchanged for a quite long time however the traffic volume (i.e., interaction intensity or weight) over its links varies constantly and fiercely. Given the fundamental role of link weights and metric space in determination of the scaling law, the time-varying network interactions can consequently impact the dynamics of the network. As a result, the failure to recognize the importance of link weight and metric space analysis will intrinsically limit our capability to characterize, predict and control the network behaviors.

Moreover, the variations of network scaling behaviors closely connect to the change of network properties, which leads us to solve a reverse research problem to characterize and quantify the heterogeneity of weighted complex networks by learning the scaling variations from a microscopic perspective of the network. We provide a general network characterization framework motivated by the observed locality and phase transition behaviors of the network scaling dependency. This characterization framework interprets the

weighted complex network by the construction of a scaling feature space spanned by the localized scaling feature vectors determined both by the surrounding environment of individual nodes and the underlying metric space defined on the network. The proposed characterization is general and not limited to complex networks that are fractal or multi-fractal. It can be easily interfaced with subsequent analytical tools to unveil the intrinsic properties of the weighted complex network. As an important application, we showed the proposed characterization framework can be employed to learn the network communities that are consistent with our biological knowledge of the human brain connectivity patterns.

A very important aspect to emphasize is that the proposed characterization framework actually gives a general similarity metric within and between networks, which can be potentially leveraged as a basis for both structural and dynamic analysis on networks in a wide spectrum of applications. For instance, it can be interfaced with brain connectivity network constructed from real-time EEG measurements to identify tasks that correspond to different sets of scaling feature vectors, or to make both diagnosis and predictive analysis on brain-related pathological anomalies (e.g., traumatic damage, epilepsy) by learning corresponding scaling feature subspace. The proposed characterization framework can also be employed as self-similarity metric that enables the detection of anomalies or attack by comparing the learned scaling feature space to that during its normal operation mode in real time. In such cases, the benefit of the proposed characterization framework comes from its capability to quantify the variation of interaction intensities (e.g., change of transmitted power between grid node or maliciously injected traffic to overload the server) while no significant network structure mutation is present. On a different direction, this proposed framework also enables the fine-grain similarity analysis among a set of nodes in the same network. Aside from the presented network community detection based on this fine-grain similarity analysis, it is also useful to combine with domain knowledge (labels and attributes of nodes, e.g., functionality of brain region) to drive an informed exploration (e.g., any functional similarity between brain regions that are topologically apart but share the same scaling law). These examples may only constitute a small portion of its potential applications which necessitate our ongoing research efforts to extend the presented work to broader domains.

# METHODS

## Multi-fractal Analysis

Formally, let us consider a geometrical object tiled by boxes $B(l)$ of size $l$. Let us define $L$, $M_0$ and $M_i(l)$ as the linear length of the fractal, the total mass and the mass of the $i$-th box of size $l$, respectively. It is possible to determine $N(M)$ that corresponds to the number of boxes sharing the same mass $M$ given the object tiled by $B(l)$. The probability density function of mass thus could be estimated by histograms in a double logarithmic plot $ln(N(M))$ against $ln(M/M_0)$ under different choice of box sizes $l$. The multi-fractal formalism33 states that if these histograms fall onto the same universal curve after rescaling both coordinates by a factor $ln(l/L)$, the object is a geometrical multi-fractal34. Alternatively stated, the above property holds if

$$M \sim M_0(l/L)^{\alpha} \tag{4}$$

and

$$N(\alpha) \sim (l/L)^{-f(\alpha)} \tag{5}$$

as the $(l/L) \to 0$, where $\alpha$ is the Holder exponent which can be determined by,

$$\alpha = \frac{ln(\mu(B))}{ln(l/L)} = \frac{ln(M/M_0)}{ln(l/L)} \tag{6}$$

$\mu(B)$ is an arbitrary measure defined on the support while it is equal to the probability to find a point in a given box. $N(\alpha)$ is the number of boxes with holder exponent $\alpha$. $f(\alpha)$ is the *singularity* or *multi-fractal spectrum* if multi-fractal formalism holds35, 36. The multi-fractal spectrum shows the distribution of fractal dimensions across different sets of points sharing the same Holder exponent. Roughly speaking, it captures the variations in scaling behaviors of different subcomponents of the object. Equivalently, this variation could be captured by *generalized dimension* $D(q)$,

$$\sum_i M_i(l)^q \sim M_0^q \left(\frac{l}{L}\right)^{\tau(q)} \tag{7}$$

$$\tau(q) = (q-1)D(q) \tag{8}$$

as we take the limit $l/L \to 0$. $\tau(q)$ is called as mass exponent. Distorting exponent $q$ can be arbitrarily real-valued which serves to distinguish the irregularity in various regions of the object by magnification of measures

scaled differently. The equivalence between the pair of ($f(\alpha)$,$\alpha$) and ($\tau(q)$, $q$) is decided by the Legendre transformation,

$$\alpha = \frac{d\tau(q)}{dq} \tag{9}$$

$$f(\alpha) = q\frac{d\tau(q)}{dq} - \tau(q) \tag{10}$$

For a fractal object that can be characterized by a single fractal dimension, Eq. (7) suggests a sufficiently minimal fluctuation in measure $\mu(B_i(l))$ across all boxes of different sizes $l$. This directly translates to a narrowly distributed Holder exponent $\alpha$ and a *linear* dependence between mass exponent $\tau(q)$ and distorting exponent $q$. In contrast, a multi-fractal is rich in fluctuations of measure $\mu$ and have a spectrum $f(\alpha)$ widely spanned over $\alpha$ horizon and a *non-linear* $\tau(q)$ as a function of $q$. These fluctuations are to be captured and magnified via different choices of distorting factor $q$. To give some intuition, when $\mu$ is a probability measure as in box covering process, bigger weights in the summation of Eq. (7) will be placed to smaller probabilities if q is negative and to greater probabilities otherwise. The generalized fractal analysis approach is also well known as *multi-fractal analysis (MFA)* that has wide applications due to its power to capture the heterogeneity underlying the structures of the objects.

## FBCw and FSBw

Box-covering and sandbox methods form the basis for MFA on weighed complex network with the following definitions.

*Box covering* method tiles the object of interest with boxes $B(l)$ of different sizes $l$. An arbitrary measure $\mu(B_i(l))$ is defined for each box $B_i$ that serves as support. Eq. (7) considers the case when $\mu$ is a probability measure such that,

$$\sum_i \mu(B_i(l))^q \sim \left(\frac{l}{L}\right)^{\tau(q)} \tag{11}$$

$$\mu(B_i(l))^q = \left(\frac{M_i(l)}{M_0}\right)^q \tag{12}$$

when the limit $l \to 0$ is considered. Therefore, the generalized fractal dimension calculated by box-covering method is given by,

$$D_{bc}(q) = lim_{l\to 0}\frac{ln(\sum_i (M_i(l)/M_0)^q)}{ln(l/L)}\frac{1}{q-1} \quad (13)$$

Eq. (13) determines $D_{bc}(q)$ asymptotically from the scaling of number of non-empty boxes of decreasing size $l$.

*Sandbox* method investigates the scaling of an arbitrary measure $\mu$ within a region embedded in a metric space, i.e., a sandbox centered at certain point, as a function of its radius $l$. Formally, let $\mathscr{X}$ be the support of the measure $\mu$. Let $\mathscr{D}: \mathscr{X} \times \mathscr{X} \to \mathscr{R}$ be a metric space defined on $\mathscr{X}$. For each $x_i \in \mathscr{X}$, we can define the following probability measure $M_i(l)/M_0$ as the chance to find an element $x_k \in \mathscr{X}$ with its distance to $x_i$ in metric space $\mathscr{D}$ less than $l$,

$$\mu_i(l) = \frac{M_i(l)}{M_0} = \frac{1}{M_0}\sum_{k\neq i}^{M_0}\mathscr{H}(l - \mathscr{D}(x_i, x_k)) \quad (14)$$

Where $M_o = |\mathscr{X}|$ and $\mathscr{H}$ is the heaviside function. However, it is known that the relation $\mu_i(l) \sim (l/L)^D$, where $D$ is the fractal dimension of the object, does not hold for all choices of sandbox centers as $l \to \infty$ unless the center is the *origin* of the fractal34. Actually, sandbox method is equivalent to box covering method only if the choice of sandbox is *randomized*. We can rewrite Eq. (11) as,

$$\left(\frac{M_i(l)}{M_0}\right)^{q-1}\frac{M_i(l)}{M_0} \sim \left(\frac{l}{L}\right)^{\tau(q)} \quad (15)$$

Equivalently,

$$E\left[\left(\frac{M_i(l)}{M_0}\right)^{q-1}\right] \sim \left(\frac{l}{L}\right)^{\tau(q)} \quad (16)$$

Therefore, the box-covering method can be understood as a sandbox method when the average is taken based on the measure distribution $M_i(l)/M_0$. Alternatively stated, the sandbox is equivalent to box counting only if choice of sandbox is randomized such that an estimate of $E[(M_i(l)/M_0)^{q-1}]$ can be obtained. Denote $\langle . \rangle$ as the operation to take average. We have,

$$D_{sb}(q) = lim_{l\to 0}\frac{ln(\langle (M_i(l)/M_0)^{q-1}\rangle)}{ln(l/L)}\frac{1}{q-1} \quad (17)$$

We propose the finite box-covering method (FBCw) and the finite sandbox covering method for weighted networks (FSBw) to address the intrinsic estimation bias introduced by the incompatible growth rule of the box in numerical determination of multi-fractality of complex network with finite resolution. Formally, a complex network with a finite resolution is defined as follows,

***Definition 6 (finite resolution)****: For a given weighted complex network* $G=(V, E)$ *with distance metric* $d_{i,j} = \min\{w^p_{i,k_1} + w^p_{k_1,k_2} + \cdots + w^p_{k_n,j}\}$. *The resolution of* $G$ *is finite if and only if the shortest path distribution* $F_{d_{i,j}}(l) = P\{d_{i,j} \leq l\}$ *has a discrete support set* $\mathscr{L}(G) = \{l_k | F_{d_{i,j}}(l_k) \neq F_{d_{i,j}}(l_{k'}), \forall k \neq k'\}$.

The fundamental principle of FBCw and FSBw is to locate the scales of box that correspond to the compatible growth rule which is a function of the complex network $G$. For each node $v_i$, the local compatible growth rule on $G$ can be easily found by a strictly ordered set $L_{<,v_i} = \{l_1, l_2, \cdots, l_n, \}$ where $l_{k+1} > l_k$ and $L_{<,v_i} \subseteq \mathscr{L}(G)$. However, it is usually difficult to find a shared compatible growth rule across the network for the sandbox method or to analytically derive the optimal box-covering strategy as we did for the Sierpinski fractal network governed by a simple generation rule. In this context, we propose a data driven filtering method to interface with the box-covering and sandbox method for FBCw and FSBw. Both algorithms stand as a two-step process. In the first step, the accumulative measure $\sum \mu(B_i(l))^q$ given the distorting factor $q$ will be first obtained by growing the scale of the box $l$ based on the unique path length of the network. Based on our discussion, this growth rule is generally incompatible. In the second step, we address this problem by a data-driven filtering procedure to obtain a subset $L_<$ of the discrete support $\mathscr{L}(G)$ of $F_{d_{i,j}(l)}$ such that it is compatible with $G$. More precisely, FBCw and FSBw can be stated as follows:

### *Step 1- Collecting the accumulative measure* $\sum \mu(B_i(l))^q$ *:*

- Given the distance metric $d_{ij}$ on $G$, calculate all pairs of distances and encapsulate them into a matrix $D$ either by the Floyd Warshall algorithm ($O(|V|^3)$) or the Dijkstra algorithm ($O(|V|(|E|+V log|V|))$). Practically, if the graph is sparse in the sense that $|E| \ll |V|^2$, it is recommended to use Dijkstra algorithm which outperforms Floy-Warshall algorithm by a significant margin.

- Given the distance matrix $D$, derive the strictly ordered unique distance sequence $D_< = \{d_1, d_2, d_3, \ldots, d_N\}$ where $d_i = d_j$ if and only if $i=j$. $d_N$ is the diameter of the network. $D_<$ serves as the tentative growth rule which, as discussed, is usually an incompatible growth rule that gives rise to the staircase effect whereas it can be alleviated by the subsequent filtering step. It should be also noted that the cardinality of $D_<$ can be a computationally prohibitive in some cases when the number of unique path length is very large (e.g., $|D_<|$ of the collaboration network is close to $10^6$). In such cases, a resampling function $\mathscr{S}: D_< \rightarrow D'_<$ where $D'_< \subseteq D_<$ will be useful to bring down the computational overhead to an acceptable level. The proper choice of the resampling function is not constrained and may be subject to change based on the target network. In most of cases, a linear resampling function should be satisfactory.
- Iterate on $D_<$ in an ascending order to perform the box-covering or sandbox covering procedure to obtain the accumulative measure $M(d_k)=\sum\mu(B_i(d_k))^q$ at the scale $d_k \in D_<$. No constraint is advised for the choice of a specific heuristic for this procedure. Practically, in the case that repeating the randomized box covering procedure for a large number of trials (to find the minimal number of boxes) is computationally impractical, Welsh–Powell algorithm usually gives satisfactory approximation after transforming the original network into its dual graph following the technique in ref. 28. Repeat the above procedure to obtain the accumulative measure sequence $M=\{M(d_1), M(d_2), \ldots, M(d_N)\}$.

***Step 2- Data-driven filtering for critical scales:*** As a consequence of growing the scale of box based on an incompatible growth rule $D_<$ for complex network $G$ of finite resolution, there exists $d_i$ and $d_{i'}$ such that $M(d_i)=M(d_{i'})$ (i.e., the staircase effect). In practice, this condition can usually be relaxed to $|M(d_i)-M(d_i')|\leq\varepsilon$ where $\varepsilon$ is a tuning threshold and conditioned on the property of the network. Therefore, for every $d_i \in D_<$, the major task of step 2 is to filter out all the $d_{i'}$ where $|M(d_i)-M(d_i')|\leq\varepsilon$ holds. Theoretically, it is possible to find a proper choice of $\varepsilon$ such that the filtering can be done by enumeratively checking the condition for all choices of $d_i$. However, picking the proper $\varepsilon$ can be tedious manual process. In this context, we propose a simple yet effective variance based sliding window filter to identify the critical $d_i$ that corresponds to a remarkable change in $M(d_i)$. Formally, the sliding window filter $\mathscr{F}(\mathbf{x}, t)$

$$\mathscr{F}(\mathbf{x}, t) = \sum((\bar{x} - x_i)^2) \tag{18}$$

where $x=[x_1, x_2, \ldots, x_W]^{\mathrm{T}}$ is a $W$-dimensional vector of observations starting at $t$. $W$ is the width of the sliding window. Then the data-driven filtering procedure can be stated as follows:

- Pick $d_i$ from $D_<$ in an ascending order and calculate $\sigma_i = \mathscr{F}(M, d_i)$. Repeat it for all choices of $d_i$ to obtain $\sigma=\{\sigma_1, \sigma_2, \ldots, \sigma_{M-W+1}\}$.
- Iterate on $\sigma$ to find the index $i$ of the peaks in $\sigma$ that correspond to the critical scale $d_i$.
- Perform the regression to Eqs (13) and (17) using the identified critical scales.

To better illustrate the efficacy of proposed data-driven filtering method, we plot in Fig. 19 the raw $M$ against the scale index obtained in Step 1 by Welsh–Powell algorithm based box-covering strategy to Sierpinski fractal network $G_4$ with $s=1/2$ and $b=3$. The peaks of $\sigma$ exactly correspond to the critical scales $d_i$ where a significant change of $M(d_i)$ appears. These scales are identified and used for numerical determination of the scaling behavior instead of all the scales to avoid stagnant observations.

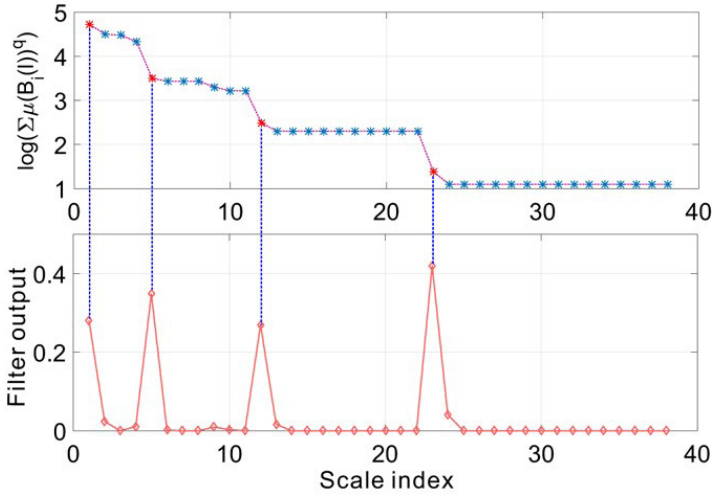


**Figure 19**: An example application of the proposed data-driven filtering method. By applying the filter sliding through the observations, the peaks of the output correspond to the critical scales where a significant change of the accumulative measure $\sum\mu(B_i(l))^q$ occurs.

Data accessibility: The datasets generated during and/or analyzed during the current study are available from the corresponding author on reasonable request.

## ACKNOWLEDGEMENTS

The authors acknowledge the support from US National Science Foundation (NSF) under CAREER Award CPS-1453860 grant, the US Army Defense Advanced Research Projects Agency (DARPA) and DARPA Young Faculty Award under grant numbers W911NF-17-1-0076 and N66001-17-1-4044.

## REFERENCES


1. Dobson, C. M. Protein folding and misfolding. *Nature* 426, 884–890 (2003).
2. Engen, J. R. Analysis of protein conformation and dynamics by hydrogen/deuterium exchange ms (2009).
3. Selkoe, D. J. Cell biology of protein misfolding: the examples of alzheimer's and parkinson's diseases. *Nature cell biology* 6, 1054–1061 (2004).
4. Landles, C. & Bates, G. P. Huntingtin and the molecular pathogenesis of huntington's disease. *EMBO reports* 5, 958–963 (2004).
5. Barabási, A.-L. & Albert, R. Emergence of scaling in random networks. *science* 286, 509–512 (1999).
6. Song, C., Havlin, S. &Makse, H. A. Origins of fractality in the growth of complex networks. *Nature Physics* 2, 275–281 (2006).
7. Song, C., Havlin, S. &Makse, H. A. Self-similarity of complex networks. *Nature* 433, 392–395 (2005).
8. Rozenfeld, H. D. &Makse, H. A. Fractality and the percolation transition in complex networks. *Chemical Engineering Science* 64, 4572–4575 (2009).
9. Rozenfeld, H. D., Song, C. &Makse, H. A. Small-world to fractal transition in complex networks: a renormalization group approach. *Physical review letters* 104, 025701 (2010).
10. Muzy, J.-F., Bacry, E. &Arneodo, A. Wavelets and multifractal formalism for singular signals: Application to turbulence data. *Physical review letters* 67, 3515 (1991).
11. Ivanov, P. C. *et al*. Multifractality in human heartbeat dynamics. *Nature* 399, 461–465 (1999).
12. Ivanov, P. C. *et al*. From 1/f noise to multifractal cascades in heartbeat dynamics. *Chaos: An Interdisciplinary Journal of Nonlinear Science* 11, 641–652 (2001).
13. Zhou, W.-X. *et al*. Multifractal detrended cross-correlation analysis for two nonstationary signals. *Physical Review E* 77, 066211 (2008).
14. Martinez, P., Schertzer, D. & Pham, K. Texture modelisation by multifractal processes for sar image segmentation (1997).
15. Kenkel, N. & Walker, D. Fractals in the biological sciences. *Coenoses* 77–100 (1996).

16. Wendt, H., Roux, S. G., Jaffard, S. &Abry, P. Wavelet leaders and bootstrap for multifractal analysis of images. *Signal Processing* 89, 1100–1114 (2009).
17. Yu, Z.-G., Anh, V. & Lau, K.-S. Measure representation and multifractal analysis of complete genomes. *Physical Review E* 64, 031903 (2001).
18. Moreno, P. A. *et al*. The human genome: a multifractal analysis. *BMC genomics* 12, 506 (2011).
19. Tessier, Y., Lovejoy, S., Hubert, P., Schertzer, D. &Pecknold, S. Multifractal analysis and modeling of rainfall and river flows and scaling, causal transfer functions. *Journal of Geophysical Research: Atmospheres* 101, 26427–26440 (1996).
20. Lovejoy, S. &Schertzer, D. Scale, scaling and multifractals in geophysics: twenty years on. In *Nonlinear dynamics in geosciences* 311–337 (Springer, 2007).
21. Meneveau, C. &Sreenivasan, K. Simple multifractal cascade model for fully developed turbulence. *Physical review letters* 59, 1424 (1987).
22. Benzi, R., Paladin, G., Parisi, G. &Vulpiani, A. On the multifractal nature of fully developed turbulence and chaotic systems. *Journal of Physics A: Mathematical and General* 17, 3521 (1984).
23. Feldmann, A., Gilbert, A. C. &Willinger, W. Data networks as cascades: Investigating the multifractal nature of internet wan traffic. In *ACM SIGCOMM Computer Communication Review*, vol. 28, 42–55 (ACM, 1998).
24. Schmitt, F., Schertzer, D. & Lovejoy, S. Multifractal analysis of foreign exchange data. *Applied stochastic models and data analysis* 15, 29–53 (1999).
25. Kantelhardt, J. W. *et al*. Multifractal detrended fluctuation analysis of nonstationary time series. *Physica A: Statistical Mechanics and its Applications* 316, 87–114 (2002).
26. Matia, K., Ashkenazy, Y. & Stanley, H. E. Multifractal properties of price fluctuations of stocks and commodities. *EPL (Europhysics Letters)* 61, 422 (2003).
27. Calvet, L. & Fisher, A. Forecasting multifractal volatility. *Journal of econometrics* 105, 27–58 (2001).
28. Song, C., Gallos, L. K., Havlin, S. &Makse, H. A. How to calculate the fractal dimension of a complex network: the box

covering algorithm. *Journal of Statistical Mechanics: Theory and Experiment* 2007, P03006 (2007).

29. Daqing, L., Kosmidis, K., Bunde, A. &Havlin, S. Dimension of spatially embedded networks. *Nature Physics* 7, 481–484 (2011).
30. Emmerich, T., Bunde, A., Havlin, S., Li, G. & Li, D. Complex networks embedded in space: Dimension and scaling relations between mass, topological distance, and euclidean distance. *Physical Review E* 87, 032802 (2013).
31. Wei, D.-J. *et al*. Box-covering algorithm for fractal dimension of weighted networks. *Scientific reports* 3, 3049 (2013).
32. Song, Y.-Q., Liu, J.-L., Yu, Z.-G. & Li, B.-G. Multifractal analysis of weighted networks by a modified sandbox algorithm. *Scientific reports* 5 (2015).
33. Olsen, L. A multifractal formalism. *Advances in mathematics* 116, 82–196 (1995).
34. Tél, T., Fülöp, Á. &Vicsek, T. Determination of fractal dimensions for geometrical multifractals. *Physica A: Statistical Mechanics and its Applications* 159, 155–166 (1989).
35. Mandelbrot, B., Calvet, L. & Fisher, A. Large deviations and the distribution of price changes. *Technical Report* 1165 (1997).
36. Christophe, C., Véhel, J. L. & Tricot, C. Continuous large deviation multifractal spectrum: definition and estimation. In *Fractals 98* (World Scientific, 1998).

# INDEX

**F**



**G**



**H**

**T**



**U**



**V**



**W**

# Fractal Analysis

Fractals are self-similar, self-repeating and scale-invariant structures which were first introduced by Mandelbrot to model the "roughness" in patterns observed in nature, a roughness that could not be described in terms of over-idealized Euclidean geometry. Fractals are not only used to model complex spatial shapes but also time patterns. This book is composed by an introductory chapter and 16 open-access articles describing various aspects of fractal analysis. It overviews concepts such as fractal dimension, fractal time series, symmetrical and asymmetrical bifurcating fractal networks. The book is divided into the following topics:

- Fractal dimension, self-similarity and self-affinity: The first chapter aims to introduce the reader to fundamental concepts in fractal analysis such as self-similarity, self-affinity, Hausdorff dimension and Hurst exponent. The second chapter introduces a unified definition of fractal dimension for self-similar and self-affine fractals.
- Fractal Antennas: The third chapter reviews the concepts of fractal dimension and its relationship with Rényi entropy, as well as describes the fractal structure behind Sierpinski Gasket and Hilbert antennas.
- Measuring the Fractal nature of observed patterns: The Chapter 5 and 6 include a practical application of the box-counting method in determining the fractal nature of rings of Saturn and the occurrence of specific words in text.
- Fractal analysis applications to digital imaging: Chapters 6 and 7 describe two examples of fractal analysis applications to digital imaging. Chapter 6 introduces the reader to used of Higuchi method for determining the fractal properties of objects represented by digital images. Chapter 7 evaluates colour fractal dimension and lacunarity as video quality metrics.
- Fractal time series analysis: Chapters 8, 9, and 10 overview the different fractal time-series analysis methods. Chapter 8 summarizes the evolution of different methods from Mandelbrot's similarity dimension to variational box-counting methods. Chapter 9 offers a tutorial to adaptive fractal analysis. Chapter 10 reviews the current mono- and multi-fractal, as well as time- and frequency-domain time series analysis.
- Examples of fractal time series applications: Chapters 11, 12, and 13 describe three cases of fractal time series applications: the characterization of remotely sensed forested landscapes, the generation of natural-looking radar echoes on coastlines, and the study of multi-fractal behaviour of corroded steel surfaces.
- L-systems as fractal models of fracture networks: Chapters 14 and 15 introduce the readers to Lindenmayer systems (L-systems) which can be utilized to model the fractal geometry of rock and hydraulic fractures.
- Multi-fractal analysis and its applications to weighted complex networks: Chapters 16 and 17 describe multi-fractal applications to weighted complex networks and overviews several algorithms such as the box-counting, edge-covering box counting, rank-driven, ball-covering, compact-box-burning, fixed-size box-counting and sandbox algorithm.

Olga Moreira is a Ph.D. in Astrophysics and B.Sc. in Physics and Applied Mathematics. She is an experienced technical writer and researcher which former fellowships include postgraduate positions at two of the most renown European institutions in the fields of Astrophysics and Space Science (the European Southern Observatory, and the European Space Agency). Presently, she is an independent scientist working on projects involving machine learning and neural networks research as well as peer-reviewing and edition of academic books.

ISBN 978-1-77407-900-3

ARCLER PRESS